### Malaysian Journal of Analytical Sciences Vol 26 No 3 2022

Articles 9-20 are selected papers from the "Symposium on Fuel Cell and Hydrogen Technology (SFCHT2021), 26-27 October 2021; organized by the Fuel Cell Institute (SELFUEL), Universiti Kebangsaan Malaysia & The Malaysian Association of Hydrogen Energy (MAHE)."

Guest Editor: Mahendra Rao Somalu

		Page
1.	PHYTOCHEMICALS AND ANTIOXIDANT ACTIVITY OF ULTRASOUND-ASSISTED AVOCADO SEED EXTRACT (Fitokimia dan Aktiviti Antioksidan Ekstrak Biji Avokado Berbantukan Ultrabunyi) Chin Xuan Tan, Renee Chin, Seok Tyug Tan, Seok Shin Tan	439
2.	A COMPARISON OF CHEMICAL COMPOSITIONS IN KELULUT HONEY FROM DIFFERENT REGIONS (Perbandingan Komposisi Kimia dalam Madu Kelulut dari Kawasan Berbeza) Hasnah Haron, Ruzita A Talib, Ponnusami Subramaniam, Zainorain Natasha Zainal Arifen, Muhammad Ibrahim	447
3.	QUANTITATIVE STRUCTURE-ACTIVITY RELATIONSHIP (QSAR) STUDY OF NEWLY SYNTHESIZED CARBONYL THIOUREA DERIVATIVES ON <i>Acanthamoeba</i> sp. (Kajian Kuantitatif Hubungan Struktur-Aktiviti (QSAR) Terhadap Terbitan Karbonil Tiourea Hasilan Sintesis Baru Terhadap <i>Acanthamoeba</i> sp.)  Maizatul Akma Ibrahim, Nor Hafizah Zakaria, Mohd Sukeri Mohd Yusof	457
4.	IMPROVING THE MORPHOLOGICAL, THERMAL, AND ACOUSTICS PROPERTIES OF POLYURETHANE-UREA BIOFOAM USING INDUSTRIAL PLYWOOD SAWDUST WASTE (Meningkatkan Morfologi, Termal dan Sifat Akustik Busa Poliuretan-Urea Menggunakan Sisa Habuk Papan Kayu Lapis)  Herlina Nofitasari, Ari Handono Ramelan, Mohammad Masykuri	478
5.	SYNTHESIS OF GREEN-RENEWABLE BIOLUBRICANT BASE STOCK FROM MALAYSIAN PALM OIL (Sintesis Stok Asas Biopelincir Hijau-Diperbaharui daripada Minyak Sawit Malaysia) Nurazira Mohd Nor and Jumat Salimon	492
6.	THE REMOVAL OF BISPHENOL-A FROM SYNTHETIC WASTEWATER USING THIN-FILM COMPOSITE MEMBRANE (Penyingkiran Bisfenol A daripada Sisa Air Sintetik Mengunakan Membran Lapisan Komposit Nipis) Taofiq Damilare Aiyelabegan , Siti Nur Alwani Shafie, Shafiq Mohd Hizam, Nik Abdul Hadi Nordin	507
7.	CONSTRUCTING Ni-DOPED ZnO/GO HETEROSTUCTURES FOR ENHANCED SUNLIGHT-TRIGGERED DEGRADATION OF METHYLENE BLUE DYE (Pembinaan Heterostruktur Ni-Didop dengan ZnO/GO untuk Meningkatkan Degradasi Pewarna Metilina Biru di Bawah Sinar Matahari) Hartini Ahmad Rafaie, Nur Shafiza Ismail, Syazni Hanun Nur Ili Dedy Dasiano, Muhd Firdaus Kasim, Nurul Infaza Talalah Ramli, Zul Adlan Mohd Hir, Mohomad Hafiz Mamat	520
8.	BIOSORPTION CAPACITY OF HEAVY METAL LEAD (Pb(II)) USING DRY SEAWEED Eucheuma denticulatum (Kapasiti Biojerapan Logam Berat Plumbum (Pb(II)) Mengunakan Rumpai Laut Kering Eucheuma denticulatum)	532

	Hamad Maalim Sharif, Yahya Makame, Mohammed Ali Sheikh, Hasrizal Shaari, Rokiah Suriadi	
9.	SYNTHESIS OF ZnO ON 3D GRAPHENE/NICKEL FOAM FOR PHOTOELECTROCHEMICAL WATER SPLITTING (Sintesis ZnO pada 3D Grafin/Busa Nikel untuk Pembelahan Molekul Air Secara Fotoelektrokimia)  Nur Rabiatul Adawiyah Mohd Shah, Rozan Mohamad Yunus, Nurul Nabila Rosman, Wai Yin Wong, Khuzaimah Arifin, Lorna Jeffery Minggu	546
10.	THE EFFECT OF MEMBRANE THICKNESS ON THE PERFORMANCE OF PASSIVE DIRECT ETHANOL FUEL CELLS USING A POLY VINYL ALCOHOL/GRAPHENE OXIDE COMPOSITE MEMBRANE (Kesan Ketebalan Membran Terhadap Prestasi Sel Fuel Etanol Langsung Pasif Menggunakan Membran Komposit Alkohol Polivinil/Grafin Oksida) Zulfirdaus Zakaria	554
11.	EFFECT OF pH IN THE SYNTHESIS OF GOLD-COPPER NANOPARTICLES SUPPORTED ON ANODIC ALUMINIUM OXIDE AS CATALYST FOR THE REDUCTION OF <i>p</i> -NITROPHENOL (Kesan pH dalam Sintesis Emas-Kuprum (Au-Cu) Partikel Nano Disokong pada Anodik Aluminium Oksida Sebagai Mangkin bagi Penurunan <i>p</i> -Nitrofenol) Norizwan Nordin, Hanani Yazid, Nor Azira Irma Muhammad, Abdul Mutalib Md Jani	562
12.	POTENTIAL OF TEXTILE WASTE AS NITROGEN DOPED POROUS CARBON FOR OXYGEN REDUCTION REACTION (Potensi Sisa Tekstil Sebagai Karbon Poros Terdop Nitrogen Berliang untuk Tindak Balas Penurunan Oksigen) Suhaila Mohd Sauid, Siti Kartom Kamarudin, Loh Kee Shyuan	571
13.	PHOTOCATALYTIC HYDROGEN GENERATION FROM WATER BY TiO <sub>2</sub> /Co <sub>3</sub> O <sub>4</sub> COMPOSITE PHOTOCATALYSIS (Penjanaan Hidrogen Fotokatalitik dari Molekul Air Mengunakan Komposi Fotomangkin TiO <sub>2</sub> /Co <sub>3</sub> O <sub>4</sub> ) Siti Nurul Falaein Moridon, Dian Anggraini, Khuzaimah Arifin, Lorna Jeffery Minggu, Mohammad B. Kassim	581
14.	THE THERMAL STABILITY AND PRELIMINARY PERFORMANCE OF SODIUM ALGINATE AND POLYVINYL ALCOHOL-BASED MEMBRANE IN DMFC: MONTMORILLONITE AS A FILLER (Kestabilan Haba dan Prestasi Awal Membran Berasaskan Natrium Alginat dan Polivinil Alkohol untuk DMFC: Montmorillonit sebagai Pengisi) Maryam Taufiq Musa and Norazuwana Shaari	589
15.	FORMULATION AND CHARACTERISATION OF LSCF/YSZ-SDC AND LSCF/YSZ-SDCC DUAL COMPOSITE CATHODES FOR INTERMEDIATE-TEMPERATURE SOLID OXIDE FUEL CELL (Formulasi dan Ciri Dwi-Komposit Katod LSCF/YSZ-SDC dan LSCF/YSZ-SDC Karbonat untuk Sel Bahan Api Oksida Pepejal Bersuhu Pertengahan) Nurul Farhana Abdul Rahman, Umira Asyikin Yusop, Yohannes Nyambong Lowrance, Hamimah Abd. Rahman, Mohd Azham Azmi, Shahruddin Mahzan, Azzura Ismail	600
16.	Ptru Supported on Porous 3d titanium dioxide-graphene Aerogel as a Potential electrocatalyst for direct methanol fuel cells (Ptru disokong pada 3d titanium dioksida-Grafin Aerogel Berliang Sebagai Potensi Elektromangkin untuk sel Bahan Bakar Metanol Langsung) Siti Hasanah Osman, Siti Kartom Kamarudin, Sahriah Basri, Nabila A. Karim	613
17.	A REVIEW ON PREPARATION, MODIFICATION AND FUNDAMENTAL PROPERTIES OF SPEEK NANOCOMPOSITE PEM FOR DIRECT METHANOL FUEL CELL APPLICATIONS (Satu Ulasan tentang Penyediaan, Pengubahsuaian dan Ciri Asas Komposit Nano Membran Elektrolit Polimer SPEEK untuk Aplikasi Sel Bahan Api)  Nor Fatina Raduwan and Norazuwana Shaari	622

18.	PHYSICAL AND ELECTROCHEMICAL CHARACTERISTICS OF LiCo <sub>0.6</sub> Sr <sub>0.402</sub> CATHODE INK FOR INTERMEDIATE-LOW TEMPERATURE SOLID OXIDE FUEL CELL (Pencirian Fizikal dan Elektrokimia Terhadap Dakwat Katod LiCo <sub>0.6</sub> Sr <sub>0.402</sub> bagi Sel Bahan Api Oksida Pepejal Bersuhu Sederhana Rendah)  Nur Nadhihah Mohd Tahir, Nurul Akidah Baharuddin, Wan Nor Anasuhah Wan Yusoff, Azreen Junaida Abd Aziz, Mahendra Rao Somalu, Andanastuti Muchtar	640
19.	TITLECHEMICAL OXYGEN DEMAND AND TURBIDITY REMOVAL OF LANDFILL LEACHATE USING ELECTROCOAGULATION TECHNIQUE WITH AI ELECTRODE (Penyingkiran Permintaan Oksigen Kimia dan Kekeruhan daripada Larut Resap Tapak Pelupusan dengan Menggunakan Elektrod AI) Norilhamiah Yahya, M. Firdaus Mamat, Suhaini Mamat, Nabila A. Karim	652
20.	ENHANCING THE OXYGEN REDUCTION REACTION OF LOW-PLATINUM AND NON-PLATINUM CATALYSTS FOR FUEL CELL APPLICATIONS (Peningkatan Tindak Balas Penurunan Oksigen Mangkin Platinum Bermuatan Rendah dan Bebas Platinum Untuk Aplikasi Sel Bahan Api)  Kazi Rumanna Rahman, Kuan Ying Kok, Nor Azillah Fatimah Othman, Wai Yin Wong, Kean Long Lim	664

# Malaysian Journal of Analytical Sciences (MJAS)



Published by Malaysian Analytical Sciences Society

### PHYTOCHEMICALS AND ANTIOXIDANT ACTIVITY OF ULTRASOUND-ASSISTED AVOCADO SEED EXTRACT

(Fitokimia dan Aktiviti Antioksidan Ekstrak Biji Avokado Berbantukan Ultrabunyi)

Chin Xuan Tan<sup>1\*</sup>, Renee Chin<sup>1</sup>, Seok Tyug Tan<sup>2</sup>, Seok Shin Tan<sup>3</sup>

<sup>1</sup>Department of Allied Health Sciences, Faculty of Science,
Universiti Tunku Abdul Rahman, Jalan Universiti Bandar Barat 31900, Kampar Perak, Malaysia

<sup>2</sup>Department of Healthcare Professional, Faculty of Health and Life Sciences,
Management and Science University, University Drive, Off Persiaran Olahraga, Seksyen 13, 40100 Shah Alam,
Selangor, Malaysia

<sup>3</sup>Jeffrey Cheah School of Medicine and Health Sciences,
Monash University Malaysia, Bandar Sunway, Selangor, Malaysia

\*Corresponding author: tancx@utar.edu.my

Received: 13 February 2022; Accepted: 14 March 2022; Published: 27 June 2022

#### **Abstract**

Avocado seed is the residue from direct food consumption and fruit processing industry, which is rich in phytochemicals. Ultrasound-assisted extraction (UAE) has been proposed as a cost-effective technique to recover the phytochemicals from plant fractions. Sonication time is one of the parameters that may influence the quantity and quality of phytochemicals isolated from the plant fractions when using UAE. Hence, this study aimed to investigate the effect of different sonication times (0, 20, 40 and 60 min) used in the UAE on the phytochemicals and antioxidant capacity of methanolic avocado seed extract. Results indicated the total phenolic, flavonoid and anthocyanin content of the seed extracts were in the range of 31.90-41.62 mg GAE/100 g, 8.25-12.51 mg RE/100 g, and 8.02-24.57 mg CGE/100 g, respectively. UAE for 60 mins generated the significant highest (p<0.05) amount of phenolic, flavonoid and anthocyanin content. Based on the antioxidant capacity tests, UAE for 60 mins resulted in the highest antioxidant activity.

Keywords: avocado seed, sonication time, phytochemicals, ultrasound-assisted extraction

#### Abstrak

Biji alpukat merupakan bahan sisa daripada penggunaan secara langsung dan/atau industri pemprosesan buah-buahan, yang kaya dengan fitokimia. Pengekstrakan berbantukan ultrabunyi (UAE) merupakan kos efektif teknologi untuk mengisolasi fitokimia daripada sumber tumbuh-tumbuhan. Dalam kaedah UAE, masa sonikasi adalah salah satu faktor yang mempengaruhi kuantiti dan kualiti fitokimia yang diisolasi daripada sumber tumbuh-tumbuhan. Kajian ini bertujuan untuk analisa kesan masa sonikasi yang berbeza (0, 20, 40 dan 60 minit) dalam UAE terhadap fitokimia dan kapasiti antioksidan ekstrak biji alpukat metanol. Hasil kajian menunjukkan jumlah kandungan fenolik, flavonoid dan antosianin dalam ekstrak biji alpukat adalah dalam lingkungan 31.90-41.62 mg GAE/100 g, 8.25-12.51 mg RE/100 g dan 8.02-24.57 mg CGE/100 g. Penggunaan masa sonikasi 60 minit dalam UAE dapat menghasilkan kandungan fenolik, flavonoid dan antosianin yang paling signifikan banyak (p < 0.05). Berdasarkan

### Tan et al: PHYTOCHEMICALS AND ANTIOXIDANT ACTIVITY OF ULTRASOUND-ASSISTED AVOCADO SEED EXTRACT

ujian kapasiti antioksidan, pengunaan masa sonikasi 60 minit dalam UAE dapat menghasilkan aktiviti antioksidan yang paling tinggi.

Kata kunci: biji alpukat, masa sonikasi, fitokimia, pengekstrakan berbantukan ultrabunyi

#### Introduction

Avocado, also known as *Persea americana* Mill. or alligator pear, is a tropical and subtropical fruit that has been gaining increasing worldwide demand in recent years due to its relevant nutritional values and health benefits. There are over 100 varieties of avocado fruits have been recorded in the database of California Avocado Society [1]. Hass variety avocado is one of the most widely sought for commercialization [2]. A major portion of Hass avocado is constituted by the pulp (65%) whereas the seed (20%) and peel (15%) make up the rest [3].

Avocado fruits have been primarily used for human consumption, and to a lesser extent, as raw material in the pharmaceutical and cosmetic industries [4]. However, only the pulp of avocado is valued for commercial usance while other fruit fractions such as the seed and peel are considered obsolete and usually throw away as waste products. Hass avocado seed is ovoid shaped with a length of 5 to 6.4 cm. The ivorycolored avocado seed is covered with a thin, browncolored seed coat that adheres to the flesh cavity when ripe [5].

Proximate analysis done by Saavedra [6] revealed that the Hass avocado seed contained 52.7% of moisture, 2.51% of protein, 1.15% of ash, 1.11% of lipids, and 42.5% of nitrogen-free extract. The seed was also rich in phytochemicals such as phenolic acids, flavonoids and condensed tannins [7]. Based on current findings with regards to the biological effects of avocado seed are known to have various extracts, they ethnopharmacological properties for health-related conditions including anti-cancer, anti-inflammatory, anti-diabetic, anti-hypertensive, hypercholesterolemic, anti-microbial and the application in dermatological [8]. Hence, there has been a growing interest in the extraction of phytochemicals from avocado seeds to be utilized in the food and pharmaceutical industries.

Techniques such as maceration, infusion, heat extraction, enzyme-assisted extraction and Soxhlet extraction are commonly used to extract bioactive compounds from plants [9]. These techniques, however, have numerous limitations including the requirement of high extraction times, solvents and/or temperatures. Although advanced techniques like supercritical fluid extraction, microwave-assisted extraction and accelerated solvent extraction have demonstrated their efficiency in the recovery of phytochemicals, but these techniques are complex in operation and/or not cost-effective.

Ultrasound-assisted extraction (UAE) has been noted as one of the most effective techniques for the isolation of phytochemicals from plant materials [1, 9]. It utilizes acoustic waves to induce cavitation force to disrupt the plant cell wall, consequently enhancing the extraction rate of phytochemicals. Sonication time, solvent composition, sonication temperature, solid-solvent ratio and sonication frequency are the parameters that may influence the quantity and quality of phytochemicals isolated from the plant materials when using UAE [1, 9]. Among these parameters, sonication time was reported to have the greatest influence on the quality of plant extracts [10].

Industrial processing of avocado fruits produces a large number of seeds as wastes. Exploiting the phytochemicals of avocado seed waste may lead to new products and add value to the food industry. Therefore, this study aimed to investigate the effect of different sonication times on the UAE of phytochemicals and antioxidant activity of avocado seed extract.

#### **Materials and Methods**

#### Sample preparation

Hass variety avocado fruits were purchased from a local retailer in 2019. The fruits were kept at room temperature  $(25 \pm 5^{\circ}\text{C})$  until ripe. Ripe avocado fruit,

as indicated by changes in peel color (from green to purplish-black) and gentle pressure felt when held in the palm, were manually separated into seed, peel, and pulp. The outer coat layer of the seed was peeled off before being cut into slices with an average thickness of 5 mm [6], followed by drying in a lab-scale freeze dryer (Liobras L101, Brazil). The lyophilized seeds were milled into fine powder by using an electrical blender (Panasonic MX-799S, Malaysia) and sieved through a 250  $\mu$ m stainless steel sieve. The powdered sample was kept in an air-tight container at -5°C until use.

#### Chemicals and reagents

Analytical reagent grade of methanol, glacial acetic acid, hydrochloric acid (37%) was purchased from Fisher Scientific (Massachusetts, U.S.). Folin-Ciocalteu reagent, sodium carbonate, gallic acid, sodium nitrite, aluminium chloride hexahydrate, sodium hydroxide, rutin, 2,4,6-Tripyridyl-S-triazine (TPTZ), 2,2-diphenyl-1-picrylhydrazyl (DPPH), iron (III) chloride and iron (II) sulphate were purchased from Sigma–Aldrich (St. Louis, USA).

#### **Ultrasound-assisted extraction**

Approximately 1 g of avocado seed powder was mixed with 15 mL of 80% methanol in a 50 mL dark reagent bottle. The mixture was subjected to different sonication times (0, 20, 40 and 60 mins) in an ultrasonic bath [Elmasonic 100 H, Germany; 37 kHz ultrasonic frequency; 600 W ultrasonic output power; 11.8" x 9.4" x 5.9" (L x W x H) internal dimensions] operated at a constant temperature of 30°C. Extraction time and ultrasonic temperature were regulated from the panel of the instrument. A centrifuge set at 4,000 rpm for 10 mins at room temperature was used to separate the methanolic seed extract from the powdered sediment. The extract was then transferred into a dark bottle using a pipette and kept at 4°C until use.

#### **Phytochemicals**

#### Determination of total phenolic content

The TPC was determined by the Folin-Ciocalteu method described by Tan and Azrina [11]. Briefly, 600  $\mu$ L of methanolic seed extract was diluted with the same amount of distilled water in a test tube and

subsequently added with 300  $\mu L$  of 1 N Folin-Ciocalteu reagent and 600  $\mu L$  of 2.0% Sodium carbonate. The mixture was incubated in the dark for 30 min. The absorbance was measured at 750 nm using a spectrophotometer (DLAB Scientific SP V1000, China) against a blank. A standard curve was plotted by using different gallic acid concentrations (0.20, 0.70 and 0.90 mg/mL) for TPC calculation. The results were expressed as mg gallic acid equivalent (GAE) per 100 g of samples on the basis of fresh weight (mg GAE/100 g).

#### Determination of total flavonoid content

The TFC was determined by the aluminium chloride colorimetric method described by Sharma and Agarwal [12]. Exactly 100 µL of methanolic seed extract was pipetted into a test tube containing 4 mL of distilled water and 0.15 mL of 5% sodium nitrite solution. After 6 min of incubation at room temperature, 0.15 mL of 10% aluminium chloride solution, 2 mL of 4% sodium hydroxide solution and 0.2 mL of distilled water were added into the mixture and vortexed. The mixture was allowed to stand for 15 mins. The absorbance was recorded at 510 nm using a spectrophotometer (DLAB Scientific SP V1000, China) against a blank. A standard curve was plotted by using different rutin concentrations (7.0, 9.0, 11.0, 13.0 and 15.0 mg/mL) for TFC calculation. The results were expressed as mg rutin equivalent (RE) per 100 g of samples on the basis of fresh weight (mg RE/100 g).

#### Determination of total anthocyanin content

The TAC was determined according to the method of Granato et al. [13]. Exactly  $1000~\mu L$  of methanolic seed extract was pipetted into a 25 mL volumetric flask and diluted with distilled water to volume. The absorbance of the mixture was measured at 535 nm using a spectrophotometer (DLAB Scientific SP V1000, China) against a blank. The results were expressed as mg cyanidin-3-glucoside equivalent (CGE) per 100~g of samples on the basis of fresh weight (mg CGE/100~g).

#### Antioxidant activity

### Determination of ferric ion reducing antioxidant power

The FRAP was determined according to the method of Bagheri et al. [14]. Freshly prepared FRAP reagent was obtained by mixing 2.5 mL of 10 mM TPTZ in 40 mM hydrochloric acid, 2.5 mL of 20 mM ferric chloride solution and 24 mL of 300 mM acetate buffer (pH 3.6). Then, 40 μL of methanolic seed extract was pipetted into 1.2 mL of the FRAP reagent and incubated at 37°C for 10 mins. The absorbance of the mixture was measured at 593 nm using a spectrophotometer (DLAB Scientific SP V1000, China) against a blank. A standard curve was plotted by using different concentrations of iron (II) sulfate solution (0.01, 0.03 and 0.06 mg/mL) for FRAP calculation. The results were expressed as mmol Fe<sup>2+</sup> per kg of samples on the basis of fresh weight (mmol Fe<sup>2+</sup>/kg).

#### Determination of DPPH radical scavenging activity

The DPPH radical scavenging activity was determined according to the method of Ghafoor et al. [15]. Briefly, 0.25 mL of methanolic seed extract was mixed with 2 mL of 30 mg/L freshly prepared DPPH solution in methanol. The mixture was vigorously shaken and incubated at room temperature for 5 mins. A decline in absorbance was measured at 517 nm using a spectrophotometer (DLAB Scientific SP V1000, China) against a blank. Pure methanol was used as a negative control. The results were expressed as the percentage of antiradical activity (AA) of the extract on DPPH radicals relative to the control.

#### Statistical analysis

Statistical analyses were performed using IBM SPSS Statistic 26.0 for Windows (SPSS Inc., Chicago, USA). Data was summarized and expressed as mean  $\pm$  standard deviation. Mean value refers to three analytical replicates. Comparison of mean differences among different sonication times (0, 20, 40 and 60 mins) was conducted using a one-way analysis of variance accompanied by Tukey's post hoc analysis. The association between bioactive compounds and antioxidant capacity was evaluated using Pearson correlation test. Statistical significance was set at p <0.05.

#### **Results and Discussion**

#### Total phenolic, flavonoid and anthocyanin content

Various extraction media (methanol, ethanol, butanol, chloroform, ethyl acetate and water) have been utilized to extract the bioactive compounds from different fractions of fruits, either in pure form or in diluted form. In the present study, 80% methanol was selected as the media to prepare avocado seed extract. This is because 80% methanol has been deemed as a common medium to isolate the lipophilic and hydrophilic bioactive compounds of plant fractions [16].

The TPC, TFC and TAC of methanolic seed extracts sonicated at different times (0-60 mins) are shown in Table 1. Generally, increased sonication time enhanced the extraction of phenolics, flavonoids and anthocyanins from the avocado seed. This could be associated with the cavitation force produced by ultrasonic waves, which disrupt the integrity of plant cell walls and aid in the release of phytochemicals [9].

Phenolic compounds are secondary products produced by the metabolism of plants. They are widely recognized to have antioxidant characteristics, which could provide protection against oxidation induced by metal cations [7]. Avocado seed has been proposed as a potential food waste product for phenolic extraction [17]. It has been reported that the medicinal properties of avocado seed are attributed by its high phenolic compounds. As reported by Bahru et al. [18], the phenolic content of avocado seed (64%) was higher than its peel (23%) and pulp (13%). The TPC of methanolic seed extracts obtained from different sonication times was in the range of 31.90 to 41.62 mg GAE/100 g (Table 1). Application of UAE for 60 mins significantly increased (p < 0.05) the yield of phenolic content for 30%, as compared with the control without UAE at 0 min. Previously, the TPC of non-ultrasound assisted avocado seed extracts obtained from 70% methanol and 80% methanol were reported to be 2.92 mg GAE/100 g and 0.09-0.13 mg catechin equivalent (CE)/100 g, respectively [19, 20]. These values were much lower than the present study, possibly due to the different experimental protocols used in TPC analysis. As stated by Singh et al. [21], there are no standard method to determine phenolic compounds of plant seed extracts and the parameters used (e.g. solute to solvent ratio, particle size of the seed samples and agitation rate) in the preparation of seed extract could affect the yield of TPC.

Flavonoid compounds are secondary metabolites corresponding to phenolics and are one of the most studied bioactive compounds due to their diverse benefits in human health. The TFC is analyzed based on color change due to the reaction between aluminium chloride and flavonoid compounds in the methanolic seed extract. Previous study reported the TFC of water and ethanolic avocado seed extract were 3.72 and 4.96 mg RE/100 mL, respectively [22]. These values were comparable with the results of the present study. In Table 1, application of UAE for 60 mins significantly increased (p < 0.05) the yield of flavonoid content for 52%, as compared with the control without UAE at 0 min. A similar observation was reported by Ramić et al. [23], in which the TFC of ethanolic chokeberries extract was highest when sonicated for 60 min.

Anthocyanins are naturally occurring pigments that belong to the group of flavonoids. The flavylium cation

form of anthocyanins requires a sufficiently acidic medium to maintain its stability, but not to the extent that can cause acyl moieties in acylated anthocyanins to be hydrolyzed [24]. It is difficult to achieve optimal protocol of extraction due to the diversity of anthocyanins structure and their sensitivity to heat, metal complexes, pH, and co-pigmentation. Hence, this study utilizes a method that quantifies TAC without requiring the use of chemical standards to plot a calibration curve. In Table 1, the application of UAE for 60 mins significantly increased (p < 0.05) the yield of anthocyanin content for 102%, as compared with the control without UAE at 0 min. This may be due to the simultaneous enhancement of fragmentation and hydration from acoustic cavitation of UAE improves the mass transfer of anthocyanin compounds into the extraction solvent [9]. There has been limited data on the anthocyanin content of avocado seed extract documented thus far. Our current study demonstrated the effectiveness of UAE application in enhancing the yield of anthocyanin in avocado seed extract. Further study on quantifying the individual anthocyanin compound of avocado seed extract following UAE of 60 mins could be conducted.

Table 1. Phenolic, flavonoid and anthocyanin content of methanolic avocado seed extract

Sonication Time (mins)	TPC (mg GAE/100 g)	TFC (mg RE/100 g)	TAC (mg CGE/100 g)
0	$31.90\pm0.09^a$	$8.25\pm0.03^{\mathrm{a}}$	$8.02\pm0.38^a$
20	$32.20 \pm 0.09^b$	$8.74\pm0.01^{b}$	$16.04\pm0.38^b$
40	$32.26 \pm 0.09^b$	$8.81\pm0.02^{c}$	$21.26\pm0.22^{c}$
60	$41.62\pm0.09^c$	$12.51\pm0.02^{d}$	$24.57 \pm 1.59^{d}$

Mean values in the same column with different letters are significantly different at p < 0.05

#### FRAP and DPPH radical scavenging activity

Antioxidant capacity of methanolic seed extract from UAE was determined using two different antioxidant capacity assays and the finding results are shown in Table 2. Both FRAP and DPPH assays involved scavenging free radicals through electron transfer mechanism. As can be seen in both antioxidant capacity methods used, application of UAE at 60 mins had the highest antioxidant capacity, followed by 40 and 20 mins, while the control had the lowest

antioxidant capacity. This shows the longest sonication time, the highest antioxidant activity in the methanolic seed extract. A similar observation was reported by Gómez et al. [25]. Their study demonstrated that the antioxidant activity of ethanolic avocado seed extract, as measured by oxygen radical antioxidant capacity assay, was the highest (158.77 mg Trolox Equivalents/g) when the longest sonication time (55 mins) was used during UAE.

### Tan et al: PHYTOCHEMICALS AND ANTIOXIDANT ACTIVITY OF ULTRASOUND-ASSISTED AVOCADO SEED EXTRACT

T 11 0	A 1	1 4 4 4 4 4 4 4 4 4 4 4 4 4 4 4 4 4 4 4	C 41	1.	1 1 , ,
Table /	$\Delta$ nti $\Delta$ vid	lant activities	ant methat	10110 23/002	do seed extract
1 4010 2. 1	MINOMIN		o or memai	ione avoca	ao seeu exitaet

Sonication Time (mins)	FRAP (mmol Fe <sup>2+/</sup> kg)	<b>DPPH</b> (%)
0	$0.72 \pm 0.00^{a}$	$28.20 \pm 1.42^{a}$
20	$0.96\pm0.00^{b}$	$36.54 \pm 0.83^{b}$
40	$1.19\pm0.02^{b}$	$83.47 \pm 0.19^{c}$
60	$1.72\pm0.00^{\rm c}$	$84.96\pm1.20^c$

Mean values in the same column with different letters are significantly different at p < 0.05

## Correlation between phytochemicals and antioxidant activity

Correlation between phytochemicals (TPC, TFC and TAC) and antioxidant activities (FRAP and DPPH) are shown in Table 3. Positive correlation (p <0.05) was found between total phenolic, flavonoid and anthocyanin content and antioxidant activity measured by FRAP and DPPH, indicating these phytochemicals contribute high antioxidant activity in the extract. This observation is in agreement with Wang et al. [26], who reported the high antioxidant capacity in Hass avocado seed extract was due to the high concentration of flavonoid and phenolic content.

Sonication time is a significant factor that influences the extraction of plant phytochemicals and their antioxidant activity. This may be contributed by the cavitation effect of the ultrasound improved the fragmentation, swelling, hydration and pore production of the plant tissue matrix where the phytochemicals are to be isolated [27]. This will enhance the exposure of the phytochemicals and the extraction medium and help their release into the solvent, thereby increasing the antioxidant activity.

Table 3. Correlation between phytochemicals and antioxidant activity of methanolic avocado seed extract

	TPC	TFC	TAC	FRAP	DPPH
TPC	1	0.995**	0.675*	0.908**	0.609*
TFC		1	0.738**	0.940**	0.657*
TAC			1	0.916**	0.916**
FRAP				1	0.859**
DPPH					1

<sup>\*\*</sup> Correlation was significant at p <0.01

#### Conclusion

Avocado seed is the by-product of direct food consumption and food processing industry which could be further utilized to develop nutraceutical products. The TPC, TFC and TAC of methanolic seed extract were in the range of 31.90-41.62 mg GAE/100 g, 8.25-12.51 mg RE/100 g and 8.02-24.57 mg CGE/100 g, respectively. All phytochemicals and antioxidant activity demonstrated a positive and significant

correlation. Efficacy of the UAE in terms of sonication time was demonstrated in this study. Sonication for 60 mins leads to the highest extraction yield of phenolic, flavonoids and anthocyanin content in methanolic seed extract. Further study to quantify the individual bioactive compound of avocado seed extract following UAE application of 60 mins could be carried out.

<sup>\*</sup> Correlation was significant at p < 0.05

#### Acknowledgement

The authors would like to acknowledge Faculty of Science, Universiti Tunku Abdul Rahman, Kampar campus for providing the research facilities.

#### References

- Tan, C. X., Tan, S. S. and Tan, S. T. (2017). Influence of geographical origins on the physicochemical properties of Hass avocado oil. *Journal American Oil Chemical Society*, 94:1431-1437
- Zafar, T. and Sidhu, J. S. (2011). Avocado: production, quality, and major processed products. In: Handb. Veg. Veg. Process. Blackwell Publishing Ltd., New Jersey, United States: pp 525-543.
- 3. Costagli, G. and Betti, M. (2015). Avocado oil extraction processes: method for cold-pressed high-quality edible oil production versus traditional production. *Journal Agriculture Engineering*, 46:115.
- Duarte, P. F., Chaves, M. A., Borges, C. D. and Mendonça, C. R. B. (2016). Avocado: characteristics, health benefits and uses. *Ciência Rural*, 46:747-754
- Abraham, J. D., Abraham, J. and Takrama, J. F. (2018). Morphological characteristics of avocado (*Persea americana* Mill.) in Ghana. *African Journal Plant Sciences*, 12: 88-97.
- Saavedra, J., Córdova, A., Navarro, R., Díaz-Calderón, P., Fuentealba, C., Astudillo-Castro, C., Toledo, L., Enrione, J. and Galvez L. (2017). Industrial avocado waste: Functional compounds preservation by convective drying process. *Journal Food Engineering*, 198: 81-90.
- Segovia, F. J., Hidalgo, G. I., Villasante, J., Ramis, X. and Almajano, M. P. (2018). Avocado seed: A comparative study of antioxidant content and capacity in protecting oil models from oxidation. *Molecules* 23:1-14.
- 8. Dabas, D., Shegog, R. M., Ziegler, G. R. and Lambert, J. D. (2013). Avocado (*Persea americana*) seed as a source of bioactive phytochemicals. *Current Pharmaceutical Design*, 19: 6133-6140.

- Fadimu, G. J., Ghafoor, K., Babiker, E. E., Al-Juhaimi, F., Abdulraheem, R. A., Adenekan, M. K. (2020) Ultrasound-assisted process for optimal recovery of phenolic compounds from watermelon (*Citrullus lanatus*) seed and peel. *Journal Food Measure Characterization*, 14:1784-1793.
- Zhang, Q. W., Lin, L. G. and Ye, W. C. (2018).
   Techniques for extraction and isolation of natural products: A comprehensive review. *China Medicine*, 13: 1-26.
- 11. Tan, C. X. and Azrina, A. (2017). Dietary fiber and total phenolic content of selected raw and cooked beans and its combinations. *International Food Research Journal*, 24:1863-1868
- Sharma, V. and Agarwal, A. (2015). Physicochemical and antioxidant assays of methanol and hydromethanol extract of ariel parts of *Indigofera tinctoria* Linn. *Indian Journal Pharmaceutical Sciences*, 77: 729-734.
- 13. Granato, D., Santos, J. S., Maciel, L. G. and Nunes, D. S. (2016). Chemical perspective and criticism on selected analytical methods used to estimate the total content of phenolic compounds in food matrices. *TrAC Trends Analytical Chemistry*, 80: 266-279.
- 14. Bagheri, E., Hajiaghaalipour, F., Nyamathulla, S. and Salehen, N. A. (2018). The apoptotic effects of Brucea javanica fruit extract against HT29 cells associated with p53 upregulation and inhibition of NF-κB translocation. *Drug Design Development Theraphy*, 12: 657-671.
- Ghafoor, K., Al-Juhaimi, F. Y. and Choi, Y. H. (2012) Supercritical fluid extraction of phenolic compounds and antioxidants from grape (*Vitis labrusca B.*) seeds. *Plant Foods Human Nutrition*, 67:407-414
- Saenjum, C., Pattananandecha, T. and Nakagawa, K. (2020). Detection of antioxidant phytochemicals isolated from Camellia japonica seeds using HPLC and EPR imaging. *Antioxidants*, 9:1-14
- Segovia, F. J., Corral-Pérez, J. J. and Almajano, M. P. (2016) Avocado seed: Modeling extraction of bioactive compounds. *Industrial Crops Production*, 85:213-220.

### Tan et al: PHYTOCHEMICALS AND ANTIOXIDANT ACTIVITY OF ULTRASOUND-ASSISTED AVOCADO SEED EXTRACT

- 18. Bahru, T. B., Tadele, Z. H. and Ajebe, E. G. (2019). A review on avocado seed: Functionality, composition, antioxidant and antimicrobial properties. *Chemical Science International Journal*, 27:1–10.
- Pahua-Ramos, M. E, Ortiz-Moreno, A., Chamorro-Cevallos, G., Hernández-Navarro, M. D., Garduño-Siciliano, L., Necoechea-Mondragón, H. and Hernández-Ortega, M. (2012). Hypolipidemic effect of avocado (*Persea americana* Mill) seed in a hypercholesterolemic mouse model. *Plant Foods Human Nutrition*, 67:10-16.
- Kosińska, A., Karama,ć M., Estrella, I., Hernández, T., Bartolomé, B. and Dykes, G. A. (2012). Phenolic compound profiles and antioxidant capacity of *Persea americana* Mill. peels and seeds of two varieties. *Journal Agriculture Food Chemistry*, 60: 4613-4619.
- Singh, B., Singh, J. P., Kaur, A. and Singh, N. (2017). Phenolic composition and antioxidant potential of grain legume seeds: A review. *Food Research International*, 101:1-16.
- 22. Noorul, H., Mujahid, M., Khalid, M., Vartika, S., Nesar, A., Zafar, K. and Zohrameena, S. (2017). Physico-phytochemical analysis and estimation of total phenolic, flavonoids and proanthocyanidin content of *Persea americana* (avocado) seed

- extracts. World Journal Pharmceutical Sciences, 5:70-77.
- Ramić, M., Vidović, S., Zeković, Z., Vladić, J., Cvejin, A. and Pavlić, B. (2015). Modeling and optimization of ultrasound-assisted extraction of polyphenolic compounds from *Aronia* melanocarpa by-products from filter-tea factory. Ultrasonic Sonochemistry, 23:360-368.
- Martín, J., Navas, M. J., Jiménez-Moreno, A. M. and Asuero, A. G. (2017). Anthocyanin pigments: Importance, sample preparation and extraction. In: Phenolic Compd. sources, importance Appl. IntechOpen, London, UK, pp 117-152.
- Gómez, F. S., Peirósánchez, S., Iradi, M. G. G., Azman, N. A. M. and Almajano, M. P. (2014). Avocado seeds: Extraction optimization and possible use as antioxidant in food. *Antioxidants*, 3:439-454.
- Wang, W., Bostic, T. R. and Gu, L (2010). Antioxidant capacities, procyanidins and pigments in avocados of different strains and cultivars. *Food Chemistry*, 122: 1193-1198.
- Kumar, K., Srivastav, S. and Sharanagat, V. S. (2021). Ultrasound assisted extraction (UAE) of bioactive compounds from fruit and vegetable processing by-products: A review. *Ultrasonic Sonochemisty*, 70:105325.

# Malaysian Journal of Analytical Sciences (MJAS)





# A COMPARISON OF CHEMICAL COMPOSITIONS IN *KELULUT* HONEY FROM DIFFERENT REGIONS

(Perbandingan Komposisi Kimia dalam Madu Kelulut dari Kawasan Berbeza)

Hasnah Haron<sup>1</sup>\*, Ruzita A Talib<sup>1</sup>, Ponnusami Subramaniam<sup>2</sup>, Zainorain Natasha Zainal Arifen<sup>1</sup>, Muhammad Ibrahim<sup>3</sup>

<sup>1</sup>Nutritional Sciences Programme, Faculty of Health Sciences

<sup>2</sup>Health Psychology Programme, Faculty of Health Sciences

Universiti Kebangsaan Malaysia, 50300, Kuala Lumpur, Malaysia

<sup>3</sup>Department of Nutrition Sciences, Kuliyyah of Allied Health Sciences,

International Islamic University Malaysia, Jalan Istana, Bandar Indera Mahkota, 25200, Kuantan, Pahang, Malaysia

\*Corresponding author: hasnaharon@ukm.edu.my

Received: 1 December 2021; Accepted: 24 March 2022; Published: 27 June 2022

#### Abstract

Kelulut honey (KH) is honey produced by stingless bees (Trigona spp.) found in Malaysia. This study investigated the difference inherent in the chemical composition of kelulut honey collected from the east coast, and the central and northern regions of Peninsular Malaysia. Total sugar content, individual sugar content, total phenolics, total flavonoids, ascorbic acid, ascorbic acid equivalent antioxidant content (AEAC), and proline content were determined. Sugar analysis revealed that kelulut honey contained 62.33-79.53 g/100g of total sugar, with maltose as the predominant sugar (15.85-37.74 g/100g), followed by fructose (9.91-53.64 g/100g), glucose (10.96-25.04 g/100g), and sucrose (0.54-3.48 g/100g). The results indicate that total flavonoids (78.95±0.70 mg QE/kg) and phenolics (1149.48±40.52 mg GAE/kg) were the highest in honey from the east coast region. The proline and ascorbic acid content were less likely to be affected by geographical factors. Kelulut honey possesses a unique sugar profile that may contribute to its unique taste. In conclusion, the geographical and floral origin of honey are the two most important factors that fundamentally affect the physical-chemical properties of honey samples.

Keywords: chemical, compositions, kelulut, honey, region

#### Abstrak

Madu kelulut (KH) ialah madu yang dihasilkan oleh lebah tidak bersengat (Trigona spp.) yang terdapat di Malaysia. Kajian ini menyelidik perbezaan komposisi madu kelulut yang dikumpul dari pantai timur, tengah dan utara Semenanjung Malaysia. Jumlah dan gula individu, jumlah fenolik, jumlah flavonoid, asid askorbik, asid askorbik kandungan antioksidan setara (AEAC) dan kandungan prolin telah ditentukan. Analisis kandungan gula menunjukkan bahawa madu kelulut mengandungi 62.33-79.53 g/100g jumlah gula dengan maltosa sebagai gula utama (15.85-37.74 g/100g), diikuti oleh fruktosa (9.91-53.64 g/100g), glukosa (10.96-25. 100g) dan sukrosa (0.54-3.48 g/100g). Jumlah flavonoid (78.95±0.70 mg QE/kg) dan fenolik (1149.48±40.52 mg GAE/kg) adalah tertinggi dalam madu dari pantai timur. Prolin dan asid askorbik adalah kurang berkemungkinan dipengaruhi oleh faktor geografi. Madu kelulut mempunyai profil gula yang unik yang mungkin menyumbang kepada rasa unik madu

### Hasnah et al: A COMPARISON OF CHEMICAL COMPOSITIONS IN *KELULUT* HONEY FROM DIFFERENT REGIONS

kelulut. Secara kesimpulannya, geografi dan floral madu adalah dua parameter kualiti penting yang pada asasnya mempengaruhi sifat fizikal-kimia sampel madu.

Kata kunci: kimia, komposisi, kelulut, madu, kawasan

#### Introduction

Honey is a natural food consisting of about 200 different compounds including sugars, phenolics, amino acids, enzymes, organic acids, and aromatic compounds. Honey composition varies by bee species, nectar source, and geographic origin [1]. Honey is not only known for its nutritional benefit, but also as traditional medicine due to its healing properties. It has been proven that honey exert antioxidant, antiinflammatory, anti-bacterial and anti-mutagenic properties. The antioxidant activity assay for any product is based on the capability of the compounds to inhibit oxidation. The DPPH and FRAP assays are typically chosen because they are simple and rapid methods for assessing a honey sample's antioxidant capacity. These two assays are based on different principles, and thus may be used to screen compounds that have different antioxidant mechanisms. Recently, there is an increase in the Malaysian consumer demand for honey, especially for health maintenance and promotion purposes. There has been a surge of interest in honey's capacity as an antioxidant and its protective effects on the brain and other organs [2]. Kelulut honey is produced by the stingless bees that are indigenous to Malaysia. A local study reported that a low dose of Kelulut honey taken orally could improve wound healing rate in epidermal keratinocyte in vitro wound healing model [3]. It has also been reported to have a potential in preventing damage to sperm and testes in diabetic rats [4]. Kelulut honey is a multifloral honey which does not have any predominant pollen present in it. The nutritional profile and composition of this honey is still understudied. Over the decades, research on Malaysian honey production has been focused on Apis spp. which left a gap to be bridged by research work on kelulut honey. The effect of different botanical and geographical environment on honey chemical composition could be studied by comparing the honey of a particular type produced in different localities. Previous studies indicated that the nectar source can affect the antioxidant content and the antibacterial and

radical scavenging activities of the honey [5]. Bioactive compounds from the plant are secreted into the nectar, thereby impacting the quality of honey and its medicinal properties that are very dependent on its bioactive composition. The present study was undertaken to study the compositional variations of *kelulut* honey collected from different locations in peninsular Malaysia.

#### **Materials and Methods**

#### Sample collection

Kelulut honey from Heterotrigona itama species were collected from three peninsular Malaysia regions, namely the east coast region, the northern region, and the central region. The honey samples were collected from each region in two different batches. Each batch were analyzed in triplicates, and the results were expressed as an average  $\pm$  standard deviation of six replicates from samples collected in two batches.

#### Individual and total sugar analysis using HPLC

The composition of individual sugars in kelulut honey samples was determined using high performance liquid chromatography (HPLC) [6]. About 1 g of honey sample was weighed and loaded into a 50 mL centrifuge tube. 25 mL of 50:50 acetonitrile/deionized water was added into the tube. The sample was then filtered using a 0.45 µM nylon filter. The purified sugar extract was analyzed using a HPLC Waters model 2707 with an XBridge Amide column (250 x 4.6mm, 3.5μM) coupled with Water RI-2414 refractive mobile index detector. The phase acetonitrile/deionized water (75:25). The injection volume was 20 µL with flow rate of 1.0 mL/min. The retention time for each sugar was determined by comparing with a known standard sugar solution consisting of fructose, glucose, sucrose, and maltose with a concentration of 0.5 g/10 mL. The composition of the individual sugar was calculated using Empower 2 software.

#### Total sugar content using chemical analysis

Total sugar content in kelulut honey were also determined using the phenol-sulphuric acid method [7]. This analysis was performed in this study because honey also contains a small amount of oligosaccharides that the HPLC method could not detect. For this analysis, 0.1 g of honey sample was diluted 100-fold and the solution was homogenized, 1 mL of the new solution was 20-fold diluted. A 2 mL aliquot of the honey solution was combined with 1 mL of 5% aqueous phenol solution in a test tube. 5 mL of concentrated sulphuric acid was then added rapidly to the mixture. The mixture was allowed to stand for 10 min and subsequently vortexed for 30 seconds. The test tube was then placed in a water bath at room temperature for 20 minutes for color development. The absorbance was then recorded on a spectrophotometer (Secomam, France) at 490 nm. Glucose solutions 0f 0.0-0.1 g/L were used as standard.

#### **Total phenolic content**

The Folin-Ciocalteu assay [8] was used to determine the total phenolic content in *kelulut* honey. 0.5 mL of the 10% honey solution was mixed with 2.5 mL of 0.2 N Folin-Ciocalteu reagent, and the mixture was left to stand for 5 minutes. Then, 2 mL of 7.5% sodium carbonate solution was added. The mixture was allowed to stand at room temperature for 2 hours. The absorbance of the mixture was then measured at 760 nm using spectrophotometer (Secomam, France) against methanol as blank. Gallic acid (50-200 mg/L) was used to produce standard curve ( $R^2 = 0.987$ ). The total phenolic content was expressed in mg of gallic acid equivalent (GAE)/kg honey.

#### **Total flavonoid content**

The total flavonoid content in the honey samples was analyzed using the method described by Zhishen et al. [9]. A 1 mL volume of 20% honey was mixed with 4 mL of distilled water and 0.3 mL of sodium nitrite. After 5 minutes, 0.3 mL of 10% aluminum chloride was added followed by 2 mL of 1 M sodium hydroxide six minutes later. The volume was made up to 10 mL by distilled water, and the mixture was shaken thoroughly. The absorbance was read using spectrophotometer (Secomam, France) at 510 nm

wavelength. A standard curve was plotted using a quercetin solution with concentrations ranging between 25 - 100  $\mu$ g/mL ( $R^2 = 0.987$ ). The results were expressed as mg quercetin equivalent (QE)/kg honey.

#### **Proline content**

The proline content in the honey sample was determined using the method described by Bogdanov et al. [10]. A 0.5 mL sample of honey (0.05 g/mL) was mixed with 1 mL of formic acid (80%) and 1 mL of ninhvdrin solution (3% in ethylene monomethylether). The mixture was shaken vigorously for 15 minutes. The mixture was incubated in a boiling water bath for 14 minutes before being transferred to a 70 °C water bath for 10 minutes. A 5 mL 50% propanol-water solution was added, and the mixture was allowed to cool for 45 minutes. Its absorbance at 510 nm was measured. Water was used as the blank and a 0.032 mg/mL proline solution was used as the standard. Proline content (mg/kg) was calculated as follow:

$$Proline = \frac{E_S}{E_a} X \frac{E_1}{E_2} X80 \tag{1}$$

where  $E_s$  is the absorbance of the sample solution;  $E_a$  is the absorbance of the proline solution;  $E_1$  is the concentration of proline in mg used for the standard;  $E_2$  is the weight of honey in g; 80 is the dilution factor.

#### Ascorbic acid content determination

The honey sample (100 mg) was extracted with 10 mL of metaphosphoric acid for 45 minutes at room temperature and the mixture was filtered through a filter paper. About 1 mL of the filtrate was mixed with 9 mL of 2,6-dichlorophenolindophenol and the absorbance was determined at 515 nm within 30 min. L-ascorbic acid (0.02-0.12 mg/mL) was used as standard [11].

#### Ascorbic acid equivalent antioxidant content

AEAC was performed according to the procedure described by Meda et al. [12]. A 0.75 mL samples of honey in methanol (0.04 g/mL) was mixed with 1.5 mL of 0.02 mg/mL methanolic DPPH radical solution. The mixture was left for 15 minutes at room temperature before its absorbance was measured using a spectrophotometer (Secomam, France) at 517 nm. The

blank sample was prepared from a mixture of 0.75 mL of honey solution and 1.5 mL of methanol.

#### Carotenoid content

The measurement of carotenoid in *kelulut* honey was performed based on the method described by Ferreira et al. [11]. A 100 mg honey sample was shaken with a 4:6 ratio mixture of acetone and hexane for 1 minute. The mixture was filtered with filter paper and the absorbance of the filtrate was measured using a spectrophotometer (Secomam, France) at 454 nm, 505 nm, and 663 nm. The content of β-carotene inside the sample was calculated using the equation  $0.216A_{663} - 0.304A_{505} + 0.452A_{453}$  while the lycopene content was calculated using the equation  $-0.0458A_{663} + 0.372$   $A_{505} - 0.0806$   $A_{453}$ . The total carotenoid content is defined as the sum of β-carotene and lycopene, and all measurements were expressed in mg/100mL.

#### **Anti-oxidative activities**

The DPPH radical scavenging capacity of kelulut honey was investigated using the procedure described Ferreira et al. [11]. Approximately 0.5 mL of the 0.2 g/mL honey extract was mixed with 2.7 mL of methanolic 0.024 mg/mL DPPH radical solution. The mixture was vigorously shaken and incubated for 15 minutes, then its absorbance was measured at 517 nm. IC<sub>50</sub> was defined as the concentration of a substance that would scavenge 50% of DPPH radicals, which means that a lower IC<sub>50</sub> value corresponds to a stronger antioxidant property. The FRAP assay was performed using the procedure described by Benzie & Strain [13]. A 200 µL sample of 0.1 g/mL honey was mixed with 1.5 mL of the FRAP reagent prepared from acetate buffer (300 mM/L), 2,4,6-tris(2-pyridyl)-s-triazine (TPTZ) solution (10 mM in 40 mM/L HCl), and ferric chloride (FeCl<sub>3.6</sub>H<sub>2</sub>O) (20mM) in the ratio of 10:1:1. The mixture was pre-warmed at 37 °C for 4 minutes before its absorbance was measured at 593 nm using a spectrophotometer (Secomam, France). Ferrous sulfate (FeSO<sub>4.7</sub>H<sub>2</sub>O) solutions with concentrations between 250-1000 µM/L was used to construct the standard curve (R<sup>2</sup>=0.991). The FRAP values were expressed as μM Fe (II) per kg honey.

#### Data analysis

IBM SPSS version 23 was employed for the statistical analyses. ANOVA with Tukey's Honest Significant

Difference (HSD) test was used for the comparisons of the chemical compositions of *kelulut* honey from three different zones. Pearson correlation was used to establish correlation between bioactive compounds and anti-oxidative activities. The significant level was set as  $\alpha$ =0.05.

#### **Results and Discussion**

The compositional analysis revealed that the kelulut honey samples from Trigona spp. Collected in this study contained fructose and glucose at the concentrations of 9.91-27.33 g/100g and 10.96-25.04 g/100g, respectively (Table 1). Maltose was the predominant sugar of kelulut honey from the east coast and central regions of Peninsular Malaysia. The total sugar content of kelulut honey was 62.3-79.53 g/100g. The honey also contained oligosaccharides as the minor sugar constituents. In this study, oligosaccharide content of kelulut honey was estimated by subtracting the individual sugars analyzed using HPLC from the total sugars analyzed using the phenolsulphuric acid method. The results showed that kelulut honey contained 3.84-14.68 g/100g of oligosaccharides.

The total phenolic content of the *kelulut* honey samples collected in the present study was in the range of 530.28-1166.77 mg GAE/kg while the total flavonoid content was in the range of 48.82-79.02 mg QE/kg (Table 2). Kelulut honey samples collected from the east coast region contained the highest level of carotenoids at 1.52  $\pm$  0.17 mg lycopene/kg and 3.09  $\pm$ 0.25 mg β-carotene/kg. The total carotenoid content of kelulut honey samples in this study ranged between 2.22-4.61 mg carotenoids/kg. The proline content of kelulut honey in the present study was 277.76-291.89 mg/kg. The ascorbic acid content of the kelulut honey was within the range of 75.71-95.85 mg/kg. The central region kelulut honey had a significantly higher (p<0.05) ascorbic acid content compared to the east coast and northern kelulut honey. Meanwhile, the AEAC of kelulut honey was 78.10-146.48 mg/kg. Ascorbic acid in the kelulut honey contributed 65.44-96.94% to AEAC.

Table 1. Types of sugar in kelulut honey

Sugars	East Coast Region Honey (n=6)	Northern Region Honey (n=6)	Central Region Honey (n=6)
Total sugars (g/ 100g)	$62.33 \pm 10.33^{a}$	$79.53 \pm 13.22^{b}$	$64.28 \pm 19.63^{ab}$
Maltose (g/100g)	$22.80\pm1.74^a$	$15.85 \pm 0.05^{b}$	$37.74\pm8.57^c$
Fructose (g/100g)	$10.41 \pm 0.18^a$	$27.33 \pm 0.15^{b}$	$9.91\pm3.99^a$
Glucose (g/100g)	$10.96 \pm 0.18^{a}$	$25.04 \pm 0.14^b$	$11.98\pm1.68^a$
Sucrose (g/100g)	$3.48\pm0.65^{\mathrm{a}}$	$0.54\pm0.01^{b}$	$0.81\pm0.22^{c}$

Total sugar was obtained from phenol-sulphuric acid method while individual sugars were analyzed using HPLC. Different superscripts across the same row indicates significant difference (p < 0.05).

Table 2. Phenolic, flavonoid, proline, ascorbic acid content and AEAC of kelulut honey

Parameters	East Coast Region Honey (n=6)	Northern Region Honey (n=6)	Central Region Honey (n=6)
TPC (mg GAE/kg)	$1166.77 \pm 47.85^a$	$728.42 \pm 58.06^b$	$530.28 \pm 30.31^{\circ}$
TFC (mg QE/kg)	$7902\pm0.59^a$	$48.82\pm0.67^b$	$55.38\pm0.37^b$
AEAC (mg/kg)	$146.48 \pm 6.43^a$	$78.10 \pm 3.75^{b}$	$96.92 \pm 1.31^{c}$
Ascorbic acid content (mg/kg)	$95.85 \pm 13.48^{a}$	$75.71 \pm 12.69^a$	$92.79\pm0.75^a$
Proline (mg/kg)	$277.76 \pm 19.75^{ab}$	$291.89 \pm 3.46^a$	$284.82 \pm 10.72^{b}$
Lycopene (mg/kg)	$1.52\pm0.17^a$	$0.64\pm0.08^{b}$	$0.76\pm0.08^{c}$
β-carotene (mg/kg)	$3.09\pm0.25^a$	$1.58\pm0.14^b$	$1.57\pm0.05^{\text{b}}$
IC <sub>50</sub> (DPPH radical scavenging) (mg/mL)	$15.17 \pm 1.02^{\rm a}$	$28.47\pm2.03^{\mathrm{b}}$	$24.27 \pm 2.68^c$
FRAP (µM Fe (II)/ kg)	$7481.08 \pm 57.57^{\rm a}$	$4122.97 \pm 424.44^b$	$3633.78 \pm 127.21^{c}$

Different superscripts across the same row indicates significant difference (p < 0.05)

The DPPH and FRAP assays were chosen because they are simple and rapid methods for assessing the antioxidant capacity of honey. The FRAP assay measures the ferric-reducing capacity of antioxidants, whereas the DPPH assay measures the ability of antioxidants to scavenge the DPPH radical. These two assays are based on different principles, and thus may be used to screen compounds that have different antioxidant mechanisms. *Kelulut* honey exhibited IC<sub>50</sub> values in the range of 15.17-28.46 mg/mL. The honey collected from the east coast region showed the strongest DPPH radical scavenging activity with the

lowest IC<sub>50</sub> value of 15.17  $\pm$ 1.02 mg/mL. The reducing power of *kelulut* honey assessed using FRAP was outlined in the order of east coast region *kelulut* honey > northern region *kelulut* honey > central region *kelulut* honey. The FRAP values were in the range of 3633.78-7481.08  $\mu$ M Fe (II)/ kg.

The IC<sub>50</sub> of the honey samples had a significant inverse correlation (p<0.01) with their bioactive compound compositions, namely total phenolics, total flavonoids, lycopene,  $\beta$ -carotene, ascorbic acid, and AEAC (Table 3). Their FRAP also had a significant and inverse

### Hasnah et al: A COMPARISON OF CHEMICAL COMPOSITIONS IN *KELULUT* HONEY FROM DIFFERENT REGIONS

correlation (p<0.01) with their bioactive compound compositions, namely total phenolics, total flavonoids, lycopene,  $\beta$ -carotene and AEAC. The IC<sub>50</sub> and FRAP had a strong inverse correlation (r=-0.868, p <0.01). The correlation matrix indicated the importance of the bioactive constituents of honey to its anti-oxidative capacity. The total phenolic content of a honey sample was negatively correlated with its IC<sub>50</sub> value (r<sup>2</sup> = -0.789; p <0.05) and positively correlated with the FRAP value (r<sup>2</sup> = 0.970; p <0.05). In addition, a significant negative correlation was found between the

honey sample's ascorbic acid composition and its  $IC_{50}$  value ( $r^2 = -0.545$ ; p < 0.05) and a positive correlation was found between its ascorbic acid composition and its lycopene value ( $r^2 = 0.634$ ; p < 0.01). These correlations between the bioactive compound content and the antioxidant activity of the extracts suggest that phenolic compounds are primarily responsible for the antioxidant activity of the honey samples as measured in the DPPH and FRAP assays.

Table 3. Correlation matrix of antioxidant content and anti-oxidative activities

	TPC	TFC	IC50	FRAP	Lycopene	β- carotene	Ascorbic Acid	AEAC
TPC	1							
TFC	$0.989^{**}$	1						
IC <sub>50</sub>	-0.789**	-0.751**	1					
FRAP	$0.970^{**}$	0.965**	-0.868**	1				
Lycopene	0.883**	$0.861^{**}$	-0.895**	0.911**	1			
β-carotene	$0.932^{**}$	0.924**	-0.868**	0.951**	0.987**	1		
Ascorbic Acid	0.228	0.172	-0.545**	0.323	$0.634^{*}$	0.527	1	
AEAC	0.812**	0.813**	-0.948**	0.909**	0.932**	0.926**	0.557	1

TPC- total phenolic content; TFC- total flavonoid content; \*\*Significant correlation at p<0.05; \*Significant correlation at p<0.01

The fructose and glucose content of the kelulut honey samples gathered in this study were lower than those reported in the literature. Honey produced by stingless bees in the semi-arid region of Northeastern Brazil [14] has fructose as its predominant sugar (50.0-59.2 g/100g), followed by glucose (37.7-45.7 g/100g) and sucrose (0.7-3.9 g/100g). Ecuadorian stingless bee honey contained similar amounts of glucose (25.5 g/100g) and fructose (25.2 g/100g) with a smaller amount of sucrose (3.72 g/100g) [15]. Biluca et al. [16] also reported that the stingless bee honey from Santa Catarina, Brazil, contained 8.21-31.3 g glucose/100g and 30.4-46.1 g fructose/100g, while the honey from Trigona fuscipennis contained 36.22 g fructose /100g and 20.4 g glucose /100g. The amount of glucose and fructose measured were in accordance with the Malaysian Standard specification on kelulut stingless honey (MS 2683:2017), which dictates that it contains less than 7.5% sucrose and less than 85% fructose. The high concentration of sugar in honey combined with an acidic pH (3-5) do retard the growth of bacteria in honey [17].

The maltose content of the honey samples collected in the current study exceeded the limit set by the Malaysian Standard on kelulut stingless honey (MS 2683:2017), which dictated that the maltose content should be less than 9.5%. However, the current findings were in line with a recent study conducted by Chuttong et al. [18] which reported that Thai stingless bee honey contained 41 g maltose /100g, 17 g fructose/100g, 14 g glucose/100g and 1.2 g

sucrose/100g. An earlier study [19] also reported the Trigona honey, specifically of Frieseomelita aff varia, contained maltose as the predominant sugar (32.3%), followed by fructose (24.2%), glucose (18.1%), and sucrose (0.2%). The total sugar in our study were higher than those reported for Thai stingless bee honey (55±21 g/100g) [18]. The total sugar content of the kelulut honey in the current study was within the range of total sugars reported for Brazilian stingless monofloral honey (62.7-71.2 g/100g) [14]. The sucrose content (0.54-3.48 g/100g) obtained in this study was within the limit set by Codex Alimentarius (2001) [20] which is less than 5g/100g. Kelulut honey has a different sugar profile compared to the typical Apis spp. honey that contains fructose and glucose as the predominant sugar. This sugar profile in kelulut honey may contribute to its distinct flavor. Previous studies indicated that honey contains the oligosaccharides nigerose  $(1.11\pm2.81\%)$ , turanose  $(0.78\pm2.03\%)$ , maltotriose (0.24±1.03%), melezitose (0.21±0.37%) and raffinose (0.10±0.25%) that may also be present in kelulut honey.

Phenolic compounds play a role in countering the damage that oxidative stress incurs on the body. Having these active compounds makes the stingless bee honey valuable for medicinal purpose [21]. The vast difference in the phenolic content of the honey samples collected from the three different regions may be attributed to the differing bee species that produce those honey. A study showed the honey samples collected from three stingless bee species, namely Geniotrigona thoracica, Heterotrigona itama, and Heterotrigona erythrogastra, had significant differences in their phenolic content, which were 99.04  $\pm$  5.14, 67.86  $\pm$  7.40, 44.72  $\pm$  6.50 mg/mL, respectively [22]. Apart from the different species of bees, geographical and botanical origins could explain the variation of phenolics content in stingless bee honey. Biluca et al. [16] reported that various stingless bee honey samples contained 10.3-98.0 mg GAE/100g phenolics while Silva et al. [23] reported a range of 1.1-1.3 mg GAE/g of phenolics found in stingless bee honey.

Furthermore, the total flavonoid content of kelulut honey were in fair agreement with results reported by Chan et al. [24], in which Trigona spp. honey from Malaysia contained 44.60-79.13 mg QE/kg. Tuksitha et al. [22] reported a higher flavonoids range (12.41-17.67 mg/mL) for stingless bee from Borneo. Previous study reported that various kinds of Hungarian honey contained 252-2283 mg proline /kg [23]. The value obtained in this study was within the range. The protein content of floral honey is 1.0-1.5% and the amino acid content is 1.0% of the total protein in honey. Proline is the main amino acid present in honey, constituting 50-85% of the total amino acids [23]. The proline content of honey decreases at a constant rate during storage; thus, it acts as an indicator of ripeness [23]. The minimum value of 180 mg/kg of proline is accepted for pure honey [26]. The value of ascorbic acid obtained in this study was lower than those obtained in Portuguese honey (140.01-145.80 mg/kg [11] and Algerian honey (159.70±0.78 mg/kg). A previous study [27] reported that Algerian honey contained 0.30-1.01 mg carotenoids/ 100 g.

A more recent study reported that floral honey from Tunisia contained 1.16-4.72 mg carotenoids/kg [28]. The carotenoid content of the *kelulut* honey samples collected from the three regions were significantly different (p <0.05), indicating the influence of geography on carotenoid content. Environmental factors and the changing seasons also contribute to the carotenoid content in honey [28]. The ascorbic acid content measured in this study was lower than those measured in Portuguese honey (140.01-145.80 mg/kg) [11] and Algerian honey (159.70±0.78 mg/kg). The value of AEAC in the present study was lower than those reported from other countries such as India (15.1-29.5 mg AEAC/100g) [29] and Bangladesh (18.4-34.1 mg AEAC/100g) [30].

The values of IC<sub>50</sub> obtained in this study agreed well with the results reported for Tunisian floral honey which had a range of IC<sub>50</sub> values from 11.08 mg/mL to 93.26 mg/mL [28]. Omani honey had higher IC<sub>50</sub> values which were 25.1 mg/mL, 49.3 mg/mL, 144.5 mg/mL as the average values for Sumer, Sidr, and multifloral honey, respectively [31]. Our results were

higher than those of Brazilian honey (3.17-8.79 mg/mL) [32]. Despite the differences, we should acknowledge the inter-laboratory differences of these studies. Silva et al. [23] and Biluca et al. [16] reported that stingless bee honey had between 10.6-12.9 mg ascorbic acid equivalent/100g and 1.46-18.5 mg ascorbic acid equivalent/100g, respectively as the concentration needed to scavenge DPPH radicals. Recently, Tuksitha et al. [22] reported that stingless bee honey from Sarawak, Malaysia, contained 25.78-50.66 µM Fe (II)/100g. Compared to that, the samples collected in this study had stronger reducing activities. Our results were in fair agreement with the FRAP values of Polish honey 0.6-5.7 mM Fe (II)/kg honey [33] and stingless bee honey reported by Biluca et al. [16] in the ranged of  $61.1-624 \mu M$  Fe (II)/100g.

#### Conclusion

Kelulut honey contains maltose as its predominant sugar and a relatively low amount of sucrose. Kelulut honey contains bioactive compounds namely phenolics and flavonoids, the compositions of which were significantly affected by the honey's botanical and geographical origin. Honey from the east coast region contained the highest amount of phenolics and flavonoids. Proline and ascorbic acid were not correlated with geographical factor.

#### Acknowledgement

This study was funded by Universiti Kebangsaan Malaysia research grant GUP-056-2014.

#### References

- Escuredo, O., Míguez, M., Fernández-González, M., and Seijo, M. C. (2013). Nutritional value and antioxidant activity of honeys produced in a european atlantic area. *Food Chemistry*, 138: 851-856.
- Arrifin, N. A. (2018). Determination of minerals in commercial honeys using atomic absorption spectrometry and inductively couple plasmaoptical emission spectrometry. Thesis of Bachelor's Degree, Universiti Teknologi Mara.
- 3. Abid, N., Shiplu, R. C., Aminuddin, S. and Ruszymah, H. I. (2018). Low dose kelulut honey improves human keratinocyte viability,

- proliferation, and wound healing. *Regenerative Research*, 7(1):143.
- 4. Budin, S. B., Jubaidi, F. F., Azam, S. N. F. M. N., Yusof, N. L. M., Taib, I. S. and Mohamed, J. (2017). Kelulut honey supplementation prevents sperm and testicular oxidative damage in streptozotocin-induced diabetic rats. *Jurnal Teknologi*, 79(3).
- Kaškonienė, V. and Venskutonis, P. R. (2010). Floral markers in honey of various botanical and geographic origins: a review. Comprehensive reviews in food science and food safety, 9(6): 620-634.
- Wills, R. B. H., Balmer, N. and Greenfield, H. (1980). Composition of Australian foods. 2. Methods of analysis. Food Technology in Australia, 32(4): 198-204.
- 7. Dubois, M., Gilles, K. A., Hamilton, J. K., Rebers, P. T. and Smith, F. (1956). Colorimetric method for determination of sugars and related substances. *Analytical chemistry*, 28(3): 350-356.
- 8. Singleton, V. L., Orthofer, R. and Lamuela-Raventos, R. M. (1999). Analysis of total phenols and other oxidation substrates and antioxidants by means of Follin–Ciocalteu reagent. *Methods in Enzymology*, 299: 152-178.
- 9. Zhishen, J., Mengcheng, T. and Jianming, W. (1999). The determination of flavonoid contents in mulberry and their scavenging effects on superoxide radicals. *Food chemistry*, 64(4): 555-559.
- Bogdanov, S., Lullmann, C., Mossel, B.L., D'arcy, B.R., Russmann, H., Vorwohl, G., Oddo, L., Sabatini, A.G., Marcazzan, G.L., Piro, R. and Flamini, C. (1999). Honey quality, methods of analysis and international regulatory standards: review of the work of the international honey commission. *Mitt Lebensmittelunters Hyg*, 90: 108-125.
- Ferreira, I. C., Aires, E., Barreira, J. C., and Estevinho, L. M. (2009). Antioxidant activity of Portuguese honey samples: different contributions of the entire honey and phenolic extract. *Food Chemistry*, 114(4): 1438-1443.

- Meda, A., Lamien, C. E., Romito, M., Millogo, J. and Nacoulma, O. G. (2005). Determination of the total phenolic, flavonoid and proline contents in burkina fasan honey, as well as their radical scavenging activity. *Food chemistry*, 91(3): 571-577.
- 13. Benzie, I. F., and Strain, J. J. (1999). Ferric reducing/antioxidant power assay: Direct measure of total antioxidant activity of biological fluids and modified version for simultaneous measurement of total antioxidant power and ascorbic acid concentration. *Methods in Enzymology*, 299: 15-27.
- 14. de Sousa, J. M. B., de Souza, E. L., Marques, G., de Toledo Benassi, M., Gullón, B., Pintado, M. M., and Magnani, M. (2016). Sugar profile, physicochemical and sensory aspects of monofloral honeys produced by different stingless bee species in Brazilian semi-arid region. LWT-Food Science and Technology, 65: 645-651.
- Guerrini, A., Bruni, R., Maietti, S., Poli, F., Rossi, D., Paganetto, G., Muzzoli, M., Scalvenzi, L. and Sacchetti, G. (2009). Ecuadorian stingless bee (Meliponinae) honey: A chemical and functional profile of an ancient health product. *Food Chemistry*, 114(4): 1413-1420.
- Biluca, F. C., Braghini, F., Gonzaga, L. V., Costa, A. C. O. and Fett, R. (2016). Physicochemical profiles, minerals and bioactive compounds of stingless bee honey (Meliponinae). *Journal of Food Composition and Analysis*, 50: 61-69.
- Lia, A. S., Muhammad, A. I., Nik, M. S. and Fareed S. (2017). Pemencilan dan pengenalpastian bakteria daripada madu kelulut (*Trigona sp.*). Undergraduate Research Journal for Biomolecular Sciences and Biotechnology, 1: 151-157.
- Chuttong, B., Chanbang, Y., Sringarm, K. and Burgett, M. (2016). Physicochemical profiles of stingless bee (Apidae: Meliponini) honey from South East Asia (Thailand). Food chemistry, 192: 149-155.
- Bogdanov, S., Vit, P. and Kilchenmann, V. (1996).
   Sugar profiles and conductivity of stingless bee honeys from Venezuela. *Apidologie*, 27(6): 445-450.

- 20. Codex Alimentarius (2001). Revised codex standard for honey. Codex Standard 12(2001): 1982.
- 21. Yaacob, M., Rajab N.F., Shahar, S. and Sharif, R. (2018). Stingless bee honey and its potential value: A systematic review. *Food Research*, 2550-2166.
- Tuksitha, L., Chen, Y. L. S., Chen, Y. L., Wong, K. Y. and Peng, C. C. (2018). Antioxidant and antibacterial capacity of stingless bee honey from Borneo (Sarawak). *Journal of Asia-Pacific Entomology*, 21(2): 563-570.
- 23. Silva, T. M. S., dos Santos, F. P., Evangelista-Rodrigues, A., da Silva, E. M. S., da Silva, G. S., de Novais, J. S. and Camara, C. A. (2013). Phenolic compounds, melissopalynological, physicochemical analysis and antioxidant activity of Jandaíra (*Melipona subnitida*) honey. *Journal of Food Composition and Analysis*, 29 (1): 10-18.
- 24. Chan, B. K., Haron, H., Talib, R. A. and Subramaniam, P. (2017). Physical properties, antioxidant content and anti-oxidative activities of Malaysian stingless kelulut (Trigona spp.) honey. *Journal of Agricultural Science*, 9(13): 32.
- 25. Czipa, N., Borbély, M. and Győri, Z. (2012). Proline content of different honey types. *Acta Alimentaria*, 41 (1): 26-32.
- Hermosín, I., Chicon, R. M. and Cabezudo, M. D. (2003). Free amino acid composition and botanical origin of honey. *Food Chemistry*, 83(2): 263-268.
- 27. Mouhoubi-Tafinine, Z., Ouchemoukh, S., & Tamendjari, A. (2016). Antioxidant activity of some Algerian honey and propolis. *Industrial Crops and Products*, 88: 85-90.
- Boussaid, A., Chouaibi, M., Rezig, L., Hellal, R., Donsì, F., Ferrari, G. and Hamdi, S. (2018). Physicochemical and bioactive properties of six honey samples from various floral origins from tunisia. *Arabian Journal of Chemistry*, 11(2): 265-274.
- Saxena, S., Gautam, S. and Sharma, A. (2010). Physical, biochemical and antioxidant properties of some indian honeys. *Food Chemistry*, 118(2): 391-397.

### Hasnah et al: A COMPARISON OF CHEMICAL COMPOSITIONS IN *KELULUT* HONEY FROM DIFFERENT REGIONS

- 30. Islam, A., Khalil, I., Islam, N., Moniruzzaman, M., Mottalib, A., Sulaiman, S. A. and Gan, S. H. (2012). Physicochemical and antioxidant properties of Bangladeshi honeys stored for more than one year. *BMC Complementary and Alternative Medicine*, 12(1): 1.
- 31. Al-Farsi, M., Al-Amri, A., Al-Hadhrami, A. and Al-Belushi, S. (2018). Color, flavonoids, phenolics and antioxidants of Omani honey. *Heliyon*, 4(10): e00874.
- Pontis, J. A., Costa, L. A. M. A. D., Silva, S. J. R.
   D. and Flach, A. (2014). Color, phenolic and flavonoid content, and antioxidant activity of

- honey from Roraima, Brazil. *Food Science and Technology*, 34(1): 69-73.
- 33. Kuś, P. M., Congiu, F., Teper, D., Sroka, Z., Jerković, I. and Tuberoso, C. I. G. (2014). Antioxidant activity, color characteristics, total phenol content and general HPLC fingerprints of six Polish unifloral honey types. *LWT-Food Science and Technology*, 55(1): 124-130.

### **Malaysian Journal of Analytical Sciences** (MJAS) Published by Malaysian Analytical Sciences Society





### QUANTITATIVE STRUCTURE-ACTIVITY RELATIONSHIP (QSAR) STUDY OF NEWLY SYNTHESIZED CARBONYL THIOUREA DERIVATIVES ON

Acanthamoeba sp.

(Kajian Kuantitatif Hubungan Struktur-Aktiviti (QSAR) Terhadap Terbitan Karbonil Tiourea Hasilan Sintesis Baru Terhadap *Acanthamoeba* sp.)

Maizatul Akma Ibrahim<sup>1\*</sup>, Nor Hafizah Zakaria<sup>1</sup>, Mohd Sukeri Mohd Yusof<sup>2</sup>

<sup>1</sup>Department of Plant Science, Kulliyyah of Science, International Islamic University Malaysia, Bandar Indera Mahkota, 25200 Kuantan, Pahang, Malaysia <sup>2</sup>Faculty of Science and Marine Environment, Universiti Malaysia Terengganu, 21030 Kuala Nerus, Terengganu, Malaysia.

\*Corresponding author: maizatulakma@iium.edu.my

Received: 3 December 2021; Accepted: 23 March 2022; Published: 27 June 2022

#### **Abstract**

This research aims to build a mathematical quantitative structure-activity relationship (QSAR) model, which could relate the relationship between newly-synthesized carbonyl thiourea derivatives with their anti-amoebic activities. Therefore, in this study, inhibition concentration of 50% cells population (IC<sub>50</sub>) was evaluated for 44 carbonyl thiourea derivatives on pathogenic Acanthamoeba sp. (Hospital Kuala Lumpur isolate). QSAR analysis was conducted using the obtained IC50 data with additional 4 thiourea compounds of the same group from our previous work by applying three linear regression techniques namely stepwise-MLR, GA-MLR, and GA-PLS. Results showed that these thiourea derivatives are positively active against the tested Acanthamoeba sp. with IC<sub>50</sub> values ranging from 2.56 to 7.81 μg/mL. From the evaluation of the obtained models, the GA-PLS technique is found to be the best model due to its best predictive ability. The final equation of GA-PLS model gave good statistical output with values of  $r^2 = 0.827$ ,  $r^2_{cv} = 0.682$  RMSEC=0.047, RMSECV=0.064, and  $r^2_{test} = 0.790$  and RMSEP=0.051. Y-randomization test has confirmed that the model did not occur from the chance of correlation with  $r^2 = 0.015$ -0.372. Small residual with values less than 0.25 from the prediction in the test set proves the robustness of the model. The information generated from this study will provide an insight into designing a new lead compound from carbonyl thiourea containing highly potential anti-amoebic properties.

**Keywords**: thiourea derivatives, *Acanthamoeba* sp., IC<sub>50</sub>, anti-amoebic activity, QSAR models

#### **Abstrak**

Kajian ini mensasarkan pembinaan model matematik kuantitatif hubungan struktur-aktiviti (QSAR) yang memberi hubungkait antara terhadap terbitan karbonil tiourea hasilan sintesis baru dengan aktiviti anti-amebik. Oleh itu, kepekatan penghambatan 50% populasi sel (IC<sub>50</sub>) dikaji ke atas 44 sebatian karbonil tiourea terhadap *Acanthamoeba* sp. (Hospital Kuala Lumpur isolat) berstatus patogenik. Analisa hubungan struktur-aktiviti kuantitatif dijalankan menggunakan data IC50 yang diperolehi bersama 4 sebatian tambahan kumpulan sama dari hasil kerja kami sebelum ini, dengan mengaplikasi tiga teknik regresi linear, iaitu

sp.

stepwise-MLR, GA-MLR dan GA-PLS dijalankan. Hasil kajian menunjukkan bahawa sebatian tiourea ini aktif secara positif terhadap *Acanthamoeba* sp.yang diuji dengan nilai IC<sub>50</sub> antara 2.56 hingga 7.81 µg/mL. Penilaian terhadap semua model QSAR yang dibina dalam kajian ini menunjukkan teknik GA-PLS adalah model yang terbaik kerana kemampuan ramalannya yang terbaik. Persamaan akhir untuk model GA-PLS menunjukkan output statistik yang baik dengan nilai  $r^2 = 0.827$ ,  $r^2_{cv} = 0.682$ , RMSEC = 0.047, RMSECV = 0.064,  $r^2_{test} = 0.790$  dan RMSEP = 0.051. Ujian perawakan-y mengesahkan bahawa model tersebut tidak terhasil secara kebetulan dengan  $r^2 = 0.015$ -0.372. Baki kecil dengan nilai kurang dari 0.25 dari ramalan set ujian membuktikan kekuatan model tersebut. Data terbina dari kajian ini akan memberi maklumat untuk mencipta sebatian penting baru dari tiourea karbonil yang mempunyai aktiviti anti-amebik yang berpotensi tinggi.

Kata kunci: tiourea terbitan, Acanthamoeba sp., IC50, aktiviti anti-amebik, model QSAR

#### Introduction

Acanthamoeba is a pathogenic protozoan that is ubiquitously found in the environment. It can cause Acanthamoeba keratitis, which commonly occurs in contact lens users [1]. There are several antimicrobial agents such as chlorhexidine gluconate polyhexamethylene biguanide that have been used to treat the disease but according to Vontobel et al. [2], both agents do not readily penetrate the cornea of the eyes, which require months of topical administration, making them ineffective for keratitis treatment. Reports showed resistance of Acanthamoeba towards these antiseptics, especially during the later stage of infection, which makes it difficult to be treated [3]. Therefore, the development of new potential antiamoebic agents is demanded to overcome these problems. Thiourea, an organosulfur compound has been reported to contain diverse biomedical benefits such as antibacterial, anticancer, antifungal, antiinflammatory, antithyroid, herbicidal, antitubercular properties [4, 5, 6]. Naz et al. evaluated the antibacterial activity of thiourea derivatives and found that these compounds significantly inhibited several pathogenic bacteria including E. faecalis, P. aeruginosa, S. typhi, and K. pneumoniae [7]. In another study, Keche and Kemble also reported the antimicrobial activity of novel thiourea compounds against several selected bacteria and fungi and they revealed that these compounds have promising antimicrobial activity [8]. Nevertheless, there is still lacking literature regarding the anti-amoebic properties of thiourea derivatives on Acanthamoeba. Therefore, a cytotoxicity test was conducted in this study to

determine the lC<sub>50</sub> values for the newly synthesized thiourea derivatives on *Acanthamoeba*.

A QSAR study was applied to analyze the molecular structures of the synthesized compounds to correlate with their anti-amoebic activities and allow for the effects of compounds of interest to be predicted [9]. In this study, QSAR methods were used to quantitatively study the relationship between the presented synthesized carbonyl thiourea analogs with their antiamoebic activity. The approach applied multiple linear regression (MLR) and partial least square (PLS) to build the QSAR equation models. Conventional stepwise methods and genetic algorithm (GA) were employed to choose the best descriptors subset in the model development. Internal and external validations were carried out to evaluate the robustness of the generated models. From the information gained in this study, optimized thiourea-based compounds that work best against pathogenic Acanthamoeba could be predicted and developed as new agents to treat Acanthamoeba keratitis.

#### **Materials and Methods**

In this study, a set of carbonyls thiourea derivatives consisting of 40 compounds were synthesized and characterized at the Faculty of Science and Marine Environment, Universiti Malaysia Terengganu. These synthesized thiourea derivatives were confirmed by spectral studies of Fourier Transformation Infrared (FT-IR) spectroscopy and <sup>1</sup>H and <sup>13</sup>C Nuclear Magnetic Resonance (NMR). The preparation of M1–M44 compounds is based on the synthesis method of the previous study with additions of compounds

labeled as M7, M8, M25, and M26 attained from the same work [10]. The other synthesized thiourea and

their molecular weights are listed in Table 1.

Table 1. Molecular structures of the newly-synthesized carbonyl thiourea derivatives

Code	Chemical Name	Molecular Weight	Structure
M1	2-(3-benzoyl thioureido)-3- mercapto propanoic acid	284.35	HO NH
M2	2-(3-benzoyl thioureido)-4- (methylthio)butanoic acid	312.41	HO S NH
M3	2-(3-benzoyl thioureido)-3-(4-hydroxyphenyl)propanoic acid	344.38	HO NH
M4	2-(3-benzoyl thioureido)succinic acid	296.30	HO S NH
M5	1-(benzoyl carbamothioyl) pyrrolodine-3-carboxyl acid	278.33	S NH
M6	2-(3-benzoyl thioureido)-3-methyl pentanoic acid	294.37	HO-ONH
M7	2-(3-benzoyl thioureido)propanoic acid	252.29	HO-NH [8]
M8	3-(3-benzoyl thioureido)propanoic acid	252.29	NH [8]
M9	3-[3-(3-methylbenzoyl) thioureido] propanoic acid	266.32	HO SNH
M10	2-[3-(3-methylbenzoyl) thioureido] acetic acid	252.29	THE SOH
M11	3-hydroxy-2-[3-(3- methylbenzoyl) thioureido]propanoic acid	282.32	H H OOH
M12	2-[3-(2- methylbenzoyl)thioureido] acetic acid	252.29	H N O OH
M13	2-(3-furan-2-carbonyl thioureido) acetic acid	228.23	HO N N N

Table 1 (cont'd). Molecular structures of the newly-synthesized carbonyl thiourea derivatives

Code	Chemical Name	Molecular Weight	Structure
M14	2-[3-(4-methylbenzoyl) thioureido]-3-phenylpropanoic acid	342.41	T H H H H H H H H H H H H H H H H H H H
M15	5-amino-2-[3-(4-methylbenzoyl) thioureido]-5-oxopentanoic acid	323.37	HN S H <sub>2</sub> N O
M16	2-[3-(4-methylbenzoyl) thioureido] propanoic acid	266.32	Т
M17	3-hydroxy-2-[3-(4- methylbenzoyl) thioureido]propanoic acid	282.32	HO N N N
M18	3-methyl-2-[3-(4-methylbenzoyl) thioureido]butanoic acid	294.37	N SHO O
M19	2-[3-(2-methylbenzoyl) thioureido] propanoic acid	266.32	H H OH
M20	3-hydroxy-2-[3-(2- methylbenzoyl) thioureido]butanoic acid	296.34	S HO OH
M21	3-hydroxy-2-[3-(4- methylbenzoyl) thioureido]butanoic acid	296.34	N N OH
M22	<i>N</i> -(3-fluorophenyl)- <i>N</i> '-phenylacetyl thiourea	288.34	S NH
M23	N-phenyl- $N$ '-phenylacetyl thiourea	270.35	
M24	N-(2,4-dimethylphenyl)- $N$ '-phenyl acetylthiourea	298.40	HN
M25	<i>N</i> -(2-chlorophenyl)- <i>N</i> '-(4-chlorobutanoyl) thiourea	291.20	SNH CI
M26	<i>N</i> -(3-chlorophenyl)- <i>N</i> '-(4-chlorobutanoyl) thiourea	291.20	ci—NH—Ci[8]
M27	<i>N</i> -(3-chlorophenyl)- <i>N</i> '- (biphenyl-4-yl) carbamoyl thiourea	366.86	HN-S

Table 1 (cont'd). Molecular structures of the newly-synthesized carbonyl thiourea derivatives

Code	Chemical Name	Molecular Weight	Structure
M28	N-(2,6-diethylphenyl)-N'- (biphenyl-4-yl)carbamoyl thiourea	388.53	HN S
M29	<i>N</i> -(2-chlorophenyl)- <i>N</i> '-(2-ethyl hexanoyl) thiourea	312.86	
M30	<i>N</i> -(3-chlorophenyl)- <i>N</i> '-(2-ethyl hexanoyl) thiourea	312.86	NH C
M31	N-(2,5-dichlorophenyl)- $N$ '-(2-ethyl hexanoyl) thiourea	347.40	CI NH NH CI S
M32	<i>N</i> -(3-fluorobenzoyl)- <i>N</i> '-(2-fluoro phenyl) thiourea	292.30	NH NH F
M33	<i>N</i> -(3-fluorobenzoyl)- <i>N</i> '-(3-fluoro phenyl) thiourea	292.30	F N N F
M34	<i>N</i> -(3-fluorobenzoyl)- <i>N</i> '-(4-fluoro phenyl) thiourea	292.30	F N N N N N N N N N N N N N N N N N N N
M35	<i>N</i> -(3-fluorobenzoyl)- <i>N</i> '-(2-chloro phenyl) thiourea	308.76	N NH CI
M36	<i>N</i> -(3-fluorobenzoyl)- <i>N</i> '-(3-chloro phenyl) thiourea	308.76	F N H H CI
M37	<i>N</i> -(3-fluorobenzoyl)- <i>N</i> '-(4-chloro phenyl) thiourea	308.76	F N S CI
M38	<i>N</i> -(3-fluorobenzoyl)- <i>N</i> '-(2-ethyl phenyl) thiourea	302.37	O NH H
M39	<i>N</i> -(3-fluorobenzoyl)- <i>N</i> '-(3-ethyl phenyl) thiourea	302.37	F N N
M40	<i>N</i> -(3-fluorobenzoyl)- <i>N</i> '-(2-bromo phenyl) thiourea	353.21	NH H HBr
M41	<i>N</i> -(3-fluorobenzoyl)- <i>N</i> '-(3-bromo phenyl) thiourea	353.21	F N H H Br
M42	<i>N</i> -(3-fluorobenzoyl)- <i>N</i> '-(2,6-diethyl phenyl) thiourea	330.42	
M43	<i>N</i> -(3-fluorobenzoyl)- <i>N</i> '-(4-ethyl phenyl)thiourea	302.37	F N N N
M44	<i>N</i> -(4- <i>tert</i> -butylbenzoyl)- <i>N</i> '-diethyl phenyl thiourea	292.44	HN S

#### Determination of IC<sub>50</sub> values

Thiourea derivatives were prepared and chlorhexidine gluconate (Raza Manufacturing, Malaysia) was used as the positive control whereas 10<sup>4</sup> cells/mL of healthy Acanthamoeba sp. without any treatment was used as the negative control [10]. The plates were incubated at 30°C for 72 hours. After incubation, the staining process was performed using the eosin dye method [11]. The absorbance was measured at 490 nm using an ELISA plate reader (Tecan, Australia). The readings were plotted in GraphPad Prism software (version 5.03) (San Diego, USA) to give a non-linear sigmoidal dose-response curve in which the cytotoxicity study was expressed as 50% cytotoxic dose (IC<sub>50</sub>). T-test (SPSS, version 11.5, USA) was used to compare mean values between untreated and treated cultures, and p < 0.05 is considered statistically significant.

#### Data set selection for QSAR study

The data set that contains thiourea derivatives with anti-amoebic activity is shown in Table 2. The IC<sub>50</sub> values in the molar (M) unit were converted to pIC<sub>50</sub> for the convenience of computational work. The data were divided into training and test set. The training set is comprised of 30 thiourea compounds while the test set consisted of the remaining 14 compounds. Compound M7 was later removed from the data set as it was detected to be an outlier throughout the model building by all selected methods of stepwise multiple linear regression (stepwise-MLR), genetic algorithm multiple linear regression (GA-MLR), and genetic algorithm partial least square (GA-PLS).

Table 2. Functional groups of carbonyl thiourea analogs with their anti-amoebic activity

Code	$\mathbf{R}_1$	R <sub>2</sub>	IC50 (µM)	pIC <sub>50</sub> (M)
M1	C <sub>4</sub> H <sub>8</sub> O <sub>2</sub> S	C <sub>8</sub> H <sub>8</sub> O	9.00	5.05
M2	$C_6H_{12}O_2S$	$C_8H_8O$	8.63	5.06
M3	$C_{10}H_{12}O_3$	$C_8H_8O$	9.65	5.02
M4	$C_5H_8O_4$	$C_8H_8O$	13.35	4.87
M5	$C_5H_{10}O_2$	$C_8H_8O$	11.06	4.96
M6	$C_7H_{14}O_2$	$C_8H_8O$	13.24	4.88
M7	$C_4H_8O_2$	$C_8H_8O$	10.85	4.97
M8	$C_4H_8O_2$	$C_8H_8O$	11.59	4.94
M9	$C_4H_8O_2$	$C_9H_{10}O$	19.26	4.72
M10	$C_9H_{10}O$	$C_3H_6O_2$	22.35	4.65
M11	$C_9H_{10}O$	$C_4H_8O_3$	18.52	4.73
M12	$C_9H_{10}O$	$C_3H_6O_2$	19.58	4.71
M13	$C_3H_6O_2$	$C_6H_6O_2$	20.16	4.70
M14	$C_9H_{10}O$	$C_{10}H_{12}O_2$	14.47	4.84
M15	$C_9H_{10}O$	$C_6H_{11}NO_3$	17.04	4.80
M16	$C_9H_{10}O$	$C_4H_8O_2$	21.79	4.66
M17	$C_9H_{10}O$	$C_4H_8O_3$	18.75	4.73
M18	$C_9H_{10}O$	$C_6H_{12}O_2$	17.20	4.76
M19	$C_9H_{10}O$	$C_4H_8O_2$	19.95	4.70
M20	$C_9H_{10}O$	$C_5H_{10}O_3$	15.58	4.81
M21	$C_9H_{10}O$	$C_5H_{10}O_3$	16.18	4.79

Table 2 (cont'd). Functional groups of carbonyl thiourea analogs with their anti-amoebic activity

Code	$\mathbf{R_1}$	$\mathbb{R}_2$	IC <sub>50</sub> (µM)	pIC <sub>50</sub> (M)
M22	C <sub>9</sub> H <sub>10</sub> O	C <sub>7</sub> H <sub>7</sub> F	14.65	4.83
M23	$C_9H_{10}O$	$C_7H_8$	19.47	4.71
M24	$C_9H_{10}O$	C9H12	19.80	4.70
M25	C <sub>5</sub> H <sub>9</sub> ClO	C <sub>7</sub> H <sub>7</sub> Cl	23.84	4.62
M26	C <sub>5</sub> H <sub>9</sub> ClO	C <sub>7</sub> H <sub>7</sub> Cl	26.81	4.57
M27	$C_{14}H_{12}O$	$C_7H_7C1$	16.31	4.79
M28	$C_{14}H_{12}O$	$C_{11}H_{16}$	14.14	4.85
M29	$C_9H_{18}O$	C <sub>7</sub> H <sub>7</sub> Cl	20.93	4.68
M30	$C_9H_{18}O$	C <sub>7</sub> H <sub>7</sub> Cl	21.52	4.67
M31	$C_9H_{18}O$	$C_7H_6Cl_2$	18.62	4.73
M32	$C_8H_7FO$	$C_7H_7F$	23.46	4.63
M33	$C_8H_7FO$	$C_7H_7F$	22.28	4.65
M34	$C_8H_7FO$	$C_7H_7F$	20.91	4.68
M35	$C_8H_7FO$	C <sub>7</sub> H <sub>7</sub> Cl	20.78	4.68
M36	$C_8H_7FO$	$C_7H_7C1$	20.23	4.69
M37	$C_8H_7FO$	$C_7H_7C1$	20.03	4.70
M38	$C_8H_7FO$	$C_9H_{12}$	19.74	4.70
M39	$C_8H_7FO$	$C_9H_{12}$	19.29	4.72
M40	$C_8H_7FO$	$C_7H_7Br$	18.41	4.74
M41	$C_8H_7FO$	$C_7H_7Br$	17.98	4.75
M42	$C_8H_7FO$	$C_{11}H_{16}$	19.02	4.72
M43	$C_8H_7FO$	$C_9H_{12}$	20.93	4.68
M44	$C_{12}H_{16}O$	$C_5H_{12}$	21.55	4.67

#### Structure entry and molecular modeling

Structure entry and molecular modeling were first carried out by acquiring a three-dimensional (3D) representation of the thiourea derivative molecules. The compounds' two-dimensional (2D) molecular structures were generated using ChemDraw Ultra (version 10.0). The structures were then converted to 3D structures using Chem3D Ultra 10.0. The 3D molecules of thiourea compounds were analyzed with the MM2 method and MOPAC (Chem3D Ultra 10.0) at default settings to acquire stable molecular structures with the lowest energy.

#### **Descriptors** generation

A total of 1661 molecular descriptors of optimized thiourea molecules were computed with DRAGON software (version 5.2). In this analysis, only 0D, 1D,

and 2D descriptors were used while the 3D descriptors were excluded since molecular structures of the compounds were not uniformly aligned.

#### **Feature selection**

The descriptors that did not contain relevant information for the model development were eliminated from the set. The next step was to find the best subset from the remaining descriptors. Stepwise multiple regression and Genetic Algorithm (GA) were used in this step using MATLAB version 7.6.0 (The Mathworks Inc.) software with PLS Toolbox version 5.2.2 (Eigenvector Research Inc.). Meanwhile, Genetic Algorithm GUI [genalg] function was used for GA selection.

sp.

#### Model development

For the model development, routines were performed in MATLAB with PLS Toolbox whereby MLR and PLS analyses were applied. The approaches for modeling utilize integrated stepwise with MLR (stepwise-MLR), GA with MLR (GA-MLR) and GA with PLS (GA-PLS). Statistical significance of the final model was characterized by the squared correlation coefficient,  $r^2$ , root mean square error of calibration, RMSEC, and root mean square error of cross validation, RMSECV. The obtained outputs were converted [regcon] to equation models. The regression coefficient in the equation indicates the significance of an individual descriptor. A plot of predicted versus experimental activity was evaluated to examine the goodness of fit for the generated models. A plot of residuals versus predicted values was used to detect outliers in the data set.

#### Model validation

The model validation process was also conducted by MATLAB with the PLS toolbox. Both internal and external validations were conducted in this study. Cross-validation by the leave-one-out (LOO) method was applied to provide a rigorous internal check on the built models. This validation process was accomplished by validating the models from their statistical outputs of cross validated squared correlation coefficient  $r_{cv}^2$ , squared correlation coefficient of test set,  $r^2_{test}$  and root mean square error of prediction, RMSEP. Data scrambling technique by the y-randomization test was performed to ensure that the constructed models were not the result of mere chance correlations. On the other hand, external validation was also performed involving the prediction of activity for compounds from the test set.

#### **Results and Discussion**

## Inhibition concentration for half of cells population (IC<sub>50</sub> values)

Thiourea derivatives that exhibited the best antiamoebic activity were 2-(3-benzoylthioureido)-3mercaptopropanoic acid and 2-(3-benzoylthioureido)-4-(methylthio)butanoic acid labeled as M1 and M2, respectively. These two thiourea compounds showed the lowest  $IC_{50}$  value suggesting that they provide the best intrinsic anti-amoebic activity. These two compounds are amino acid types of derivatives that could be recognized by the presence of hydroxyl (-COOH) with an amine group in the molecule. In general, all derivatives of amino acid groups in this study showed lower IC50 values compared to other compounds in the series. This indicates that amino acids could enhance the activity of the thiourea derivatives. Xu et al. [12] supported this finding by highlighting that in general, amino acid derivatives of the compounds could exhibit a variety of biological properties. Meanwhile, Hauck et al. [13] emphasized that amino acid derivatives in the compounds contribute to a hydrophilic moiety, which gives high selectivity toward receptors. Ibrahim et al. [8] that came out with thiourea derivatives labeled as M7, M8, M25, and M26 also suggested that the mechanism of action for the proposed thiourea derivatives toward the protozoan parasite Acanthamoeba should focus on the hydrophobicity of thiourea molecules to explain their actions. The suggested drug-receptors for the compounds' main target in the amoeba cells are the transport proteins that are distributed throughout the cell membrane.

Chlorhexidine gluconate was used as a positive control as it is a general biocidal effective against a wide variety of microorganisms [14]. The chlorhexidinetreated amoeba in the experiment exhibited a slightly lower IC<sub>50</sub> of 6.30  $\pm$  0.49  $\mu M$ . From the T-test analysis, absorbance readings from the untreated and treated cells showed statistical significance (p < 0.05). Thiourea in its basic structure has one sulfur atom. A sulfur atom has six valence electrons, and its electronic configuration is similar to oxygen [15]. Most sulfurcontaining organics exhibit a low order of toxicity. However, their toxicity may be enhanced by substitution in the molecules. Patnaik [16] explained that an -SH group attached to a benzene ring imparts greater toxicity to the molecule than that attached to an alkyl group. Therefore, the thiourea derivatives were synthesized with at least one benzene ring as an attachment in this study with an attempt to increase their activity on the tested cells.

Table 3. IC<sub>50</sub> values of 45 carbonyl thiourea derivatives compound on *Acanthamoeba* sp.

Code	Chemical Name	$IC_{50}\mu g/mL$
M1	2-(3-benzoylthioureido)-3-mercaptopropanoic acid	$2.56 \pm 0.46$
M2	2-(3-benzoylthioureido)-4-(methylthio)butanoic acid	$2.70\pm0.27$
M3	2-(3-benzoylthioureido)-3-(4-hydroxyphenyl)propanoic acid	$3.32 \pm 0.18$
M4	2-(3-benzoylthioureido)succinic acid	$3.96 \pm 0.26$
M5	1-(benzoylcarbamothioyl)pyrrolodine-3-carboxyl acid	$3.08\pm0.34$
M6	2-(3-benzoylthioureido)-3-methylpentanoic acid	$3.90\pm0.20$
M7	2-(3-benzoylthioureido)propanoic acid	$2.74 \pm 0.42$
M8	3-(3-benzoylthioureido)propanoic acid	$2.92\pm0.24$
M9	3-[3-(3-methylbenzoyl)thioureido]propanoic acid	$5.13 \pm 0.59$
M10	2-[3-(3-methylbenzoyl)thioureido]acetic acid	$5.64 \pm 0.63$
M11	3-hydroxy-2-[3-(3-methylbenzoyl)thioureido]propanoic acid	$5.23 \pm 0.41$
M12	2-[3-(2-methylbenzoyl)thioureido]acetic acid	$4.94 \pm 0.20$
M13	2-(3-furan-2-carbonylthioureido) acetic acid	$4.60\pm0.61$
M14	2-[3-(4-methylbenzoyl)thioureido]-3-phenylpropanoic acid	$4.95 \pm 0.49$
M15	5-amino-2-[3-(4-methylbenzoyl)thioureido]-5-oxopentanoic acid	$5.51 \pm 0.47$
M16	2-[3-(4-methylbenzoyl)thioureido]propanoic acid	$5.80 \pm 0.20$
M17	3-hydroxy-2-[3-(4-methylbenzoyl)thioureido]propanoic acid	$5.29 \pm 0.10$
M18	3-methyl-2-[3-(4-methylbenzoyl)thioureido]butanoic acid	$5.06 \pm 0.40$
M19	2-[3-(2-methylbenzoyl)thioureido]propanoic acid	$5.31 \pm 0.22$
M20	3-hydroxy-2-[3-(2-methylbenzoyl)thioureido]butanoic acid	$4.62\pm0.43$
M21	3-hydroxy-2-[3-(4-methylbenzoyl)thioureido]butanoic acid	$4.80\pm0.48$
M22	<i>N</i> -(3-fluorophenyl)- <i>N</i> '-phenylacetylthiourea	$4.23 \pm 0.95$
M23	<i>N</i> -phenyl- <i>N</i> '-phenylacetylthiourea	$5.26 \pm 0.55$
M24	N-(2,4-dimethylphenyl)- $N$ '-phenylacetylthiourea	$5.91 \pm 0.51$
M25	<i>N</i> -(2-chlorophenyl)- <i>N</i> '-(4-chlorobutanoyl)thiourea	$6.94 \pm 0.79$
M26	<i>N</i> -(3-chlorophenyl)- <i>N</i> '-(4-chlorobutanoyl)thiourea	$7.81 \pm 0.34$
M27	<i>N</i> -(3-chlorophenyl)- <i>N</i> '-(biphenyl-4-yl)carbamoylthiourea	$5.98 \pm 0.79$
M28	<i>N</i> -(2,6-diethylpehnyl)-N'-(biphenyl-4-yl)carbamoylthiourea	$5.49 \pm 0.38$
M29	N-(2-chlorophenyl)-N'-(2-ethylhexanoyl)thiourea	$6.55 \pm 0.56$
M30	N-(2-chlorophenyl)-N'-(2-ethylhexanoyl)thiourea	$6.73 \pm 0.30$
M31	<i>N</i> -(2,5-dichlorophenyl)- <i>N</i> '-(2-ethylhexanoyl)thiourea	$6.47 \pm 0.70$
M32	<i>N</i> -(3-fluorobenzoyl)- <i>N</i> '-(2-fluorophenyl)thiourea	$6.86 \pm 0.36$
M33	<i>N</i> -(3-fluorobenzoyl)- <i>N</i> '-(3-fluorophenyl)thiourea	$6.51 \pm 0.27$
M34	N-(3-fluorobenzoyl)-N'-(4-fluorophenyl)thiourea	$6.11 \pm 0.17$
M35	<i>N</i> -(3-fluorobenzoyl)- <i>N</i> '-(2-chlorophenyl)thiourea	$6.42\pm0.28$
M36	N-(3-fluorobenzoyl)-N'-(3-chlorophenyl)thiourea	$6.25\pm0.35$
M37	N-(3-fluorobenzoyl)-N'-(4-chlorophenyl)thiourea	$6.18 \pm 0.32$
M38	<i>N</i> -(3-fluorobenzoyl)- <i>N</i> '-(2-ethylphenyl)thiourea	$5.97 \pm 0.63$
M39	<i>N</i> -(3-fluorobenzoyl)- <i>N</i> '-(3-ethylphenyl)thiourea	$5.83 \pm 0.49$
M40	<i>N</i> -(3-fluorobenzoyl)- <i>N</i> '-(2-bromophenyl)thiourea	$6.50\pm0.52$
M41	<i>N</i> -(3-fluorobenzoyl)- <i>N</i> '-(3-bromophenyl)thiourea	$6.35\pm0.71$
M42	<i>N</i> -(3-fluorobenzoyl)- <i>N</i> '-(2,6-diethylphenyl)thiourea	$6.29 \pm 0.21$

Table 3 (cont'd). IC<sub>50</sub> values of 45 carbonyl thiourea derivatives compound on *Acanthamoeba* sp.

Code	Chemical Name	IC <sub>50</sub> μg/mL
M43	N-(3-fluorobenzoyl)-N'-(4-ethylphenyl)thiourea	$6.33 \pm 0.44$
M44	<i>N</i> -(4- <i>tert</i> -butylbenzoyl)- <i>N</i> '-diethylphenylthiourea	$6.30\pm0.59$
M45	N-(3-fluorobenzoyl)- $N$ '-(2-chlorophenyl)thiourea	$6.42\pm0.28$

#### **QSAR** study

QSAR utilizes linear regression of statistical analysis to build mathematical equation models, which could elucidate the relationship for molecular structures of the compounds with their potential biological activities. QSAR will also help to create a preliminary hypothesis regarding the mechanism of action by investigating the compounds on a particular biological system. Through this approach, it is assumed that the compounds that fit in a QSAR model are acting with the same mechanism of action [17].

### Development of QSAR model by stepwise-multiple linear regression (stepwise-MLR) analysis

In order to build a QSAR model, feature selection was primarily conducted to discard unnecessary variables from the pool of 202 descriptors. Stepwise multiple regression chose 7 descriptors that fit best with the equation model, which were MATS1m, GATS5m, GATS3e, ESpm01d, ESpm05d, JGI1, and JG12. To avoid the overfitting problem, the proportion of the descriptors to the compound was maintained in a 5:1 ratio of the thumb rule. The descriptors set were maintained to contain five or fewer variables that contain the best information to represent the model.

This was done by single exclusion practice of each variable from the selected obtained descriptors. The variables were tested for their significance by removing each one of them and their predictive power was tested each time by using the proposed model. From this technique, two variables, GATS5m and GATS3e, were found to be insignificant for the model and were removed. From the verification by correlation matrix, a high degree of correlation was found between descriptor ESpm01d and ESpm05d with a value of > 0.8. ESpm05d was chosen from the two since it was more significant by giving a statistically better model with higher predictive ability. The regression model was constructed with four descriptors namely MATS1m, ESpm05d, JGI1, and JGI2. According to Hadanu et al. [18], the best model could be selected based on the value of correlation coefficient (r), squared correlation coefficient  $(r^2)$ , Standard Error of Estimation (SE), degree of freedom (F) or Predictive Residual Sum of Square (PRESS). Frimayanti et al. [19] proposed that the accepted value range for QSAR models is  $r^2 > 0.6$  and  $r^2_{cv} > 0.5$ . The final statistical output for the generated model of stepwise-MLR is shown in Table 4.

Table 4. Statistics for a model developed using the stepwise-MLR method

Statistical Output	Value	
$r^2$	0.732	
$r^2_{cv}$	0.522	
RMSEC	0.058	
RMSECV	0.080	

 $r^2$  = squared correlation coefficient;

*RMSEC*= root mean square error of calibration;

RMSECV= root mean square error of cross validation

 $r^2_{cv}$  = cross validated squared correlation coefficient;

Based on the statistical evaluation, high  $r^2$  and  $r^2_{cv}$  values with very low *RMSEC* and *RMSECV* indicate that the constructed model is statistically robust to predict the activity of other compounds outside the training set. This statistical outcome shows that the model is capable to elucidate 73.2% of the variance in anti-amoebic activity.

The final QSAR equation model given by the stepwise-MLR method is shown in Equation 1.

The generated regression model shows the order of significance for used descriptors is as follow: ESpm05d > JGI1 > MATS1m > JGI2. The observed and calculated or predicted activity by using this model was compared and it showed that the predicted pIC<sub>50</sub> values did not greatly differ from the pIC<sub>50</sub> values obtained from the ex periments with residual values less than 0.95. The observed values are in the range of 4.57 to 5.05 M while the predicted values range from 5.50 to 5.54 M.

$$pIC_{50} = -0.0145*MATS1m + 0.1013*ESpm05d - 0.0733*JGI1 - 0.0090*JGI2 + 4.7592$$
 (1)

### Validation of QSAR regression model from stepwise multiple linear regression (stepwise-MLR)

The statistical output of model validation is shown in Table 5. It proves that the developed model has a high predictive ability. It was given that  $r^2_{test}$  was 0.739, which is above 0.5 with an *RMSEP* value of 0.062, which is low enough for roots mean square error of prediction.

The built of the QSAR models must be properly validated prior to use for interpreting and predicting biological responses of non-investigated compounds. Qin et al. [20] emphasized the importance of vigorous validation of QSAR models despite the high fitting accuracy for the training set and apparent mechanistic appeal. The model equation was later used to predict thiourea analogs' anti-amoebic activity in the test set data. The comparison showed that the observed values

are in the range of 4.63 to 5.05 M. Meanwhile, the range of the predicted values was 5.49 to 5.56 M. The residuals obtained gave values less than 0.90. This indicates the robustness and high predictive power of the built model. The robustness of a QSAR model should be also validated by a v-randomization test to ensure that the statistical output in the original model, which gave high  $r^2$  and  $r^2_{cv}$  values, were not merely from a chance correlation or structural dependency of the training set. If a true QSAR relationship existed with the real dependent variable, the results for the y-random runs should be very low [21]. Yrandomization test was run 20 times and gave  $r^2$  values between 0.052 to 0.233, which shows low  $r^2$  and  $r^2_{test}$ (Table 6). Thus, it is concluded that the generated model by stepwise-MLR was not obtained from a random chance of correlation.

Table 5. Statistics of prediction for stepwise-MLR model

Statistical Output	Value
$r^2_{test}$	0.739
RMSEP	0.062

 $r^2_{test}$  = correlation coefficient of test; RMSEP= root mean square error of prediction Maizatul Akma et al: QUANTITATIVE STRUCTURE-ACTIVITY RELATIONSHIP (QSAR) STUDY OF NEWLY SYNTHESIZED CARBONYL THIOUREA DERIVATIVES ON *Acanthamoeba* sp.

Table 6.	Y- randomization test of stepwise-MLR model

Iteration	$r^2$	$r^2_{test}$	Iteration	$r^2$	$r^2_{test}$
1	0.055	0.016	11	0.181	0.052
2	0.180	0.010	12	0.248	0.034
3	0.143	0.083	13	0.152	0.007
4	0.059	0.007	14	0.147	0.042
5	0.089	0.146	15	0.089	0.334
6	0.182	0.011	16	0.060	0.015
7	0.055	0.034	17	0.110	0.233
8	0.052	0.006	18	0.233	0.004
9	0.129	0.115	19	0.082	0.025
10	0.182	0.003	20	0.141	0.001

 $r^2$  = squared correlation coefficient;

### Development of QSAR model by genetic algorithm multiple linear regression (GA-MLR) analysis

The regression model was constructed with five descriptors namely RBN, MATS2m, EEig07x, JGI1, and N-070. The correlation matrix was investigated to detect highly correlated variables that would be less important for the model, which detected 135 that represents ESpm05d to be highly correlated with 198, representing N-070 by giving a value higher than 0.80 from the correlation matrix. The analysis was executed again to find out which variable was more significant than others by removing each of them from the model. The final analysis concluded that N-070 was more significant compared to ESpm05d and, therefore, it was included in the model. The statistical output of the final model is shown in Table 7. Statistical result of the constructed GA-MLR model shows a high  $r^2$  value that concludes the equation could explain 84.8% of the variance in the compounds' activity. Meanwhile,  $r^2_{cv}$  is also quite high with a value of 0.767. RMSEC and RMSECV obtained are very low with values of 0.044 and 0.055, respectively. The statistical output shows

that the GA-MLR method was a good technique to obtain a good model. This result also proves that the hybrid GA-MLR approach produced a better QSAR model compared to the stepwise-MLR method for this study.

The final QSAR equation model of the GA-MLR method is elaborated in Equation 2 in which it shows a significant order of the five selected variables as follows; N-070 > MATS2m > JGI1 > EEig07x > RBN. The variables of MATS2m, JGI1, and N-070 were shown to work reversibly with pIC50 while RBN and EEig07x both worked positively with pIC50. The predicted pIC50 values were compared to the experimental data. The data revealed that the predicted values ranging from 4.93 to 5.21 M and the experimental values ranging from 4.57 to 5.05 M. Low residual values in the range of less than 0.55 from the activity prediction proves that the constructed model was robust.

$$pIC_{50} = 0.0301*RBN - 0.0576*MATS2m + 0.0445*EEig07x - 0.0529*JGI1 - 0.0896*N-070 + 4.7602$$
 (2)

 $r^2_{test}$  = correlation coefficient of test

Table 7. Statistics for the model developed using GA-MLR method

Statistical Output	Value
$r^2$	0.848
$r^2_{cv}$	0.767
RMSEC	0.044
RMSECV	0.055

 $r^2$  = squared correlation coefficient;

### Validation of QSAR regression model from genetic algorithm multiple linear regression (GA-MLR)

The statistical result in Table 8 confirms the robustness of the generated GA-MLR model with acceptable values of  $r^2_{test}$  and RMSEP. Tropsha et al. [22] suggested that a proposed QSAR model is considered predictive if it satisfies the condition of  $r^2_{test} > 0.6$ . The predicted pIC<sub>50</sub> values were compared to the experimental data. The predicted values ranged from 4.92 to 5.20 M and the experimental values ranged from 4.63 to 5.06 M. The residuals gave values less

than 0.45 suggesting that the model is robust and has high predictive power.

Validation by y-randomization was run 20 times and the test showed that the squared correlation coefficient,  $r^2$  were in the range of 0.004 to 0.300 (Table 9). The difference between randomized models compared to the original GA-MLR statistical representation was significant. Therefore, this proves that chance correlation was negligible in the model development.

Table 8. Statistics of prediction for GA-MLR model

Statistical Output	Value	
$r^2_{test}$	0.777	
RMSEP	0.057	

 $r^2_{test}$  = correlation coefficient of test;

*RMSEP*= root mean square error of prediction

Table 9. Y- randomization test of GA-MLR model

Iteration	r <sup>2</sup>	r <sup>2</sup> test	Iteration	r <sup>2</sup>	$r^2_{test}$
1	0.151	0.008	11	0.227	0.457
2	0.047	0.240	12	0.176	0.288
3	0.233	0.099	13	0.226	0.064
4	0.130	0.113	14	0.127	0.122
5	0.046	0.066	15	0.212	0.126

 $r^2_{cv}$  = cross validated squared correlation coefficient;

*RMSEC*= root mean square error of calibration;

RMSECV= root mean square error of cross validation

Table 9 (cont'd). Y-1	randomization test of	GA-MLR model
-----------------------	-----------------------	--------------

Iteration	$r^2$	$r^2_{test}$	Iteration	$r^2$	$r^2_{test}$
6	0.167	0.015	16	0.218	0.045
7	0.087	0.051	17	0.083	0.081
8	0.176	0.002	18	0.230	0.010
9	0.068	0.143	19	0.215	0.001
10	0.300	0.002	20	0.004	0.195

 $r^2$  = squared correlation coefficient;

### Development of QSAR model by genetic algorithm partial least square (GA-PLS) analysis

The third method of QSAR in this study applied GA in combination with the PLS technique. The selected variables used MATS2m, MATS3m, EEig09d, JGI6, and N-070. The correlation matrix of the selected variables showed that no higher correlation than 0.8 for the variables was used hence this explains the consistency to be used in the model. The statistical output for the GA-PLS model is shown in Table 10. The statistical result proves the reliability of the built

QSAR model from GA-PLS regression with squared correlation coefficient,  $r^2$  of 0.827 and cross-validated,  $r^2_{cv}$  of 0.682. This result is in accordance with a study by Edraki et al. [23] in QSAR analysis of 3,5-bis (arylidene)-4-piperidone derivatives in cytotoxicity models. The statistical output using the GA-PLS model revealed the  $r^2$  of 0.86 and  $r^2_{cv}$  of 0.66. The model also gave low root mean square error values for *RMSEC* and *RMSECV*.

Table 10. Statistics for the model developed using the GA-PLS method

Statistical Output	Value
$r^2$	0.827
$r^2_{cv}$	0.682
RMSEC	0.047
RMSECV	0.064

 $r^2$  = squared correlation coefficient;

*RMSEC*= root mean square error of calibration;

*RMSECV*= root mean square error of cross validation.

This statistical output of the model proves to be able to explain 82.7% of the variance in the experimental activity and  $r^2_{cv}$ , which manifests good predictive ability. The best combination of a selected variable by the GA-PLS method is illustrated in Equation 3.

The order of variables are as follows; EEig09d > N-070 > JGI6 > MATS2m > MATS3m in which this QSAR model was used to predict the activity of compounds in the training set. The values of calculated

compared to observe activity. The predicted values were in the range of 4.72 to 4.82 M and the experimental values were in the range of 4.63 to 5.06 M. The residuals observed were compared to the predicted values, which were less than 0.25. This explains the robustness of the model. However, the predictive ability of the model was further evaluated in external validation to ensure that the QSAR model also has a good predictive ability for compounds that were not included in the training set.

 $r^2_{test}$  = correlation coefficient of test

 $r^2_{cv}$  = cross validated squared correlation coefficient;

$$pIC_{50} = -0.0457*MATS2m + 0.0242*MATS3m + 0.0638* EEig09d - 0.0511*JGI6 - 0.0609*N-070 + 4.7554$$
 (3)

## Validation of QSAR regression model from genetic algorithm partial least square (GA-PLS)

The result gave good statistical output with  $r^2_{test}$  and *RMSEP* of 0.790 and 0.051, respectively (Table 10). The robustness of the GA-PLS QSAR model was also assessed through its predictive power for the comparison of the observed to predicted activity. The predicted values were in the range of 4.72 to 4.82 M while the experimental values were in the range of 4.57 to 5.05 M. Small residual with values less than

0.25 proved the robustness of the equation model, which could be used to predict other compounds that were not included in the model development. The test of y-randomization was run 20 times and confirmed that the model does not occur merely by random chance correlation of statistics since it gave low squared correlation coefficients,  $r^2$  in the range of 0.015-0.372 (Table 11).

Table 10. Statistics of prediction for GA-PLS method

Statistical Output	Value
$r^2_{test}$	0.790
RMSEP	0.051

 $r^2_{test}$  = correlation coefficient of test;

*RMSEP*= root mean square error of prediction

Table 11. Y- randomization test of GA-PLS model

Iteration	$r^2$	r <sup>2</sup> test	Iteration	$r^2$	$r^2_{test}$
1	0.078	0.006	11	0.087	0.085
2	0.350	0.158	12	0.055	0.007
3	0.123	0.001	13	0.118	0.008
4	0.084	0.088	14	0.172	0.007
5	0.015	0.004	15	0.210	0.003
6	0.136	0.183	16	0.167	0.090
7	0.026	0.021	17	0.120	0.077
8	0.066	0.021	18	0.148	0.088
9	0.372	0.148	19	0.079	0.001
10	0.074	0.010	20	0.041	0.016

 $r^2$  = squared correlation coefficient;

#### Comparisons of constructed QSAR models

QSAR mathematical models from three different techniques namely stepwise-MLR, GA-MLR, and GA-PLS were evaluated and compared (Table 12). A

genetic algorithm (GA) is a well-suited approach to the problem of variable selection and optimization. GA performs its optimization by comparing root-mean-square error of cross validation, *RMSECV* of proposed

 $r^2_{test}$  = correlation coefficient of test

models as the measure of fitness [24]. The hybrid approach (GA-MLR) which combines GA with MLR may be useful in the derivation of highly predictive and interpretable QSAR models [17]. Therefore, this approach, as well as the conventional stepwise-MLR technique, was applied in this study. The method of stepwise-MLR gave four selected variables that are well fitted in the equation model. The model gave good statistical output with high  $r^2$  and  $r^2_{cv}$  and low *RMSEC* and *RMSECV*. This indicates that the constructed model has good fitness and is robust. On the other hand, the model obtained from the GA-MLR method contains five descriptors and produced a statistically

better model compared to the stepwise-MLR. This showed that GA-MLR is a good technique to obtain a better QSAR model in this study. However, the weaknesses of using the MLR technique are that the data are often crude, imprecise, and strongly collinear. These imply that this traditional regression technique, which assumes the selected descriptors to be exact and 100% relevant and independent of each other, will not always work well. Thus, in situations where many strongly collinear descriptors and biological responses operate together, data analytical methods, other than the classical MLR techniques, must be used [25].

Table 12. Summary of constructed models

	Stepwise-MLR	GA-MLR	GA-PLS
Statistical output:			
$r^2$	0.732	0.848	0.827
$r^2_{cv}$	0.522	0.767	0.682
RMSEC	0.058	0.044	0.047
RMSECV	0.080	0.055	0.064
$r^2_{test}$	0.739	0.777	0.790
RMSEP	0.062	0.057	0.051
Y-random $(r^2)$	0.055-0.248	0.004-0.300	0.015-0.372
No. of descriptors	4	5	5
Residual in train. set	<u>≤</u> 0.93	$\leq$ 0.54	≤ 0.23
Residual in test set	<u>≤</u> 0.87	$\leq$ 0.42	≤ 0.24
Descriptors:			
1	MATS1m	RBN	MATS2m
2	ESpm05d	MATS2m	MATS3m
3	JGI1	EEig07x	EEig09d
4	JGI2	JGI1	JGI6
5	-	N-070	N-070

 $r^2$  = squared correlation coefficient;

 $r^2_{test}$  = correlation coefficient of test;

 $r^2_{cv}$  = cross validated squared correlation coefficient;

*RMSEC*= root mean square error of calibration;

RMSECV= root mean square error of cross validation

PLS is well suited to overcome overfitting and multicollinearity problems. It has been used to alleviate the effect of multicollinearity and to prevent overfitting by reducing the dimension size [tran 26]. This approach has also successfully come out with a statistically robust model of five variables that were better compared to the model developed from stepwise MLR and GA-MLR techniques based on the predictive ability. PLS also gave much lower residual values in both training and the test set with < 0.23 and < 0.24, respectively compared to the MLR models that gave higher residual values from their prediction. The descriptors or variables, which demonstrate to be important, are those that have been used more than once from the three approaches. It is suggested that these variables namely JGI1, MATS2m, and N-070 are found to be the influential factors and contributors in the models' development for this study and could possibly have a significant role in modulating the antiamoebic activity for the thiourea derivative compounds. These variables are in the groups of topological charge indices, 2D-autocorrelations, and atom centered fragments.

GA, MLR, and PLS were also implemented by many authors in their studies for prediction in highdimensional linear regressions [27,28]. GA is suitable to solve optimization and variable selection problems while MLR yields models that are simpler and easier to interpret compared to PLS because these methods perform regression on latent variables that do not have physical meaning [28]. Due to the co-linearity problem in MLR analysis, one may remove the collinear descriptors before MLR model development. MLR describe equations can the structure-activity relationships but some information will be discarded in the MLR analysis. On the other hand, factor analysisbased methods such as PLS regression can handle the collinear descriptors and, therefore, PLS analysis provides a better analysis with a highly predictive QSAR model [29]. In a previous study, the QSAR model built using PLS and GA-MLR methods showed a remarkable coefficient of determination  $(r^2)$  in predicting the anticholinergic side effects of drugs in lower urinary tract infection (PLS: R<sup>2</sup>=0.808 and GA-MLR:  $R^2 = 0.804$ ) [26]. A series of 3-hydroxypyridine4-one and 3-hydroxypyran-4-one derivatives were subjected to QSAR methods using factor analysis-based multiple linear regression (FA-MLR), principal component regression (PCR), and partial least squares combined with genetic algorithm for variable selection (GA-PLS). The result revealed that GA-PLS showed the most significant QSAR model with 96% and 91% predicted variances in the pIC<sub>50</sub> data (compounds tested against *S. aureus*) [28]. The studies proved that GA-PLS is a reliable QSAR model in predicting the biological activities of chemical compounds based on mathematical and statistical relations.

#### **Descriptors interpretation**

In this study, all applied approaches offered a few similar descriptors or variables for the equations, which are JGI1, MATS2m, and N-070. The finding suggests that they might be the most influential descriptors that contribute to the QSAR models and provide a significant role in the anti-amoebic activity for the thiourea derivatives. Meanwhile, the selected and best QSAR model, which was obtained from the GA-PLS technique, gave 5 variables that include EEig09d, N-070, JGI6, MATS2m, and MATS3m. These variables belong to 2D autocorrelation (Moran autocorrelation lag2/weighted, and -lag3/weighted by atomic masses), edge adjacency indices (Eigenvalue 09 from edge adjacency matrix weighted by dipole moments), topological charge indices (mean topological charge index of order 6), and atom-centered fragment class (Ar-NH-Al). According to Speck-Planche et al. [30], atom-centered fragments are simple molecular descriptors that are defined as the number of specific atom types in a molecule. They are calculated from molecular composition and atom connectivities. Each type of atom in the molecule is described in terms of its neighboring atoms. The atom-centered fragment descriptors have been demonstrated to be very useful descriptors and have been employed in previous QSAR studies. Meanwhile, Viswanadha et al. [31] reported that these atom-centered fragments descriptors provide important information about hydrophobic dispersive interactions, which are involved in biological processes such as transport and distribution of compounds through cells membrane, as well as the information about the compound's receptor interactions. From the variables that have been selected in the model of this study, it could be concluded that the atom-centered fragment plays a major role in providing the information on the thiourea molecules' preliminary penetration into *Acanthamoeba* through the cells membrane.

On the other hand, another representative descriptor or variable selected in the generated model of this study is topological structural descriptors, which are a representation of a molecular structure that arises from the chemical identity of each atom. In this study, two Moran autocorrelation descriptors were used in the descriptors **GA-PLS** model. These describe hydrophobicity scale, average flexibility index, polarizability parameter, the free energy of amino acid solution in water, residue accessible surface area, amino acid residue volume, steric parameters, and relative mutability [32]. In the meantime, physical interpretation of Burden eigenvalues and topological charge indices is difficult because they condense a large amount of structural and property information into a single number [33]. However, these descriptors have been extensively used in medicinal chemistry [34]. Todeschini and Consonni [35] reviewed that due to the relevancy and complexity of amino acid chains and macromolecules, some descriptors were defined to represent amino acid chains and sequences of amino acids. Amino acid properties were modeled for example by connectivity indices, substituent descriptors, charge descriptors, and principal properties. Raychaudury et al. [36] used a topological descriptor to characterize the size and shape of the side chains in the amino acids, which was based on a graphapproach applied to root weighted theoretical molecular graphs with hydrogen included. Substantially, it was relevant with the result obtained from analysis in this study that concentrated on topological descriptors in the model since the thiourea compound series contained 21 amino acids of the side chain of the molecules. Todeschini et al. [37] explained the interpretability of descriptors whereby it is important to take into account that model response is frequently the result of a series of complex biological or physicochemical mechanisms. Therefore, it is very difficult and reductionist to ascribe to the mechanistic

meaning of the selected molecular descriptors in a QSAR model. Furthermore, it must also be highlighted that in multivariate models, even though the interpretation of a singular molecular descriptor can be certainly useful, it is only the combination of a selected set of descriptors that is able to model the studied biological end-point. It was also stressed that in QSAR modeling, attention should be focused on the model quality through its predictive ability.

#### Conclusion

QSAR models were constructed from the obtained IC<sub>50</sub> values of 44 carbonyl thiourea analogues toward *Acanthamoeba* sp. (HKL isolate) ranging from 2.56 to 7.81 μg/mL. Linear regression techniques, stepwise-MLR, GA-MLR, and GA-PLS were applied to build the best QSAR model to correlate the compounds with their anti-amoebic activity. Three equation models were successfully generated with the hybrid GA-PLS approach that gave the best output with a statistically robust model of five variables. Thus, this GA-PLS QSAR model could be applied in the future for the development of a new lead compound based on carbonyl thiourea with optimized anti-amoebic activity to design a new anti-amoebic agent for A*canthamoeba* keratitis disease.

#### Acknowledgement

The authors would like to acknowledge and thank International Islamic University Malaysia (IIUM), Universiti Malaysia Terengganu (UMT), and Universiti Teknologi Malaysia (UTM) for providing the space and facilities to conduct this work. This paper is especially dedicated to the research team, Professor Dr. Nakisah Mat Amin and Professor Mohamed Noor Hasan, who has retired from UMT and UTM.

#### References

 Kang, H., Sohn, H. J Park, A. Y. et al. (2021). Establishment of an *Acanthamoeba* keratitis mouse model confirmed by amoebic DNA amplification. *Scientific Report*, 11: 4183.

- Vontobel, S. F, Abad-Villar, E. M., Kaufmann, C., Zinkernagel, A. S., Hauser, P. C. et al. (2015). Corneal Penetration of Polyhexamethylene Biguanide and Chlorhexidine Digluconate. *Journal of Clinical and Experimental Ophthalmology*, 6: 430.
- Turner, N. A., Russell, A. D., Furr, J. R. and Lloyd, D. (2000). Emergence of resistance to biocides during differentiation of Acanthamoeba castellanii. *Journal of Antimicrobial Chemotherapy*, 46: 27-34.
- Lorenzo-Morales, J., Khan, N. A. and Walochnik, J. (2015). An update on Acanthamoeba keratitis: diagnosis, pathogenesis and treatment. *Parasite*, 22: 10.
- Chen, S., Wu, G. and Zeng, H. (2005). Preparation of high antimicrobial activity chitosan-Ag<sup>+</sup> complex. *Carbohydrate Polymers*, 60: 33-38.
- Alcolea, V., Plano, D., Karelia, D. N., Palop, J. A., Amin, S., Sanmartín, C. et al. (2016). Novel seleno- and thio-urea derivatives with potent in vitro activities against several cancer cell lines. European Journal of Medical Chemistry, 113: 134-144.
- Sadeghian-Rizi, S., Sakhteman, A. and Hassanzadeh, F. (2016). A quantitative structureactivity relationship (QSAR) study of some diaryl urea derivatives of B-RAF inhibitors. Research in Pharmaceutical Sciences, 11(6): 445-453.
- 8. Naz, S., Zahoor, M., Umar, M., Alghamdi, S., Sahibzada, M. and UlBari, W. (2020). Synthesis, characterization, and pharmacological evaluation of thiourea derivatives. *Open Chemistry*, 18(1): 764-777.
- 9. Keche, A. P. and Kamble, V. M. (2019). Synthesis and anti-inflammatory and antimicrobial activities of some novel 2-methylquinazolin-4(3H)-one derivatives bearing urea, thiourea and sulphonamide functionalities, *Arabian Journal of Chemistry*, 12(7): 1522-1531.
- 10. Asadollahi-Baboli, M. and Dehnavi, S. (2018). Docking and QSAR analysis of tetracyclic oxindole derivatives as α-glucosidase inhibitors. *Computational Biology and Chemistry*, 76: 283-292.

- 11. Ibrahim, M. A., Yusof, M. S. and Amin, N. M. (2014). Anti-amoebic properties of carbonyl thiourea derivatives. *Molecules*, 19(4): 5191-5204.
- Wiji Prasetyaningrum, P., Bahtiar, A. and Hayun, H. (2018). Synthesis and cytotoxicity evaluation of novel asymmetrical mono-carbonyl analogs of Curcumin (AMACs) against Vero, HeLa, and MCF7 Cell Lines. Scientia Pharmaceutica, 86(2): 25.
- 13. Xu, Q., Deng, H., Li, X. and Quan, Z. S. (2021). Application of amino acids in the structural modification of natural products: A review. *Frontiers in Chemistry*, 9: 650569.
- 14. Hauck, M., Jürgens, S. R. and Leuschner, C. (2010). Effect of amino acid moieties on metal binding in pulvinic acid derivatives and ecological implications for lichens producing these compounds. *The Bryologist*, 113(1): 1-7.
- 15. Ahmadi, S. and Habibpour, E. (2017). Application of GA-MLR for QSAR modeling of the arylthioindole class of tubulin polymerization inhibitors as anticancer agents. *Anticancer Agents in Medical Chemistry*, 17(4): 552-565.
- Rahman, F. U., Bibi, M., Khan, E., Shah, A. B., Muhammad, M., Tahir, M. N., Shahzad, A., Ullah, F., Zahoor, M., Alamery, S. et al. (2021). Thiourea derivatives, simple in structure but efficient enzyme inhibitors and mercury sensors. *Molecules*, 26: 4506.
- 17. Patnaik, P. (2007). A comprehensive guide to the hazardous properties of chemical substances: Thiourea. Wiley-Interscience, Hoboken, New Jersey: pp. 904.
- 18. Saxena, A. K. and Prathipati, P. (2003). Comparison of MLR, PLS and GA-MLR in QSAR analysis. *SAR QSAR Environmental Research*, 14(5-6): 433-445.
- Hadanu, R., Mastjeh, S., Mustofa, J., Sholikhah, E. N., Wijayanti, M. A. and Tahir, I. (2007). Quantitative structure-activity relationship analysis (QSAR) of antimalarial 1,10-phenanthroline derivatives compounds. *Indonesian Journal of Chemistry*, 7(1): 72-77.

- Frimayanti, N., Yam, M. L., Lee, H. B., Othman, R., Zain, S. M. and Rahman, N. A. (2011).
   Validation of quantitative structure-activity relationship (QSAR) model for photosensitizer activity prediction. *International Journal of Molecular Sciences*, 12(12), 8626–8644.
- 21. Qin, L., Zhang, X., Chen, Y., Mo, L., Zeng, H. and Liang, Y. (2017). Predictive QSAR Models for the toxicity of disinfection byproducts. *Molecules*, 22(10): 1671.
- Ravichandran, V., Mourya, V. K. and Agrawal, R. K. (2009). Prediction of anti-HIV activity of phenyl ethyl thiourea (PET) derivatives: QSAR approach. *Digest Journal of Nanomaterials and Biostructures*, 4: 213-221.
- 23. Tropsha, A., Gramatica, P. and Gombar, V. K. (2003). The importance of being earnest: validation is the absolute essential for successful application and interpretation of QSPR Models. *QSAR and Combinatorial Science*, 22: 69-77.
- 24. Edraki, N., Das, U., Hemateenejad, B., Dimmock, J. R. and Miri, R. (2016). Comparative QSAR analysis of 3,5-bis (arylidene)-4-piperidone derivatives: The development of predictive cytotoxicity models. *Iranian Journal of Pharmaceutical Research*, 15(2): 425-437.
- Katoch, S., Chauhan, S. S. and Kumar, V. (2021).
   A review on genetic algorithm: past, present, and future. *Multimedia Tools Application*, 80: 8091

  8126.
- Filzmoser, P., Gschwandtner, M. and Todorov, V. (2012). Review of sparse methods in regression and classification with application to chemometrics. *Journal of Chemometrics*, 26: 42-51.
- Tran, T. N., Afanador, N. L., Buydens, L. M. C. and Blanchet, L. (2014). Interpretation of variable importance in partial least squares with significance multi-variate correlation (sMC). Chemometrics and Intelligent Laboratory System, 138: 153-160.
- 28. Yuyama, M., Ito, T., Arai, Y., Kadowaki, Y., Iiyama, N. et al., (2020). Risk prediction method for anticholinergic action using auto-quantitative structure–activity relationship and docking study with molecular operating environment. *Chemical*

- and Pharmaceutical Bulletin, 68(8): 773-778.
- Sabet, R. and Fassihi, A. (2008). QSAR study of antimicrobial 3-hydroxypyridine-4-one and 3hydroxypyran-4-one derivatives using different chemometric tools. *International Journal of Molecular Sciences*, 9(12): 2407-2423.
- 30. Deeb, O., Hemmateenejad, B, Jaber, A., Garduno-Juarez, R., Miri, R. (2007). Effects of the electronic and physicochemical parameters on the carcinogenecis activity of some sulfa drug using QSAR analysis based on genetic-MLR & genetic-PLS. Chemosphere, 67: 2122-2130.
- Speck-Planche, A., Kleandrova, V.V., Luan, M.F., and Cordeiro, N.D.S. (2011). Fragment-based QSAR model toward the selection of versatile anti-sarcoma leads. *European Journal of Medicinal Chemistry*, 46: 5910-5916.
- 32. Viswanadhan, V. N., Reddy, M. R., Bacquet, R. J. and Erion, M. D. (1993). Assessment of methods used for predicting lipophilicity: application to nucleosides and nucleoside bases. *Journal of Computational Chemistry*, 14: 1019-1026.
- 33. Horne, D. S. (1988). Prediction of protein helix content from an autocorrelation analysis of sequence hydrophobicities. *Biopolymers*, 27: 451-477.
- 34. Helguera, A.M., Natália, M., Cordeiro, D.S., González, M.P., Pérez, M.A.C., Ruiz, R.M., and Castillo, Y.P. (2007). QSAR modeling for predicting carcinogenic potency of nitrosocompounds using 0D-2D molecular descriptors. 11th International Electronic Conference on Synthetic Organic Chemistry, 1-30 November 2007.
- 35. Jain, H.K., and Agrawal, R.K. (2006). QSAR analysis of indomethacin derivatives as selective COX-2 inhibitors. *Internet Electronic Journal of Molecular Design*, 5: 224-236.
- Todeschini, R., and Consonni, V. 2000. Handbook of Molecular Descriptors: Methods and Principles in Medicinal Chemistry. Volume 11, pp. 11. Weinheim: Wiley-VCH.

- 37. Raychaudhury, C., Banerjee, A., Bag, P., and Roy, S. (1999). Topological shape and size of peptides: Identification of potential allele specific helper T cell antigenic sites. *Journal of Chemical Information and Computer Sciences*, 39(2): 248-254.
- 38. Todeschini, R., Consonni, V., and Gramatica, P. (2009). Chemometrics in QSAR. In: Brown S, Tauler R, Walczak R. eds. Comprehensive

Chemometrics: Chemical and biochemical analysis, pp. 129-172. Oxford: Elsevier.

## **Malaysian Journal of Analytical Sciences** (MJAS)



## Published by Malaysian Analytical Sciences Society

## IMPROVING THE MORPHOLOGICAL, THERMAL, AND ACOUSTICS PROPERTIES OF POLYURETHANE-UREA BIOFOAM USING INDUSTRIAL PLYWOOD SAWDUST WASTE

(Meningkatkan Morfologi, Termal dan Sifat Akustik Busa Poliuretan-Urea Menggunakan Sisa Habuk Papan Kayu Lapis)

Herlina Nofitasari<sup>1\*</sup>, Ari Handono Ramelan<sup>2</sup>, Mohammad Masykuri<sup>3</sup>

<sup>1</sup>Master's Degree Program in Environmental Science <sup>2</sup>Faculty of Mathematics and Natural Sciences <sup>3</sup>Faculty of Teacher Training and Education Universitas Sebelas Maret, Surakarta 57126, Indonesia

\*Corresponding author: henosa25@gmail.com

Received: 29 December 2021; Accepted: 27 February 2022; Published: 27 June 2022

Abstract

Majority of the polyurethane-urea (PUU) foam is made from petroleum raw materials. Concerns regarding the loss of petroleum resources promote the environmentally sustainable manufacture of foam. The production of PUU foam synthesis from natural materials and waste composites was then developed. The PUU/industrial plywood sawdust waste (IPSW) biofoam was synthesized from a mixture of polyethylene glycol (PEG), methylene diisocyanate (MDI), ethylenediamine (EDA), maleic anhydrate (MAH), and IPSW by using a one-shot method. 5% IPSW was applied to the composition of the synthesized biofoam and the MDI ratio was increased. Fourier Transform Infrared Spectroscopy (FTIR) was used to identify functional groups of biofoam. The pore morphology of the biofoam was observed with Microscope Camera and Scanning Electron Microscopy (SEM), the thermal ability was measured with Thermogravimetric Analysis (TGA), and the sound absorption ability was measured by using a two-microphone impedance tube according to the ASTM E-1050 standard. Based on FTIR spectra identification, the biofoam contains OH, CH, CO, and NH chemical groups. The results reveal that the PUU/IPSW biofoam had intermediate macropore morphology (closed and open cells), thermal resistance above 120°C, and potential materials as soundabsorbing. The improvement in the biofoam properties upon the addition of organic filler shows that the biofoam is promotable as renewable material. This study suggests better formulation design to enhance the biofoam property performance.

Keywords: acoustics, polyurethane-urea foam, sawdust, scanning electron microscopy, thermogravimetric analysis

#### Abstrak

Kebanyakan busa poliuretan-urea (PUU) diperbuat daripada bahan mentah petroleum. Kebimbangan mengenai kehilangan sumber petroleum menggalakkan pembuatan busa yang mampan secara alam sekitar. Penghasilan sintesis busa PUU daripada bahan alam dan komposit sisa telah dibangunkan. Busa PUU telah disintesis daripada campuran polietilen glikol (PEG), metilen diisosianat (MDI), etilen diamin (EDA), maleat anhidrat (MAH), dan sisa habuk papan industri kayu lapis (IPSW) dengan menggunakan kaedah satu pukulan. Lima peratus IPSW telah digunakan pada komposisi biofoam tersintesis dan nisbah MDI

## Herlina et al: IMPROVING THE MORPHOLOGICAL, THERMAL, AND ACOUSTICS PROPERTIES OF POLYURETHANE-UREA BIOFOAM USING INDUSTRIAL PLYWOOD SAWDUST WASTE

telah meningkat. Spektroskopi Infra-Merah Transformasi Fourier (FTIR) digunakan untuk mengenal pasti struktur biofoam. Morfologi liang biofoam diperhatikan menggunakan mikroskop kamera dan SEM, TGA untuk pengukuran haba, dan keupayaan biofoam untuk menyerap bunyi diukur menggunakan tabung impedansi dua mikrofon mengikuti standar ASTM E-1050. Berdasarkan pengenalpastian spektrum FTIR, biofoam mengandungi kumpulan kimia OH, CH, CO, dan NH. Keputusan menunjukkan bahawa biofoam PUU/IPSW mempunyai morfologi makropori perantaraan (sel tertutup dan sel terbuka), rintangan haba melebihi 120 °C, dan berpotensi menjadi bahan penyerapan bunyi. Kemajuan kinerja ketika ditambahkan pengisi organik menunjukkan bahawa ini dapat dipromosikan sebagai bahan terbarukan. Studi ini menyarankan agar membuat formulasi yang lebih baik untuk meningkatkan prestasinya.

Kata kunci: akustik, busa poliuretan-urea, habuk papan, mikroskopi imbasan elektron, analisis termogravimetrik

#### Introduction

Population growth and rapid transportation progress have led to environmental problems in the community, including noise pollution. The effects are severe for those who have been exposed, both physically and mentally. This condition can be regulated by using sound-absorbing materials. There are two types of sound-absorbing materials: resonant and porous sound-absorbing materials. The morphology of the latter is made up of channels, gaps, and holes that allow sound waves to pass through [1-3].

Foam is a porous material that can be used to absorb sound. The foam production is synthesized from diols and polyols i.e. polyurethane chemical compounds [2, 4]. Polyurethanes are widely used for other applications such as paints, jacket coatings, elastomers, insulators, elastic fibers, and leather equipment. Polyurethane production and demand projections rose through 2020 [5]. The production of polyurethane foam is incompatible with sustainable development because it uses petroleum as raw material. Therefore, it is necessary to find alternative raw materials that are less harmful to the environment.

Renewable polyol modification is developed in the production of polyurethane by using biomass as raw material through oxypropylation or acid liquefaction process. The production of bio-polyol using oxypropylation method includes the use of palm oil, *Sapium sabiferum* oil, castor oil, soybean oil, grapeseed oil, sunflower oil, tung oil and canola oil. The current bio-polyol production process using liquefaction acid is derived from eucalyptus and pine woods, bamboo, Cellulose nanofibrils, Yaupon holly

(*Ilex vomitoria*), sugar-cane bagasse, bagasse, and jute fiber. Both processes can produce environmentally friendly polyurethane foam raw materials [4-8].

In addition to bio-polyols, the use of isocyanate alternatives such as Non-isocyanate polyurethane (NIPU), which is derived from mimose tannins [9], lysine, sorbitol, vegetable oils, and other sources, is another way to keep polyurethane foam production sustainable. Recycling polyurethane foam [4] and integrating natural waste materials into the production process are also green choices. Natural fiber blends of various concentrations and thicknesses in polyurethane foam composites have varied sound absorption capabilities [10]. The addition of Shorea leprosa wood fibers to the polyurethane foam affects its acoustic performance [11]. Production of biofoam from polyurethane-urea blends with various concentration of industrial plywood sawdust has a good sound absorption coefficient [12].

It was reported that polyurethane foam composites containing nanosilica and nanosilica solution at an optimum level of 2 wt.% had a negative impact on foam cell morphology, and the TGA test results for rigid polyurethane foam composites containing 1 wt.% nanosilica solution had poor thermal resistance [13]. As compared to foams without the addition of halloysite nanocomposites, rigid polyurethane foam with palm oil as raw material and halloysite nanocomposite had stable thermal resistance, and SEM results showed a smooth cell surface structure and larger cell size [2]. Polyurethane foam synthesized with clove composites (*Syzygium aromaticum*) at various concentrations had rheological behavior, cellular

and further mechanical structure. thermal performance of the modified material [8].

The other research studied polyurethane foam with addition of diatomite and hydroxyapatite. The thermal degradation of diatomite porous polyurethane foam biocomposites was lower than that of hydroxyapatite porous polyurethane foam biocomposites. Diatomite and hydroxyapatite increase the surface area of the polyurethane foam and harden the pores [14]. Rigid foam made by combining non-isocyanate polyurethane (NIPU) tannins with addictive glutaraldehyde and citric acid had the same morphology, called Open-Cell, but the number of cell wall pores decreased as glutaraldehyde was added, while citric acid increased the number of foam cells. The thermal resistance of the NIPU foam in all compositions was the same except for the composition of 2 grams of hexamine and 6 grams of citric acid which was higher at a temperature of 790 °C and a residue of 18.7% [9].

This research described the synthesis of polyurethaneurea (PUU) biofoam with industrial plywood sawdust waste composites (IPSW). The PUU/IPSW biofoam was synthesized by adding a chain extender in the form of ethylene diamine (EDA), coupling agent in the form of maleic anhydrate (MAH), and industrial plywood sawdust waste as filler. The chain extender is a low molecule containing an amine group at the end that plays a major role in polymer morphology. The addition of a chain extender and diisocyanate provided a wide range of hard segment characteristics and the

polyurethane. physical performance of The morphological structures were characterized by SEM and Microscope Camera. Meanwhile, thermal ability was analyzed by TGA, and acoustics test was conducted through impedance tube.

#### **Materials and Methods**

#### **Materials**

The materials used to synthesize the PUU/IPSW biofoam were chemical compounds and biomass. The chemical compounds included polyethylene glycol (PEG) 400 (Polyol), 4.4'-diphenylmethane diisocyanate (4.4'-MDI), ethylenediamine (EDA), and maleic anhydrate (MAH) while the biomass was in the form of industrial plywood sawdust waste (IPSW). The detail of various compositions of the PUU/IPSW biofoam are shown in Table 1.

#### Sample preparation

The biofoam was synthesized by using a one-shot method. This method worked by combining all of the ingredients until they were fully homogeneous, as detailed in Figure 1. First, the polyol and diisocyanate were mixed and stirred. Then, the chain extender (EDA), the coupling agent (MAH), and the IPSW filler were added. The composition of the ingredients was calculated by the mass ratio. The samples were coded as BP0, BP1, BP2, BP3, BP4, and BP5 for the PUU/IPSW biofoam with 0%, 1%, 2%, 3%, 4%, and 5% IPSW respectively with a ratio of PEG:MDI (1:1), and BP1.5 for the PUU/IPSW biofoam of 5% with a ratio of PEG:MDI (1:1.5).

	Table 1.	Variation of	of the PUU/IPSW	biofoam compositio	n
Samples	PEG (g)	MDI (g)	EDA 0.1% (g) (w/w)	MAH 0.01% (g) (w/w)	Wa

Samples	PEG (g)	MDI (g)	EDA 0.1% (g) (w/w)	MAH 0.01% (g) (w/w)	Waste % (g) (w/w)
BP0	15	15	0.3	0.03	0
BP1	15	15	0.3	0.03	0,31
BP2	15	15	0,3	0.03	0,62
BP3	15	15	0,3	0.03	0,94
BP4	15	15	0,3	0.03	1,26
BP5	15	15	0,3	0.03	1,6
BP1,5	15	22,5	0.3	0.03	1,6

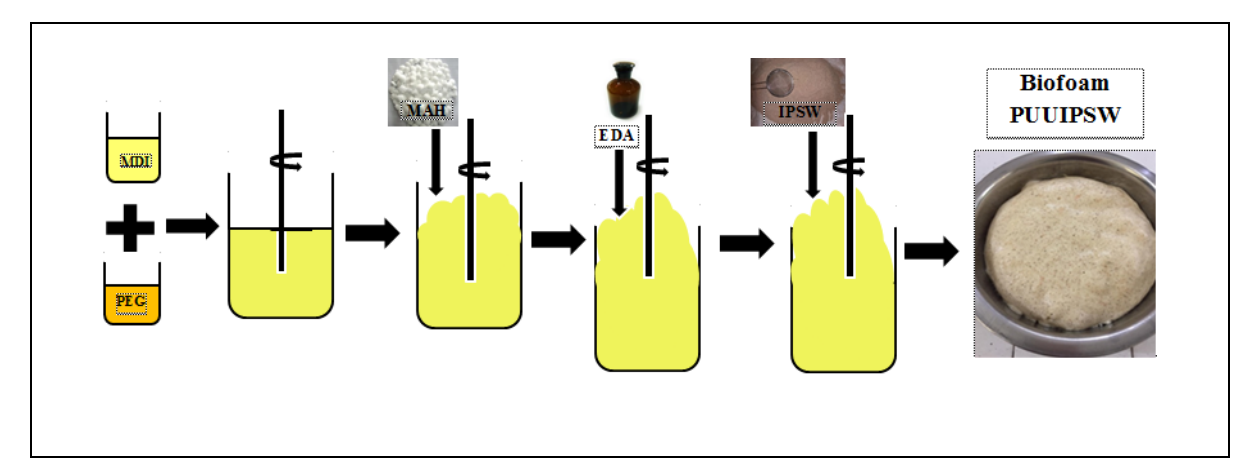


Figure 1. Procedural scheme for the PUU/IPSW biofoam synthesis

#### Microscope camera

The biofoam pore morphology in was observed by using a Nikon Eclipse 80i microscope camera for 10x magnification. The resulted pore distribution was calculated by using Image J software. The pore distribution data were analyzed by using OriginLab software.

#### **Scanning Electron Microscopy**

The morphological properties of biofoam cells were observed by using Scanning Electron Microscopy (SEM) Phenom ProX. the PUU/IPSW biofoam samples were ground into powders and then plated with gold and subjected to 10kV voltage. Prior to the test, the samples' surfaces were gold-plated in order to have conductive properties and to be detectable by the SEM detector Phenom ProX secondary electron detector (SED).

#### Fourier transform infrared spectroscopy

The PUU/IPSW biofoam chemical structure was analyzed with FTIR spectroscopy by using KBr pellet technique with measurements at 3500-400 cm<sup>-1</sup> wavenumber.

#### Thermogravimetric analysis

The PUU/IPSW biofoam was subjected to TGA to obtain its thermal resistance with the TGA DSC 200 of Seiko SSC 5200H at a temperature of 25-600 (°C) with a heating rate of 10°C/minute.

#### Impedance tube testing

The PUU/IPSW biofoam sound-proofing ability was measured with an acoustic test that followed the ASTM E-1050 standard. The biofoam samples were shaped into a 28mm-diameter circle. Two microphone techniques and automated frequency analysis systems were used to quantify the effect of normal sound absorption coefficient and precise normal acoustic impedance comparisons of materials, with frequencies ranging from 0 to 6400 (Hz) [10, 11,15].

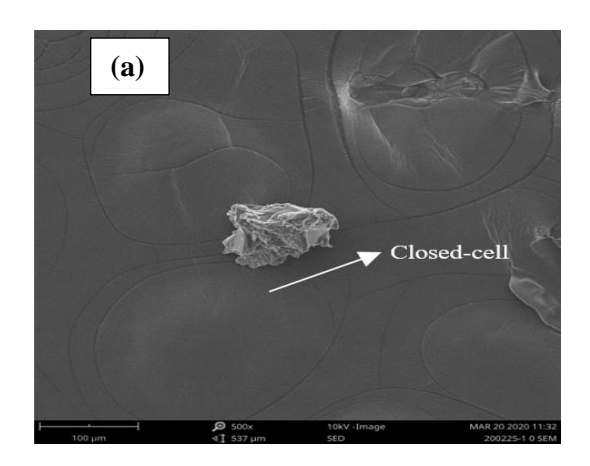
#### **Results and Discussion**

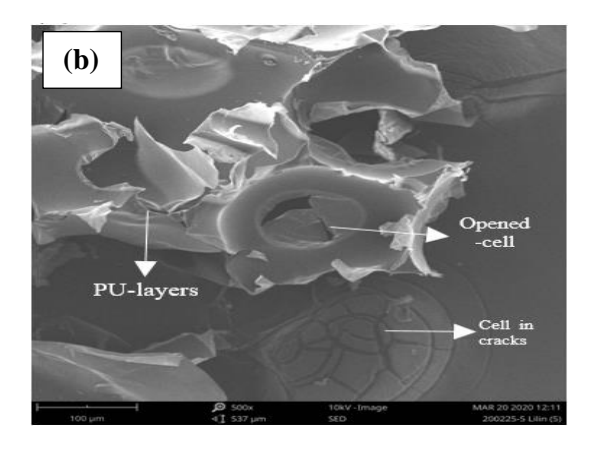
#### Cell morphology

microscopes, SEM for 500x magnification Two (Figure 2) and Microscope Camera for 10x magnification (Figure 3), were used to examine the biofoam pore morphology. Three samples, namely BP0, BP5, and BP1.5 were observed on SEM as representative treatments. The results show that majority of the pores formed were macropores since the size was found to be more than 50µm. Three types of biofoam morphology were then determined: 1) open-celled, meaning that the biofoam pores were found to have interconnecting holes between each other; 2) closed-celled, meaning that the biofoam pores were found to not have interconnecting holes between each other; and 3) intermediate-celled, meaning that the biofoam pores were found in a combination of the two. BP0 was found to be closed-celled, with circular to oval shape when it expanded. BP5 was found to be

intermediate-celled with oval shape [3]. Other microstructures were observed in PU layers. BP1.5 had closed-celled microstructure with polygonal shape. It had another microstructure, namely interconnecting hole. According the SEM images, filler addition influenced the biofoam morphology. It was observed that the filler could make a closed-celled sample to be an open-celled one, since it filled the biofoam matrices. Meanwhile, the effect of filler addition to MDI ratio enhancement was found to be not significant. The SEM image results were smooth, demonstrating MAH's ability to act as a coupling agent. The smoothest the sample captured by SEM causes the role of MAH which can relate the filler and the biofoam matrices. Therefore, the surface of samples seemed smooth.

The structure of the cavities and pores created during the polymerization process and the cell size were determined by the gelling and blowing reactions. If the cavity pressure is greater than the wall strength, biofoam with an open-celled structure may be created. At low channel flow rates, the cavity wall thickness retains hardness. However, if the hardening process is completed before the open pore formation, some open pores can form. Closed cells will remain if the cavity wall hardens completely before fracturing [2, 16, 17]. With the addition of filler, the pore distribution continued to reduce in size (Figure 3). It was identified that sample BP0 had the highest pore distribution with pore size in the range of 250-300 µm, while Samples BP1, BP3, BP4, BP5, and BP1.5 had pore sizes in the range of 100-150 µm. Meanwhile, Sample BP2 had pore distribution with pore size in the range of 150-200 um. The factor which caused different sizes of pore distribution might occur when the minimum biofoam synthesis period and stirring velocity were not fulfilled. It was suggested that foaming under this kind of condition impacted the cell sizes of Sample BP2. This demonstrated that the presence of filler had a direct impact on the morphological properties distribution. The biofoam mechanical and thermal efficiency depended on these factors [8].





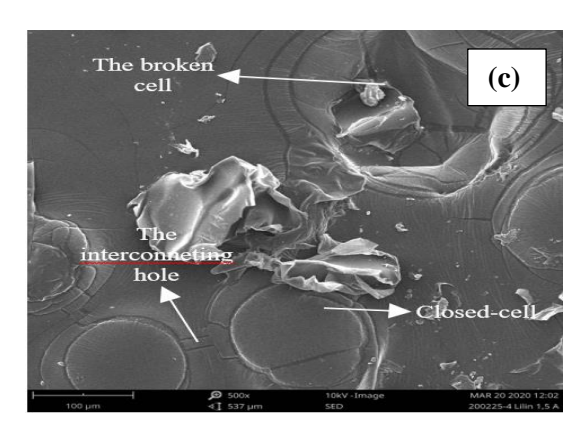
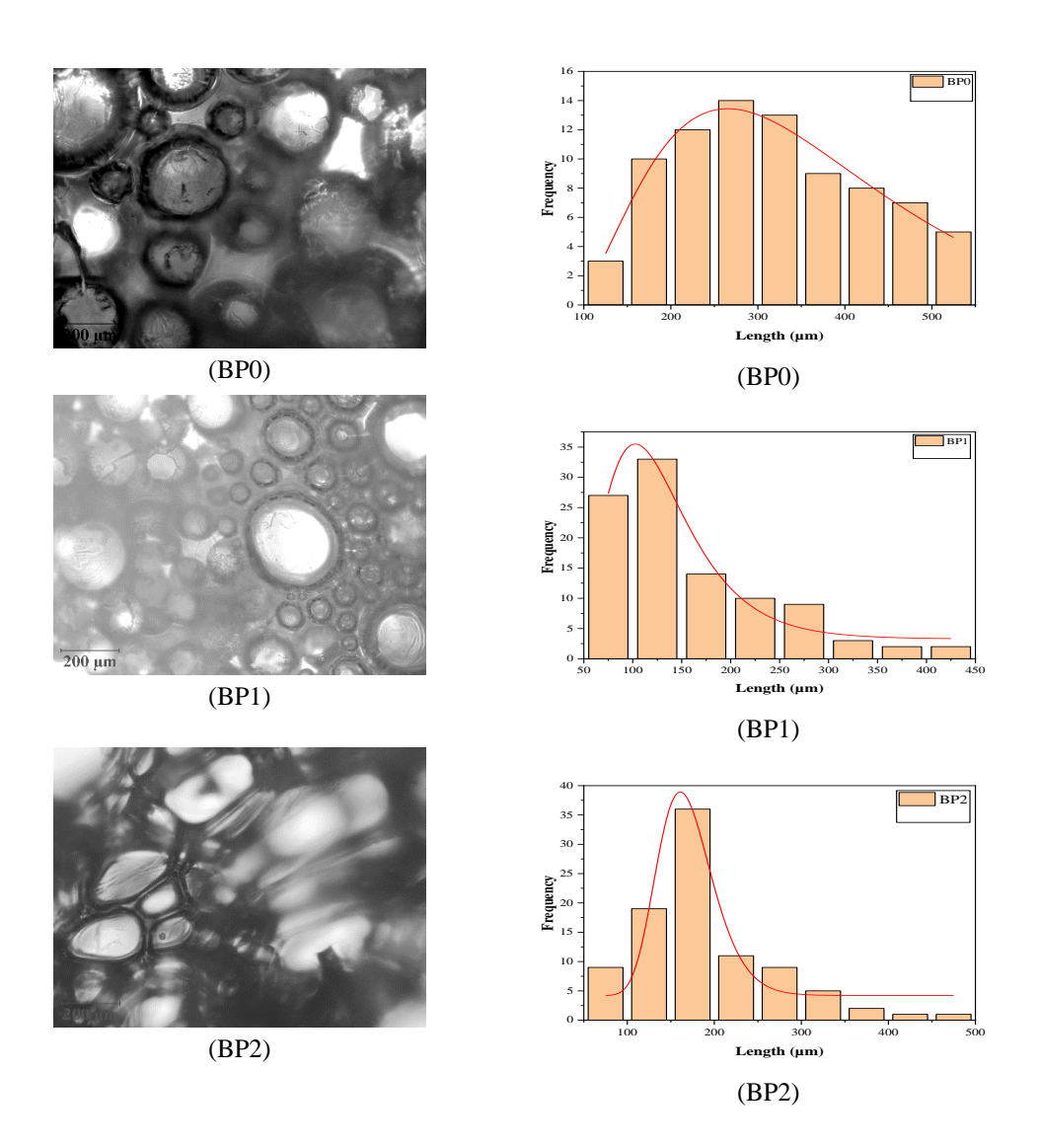


Figure 2. SEM images from the PUU/IPSW biofoam samples of (a) BP0, (b) BP5, and (c) BP1.5.



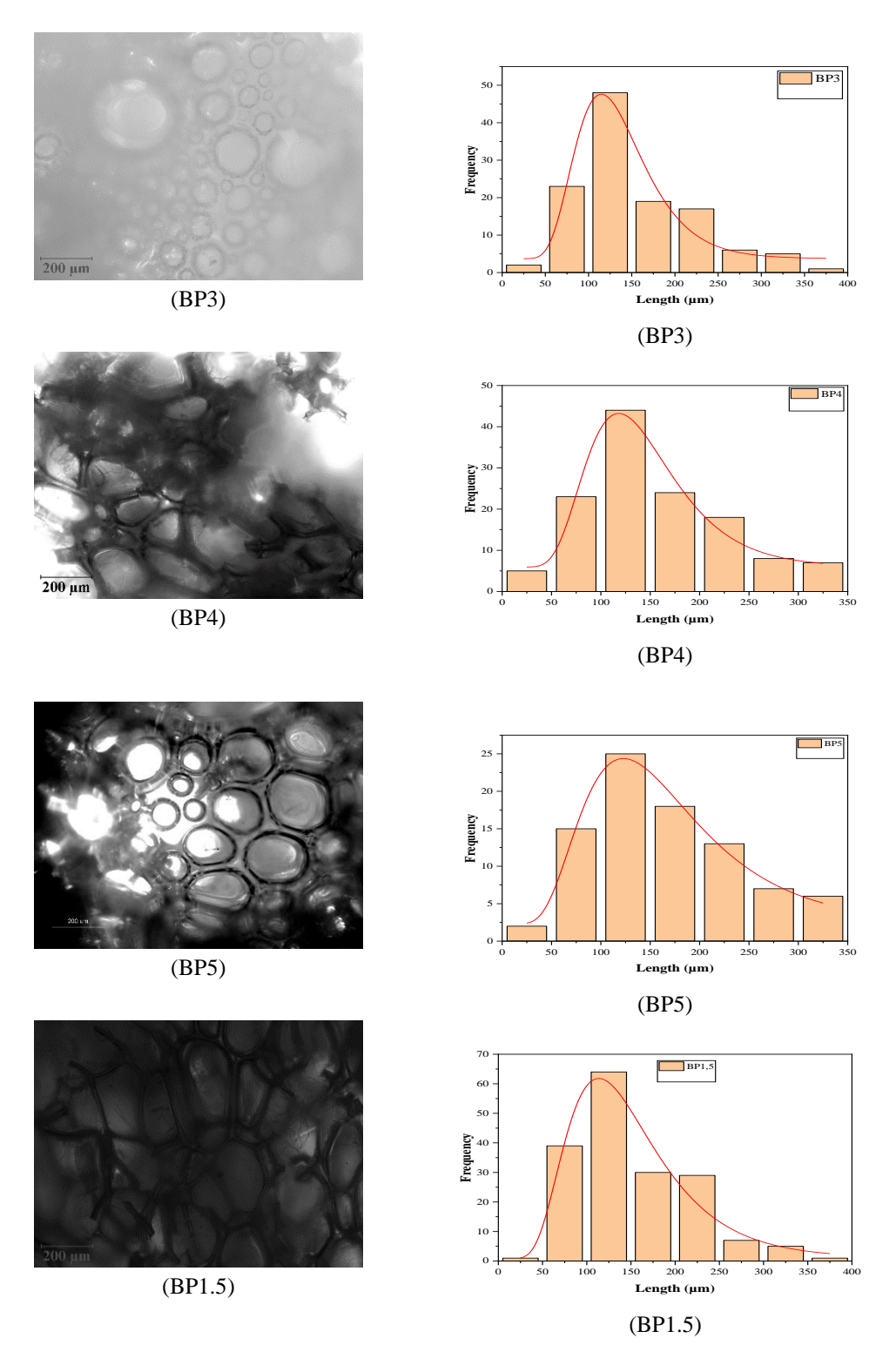


Figure 3. The PUU/IPSW biofoam microscope camera profile and pore distribution curves

#### **Chemical structure**

Urethane and urea are two forms of carbonyl groups formed by hydrogen bonds [18]. The PUU biofoam is derived from polyol and diisocyanate raw materials. Samples of MDI, PEG, BPO, and BP5 were observed to understand the PUU/IPSW biofoam chemical reaction. According to the absorption observed in the FTIR spectra, the -NH functional group was found in the wavenumber range of 3808-3308 cm<sup>-1</sup> with broad intensity. This covered Samples BP0 (3516 cm<sup>-1</sup>) and BP5 (3527 cm<sup>-1</sup>). Samples BP0 (3382 cm<sup>-1</sup>), MDI (3384 cm<sup>-1</sup>) and BP5 (3382 cm<sup>-1</sup>) belonged to -OH functional group found in the wavenumber range 3422-3314 cm<sup>-1</sup>. The absorption peak of the PUU biofoam formed shifted to a lower wavenumber, suggesting a looser bond [13, 19]. Methylene functional group was detected at the absorption peak wavenumbers of 2972 cm<sup>-1</sup> and 2971 cm<sup>-1</sup> which was the -CH asymmetric stretching vibration of CH<sub>3</sub> [9, 19].

The absence of an isocyanate functional group absorption band at wavenumbers 2270-2250 cm<sup>-1</sup> suggested that the isocyanate reacted properly with polyol (Figure 4). The first explanation is that due to

the steric disturbance molecule, the -OH functional group interacted with the -NCO group. Another explanation is that the -NCO functional group interacted with the -OH group in the air, which was caused by humidity [6, 20]. The characteristics of amide III and C = O (-RNHCOO- / urethane linkage) functional groups in the absorption bands of 1230 cm<sup>-1</sup> and 1077 cm<sup>-1</sup> suggested that the PUU biofoam was successfully formed and chemically bonded [6, 19, 21]. In addition, another absorption peak was detected, namely the aromatic group C-C/C = C stretching modes in the wavenumber range 1600-1607 cm<sup>-1</sup> [22]. The properties of EDA as a chain extender contributed to the PUU biofoam's hard segment character, which can be detected when the biofoam is heated or cooled. When PUU biofoam is heated to a specific temperature, it has a peak intensity –H bonded urethane C = O groups while urea groups decrease. This also applies if it is cooled to a temperature of 120-30 (°C) so that the peak intensity of -H bonded urethane C=O groups increases while the peak intensity of free urethane C=O decreases [18]. More information is presented in Table 2.

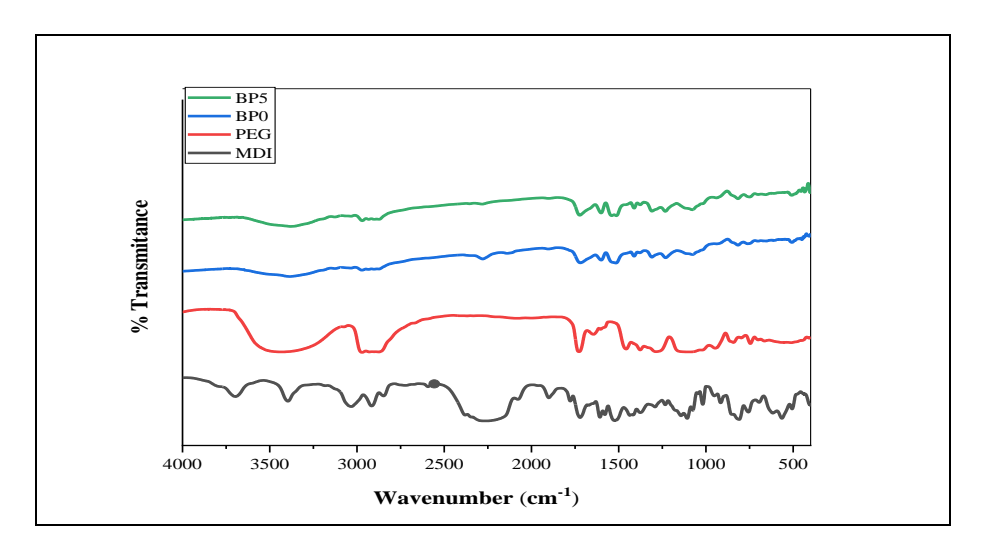


Figure 4. FTIR spectra of BP0, PEG, and MDI

Wavenumber (cm <sup>-1</sup> )		Wavenumber Range	Functional Groups				
MDI	PEG	PEG BP0 BP5 (cm <sup>-1</sup> )		(cm <sup>-1</sup> )	•		
-		3516	3527	3808-3308	The stretching vibration of -NH		
3384	-	3382	3382	3422-3314	-OH stretching modes from hydroxy groups		
-	2972	2972	2971	3000-2970	-CH asymmetric stretching vibration CH <sub>3</sub> (methylene groups)		
2257	-	-	-	2270-2250	-NCO- (isocyanate asymmetric stretching)		
1720	-	1719	1724	1724-1705	Disorder H-bonded (C=O)OC in urethane		
-	1644	1638	1635	1648-1627	Order H-bonded urea C=O		
1607	1602	1600	1600	1615-1580	Aromatic C-C/C=C Stretching Modes		
1233	-	1230	1230	1257-1222	υC-N+ δN-H (Amide III)		
1075	-	1077	1075	1083-1070	H-Bonded (C=O)OC in urethane		

Table 2. Peaks of FTIR spectra of BP0, PEG, and MDI

#### TGA analysis

Thermogravimetric Analysis (TGA) is used to calculate the effect of filler addition (industrial plywood sawdust waste) and the ratio of MDI to its thermal performance, while DTG is a derivative of its mass loss. Samples BP0, BP5, and BP1.5 were observed because they were representatives to the treatment. Figure 5 and Table 3 show the results of the TG and DTG tests. Temperature characteristics were divided into Tonset and Tmax. Tonset was the degradation of temperature when the mass loss was 5%, while  $T_{max}$ was the maximum degradation temperature of all samples [6]. All samples had T<sub>max</sub> which was divided into three stages. Before the samples were degraded at the T<sub>Onset</sub> temperature in the initial stage, there was a small degradation below 100°C which was the degradation of moisture, solvent light organic molecules, and impurities from the biofoam [23]. The T<sub>Onsets</sub> of the three samples were all above 120 °C, with BP1.5 having the highest value of 130 °C. The first and second stages of degradation occurred at temperatures of 190-209 (°C) and 294-295 (°C) respectively, and involved the decomposition of polymer urethane bonds [7, 13, 21]. The last degradation that occurred was the soft segment decomposition of the MDI biofoam at a temperature above 500°C. This stage involved combustion and aromatic oxidation [7, 24], as well as the degradation of lignin (industrial plywood sawdust) and other molecules that were difficult to separate from the previous stage [21, 25]. Furthermore, the DTG curve (Figure 5) shows that the greatest mass loss occurred at 294 °C which was the hard segment decomposition stage while the temperature above 525 °C was the soft segment decomposition stage.

Figures 5(a)-(c) show the TGA results. It was found that BPO, or the biofoam without the addition of waste or MDI ratio, had better thermal resistance. This is because its thermal degradation profile showed that mass loss generally occurred at higher temperature compared to BP1 and BP1.5 (Figure 5 (a)). When biofoam filler was added, it is suggested that two things might have occurred: 1) the organic filler might contain a small amount of water residue as a result of the formation of urea bonds which increases the activation energy for thermal degradation [8], or 2) the addition of filler improved strength by giving the part a hard segment character, which increased thermal resistance [23]. Based on the results found, it should be the result that led to the second reason but this research showed that BP0 had highest thermal conductivity. It means that the filler-free biofoam had good thermal resistance. Another factor that caused a decrease in thermal performance was the uneven distribution of the filler in the polymer matrix which affected density. Besides, the TGA results were also influenced by pore

morphology. The modified biofoam's high pores and open cavities hastened the degradation process, thus reducing the thermal efficiency of the substance being analyzed [8].

DSC analysis was used to measure the change in mass of the heat-treated samples. TGA cannot normally detect physical changes in polymer structures such as glass transition, crystallization, or melting, but these can be determined through DSC [23]. The DSC analysis (Figure 5) reveals that none of the biofoam samples had endothermic melting peaks. This could be caused by a physical changeover of the polymer, or the density from melting at a fast cooling rate to a glassy amorphous state or impure samples. Samples B5 and BP1.5 had a single exothermic peak at 522 °C and 538 °C respectively, while Sample BP0 had two exothermic peaks at 539 °C and 551 °C.

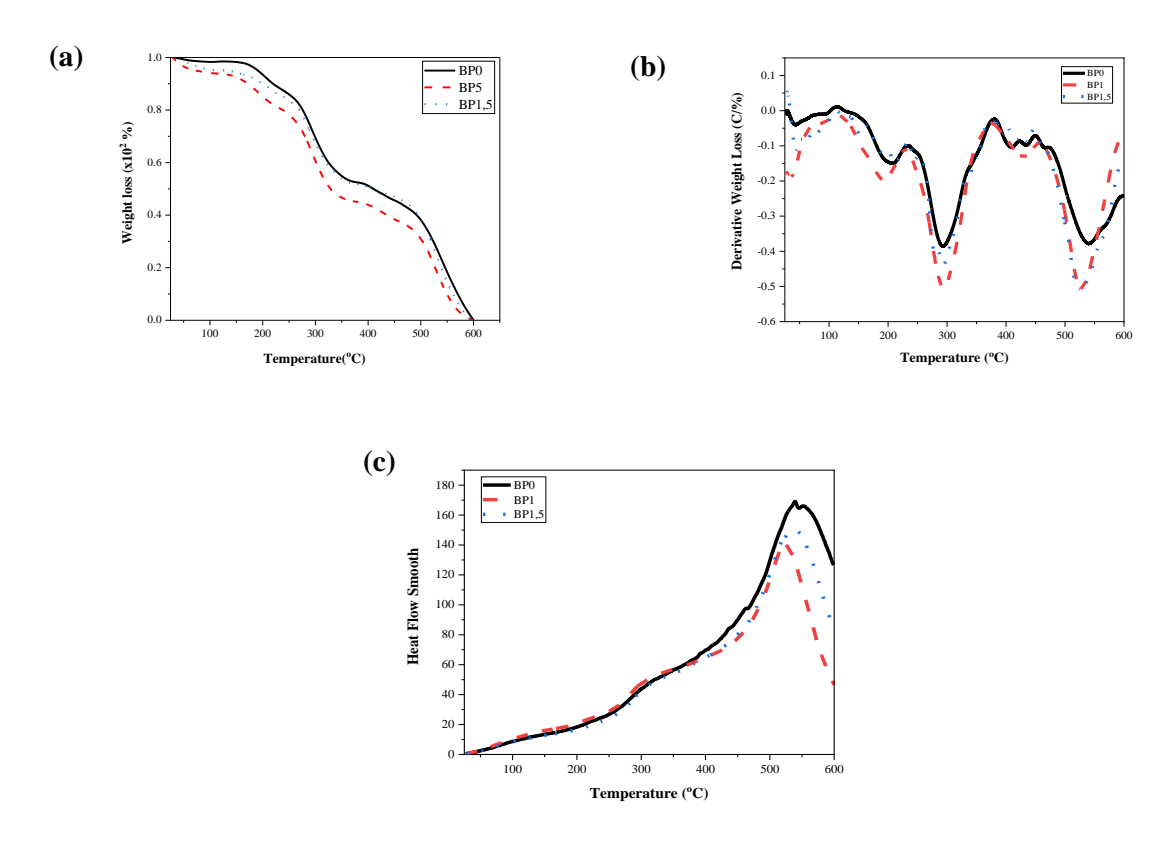


Figure 5. TGA (a), DTGA (b), and DSC (c) of the PUU/IPSW biofoam

Table 3. The sections of thermal degradation on the PUU/IPSW biofoam

Sample Codes	T(0C)	(Stage	es) T <sub>ma</sub>	x (OC)	Residual Mass	
Sample Codes	Tonset (OC)	I	II	III	600 °C (%)	
BP0	126	206	294	539	37.29	
BP5	130	190	295	528	23.00	
BP1.5	130	209	294	527	33.48	

#### Sound absorption coefficient

The sound absorption coefficient (α) for all samples is shown in Figure 6. The three samples (BP0, BP4, and BP1.5) were measured in the wavenumber range of 0-6400 (Hz) with two microphone impedance tubes and with similar sample thickness of 1.5 cm. Sample BP4 was selected as the representative to the treatment for 1:1 ratio, and the addition of IPSW with highest SAC compared to the other samples. The detailed information regarding SAC for all samples can be found in previous publication [12]. The results showed that BP4 had the highest sound absorption, with a value of 0.69 at 3864 Hz, followed by BP0 with a value of

0.65 at 4552 Hz, and BP1.5 with a value 0.45 at 4760 Hz. All samples showed the best acoustic performance at high frequencies above 3800 Hz. Based on these results, it was found that BP4 had the best acoustic performance, showing that that of BP0 and BP1.5 was not optimal. The addition of filler to the synthesis of polyurethane foam can enhance sound absorption [10, 11]. But this did not apply to the PUU/IPSW biofoam sample with IPSW of above 4% [12] and did not enhance MDI ratio. Several other factors influenced the biofoam sample ability to absorb sound which are explained in the following.

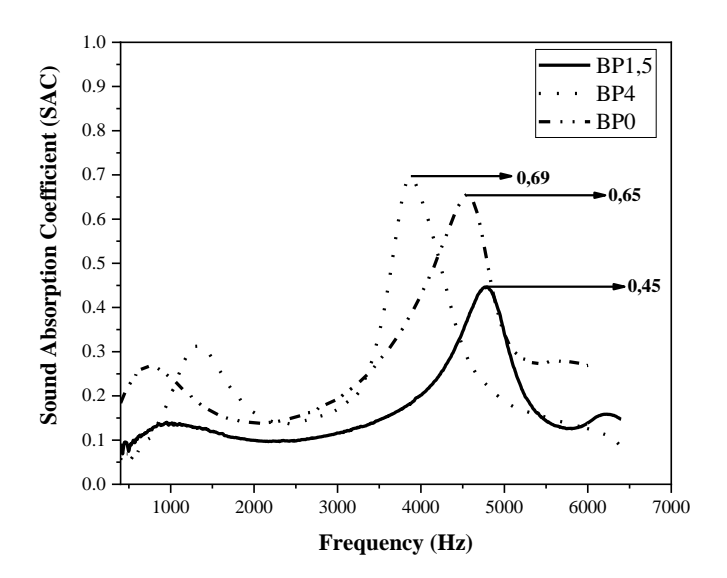


Figure 6. The PUU/IPSW biofoam sound absorption coefficient

#### Effect of texture, pore morphology, and density

Sound-absorbing foam will have a high SAC value if it has the following material characteristics [20, 25, 26]:

- 1. Flexible foam texture
- 2. Open-celled microstructure
- 3. Small-sized pores in large numbers
- 4. Higher density (not measured in this research)

The synthesized PUU/IPSW biofoam had the characteristics of semirigid texture, intermediate microstructure, smaller pore size, and higher SAC

value than the control biofoam. This can be caused by other influencing factors such as the characteristics of the pores. Even if the size is small and numerous, it may not meet aspects such as structure and pore characteristics of sound-absorbing materials, including those mentioned below [17].

- The material contains several pores and holes, all of which are small and uniform in size
- 2. The pores and holes must be connected.
- The pores and holes inside the material must connect with the outer surface.

#### Effect of filler addition

The biofoam filler used, called IPSW, was measured by 30 mesh size. The filler had an impact on pore size in such a way that biofoam with added filler had smaller pores than those without filler addition. The smaller pore size was closely related to improved sound absorption mechanism. It is suggested that smaller pores allowed sound waves to dissipate sound energy and dampened it as they move through the sound-absorbing material. Therefore, smaller pores in large numbers allowed more sound wave to collide with the cell wall, lengthening the reflection & bending portion and causing more energy to be absorbed, resulting in higher SAC [10, 15, 20, 27]. The smaller pore size in the synthesized biofoam is shown in Figure 3. The existence of other factors that predominantly affect sound absorption such as the unfulfilled criteria for pores as sound absorbers had resulted in the reduced acoustic performance of the PUU/IPSW biofoam. However, if adjusted and designed with a better formula, the PUU/IPSW biofoam had a great potential as a noise-absorbing material with wide range frequency.

#### Effect of MDI ratio enhancement

Isocyanate (MDI) is composed of hard segment. Enhancing the MDI ratio can reduce SAC, as shown in Sample BP1.5. Biofoam with added MDI ratio had leaning rigid texture. The texture rigidity was caused by the closed-celled microstructure. Another factor which could make the biofoam texture rigid was chain extender [19, 20].

#### Conclusion

The PUU/IPSW biofoam was successfully synthesized after its functional groups (-NH, -OH, -CH, -CO and C-C) were identified in the FTIR spectra. Addition of filler and increase in MDI affect pore morphology, thermal resistance, and acoustic performance. Samples BPO and BP1.5 of the synthesized biofoam had close-celled microstructure morphological type while Sample BP5 had intermediate-celled type. All samples had thermal resistance above 120 °C. Sample BP4 had the highest SAC with the value of 0.69. The acoustic output was poor, resulting in lower-frequency SAC when tested.

However, if adjusted and designed with a better formula, PUU/IPSW biofoam can absorb sound at wide-range frequency. Lastly, filler addition could enhance the biofoam property performance. Therefore, IPSW is promotable as an organic filler for renewable material.

#### Acknowledgement

The authors thank Rosid Eka Mustofa for assisting with the OriginLab analysis, Iklima Maharani for directing the sample preparation stages, Safira C for laboratory access to the Microscope Camera tool, and all SEM, TGA, FTIR, and Acoustic laboratory test equipment operators who tested all samples in this research.

#### References

- Aditya, V. T., Masykuri, M. and Setyono, P. (2019). Analysis of noise in the green open space Putri Kaca Mayang, Pekanbaru City. AIP Conference Proceedings: International Conference on Biology and Applied Science (ICOBAS), 2019.040020.
- 2. Cao, L., Fu, Q., Si, Y., Ding, B. and Yu, J. (2018). Porous material for sound absorption. *Composites Communications*, 10(2018): 25-35.
- 3. Rojo-Gomez, R., Alameda, L., Rodriguez, A., Calderon, V. and Guiterrez-Gonzalez, S. (2019). Characterization of polyuretane foam waste for reuse in eco-efficient building materials. *Polymers*, 11: 359.
- 4. Gama, N.V., Ferreira, A. and Timmons, A. B. (2018). Polyurethane foams: Past, present and future. *Materials*, 11(10): 1-35.
- Akindoyo, J. O., Beg, M. D. H., Ghazali, S., Islam, M. R., Jeyaratman, N. and Yufaraj, A. R. (2016). Polyurethane types, synthesis and applications- a review. *Royal Society of Chemistry*, 6(1): 114453-114482.
- Alis, A., Majid, R. A., and Mohammad, Z. (2019). Morphologies and thermal properties of palm-oil based rigid polyurethane/halloysite nanocomposite foam. *Chemical Engineering Transactions*, 72(2019): 415-420.

- Bundjali, B., Masykuri, M., Hartanti, F. W. and Arcana, I. M. (2018). Poly (urethane-urea) synthesized from 9-ethoxy-1, 10-octadecanediol obtained by modification of palm oil oleic acid. *Journal of Mathematics and Fundamental Sciences*, 50(1): 13-27.
- 8. Czlonka, S., Strakowska, A., Strzelec, K., Kairyte, A., and Kremensas, A. (2020). Biobased polyurethane composite foams improved mechanical, termal, and antibacterial properties. *Materials*, 13(1):1-20.
- Chen, X., Xi, X., Pizzi, A., Fredon, E., Zhou, X., Li, J., Gerardin, C. and Du, G. (2020). Preparation and characterization of condensed tannin non-isocynate polyurethane (NIPU) rigid foams by ambient temperature blowing. *Polymers*, 12(4):1-20.
- Azahari, M. S. M., Rus, A. Z. M., Kormin, S. and Zaliran, M. T. (2017). Acoustic properties of polymer foam composites blended with different percentage loadings of natural fiber. *IOP Conferences Series: Materials Science and Engineering*, 244(2017):1-6.
- Azahari, M. S. M., Rus, A. Z. M., Kormin, S. and Zaliran, M. T. (2018). An acoustic study of Shorea leprosula wood fiber filled polyurethane composite foam. Malaysian Journal of Analytical Science, 22(6): 1031-1039.
- Nofitasari, H., Masykuri, M. and Ramelan, A. H. (2020). Reducing room noise using polyurethane-urea biofoam/industrial plywood sawdust waste (PUU/IPSW). AIP Conferences Proceedings: International Conference on Science and Applied Science, 2296(2020): 020061-020066.
- 13. Czlonka, S., Strakowska, A., Strzelec, K., Kairyte, A., and Vaitkus, S. (2019). Composites of rigid polyurethane foams and silica powder filler enhanced with ionic liquid. *Polymer Testing*, 75(2019): 12-25.
- Mustafov, S. D., Sen, F. and Seydibeyoglu, M. O. (2020). Preparation and characterization of diatomite and hidroxyapatite reinforced porous polyurethane foam biocomposites. *Scientific Reports*, 1(2020): 1-9.

- 15. Rus, A. Z. M. and Shafizah, S. (2015). Acoustic behavior of polymer foam composite of *Shorea leprosula* after UV-irradiation exposure *International Journal Mechanical Aerospace, Industry Mechatronics*, 9(2015):188-192.
- Sung, G., Kim, S. K., Kim, J. W. and Kim, J. H. (2016). Effect of isocyanate molecular structures in fabricating flexible polyurethane foams on sound absorption behavior, *Polymer Test*, 53(2016): 156-164.
- 17. Zhao, C., Wang, P., Wang, L. and Liu, D. (2014). Reducing railway noise with porous sound-absorbing concrete slabs. *Advance Material Science Engineering*, 2014: 1-11.
- Kayalvizhi, M., Vakees, E., Suresh, J. and Arun,
   A. (2019). Poly(urethane-urea) based on functionalized polystyrene with HMDI: Synthesis and characterization. *Arabian Journal of Chemistry*, 12(8): 2484-2491.
- 19. Jiang, L., Ren, Z., Zhao, W., Liu, W., Liu, H. and Zhu, C. (2018). Synthesis and structure/properties characterizations of four polyurethane model hard segments. *The Royal Society Open Science*, 5(7): 1-11.
- Tiuc, A. E., Vasile, O., Usca, A-D., Gabor, T. and Vermesan, H. (2014). The analysis of factors that influnce the sound absorption coefficient in porous materials. *Romanian Journal of Acoustics and Vibration*, 11 (2):105-108.
- Zhao, X., Qi, Y., Li, K. and Zhang, Z. (2019).
   Hydrogen bonds and FTIR peaks of polyether polyurethane-urea. *Key Engineering Materials*, 815(2019):151-156.
- Bayu, A., Nandiyanto, D., Oktiani, R. dan Ragadhita, R. (2019). How to read and interpret FTIR spectroscope of organic material. *Indonesian Journal of Science and Technology*, 4(1): 97-118.
- Ng, H. M., Omar, F. S., Saidi, N. M. and Kasi, R. (2018). Encyclopedia of Polymers Science and Technology. Jhon Waley Sons Inc, New York: pp. 1-29.

- Kripluks, M., Cabulis, U., Ivdre, A., Kuranska, M., Zileniewska, M. and Auguscik, M. (2016).
   Mechanical and thermal properties of high-density rigid polyurethane foams from renewable resources. *Journal Renewable Material*, 4(1): 86-100.
- 25. Huang, X.Y., Hoop, C. F., Peng, X. P., Xie, J. L., Qi, J. Q., Jiang, Y. Z., Xiao, H. and Nie, S. X. (2018). Thermal stability analysis of polyurethane foams made from microwave liquefaction bio-polyols with and without solid residue. *BioResources*, 13(2): 3346-3361.
- Amares, S., Sujatmika, E., Hong, T. W., Durairaj, R. and Hamid, H. S. H. B. (2017). A review: characteristic of noise absorption material. *IOP Conferences Series: Journal of Physics: Conferences Series*, 908(2017): 012005.
- Hassan, N. N. M. and Rus, A. Z. M. (2016). Influences of thickness and fabric for sound absorption of biopolymer composite. *Applied Mechanics and Materials*, 393(1): 102-107.

## **Malaysian Journal of Analytical Sciences** (MJAS)



### SYNTHESIS OF GREEN-RENEWABLE BIOLUBRICANT BASE STOCK FROM MALAYSIAN PALM OIL

(Sintesis Stok Asas Biopelincir Hijau-Diperbaharui daripada Minyak Sawit Malaysia)

Nurazira Mohd Nor1\* and Jumat Salimon2

<sup>1</sup>MaterOleo Research Group, Faculty of Applied Sciences,

Universiti Teknologi MARA, Cawangan Negeri Sembilan, Kampus Kuala Pilah, 72000 Kuala Pilah, Negeri Sembilan, Malaysia <sup>2</sup>Department of Chemical Sciences, Faculty of Science and Technology, Universiti Kebangsaan Malaysia, 43600 UKM Bangi, Selangor, Malaysia

\*Corresponding author: nurazira@uitm.edu.my

Received: 20 August 2021; Accepted: 3 February 2022; Published: 27 June 2022

#### **Abstract**

Palm oil has become one of the potential renewable resources in biolubricant application. However, the direct application of palm oil as a biolubricant is restricted due to its low oxidative stability and poor low temperature properties. These drawbacks can be overcome by molecule structural redesign through chemical modification process. Palm oil (PO) was modified via epoxidation, ring opening and esterification process. The epoxidized palm oil (EPO) was prepared by using an in-situ performic acid catalyst. Then, EPO was ring-opened using oleic acid in the presence of p-toluenesulfonic acid (PTSA) as a catalyst and further esterification with oleic acid using sulfuric acid as catalyst. The molecular structure confirmation of modified palm oils was proven through the oxirane oxygen content (OOC) value, iodin value, hydroxyl value, Fourier transformation infra-red (FTIR), proton and carbon nuclear magnetic resonance (<sup>1</sup>H-NMR and <sup>13</sup>C-NMR) spectroscopy analysis. Results showed that the conversion of PO into EPO has improved its oxidative stability (190 °C). While, the esterification process has resulted in branching and bending in the molecule structure of the final product (palm oil dioleate, PODO), which improved its pour point (-10 °C), flash point (315 °C) and viscosity index (146). These make PODO suitable to be used in biolubricant application.

Keywords: biolubricant, epoxidation, esterification, ring opening, palm oil

#### **Abstrak**

Minyak sawit merupakan salah satu sumber yang boleh diperbaharui yang berpotensi dalam penghasilan biopelincir. Walaubagaimanapun, penggunaan secara terus minyak sawit sebagai biopelincir adalah terhad disebabkan oleh kestabilan oksidatif yang rendah dan sifat suhu rendah yang lemah. Kelemahan ini boleh diatasi dengan ubahsuai struktur molekul melalui proses pengubahsuaian kimia. Minyak sawit (PO) diubahsuai melalui proses pengepoksidaan, pembukaan gelang dan pengesteran. Minyak sawit terepoksida (EPO) dihasilkan menggunakan mangkin asid performik yang dijana secara in-situ. Seterusnya, EPO ditindakbalaskan melalui pembukaan gelang menggunakan asid oleik dengan kehadiran p-toluena asid sulfonik (PTSA) sebagai mangkin dan diikuti dengan pengesteran dengan asid oleik dengan menggunakan mangkin asid sulfurik. Pengecaman struktur molekul minyak sawit terubahsuai dibuktikan melalui nilai kandungan oksigen oksiran, nilai iodin, nilai

hidroksil, spektroskopi infra-merah transformasi Fourier (FTIR), proton dan karbon nuklear magnetik resonans (¹H-NMR dan ¹³C-NMR). Keputusan menunjukkan penukaran PO kepada EPO telah memperbaiki nilai kestabilan oksidatifnya (190 °C). Manakala proses pengesteran telah menghasilkan struktur molekul yang bercabang dan bengkok bagi hasil akhir (dioleate minyak sawit, PODO) dan telah memperbaiki nilai takat tuang (-10 °C), takat kilat (315 °C) dan indeks kelikatan (146). Ini menjadikan PODO sesuai untuk digunakan dalam aplikasi biopelincir.

Kata kunci: biopelincir, pengepoksidaan, pengesteran, pembukaan gelang, minyak sawit

#### Introduction

Currently, there are wide ranges of base oils used in lubricant application, which include mineral oils, synthetic oils, re-refined oils and plant oils. Among these, mineral oils are the most commonly used [1]. However, mineral oils pose a constant threat to ecology and vast ground water reserves due to their inherent toxicity and non-biodegradable nature [1, 2]. The reduction of petroleum oil resources and increasing greenhouse gas emissions also provide a clear picture of the importance of the move towards sustainable development [3]. The use of renewable sources in the industry is vital to ensure sustainable development.

Plant oils are found to be the best alternative source to replace mineral oils in the production of biolubricant because they are renewable raw materials, biodegradable, non-toxic and environmentally friendly. Plant oil itself exhibits good lubrication properties with high viscosity index [4]. Biolubricants hold great potential for environmental conservation as an alternative lubricant. The global market size for biolubricants was USD 2.20 billion in 2019 and is projected to reach USD 2.46 billion by 2025, at a compound annual growth rate (CAGR) of 4.1% between 2020 and 2025 [5]. Stringent regulations and the growing acceptance among end-users are projected to drive the biolubricants market [5].

However, plant oils have several drawbacks that will restrict their direct application in the lubricant industries such as low oxidative stability [6, 7] and poor low temperature properties [3, 8]. The low oxidative stability is due to the presence of bis-allylic protons in plant oil's structure which are highly susceptible to free radical attack and therefore undergo oxidative degradation to form polar oxy compounds [9-13]. The rate of the oxidation process can be attributed

to the number of unsaturated fatty acids present in its composition [10,14]. Meanwhile, poor low temperature properties include cloudiness, precipitation, poor flowability and solidification at relatively high temperatures [8, 15]. The poor low temperature properties also will limit its use at a low operating temperature [6].

The oxidative stability and poor low temperature drawbacks that occur in the plant oils can be overcome by molecule structural redesign through chemical modifications. The presence of the double bonds and their reactivity have allowed the functional addition reactions into the unsaturated fatty acids. The epoxidation process is one of the most important functionalization reactions of the double bond to other stable functional groups to improve the plant oil's oxidative stability [6, 16, 17]. The epoxidation of plant oil using peracids is one of the most important steps and a useful modification process toward the double bonds because the epoxides are reactive intermediates that can be converted to other functional groups through ring-opening reactions [18]. Plant oils with high content of unsaturated fatty acid are used to produce high epoxy functionality materials [19]. Epoxidized plant oils products from the epoxidation process can be used as high-temperature lubricants [20], plasticizers [21] and high temperature coating materials [22].

Meanwhile, the modification that can be used to improve poor low temperature properties of plant oil is ring opening and esterification reactions. The oxirane ring opening by acidic or alkaline catalyzed reaction with suitable reagent provides interesting polyfunctional compounds [15, 23], whereas reducing structural uniformity of the oil by attaching alkyl side chains would improve the low-temperature performance [15, 24]. The branching group which resulted from ring opening reaction will interfere with the formation of macro-crystalline structures during low-temperature applications and provide enhanced fluidity to plant oils. These modified plant oils with chain branching were reported to have the superior performance of the physicochemical properties and are promising as biolubricants [25]. Products obtained from ring opening can be used as low-temperature lubricants [20].

Palm oil which is abundantly available all over Malaysia become one of the potential plant oils that can be used as biolubricant base stock [26, 27]. In this

paper, the modification of palm oil molecule structure to produce a base stock oil for lubricant application as shown in Figure 1 is reported. Palm oil contains a high percentage of unsaturated fatty acid (49.4%) [28], which serves as good starting material for the epoxidation process. Palm oil was converted into epoxidized palm oil followed by the ring opening and esterification reactions with oleic acid to enhance the lubrication properties. The structure of products was confirmed by FTIR and NMR spectroscopy. Physicochemical properties of products were examined by using several tests such as oxidative stability, pour point, flash point and viscosity index.

Figure 1. The schematic reaction for the modification of palm oil

#### **Materials and Methods**

#### **Materials**

Palm oil was obtained from Jomalina Refinery, Teluk Panglima Garang, Selangor, Malaysia. Formic acid (88%) was obtained from Fisher Scientific and hydrogen peroxide (30%) from Merck. Oleic acid (90%) was purchased from Sigma Aldrich. Ethyl acetate, toluene, sodium hydrogen carbonate and sodium chloride were purchased from Systerm.

#### **Chemical modification processes**

The epoxidation process was carried out based on the optimum conditions reported by Nurazira et al. [27]; mole ratio of PO: HCOOH: H<sub>2</sub>O<sub>2</sub> (1:5.91:3.6), reaction temperature of 40 °C and reaction time of 2.55 hours. Next, the ring opening process was carried out based on the optimum conditions reported by Nurazira et al. [29]; mole ratio of EPO: oleic acid (1:3), reaction temperature of 119 °C, reaction time of 4.73 hours and 1.02% of *p*-toluenesulfonic acid (PTSA). The next esterification was carried out by using a mole ratio of POHO and oleic acid at 1:3, reaction temperature of 135 °C, reaction time of 4.96 hours and 1.86% of sulphuric acid.

#### Characterization of modified palm oils

The unsaturation of oil was determined by iodine value (IV) test using the Wijs method [30]. Oxirane oxygen content (OOC) value was determined by direct method using hydrobromic acid solution in glacial acetic acid (AOCS Cd 9-57) [31]. Hydroxyl value (HV) was performed according to analysis method (AOCS Tx 1a-66) [31]. The structure of modified oils was confirmed by using Fourier Transformation Infra-red (FTIR), proton and carbon Nuclear Magnetic Resonance (<sup>1</sup>H-NMR and <sup>13</sup>C-NMR). FTIR spectra were recorded on a Perkin Elmer Infrared Spectrophotometer in the range of 400-4000 cm<sup>-1</sup>. <sup>1</sup>H and <sup>13</sup>C NMR were recorded on JEOL-ECP 400 spectrometer (400 MHz <sup>1</sup>H/100.61 MHz <sup>13</sup>C) using CDCl<sub>3</sub> as a solvent.

## Physicochemical properties tests of modified palm

The American Society for Testing Materials standards such as ASTM D-6186, ASTM D-5853, ASTM D-92

and ASTM D-2270 were used to measure oxidative stability, pour point, flash point and viscosity index [32]. The oxidative stability test was conducted using Differential Scanning Calorimetry (DSC). 1.5 mg of sample was placed into an aluminum pan with a pinhole cover to allow interaction between ester product and oxygen gas which acts as reaction gas. Then, aluminum pan was put into DSC and heated for 20 minutes up to temperatures of 250 °C by using nitrogen gas. Onset temperature was recorded to determine the oxidative stability.

In the pour point test, the sample was filled into a U-shaped glass tube until it reached a height of 4 cm. The thermometer was placed at one end of the U-shaped tube and both ends of the U-shaped tube was covered with parafilm. The U-shaped tube containing the sample was placed in the refrigerator (minimum temperature -80 °C) for 24 hours to ensure that the sample froze completely. After being left overnight, the U tube was removed and flipped upside down. The lowest temperature at which movement of the sample was observed was recorded as the pour point.

For flash point testing, 2 mL of sample was placed in a crucible and heated on a heating plate. A thermometer with a maximum reading temperature of 360 °C was placed on the sample to measure the sample's temperature. The temperature was rapidly increased at first and then at a slow constant rate as the flash point was approached. The lowest temperature at which the vapors above the surface of the liquid ignited was taken as the flash point.

For the viscosity index test, the Rheometer Anton Paar (Physica MCR 301 model) was used to measure the viscosity and viscosity index of the tested sample. The diameter used for both samples was 0.051 mm. Samples was tested at 40 °C and 100 °C [32]. The sample viscosity index was calculated based on the formula below:

Viscosity index=  $(L-U)/(L-H)\times 100$ 

where: U= oil's kinematic viscosity at 40  $^{\circ}$ C, L and H = values based on the oil's kinematic viscosity at 100  $^{\circ}$ C.

#### **Results and Discussion**

Palm oil is golden yellow and exists in the semi-solid form at room temperature. The liquid fraction contains unsaturated triacylglycerol (TAG), whereas the solid fraction contains more saturated TAG. The epoxidation process is more likely to occur at unsaturated TAG.

In epoxidation reaction, hydrogen peroxide acts as an oxygen donor, while formic acid acts as an oxygen carrier and gets regenerated once the epoxidation reaction takes place [33]. Formic acid also takes part in the overall reaction as a catalyst in the formation of the oxirane ring and as a reactant in the hydrolysis of the oxirane ring. To attain the maximum oxirane oxygen content, the level of the formic acid should be such that these two effects are balanced [34,35]. Figure 2 shows the mechanism of the epoxidation reaction.

The results for the epoxidation of palm oil are shown in Table 1. The average percentage yield of epoxidation was 86% (w/w). The epoxi dation process can be monitored through the IV and OOC values. The IV should be as small as possible after epoxidation, while OOC should be as large as possible. There was a

difference between the IV before and after epoxidation. The initial IV of palm oil before epoxidation was 57.8 m/g, while the IV obtained for EPO after epoxidation was low approaching zero (0.09 mg/g). EPO showed a high OOC value which was 3.46% with 99.43% of relative conversion oxirane (RCO). The theoretical value of OOC was 3.49%. It means almost all unsaturated fatty acids in PO were successfully epoxidized and converted to oxirane rings to produce EPO.

Many nucleophilic reagents are known to add to an oxirane ring, resulting in ring opening. The ester branching groups produced from oxirane ring opening based esterification reactions are effective for attaining the desired molecular spacing. Most of the oxirane ring groups were opened and converted into ester bonds in the molecule with the hydroxyl group [26, 36]. The modified plant oils with chain branching were reported to have superior performance properties and are promising as biodegradable lubricants [26,36,37]. Figure 3 shows the mechanism of ring opening reaction.

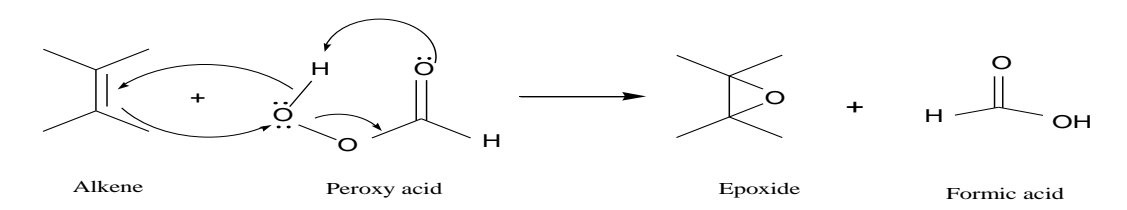


Figure 2. The mechanism of the epoxidation reaction

Table 1. Analysis results for modified palm oils

Compound	PO	EPO	РОНО	PODO
Yield (%)	-	86	84	80
Iodine value (mg/g)	57.8	0.09	59.4	109.8
OOC value (%)	-	3.46	0.041	-
RCO (%)	-	99.43	-	-
Hydroxyl value (mgKOH/g)	19	23	118.7	25.4

Figure 3. The mechanism of the ring opening reaction

This study reports the oxirane ring opening reaction of epoxidized palm oil (EPO) by the nucleophilic addition of oleic acid (OA) in the presence of homogenous acid catalysts which was *p*-toluenesulfonic acid (PTSA). PTSA was preferred to be used in the reactions due to the maximum yield of epoxy ring opening and no evidence of any side reaction occurred during the reaction [38]. The nucleophilic attack by the fatty acid molecule which was oleic acid on the oxirane ring of epoxidized palm oil (EPO) in the presence of PTSA as catalyst resulted in the ring opened product: palm oil hydroxy oleate (POHO).

The results for the ring opening process are shown in Table 1. The average percentage yield of ring opening was 84% (w/w). The ring opening process can be monitored through IV, HV and OOC values. The OOC value should be as small as possible. This is because the reduction of OOC value is proportional to the number of epoxides opened. OOC value obtained after ring opening process was low approaching zero (0.041%). It showed that the entire epoxide ring was successfully opened during the ring opening reaction with the oleic acid to produce POHO. The entire epoxide ring had been successfully converted to hydroxyl oleate ester functional groups. This can be evidenced by the increase of IV and HV of the product. The addition of the olefin which exists from the oleate acyl group had increased the IV of POHO to 59.4 mg/g. There was also an increase in HV from 23 mg KOH/g to 118.7 mg KOH/g after the ring opening process. Further esterification of POHO with oleic acid produced the final product: palm oil dioleate (PODO). The average percentage yield of the final esterification process was 80% (w/w). There was a decrease in HV of PODO to 25.4 mgKOH/g and an increase of IV (109.8 mg/g) after esterification. It means that the hydroxyl group of POHO was reacted with oleic acid to produce the oleate acyl group.

#### FTIR spectra

The presence of functional groups in all modified oils was identified by using FTIR spectroscopy. Figure 4 shows the FTIR spectra of PO, EPO, POHO and PODO. The disappearance of the double bond functional group peak at 3005 cm<sup>-1</sup> which was initially present in the PO spectrum indicated the conversion of the double bond to the epoxy group. It can be proven by the presence of a C-O-C oxirane peak at 843 cm<sup>-1</sup> in the EPO spectrum. Pavia et al. [39] reported the presence of epoxy group can be monitored at wavenumber range of 815-950 cm<sup>-1</sup> which agrees well for this study.

The disappearance of the epoxide peak showed that the entire oxirane ring had been successfully converted to hydroxyl oleate ester functional groups during the ring opening reaction with oleic acid. This is evidenced by the increase of peaks intensity of the hydroxyl (OH) functional group at 3463 cm<sup>-1</sup> and C=O stretching at 1740 cm<sup>-1</sup> in the POHO spectrum. A significant change in the ring opening process also can be evidenced by

the existence of the C=C olefin peak of the oleate acyl group at 3003 cm<sup>-1</sup> in the POHO spectrum. The final esterification product (PODO) was evidenced by the

reduction of the peak intensity of the hydroxyl group in the PODO spectrum.

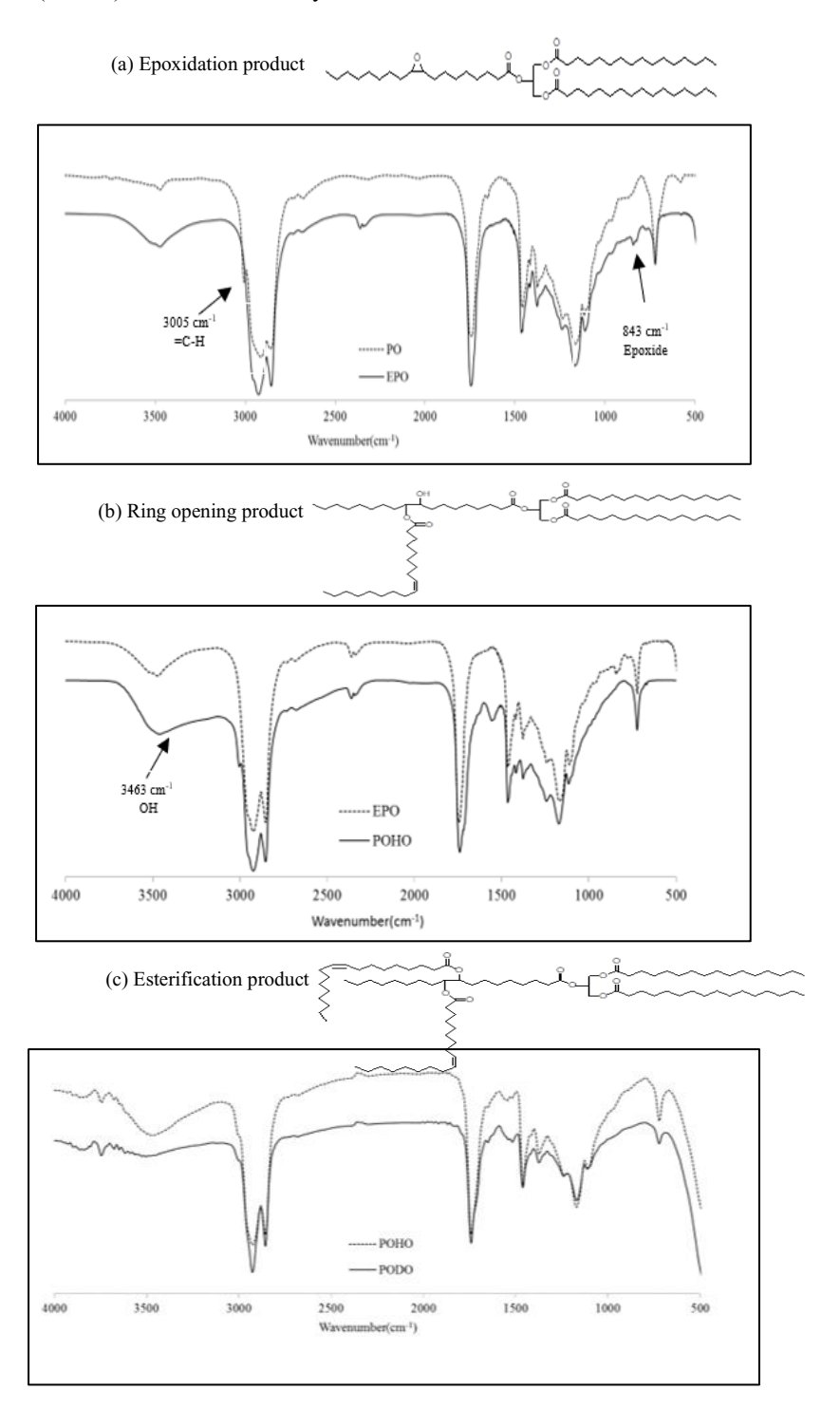
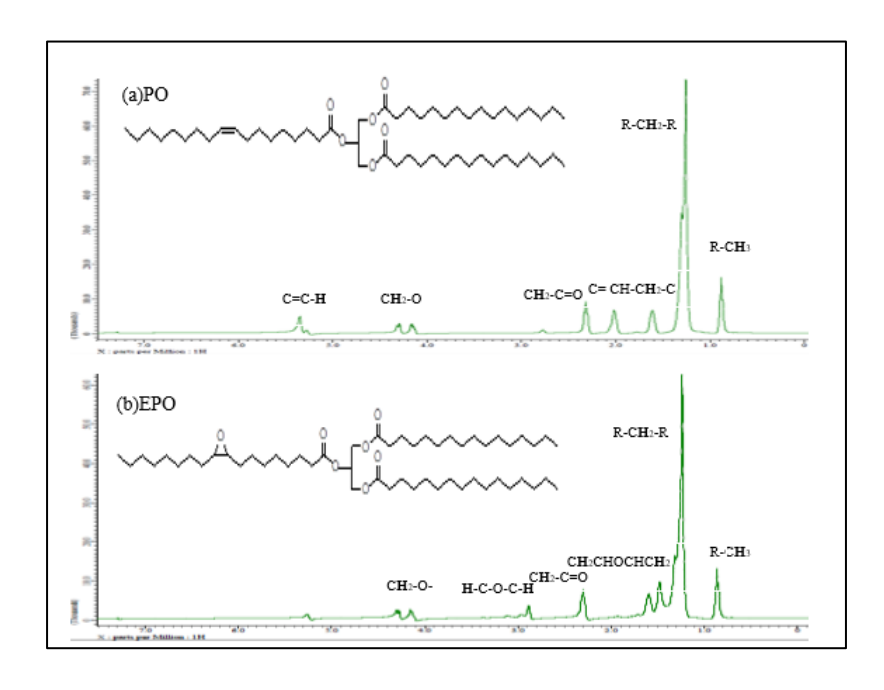


Figure 4. FTIR spectra of (a) epoxidation; (b) ring opening; (c) esterification products

### **NMR** spectra

Figure 5 shows <sup>1</sup>H NMR spectra of PO, EPO, POHO and PODO and Table 2 shows the chemical shift for all products. The epoxidation process (EPO) can be proven by the disappearance of olefin proton at 5.34 ppm (C=C-H) and allylic proton at 2.0-2.05 ppm (C=C-C-H), which initially were present in the PO spectrum. They were replaced by the existence of a peak signal at 2.89 ppm, which corresponds to the proton of oxirane ring (CHOCH) and a peak signal at 1.49 ppm that represents epoxy proton (CH2-CHOCH-CH<sub>2</sub>) in the EPO spectrum. The result of ring opening reaction can be confirmed by the disappearance of peak signal of oxirane ring proton (CHOCH) in the POHO spectrum. Peak signal for olefin proton and allylic proton can be detected at 5.30-5.36 ppm (C=C-H) and 1.97-2.09 ppm (C=C-C-H) in the POHO spectrum. The final product showed that there was a disappearance of the C-O-H peak signal (C-O-H) in the PODO spectrum.

Figure 6 shows <sup>13</sup>C NMR spectra of PO, EPO, POHO and PODO and Table 3 shows the chemical shift for all products. The peaks at 127.85- 130.17 ppm in the PO spectrum represented the double bond (C=C). Conversion of the double bond to oxirane ring can be proven by the disappearance of double bond peak and existence of carbon atom of epoxy (C-O) at 54.19-57.22 ppm in EPO spectrum. The results of ring opening reaction can be evidenced by disappearance of epoxy carbon, the existence of carbon olefin (C=C) at 129.60-129.97 ppm and also the existence of peak signal at 73.50 ppm, which represents the carbon next to the hydroxyl group (HC-OH) in POHO spectrum. The final product showed that there was a disappearance of the HC-OH signal peak in the PODO spectrum.



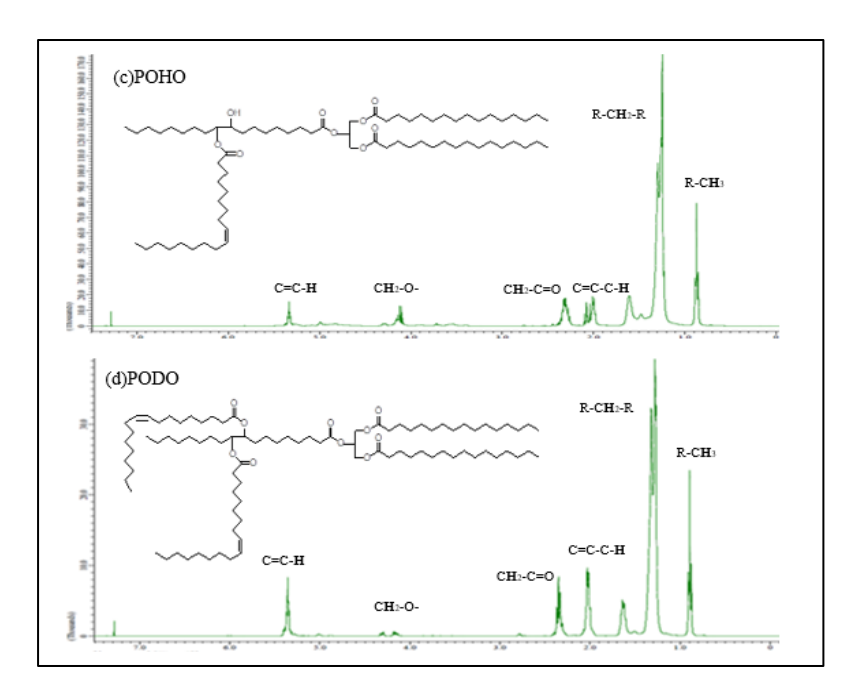


Figure 5. <sup>1</sup>H NMR spectra of (a) PO; (b) EPO; (c) POHO and (d) PODO

Table 2. The chemical shifts for <sup>1</sup>H NMR PO, EPO, POHO and PODO spectra

Compound	Chemical Shift, ppm	Chemical Shift, ppm (Reference <sup>36</sup> )	Remarks
PO	5.34	4.5-6.5	С=С-Н
	2.00 - 2.05	1.6-2.6	C=C-C-H
EPO	2.89	2.5-3.5	СНОСН
РОНО	5.30-5.36	4.5-6.5	C=C-H
	1.97-2.09	1.6-2.6	C=C-C-H
	4.99	0.5-5.0	С-О-Н
PODO	5.34-5.37	4.5-6.5	C=C-H
	2.00-2.07	1.6-2.6	C=C-C-H

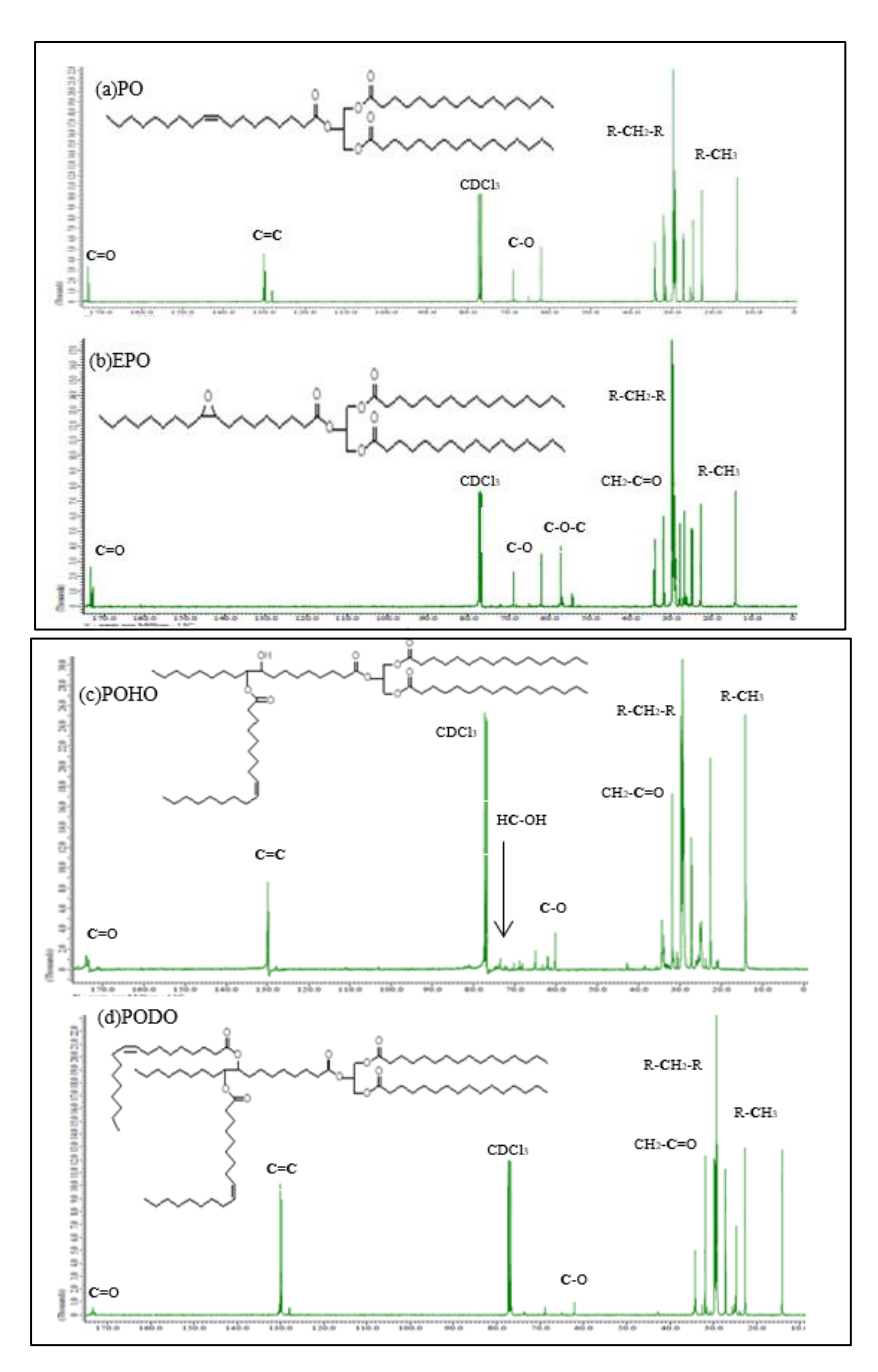


Figure 6. <sup>13</sup>C NMR spectra of (a) PO; (b) EPO; (c) POHO and (d) PODO

Table 3. The chemical shifts for <sup>13</sup>C NMR PO, EPO, POHO and PODO spectra

Compound	Chemical Shift, ppm	Chemical Shift, ppm (Reference <sup>36</sup> )	Remarks
PO	127.85- 130.17	100-150	C=C
EPO	54.19-57.22	56.9-58.5	C-O-C
РОНО	129.60-129.97	100-150	C=C
	60.18-63.30	40-80	C-O
PODO	127.88-130.16	100-150	C=C

#### Physicochemical properties

There were several tests conducted to determine the physicochemical properties of the modified oils. The physicochemical properties results obtained are shown in Table 4. The ability of a substance to resist oxidative degradation is an important property of biolubricant. Oxidative stability is determined by the onset temperature (OT) using Differential Scanning Calorimetry (DSC). OT is the temperature at which the occurrence of a sharp increase in the rate of oxidation of the sample. Higher onset temperature indicates that

the lubricant has high oxidation stability [6]. Based on the DSC analysis, there was an improvement in oxidative stability for EPO (190 °C) compared to PO (181 °C). It was due to the conversion of the double bond group to the epoxy group which will reduce the active site of oxidation and make it less susceptible to radical attack. However, POHO and PODO showed low oxidative stability due to increasing double bond content and carbon chain, which will increase the potential active site for the oxidation process.

Table 4. Physicochemical properties of PO, EPO, POHO, PODO and commercial lubricants (100A and 100B)

Compound	PO	EPO	РОНО	PODO	100A <sup>a</sup>	100B <sup>b</sup>
Oxidative stability (°C)	181	190	170	157	n/a	n/a
Pour point (°C)	7	18	-8	-10	-19	-27
Kinematic viscosity (40 °C)	56.97	97.72	616.46	83.45	96	96.7
Kinematic viscosity (100 °C)	9.24	14.56	60.73	15.30	10.9	11
Viscosity index (VI)	130	133	125	146	97	100
Flash point (°C)	240	255	295	315	276	254
ISO viscosity grade	46	100	680	100	100	100

a:100A: Denicol Compressor Oil ISO VG 100 [41],

b: SubsTech Hydraulic Oil ISO 100 [42]

Pour point is one of the important quality parameters to determine cold flow or low temperature properties of the lubricant. The cold flow properties of plant oils are extremely poor and these limit their use at low operating temperatures especially as automotive and industrial fluids. Plant oils tend to form

macrocrystalline structures at low temperatures through uniform self-stacking of the linear triacylglycerol molecules. The macrocrystals restrict the easy flow of the system due to the loss of kinetic energy of individual molecules during self-stacking [6, 15, 40]. PODO has the lowest pour point (-10 °C) compared to other products due to the branched carbon chain and bent structure. It makes it more restricted to selfstacking and more hollows in the structure, thus easier for it to flow, which contributed to the lowest pour point. In general, the presence of a branching group at the end of the molecule will disrupt this stacking process and create a steric barrier around the individual molecules and inhibit crystallization [18]. This will result in the formation of microcrystalline structures rather than macro structures. At lower temperatures, the microcrystalline structures can easily tumble and glide over one another resulting in better fluidity of the total matrix [6], resulting in a lower pour point. Moreover, the disappearance of the hydroxyl group in PODO esters means that no hydrogen bonds exist in the molecule, which causes the molecules to be less sticky to each other and to move freely around.

Viscosity also becomes one of the important quality parameters for lubricating oils. The efficiency of the biolubricant in reducing friction and wear is greatly influenced by its viscosity. The viscosity of PO is lower than EPO due to the existence of a double bond, which provides the lubricating properties of liquids by degrees of unsaturation. POHO has a higher viscosity due to the presence of intermolecular hydrogen bonding from the hydroxyl group resulted from the ring opening reaction. The hydroxyl group gives a higher polarity that influences the viscosity of the oil, in which more polar molecule of oil, the higher the viscosity [40]. In general, the hydroxyl group will form a bond between molecules and cause lubricating oil to become more viscous. After the final esterification process, the viscosity of PODO decreased due to the disappearance of the hydroxyl group. The viscosity of PODO was in the medium range, which was 83.45 centistokes (cSt) at 40 °C and decreasing to 15.30 cSt at 100 °C. It shows the viscosity of biolubricant decreases as temperature increases. The least viscous biolubricant which still forces the two moving surfaces

apart is desired. If the biolubricant is too viscous, it will require a large amount of energy to move and if is too thin, the surfaces will rub and friction will increase [6]. The viscosity index highlights how the viscosity of biolubricant changes with variations in temperature [6]. PODO showed the highest viscosity index (146) compared to other products. It shows the viscosity of PODO is less affected by temperature changes and does not drastically change when the temperature varies. This is a good indicator and it is suitable for use at a large temperature range.

The flash point is often used as a descriptive characteristic of fuel oil and it is also used to describe oils that are not used as fuels such as a lubricant. Flash point refers to both flammable oils and combustible oils. The oils with a flash point of less than 43 °C are flammable, while those having a flash point above this temperature are combustible. Biolubricant which has a low flash point value is considered to have been contaminated by volatile and usually requires special precautions when handling these biolubricant [6]. PODO showed the highest flash point (315 °C) compared to other products. It is due to the increasing carbon number which causes an increasing molecular weight that gives a higher flash point. In addition, PODO also has a big branched molecular structure which requires more energy to burn. This will increase the flash point of PODO. A high flash point is important to ensure that the lubricant is not burned in the engine during its operation.

Table 4 also shows a comparison of lubrication properties between the biolubricant base stock produced (PODO) with commercial lubricants in the market. The selected commercial lubricants are ISO VG 100 grade lubricants, namely Denicol Compressor Oil (100A) [41] and SubsTech Hydraulic Oil (100B) [42]. Based on the comparison made, PODO has a higher viscosity index compared to 100A and 100B lubricants. The pour point value of PODO is also lower than 100A and 100B lubricant. In addition, PODO also recorded much higher flash point value than 100A and 100B lubricants.

#### Conclusion

The chemically modified palm oils showed improvement in physicochemical properties. The epoxidized palm oil (EPO) has the highest oxidative stability due to the reduction of double bond content, while the final esterification product, palm oil dioleate (PODO) has the lowest pour point due to the greater ability of the branched chain esters to disrupt crystalline formation. A bigger, bending, branching and hollow structure makes the molecule less compact, thus improve the lubricity of the lubricant. PODO also showed the highest viscosity index and flash point due to the big branched molecular structure. This makes PODO as plausible to be used as a biolubricant with better lubrication properties.

#### Acknowledgement

The authors gratefully acknowledge Universiti Kebangsaan Malaysia for financial support under research grant GUP-2016-012 and GUP-2016-058. The authors also thank the Ministry of Education, Malaysia for providing scholarship support (MyPhD) for the author.

#### References

- Salimon, J. and Salih, N. (2009). Oleic acid diesters: Synthesis, characterization and low temperature properties. *European Journal of Scientific Research*, 32(2): 216-222.
- Farhoosh, R., Einafshar, S. and Sharayei, P. (2009). The effect of commercial refining steps on the rancidity measures of soybean and canola oils. *Food Chemistry*, 115: 933-938.
- 3. Erhan, S. Z. and Asadauskas, S. (2000). Lubricant basestocks from vegetable oils. *Industrial Crops and Products*, 11: 277-282.
- 4. Nirmal, V. P. and Dineshbabu, D. (2015). Performance and emission of *Pongamia pinnata* oil as a lubricant in diesel engine. *International Journal of Innovative Research in Science, Engineering and Technology*, 4(2): 75.
- Salih, N. and Salimon, J. (2021). A review on ecofriendly green biolubricants from renewable and sustainable plant oil sources. *Biointerface Research in Applied Chemistry*, 11(5): 13303-13327.
- Salimon, J., Salih, N. and Yousif, E. (2011). Chemically modified biolubricant basestocks from epoxidized oleic acid: Improved low temperature

- properties and oxidative stability. *Journal of Saudi Chemical Society*, 15: 195-201.
- 7. Wu, X., Zhang, X., Yang, S., Chen, H. and Wang, D. (2000). The study of epoxidized rapeseed oil used as a potential biodegradable lubricant. *Journal of the American Oil Chemist Society*, 77: 561-563.
- 8. Salimon, J. and Salih, N. (2010). Modification of epoxidized ricinoleic acid for biolubricant base oil with improved flash and pour points. *Asian Journal of Chemistry*, 22(7): 5468-5476.
- 9. Adhvaryu, A., Liu, Z. and Erhan, S. Z. (2005). Synthesis of novel alkoxylated triacylglycerols and their lubricant base oil properties. *Industrial Crops and Products*, 21:113-119.
- Borugadda, V. B. and Goud, V. V. (2015). Response surface methodology for optimization of biolubricant basestock synthesis from high free fatty acids castor oil. *Energy Science & Engineering*, 3(4): 371-383.
- Erhan, S. Z., Sharma, B.K. and Perez, J. M. (2006). Oxidation and low temperature stability of vegetable oil-based lubricants. *Industrial Crops* and *Products*, 24: 292-299.
- Sharma, B. K., Perez, J. M. and Erhan, S. Z. (2007). Soybean oil-based lubricants: A search for synergistic antioxidants. *Energy Fuels*, 21: 2408-2414.
- 13. Singh, C. P. and Chhibber, V. K. (2013). Chemical modification in karanja oil for biolubricant industrial applications. *Journal Drug Delivery Therapeutics*, 3:117-122.
- 14. Borugadda, V. B. and Goud, V. V. (2013). Comparative studies of thermal, oxidative and low temperature properties of waste cooking oil and castor oil. *Journal Renewable Sustainable Energy*, 5: 063104.
- 15. Salimon, J. and Salih, N. (2009). Substituted esters of octadecanoic acid as potential biolubricants. *European Journal of Scientific Research*, 31(2): 273 227.
- 16. Moser, B. R. and Erhan, S. Z. (2007). Preparation and evaluation of a series of α-hydroxy ethers from
  9, 10-epoxystreates. European Journal Lipid Science Technology, 109: 206-213

- 17. Salimon, J., Ahmed, W. A., Salih, N., Yarmo, M. A. and Derawi, D. (2015). Lubricity and tribological properties of dicarboxylic acids and oleyl alcohol based esters. *Sains Malaysiana*, 44(3): 405-412.
- 18. Wang, R. and Schuman, T. P. (2013). Vegetable oil-derived epoxy monomers and polymer blends: A comparative study with review. *eXPRESS Polymer Letters*, 7(3):272–292.
- Meyer, P. P., Techaphattana, N., Manundawee, S., Sangkeaw, S., Junlakan, W. and Tongurai, C. (2008). Epoxidation of soybean oil and jatropha oil. *Thammasat International Journal Science Technology*, 13: 1-5.
- Lathi, P. S. and Mattiasson, B. (2007). Green approach for the preparation of biodegradable lubricant base stock from epoxidised vegetable oil. Applied Catalysis B: Environmental, 69: 207-212.
- Joseph, R., Madhusoodhanan, K. N., Alex, R., Varghese, S., George, K. E. and Kuriakose, B. (2014). Studies on epoxidised rubber seed oil as secondary plasticiser/stabiliser for polyvinyl chloride. *Plastics Rubber and Composites*, 33(5): 217-222.
- 22. Derawi, D. and Salimon, J. (2016). Sintesis sebatian hidroksi-eter minyak sawit olein. *Sains Malaysiana*, 45(5): 817-823.
- Yunus, R., Razi, A. F., Iyuke T. L. and Idris, A. (2003). Preparation and characterization of trimethylolpropane esters from palm kernel oil methyl esters. *Journal of Oil Palm Research*, 15(2):42-49.
- Sharma, B. K., Doll, K. M. and Erhan, S. Z. (2008). Ester hydroxy derivatives of methyl oleate: tribological, oxidation and low temperature properties. *Bioresource Technology*, 99: 7333-7340.
- 25. Salimon, J., Abdullah, B. M., Yusop, R. M., Salih, N. and Yousif, E. (2013). Synthesis and optimization ring opening of monoepoxide linoleic acid using *p*-toluenesulfonic acid. *SpringerPlus*, 2: 429.
- Nor, M. N., Derawi, D. and Salimon, J. (2017). Chemical modification of epoxidized palm oil for biolubricant application. *Malaysian Journal of Analytical Sciences*, 21(6):1423-1431.

- Nor, M. N., Derawi, D. and Salimon, J. (2018).
   The optimization of RBD palm oil epoxidation process using D-optimal design. Sains Malaysiana, 47(7):1359-1367.
- Njoku, P. C., Egbukole, M. O. and Enenebeaku, C. K. (2010). Physio-chemical characteristics and dietary metal levels of oil from *Elaeis guineensis* species. *Pakistan Journal of Nutrition*, 9(2):137-140.
- 29. Nor, M. N., Salih, N. and Salimon, J. (2021). Optimization of the ring opening of epoxidized palm oil using D-optimal design. *Asian Journal of Chemistry*, 33(1):67-75.
- 30. Kuntom, A., Lin, S. W., Ai, T. Y., Idris, N. A., Yusof, M., Sue, T. T. and Ibrahim, N. A. (2004). MPOB test methods: A compendium of test on palm oil products, palm kernel products, fatty acids, food related products and others. MPOB, Bangi.
- 31. A.O.C.S. (1998). *Official Methods and Recommended Practices of AOCS*, AOCS, Illionis.
- Nadkarni, R. A. (2007). Guide to ASTM test methods for the analysis of petroleum products and lubricants. ASTM International, West Conshohocken
- 33. Mungroo, R., Pradhan, N. C, Goud, V. V. and Dalai, A. K. (2008). Epoxidation of canola oil with hydrogen peroxide catalyzed by acidic ion exchange resin. *Journal of the American Oil Chemist Society*, 85:887-896.
- Goud, V.V., Patwardhan, A.V. and Pradhan, N. C. (2006). Studies on the epoxidation of mahua oil (*Madhumica indica*) by hydrogen peroxide. *Bioresource Technology*, 97:1365-1371.
- 35. Goud, V.V., Patwardhan, A.V., Dinda, S. and Pradhan, N. C. (2007) Kinetics of epoxidation of *Jatropha* oil with peroxyacetic and peroxyformic acid catalysed by acidic ion exchange resin. *Chemical Engineering Science*, 62: 4065-4076.
- 36. Baumann, H., Buehler, M., Fochem, H., Hirsinger, F., Zoebelein, H. and Falbe, J. (1988). Natural fats and oils renewable raw materials for the chemical industry. *Angewandte Chemie*, 27(1): 41-62.

- Hwang, H. S. and Erhan, S. Z. (2001). Modification of epoxidized soybean oil for lubricant formulation with improved oxidative stability and low pour point. *Journal of the American Oil Chemist Society*, 78(12): 1179-1184.
- 38. Salimon, J., Abdullah, B. M., Yusop, R. M., Salih, N. and Yousif, E. (2013). Synthesis and optimization ring opening of monoepoxide linoleic acid using *p*-toluenesulfonic acid. *SpringerPlus*, 2: 429.
- Pavia, D. L., Lampman, G. M., Kriz, G. S. and Vyvyan, J. R. (2009). Introduction of spectroscopy, Fourth edition. Cengage Learning, United States: pp. 51-52

- 40. Sharma, A., Adhvaryu, A., Liu, Z. and Erhan, S. Z. (2006). Chemical modification of vegetable oils for lubricant applications. *Journal of the American Oil Chemist Society*, 83:129-136.
- 41. Denicol Motor Oils N.V (2020). Denicol compressor oil. Access from https://pdf4pro.com/view/compressor-oil-iso-vg-32-46-68-100-150-denicol-5786bc.html. [Access online 25 December 2020].
- 42. SubsTech: Substances and Technologies (2012). SubsTech hydraulic oil. Access from http://www.substech. com /dokuwiki/doku.php? id=hydraulic\_oil\_iso\_100 .[Access online 25 December 2020].

# Malaysian Journal of Analytical Sciences (MJAS)



Published by Malaysian Analytical Sciences Society

## THE REMOVAL OF BISPHENOL-A FROM SYNTHETIC WASTEWATER USING THIN-FILM COMPOSITE MEMBRANE

(Penyingkiran Bisfenol A daripada Sisa Air Sintetik Mengunakan Membran Lapisan Komposit Nipis)

Taofiq Damilare Aiyelabegan, Siti Nur Alwani Shafie, Shafiq Mohd Hizam, Nik Abdul Hadi Nordin\*

Department of Chemical Engineering, Universiti Teknologi PETRONAS, 32610 Seri Iskandar, Perak, Malaysia

\*Corresponding author: nahadi.sapiaa@utp.edu.my

Received: 22 August 2021; Accepted: 24 March 2022; Published: 27 June 2022

#### Abstract

In this study, the removal performance of bisphenol A (BPA) from synthetic wastewater using the forward osmosis method was compared between polyamide thin film composite membrane (PA -TFC) and polysulfone (PSf) membrane substrate. The thin-film composite membrane was prepared by using flat polysulfone (PSf) sheets as membrane substrate through in-situ interfacial polymerization technique. To generate the thin film surface on the PSf substrate, M-phenylenediamine (MPD) and 1,3,5-benzene trichloride (TMC) were utilized as monomers in aqueous and organic solutions, respectively. The BPA retention efficiency of the PSf and TFC membranes was examined and compared accordingly. The membranes were characterized by using atomic force microscopy (AFM), field emission scanning electron microscope (FESEM), Fourier transform infrared spectroscopy (FTIR), and contact angle analysis. The fabricated thin film on the PSf substrate membrane has enhanced its hydrophilicity which aids in wastewater treatment by increasing the membrane's water flow rate. A synthetic BPA wastewater solution of 100 mgL-1 was prepared to evaluate the performance of the membrane. Based on the finding of this study, the PSf substrate and PA -TFC membrane yielded 25% and 91% of BPA removal from the feed solution, respectively.

Keywords: bisphenol-a, polyamide, thin-film composite membrane, forward osmosis

#### Abstrak

Dalam kajian ini, penyingkiran bisfenol A (BPA) dari air sisa sintetik disiasat menggunakan membran filem komposit nipis poliamida (PA -TFC) dan dibandingkan dengan substrat membran polisulfon (PSf) menggunakan proses osmosis hadapan. Membran TFC diperbuat melalui teknik pempolimeran dengan menggunakan permukaan PSf sebagai substrat membran. M-fenildiamina (MPD) dan 1,3,5-benzena triklorida (TMC) digunakan sebagai monomer dalam larutan berair dan organik untuk menghasilkan permukaan filem nipis pada substrat PSf. Penyingkiran BPA melalui membran PSf dan TFC disiasat dan dibandingkan. Setiap membran dicirikan dengan mikroskopi tekanan atom (AFM), mikroskopi imbasan elektron pancaran medan (FESEM), spektroskopi inframerah transformasi Fourier (FTIR) dan analisa sudut sentuhan. Lapisan filem nipis yang dihasilkan pada membran substrat PSf meningkatkan daya hidrofiliknya, yang membantu dalam rawatan air sisa dengan meningkatkan kadar pengeluaran air. 100 ppm larutan sisa air BPA sintetik disediakan untuk menguji prestasi membran. Dari data yang diperoleh dari kajian ini, substrat PSf dan membran PA -TFC menghasilkan 25% dan 91% penurasan BPA dari sisa tersebut.

Kata kunci: bisfenol a, poliamida, membran filem komposit nipis, osmosis hadapan

#### Introduction

The rapid growth and development of modern industries have led to serious environmental issues nowadays. The threats posed by organic micropollutants especially pharmaceutically active and endocrine-disrupting compounds have been of great concern over the previous years. Numerous studies have been performed on investigating their removal mechanism from the wastewater [1]. These compounds are highly related to the effluents of industrial sectors such pharmaceutical, plastic, dye and textiles, oil refineries, and petrochemical industries [2]. Industrial wastewater treatment plant (WWTP) effluent is an important source of these compounds, as these micropollutants are hardly removed by the conventional treatment processes [3, 4]. Thus, advanced membrane treatment of WWTP effluents to remove these pollutants could be an effective approach to reduce their presence in the ecosystem and thus contribute to mitigating the environmental risk.

Bisphenol-A (BPA) is an endocrine disruptor that is commonly utilized in the manufacturing polycarbonate, epoxy resins, dental composites, and medical equipment [5]. This organic pollutant has huge potential to cause serious health hazards to humans, wildlife, and the ecosystem even at low concentrations [6, 7]. Structurally, BPA consists of phenolic and hydroxyl groups in combination with an aromatic ring. BPA has a molecular weight of 228 g/mol and shows relatively low solubility in water with the range of 120-300mg/L at 25 °C [8]. However, its solubility increases if dissolved in polar organic solvents or aqueous solutions with alkaline concentrations. The total daily intake (TDI) of BPA has been regulated at 50µg/kg/day, while the oral reference dosage for BPA has been set at 100 µg/L as the maximum allowable concentration in drinking water according to the United States Environmental Protection Agency [9].

BPA can cause adverse health effects because it is an endocrine disruptor that binds to receptors in living organisms [38]. BPA acts as a hormone receptor blocker for various hormones and interferes with their activity which leads to damage to the human body. For instance, it acts as an antiestrogen by competing with endogenous

E and inhibiting its estrogenic response [10]. Previous laboratory studies reported that this compound may also bind directly to the sex hormone receptors (androgen receptors) and inhibit the activity of endogenous androgen [11]. These hormone-inhibiting effects may lead to fertility problems such as decreased sperm quality, polycystic ovary syndrome, and sex hormone concentrations. Increases in chronic diseases such as type 2 diabetes, obesity, cardiovascular disease, prostate, and breast cancer have been linked to early exposure to BPA [12]. In addition, there is a high probability that maternal exposure to BPA can cause postnatal abnormalities in DNA methylation status, disrupting the expression of some particular genes and the epigenetic programming of gene expression during child development [13]. Due to their widespread dispersion in the environment and continuous usage in industry, it is critical to develop new treatment techniques for their degradation, detoxification, and removal in wastewater effluents.

Concentrative processes such as absorption, ozonation, and Fenton have effectively removed the major microbial contaminants and chemicals from wastewater treatment facilities. However, the application of these techniques for the removal of endocrine disruptors is restricted [14, 15, 16]. In addition, due to stringent water quality requirements, it is becoming increasingly important to remove BPA from water sources, even if it presents in extremely low concentrations. Pressuredriven membrane separation methods such as reverse osmosis (RO), nanofiltration (NF), ultrafiltration (UF), and microfiltration (MF) in pore sizes ascending order, have been demonstrated to be effective in removing BPA from wastewater and producing high-quality water from WWTP secondary effluent [17]. According to Schrotter et al., membrane technology has been utilized to treat approximately 60 million m<sup>3</sup> of water per day, with RO being the most widely used membrane process for wastewater treatment. Meanwhile, microfiltration and ultrafiltration have a combined average capacity of 20 million m<sup>3</sup> per day, accounting for 60% of total drinking water production [17].

Unlike chemical oxidation and biodegradation, membrane filtration does not utilize chemicals or generate by-products/new metabolites, making it more suitable for treating drinking water due to its environmentally friendly's characteristic [17]. The membrane process uses a variety of mechanisms to remove micropollutants from wastewater. For example, BPA removal in NF and RO is performed by sieving and electrostatic interactions, while the removal mechanism in MF and UF is generally based on the adsorption process [18, 19]. When compared to traditional techniques, the employment of membrane separation processes has numerous advantages: low energy cost, easy operational control, no use of chemicals, and compact structure with possible material recovery [20].

Zhao et al. examined the removal of BPA using a commercial UF hollow fibre membrane at a dosage of 1000 μg/L. Due to the large pore size of the UF membrane (0.04 microns), the BPA removal efficiency was found to be < 5%. The removal approach applied the adsorption mechanism of the membrane rather than the size exclusion technique [21]. The UF-Koch membrane was tested for the removal performance of BPA at the concentration of 1µM. This membrane showed significant retention efficiency of BPA (> 40%), which was attributed to the adsorption process on the membrane surface [22]. Bing-Zhi et al. [2010] investigated the removal of BPA from wastewater using a commercial MF membrane. They found that this membrane showed poor BPA retention performance, with the removal rate decreasing from 95% to 20% at the end of the filtration process as the membrane got saturated with BPA [23].

Yuskel et al. observed that the RO and NF membranes performed well when tested for removing BPA from synthetic wastewater at a concentration of 50 mg/L with an operating pressure of 10 bar. The NF membranes made of compressed and loose polyamide were used in the experiment. A polyamide and cellulose acetate RO membrane was also tested. The dense RO and NF membranes demonstrated excellent BPA removal (> 98%), while the loose NF membrane demonstrated much lower rejection (80%), and the cellulose acetate RO membrane demonstrated low rejection of BPA of 10-40%, which was attributed to BPA adsorption on the membrane surface [24]. These technologies, however,

fall short because they are particularly susceptible to membrane fouling, have large pore sizes (MF and UF), and rely on high pressure to work [17].

Forward osmosis (FO) is an alternative membrane filtration process that has been utilized in recent decades for desalination, wastewater treatment, and production of high-quality water. The FO method uses the osmotic differential pressure between the draw and feed solutions to reject the trace organic pollutants. [25]. This process has a great advantage over the conventional membrane filtration process as it does not require the application of hydraulic pressure to operate, and fouling propensity is minimal due to the generation of osmotic pressure from the concentrated draw solution [26]. Even when fouling occurs, it can easily be reversed and controlled via chemical, physical, or physiochemical cleanings unlike the RO and NF methods [27, 28].

Presently, there have been advancements in the type of membranes fabricated using interfacial polymerization (IP) that can be used with the forward osmosis process, such as the thin film composite and thin film nanocomposite membranes. these membranes are controlled by the osmotic pressure of water and are usually utilized in the wastewater separation and desalination processes in pharmaceuticals and chemical industries [29]. TFC membranes are believed to be a viable method for eliminating tiny organic contaminants such as BPA from industrial and pharmaceutical effluents since they are modified to have smaller pore sizes as compared to RO, NF, and UF membranes. Nowadays, TFC membranes made from modifying a thin-film layer of aromatic polyamide on a porous membrane substrate are employed in wastewater treatment operations [30, 31]. The greater retention of feed solution components, along with an increase in permeate flow has led to their widespread adoption. TFC membranes can remove heavy metals, organic micropollutants such as pharmaceuticals, endocrine disruptors, and pesticides from wastewater [17]. In general, polyamide membranes have been reported in the literature that they performed better than cellulose acetate-based membranes in rejecting organic micropollutants. This is because they have lower pressure requirements and operate under more flexible settings [32].

Thus, the goal of this study is to determine if employing a thin-film composite membrane to remove BPA from pharmaceutical effluent is more feasible and efficient than using conventional polysulfone substrates. The interfacial polymerization method was used to fabricate the TFC membrane on the polysulfone membrane substrate layer. Both membranes' efficiency in removing BPA from the synthetic wastewater was compared in this study.

#### **Materials and Methods**

#### Materials and reagents

Bisphenol A (BPA), polysulfone (PSf), polyvinylpyrrolidone (PVP), N-methyl-2-pyrrolidinone (NMP), M-phenylenediamine (MPD), 1,3,5-benzenecarbon trichloride (TMC) were procured from Sigma Aldrich Chemicals Company. These materials were all of the analytical grades and were used exactly as they were received. All of the experiments were conducted using distilled water.

## Forward osmosis membrane fabrication: Membrane substrate preparation (Psf substrate)

The wet phase inversion method was used to prepare the PSf membrane substrate. Firstly, a dope solution with the composition of PSf/NMP/PVP (wt.%) = (15/82/3)

was prepared. The NMP was then dissolved in PSf pellets, and PVP was added as an additive to increase the porosity of the membrane substrate. The casting solution was continuously stirred until the polysulfone pellets were completely dissolved in the solution. The dock solution was then poured on the glass surface with a 200µm casting rod. The casted membrane on the glass surface was instantly submerged in a water bath for the wet phase inversion. The generated PSf support membrane was kept in distilled water before use.

#### Thin-film composite membrane fabrication

The thin-film polyamide layer was fabricated by using the interfacial polymerization method as shown in Figure 1. Two solutions were prepared: an aqueous solution comprising of 2 wt.% MPD in distilled water and an organic solution comprising of 0.05 wt.% TMC dissolved in heptane. The PSf membrane substrate was immersed in the MPD solution for 3 minutes. After that, a thin-film polyamide layer was formed by carefully pouring the TMC solution on top of the membrane for 3 minutes. The generated Polyamide Thin-Film Composite (PA-TFC) membranes were stored in distilled water and kept at room temperature before use.

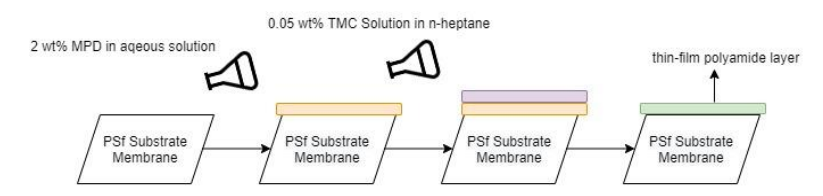


Figure 1. Preparation of polyamide TFC layer via interfacial polymerization method

## Characterization of the PA-TFC FO membrane: Morphological Analysis

The morphological structures including top surface and cross-section of the PSf substrate and PA -TFC membrane were examined using field emission scanning electron microscopy (FESEM, Zeiss, supra 55VP, 12-2,000,000x). The samples were then further examined using a Zeiss Supra V55 microscope.

#### Contact angle analysis

The contact angle of the membranes was measured at room temperature with a GSPJ-360 goniometer and distilled water was used as the measuring liquid. When water was dropped onto the membrane's surface, the CA was instantaneously calculated and recorded. To reduce experimental errors, 10 measurements were conducted at random points on the membrane surface, and the average CA was calculated.

#### Fourier-transform infrared spectroscopy

An infrared spectroscope (Perkin Elmer, Frontier 01) with a range of 550-4000 cm<sup>-1</sup> was used to investigate the chemical changes on the membrane surface before and after the TFC treatment. FTIR spectroscopy was used to detect the active polyamide layer as well as other functional groups.

#### Atomic force microscopy analysis

The surface roughness of the membrane was measured using an AFM (Hitachi AFM500II). The membrane samples were cut into sections of 5 cm  $\times$  5 cm. The samples were then mounted on the device for AFM investigation using a metal block.

## Preparation of the Synthetic Wastewater and Determination of the PA-TFC Performance

Due to BPA's insolubility in water, a working feed solution with a concentration of 100 mgL<sup>-1</sup> was prepared by dissolving the prescribed amount of BPA in a small amount of methanol before it was introduced to the experimental feed solution. The solution was then stirred at 120 °C with a magnetic stirrer until the BPA particles were completed dissolved. The draw solution consisted of 4M NaCl. The active layer of the membrane was positioned toward the feed solution.

The forward osmosis experiment was conducted according to the setup as shown in Figure 2. The initial quantities of the feed and draw solutions were 500 and 800 mL, respectively. The draw and feed solutions were interacting directly with each other through the membrane module. The temperature of both solutions was maintained at room temperature. Membrane

orientation was kept on AL-FS mode to mitigate the fouling effect [14]. The feed and draw solutions were recirculated in co-current mode to the membrane module at 200 mL/min using a BT600M dual-channel pump. The feed solution was placed on a precision balance (Huazhi Scientific Instrument HZK-3102) to record the weight variations associated with the water flux calculation. The precision weight balance was linked to a computer for data logging via the Serial-Portto-Keyboard software provided by Huazhi Scientific Instrument. The samples were taken at predetermined intervals, and the concentrations of the feed and draw solutions were measured using UV-Vis spectrophotometer. Each of the experiments was conducted twice in order to ascertain the accuracy and precision of the results.

Water permeation flux,  $J_w$  in  $L/m^2h$  was calculated using the change in weight of the feed solution over time and the membrane area,  $A_m$  (m<sup>2</sup>) as shown in equation (1):

$$J_{w} = \frac{\Delta w}{A_{m}\Delta t} \tag{1}$$

 $\Delta w$  = The recorded weight change of the feed solution, and  $\Delta t(h)$  = Experimental test time

Equation (2) is used to calculate BPA rejection in the FO process

$$R (\%) = \frac{(C_i - C_f)}{C_f} \quad x \ 100\% \tag{2}$$

where, R = The rejection percentage of BPA,  $C_i$  = Concentration of BPA in the feed solution at the start of the experiment (mg/L), and  $C_f$  = Final concentration of BPA in the draw solution after the experiment (mg/L).

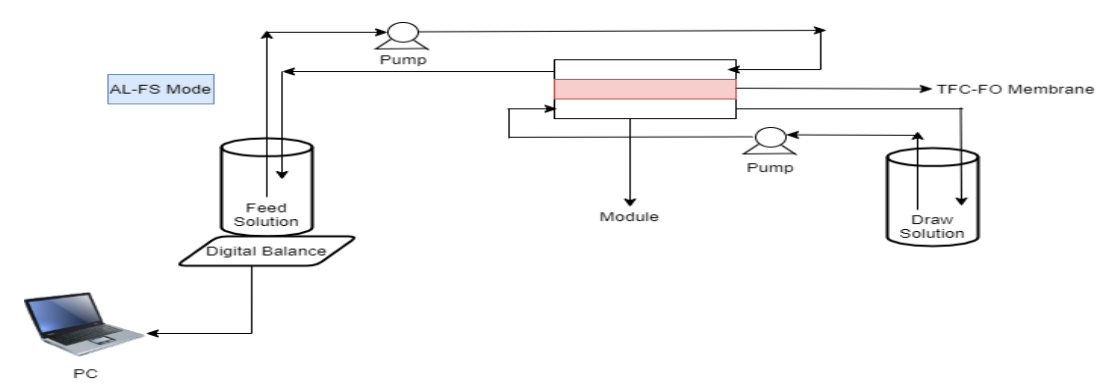


Figure 2. Illustration diagram of the forward osmosis setup (AL-FS mode)

## Results and Discussion Morphological analysis (FESEM)

The morphological structures of the surface and crosssection of the PA-TFC membrane were examined using FESEM (Zeiss, supra 55VP). In addition, the FESEM images were used to confirm the presence of the selective layer (PA layer) on top of the PSF membrane substrate. As depicted in Figure 3a, the thin polyamide layer can be seen on top of the PSf membrane substrate, which contains dense and porous layers. The denser layer of the membrane was found on top of the porous support layer, and it was believed to be a polyamide thinfilm layer formed via interfacial polymerization. This morphological evidence indicates that the membrane's rejection capability is improving while its permeability is decreasing [33]. According to Khorshidi et al., one disadvantage of the denser layer of the membrane is the low water flow, and the only option to address this issue is for the dense layer to be extremely thin. The PA selective layer as depicted in Figure 3a was estimated to be roughly 4.4µm thick, which is sufficient because the typical thickness of PA thin film is around 200nm. The

thickness of the PA layer is proportional to the concentration of TMC, which best explains the formation of the PA layer because low TMC concentrations were used in the preparation of the membrane (0.05%) [30].

There is a difference in the membrane surface appearance between the PSf and PA-TFC membranes, as shown by the FESEM surface images in Figures 3(b) and 3(c). The PSf substrate has a smooth and porous surface, but the PA-TFC membrane has a ridge-andvalley structure that results in a rough surface texture, as shown in Figure 3(b). The PSf membrane substrate has a porous structure with long finger-like pores formed under a thin sponge-like layer, making it excellent for FO membranes to minimize the structural parameters. The polyamide layer produced in this study has a ridgevalley structure, which is typical of TFC polyamide membranes prepared with the monomers MPD and TMC [34]. Miao et al. found that the ridge-and-valley structure is a significant indicator of the formation of the polyamide layer on the PSf membrane [35].

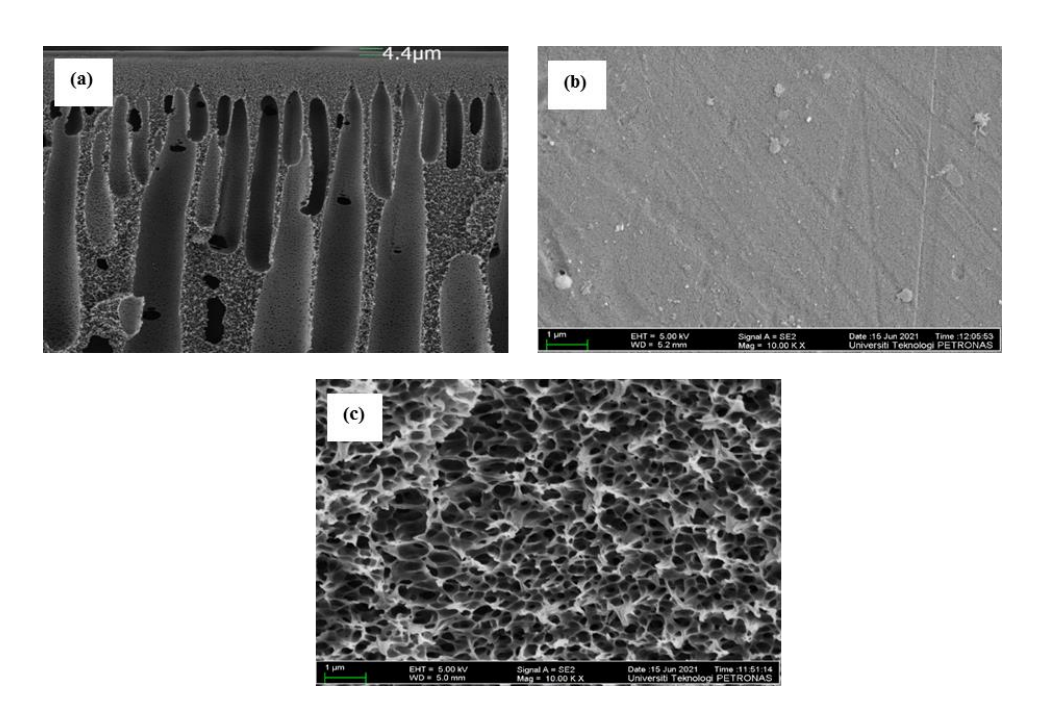


Figure 3. FESEM top surface morphologies of (a) cross section images of the PA-TFC membrane, surface images of (b) Polysulfone substrate and (c) Polyamide-TFC membrane

#### Fourier-transform infrared spectroscopy studies

The top surface of the modified PA-TFC membrane and Polysulfone substrate layer was analyzed using FTIR to examine the chemical compositions. Figure 4 shows the IR spectra of the Polysulfone and PA-TFC membrane. The transmittance peak at wavelengths of 1150 cm-1 (O-S-O stretching), 1243 cm-1 (C-O-C stretching) and 1106 cm-1 (S=O stretching) are the characteristics of sulfone group. Also, the absorption at 1013 and 833 cm-1 are assigned to the C-H stretching of the polysulfone aromatic rings. The peaks at 1605, 1538, 1486, 1247,

997 and 750 cm-1 are attributed to C=O of the amide linkage, O-H bending of the carboxylic acid, C-H bending, C-N stretching, C=O stretching and C-Cl stretching, respectively. These observations indicate the formation of polyamide layer on the polysulfone substrate. The absorbance at 3320 cm-1 suggests the N-H stretching of the amine functional group, indicating that the polyamide structure was formed through the interfacial polymerization of MPD and TMC [36].

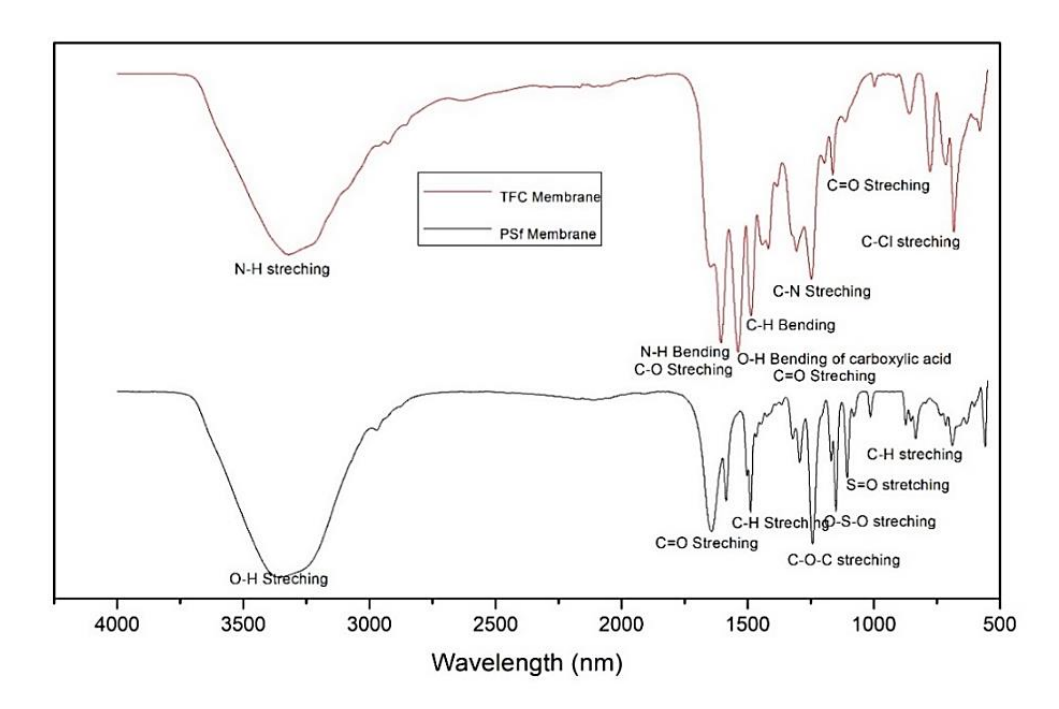


Figure 4. FTIR Spectra of PA-TFC and PSf membranes

#### Atomic force microscopy

The AFM was utilized to examine the surface morphology of polyamide layer (Figure 5). The threedimensional images show the PSf substrate and the coated TFC-PA membrane via interfacial polymerization with different top surface roughness. The PSf membrane has a smooth surface with a root mean square (RMS) value of 4.5nm while the TFC-PA membrane has a higher root mean square value of 20.76 nm with increased surface roughness. This is because the polyamide layer was effectively polymerized over the porous PSf substrate layer [37]. The polymerization of the PA layer results in increased ridge-and-valley

microstructure, raising the surface roughness value to 20.76nm. The increased surface roughness of the TFC membrane was also attributable to nodules generated on its surface as a result of MPD and TMC interaction. The advantage of having a higher surface roughness on the TFC membrane is that it will have a larger surface area for water to interact, resulting in a higher water flux performance for the membrane [38]. Morgan's theory states that the membrane roughness is related to the heterogeneity of different reactions between the amide and diacid chloride reactions following the initial formation of the Polyamide film [39].

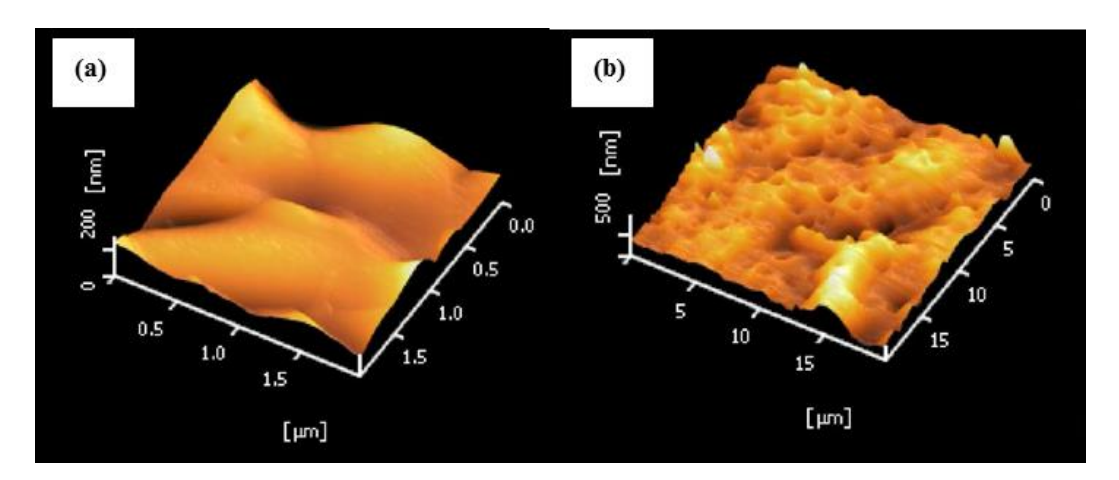


Figure 5. AFM surface morphology of (a) Polysulfone membrane substrate and (b) the thin-film composite membrane

#### Contact angle test

The contact angle of a membrane is one of its most important physical characteristics since it reveals its hydrophilicity and fouling susceptibility. An ideal membrane should be hydrophilic with high water flow rate and low fouling properties. The contact angle of the PSf substrate and the TFC membrane was assessed using a goniometer to determine their hydrophilicity. Figure 6 shows that the average contact angle for both membranes was less than 90°, which indicates its hydrophilicity. The hydrophilicity of the TFC membrane (36.04°) is higher than that of the PSf membrane (65.57°), indicating that more amide groups

are generated on the TFC membrane surface. TFC membranes have lower contact angle values because the polyamide layer structure contains strong polar amide functional groups that are hydrophilic in nature [40]. The presence of the pendant carboxylic acid groups inside the main chain has contributed to the increased hydrophilicity of the TFC membrane [33]. The TFC membrane thickened as the interfacial polymerization reaction time increased, contributing to its dense structure. This also explains why the contact angle of TFC membrane is decreasing [34].

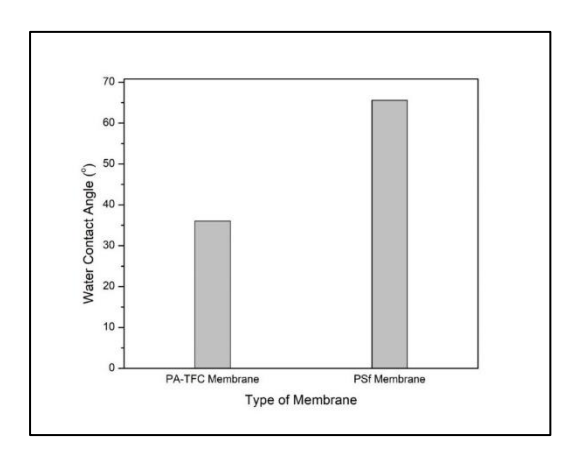


Figure 6. Comparison of contact angle values between PA-TFC and PSf membranes

#### Water permeability flux

The water flux change between TFC and PSf membrane was examined (Figure 7). Permeate flow is known to be highly related to membrane pore size, hence the increase in water flux in PSf substrate was expected. TFC

membranes have a low water flux because of their dense structure, which obstructs water flow and hence reduces the water flux value across the membrane [29]. In addition, it is worth noting that a denser active layer offers better rejection and lower fouling propensity [41].

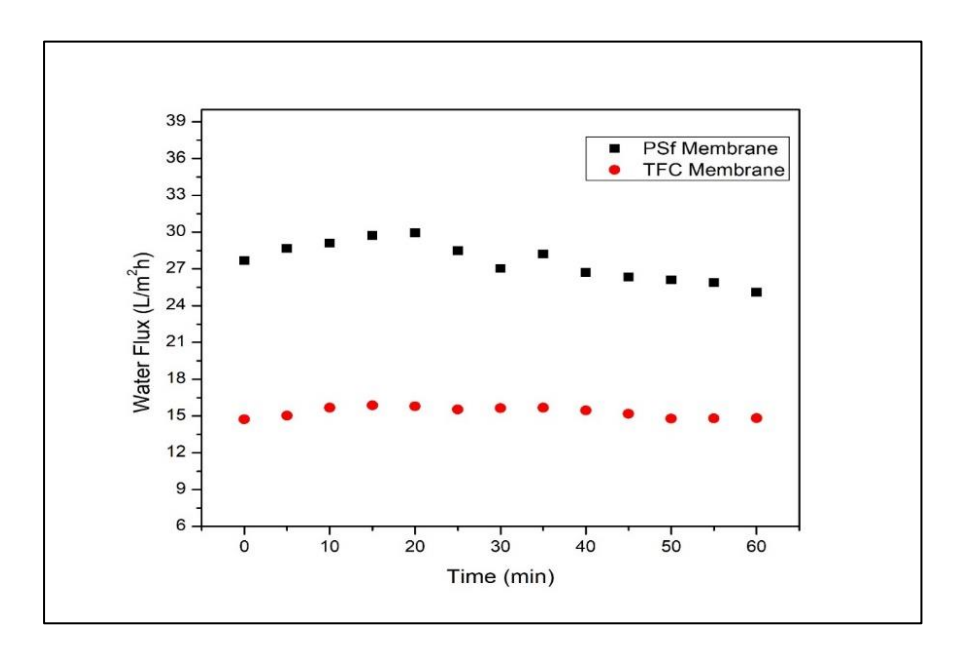


Figure 7. Water flux of FO with the model solution and pure water as feed (experimental conditions: AL-FS, 4M NaCl as DS

#### **BPA** removal

The retention of BPA was investigated utilizing both the PA-TFC and PSf membranes, and the results were compared accordingly. Figure 8 demonstrates that the overall rejection of BPA was within the range of 91% with the membrane orientation mode at AL-FS, whereas the PSf membrane yielded a rejection of 25%. The thinfilm active layer produced on the membrane substrate was predicted to increase the retention capacity of TFC forward osmosis membrane. The thin-film layer which has a higher ridge-and-valley microstructure, entraps the BPA at the active layer. BPA rejection of more than 90% suggested that its pore size is substantially smaller than BPA particle size, which explains the high removal from the feed solution. The dense top coating of the TFC membrane was believed to have contributed to the significant BPA rejection due to its excellent substance retention properties [29, 34]. The result shows that the thin-film composite membrane fabricated through the IPIS method can be used to remove BPA from industrial and pharmaceutical wastewaters.

In terms of the forward osmosis rejection efficiency of BPA, the result from this study is slightly higher than the values reported by Zhu et al. (approx. 80%) [42], Hancock et al. (approx. 70%) [43] and Linares et al. (approx. 49%) [44]. These above-mentioned studies were basically carried out using the cellulose triacetate forward osmosis membranes. The interfacial polymerization of the polyamide layer on the polysulfone substrate could improve the BPA rejection by FO according to the findings of this study and comparisons with earlier research. This modification will enhance hydrophilicity, increase rejection from feed solution, and maintain the highest possible flow rates [29].

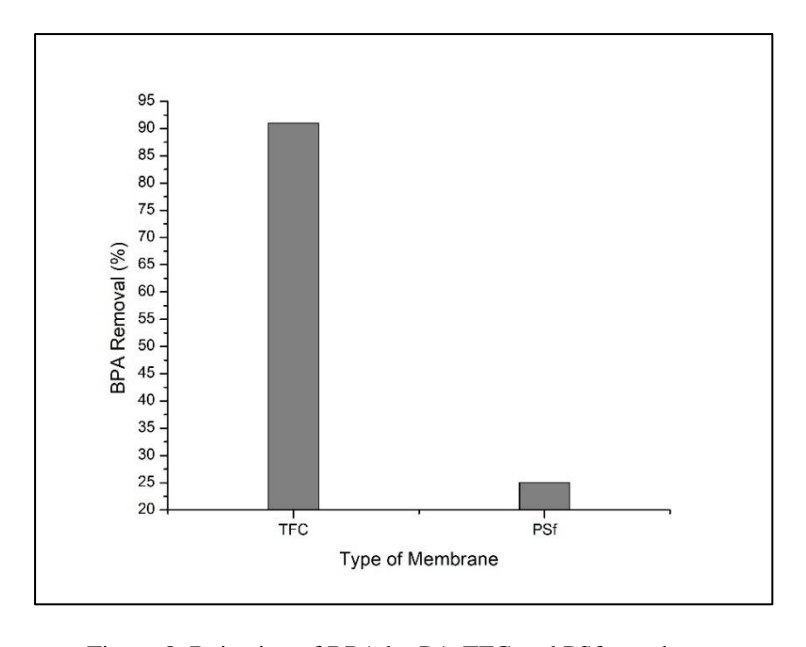


Figure 8. Rejection of BPA by PA-TFC and PSf membrane

#### Conclusion

This study assessed the effectiveness of a successfully fabricated PA-TFC membrane on a polysulfone membrane substrate using the interfacial polymerization method. Both membranes were examined and compared for their retention performance of bisphenol-A from a synthetic wastewater solution of 100mg/L using the forward osmosis process. The polyamide-based membrane performed well with a retention efficiency of 91%, whereas the polysulfone membrane retained just approximately 25%. The performance results of both membranes indicate that the fabricated membrane appears to be more promising and provides greater BPA retention than the polysulfone membrane substrate using the forward osmosis technique. It can be used to treat pharmaceutical and industrial wastewaters, which primarily contain small organic pollutants like phenols that are difficult to remove using other conventional or membrane treatment processes.

#### Acknowledgement

This research work was supported by the Yayasan Universiti Teknologi PETRONAS (Grant No: 015MD0-

056) research grant. In addition, the authors thankfully acknowledge the support from the Centralized Analytical Lab (CAL) and the technical assistance offered by the Chemical Engineering Department throughout the experimental work.

#### References

- 1. Li, J., Liu, Q., Liu, Y. and Xie, J. (2017). Development of electro-active forward osmosis membranes to remove phenolic compounds and reject salts. *Environmental Science: Water Research & Technology*, 3(1): 139-146.
- 2. Silva, C. P., Otero, M. and Esteves, V. (2012). Processes for the elimination of estrogenic steroid hormones from water: A review. *Environmental Pollution*, 165: 38-58.
- Xiao, M., Zhou, J., Tan, Y., Zhang, A., Xia, Y. and Ji, L. (2006). Treatment of highly-concentrated phenol wastewater with an extractive membrane reactor using silicone rubber. *Desalination*, 195(1-3): 281-293.

- Mohammadi, S., Kargari, A., Sanaeepur, H., Abbassian, K., Najafi, A. and Mofarrah, E. (2015). Phenol removal from industrial wastewaters: a short review. *Desalination and Water Treatment*, 53(8): 2215-2234.
- Huang, Y. Q., Wong, C. K. C., Zheng, J. S., Bouwman, H., Barra, R., Wahlström, B., Neretin, L., & Wong, M. H. (2012). Bisphenol A (BPA) in China: A review of sources, environmental levels, and potential human health impacts. *Environment International*, 42: 91-99.
- Kumar, A., Gupta, K., Tomer, V., Kaur, A., & Kumar, V. (2018). Bisphenols as human health hazard: A systematic review on potent sources, route of exposure, harmful effects and safe alternatives. *Toxicology International*, 25(1): 78–92.
- Katibi, K. K., Yunos, K. F., Man, H. C., Aris, A. Z., Mohd Nor, M. Z. and Azis, R. S. (2021). Recent advances in the rejection of endocrine-disrupting compounds from water using membrane and membrane bioreactor technologies: A review. *Polymers*, 13(3): 392.
- 8. Tsai, W. T. (2006). Human health risk on environmental exposure to bisphenol-A: A review. Journal of Environmental Science and Health - Part C Environmental Carcinogenesis and Ecotoxicology Reviews, 24(2), 225-255.
- 9. Rubin, B. S. (2011). Bisphenol A: An endocrine disruptor with widespread exposure and multiple effects. *Journal of Steroid Biochemistry and Molecular Biology*, 127(1–2): 27-34.
- Viñas, R., Jeng, Y. J. and Watson, C. S. (2012).
   Non-genomic effects of xenoestrogen mixtures.
   International Journal of Environmental Research and Public Health, 9(8): 2694-2714.
- 11. Zoeller, R. T., & Belcher, S. M. (2007). In vitro molecular mechanisms of bisphenol A action. *Reproductive Toxicology*, 24(2): 178-198.
- 12. Rochester, J. R. (2013). Bisphenol A and human health: A review of the literature. *Reproductive Toxicology*, 42: 132-155.
- 13. Kundakovic, M. and Champagne, F. A. (2011). Epigenetic perspective on the developmental effects of bisphenol A. *Brain, Behavior, and Immunity*, 25(6): 1084-1093.

- 14. Chen, H. W., Liang, C. H., Wu, Z. M., Chang, E. E., Lin, T. F., Chiang, P. C. and Wang, G. S. (2013). Occurrence and assessment of treatment efficiency of nonylphenol, octylphenol and bisphenol-A in drinking water in Taiwan. *Science of the Total Environment*, 449: 20-28.
- 15. Kleywegt, S., Pileggi, V., Yang, P., Hao, C., Zhao, X., Rocks, C., Thach, S., Cheung, P. and Whitehead, B. (2011). Pharmaceuticals, hormones and bisphenol A in untreated source and finished drinking water in Ontario, Canada Occurrence and treatment efficiency. *Science of the Total Environment*, 409(8): 1481-1488.
- Sodré, F. F., Locatelli, M. A. F. and Jardim, W. F. (2010). Occurrence of emerging contaminants in Brazilian drinking waters: A sewage-to-tap issue. Water, Air, and Soil Pollution, 206(1–4): 57-67.
- 17. Muhamad, M. S., Salim, M. R., Lau, W. J. and Yusop, Z. (2016). A review on bisphenol A occurrences, health effects and treatment process via membrane technology for drinking water. *Environmental Science and Pollution Research*, 23(12): 11549-11567.
- 18. Yüksel, S., Kabay, N. and Yüksel, M. (2013). Removal of bisphenol A (BPA) from water by various nanofiltration (NF) and reverse osmosis (RO) membranes. *Journal of Hazardous Materials*, 263: 307-310.
- 19. Mehwish, N., Kausar, A. and Siddiq, M. (2014). Advances in Polymer-based Nanostructured Membranes for Water Treatment. *Polymer Plastics Technology and Engineering*, 53(12): 1290-1316.
- 20. Kim, I. C. And Lee, K. H. (2003). Effect of various additives on pore size of polysulfone membrane by phase-inversion process. *Journal of Applied Polymer Science*, 89(9): 2562-2566.
- Zhao, F. B., Tang, C. C., Liu, X. Y., Shi, F. J., Song, X. R., Tian, Y. and Li, Z. S. (2015). Transportation characteristics of bisphenol A on ultrafiltration membrane with low molecule weight cut-off. *Desalination*, 362: 18-25.

- Heo, J., Flora, J. R. V., Her, N., Park, Y. G., Cho, J., Son, A. and Yoon, Y. (2012). Removal of bisphenol A and 17β-estradiol in single walled carbon nanotubes-ultrafiltration (SWNTs-UF) membrane systems. Separation and Purification Technology, 90: 39-52.
- 23. Bing-zhi, D., Hua-qiang, C., Lin, W., Sheng-ji, X. and Nai-yun, G. (2010). The removal of bisphenol A by hollow fiber microfiltration membrane. *Desalination*, 250(2): 693-697.
- Yüksel, S., Kabay, N. and Yüksel, M. (2013).
   Removal of bisphenol A (BPA) from water by various nanofiltration (NF) and reverse osmosis (RO) membranes. *Journal of Hazardous Materials*, 263: 307-310.
- Lutchmiah, K., Verliefde, A. R. D., Roest, K., Rietveld, L. C. and Cornelissen, E. R. (2014). Forward osmosis for application in wastewater treatment: A review. *Water Research*, 58: 179-197.
- Cartinella, J. L., Cath, T. Y., Flynn, M. T., Miller, G. C., Hunter, K. W. and Childress, A. E. (2006). Removal of natural steroid hormones from wastewater using membrane contactor processes. *Environmental Science and Technology*, 40(23): 7381-7386.
- 27. Lee, S., Boo, C., Elimelech, M. and Hong, S. (2010). Comparison of fouling behavior in forward osmosis (FO) and reverse osmosis (RO). *Journal of Membrane Science*, 365(1-2): 34-39.
- 28. Mi, B. and Elimelech, M. (2010). Organic fouling of forward osmosis membranes: Fouling reversibility and cleaning without chemical reagents. *Journal of Membrane Science*, 348(1-2): 337-345.
- Adamczak, M., Kamińska, G. and Bohdziewicz, J. (2019). Preparation of polymer membranes by in situ interfacial polymerization. *International Journal of Polymer Science*, 2019: 6217924.
- Khorshidi, B., Thundat, T., Fleck, B. A. and Sadrzadeh, M. (2016). A novel approach toward fabrication of high performance thin film composite polyamide membranes. *Scientific Reports*, 6(1): 1-10.
- 31. Al-Hobaib, A. S., El Ghoul, J., Ghiloufi, I. and El Mir, L. (2016). Synthesis and characterization of polyamide thin-film nanocomposite membrane

- reached by aluminum doped ZnO nanoparticles. *Materials Science in Semiconductor Processing*, 42: 111-114.
- 32. Mehwish, N., Kausar, A. and Siddiq, M. (2014). Advances in polymer-based nanostructured membranes for water treatment. *Polymer Plastics Technology and Engineering*, 53(12): 1290-1316.
- 33. Wei, J., Qiu, C., Tang, C. Y., Wang, R. and Fane, A. G. (2011). Synthesis and characterization of flat-sheet thin film composite forward osmosis membranes. *Journal of Membrane Science*, 372(1–2): 292–302.
- 34. Syahida Mat Anan, N., Jaafar, J., Sato, S. and Mohamud, R. (2021). Titanium dioxide incorporated polyamide thin film composite photocatalytic membrane for bisphenol a removal. *IOP Conference Series: Materials Science and Engineering*, 1142(1): 012015.
- 35. Miao, L., Jiang, T., Lin, S., Jin, T., Hu, J., Zhang, M. and Liu, G. (2020). Asymmetric forward osmosis membranes from p-aramid nanofibers. *Materials & Design*, 191: 108591.
- El-Arnaouty, M. B., Abdel Ghaffar, A. M., Eid, M., Aboulfotouh, M. E., Taher, N. H. and Soliman, E.-S. (2018). Nano-modification of polyamide thin film composite reverse osmosis membranes by radiation grafting. *Journal of Radiation Research* and Applied Sciences, 11(3): 204-216.
- 37. Park, H. M., Takaba, H., & Lee, Y. T. (2020). Preparation and characterization of TFC NF membrane with improved acid resistance behavior. *Journal of Membrane Science*, 616: 118620.
- 38. Song, X., Qi, S., Tang, C. Y. and Gao, C. (2017). Ultra-thin, multi-layered polyamide membranes: Synthesis and characterization. *Journal of Membrane Science*, 540: 10-18.
- 39. Morgan, P. W. and Kwolek, S. L. (1996). Interfacial polycondensation. II. Fundamentals of polymer formation at liquid interfaces. *Journal of Polymer Science Part A: Polymer Chemistry*, 40(137): 299-327
- Rajaeian, B., Rahimpour, A., Tade, M. O. and Liu,
   S. (2013). Fabrication and characterization of polyamide thin film nanocomposite (TFN) nanofiltration membrane impregnated with TiO<sub>2</sub> nanoparticles. *Desalination*, 313: 176-188.

- 41. McGinnis, R. L., Hancock, N. T., Nowosielski-Slepowron, M. S. and McGurgan, G. D. (2013). Pilot demonstration of the NH<sub>3</sub>/CO<sub>2</sub> forward osmosis desalination process on high salinity brines. *Desalination*, 312: 67-74.
- 42. Zhu, H. and Li, W. (2013). Bisphenol A removal from synthetic municipal wastewater by a bioreactor coupled with either a forward osmotic membrane or a microfiltration membrane unit. Frontiers of Environmental Science and Engineering, 7(2): 294-300.
- 43. Hancock, N. T., Xu, P., Heil, D. M., Bellona, C. and Cath, T. Y. (2011). Comprehensive bench- and pilot-scale investigation of trace organic compounds rejection by forward osmosis. *Environmental Science and Technology*, 45(19): 8483-8490.
- 44. Valladares Linares, R., Yangali-Quintanilla, V., Li, Z. and Amy, G. (2011). Rejection of micropollutants by clean and fouled forward osmosis membrane. *Water Research*, 45(20): 6737-6744.

## Malaysian Journal of Analytical Sciences (MJAS)



Published by Malaysian Analytical Sciences Society

# CONSTRUCTING NI-DOPED ZnO/GO HETEROSTUCTURES FOR ENHANCED SUNLIGHT-TRIGGERED DEGRADATION OF METHYLENE BLUE DYE

(Pembinaan Heterostruktur Ni-Didop dengan ZnO/GO untuk Meningkatkan Degradasi Pewarna Metilina Biru di Bawah Sinar Matahari)

Hartini Ahmad Rafaie<sup>1,5</sup>\*, Nur Shafiza Ismail<sup>1</sup>, Syazni Hanun Nur Ili Dedy Dasiano<sup>2,4</sup>, Muhd Firdaus Kasim<sup>3</sup>, Nurul Infaza Talalah Ramli<sup>1</sup>, Zul Adlan Mohd Hir<sup>1</sup>, Mohomad Hafiz Mamat<sup>4</sup>

<sup>1</sup>Faculty of Applied Science,
Universiti Teknologi MARA Pahang, 26400 Bandar Tun Abdul Razak Jengka, Pahang, Malaysia

<sup>2</sup>Faculty of Applied Sciences

<sup>3</sup>Center for Nanomaterials Research, Institute of Science

<sup>4</sup>NANO-Electronic Centre, Faculty of Electrical Engineering
Universiti Teknologi MARA, 40450 Shah Alam, Selangor, Malaysia

<sup>5</sup>Centre of Foundation Studies,
Universiti Teknologi MARA, Selangor Branch, Dengkil Campus, 43800 Dengkil, Selangor, Malaysia

\*Corresponding author: hartinirafaie@uitm.edu.my

Received: 15 November 2021; Accepted: 3 February 2022; Published: 27 June 2022

#### Abstract

Chemical pollutants emitted by the textile industry are a major source of water contamination, resulting in dangerous diseases and most of the effluent treatment techniques are relatively ineffective. As a result, metal oxide-based photocatalysts emerged as a viable alternative to the already existing dye treatment methods. The current work focused on the synthesis and characterization of Ni-doped ZnO/GO heterostructures and evaluation of its photoactivity under sunlight irradiation. The nanocomposite was prepared via a simple mixing approach, by varying the weight ratio of graphene oxide (GO) ranging from 0.1 to 0.4 g prior to the incorporation into Ni-doped ZnO surfaces. The X-ray diffraction analysis revealed that Ni and GO were successfully incorporated into the wurtzite-structure of ZnO nanocomposites. FESEM images showed a uniformed particle with the average size of about 100-500 nm for all samples. The photocatalytic activity was assessed by monitoring the degradation of methylene blue (MB) dye under direct sunlight irradiation. Ni-doped ZnO/GO<sub>0.1</sub> nanocomposite exhibited the greatest degradation performance by degrading 94% MB. The highest degradation rate constant of 0.0250 min<sup>-1</sup> was obtained within 120 minutes of reaction time. The current study is easy, effective, and compatible; hence it can be employed in the future to treat textile dye wastewater.

Keywords: graphene oxide, methylene blue, nickel, photodegradation, sunlight

#### Abstrak

Bahan pencemar kimia yang dikeluarkan oleh industri tekstil merupakan sumber utama pencemaran air, mengakibatkan penyakit berbahaya dan kebanyakan kaedah rawatan sisa bahan buangan yang dicipta masih tidak berkesan sepenuhnya. Justeru,

#### Hartini et al: CONSTRUCTING NI-DOPED ZnO/GO HETEROSTUCTURES FOR ENHANCED SUNLIGHT-TRIGGERED DEGRADATION OF METHYLENE BLUE DYE

fotomangkin berasaskan logam oksida dihasilkan sebagai alternatif yang berdaya maju bagi kaedah rawatan pewarna sedia ada. Penumpuan kepada sintesis dan pencirian yang mudah bagi heterostruktur ZnO/GO yang didopkan dengan Ni dan penilaian fotoaktivitinya di bawah cahaya matahari. Nanokomposit disediakan melalui kaedah campuran yang ringkas dengan mengubah nisbah berat grafin oksida (GO) diantara 0.1 hingga 0.4 g sebelum dimasukkan ke dalam permukaan ZnO berdop Ni. Analisis pembelauan sinar-X mendedahkan bahawa Ni dan GO telah berjaya dimasukkan ke dalam struktur ZnO. Imej FESEM menunjukkan partikel seragam dengan saiz purata diantara 100-500 nm untuk semua sampel. Aktiviti fotokatalitik dinilai dengan memantau degradasi pewarna metilina biru (MB) di bawah penyinaran cahaya matahari secara lansung. Nanokomposit ZnO/GO<sub>0.1</sub> berdop Ni mempamerkan prestasi degradasi yang paling tinggi dengan nilai peratus degradasi 94% MB. Pemalar kadar degradasi tertinggi ialah 0.0250 min<sup>-1</sup> diperolehi dalam masa 120 minit masa tindak balas. Kajian ini didapati mudah, berkesan dan sesuai, justeru ia boleh digunakan pada masa hadapan untuk merawat sisa buangan pewarna dari industri tekstil.

Kata kunci: grafin oksida, metilina biru, nikel, fotodegradasi, cahaya matahari

#### Introduction

In the past decades, contamination of freshwater resources with a large amount of dyes has been widely reported, mainly due to the rapid industrialization. They are employed in textile, paper, foods, cosmetics, pharmaceuticals, and printing industries [1]. The dyes are believed to have found their way entering the groundwater through dyeing process, leaching from various dye industries, and inappropriate discharge of untreated dye effluents [2, 3]. Human exposures to dyes occurred through consumption of food, water, air inhalation and direct contact with body and skin. This exposures hence have affected the human health and aquatic lives due to their toxicity [4, 5]. It is therefore essential to use promising treatment strategies, aiming to restore the quality of contaminated water by ensuring the sustainability of the environments economically viable approach.

Presently, photocatalytic advanced oxidation processes (AOPs) have been studied extensively for water restoration, mainly due to its favorable degradation activity toward recalcitrant organic pollutants as compared to conventional water treatment approaches [6, 7]. The method highlights on the use of semiconductor oxides as the catalyst assisted with UV or solar irradiation during the process. It is a cost-effective method in such a way that it operates at/near ambient temperature and pressure for the *in-situ* production of reactive radical species such as •OH and  $\bullet$ O<sub>2</sub> $^-$  on the surface of the photocatalyst [8]. The process aims for the mineralization of the contaminants to harmless inorganic by-products, water, and carbon

dioxide through a series of redox reaction [9]. Of various semiconductor metal oxides, zinc oxide (ZnO) is most likely to be of the highest interest and regarded as an ideal catalyst due to its exceptional capability such as wide and direct bandgap semiconductor materials, higher photocatalytic efficiency, ability to absorb over a larger fraction of the UV or solar spectrum, non-toxic, low cost and environmentally sustainable [10–13].

Nonetheless, ZnO has their own limitation such as lower reusability and adsorption ability, wide band gap energy (3.37 eV) which can only be fully utilized under UV ( $\lambda$ < 387 nm) [14]. It is well-established that solar light consists of merely ~4% UV, so it is not very effective for large band gap materials. Also, rapid charge recombination is believed to be a major loss for the photoexcited charge carriers and a critical factor that limits the photo-efficiency for wide band gap photocatalyst [15-17]. To overcome these drawbacks, the construction of heterojunctions by coupling ZnO with suitable band potentials materials has been revealed to be an efficient strategy to simultaneously improve its photoactivity and photostability. Researchers found that modifying ZnO surface by doping with metal such as nickel (Ni) could extend the light absorption range towards visible region [18]. In this respect, Tawale et al. [19] investigated different microstructural and photoluminescence performance of bare ZnO, Ni doped ZnO and Cr doped ZnO. The result revealed that the Nidoped ZnO nanostructures had the stronger PL intensity compared to Cr doped and undoped ZnO nanostructures. Apparently, high quality and good physicochemical properties will enhance the photocatalytic properties.

Wang et al. [18] reported on the recyclable photocatalyst based flower-like nickel zinc οn ferrite nanoparticles/ZnO (NZF/ZnO) using a hydrothermal method. It was found that the samples prepared using 2.0 wt.%, 4.0 wt.% and 6.0 wt.% NZF nanoparticles exhibit better degradation performance towards rhodamine B (RhB) with increasing amounts of NZF, and 6.0 wt.% NZF has the best photocatalytic activity under visible irradiation. This result may come from the fact that the sample grown with 6.0 wt.% NZF has a smaller diameter and a larger surface area. Moreover, the much higher photocatalytic performance comes from the charge separation effect due to the band alignment between NZF and ZnO.

Combination of semiconductor oxide on carbonaceous materials such as graphene oxide is also attractive to improve the charge separation efficiency for enhanced photoactivity. This is due to the fascinating properties of GO such as high adsorption capacity, high electron mobility, large surface area and high thermal conductivity [4, 20-23]. This can be seen from the research conducted by Wu and Wang [24], where they conducted a study on the preparation of graphene oxide/hexagonal flower-like (GO/ZnO) ZnO micro/nanoparticles through hydrothermal method. It was found that the degradation percentage of rhodamine (RhB) dye reached 90.8% in 60 min, which was much higher than pure ZnO. The micro/nanostructure of GO/ZnO significantly improved the photocatalytic ability compared to pure ZnO. Kherabadi and his coworkers [4] reported on the synthesis, physicochemical properties and performance of three-dimensional (3D) Ag/ZnO/graphene as photocatalyst using a combined hydrothermal-photo deposition method. The dye degradation under both UV and visible light irradiation exhibited an enhanced photoactivity in comparison to ZnO/graphene and graphene alone. The deposition of Ag nanoparticles onto the surface of ZnO/graphene enhanced the photocatalytic efficiency due to the electron capturing properties.

In this research, an attempt has been made to synthesize Ni-doped ZnO/GO nanocomposites using a simple mixing approach. The morphological, structural properties, and photocatalytic activities of the

nanocomposites were also investigated utilizing methylene blue (MB) dye as the probe molecule. Attempts has made to investigate the influence of variation GO weight ratio to Ni-doped ZnO on its photocatalyst. The performance as resultant nanocomposite photocatalyst certainly tends to harvest direct sunlight absorption effectively for photoexcited electron-holes formation, enhance the interfacial charge migration and hold better photostability during the photocatalytic reaction. The growth of Ni-doped ZnO/GO provides a simple, environmentally friendly and cost saving approach.

#### **Materials and Methods**

#### Materials

Commercial zinc oxide powder (ZnO, purity > 99%), Graphene oxide powder (GO, purity > 99%), nickel powder (Ni, purity > 99%), and methylene blue dye were purchased from Merck (Selangor, Malaysia). All chemicals and reagents were used as received and no purification step was performed. Deionized water was utilized throughout the synthesis and other experimental process.

#### Synthesis of Ni-doped ZnO/GO nanocomposites

In this work, a simple mixing approach was employed to prepare the heterostructures photocatalyst. Firstly, 0.5 g of Ni and 9.5 g of ZnO powder were mixed in a 100 mL of deionized water under continuous magnetic stirring for 30 min. After that, GO was added into the mixture and the amount was varied from 0.1 to 0.4 g. The amount of Ni and ZnO powder was kept constant throughout the process. The mixed solution went through an ultrasonic agitation using a sonicator (Powersonic 405) at a power of 350 W with a 40 KHz working frequency for 60 min. Following that, the mixtures solution was continuously stirred with a heating temperature of 60°C for 1 h on magnetic stirrer. Subsequently, the obtained Ni-doped ZnO/GO catalysts in the form of a fine powder were filtered, washed several times with deionized water and dried at 300°C for 1 h, yielding a greyish powder. The samples were labelled as ZnO/Ni, ZnO/Ni/GO<sub>0.1</sub>, ZnO/Ni/GO<sub>0.2</sub> ZnO/Ni/GO<sub>0.3</sub>, and ZnO/Ni/GO<sub>0.4</sub> accordingly. The morphology of the Ni-doped ZnO/GO nanocomposites was examined using a field emission scanning electron

microscopy (JEOL JSM-7600F). X-ray diffraction patterns were obtained by PANalytical X'pert Pro powder diffraction equipment at room temperature (Cu K $\alpha$  radiations of  $\lambda$  =1.5418 Å) between 2 $\theta$  range of 10–90° with a scanning speed of 2°/min. Following that, the Ni-doped ZnO/GO samples then underwent photocatalytic degradation measurement.

#### Photocatalytic degradation study

The photocatalytic degradation of the Ni-doped ZnO/GO nanocomposites were evaluated using methylene blue (MB) dye on each interval under direct sunlight irradiation as shown in Figure 1. In a typical procedure, 10 mg of photocatalyst was dispersed in 100 mL of 10 mg/L of MB aqueous solution for every run. Prior to irradiation, the suspension was magnetically stirred for 30 min under dark condition to reach the adsorption/desorption equilibrium.

Following that, the suspensions were subsequently exposed to sunlight irradiation under continuous stirring for 120 min. At predetermined time intervals, an aliquot of 5 mL of sample was extracted out and the residual was monitored using concentration UV-vis spectrophotometer at  $\lambda_{max} = 664$  nm. The percentage of degradation of MB was calculated using equation (1). All the photocatalytic degradation experiments were carried out under similar condition on a sunny day from 12.00 to 2 pm, in the month of Mac where the temperature was T= (34±2) °C at Bandar Tun Abdul Razak Jengka, Pahang.

Percentage of degradation (%) =  $(C_o-C_t)/C_o * 100$  (1) where  $C_0$  is the concentration of MB before irradiation, while  $C_t$  is the concentration of MB at time 't'.

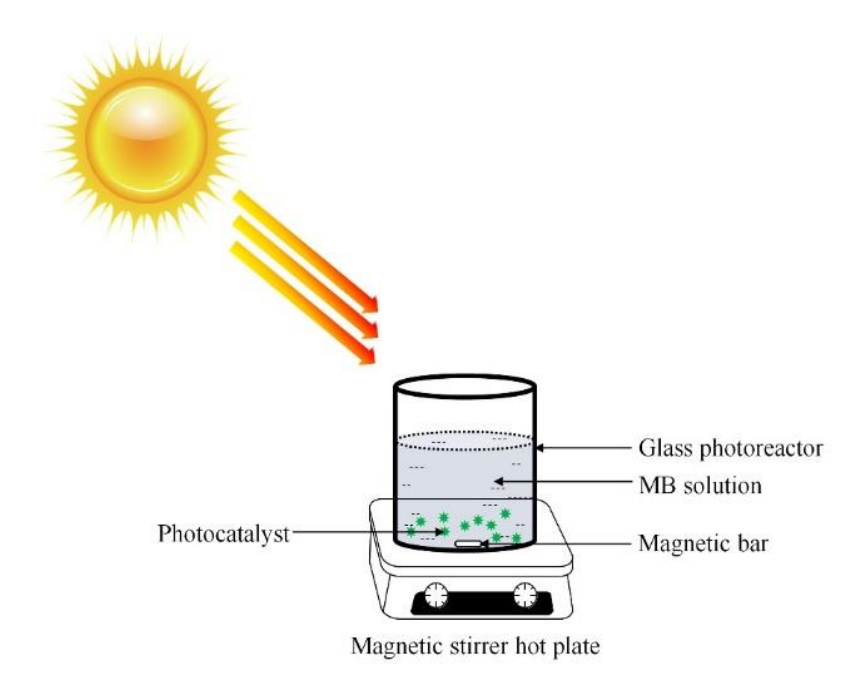


Figure 1. Illustration of the degradation process of Ni-doped ZnO/GO nanocomposites against MB under sunlight irradiation

#### **Results and Discussion**

#### X-ray diffraction pattern analysis

The crystalline phases of the pure and nanocomposites samples were analyzed by XRD, and the corresponding diffraction patterns are shown in Figure 2. Typically, all the diffraction peaks of pure ZnO (Figure 2a) are indexed according to the standard reference of hexagonal ZnO wurtzite structure (JCPDS No. 36-1451). The diffraction peaks at  $2\theta$  of  $31.8^{\circ}$ ,  $34.4^{\circ}$ ,  $36.4^{\circ}$ ,  $47.6^{\circ}$ ,  $62.9^{\circ}$ ,  $66.6^{\circ}$ ,  $67.9^{\circ}$  and  $69.2^{\circ}$  were respectively

assigned to the (100), (002), (101), (102), (103), (112) and (201), and were consistent with hexagonal zincite structure of pure ZnO [25, 26].

Meanwhile, Figure 2b shows the pattern for the peak of Ni obtained at 44.59° and 51.97° that corresponded to the (111) and (200) crystal faces of Ni standard pattern (JCPDS No. 04-0850) [27]. GO powder exhibits a diffraction peak at 26° corresponding to the (002) plane as can be seen in Fig. 2c. Interestingly, the presence of ZnO wurtzite structure with a very small peak of Ni were identified in the Ni-doped ZnO sample (Figure 2d). The existing of small Ni peak might be due to very small doping content of Ni element. All samples of Ni-doped

ZnO/GO displayed the characteristic peaks belonging to ZnO (Figure 2e–h). However, the characteristic peak of Ni and GO was not observed in the XRD patterns possibly because of the low Ni and GO content (0.1 to 0.4 g), which is below the detection range of the XRD instrument. Also, no shift was observed in the position of ZnO diffraction peaks as compared to pure ZnO, proving that the native crystalline structure of ZnO had been maintained after the preparation of the hybrid heterostructure materials. The XRD analysis also revealed that the Ni and GO were incorporated into the wurtzite structure of ZnO crystal as there was no impurity or secondary phases existed in the pattern for all Ni-doped ZnO/GO samples.

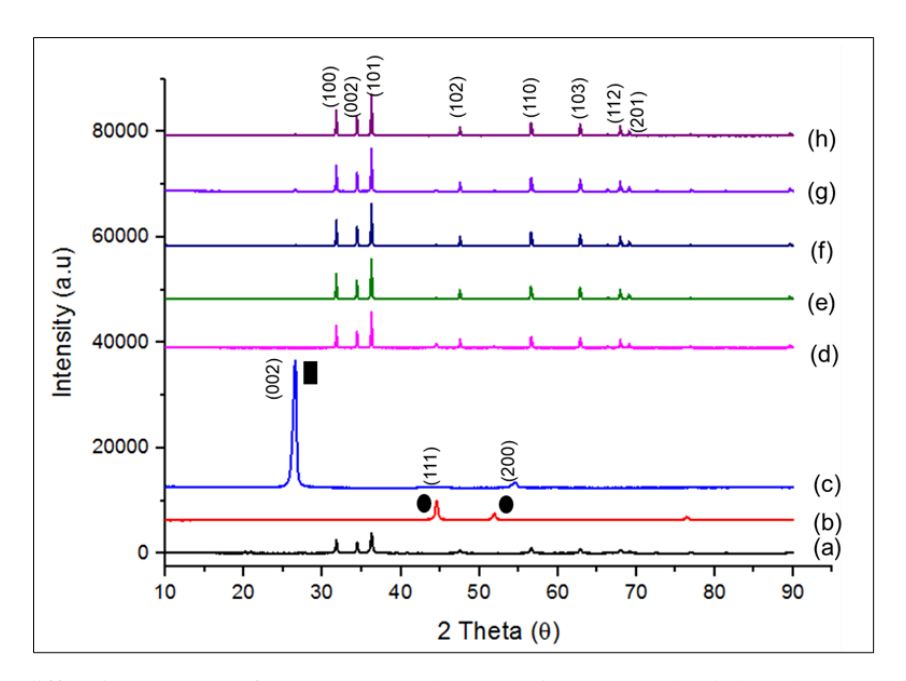


Figure 2. X-ray diffraction patterns of (a) pure ZnO, (b) pure Ni, (c) GO, (d) Ni-doped ZnO, and (e-h) Ni-doped  $ZnO/GO_{0.1-0.4}$ . (GO and Ni labelled as black square and circle in the graph respectively)

#### Surface morphological and structural analysis

The surface morphological and structural of pure ZnO, Ni-doped ZnO and Ni-doped ZnO/GO<sub>0.1-0.4</sub> nanocomposites were characterized by FESEM analysis (Figure 3). It could clearly be seen that similar structure particles with average size of about 100–500 nm was

observed for pure ZnO, Ni-doped ZnO and Ni-doped ZnO/GO<sub>0.1-0.4</sub> nanocomposites. The incorporation of nickel and GO were not visible in the FESEM images. Nonetheless, the overall shapes for all samples composed of rod-like and cubic-like structures.

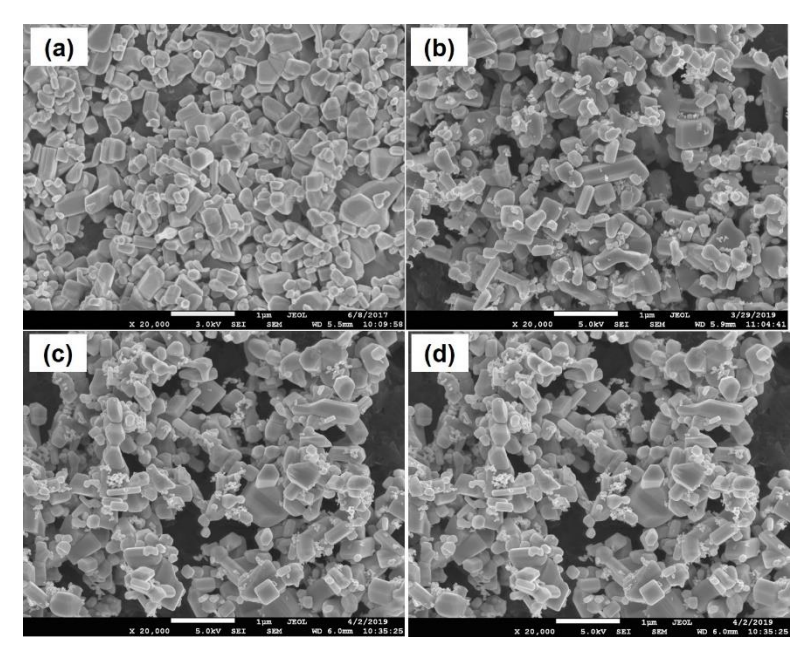


Figure 3. Selected FESEM images for (a) pure ZnO, (b) Ni-doped ZnO, (c) Ni-doped ZnO/GO $_{0.1}$ , and (d) Ni-doped ZnO/GO $_{0.4}$ 

#### Evaluation of photocatalytic activity

Photocatalytic measurement of Ni-doped ZnO/GO nanocomposites photocatalyst in the removal of MB based on UV-vis spectra is depicted in Figure 4. The overall results revealed that the maximum absorption of MB at 664 nm decreased gradually as a function of time in the presence of different photocatalysts.

All the degradation behaviours were analysed and extrapolated in the following graph as presented in Figure 5. As depicted in the insert of Figure 5, no change was observed in the first 30 min before being exposed to sunlight for photodegradation of MB using ZnO/Ni/GO<sub>0.1</sub> catalyst because the MB was adsorbed on the surface of catalyst which led to an unchanged concentration and this unable the degradation of MB under dark condition. The photolysis of MB also seems negligible, indicating the stability of MB under sunlight. This is supported from our previous findings where the photolysis of MB under UV light was also insignificant even though UV contains high photon energy (shorter wavelength) as compared to sunlight (longer wavelength) [28]. The photocatalytic activity of pure ZnO reached almost 80% percentage of degradation

against MB in aqueous phase. In contrast, the addition of Ni onto the ZnO surface did not improve the degradation efficiency since the percentage obtained was reduced to 15%. The addition of small amount of Ni to the ZnO might contribute to the decreasing of the percentage of degradation. Some researchers had found that the existence of Ni acted as a co-catalyst that reduced the over-potential of electrons at conduction band of ZnO which gave negative effect by lowering the degradation efficiency of ZnO itself. Previously, it was reported that there is high tendency for the occurrence of NiO (as a secondary phase) alongside Ni/ZnO on the catalyst surface which might impose undesirable defects and hence acted as a barrier to light absorption [29]. The transitions of metal ions substituted into the ZnO lattice also act as a recombination centre for electron-hole pairs and subsequently, producing lower percentage of degradation [30]. However, the incorporation of GO (0.1 g) into the samples shows a significant change in photocatalytic activity as compared to pure ZnO and Nidoped ZnO samples with percentage obtained was around 95%. This was ascribed to the increase in the active sites and enhanced electron mobility which was responsible for the MB degradation.

The photocatalytic enhancement is also attributed by the strong and synergistic interaction between Ni/ZnO and GO in which the GO itself acts as an electron trapping site. The active sites here is referring to the GO surfaces which contain oxygenated functional groups (such as C=O, OH, etc.) that help in enhancing the electron mobility. Graphene itself is known to have superior charge carrier mobility properties  $(2 \times 10^5 \text{ cm}^2 \text{ V}^{-1} \text{ s}^{-1})$ which allow for better electron transfer [31]. Theoretically, when ZnO is receiving the photon energy, the electrons (e<sup>-</sup>) excited from the valence band (VB) to the conduction band (CB), leaving positive holes (h<sup>+</sup>) behind. These excited electrons are then migrated to the Ni atom and GO sheet and subsequently avoiding the recombination behaviour through effective separation of electron-hole pairs. In this view, more charge carriers are produced from series of redox reactions with subsequent reactive oxidative species (such as •OH and •O<sub>2</sub><sup>-</sup>) for efficient MB degradation [31]. The recombination could not be avoided if the electrons fall back to the valence band and no photocatalytic reaction could be observed. Thus, an appropriate amount of GO played a crucial role to facilitate the electron transfer and to support ZnO for effective electron mobility and separation of photogenerated charges. The percentage of degradation however decreased significantly at a higher GO content (0.2–0.4 g) due to the agglomeration of the nanocomposites which reduced the surface area and

light absorption capacity of the photocatalysts. The percentage obtained for those nanocomposites with varied concentrations of GO displayed were almost comparable to each other.

Even though GO serves as an electron acceptor and mediator for an efficient carrier mobility [32], the presented results also suggested that, different GO content that was incorporated to the Ni-doped ZnO samples significantly affected the degradation efficiency. It might be due to the hindrance of actives sites by excess molecules that simultaneously prevented the light to reach and maximumly absorb the number of dye molecules on the photocatalyst surface. The light scattering and low penetration of light towards the catalyst surface decreased the effective irradiation for the reaction to progress [33]. This phenomenon further reduced the generation of photoexcited electron-hole pairs which leads to the decreased in the photocatalytic performances. This statement is in a good agreement with You et al. in which the decrease in the photocatalytic performance might be due to an excessive presence of GO content which resulted in agglomeration of particles. Hence, the photodegradation rate became more saturated. Furthermore, the higher content of GO in the catalyst lattice could cause a "shielding effect" that might shade the light and limited the light absorption capacity of the photocatalyst [34].

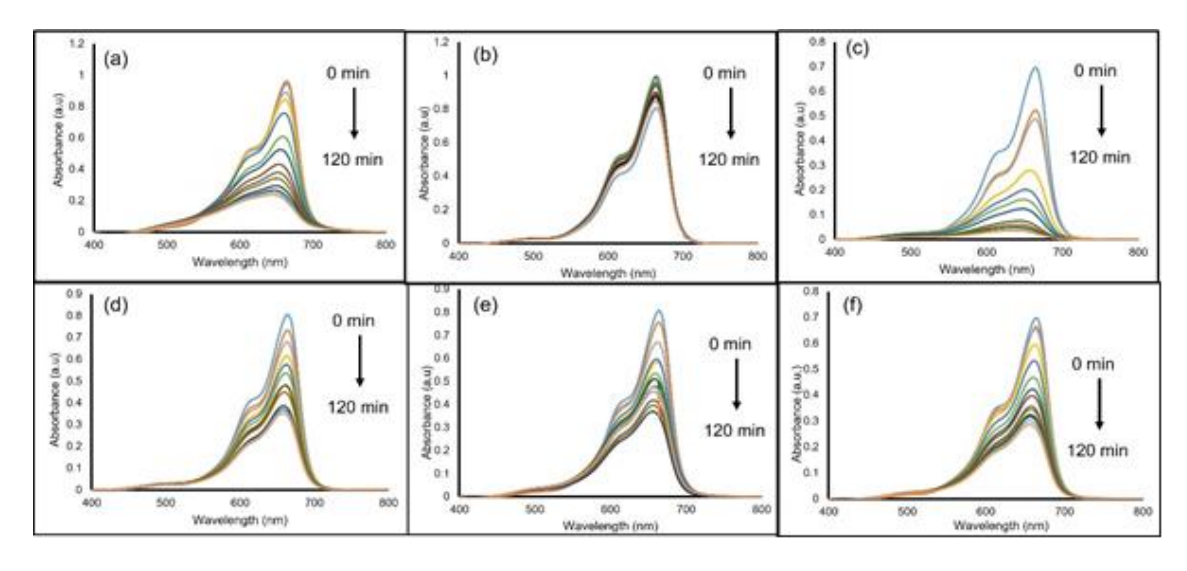


Figure 4. UV-vis absorbance spectra as a function of time for the degradation of MB using (a) pure ZnO, (b) Nidoped ZnO, and (c - f) Ni-doped ZnO/GO<sub>0.1-0.4</sub> nanocomposites

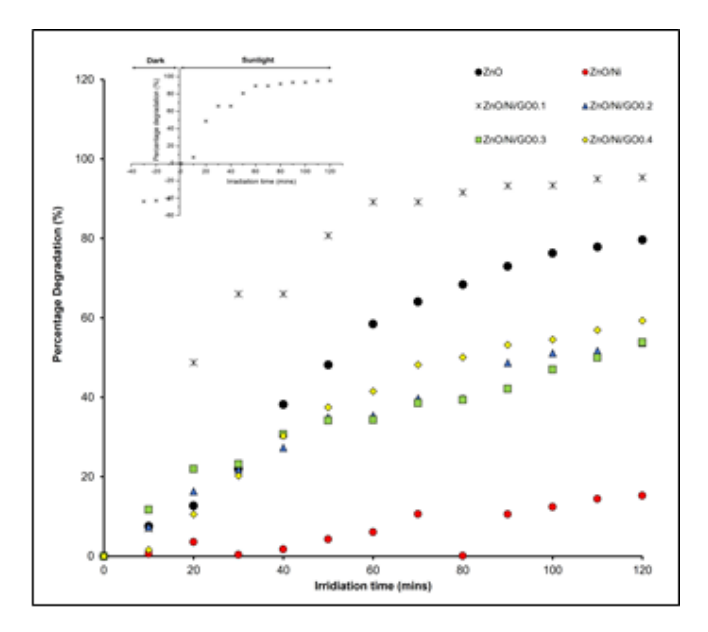


Figure 5. Percentage of degradation of MB under sunlight irradiation in the presence of different photocatalysts and the insert shows the photodegradation of MB under dark and sunlight irradiation using ZnO/Ni/GO<sub>0.1</sub> catalyst

Further analysis on the kinetic of MB disappearance had been carried out by plotting a first order decay plot of the characteristic of MB absorption peak. The experimental data were fitted based on the Langmuir–Hinshelwood (L–H) kinetic model as expressed by equations (2) and (3), hence the rate constant, k of the photocatalyst can be evaluated and quantified.

$$r = dC/dt = kC$$
 (2)

where r and k represent the pseudo first-order reaction rate and rate constant, respectively. The equation can be rewritten as

$$ln (C/C_o) = -kt$$
(3)

The pseudo first-order rate constant was determined from the slope of the plot of -ln (Co/Ct) versus irradiation time, t as illustrated in Figure 6. Linear plots were observed (with R² values higher than 0.9) which attested that photodegradation of MB obeyed pseudo-first order kinetics. The calculated pseudo-first order rate constant and corresponding R² values are presented in Table 1.

The results showed that the Ni-doped ZnO/GO<sub>0.1</sub> exhibited the highest k value of 0.025 min<sup>-1</sup> compared to other samples which were found to be 0.0138, 0.0013, 0.070, 0.066 and 0.0081 min-1 for pure ZnO, Ni-doped ZnO, Ni-doped ZnO/GO<sub>0.2</sub>, Ni-doped ZnO/GO<sub>0.3</sub>, and Ni-doped ZnO/GO<sub>0.4</sub>, respectively. As depicted in Table 1, the incorporation of GO into the Ni-doped ZnO composite influenced the photocatalytic performance as ZnO/Ni/GO<sub>0.1</sub> nanocomposite exhibited the highest percentage degradation of MB under direct sunlight. It can be suggested that Ni-doped ZnO/GO<sub>0.1</sub> should be regarded as the best photocatalyst as compared to pure ZnO and other samples. Nevertheless, the incorporation of excess amount of GO to ZnO did not give a significant trend of photodegradation performance due to the hindrance of actives sites by excess molecules that simultaneously prevents the light to reach and maximumly absorbed on the photocatalyst surface. The light scattering and low penetration of light towards the catalyst surface decreasing the effective irradiation for the reaction to progress [9].

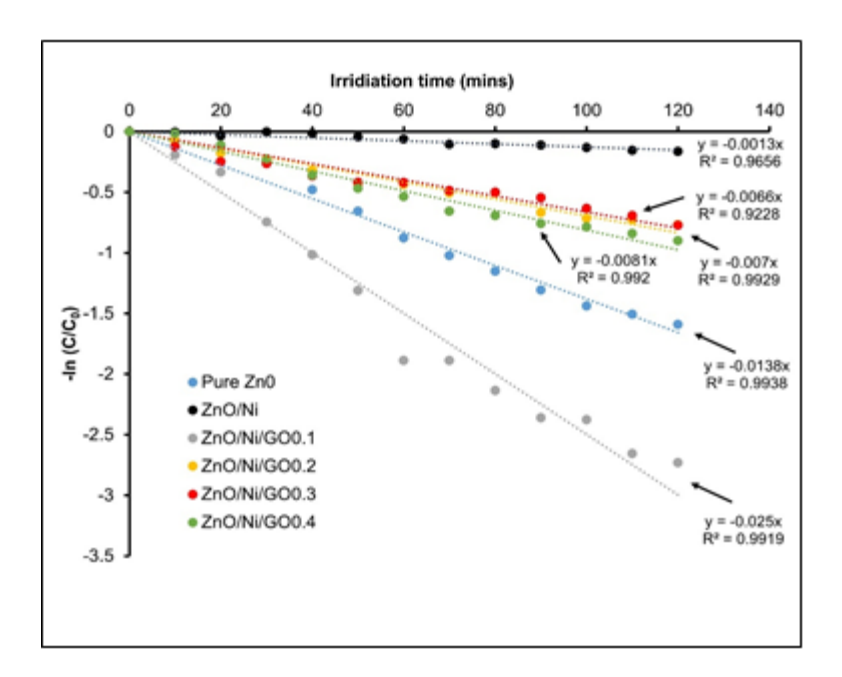


Figure 6. Plots of -ln (C/Co) versus irradiation time for the kinetic of disappearance of MB in the presence of different photocatalysts

Table 1. Photodegradation activities of MB using pure ZnO, Ni-doped ZnO, and Ni-doped ZnO/GO nanocomposites at different GO contents under sunlight irradiation

Sample	Percentage Degradation (%)	Photodegradation Rate Constant, k (min <sup>-1</sup> )	R <sup>2</sup> Value
Pure ZnO	79.64	0.0138	0.9808
ZnO/Ni	15.24	0.0013	0.9102
$ZnO/Ni/GO_{0.1}$	95.33	0.0250	0.9705
$ZnO/Ni/GO_{0.2}$	53.68	0.0070	0.9710
$ZnO/Ni/GO_{0.3}$	53.83	0.0066	0.9228
ZnO/Ni/GO <sub>0.4</sub>	59.32	0.0081	0.9717

#### Conclusion

In this study, the XRD analysis revealed that the Ni and GO were successfully incorporated into the wurtzite structure of ZnO crystal as there were no impurity or secondary phases existed in the XRD pattern for sample Ni-doped ZnO/GO<sub>0.1-0.4</sub> nanocomposites. Other than that, it also showed the absence of Ni peak in the nanocomposite samples and this might be due to very small doping content of Ni element. The FESEM images with average size of about 100–500 nm was observed

for pure ZnO, Ni-doped ZnO/GO $_{0.1}$  and Ni-doped ZnO/GO $_{0.4}$  nanocomposites. Moreover, the morphological characteristics for all prepared samples composed of rod-like and cubic-like structures. The Ni-doped ZnO/GO $_{0.1}$  nanocomposite exhibited the best photocatalytic degradation of MB under direct sunlight within 120 min of reaction with percentage of degradation reaching 93.49% and photodegradation rate constant, k value of 0.0250 min<sup>-1</sup> as compared to other samples. Overall, this research suggests a viable method

for improving the photocatalytic activity of ZnO-based photocatalysts, and it has promising implications for environmental issues.

#### Acknowledgement

This research is supported by FRGS-RACER: 600-RMI/FRGS/RACER 5/3 (041/2019). The authors fully acknowledged Ministry of Higher Education (MOHE) and Universiti Teknologi MARA Pahang for the approved fund which makes this important research viable and effective.

#### References

- 1. Jeyasubramanian, K., Hikku, G. S. and Sharma, R. K. (2015). Photo-catalytic degradation of methyl violet dye using zinc oxide nano particles prepared by a novel precipitation method and its antibacterial activities. *Journal of Water Process Engineering*, 8: 35-44.
- 2. Subbaiah, M. V. and Kim, D. S. (2016). Adsorption of methyl orange from aqueous solution by aminated pumpkin seed powder: Kinetics, isotherms, and thermodynamic studies. *Ecotoxicology and environmental safety*, 128:109-117.
- 3. Peter, A., Mihaly-Cozmuta, A., Nicula, C., Mihaly-Cozmuta, L., Jastrzębska, A., Olszyna, A. and Baia, L. (2017). UV light-assisted degradation of methyl orange, methylene blue, phenol, salicylic acid, and rhodamine B: photolysis versus photocatalyis. *Water, Air, & Soil Pollution*, 228(1): 1-12.
- Kheirabadi, M., Samadi, M., Asadian, E., Zhou, Y., Dong, C., Zhang, J. and Moshfegh, A. Z. (2019). Well-designed Ag/ZnO/3D graphene structure for dye removal: Adsorption, photocatalysis and physical separation capabilities. *Journal of Colloid* and Interface Science, 537: 66-78.
- Jothibas, M., Manoharan, C., Jeyakumar, S. J., Praveen, P., Punithavathy, I. K. and Richard, J. P. (2018). Synthesis and enhanced photocatalytic property of Ni doped ZnS nanoparticles. *Solar Energy*, 159: 434-443.
- Rafaie, H. A., Nor, R. M., Azmina, M. S., Ramli, N. I. T. and Mohamed, R. (2017). Decoration of ZnO microstructures with Ag nanoparticles enhanced the

- catalytic photodegradation of methylene blue dye. *Journal of Environmental Chemical Engineering*, 5(4): 3963-3972.
- Syazwani, O. N., Mohd Hir, Z. A., Mukhair, H., Mastuli, M. S. and Abdullah, A. H. (2019). Designing visible-light-driven photocatalyst of Ag<sub>3</sub>PO<sub>4</sub>/CeO<sub>2</sub> for enhanced photocatalytic activity under low light irradiation. *Journal of Materials Science: Materials in Electronics*, 30(1): 415-423.
- 8. Asghar, A., Raman, A. A. A. and Daud, W. M. A. W. (2015). Advanced oxidation processes for in-situ production of hydrogen peroxide/hydroxyl radical for textile wastewater treatment: a review. *Journal of Cleaner Production*, 87: 826-838.
- 9. Mohd Hir, Z. A., Abdullah, A. H., Zainal, Z. and Lim, H. N. (2017). Photoactive hybrid film photocatalyst of polyethersulfone-ZnO for the degradation of methyl orange dye: Kinetic study and operational parameters. *Catalysts*, 7(11): 313.
- Khaki, M. R. D., Shafeeyan, M. S., Raman, A. A. A. and Daud, W. M. A. W. (2017). Application of doped photocatalysts for organic pollutant degradation-A review. *Journal of Environmental Management*, 198: 78-94.
- 11. Bora, L. V. and Mewada, R. K. (2017). Visible/solar light active photocatalysts for organic effluent treatment: Fundamentals, mechanisms and parametric review. *Renewable and Sustainable Energy Reviews*, 76: 1393-1421.
- Ahmed, S. N. and Haider, W. (2018). Heterogeneous photocatalysis and its potential applications in water and wastewater treatment: a review. *Nanotechnology*, 29(34): 342001.
- 13. Wang, P., Wu, D., Ao, Y., Wang, C. and Hou, J. (2016). ZnO nanorod arrays co-loaded with Au nanoparticles and reduced graphene oxide: Synthesis, characterization and photocatalytic application. *Colloids and Surfaces A: Physicochemical and Engineering Aspects*, 492: 71-78.

- 14. Zhu, P., Duan, M., Wang, R., Xu, J., Zou, P. and Jia, H. (2020). Facile synthesis of ZnO/GO/Ag<sub>3</sub>PO<sub>4</sub> heterojunction photocatalyst with excellent photodegradation activity for tetracycline hydrochloride under visible light. *Colloids and Surfaces A: Physicochemical and Engineering Aspects*, 602: 125118.
- Upadhyay, G. K., Rajput, J. K., Pathak, T. K., Kumar, V. and Purohit, L. P. (2019). Synthesis of ZnO: TiO<sub>2</sub> nanocomposites for photocatalyst application in visible light. *Vacuum*, 160: 154-163.
- Muñoz-Fernandez, L., Sierra-Fernández, A., Milošević, O. and Rabanal, M. E. (2016). Solvothermal synthesis of Ag/ZnO and Pt/ZnO nanocomposites and comparison of their photocatalytic behaviors on dyes degradation. Advanced Powder Technology, 27(3): 983-993.
- 17. Xie, M., Zhang, D., Wang, Y. and Zhao, Y. (2020). Facile fabrication of ZnO nanorods modified with RGO for enhanced photodecomposition of dyes. *Colloids and Surfaces A: Physicochemical and Engineering Aspects*, 603: 125247.
- 18. Wang, W., Li, N., Hong, K., Guo, H., Ding, R. and Xia, Z. (2019). Z-scheme recyclable photocatalysts based on flower-like nickel zinc ferrite nanoparticles/ZnO nanorods: enhanced activity under UV and visible irradiation. *Journal of Alloys and Compounds*, 777: 1108-1114.
- Tawale, J. S., Kumar, A., Swati, G., Haranath, D., Dhoble, S. J. and Srivastava, A. K. (2018). Microstructural evolution and photoluminescence performanance of nickel and chromium doped ZnO nanostructures. *Materials Chemistry and Physics*, 205: 9-15.
- Gao, P., Ng, K. and Sun, D. D. (2013). Sulfonated graphene oxide–ZnO–Ag photocatalyst for fast photodegradation and disinfection under visible light. *Journal of Hazardous Materials*, 262: 826-835.
- Ahmad, M., Ahmed, E., Hong, Z. L., Khalid, N. R., Ahmed, W. and Elhissi, A. (2013). Graphene– Ag/ZnO nanocomposites as high performance photocatalysts under visible light irradiation. *Journal of Alloys and Compounds*, 577: 717-727.
- 22. Haghshenas, S. S. P., Nemati, A., Simchi, A. and Kim, C. U. (2019). Dispute in photocatalytic and

- photoluminescence behavior in ZnO/graphene oxide core-shell nanoparticles. *Materials Letters*, 240: 117-120.
- 23. Moussa, H., Girot, E., Mozet, K., Alem, H., Medjahdi, G. and Schneider, R. (2016). ZnO rods/reduced graphene oxide composites prepared via a solvothermal reaction for efficient sunlight-driven photocatalysis. *Applied Catalysis B: Environmental*, 185: 11-21.
- Wu, Z. and Wang, L. (2019). Graphene oxide (GO) doping hexagonal flower-like ZnO as potential enhancer of photocatalytic ability. *Materials Letters*, 234: 287-290.
- 25. Długosz, O., Szostak, K., Krupiński, M. and Banach, M. (2021). Synthesis of Fe<sub>3</sub>O<sub>4</sub>/ZnO nanoparticles and their application for the photodegradation of anionic and cationic dyes. *International Journal of Environmental Science and Technology*, 18(3): 561-574.
- Huszla, K., Wysokowski, M., Zgoła-Grześkowiak, A., Staszak, M., Janczarek, M., Jesionowski, T. and Wyrwas, B. (2022). UV-light photocatalytic degradation of non-ionic surfactants using ZnO nanoparticles. *International Journal of Environmental Science and Technology*, 19(1): 173-188.
- Li, J., Li, P., Li, J., Tian, Z. and Yu, F. (2019).
   Highly-dispersed Ni-NiO nanoparticles anchored on an SiO<sub>2</sub> support for an enhanced CO methanation performance. *Catalysts*, 9(6): 506.
- 28. Rafaie, H. A., Embong, N. A., Ramli, N. I., Mohamed, R. and Kasim, M. F. (2018). Synthesis of ZnO microstructure decorated with ag nanoparticles at different annealing temperature and their photocatalytic activity. Recent Innovations in Chemical Engineering (Formerly Recent Patents on Chemical Engineering), 11(3): 192-200.
- Behnood, R. and Sodeifian, G. (2020). Synthesis of N doped-CQDs/Ni doped-ZnO nanocomposites for visible light photodegradation of organic pollutants. *Journal of Environmental Chemical Engineering*, 8(4), 103821.

#### Hartini et al: CONSTRUCTING NI-DOPED ZnO/GO HETEROSTUCTURES FOR ENHANCED SUNLIGHT-TRIGGERED DEGRADATION OF METHYLENE BLUE DYE

- Yin, Q., Qiao, R., Li, Z., Zhang, X. L. and Zhu, L. (2015). Hierarchical nanostructures of nickel-doped zinc oxide: Morphology controlled synthesis and enhanced visible-light photocatalytic activity. *Journal of Alloys and Compounds*, 618: 318-325.
- 31. Julkapli, N. M. and Bagheri, S. (2015). Graphene supported heterogeneous catalysts: an overview. *International Journal of Hydrogen Energy*, 40(2): 948-979.
- Ahmad, M., Ahmed, E., Ahmed, W., Elhissi, A., Hong, Z. L. and Khalid, N. R. (2014). Enhancing visible light responsive photocatalytic activity by decorating Mn-doped ZnO nanoparticles on graphene. *Ceramics International*, 40(7): 10085-10097.
- 33. Qin, J., Zhang, X., Xue, Y., Kittiwattanothai, N., Kongsittikul, P., Rodthongkum, N. and Liu, R. (2014). A facile synthesis of nanorods of

- ZnO/graphene oxide composites with enhanced photocatalytic activity. *Applied Surface Science*, 321: 226-232.
- 34. Tju, H., Shabrany, H., Taufik, A. and Saleh, R. (2017). Degradation of methylene blue (MB) using ZnO/CeO2/nanographene platelets (NGP) photocatalyst: Effect of various concentration of NGP. In AIP Conference Proceedings, 1862: p. 030037.

## **Malaysian Journal of Analytical Sciences** (MJAS) Published by Malaysian Analytical Sciences Society



#### BIOSORPTION CAPACITY OF HEAVY METAL LEAD (Pb(II)) USING DRY SEAWEED Eucheuma denticulatum

(Kapasiti Biojerapan Logam Berat Plumbum (Pb(II)) Mengunakan Rumpai Laut Kering *Eucheuma denticulatum*)

Hamad Maalim Sharif<sup>1</sup>, Yahya Makame<sup>2</sup>, Mohammed Ali Sheikh<sup>3</sup>, Hasrizal Shaari<sup>1,4\*</sup>, Rokiah Suriadi<sup>1</sup>, Fatin Izzati Minhat<sup>4</sup>

> <sup>1</sup>Institute of Oceanography and Environment, Universiti Malaysia Terengganu, 21030, Kuala Nerus, Terengganu, Malaysia <sup>2</sup>Chemistry Department, School of Natural and Applied Sciences, University of Dar es Salaam, P.O. Box 35065, Dar es Salaam, Tanzania <sup>3</sup>School of Natural and Social Sciences, The State University of Zanzibar, P. O. Box 146, Zanzibar, Tanzania <sup>4</sup>Faculty of Science and Marine Environment, Universiti Malaysia Terengganu, 21030, Kuala Nerus, Terengganu, Malaysia

> > \*Corresponding author: riz@umt.edu.my

Received: 29 October 2021; Accepted: 27 February 2022; Published: 27 June 2022

#### **Abstract**

The seaweed industry plays a significant socio-economic role in tropical coastal communities. This study presents the biosorption behaviour of Pb(II) aqueous solution onto seaweed E. denticulatum. The impact of pH contact time, the initial concentration of the metals, and the adsorption activities were studied. The findings demonstrated that the Pb(II) uptake rate rose with increased concentration and contact time. The Pb(II) uptake reached saturation at 1000 mg/L after 120 min at room temperature. Pb(II) biosorption onto Eucheuma denticulatum fitted well to the Langmuir isotherm, with a maximum adsorption capacity  $(q_{max})$  of 416.67 mg/g. The results suggest that this type of seaweed, E. denticulatum, is an effective biosorbent for removing Pb (II) and may control toxic metal pollution in tropical aquatic ecosystems.

Keywords: biosorption, Eucheuma denticulatum, heavy metals, Langmuir and Freundlich models

#### Abstrak

Industri rumpai laut memainkan peranan sosio-ekonomi yang sangat penting bagi masyarakat pesisir pantai tropika. Kajian ini menunjukkan tingkah laku biojerapan larutan akues Pb(II) ke atas Eucheuma denticulatum. Pengaruh hubungan masa pH, kepekatan awal logam, dan kajian penjerapan-penyerapan telah dilakukan. Hasil kajian menunjukkan bahawa kadar pengambilan Pb(II) meningkat dengan peningkatan kepekatan dan masa hubungan. Pengambilan Pb(II) mencapai titik tepu pada 1000 mg/L setelah 120 minit pada suhu bilik. Biojerapan Pb(II) ke atas E. denticulatum dipasang dengan baik pada isoterm Langmuir dengan kapasiti penjerapan maksimum ( $q_{max}$ ) 416.67 mg/g. Hasilnya menunjukkan bahawa rumpai laut *E. denticulatum* adalah biopenjerap yang berkesan untuk menghilangkan Pb(II) dan mungkin boleh digunakan untuk mengawal pencemaran logam toksik di ekosistem perairan tropika.

Kata kunci: biojerapan, Eucheuma denticulatum, logam berat, model Langmuir dan Freundlich

#### Introduction

Heavy metal pollution is a serious concern due to its profound impact, even at small concentrations. It is caused by enhanced industrialisation and human activities that release various contaminants into the environment [1, 2, 3]. Heavy metals are considered among the most toxic groups reaching the food chain via waste disposal in water bodies and on land [4]. Therefore, eliminating heavy metal ions in wastewater is crucial for public health protection. The conventional methods for treating toxic metals are expensive and difficult to manage. Some methods lead to ineffective metals removal, restricted tolerance to pH change, slight metal selectivity, and the generation of toxic by-product waste that must be appropriately disposed of [5]. Attention has focused on heavy metals biosorption using various biological materials as this enables a higher metal binding capacity than chemical-based methods [6, 7].

Biosorption is a subtraction technique directed at contaminants or pollutants through inactive biomass, which allows the contaminants to be passively concentrated and bound to their cellular structure. Several absorbent materials have previously been used, including algae [8], fungi [9], bacteria [10], seaweeds [11], and some higher plants [12]. Several studies have assessed the efficiency of using different biosorbent materials for treating heavy metals in wastewater. For example, Tabaraki et al. [13] assessed the efficiency of brown seaweed on Pb(II) ions biosorption. At optimal conditions, they found the maximum seaweed uptake for the Pb(II) ions uptake to be 195±3.3 mg/g. The study of peanut shell efficacy on Pb2+ ions was carried out by Taşar et al. [14], and 39 mg/g was the maximum uptake obtained. The biosorption capacities of olive mill solid (OMS) and olive stone (OS) on Pb2+ ions uptake were examined by Blázquez et al. [15] in batch experiments under varied temperatures. The results revealed that the maximum Pb uptake was 6.57 mg/g on OS and 23.69 mg/g on OMS at 25 °C. Gerola et al. [16] investigated the biosorption capacity of the residue of passionfruit

skin onto Pb2+ ions and found that the maximum biosorption capacity was 204 mg/g at pH 4 for 170 min. Senthilkumar et al. [17] evaluated the biosorption functions of ten (10) different seaweed species on Pb<sup>2+</sup> ions uptake under varied pH environments. The brown seaweed Turbinaria Conoides displayed optimal Pb2+ ions uptake of 439.4 mg/g at pH 4.5 and a temperature of 30 °C. The work of Abdel-Aty et al. [18] presented the applicability of Blue-Green Alga Anabaena Sphaerica as a biosorbent of Cd<sup>2+</sup> and Pb<sup>2+</sup> ions from aqueous solutions. The ideal biosorption capacity was 111.1 mg/g and 121.95 mg/g, respectively, at peak conditions. The adsorption capacities of Macroalgae Eucheuma Spinosum, Padina Minor, and Sargassum Crasifollum were assessed by Putri [19] for their Pb<sup>2+</sup> biosorption. The maximum biosorption capacity (55.56 mg/g) was demonstrated by Sargassum Crasifollum, followed by Padina Minor (40.00 mg/g), while the lowest (32.26 mg/g) was demonstrated by Eucheuma *Spinosum*. Studies on Pb<sup>2+</sup> ions adsorption from aqueous solutions using raw and chemically modified green freshwater algae (Scenedesmus Obliquus) were conducted by Abdel Ghafar et al. [20]. The modified biomass was found to have higher biosorption capacity (207.2 mg/g) compared to raw biomass (112.0 mg/g). Therefore, algae have proven to be a more efficient and promising biosorbent to use for heavy metal removal from wastewater. The biosorption method is comparatively inexpensive and it offers elevated efficiency in terms of metal removal, as well as minimum chemical and/or biological sludge production, among others [21].

Algae biosorbent materials are gaining significant attention due to their abundance in the oceanic environment, relative easiness to process, and high accumulated ability of metal content. Algal-like seaweed is sufficient to facilitate a complex solid-liquid separation process, thus making seaweed a suitable form of biomass for heavy metal biosorption in the marine environment [22]. Seaweeds are marine algae found in coastal areas. The red algae *Eucheuma cottonii* and

Eucheuma denticulatum are grown in eastern Africa's tropical coastal regions [23, 24]. The seaweed industry in Tanzania employs more than 30,000 people [25]. Approximately 5,000 tons of dry seaweed are exported annually from Tanzania [25]. The high production of seaweed in Tanzania has motivated the authors to propose this substance as a potential biosorption material.

Heavy metal pollution has recently gained scientific attention due to its ubiquity in marine and coastal ecosystems [26]. Heavy metals' pathways into the human body are through food, water, and air. They are absorbed through the skin or by exposure from various agricultural, manufacturing, pharmaceutical, and urbanisation activities. Lead (Pb) is among the heavy metals proving to be the most serious toxic contaminant in Tanzania [27, 28, 29].

Previous studies have demonstrated the high metal-binding abilities of brown and green seaweeds [30, 31, 32]. However, there is a lack of data on the heavy metal biosorption by red seaweed species (*E. denticulatum*) in Tanzania. Therefore, this study discusses the biosorption behaviour of Pb(II) solution onto *E. denticulatum*. The findings from this study on *E. denticulatum* as a potential biosorption material of toxic metals have extensive consequences for the economy and health of farmers engaged in seaweed aquaculture in the coastal areas of Tanzania.

#### **Materials and Methods**

#### Study area

This study was conducted in three locations (Unguja Ukuu, Tumbe, and Kiungoni) along the coastal areas of Zanzibar. Tumbe and Kiungoni are located in the northern part of Pemba Island (Figure 1), while Unguja Ukuu is situated in the southern part of Unguja island (Figure 2). Seaweed farming is mainly found in these areas. Fresh seaweed *E. denticulatum* samples were cleaned carefully on-site with ocean water to eliminate impurities.

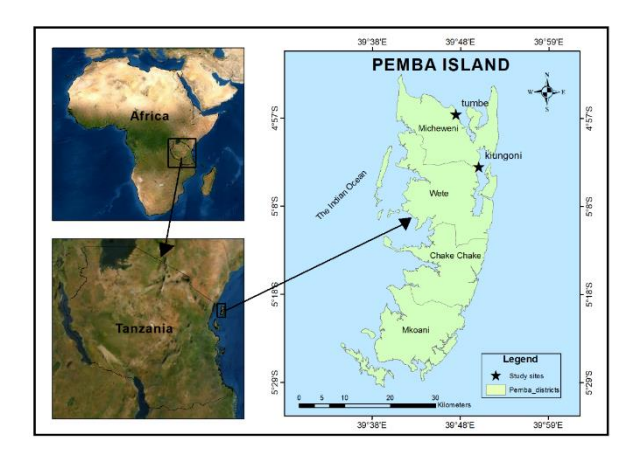


Figure 1. The sampling areas in the Pemba Island coastal region

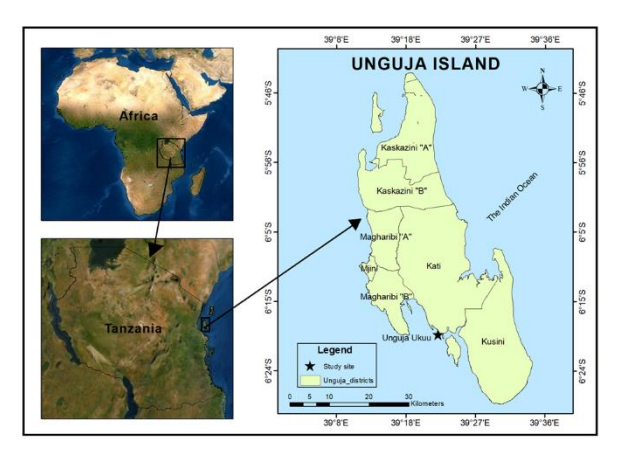


Figure 2. The sampling area in the Unguja Island coastal region

#### Sample preparation

The seaweed samples were washed with tap water, before being washed again with deionised water to eradicate salts and particulate matter from the surface of samples. The samples were then air-dried for 48 hours and then oven-drying at 80 °C for 24 hrs. The dried samples were ground into a homogeneous powder using a laboratory blender and stored in a desiccator before the biosorption experiments were conducted.

#### Pb(II) ions solution preparation

Pb(II) ions stock solution was prepared by dissolving 1.60g of Pb (NO)<sub>3</sub> in 1000 ml of deionised water. The different concentrations of Pb(II) solutions (50, 100, 250, 500, 1000, 1500, and 2000 mg/L were prepared by diluting the stock solution. The initial pH of the standard solutions was adjusted to the desired value by adding 0.1 M HCl or 0.1 M NaOH. The analytical grade of chemicals from Merck was used in this study. The concentrations of the standard solutions of 0.20, 1.00, 2.00, 7.00, 10.00, and 20.00 mg/L were precisely prepared.

## Preliminary concentration of Pb(II) in E. Denticulatum

The initial Pb(II) ions levels were determined using a modified version of the methods devised by Luis et al. [33] and Rubio et al. [34]. Next, 25 g of *E. denticulatum* was oven-dried at 70 °C for 12 hours. Then, the sample was burned in a furnace at 550 °C for 20 hours to remove the organic matter. The ash of the sample was digested in 2 mL of HNO<sub>3</sub> (v/v) for 18 hours. The digested solution was filtered with a filter paper (Whatman no 2) and transferred into a 50 mL test tube. The solution was meshed up to 30 mL with deionised water. The atomic absorption spectrometer (AAS) Thermo Scientific model iCE 3300 was used to determine the Pb(II) ion concentrations.

#### **Batch biosorption experiments**

The batch biosorption experiments were established using a magnetic stirrer (120 - 180 min) at 120 rpm in a 250 mL beaker. Next, 50 mL of the standard solution was introduced into the beaker and biosorbent was added appropriately. The different parameters were organised as follows: solution pH (2-8), contact time (0-150 minutes), initial Pb(II) ion concentration (50-2000 mg/L). The Pb (II) ion biosorption characteristics were evaluated using a biomass weight of 0.5 g. The solution was separated using a Whatman filter paper No 2 or centrifuging and decanting.

#### Optimum pH for Pb(II) biosorption

The Pb(II) biosorption optimum pH was established by adding 50 mL solutions of 50 mg/L Pb (II) ions into a 100 mL centrifuge tube with 0.5 g of dry seaweed. The samples, which were of varying pH (2.0 to 8.0), were adjusted using 0.1 M NaOH or 0.1 M HNO<sub>3</sub> [35]. The mixtures were stirred for 180 minutes with a magnetic stirrer at room temperature. The supernatant was collected after centrifuging the mixture using the Gallen Kamp Centrifuge 200 at the lowest rate for 10 minutes. The AAS was used to determine the Pb(II) ion concentration in the supernatant. The analysis of each sample was performed in a duplication setting.

#### Optimum contact time for Pb(II) adsorption

The optimum contact time for Pb(II) adsorption was determined at optimum pH by adding 0.5 g biomass to 50 mL of the 50 mg/L metal solution. The mixture was stirred for 180 min using a magnetic stirrer at moderate speed at room temperature. At 5, 10, 30, 60, 120, and 180 min, the samples were removed, centrifuged, decanted. The supernatant was collected and stored for AAS analysis. The samples were prepared in duplicate.

#### The effect of Pb(II) ion concentration on biosorption

The effect of Pb(II) ion concentration on biosorption was investigated by mixing 0.5 g of seaweed and 50 mL of solutions of known concentrations at room temperature. The Pb(II) ion concentration levels were 50, 100, 250, 500, 1000, 1500, and 2000 mg/L. The solution mixture was corrected to the required pH with HNO<sub>3</sub> or NaOH solution before it was stirred with a magnetic stirrer at moderate speed and room temperature for 120 minutes. The samples were decanted using a Gallen Kamp Centrifuge 200 centrifuge for 20 minutes. The supernatants were then kept in centrifuge tubes and determined using the Atomic Absorption Spectrometer (AAS). This process was performed in duplicate.

#### **Biosorption models**

The Langmuir and Freundlich isotherm models were used to calculate Pb(II) biosorption from the aqueous solutions. The following is a linearised Langmuir equation [36]:

$$\frac{1}{q} = \frac{1}{q_{max}} + \frac{1}{b \cdot q_{max} C_f} \tag{1}$$

where  $q_{max}$  is the Langmuir adsorption capacity (mg/g) and b is the adsorption energy (l/mg). The intercept and slope from the 1/q Vs 1/C<sub>f</sub> graph were used to calculate  $q_{max}$  and b.

The following equation represents the Freundlich isotherm linear form [37]:

$$\log q = \log K + \frac{1}{n} \log C_f \tag{2}$$

where K is the Freundlich constant correlated to adsorption capacity, and n is the adsorption intensity. Furthermore, the separation factor  $R_L$  describes the essential characteristics of the Langmuir isotherm [38]:

$$R_L = \frac{1}{1 + bq_{max}} \tag{3}$$

#### Kinetic adsorption study

Adsorption kinetics is a significant aspect of biosorption studies since it presents valuable information concerning adsorption mechanisms and allows the investigation of the controlling biosorption mechanism. The assessment of  $Pb^{2+}$  ions adsorption kinetics onto *E denticulatum* was conducted using pseudo-first-order and pseudo-second-order kinetics. The pseudo-first-order equation was devised by Febrianto et al. [39]

$$\log(q_e - q_t) = \log q_e - \frac{k_1 t}{2303} \tag{4}$$

where  $q_e$  and  $q_t$  (mg/g) are the equilibrium and time t, respectively, of the adsorption capacities.  $k_1$  (min<sup>-1</sup>) is the pseudo-first-order adsorption rate constant. The linear correlation of  $\log(q_e-q_t)$  versus t implies that the reaction fits with the pseudo-first-order reaction. The slope and the model's intercept, respectively, give  $k_1$  and  $q_e$ .

According to Ho and Ofomaja [40], the pseudo-second-order reaction is expressed as:

$$\frac{t}{q_t} = \frac{1}{k_2 q_e^2} + \frac{t}{q_e} \tag{5}$$

where  $k_2$  (g mg<sup>-1</sup>min<sup>-1</sup>) is the rate constant for the pseudo-second-order adsorption model. The linear

relationship from the  $\frac{t}{q_t}$  versus t plot gives the values of  $q_e$  and  $k_2$  from the slope and intercept, respectively.

#### **Results and Discussion**

#### The initial levels of Pb(II) in seaweed

The initial concentration of Pb (II) detected in E. denticulatum was 0.084  $\mu g/g$ . The results indicate that only trace amounts of Pb(II) were present in the E. denticulatum samples. The lead levels in Zanzibar's coastal areas range from 228 to 1150 ppm [41]. It was surmised that the trace value might be attributed to the anthropogenic sources and/or the natural background value.

#### Optimum pH for the biosorption of Pb(II)

The solution pH plays a vital role in controlling the metal ions biosorption of metal ions from aqueous solutions [42]. The findings presented in Figure 3 indicate that the removal of Pb(II) was low in an acidic medium (pH < 4). As pH increased, the metal uptake also increased until pH 4. Afterwards (beyond pH > 4), it showed a rapid decline. At low pH, the biosorption capacity was low due to the competition for binding sites on the biomass surface between the H+ ions and the metal ions [43, 44]. Therefore, repulsive forces between the metal ions and the protonated biomass cell wall prevent the metal ions from approaching the cell wall [38]. However, as pH increased, the concentration of H<sup>+</sup> ions declined. The biomass became more negatively charged, resulting in the electrostatic attraction of the positive charge metal ions. Therefore, biosorption rose to its maximum point [45, 46, 47] before the precipitation of metal hydroxides occurred at higher pH due to the high OH- ion concentration. This resulted in a decline in uptake capacity [48] and the electrostatic repulsion between the negatively charged anionic species in the solution [49]. This study revealed that the adsorption rate of Pb(II) ions was optimum at pH 4 and with a concentration of 4.7 mg/g. Therefore, the findings suggest that pH 4 is the most effective pH to use for Pb (II) biosorption, based on the range investigated (Figure 3).

Various biosorption studies employing algal biomass have demonstrated similar results (that pH 4 is the optimum pH). These include the works by Yipmantin et al. [50] using *Chondracanthus* (red alga); Lee and Park,

[51] using brown seaweeds; and Nessim et al. [52] using *Ulva fasciata*, green seaweed and *Sargassum sp.*, brown seaweed.

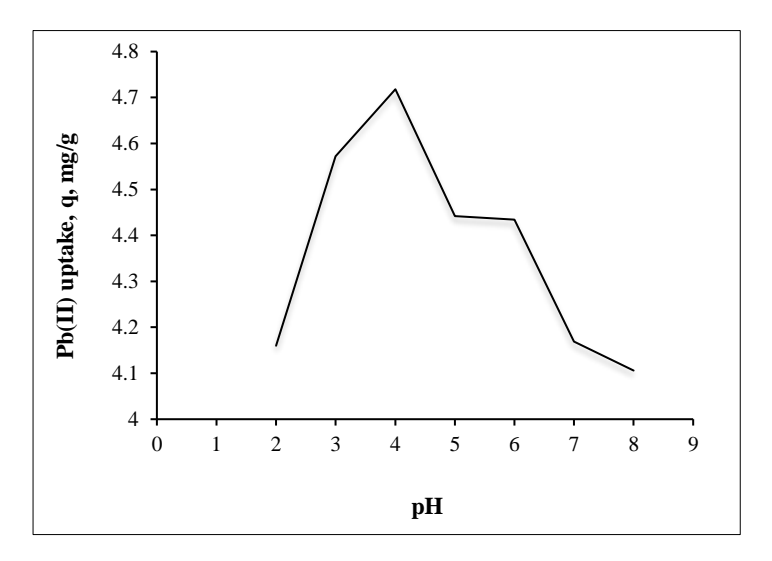


Figure 3. Variation of Pb(II) uptake of E. denticulatum with pH

#### Optimum contact time for Pb(II) biosorption

The metal ions biosorption in aqueous solutions is highly influenced by contact time, as shown in Figure 4. The results from this research study demonstrated that Pb(II) uptake onto *E. denticulatum* increased with longer contact times. Initially, during the first 20 minutes, there was a rapid Pb (II) uptake and a gradual increase until equilibrium at 120 minutes. Meanwhile, no further changes in biosorption were noticed beyond 120 minutes. Thus, 120 minutes can be considered the ideal contact time in other biosorption experiments.

The sharp increase in biosorption during the early stage was likely due to the high solute concentration gradient [53] and the availability of vacant active sites on the biomass surface. Thus, the adsorption of metal ions took

place on these sites [54, 55]. In the subsequent stages, the metal removal declined because the active sites were gradually occupied [56] and there was difficulty occupying the residual binding spots due to the forces between the solid and bulk phases [57, 58].

Several biosorption studies have demonstrated that metal ions adsorption employing algal biomass attained maximum adsorption in the interval between 60 and 120 min. These include the works of Ibrahim, [59] using *Corallina mediterranea, Galaxaura oblongata, Jania rubens*, and *Pterocladia capillacea* (red macroalgae); Ozudogru, [60] using *Padina pavonica* (brown algae); and Abdel-Aty et al. [18] using *Anabaena sphaerica* (freshwater alga).

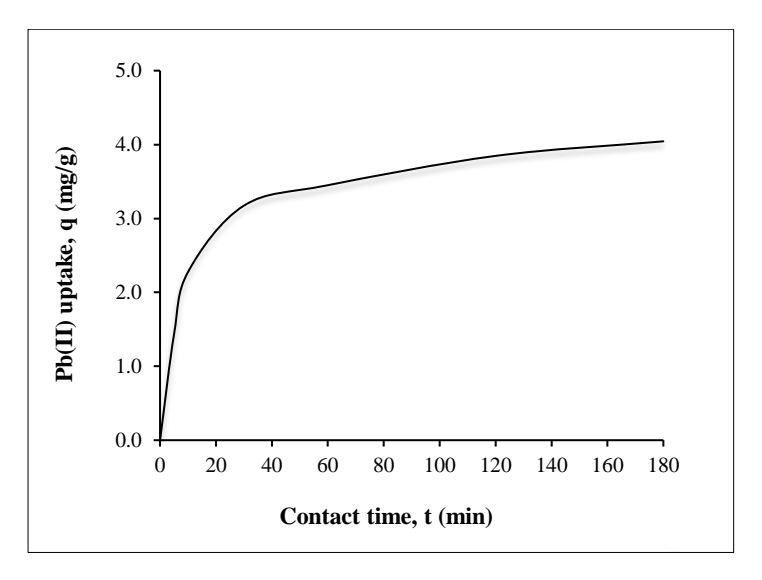


Figure 4. Effect of contact time on Pb(II) adsorption

## Effect of initial metal ion concentration on Pb(II) biosorption

The initial metal ion concentration highly affects the biosorption capacity due to a substantial driving force that eliminates the resistance of all the metal ions between the aqueous and solid phases [61]. The present study demonstrated a rapid increase in Pb(II) biosorption with increased metal ion concentration until 1000mg/L, as shown in Figure 5. The metal uptake increased slowly, implying that the biomass had approached the saturation point [62].

The increased Pb(II) uptake during the early stage might be due to the enhanced driving force of metal ions into the biomass surface and the presence of abundant binding spots on the biosorbent surface areas [63, 64]. Consequently, when the Pb(II) ion concentration increases further, the active sites are overburdened by the ions, thereby preventing further metal ions adsorption [64, 65]. Thus, the metal uptake was enhanced with an increase in the initial levels of Pb(II) ions, reaching saturation when Pb(II) concentration attained a threshold value.

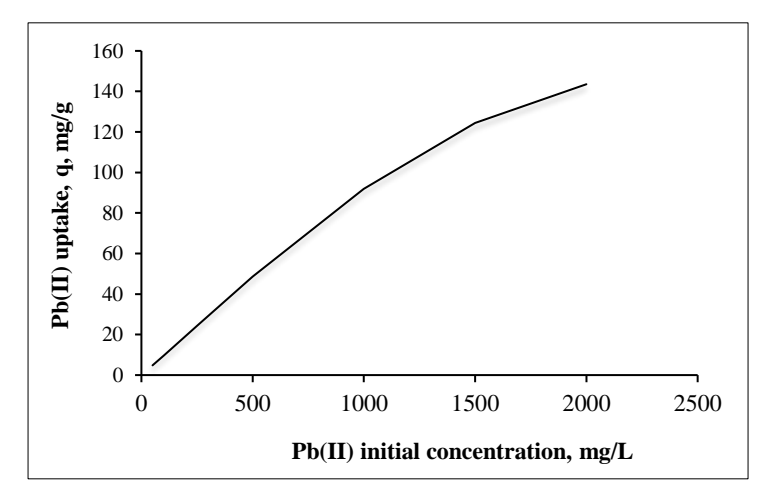


Figure 5. Effect of initial Pb (II) concentration on Pb(II) biosorption onto E. denticula

#### **Biosorption models**

The Freundlich and Langmuir models are isotherm models used to present the relation between equilibrium metal biosorption (q) and final concentration (C<sub>f</sub>) at equilibrium [66]. Both adsorption models were used to measure the relationship between the Pb (II) uptake capability (q) and equilibrium concentration  $(C_f)$ . The constants and correlation coefficients of the adsorption models employed were determined from the respective adsorption isotherms (Table 1). It was found that the Langmuir model ( $R^2 = 0.9935$ ) fitted well, compared with the Freundlich model ( $R^2 = 0.9534$ ). The high Langmuir correlation coefficient suggests conformity of the P(II) adsorption to the model, implying the existence of monolayer adsorption conditions in the Pb (II) – E. denticulatum system [67].

The maximum Langmuir monolayer Pb(II) uptake capacity  $(q_m)$  and the Langmuir constant (b) isotherm were 175.13 mg/g and 0.01476 l/mg, respectively, implying the high uptake of Pb(II) by the biomass, which might have been due to its low capability of

forming complex [68]. The presence of carboxylate polysaccharides in seaweed promotes the binding of cations with large ionic areas [69]. Moreover, the range of the Pb(II) ions separation factor,  $R_L = 0.2789$ , fell between 0 and 1 (0 <  $R_L$ < 1), implying that Pb(II) adsorption is favourable at all the concentrations studied [70].

The slopes and intercepts from the linear graphs (Figures 6 and 7) were used to compute the Langmuir and Freundlich isotherm constants, and the results are summarised in Table 1.

The magnitude of the Freundlich constant K suggests the high adsorption capacity of Pb(II) ions on E. denticulatum. The value of n = 1.67 (n > 1) indicates that under the given experimental conditions, the heterogeneity of the biomass surface and the metal ions were adequately and intensively adsorbed by the dried seaweed E. denticulatum.

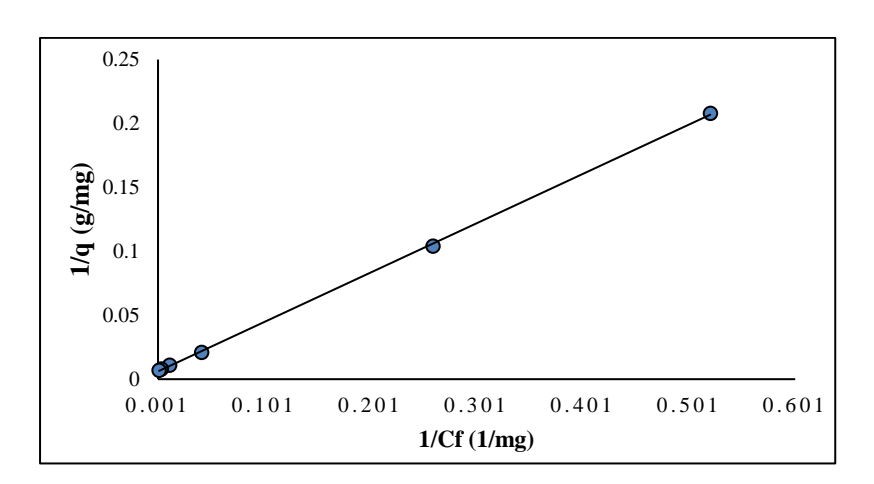


Figure 6. Langmuir isotherm for Pb (II) biosorption by E. denticulatum

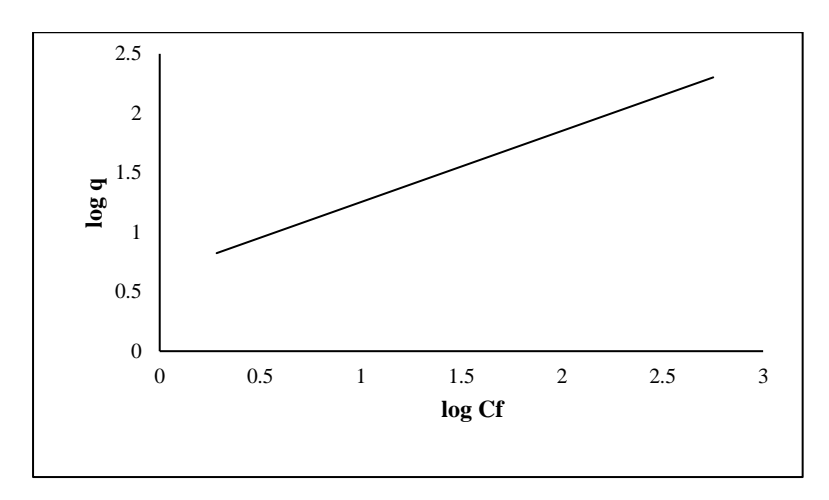


Figure 7. Linearised Freundlich isotherm for Pb(II) biosorption by E. denticulatum

Table 1. The Langmuir and Freundlich parameters and correlation coefficients for the biosorption of Pb (II) onto *E. denticulatum* 

Metal	Langmuir Isotherm Parameters			Freundlich Isotherm Parameters			
	$q_{max}$ , mg/g	<i>b</i> , l/mg	$R^2$	K, mg/g	1/n	n	$R^2$
Pb	175.13	0.01476	0.9991	4.517	0.632	1.67	0.9272

#### **Kinetic studies**

The Pb<sup>2+</sup> ions adsorption rate onto *E.denticulatum* was estimated for contact times ranging from (0-180) min. The experimental data were interpreted using pseudofirst-order and pseudo-second-order kinetic models. The kinetic parameters and regression coefficients were obtained from their corresponding linear graphs (Figures 8 (a) and (b)) and these are summarised in Table 2. The  $\log(q_e-q_t)$  Vs. t plot gives an approximate line, and the rate constant  $(k_1)$  and  $q_e$  can be estimated from the slope and the intercept, respectively. The  $k_1$ ,  $q_e$ , and  $R^2$  are shown in Table 2. Even though the plot is linear and the  $R^2$  is 0.911, the

value of  $q_e$  does not agree with the experimental  $q_e$  value (4.044). Therefore, Pb(II) adsorption does not follow pseudo-first-order kinetics.

The pseudo-second-order kinetic model was employed to find a more trustworthy Pb (II) adsorption kinetics description. The results from the  $\frac{t}{q_t}$  Vs. t plot indicates that the pseudo-second-order kinetic model fits the metal adsorption experiment. The regression coefficient (R<sup>2</sup>) was 0.998, and the  $q_e$  equals 4.3802 mg/g, which is close to the experimental  $q_e$  (4.044mg/g).

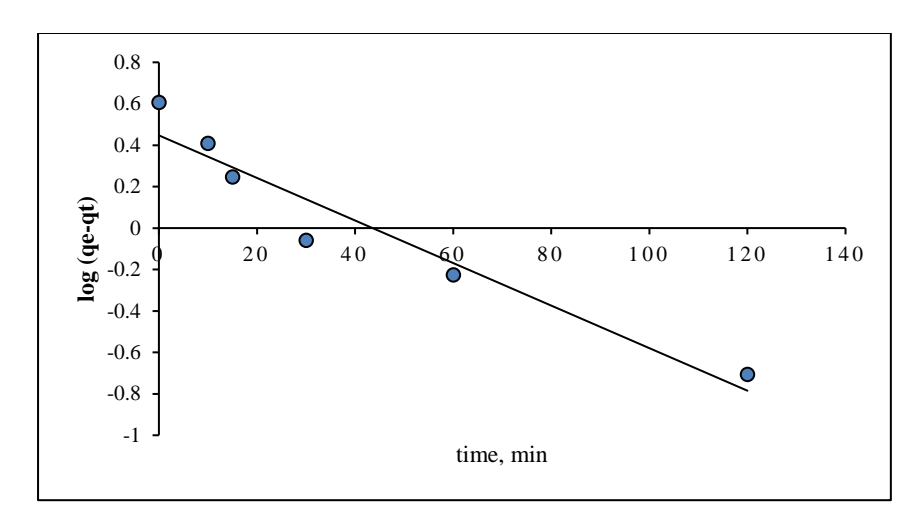


Figure 8(a). Pseudo-first-order for Pb(II) adsorption kinetics onto E. denticulatum

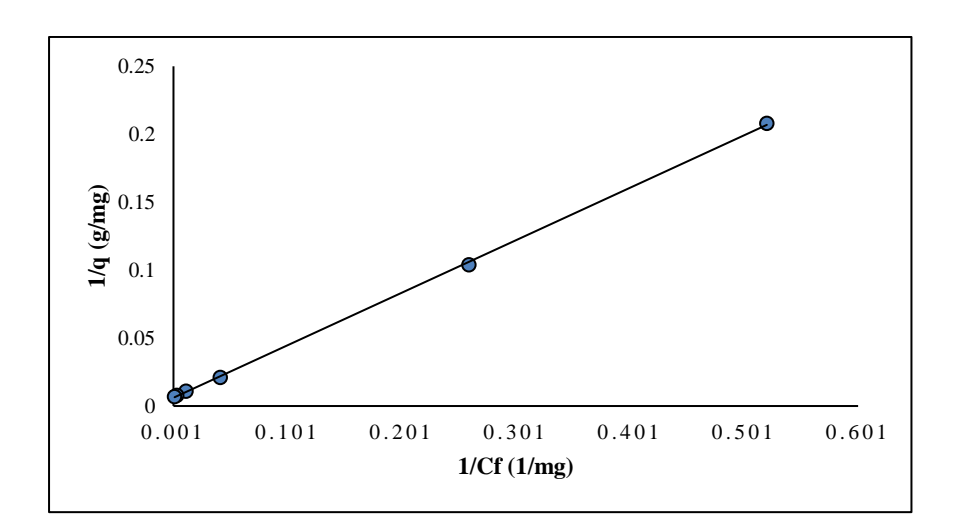


Figure 8(b). Pseudo-second-order for Pb(II) adsorption kinetics onto E. denticulatum

Table 2. The pseudo-first-order and pseudo-second-order kinetics parameters and correlation coefficients for the Pb (II) adsorption kinetics onto *E. denticulatum* 

Pseudo-first-order kinetics			Pseudo-second-order kinetics		
K <sub>1</sub> (min <sup>-1</sup> )	qe (mg g <sup>-1</sup> )	$\mathbb{R}^2$	K <sub>2</sub> (g mg <sup>-1</sup> min <sup>-1</sup> )	q <sub>e</sub> (mg g <sup>-1</sup> )	$\mathbb{R}^2$
20.0237	2.801	0.911	0.0148	4.3802	0.998

#### Conclusion

The present study demonstrated that the seaweed E. denticulatum was an effective biosorbent of  $Pb^{2+}$  from aqueous solutions. The availability of biomass and its

cost-effectiveness are additional benefits that make it a potential biosorbent for treating heavy metals in the marine environment. The impact of processing constraints - including pH, metal ion concentrations, and

absorption period - significantly affected the equilibrium process. The Pb<sup>2+</sup> uptake increased with the increase in metal ion concentration. It was also ascertained that the metal uptake increased with the rise in pH until pH 4; thereafter, the metal uptake began to decline. The Langmuir model might better represent the adsorption isotherms compared to the Freundlich model. According to these findings, the seaweed *E. denticulatum* can be considered a potential biosorbent for removing heavy metal from marine and coastal areas due to its high biosorption capability.

#### Acknowledgements

The authors of this paper are thankful to the Institute of Oceanography and Environment (INOS) and the State University of Zanzibar (SUZA) for their support.

#### References

- Asnani, P. U. and Zurbrugg, C. (2007). Improving municipal solid waste management in India: A sourcebook for policymakers and practitioners. World Bank Publications.
- Tian, H. Z., Lu, L., Cheng, K., Hao, J. M., Zhao, D., Wang, Y., Jia, W. X. and Qiu, P. P. (2012). Anthropogenic atmospheric nickel emissions and its distribution characteristics in China. *Science of the Total Environment*, 417–418: 148-157.
- 3. Yoon, J., Cao, X., Zhou, Q. and Ma, L. Q. (2006). Accumulation of Pb, Cu, and Zn in native plants growing on a contaminated Florida site. *Science of the Total Environment*, 368(2–3): 456-464.
- 4. Dixit, R., Wasiullah, Malaviya, D., Pandiyan, K., Singh, U. B., Sahu, A., Shukla, R., Singh, B. P., Rai, J. P., Sharma, P. K., Lade, H. and Paul, D. (2015). Bioremediation of heavy metals from soil and aquatic environment: An overview of principles and criteria of fundamental processes. *Sustainability* (*Switzerland*), 7(2): 2189-2212.
- 5. Das, N. (2005). Heavy metals biosorption by mushrooms. *Indian Journal of Natural Products and Resources*, 4(6): 454-459.
- 6. Volesky, B. (2007). Biosorption and me. *Water Research*, 41(18): 4017-4029.
- Zeraatkar, A. K., Ahmadzadeh, H., Talebi, A. F., Moheimani, N. R. and McHenry, M. P. (2016). Potential use of algae for heavy metal

- bioremediation, a critical review. *Journal of Environmental Management*, 181: 817–831.
- 8. Mousavi, S. A., Almasi, A., Navazeshkh, F. and Falahi, F. (2019). Biosorption of lead from aqueous solutions by algae biomass: Optimization and modeling. *Desalination and Water Treatment*, 148: 229-237.
- 9. Dwivedi, S., Mishra, A. and Saini, D. (2012). Removal of heavy metals in liquid media through fungi isolated from waste water. *International Journal of Science and Research*, 1: 2319-7064.
- 10. Vijayaraghavan, K. and Yun, Y. S. (2008). Bacterial biosorbents and biosorption. *Biotechnology Advances*, 26(3): 266-291.
- 11. Elangovan, R., Philip, L. and Chandraraj, K. (2008). Biosorption of chromium species by aquatic weeds: Kinetics and mechanism studies. *Journal of Hazardous Materials*, 152(1): 100-112.
- 12. Rahman, H. U., Shakirullah, M., Ahmad, I., Shah, S. and Shah, A. A. (2005). Removal of copper (II) ions from aqueous medium by sawdust of wood. In *Journal of the Chemical Society of Pakistan*, 27(3): 233-238.
- Tabaraki, R., Nateghi, A. and Ahmady-Asbchin, S. (2014). Biosorption of lead (II) ions on Sargassum ilicifolium: Application of response surface methodology. International Biodeterioration and Biodegradation, 93: 145-152.
- 14. Taşar, Ş., Kaya, F. and Özer, A. (2014). Biosorption of lead(II) ions from aqueous solution by peanut shells: Equilibrium, thermodynamic and kinetic studies. *Journal of Environmental Chemical Engineering*, 2(2): 1018-1026.
- 15. Blázquez, G., Calero, M., Hernáinz, F., Tenorio, G. and Martín-Lara, M. A. (2010). Equilibrium biosorption of lead(II) from aqueous solutions by solid waste from olive-oil production. *Chemical Engineering Journal*, 160(2): 615-622.
- Gerola, G. P., Boas, N. V., Caetano, J., Tarley, C. R. T., Gonçalves, A. C. and Dragunski, D. C. (2013). Utilization of passion fruit skin by-product as lead(II) ion biosorbent. Water, Air, and Soil Pollution, 224(2): 1-11.

- 17. Senthilkumar, R., Vijayaraghavan, K., Thilakavathi, M., Iyer, P. V. R. and Velan, M. (2007). Application of seaweeds for the removal of lead from aqueous solution. *Biochemical Engineering Journal*, 33(3): 211-216.
- 18. Abdel -Aty, A. M., Ammar, N. S., Abdel Ghafar, H. H. and Ali, R. K. (2013). Biosorption of cadmium and lead from aqueous solution by freshwater alga *Anabaena sphaerica* biomass. *Journal of Advanced Research*, 4(4): 367-374.
- 19. Putri, L. S.(2016). Biosorption of lead using macroalgae *Eucheuma spinosum*, *Padina minor*, and *Sargassum crassifolium* in an aqueous solution. *Asian Journal of Applied Sciences*, 4: 520-525.
- Abdel Ghafar, H. H., Abdel-Aty, A. M., Ammar, N. S. and Embaby, M. A. (2014). Lead biosorption from aqueous solution by raw and chemically modified green freshwater algae *Scenedesmus obliquus*. *Desalination and Water Treatment*, 52(40–42): 7906-7914. https://doi.org/10.1080/19443994.2013.856345
- Shrestha, R., Ban, S., Devkota, S., Sharma, S., Joshi, R., Tiwari, A. P., Kim, H. Y. and Joshi, M. K. (2021). Technological trends in heavy metals removal from industrial wastewater: A review. *Journal of Environmental Chemical Engineering*, 9(4): 105688.
- Pan, Y., Wernberg, T., de Bettignies, T., Holmer, M., Li, K., Wu, J., Lin, F., Yu, Y., Xu, J., Zhou, C., Huang, Z. and Xiao, X. (2018). Screening of seaweeds in the East China Sea as potential biomonitors of heavy metals. *Environmental Science and Pollution Research*, 25(17): 16640-16651. https://doi.org/10.1007/s11356-018-1612-3.
- 23. Valderrama, D., Cai, J., Hishamunda, N., Ridler, N., Neish, I. C., Hurtado, A. Q., Msuya, F. E., Krishnan, M., Narayanakumar, R., Kronen, M., Robledo, D., Gasca-Leyva, E. and Fraga, J. (2015). The economics of Kappaphycus seaweed cultivation in developing countries: A comparative analysis of farming systems. Aquaculture Economics and Management, 19(2): 251-277.
- 24. Rönnbäck, P., Bryceson, I. and Kautsky, N. (2002). Coastal aquaculture development in eastern Africa and the western Indian Ocean: Prospects and problems for food security and local economies.

- Ambio, 31(7-8): 537-542.
- 25. TWAS. (2004). TWAS newsletter. pp. 1-84.
- 26. Vijayaraghavan, K., Raj Jegan, J., Palanivelu, K. and Velan, M. (2004). Copper removal from aqueous solution by marine green alga *Ulva reticulata*. *Electronic Journal of Biotechnology*, 7(1): 47-54.
- 27. Chove, B. E., Ballegu, W. R. and Chove, L. M. (2006). Copper and lead levels in two popular leafy vegetables grown around Morogoro Municipality, Tanzania. *Tanzania Health Research Bulletin*, 8(1): 37-40.
- Mwegoha, W. J. S. and Kihampa, C. (2010). Heavy metal contamination in agricultural soils and water in Dar es Salaam city, Tanzania. *African Journal of Environmental Science and Technology*, 4(11): 763-769.
- 29. Shemdoe, R. S. (2010). Heavy metal concentrations in soils and leachates of Mtoni dumpsite bordering the Indian Ocean in Dar es salaam, Tanzania. *Scientific Research and Essays*, 5(16): 2143-2147.
- 30. Awasthi, M. K., Guo, D., Awasthi, S. K., Wang, Q., Chen, H., Liu, T., Duan, Y., Soundari, P. G. and Zhang, Z. (2020). Recent advances in phytoremediation of toxic metals from contaminated sites: A road map to a safer environment. *Bioremediation of Industrial Waste for Environmental Safety*, 2: 77-112.
- 31. Diniz, V. and Volesky, B. (2005). Biosorption of La, Eu, and Yb using Sargassum biomass. *Water Research*, 39(1): 239-247.
- 32. Nirmal Kumar, J. I., Oommen, C. and Kumar, R. N. (2009). Biosorption of heavy metals from aqueous solution by green marine macroalgae from Okha Port, Gulf of Kutch, India. *American Eurasian Journal Agriculture and Environmental Sciences*, 6(3): 317-323.
- 33. Luis, G., Rubio, C., Gutiérrez, Á. J., González-Weller, D., Revert, C. and Hardisson, A. (2014). Evaluation of metals in several varieties of sweet potatoes (*Ipomoea batatas* L.): Comparative study. *Environmental Monitoring and Assessment*, 186(1): 433-440.

- 34. Rubio, C., Lucas, J. R. D., Gutiérrez, A. J., Glez-Weller, D., Pérez Marrero, B., Caballero, J. M., Revert, C. and Hardisson, A. (2012). Evaluation of metal concentrations in mentha herbal teas (*Mentha piperita*, *Mentha pulegium* and Mentha species) by inductively coupled plasma spectrometry. *Journal of Pharmaceutical and Biomedical Analysis*, 71: 11-17.
- 35. Vieira, D. M., Da Costa, A. C. A., Henriques, C. A., Cardoso, V. L. and De França, F. P. (2007). Biosorption of lead by the brown seaweed *Sargassum filipendula* Batch and continuous pilot studies. *Electronic Journal of Biotechnology*, 10(3): 368-375. https://doi.org/10.2225/vol10-issue3-fulltext-3
- 36. Dabrowski, A. (2001). Adsorption From theory to practice. *Advances in Colloid and Interface Science*, 93(1–3): 135-224.
- 37. Yang, C. hai. (1998). Statistical mechanical study on the Freundlich isotherm equation. *Journal of Colloid and Interface Science*, 208(2): 379-387.
- 38. Hall, K. R., Eagleton, L. C., Acrivos, A. and Vermeulen, T. (1966). Pore- and solid diffusion kinetics in fixed-bed adsorption under constant pattern conditions. *Industrial and Engineering Chemistry Fundamentals*, 5(2): 212-223. https://doi.org/10.1021/i160018a011
- Febrianto, J., Kosasih, A. N., Sunarso, J., Ju, Y. H., Indraswati, N. and Ismadji, S. (2009). Equilibrium and kinetic studies in adsorption of heavy metals using biosorbent: a summary of recent studies. *Journal Of Hazardous Materials*, 162(2-3): 616-645.
- 40. Ho, Y. S. and Ofomaja, A. E. (2006). Pseudosecond-order model for lead ion sorption from aqueous solutions onto palm kernel fiber. *Journal of Hazardous Materials*, 129(1–3): 137-142.
- 41. Sheikh, M. A., Noah, N. M., Tsuha, K. and Oomori, T. (2007). Occurrence of tributyltin compounds and characteristics of heavy metals. *International Journal of Environmental Science and Technology*, 4(1): 49-59.
- 42. Yoonaiwong, W., Kaewsarn, P. and Reanprayoon, P. (2011). Biosorption of lead and cadmium ions by non-living aquatic macrophyte, *Utricularia aurea*. *Sustainable Environment Research*, 21(6): 369-

- 374.
- 43. Oyedepo, T. A. (2011). Biosorption of lead (II) and copper (II) metal ions on *Calotropis procera* (Ait.). *Science Journal of Purel & Applied Chemistry*, 2011: 1-7.
- 44. Vilar, V. J. P., Botelho, C. M. S. and Boaventura, R. A. R. (2008). Copper removal by algae Gelidium, agar extraction algal waste and granulated algal waste: Kinetics and equilibrium. *Bioresource Technology*, 99(4): 750-762.
- 45. Ali Redha, A. (2020). Removal of heavy metals from aqueous media by biosorption. *Arab Journal of Basic and Applied Sciences*, 27(1): 183-193.
- Murphy, V., Hughes, H. and McLoughlin, P. (2007). Cu(II) binding by dried biomass of red, green, and brown macroalgae. Water Research, 41(4): 731-740.
- 47. Vilar, V. J. P., Botelho, C. M. S. and Boaventura, R. A. R. (2008b). Lead uptake by algae Gelidium and composite material particles in a packed bed column. *Chemical Engineering Journal*, 144(3): 420-430.
- 48. Farooq, U., Kozinski, J. A., Khan, M. A. and Athar, M. (2010). Biosorption of heavy metal ions using wheat-based biosorbents A review of the recent literature. *Bioresource Technology*, 101(14): 5043-5053.
- Escudero, C., Fiol, N., Villaescusa, I. and Bollinger,
   J. C. (2009). Arsenic removal by a waste metal hydroxide entrapped into calcium alginate beads. *Journal of Hazardous Materials*, 164(2–3), 533– 541.
- 50. Yipmantin, A., Maldonado, H. J., Ly, M., Taulemesse, J. M. and Guibal, E. (2011). Pb(II) and Cd(II) biosorption on *Chondracanthus chamissoi* (a red alga). *Journal of Hazardous Materials*, 185(2–3): 922-929.
- 51. Lee, S. H., & Park, C. H. (2012). Biosorption of heavy metal ions by brown seaweeds from the southern coast of Korea. *Biotechnology and Bioprocess Engineering*, 17(4): 853-861.
- Nessim, R. B., Bassiouny, A. R., Zaki, H. R., Moawad, M. N. and Kandeel, K. M. (2011). Biosorption of lead and cadmium using marine algae. *Chemistry and Ecology*, 27(6): 579-594.

- 53. Akpomie, K. G., Ezeofor, C. C., Olikagu, C. S., Odewole, O. A. and Ezeorah, C. J. (2018). Abstraction and regeneration potential of temperature-enhanced rice husk montmorillonite combo for oil spill. *Environmental Science and Pollution Research*, 25(34): 34711-34719.
- Aroua, M. K., Leong, S. P. P., Teo, L. Y., Yin, C. Y. and Daud, W. M. A. W. (2008). Real-time determination of the kinetics of lead(II) adsorption onto palm shell-based activated carbon using an ion-selective electrode. *Bioresource Technology*, 99(13): 5786-5792.
- 55. Wu, Y., Zhang, S., Guo, X. and Huang, H. (2008). Adsorption of chromium(III) on lignin. *Bioresource Technology*, 99(16): 7709-7715.
- Bishnoi, N. R. and Pant, A. (2004). Biosorption of copper from an aqueous solution using algal biomass. *Journal of Scientific and Industrial Research*, 63: 813-816.
- 57. Wang, G., Zhang, S., Yao, P., Chen, Y., Xu, X., Li, T. and Gong, G. (2018). Removal of Pb(II) from aqueous solutions by *Phytolacca americana* L. biomass as a low-cost biosorbent. *Arabian Journal of Chemistry*, 11(1): 99-110.
- 58. Ghasemi, M., Naushad, M., Ghasemi, N. and Khosravi-fard, Y. (2014). Adsorption of Pb(II) from aqueous solution using new adsorbents prepared from agricultural waste: Adsorption isotherm and kinetic studies. *Journal of Industrial and Engineering Chemistry*, 20(4): 2193-2199.
- Ibrahim, W. M. (2011). Biosorption of heavy metal ions from an aqueous solution by red macroalgae. *Journal of Hazardous Materials*, 192(3): 1827-1835.
- Ozudogru, Y. (2017). Biosorption of Cu (II) and Pb (ii) ions by using marine brown algae *Padina pavonica*. Fresenius Environmental Bulletin, 22: 3725-3729.
- 61. Arshadi, M., Amiri, M. J. and Mousavi, S. (2014). Kinetic, equilibrium, and thermodynamic investigations of Ni(II), Cd(II), Cu(II), and Co(II) adsorption on barley straw ash. *Water Resources and Industry*, 6: 1-17.

- 62. Naiya, T. K., Bhattacharya, A. K., Mandal, S. and Das, S. K. (2009). The sorption of lead(II) ions on rice husk ash. *Journal of Hazardous Materials*, 163(2–3): 1254-1264.
- 63. Meitei, M. D. and Prasad, M. N. V. (2014). Adsorption of Cu(II), Mn(II), and Zn(II) by *Spirodela polyrhiza* (L.) Schleiden: Equilibrium, kinetic and thermodynamic studies. *Ecological Engineering*, 71: 308-317.
- 64. Al-Homaidan, A. A., Al-Houri, H. J., Al-Hazzani, A. A., Elgaaly, G. and Moubayed, N. M. S. (2014). Biosorption of copper ions from aqueous solutions by Spirulina platensis biomass. *Arabian Journal of Chemistry*, 7(1): 57-62.
- 65. Onwuka, J. C., Ajibola, V. O., Kagbu, J. A. and Manji, A. J. (2011). Biosorption of Cr(VI) and Co(II) ions from synthetic wastewater using dead biomass of freshwater green algae *Cosmarium panamense*. *Archives of Applied Science Research*, 3(6): 191-207.
- 66. Ashraf, M. A., Mahmood, K., Wajid, A., Maah, M. J. and Yusoff, I. (2011). Study of low-cost biosorbent for biosorption of heavy metals. In *Proceedings of the International Conference on Food Engineering and Biotechnology*, 9: pp. 60-68.
- 67. Ayawei, N., Ekubo, A. T., Wankasi, D. and Dikio, E. D. (2015). Adsorption of congo red by Ni/Al-CO<sub>3</sub>: Equilibrium, thermodynamic and kinetic studies. *Oriental Journal of Chemistry*, 31(3): 1307-1318.
- 68. Lasheen, M. R., Ammar, N. S. and Ibrahim, H. S. (2012). Adsorption/desorption of Cd(II), Cu(II), and Pb(II) using chemically modified orange peel: Equilibrium and kinetic studies. *Solid-State Sciences*, 14(2): 202-210.
- 69. Yalçın, S. (2014). The mechanism of heavy metal biosorption on green marine macroalga *Enteromorpha linza. CLEAN–Soil, Air, Water*, 42(3): 251-259.
- 70. Weber, T. W. and Chakravorti, R. K. (1974). Pore and solid diffusion models for fixed-bed adsorbers. *AIChE Journal*, 20(2): 228-238.

### **Malaysian Journal of Analytical Sciences** (MJAS)



### SYNTHESIS OF ZnO ON 3D GRAPHENE/NICKEL FOAM FOR PHOTOELECTROCHEMICAL WATER SPLITTING

(Sintesis ZnO pada 3D Grafin/Busa Nikel untuk Pembelahan Molekul Air Secara Fotoelektrokimia)

Nur Rabiatul Adawiyah Mohd Shah, Rozan Mohamad Yunus\*, Nurul Nabila Rosman, Wai Yin Wong, Khuzaimah Arifin, Lorna Jeffery Minggu

> Fuel Cell Institute. Universiti Kebangsaan Malaysia, 43600 UKM Bangi, Selangor, Malaysia

> > \*Corresponding author: rozanyunus@ukm.edu.my

Received: 13 December 2021; Accepted: 27 February 2022; Published: 27 June 2022

#### Abstract

Photoelectrochemical (PEC) water splitting is a promising method that involves a direct route to produce green hydrogen (H<sub>2</sub>). An efficient semiconductor photoelectrode that has a suitable band gap between the valence and conduction band is stable in an aqueous solution and cost-effective. Efficient charge transfer and outstanding light absorption are required to achieve enhanced PEC water splitting performance. However, the wide band gap of current photoelectrode such as zinc oxide (ZnO) limits their ability to transport electron, causing photogenerated electron-hole pair recombination and poor PEC performance. This study aims to design an efficient photoelectrode by incorporating a three-dimensional (3D) graphene with ZnO, where 3D graphene serves as a co-catalyst/support to enhance the photocatalytic activity of ZnO. The 3D graphene was first synthesized on nickel foam (Nifoam) via chemical vapor deposition method with the flow of argon, H<sub>2</sub>, and methane gas flow in a quartz tube, followed by the growth of ZnO via a hydrothermal method at 150 °C and 200 °C. FESEM, EDX and Raman confirmed the successful growth of ZnO on 3D graphene/Ni-foam. The flower-like ZnO was observed by FESEM after the hydrothermal method, and the highest photocurrent density was measured at 150 °C (108.2 mA cm<sup>-2</sup>). Therefore, flower-like ZnO flower-like on 3D graphene/Ni-foam can be used as an efficient semiconductor photoelectrode in PEC water splitting.

Keywords: 3D graphene, zinc oxide, photoelectrode, photoelectrochemical water splitting

#### **Abstrak**

Pembelahan molekul air secara fotoelektrokimia (PEC) merupakan kaedah yang menggunakan laluan yang mudah untuk menghasilkan hidrogen (H2). Fotoelektrod semikonduktor yang cekap mempunyai jurang jalur yang sesuai antara jalur valensi dan konduksi, stabil dalam larutan berair dan kos yang rendah. Pemindahan cas yang cekap dan penyerapan cahaya yang baik diperlukan untuk mencapai prestasi pembelahan molekul air PEC yang tinggi. Walau bagaimanapun, jurang jalur fotoelektrod yang lebar seperti zink oksida (ZnO) menghadkan kebolehannya untuk pengangkutan elektron, menyebabkan penggabungan semula lubang-elektron terjana dan prestasi PEC yang rendah. Kajian ini bertujuan untuk merekacipta fotoelektrod yang cekap dengan menggabungkan tiga-dimensi (3D) grafin dengan ZnO, di mana 3D grafin bertindak sebagai pemangkin bersama/sokongan untuk meningkatkan aktiviti fotokatalitik ZnO. 3D grafin disintesis pada busa nikel (busa-Ni) melalui kaedah pemendapan wap kimia dengan aliran gas argon, H2 dan metana dalam tiub kuarza, diikuti dengan pertumbuhan ZnO melalui kaedah hidrotherma pada

150 °C and 200 °C. FESEM, EDX dan Raman mengesahkan pertumbuhan ZnO pada 3D grafin/busa-Ni. Pertumbuhan ZnO seperti bunga dapat dilihat dengan alat FESEM selepas melalui kaedah hidrotherma dan ketumpatan foto arus yang tinggi diukur pada suhu 150 °C (108.2 mA cm<sup>-2</sup>). Oleh itu, ZnO berbentuk seperti bunga pada 3D grafin/busa-Ni boleh digunakan untuk fotoelektrod semikondutor yang cekap dalam pembelahan air secara PEC.

Kata kunci: 3D grafin, zink oksida, fotoelektrod, pembelahan molekul air secara fotoelektrokimia.

#### Introduction

Photoelectrochemical (PEC) water splitting is a potential technology that involves a direct route using sunlight and water to produce green hydrogen (H<sub>2</sub>) for a variety of applications [1, 2]. Water is a primary source of H<sub>2</sub>, and the consumption and cycle of H<sub>2</sub> are in a continuous loop. In addition, as compared to a photovoltaic-electrolysis system, the PEC system is simple and space saving with fewer components [3]. However, current solar-to-hydrogen (STH) efficiencies of the PEC system, 16.2% produced by a multijunction semiconductor, are insufficient compared with existing technologies. Thus, continuous, high-efficiency, and sustainable photocatalytic H<sub>2</sub> evolution from water without the assistance of electron donors with STH values greater than 10% is necessary [4–6].

In general, semiconductor materials with an appropriate band gap are often used as photoelectrode for light absorption in the PEC system. Nevertheless, not all semiconductors fulfill the band gap requirements for overall water splitting, which require the conduction band (CB) to be more negative than the reduction potential of water to produce H<sub>2</sub> and the valence band to

be more positive than the oxidation potential of water to produce oxygen [7, 8]. The wide band gap of current photoelectrode, such as zinc oxide (ZnO), which is approximately 3.37 eV, inhibits the ability to transport electrons, resulting in the recombination of photogenerated electron-hole pairs [9–11]. Hence, three-dimensional (3D) graphene with a high surface area, high conductivity, and fast charge carrier transport as a co-catalyst/support can overcome the limitations of ZnO by extending the light absorption range and improving charge separation and transportation properties [12, 13].

In this work, 3D graphene was synthesized on nickel foam (Ni-foam) using chemical vapor deposition (CVD) method, followed by hydrothermal method to synthesize ZnO on 3D graphene/Ni-foam by using two different reaction temperature (150 °C and 200 °C) for 2 hours (Figure 1). The photocatalytic performance of 3D graphene/Ni-foam hierarchical flower-like ZnO exhibits a large surface area that can increase the charge separation efficiency, resulting in excellent photocatalytic performance.

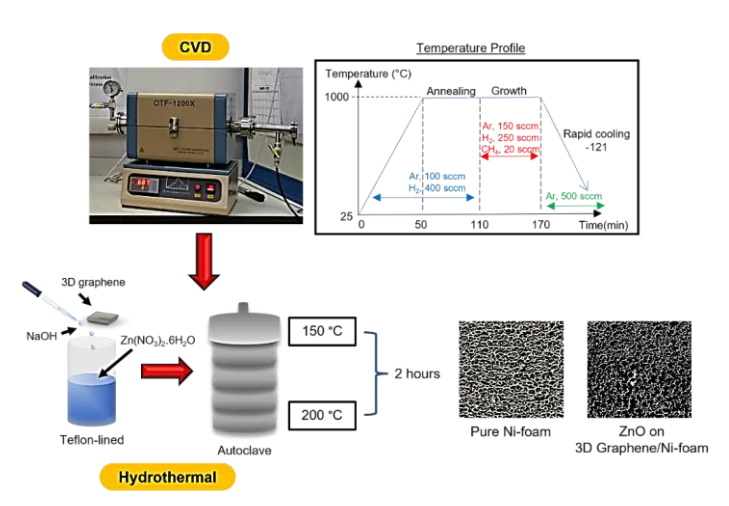


Figure 1. Schematic illustration for preparation of ZnO on 3D graphene/Ni-foam

#### Materials and Methods

#### Preparation of three-dimensional (3D) graphene

The nickel foam (Ni-foam; 1.5 cm x 1.5 cm x 0.16 cm, Brand TOB) was used as a template to grow graphene via chemical vapor deposition (CVD) method. Acetone, ethanol, and deionized water were used during ultrasonic cleaning and dried using nitrogen blow. Then, the Ni-foam was placed in the center of the quartz tube and heated up to 1000 °C for 50 min at 20 °C/min. The temperature was maintained for another 60 min with argon (Ar, 100 sccm) and H<sub>2</sub>/Ar (400 sccm) gas flow. For 60 min of growth time, methane (CH<sub>4</sub>) with 20 sccm gas flow was introduced as the carbon source. The sample is rapidly cooled to room temperature.

### Synthesis of 3D Graphene/ZnO on nickel foam (Nifoam)

Zinc nitrate hexahydrate (Zn(NO<sub>3</sub>)<sub>2</sub>.6H<sub>2</sub>O), sodium hydroxide (NaOH) from Sigma-Aldrich, and deionized water were used throughout the experiment. 0.5 M Zn(NO<sub>3</sub>)<sub>2</sub>.6H<sub>2</sub>O solutions were prepared in 30 mL deionized water under stirring for 30 min. Simultaneously, 5 M NaOH solutions were prepared in 30 mL deionized water under stirring for the same duration. Zn(NO<sub>3</sub>)<sub>2</sub>.6H<sub>2</sub>O solution was transferred to a sealed Teflon-lined stainless-steel autoclave. Next, 3 drops of NaOH solution were added to the former solution to change the pH of the reactants, and the 3D graphene/Ni-foam was immersed into the reaction before being kept in a box furnace at 150 °C and 200 °C for 2 hours. Finally, the autoclave was taken outside, and the as-sample were dried for 2 hours at 80 °C.

#### **Characterization techniques**

Raman analysis was conducted using DXR2xi, Thermo Scientific, to confirm the presence of graphene on Ni foam. The morphology of the samples was examined by field emission scanning electron microscopy (FESEM) and energy dispersive X-ray (EDX) analysis to confirm the existence of graphene and ZnO (Carl Zeiss/GeminiSEM 500).

#### Photocatalytic measurements

UV-Vis Spectroscopy (Perkin Elmer/Lambda 35) was used to evaluate the band gap energy for ZnO on 3D graphene/Ni-foam at 150 °C and 200 °C for 2 hours. A three-electrode system was used to study the photocurrent of the as-samples, where the working electrode is ZnO on 3D graphene/Ni-foam, the counter electrode is Pt wire, and the reference electrode is Ag/AgCl (3.0 M KCl). A 0.5 M sulfuric acid (H<sub>2</sub>SO<sub>4</sub>) aqueous solution was used as the electrolyte, and it was purged with nitrogen before testing. 100 mW cm<sup>-2</sup> Xe lamp was used as the light source, and the area of the ZnO on 3D graphene/Ni-foam exposed to light was 1.5 cm<sup>2</sup>.

#### **Result and Discussion**

Typically, 3D graphene can be synthesized by using CVD method based on the previous study [14]. FESEM was used to study the physical and structural characteristics of the resulting 3D graphene/Ni-foam, ZnO on 3D graphene/Ni-foam, and ZnO nanoparticles, as shown in Figure 2(a). Combining 3D graphene with metal oxide like ZnO can enhance the PEC performance through shifting the band gap energy, lowering electronhole pair recombination, increasing charge separation efficiency, and producing smaller particle size with larger surface area [15]. Figure 2(b - c) shows the FESEM image of pristine graphene taken after the CVD growth. Two different color contrasts were observed on the image where the dark contrast corresponds to graphene, which will be validated through Raman and EDX analysis. The hydrothermal method was then performed to develop ZnO on 3D graphene/Ni-foam at 150 °C and 200 °C. The morphological images of flower-like ZnO on 3D graphene/Ni-foam in Figure 2(d – e) demonstrate a high coverage area of ZnO on 3D graphene/Ni-foam. During the hydrothermal process, ZnO nanoparticles were formed (Figure 2(f - g)), and the presence of graphene influenced the growth of hierarchical flower-like ZnO structures. The mechanism of flower-like ZnO was well explained in previous study [16].

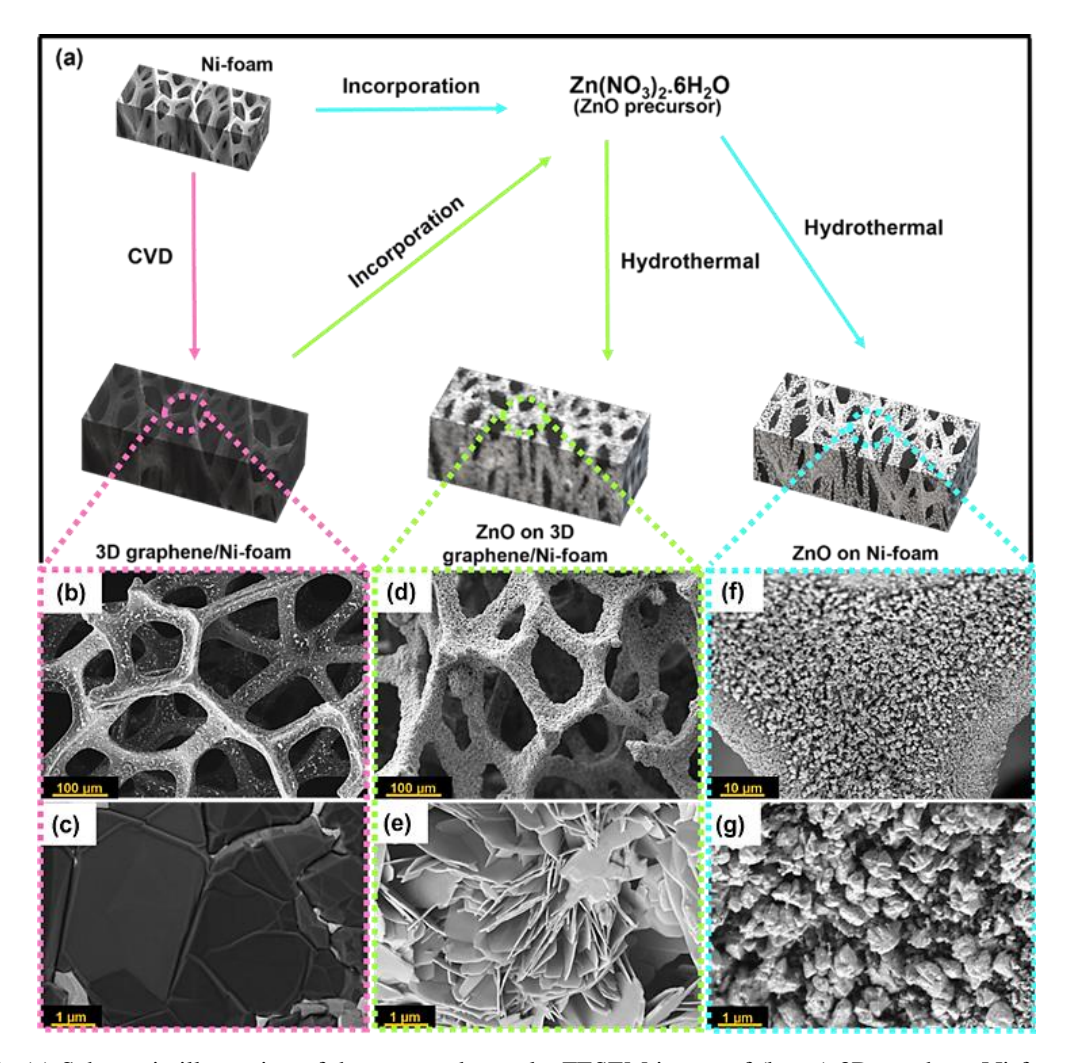


Figure 2. (a) Schematic illustration of the prepared sample. FESEM image of (b-c) 3D graphene/Ni-foam, (d-e) ZnO on 3D graphene/Ni-foam, and (f-g) ZnO on Ni-foam at the low and high magnification, respectively.

Raman spectra for 3D graphene/Ni-foam (Figure 3(a)) were determined. Two graphene fingerprint peaks, including G and 2D bands at ~1581 and ~2700 cm<sup>-1</sup>, respectively, were observed (Figure 3(b)). The graphene is successfully growth with high quality as there is no D band (~1350 cm<sup>-1</sup>) observed, in which the D band corresponds to the disorder and defect in graphene [17]. Thus, a sample at low temperature (150 °C) was selected to confirm the successful growth of ZnO using EDX mapping due to the good coverage and flower-like structure of ZnO. As shown in Figure 3(c - d), the

existence of carbon (C), zinc (Zn), oxygen (O) and nickel (Ni) indicates the successful growth of ZnO using the hydrothermal method.

Photocatalysts with a narrow band gap can harvest visible light and generate excellent efficiency in photocatalytic applications. The reflectance spectra and Kubelka-Munk plot were used to determine the band gap energy for pure Ni-foam, 3D graphene/Ni-foam and ZnO on 3D graphene/Ni-foam at 150 °C and 200 °C at 2 hours, respectively. Figure 4(a) shows a significance

decrease around 380 nm. This decrease is related to the electron transitions occurring the optical band gap. The Kubelka-Munk function was used to convert the UV-Vis reflectance spectrum to measure the precise value of the band gap. As a result, the band gap energy of pure Nifoam and 3D graphene/Ni-foam are E<sub>g</sub>= 3.217 eV and ZnO on 3D graphene/Ni-foam at 150 °C and 200 °C for 2 hours are  $E_g$ = 3.218 eV, respectively (Figure 4(b)). There are no significance changes of band gap energy with the introduction of ZnO. However, the presence of ZnO enhances the photocatalytic performance, where the highest photocurrent density is achieved with ZnO on 3D graphene/Ni-foam at 150 °C, approximately 108.2 mA cm<sup>-2</sup> (Figure 4(c)). Considering that the coverage of ZnO for 150 °C is larger than that for 200 °C, the structure of ZnO starts to agglomerate with the increase of temperature to 200 °C, thereby decreasing the surface area and resulting in a low

photocurrent density [18]. In addition, the electron transfer rate of reaction for all samples is evaluated. Electrochemical impedance spectroscopic analysis (Figure 4(d)) demonstrates that ZnO on 3D graphene/Ni-foam at 150 °C has the smallest arc radius of a semicircle, implying that the sample experienced faster interfacial electron charge transfer. This finding could be explained by the porous structure of 3D graphene, which has a large surface area, excellent mechanical and electrical properties, good electron transport, and electron-hole separation, making them suitable for PEC applications [7,8,14]. As shown in Table 1, ZnO on 3D graphene/Ni foam shows higher photocurrent density as compared with conventional methods and materials for PEC water splitting.

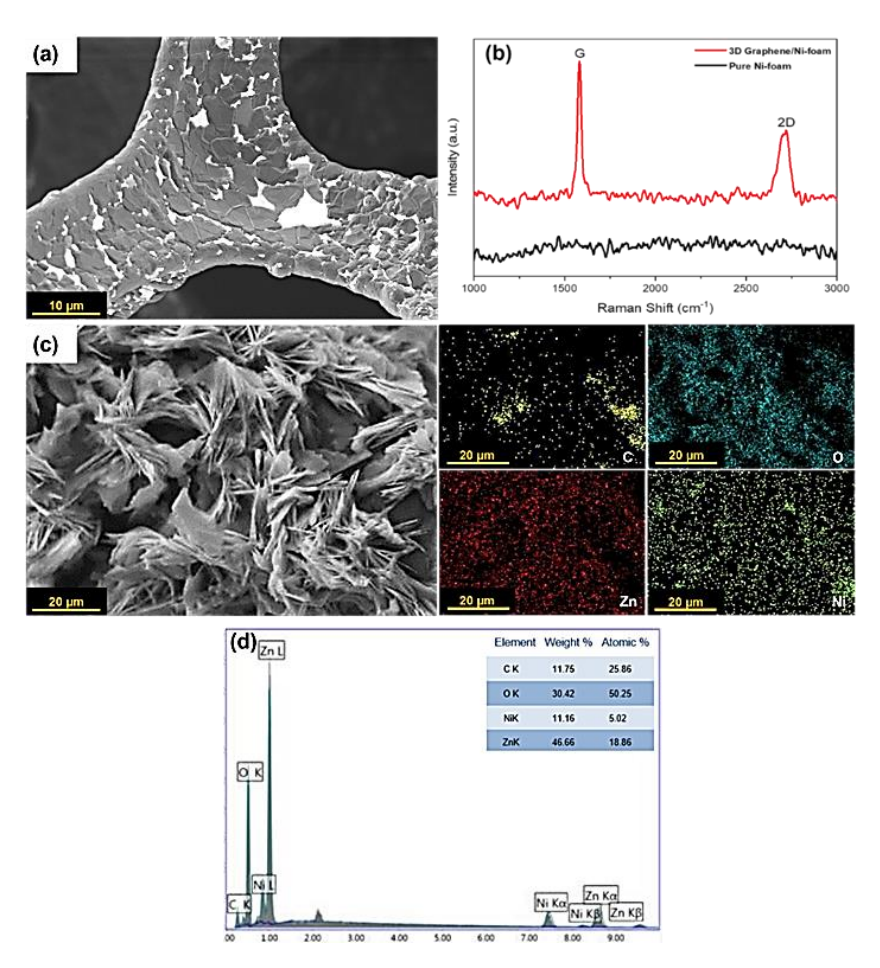


Figure 3. (a) FESEM image and (b) Raman spectra of 3D graphene/Ni-foam. EDX (c) mapping and (d) analysis of

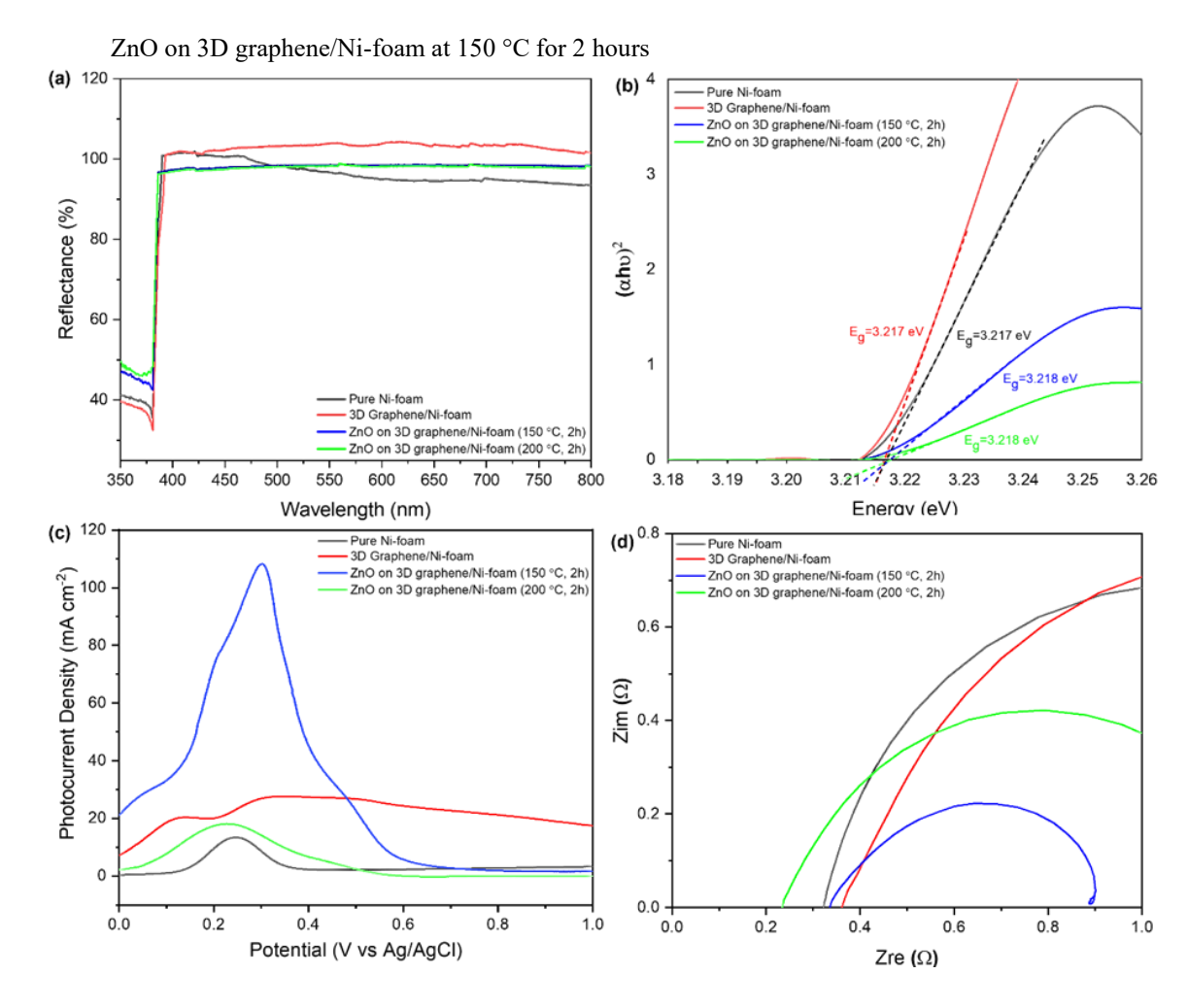


Figure 4. (a) Diffuse reflectance spectra, (b) Kubelka-Munk plot, (c) Photocurrent density at 0.0-1.0 V vs Ag/AgCl and (d) EIS analysis using Nyquist plot for pure Ni-foam, 3D graphene/Ni-foam, ZnO on 3D graphene/Ni-foam at 150 °C and 200 °C for 2 hours

Table 1. PEC performance of modified ZnO using various methods

Materials	Methods	Structures of ZnO	Photocurrent Densities (mA cm <sup>-2</sup> )	Reference
ZnO on 3D graphene/Ni-foam	CVD and hydrothermal	Flower-like	108.2 at 0 – 1.0 V vs Ag/AgCl	This work
ZnO-C@Ni-foam	Hydrothermal	Mixed of nanorods and flower-like	$100 \text{ at } 0 - 0.9 \text{ V vs} \\ Ag/AgCl$	[19]
ZnO@Ni-foam	Hydrothermal	Mixed of nanorods and flower-like	30  at  0 - 0.9  V vs $Ag/AgCl$	[19]
ZnO/rGO foam	One-step hydrothermal	Nanorods	0.27 at 1.0 V vs Ag/AgCl	[20]

Figure 5 illustrates a possible mechanism for efficient electron transport in ZnO on 3D graphene/Ni-foam based on the results of the PEC test. When sunlight illuminates ZnO on 3D graphene/Ni-foam, electrons in the VB of ZnO are excited to jump to the CB using 3D graphene/Ni-foam as a co-catalyst/support. Hydrogen

was produced on the surface of ZnO and 3D graphene/Ni-foam. The incorporation of 3D graphene/Ni-foam provides a good electron transport channel in the ZnO on 3D graphene/Ni-foam structure.

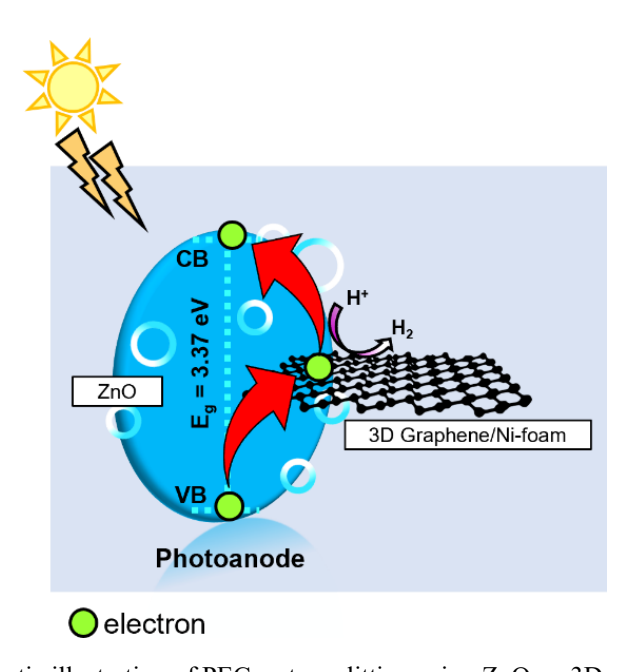


Figure 5. Schematic illustration of PEC water splitting using ZnO on 3D graphene/Ni-foam.

#### Conclusion

ZnO on 3D graphene/Ni-foam was successfully synthesized by a two-step approach, CVD and hydrothermal methods. The highest photocurrent density was achieved at 150 °C for 2 hours (108.2 mA cm<sup>-2</sup>). Therefore, a photoelectrode with a high surface area, which provides more active sites, can enhance the photocatalytic performance by increasing charge separation efficiency. Thus, ZnO on 3D graphene/Ni-foam could be a potential photoelectrode for PEC water splitting.

#### Acknowledgement

This work is funded by Ministry of Higher Education (MOHE) and Universiti Kebangsaan Malaysia (UKM) through FRGS/1/2019/STG07/UKM/02/2 and DIP-2019-020, respectively. The authors would also like to express their gratitude to all UKM staff and technicians

who contributed to this study, especially from the Fuel Cell Institute and Faculty of Science and Technology.

#### References

- Li, Y. and Tsang, S. C. E. (2020). Recent progress and strategies for enhancing photocatalytic water splitting. *Mater. Today Sustain.*, 9: 100032.
- Li, X., Zhao, L., Yu, J., Liu, X., Zhang, X., Liu, H. and Zhou, W. (2020). Water splitting: From electrode to green energy system. *Nano-Micro Letters*, Springer Singapore 12.
- Dias, P. and Mendes, A. (2018). Hydrogen production from photoelectrochemical water splitting. In encyclopedia of sustainability science and technology (Meyers, R. A., ed.). Springer New York, New York: pp 1-52.

- 4. Cao, S., Piao, L. and Chen, X. (2020). Emerging photocatalysts for hydrogen evolution. *Trends Chemistry*, Elsevier Inc. 2: pp. 57-70.
- Hisatomi, T. and Domen, K. (2019). Reaction systems for solar hydrogen production via water splitting with particulate semiconductor photocatalysts. *Nature Catalyst*, 2: 387-399.
- Young, J. L., Steiner, M. A., Döscher, H., France, R. M., Turner, J. A. and Deutsch, T. G. (2017). Direct solar-to-hydrogen conversion via inverted metamorphic multi-junction semiconductor architectures. *Nature Energy*, 2: 1-8.
- Kuang, P., Sayed, M., Fan, J., Cheng, B. and Yu, J. (2020). 3D graphene-based H<sub>2</sub>-production photocatalyst and electrocatalyst. *Advance Energy Materials*, 10: 1-53.
- Mohd Shah, N. R. A., Mohamad Yunus, R., Rosman, N. N., Wong, W. Y., Arifin, K. and Jeffery Minggu, L. (2021). Current progress on 3D graphene-based photocatalysts: From synthesis to photocatalytic hydrogen production. *International Journal Hydrogen Energy*, 46: 9324-9340.
- 9. Gowtham, M., Chandrasekar, S., Mohanraj, C. and Senthil Kumar, N. (2020). Morphology dependent photocatalytic activity of ZnO nanostructures-A short review. *NanoNEXT*, 1: 30-38.
- 10. Baruah, S. and Dutta, J. (2009). Hydrothermal growth of ZnO nanostructures. *Science Technology Advance Materials*, 10: 013001.
- 11. Vaseem, M., Umar, A. and Hahn, Y. (2010). ZnO nanoparticles: Growth, properties, and applications. *Metal Oxide Nanostructures Their Applications*, 5: 1-36
- Singh, P., Shandilya, P., Raizada, P., Sudhaik, A., Rahmani-Sani, A. and Hosseini-Bandegharaei, A. (2020). Review on various strategies for enhancing photocatalytic activity of graphene based nanocomposites for water purification. *Arabian Journal Chemistry*, 13: 3498-3520.
- 13. Gao, C., Zhong, K., Fang, X., Fang, D., Zhao, H., Wang, D., Li, B., Zhai, Y., Chu, X. and Li, J. (2021). Brief review of photocatalysis and photoresponse properties of ZnO–graphene nanocomposites. *Energies*, 14: 6403.

- Mohd Shah, N. R. A., Rosman, N. N., Wong, W. Y., Arifin, K., Jeffery Minggu, L. and Mohamad Yunus, R. (2021). Effect of annealing time on chemical vapor deposition growth of 3D graphene for photoelectrochemical water splitting. *Material Today Proceeding*, 57(3): 1215-1219.
- Ong, C. B., Ng, L. Y. and Mohammad, A. W. (2018). A review of ZnO nanoparticles as solar photocatalysts: Synthesis, mechanisms and applications. *Renewable Sustainable Energy Review*, 81: 536–551.
- Mohamed, M. A., M. Zain, M. F., Jeffery Minggu, L., Kassim, M. B., Jaafar, J., Saidina Amin, N. A., Mastuli, M. S., Wu, H., Wong, R. J. and Ng, Y. H. (2019). Bio-inspired hierarchical heteroarchitectures of in-situ C-doped g-C3N4 grafted on C, N co-doped ZnO micro-flowers with booming solar photocatalytic activity. *Journal Industry Engineering Chemistry*, 77: 393-407.
- 17. Wang, W. X., Zhang, S. C., Xing, Y. L., Wang, S. B. and Ren, Y. B. (2016). The closed-environment CVD method for preparing three-dimensional defect controllable graphene foam with a conductive interconnected network for lithium-ion battery applications. *RSC Advance*, 6: 75414-75419.
- 18. Ghorbani, M., Abdizadeh, H., Taheri, M. and Golobostanfard, M. R. (2018). Enhanced photoelectrochemical water splitting in hierarchical porous ZnO/Reduced graphene oxide nanocomposite synthesized by sol-gel method. *Int. J. Hydrogen Energy*, 43, 7754–7763.
- Gadisa, B. T., Baye, A. F., Appiah-Ntiamoah, R. and Kim, H. (2021). ZnO@Ni foam photoelectrode modified with heteroatom doped graphitic carbon for enhanced photoelectrochemical water splitting under solar light. *International Journal Hydrogen Energy*, 46: 2075-2085.
- Men, X., Chen, H., Chang, K., Fang, X., Wu, C., Qin, W. and Yin, S. (2016). Three-dimensional freestanding ZnO/graphene composite foam for photocurrent generation and photocatalytic activity. *Applied Catalyst B Environment*, 187: 367-374.

## **Malaysian Journal of Analytical Sciences** (MJAS) Published by Malaysian Analytical Sciences Society



### THE EFFECT OF MEMBRANE THICKNESS ON THE PERFORMANCE OF PASSIVE DIRECT ETHANOL FUEL CELLS USING A POLY VINYL ALCOHOL/GRAPHENE OXIDE COMPOSITE MEMBRANE

(Kesan Ketebalan Membran Terhadap Prestasi Sel Fuel Etanol Langsung Pasif Menggunakan Membran Komposit Alkohol Polivinil/Grafin Oksida)

Zulfirdaus Zakaria\*

Fuel Cell Institute, Universiti Kebangsaan Malaysia, 43600 UKM Bangi, Selangor, Malaysia

\*Corresponding author: zulfirdaus@ukm.edu.my

Received: 27 November 2021; Accepted: 3 February 2022; Published: 27 June 2022

#### Abstract

Ethanol is a renewable fuel because it can be produced from a variety of production sources that are non-toxic and environmentally friendly. Thus, the consumption of passive direct ethanol fuel cells (DEFCs) as a power supply for portable devices is intriguing and potentially marketable in the future. Unfortunately, one constraint in the application of passive DEFCs is the lack of a Nafion membrane replacement. The Nafion membrane is expensive and has high ethanol permeability. We previously synthesised a crosslinked poly vinyl alcohol/graphene oxide (PVA/GO) composite membrane for passive DEFCs using low-cost polymer materials and successfully achieved low ethanol permeability. Furthermore, the characterization and performance of a crosslinked PVA/GO composite membrane outperformed that of the Nafion membrane. In the passive DEFCs, the optimal membrane thickness is a critical parameter that influences the membrane and single-cell performance. This experimental study attempted to examine the effect of a crosslinked PVA/GO composite membrane thickness on proton conductivity, ethanol permeability, membrane selectivity, and single-cell performance. The passive DEFCs achieved a maximum performance of 7.54 mW cm<sup>-2</sup> at 60 °C by using a crosslinked PVA/GO composite membrane with a membrane thickness of 0.24 mm.

Keywords: polymer electrolyte membrane, membrane thickness, passive direct ethanol fuel cells, poly (vinyl)/graphene oxide

#### Abstrak

Etanol merupakan bahan api yang boleh diperbaharui kerana ia boleh dihasilkan daripada pelbagai sumber pengeluaran, tidak toksik, dan mesra alam. Oleh itu, penggunaan sel fuel etanol langsung pasif (DEFCs) sebagai bekalan kuasa untuk peranti mudah alih adalah menarik dan berpotensi untuk dipasarkan pada masa hadapan. Walau bagaimanapun, satu kekangan terhadap penggunaan DEFCs pasif adalah ketiadaan penggantian membran Nafion. Membran Nafion adalah mahal dan mempunyai kebolehtelapan etanol yang tinggi. Sebelum ini, kami telah mensintesis membran komposit alkohol polivinil/grafin oksida (PVA/GO) terpaut silang untuk DEFC pasif menggunakan bahan polimer berkos rendah dan berjaya mencapai kebolehtelapan etanol yang rendah. Tambahan lagi, pencirian dan prestasi membran komposit PVA/GO silang mengatasi prestasi membran Nafion. Dalam DEFCs pasif, ketebalan membran optimum ialah parameter kritikal yang mempengaruhi prestasi membran dan sel tunggal. Kajian eksperimen ini cuba untuk mengkaji kesan ketebalan membran komposit PVA/GO terpaut silang terhadap kekonduksian

Zulfirdaus: THE EFFECT OF MEMBRANE THICKNESS ON THE PERFORMANCE OF PASSIVE DIRECT ETHANOL FUEL CELLS USING A POLY VINYL ALCOHOL/GRAPHENE OXIDE COMPOSITE MEMBRANE

proton, kebolehtelapan etanol, selektiviti membran, dan prestasi sel tunggal. DEFC pasif telah memperoleh prestasi maksimum 7.54 mW cm<sup>-2</sup> pada 60 °C melalui penggunaan membran komposit PVA/GO bersilang dengan ketebalan membran 0.24 mm.

Kata kunci: membran elektrolit polimer, ketebalan membrane, sel bahan api etanol langsung pasif, alkohol polivinil/grafin oksida

#### Introduction

High reliance on fossil fuel consumption tends to increase greenhouse gas emissions, resulting in impending climate change. Furthermore, as fossil fuel sources deplete, researchers and industry are attempting to boost the use of renewable fuels such as fuel cells. Fuel cells of many forms have been investigated, including proton exchange membrane fuel cells (PEMFCs), direct alcohol fuel cells (DAFCs), and solid oxide fuel cells (SOFCs). According to the fuel cell design, each type of fuel cell has a specific application based on the physical fuel condition and type of electrolyte used [1]. For example, direct ethanol fuel cells (DEFCs) are commonly utilised for portable device applications such as electrical and electronic devices due to the fact that these fuel cell systems can be manufactured on a small micrometre scale. Although methanol is more commonly used in the systems of DAFCs for portable device applications, there are numerous advantages to using ethanol in fuel cell systems over methanol. Ethanol is a low-cost, less-toxic, naturally existing, green, and renewable fuel that can be easily manufactured through the fermentation process [2]. Besides, the energy density of ethanol (i.e., 8.00 kW h kg<sup>-1</sup>) is higher than that of methanol (i.e., 6.09 kW h kg<sup>-1</sup>). Furthermore, ethanol is safe for human

consumption (i.e., used in medicine). Thus, ethanol is easier to handle for the processes of storage, transfer, and management [3].

Passive DEFCs are appropriate for small portable device applications due to the unavailability of an external component required. For example, this fuel cell system does not require an external fuel pump or air blower to supply the fuel and oxidant needed for energy generation [4]. Passive DEFCs can be operated in the single-cell mode with a polymer electrolyte membrane (PEM) located in the centre cell and a pair of electrodes, as presented in Figure 1. PEM is a critical component that influences the overall performance of passive DEFCs. To achieve excellent long-term operating conditions for fuel cells, PEM should exhibit high chemical and mechanical stability, high proton conductivity, and low ethanol permeability to obtain high membrane selectivity [5]. Unfortunately, the conventional membrane that is widely used in fuel cell systems, which is a perfluorinated sulfonic acid electrolyte membrane (Nafion membrane, manufactured by DuPont), has significant ethanol permeability and leads to rapid ethanol crossover. As a result, the performance of the cell is degraded and damaged on the cathode side [6].

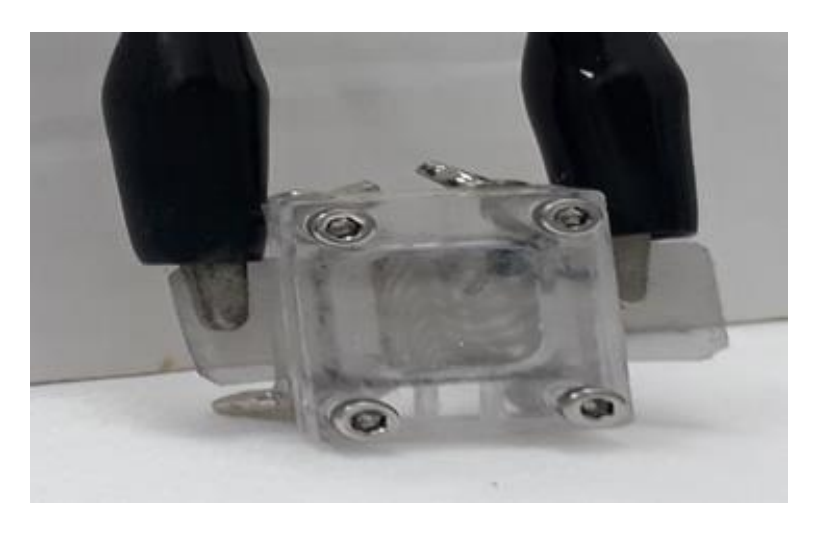


Figure 1. DIY single-cell passive DEFCs

The thickness of the membrane has a considerable effect on the membrane properties and performance of the fuel cell. Numerous studies have examined the influence of membrane thickness on fuel cell performance [7, 8]. For example, Sudaroli et al. [9] tested two distinct types of Nafion membranes with varying membrane thicknesses for fuel cell applications, Nafion 117 and Nafion 1110. According to Sudaroli et al. [9], that thicker membranes substantially decrease fuel crossover and improve single-cell efficiency. While raising the membrane thickness is efficient at decreasing fuel crossover, it has a detrimental effect on the polymeric membrane's conductivity qualities. Thus, the optimal membrane thickness is necessary to achieve the appropriate conductivity-fuel crossover balance [10].

Previously, the performance of a crosslinked poly vinyl alcohol/graphene oxide (PVA/GO) composite membrane in the use of passive DEFCs has been described. Compared to the Nafion membrane, the crosslinked PVA/GO composite membrane has a 15 wt.% loading of GO and demonstrated low ethanol permeability and good membrane selectivity [11]. In this study, the effect of the membrane thickness of a crosslinked PVA/GO composite membrane was studied to enhance the cell performance of passive DEFCs. In order to achieve the optimal membrane thickness for the crosslinked PVA/GO composite membrane, several evaluations were performed, including membrane composite self-performance and performance on singlecell passive DEFCs.

#### **Materials and Methods**

All chemicals and procedures for fabricating the membranes used in this study were previously described in our prior study utilising the simple casting solution method [11]. The GO loading was maintained at 15% by weight throughout this research. Additionally, the membrane thickness was modified according to the volume of the solution created, resulting in four distinct membrane thicknesses (i.e., 0.16 mm, 0.20 mm, 0.24 mm, and 0.28 mm). The membrane self-performance was evaluated for proton conductivity, ethanol permeability, and membrane selectivity with various membrane thicknesses. Next, the performance of singlecell passive DEFCs was measured with different membrane thicknesses of crosslinked QPVA/GO composite membranes. The cell condition was constant with 4 mg cm<sup>-2</sup> of Pt/Ru catalyst (i.e., anode), 2 mg cm<sup>-2</sup> <sup>2</sup> of Pt catalyst (i.e., cathode), and 2 cm<sup>2</sup> of active cell area at 30 °C. The technical and calculation information followed the details of the experiment from our previous work [11].

#### **Results and Discussion**

The self-performance of a crosslinked QPVA/GO composite membrane, comprising proton conductivity, ethanol permeability, and membrane selectivity, is shown in Table 1. According to the self-performance results, lowering the membrane thickness substantially boosted proton conductivity. This indicated that decreasing the membrane thickness reduced the ohmic resistance slightly and shortened the proton pathway. As a result, proton transfer within the PEM was rapid. The mechanism of proton conductivity inside the crosslinked PVA/GO composite membranes is depicted in Figure 2. The proton is mostly diffused via the vehicle and hopping mechanisms. Thus, the thin membrane thickness is generated during the proton transfer process, which is accelerated due to the resistance effect, resulting in lower resistance and a shorter diffusion pathway [12].

Table 1. Self-performance of a crosslinked PVA/GO composite membrane with varying membrane thicknesses

Membrane thickness (mm)	σ, × 10 <sup>-3</sup> S cm <sup>-1</sup>	$ ho, \times 10^{-7}$ cm <sup>2</sup> s <sup>-1</sup>	Membrane selectivity, × 10 <sup>4</sup> S s cm <sup>-3</sup>
0.16	11.3	2.34	4.829
0.20	9.5	1.78	5.337
0.24	8.4	1.51	5.562
0.28	7.6	1.46	5.241

Zulfirdaus: THE EFFECT OF MEMBRANE THICKNESS ON THE PERFORMANCE OF PASSIVE DIRECT ETHANOL FUEL CELLS USING A POLY VINYL ALCOHOL/GRAPHENE OXIDE COMPOSITE MEMBRANE

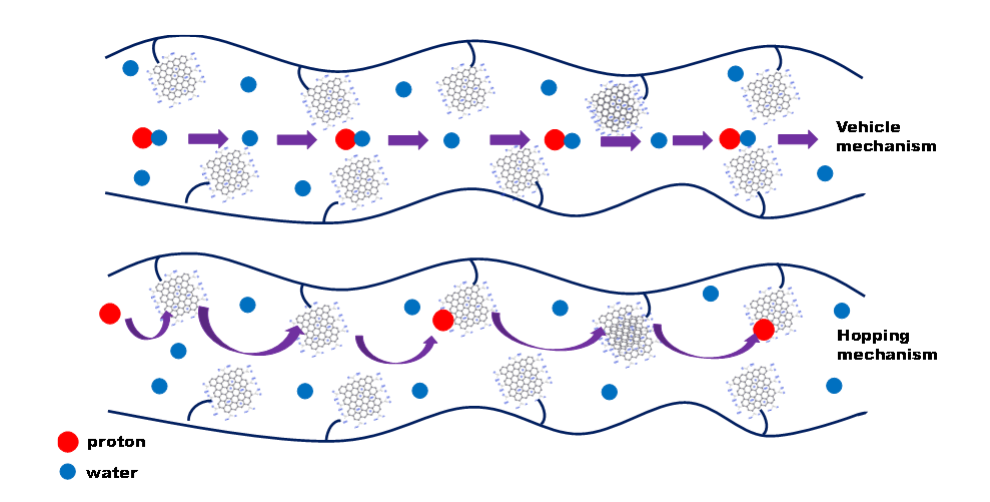


Figure 2. The mechanism of proton conductivity within the crosslinked PVA/GO composite membranes

Unfortunately, the thin membrane thickness allowed for high ethanol permeability to occur quickly due to the reduction of obstacle regions within the matrix polymer. Based on Table 1, the increasing membrane thickness is beneficial for the ethanol barrier because the fuel movement becomes more difficult to penetrate the threedimensional matrix polymer structure between PVA, GO, and crosslinking interaction [13]. However, the proton conductivity is sacrificed due to the large membrane thickness. As a result, determining the optimal membrane thickness is critical for balancing both the membrane's self-performance and the membrane's performance. Thus, membrane selectivity is a precise metric that demonstrates the optimal membrane thickness, which balances conductivity and ethanol permeability [14]. According to Table 1, the maximum membrane selectivity is 5.562 × 10<sup>4</sup> S s cm<sup>-3</sup> for a crosslinked OPVA/GO composite membrane with a membrane thickness of 0.24 mm. This indicated that the optimum membrane thickness is 0.24 mm and that the higher power density should be shown during the single-cell performance.

Overall, all membrane thicknesses have good results in terms of proton conductivity in the range of  $\sim 10^{-3}$  S cm<sup>-1</sup> and ethanol permeability in the range of  $\sim 10^{-7}$  cm<sup>2</sup> s<sup>-1</sup>. As illustrated in Figure 3, the characterization of a crosslinked PVA/GO composite membrane demonstrated suitable morphologies and structures for

usage as a PEM in applying passive DEFCs. Figure 1 presents our previous characterization results, which include the analyses of FTIR, XRD, and FESEM [11]. As illustrated in Figure 3(a), the modification of PVA with GO and a crosslinked agent resulted in the presence of numerous oxygenic functional groups necessary for the hopping mechanism and the retention of water in the vehicle mechanism for proton transfer within the PEM. The crystalline and amorphous structures of a crosslinked PVA/GO composite membrane are then balanced to enhance the self-performance of the membrane, particularly in terms of proton conductivity and ethanol permeability, as shown in Figure 3(b). Besides, the dense morphology of a crosslinked PVA/GO composite membrane that was successfully synthesised as presented in Figures 3(c) and 3(d) has contributed to the critical function of managing the issue of ethanol crossover [15, 16].

All the different membrane thicknesses of a crosslinked PVA/GO composite membrane were evaluated in single-cell passive DEFCs with 2 M ethanol. Figure 4 shows the cell voltage and power density performance for all samples. The result has proven that the highest membrane selectivity with 0.24 mm membrane thickness obtained the highest power density with 5.71 mW cm<sup>-2</sup>. Besides, the open cell voltage of 0.24 mm membrane thickness produced a maximum voltage of 0.85 V. This indicates that the minimum ethanol crossover was obtained with the optimal membrane

thickness [17]. Furthermore, the high proton conductivity of a crosslinked PVA/GO composite membrane enhanced the electrochemical properties that rapidly transferred the proton within the matrix polymer. As a result, the redox reaction occurred smoothly and

produced high cell voltage and power density [18]. Hence, the optimal membrane thickness of a crosslinked PVA/GO composite membrane for this study was 0.24 mm.

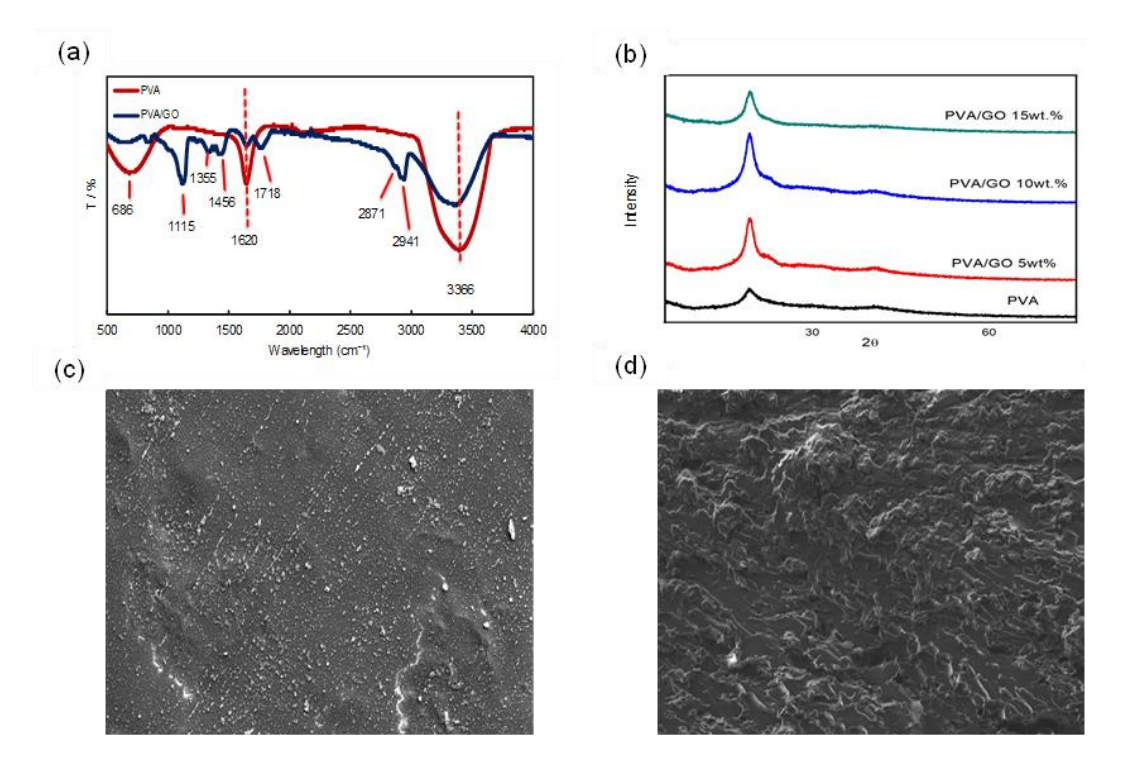


Figure 3. (a) FTIR analysis of a crosslinked PVA/GO composite membrane; (b) XRD analysis of membranes; FESEM analysis of membrane; (c) surface; (d) cross-section [11]

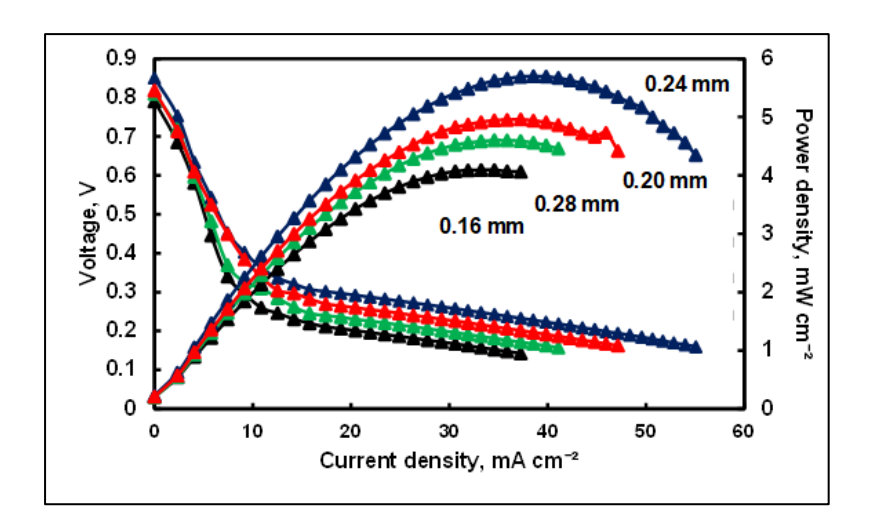


Figure 4. Cell voltage and power density of a crosslinked PVA/GO composite membrane in the passive DEFCs by varying the membrane thickness.

Finally, the optimal membrane thickness was determined using various ethanol concentrations in order to improve the cell performance of single-cell passive DEFCs using a crosslinked PVA/GO composite membrane. Three ethanol concentration values were used with the constant parameters of catalyst loading and cell operating temperature. Figure 3 presents the effect of varying ethanol concentrations, ranging from 2 M ethanol to 6 M ethanol. Obviously, the maximum power density of passive DEFCs utilising a crosslinked PVA/GO composite membrane increased from 5.71 mW cm<sup>-2</sup> to 7.04 mW cm<sup>-2</sup> when the ethanol concentration was changed from 2 M to 4 M. This indicates that a fuel concentration of 4 M of ethanol is a good fuel concentration to consume that can significantly improve the electrochemical activity for this investigation and boost the attainment of current density. In fact, the increment in ethanol concentration will result in a high density of ethanol molecules that can be converted to energy during the oxidation reaction at the anode [19, 20]. Unfortunately, the increment level of ethanol concentration has a limited level. Thus, this study provided a significant discovery for fuel limitation concentration. As shown in Figure 5, when 6 M ethanol was applied in passive DEFCs, the power density of a crosslinked PVA/GO composite membrane significantly decreased, going from 7.04 mW cm<sup>-2</sup> to 4.45 mW cm<sup>-2</sup>. This indicates that the high ethanol concentration caused the ethanol crossover to occur quickly due to the high density of ethanol molecules present at the anode. As a result, the ethanol osmotic state within the cell and ethanol transfer significantly occurred due to the different ethanol concentration conditions between the anode side and cathode side. Thus, ethanol transfers to the cathode side from the anode side through a crosslinked PVA/GO composite membrane without being affected by the oxidation process. Furthermore, this circumstance may result in both a potential problem on the cathode side and a reduction in cell performance [21, 22]. As a result, the ideal ethanol concentration was set at 4 M for this study in order to boost the performance of a crosslinked PVA/GO composite membrane in passive DEFCs.

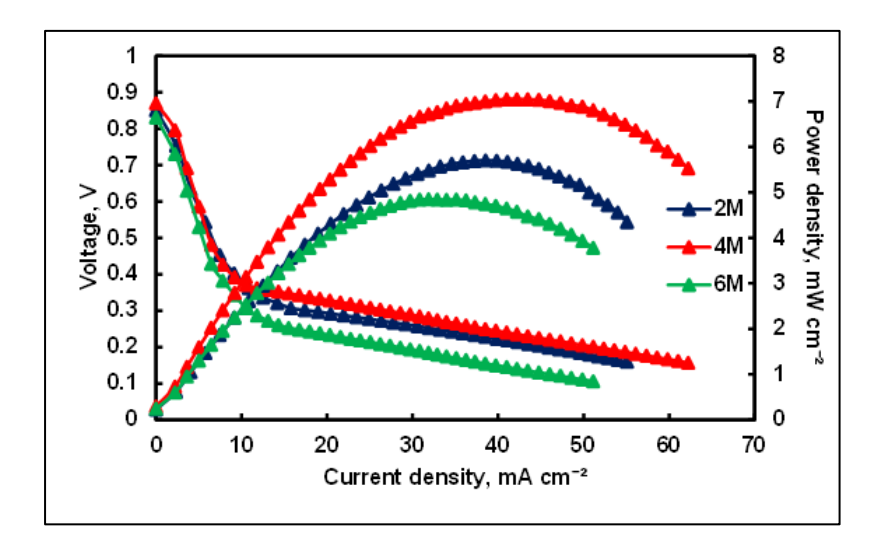


Figure 5. Cell voltage and power density of a crosslinked PVA/GO composite membrane in the passive DEFCs with optimum membrane thickness by varying the ethanol concentration

#### Conclusion

A simple casting solution method managed to synthesise a crosslinked PVA/GO composite membrane with good morphology and characterization. Furthermore, the thermal, mechanical, and chemical stability of this membrane has been demonstrated in our previous study, as has the excellent performance of single-cell passive

DEFCs. In this study, the membrane thickness of a crosslinked PVA/GO composite membrane was manipulated to improve the cell performance of this membrane in passive DEFCs. The 0.24 mm membrane thickness demonstrated good membrane selectivity with 5.562 104 S s cm<sup>-3</sup>. Thus, 0.24 mm was obtained as an optimal membrane thickness that effectively balanced

the crucial parameters of a PEM (i.e., proton conductivity and ethanol permeability). At 30 °C, the power density of single-cell passive DEFCs using a crosslinked PVA/GO composite membrane was 7.04 mW cm<sup>-2</sup> at an optimal ethanol concentration of 4 M. In conclusion, the membrane thickness of a PEM significantly influences the performance of passive DEFCs.

#### Acknowledgement

The authors gladly acknowledge their gratitude to the University of Kebangsaan Malaysia for providing this research with financial support under the Dana Modal Insan grant.

#### References

- Zakaria, Z., Kamarudin, S. K., Abd Wahid, K. A. and Hassan, S. H. A. (2021). The progress of fuel cell for Malaysian residential consumption: Energy status and prospects to introduction as a renewable power generation system. *Renewable and Sustainable Energy Reviews*, 144: 110984.
- 2. Akhairi, M. A. F. and Kamarudin, S. K. (2016). Catalysts in direct ethanol fuel cell (DEFC): An overview. *International Journal of Hydrogen Energy*, 41(7): 4214-4228.
- 3. Zakaria, Z., Kamarudin, S. K. and Timmiati, S. N. (2016). Membranes for direct ethanol fuel cells: an overview. *Applied Energy*, 163: 334-342.
- Abdullah, S., Kamarudin, S. K., Hasran, U. A., Masdar, M. S. and Daud, W. R. W. (2015). Development of a conceptual design model of a direct ethanol fuel cell (DEFC). *International Journal of Hydrogen Energy*, 40(35): 11943-11948.
- Ying, Y. P., Kamarudin, S. K. and Masdar, M. S. (2018). Silica-related membranes in fuel cell applications: An overview. *International Journal of Hydrogen Energy*, 43(33): 16068-16084.
- Kamarudin, M. Z. F., Kamarudin, S. K., Masdar, M. S. and Daud, W. R. W. (2013). Direct ethanol fuel cells. *International Journal of Hydrogen Energy*, 38(22): 9438-9453.
- 7. Liu, J. G., Zhao, T. S., Liang, Z. X. and Chen, R. (2006). Effect of membrane thickness on the performance and efficiency of passive direct

- methanol fuel cells. *Journal of Power Sources*, 153(1): 61-67.
- 8. Kienitz, B. (2021). Optimizing polymer electrolyte membrane thickness to maximize fuel cell vehicle range. *International Journal of Hydrogen Energy*, 46(19): 11176-11182.
- 9. Sudaroli, B. M. and Kolar, A. K. (2016). An experimental study on the effect of membrane thickness and PTFE (polytetrafluoroethylene) loading on methanol crossover in direct methanol fuel cell. *Energy*, 98: 204-214.
- Shaari, N., Zakaria, Z. and Kamarudin, S. K. (2019). The optimization performance of cross-linked sodium alginate polymer electrolyte biomembranes in passive direct methanol/ethanol fuel cells. *International Journal of Energy Research*, 43(14): 8275-8285.
- Zakaria, Z., Kamarudin, S. K., Timmiati, S. N. and Masdar, M. S. (2019). New composite membrane poly (vinyl alcohol)/graphene oxide for direct ethanol–proton exchange membrane fuel cell. Journal of Applied Polymer Science, 136(2): 46928.
- Hren, M., Hribernik, S., Gorgieva, S., Motealleh, A., Eqtesadi, S., Wendellbo, R. and Božič, M. (2021). Chitosan-Mg (OH)<sub>2</sub> based composite membrane containing nitrogen doped GO for direct ethanol fuel cell. *Cellulose*, 28(3): 1599-1616.
- 13. Pereira, J. P., Falcão, D. S., Oliveira, V. B. and Pinto, A. M. F. R. (2014). Performance of a passive direct ethanol fuel cell. *Journal of Power Sources*, 256: 14-19.
- 14. Jiang, X., Sun, Y., Zhang, H. and Hou, L. (2018). Preparation and characterization of quaternized poly (vinyl alcohol)/chitosan/MoS<sub>2</sub> composite anion exchange membranes with high selectivity. *Carbohydrate Polymers*, 180: 96-103.
- Taufiq Musa, M., Shaari, N. and Kamarudin, S. K. (2021). Carbon nanotube, graphene oxide and montmorillonite as conductive fillers in polymer electrolyte membrane for fuel cell: an overview. *International Journal of Energy Research*, 45(2): 1309-1346.

## Zulfirdaus: THE EFFECT OF MEMBRANE THICKNESS ON THE PERFORMANCE OF PASSIVE DIRECT ETHANOL FUEL CELLS USING A POLY VINYL ALCOHOL/GRAPHENE OXIDE COMPOSITE MEMBRANE

- 16. Shaari, N. and Kamarudin, S. K. (2017). Characterization studies of sodium alginate/sulfonated graphene oxide based polymer electrolyte membrane for direct methanol fuel cell. *Malaysian Journal of Analytical Sciences*, 21(1), 113-118.
- 17. Hamid, N. S., Kamarudin, S. K. and Karim, N. A. (2021). Potential of Nafion/eggshell composite membrane for application in direct methanol fuel cell. *International Journal of Energy Research*, 45(2), 2245-2264.
- Thiam, H. S., Daud, W. R. W., Kamarudin, S. K., Mohamad, A. B., Kadhum, A. A. H., Loh, K. S. and Majlan, E. H. (2013). Nafion/Pd-SiO<sub>2</sub> nanofiber composite membranes for direct methanol fuel cell applications. *International Journal of Hydrogen Energy*, 38(22): 9474-9483.
- 19. Yang, C. C., Chiu, S. J., Chien, W. C. and Chiu, S. S. (2010). Quaternized poly (vinyl alcohol)/alumina

- composite polymer membranes for alkaline direct methanol fuel cells. *Journal of Power Sources*, 195(8): 2212-2219.
- 20. An, L. and Zhao, T. S. (2011). Performance of an alkaline-acid direct ethanol fuel cell. *International Journal of Hydrogen Energy*, 36(16): 9994-9999.
- 21. Seweryn, J. and Lewera, A. (2014). High selectivity of ethanol electrooxidation to carbon dioxide on platinum nanoparticles in low temperature polymer electrolyte membrane direct ethanol fuel cell. *Applied Catalysis B: Environmental*, 144: 129-134.
- 22. An, L., Zhao, T. S., Chen, R. and Wu, Q. X. (2011). A novel direct ethanol fuel cell with high power density. *Journal of power sources*, 196(15): 6219-6222.

## Malaysian Journal of Analytical Sciences (MJAS)

Published by Malaysian Analytical Sciences Society



# EFFECT OF pH IN THE SYNTHESIS OF GOLD-COPPER NANOPARTICLES SUPPORTED ON ANODIC ALUMINIUM OXIDE AS CATALYST FOR THE REDUCTION OF p-NITROPHENOL

(Kesan pH dalam Sintesis Emas-Kuprum (Au-Cu) Partikel Nano Disokong pada Anodik Aluminium Oksida Sebagai Mangkin bagi Penurunan *p*-Nitrofenol)

Norizwan Nordin<sup>1</sup>, Hanani Yazid<sup>1,2</sup>, Nor Azira Irma Muhammad<sup>2</sup>, Abdul Mutalib Md Jani<sup>3</sup>\*

<sup>1</sup>Faculty of Applied Sciences,
Universiti Teknologi MARA, 40450 Shah Alam, Selangor, Malaysia

<sup>2</sup>Faculty of Applied Sciences,
Universiti Teknologi MARA, Perlis Branch, Arau Campus, 02600 Arau, Perlis, Malaysia

<sup>3</sup>Faculty of Applied Sciences,
Universiti Teknologi MARA, Perak Branch, Tapah Campus, 35400 Tapah Road, Perak, Malaysia

\*Corresponding author: abdmutalib@uitm.edu.my

Received: 9 December 2021; Accepted: 6 March 2022; Published: 27 June 2022

#### Abstract

Gold–copper (Au–Cu) bimetallic catalysts were prepared through chemical reduction with Cu and Au precursors at the pH of 3, 5, 7 and 9 and hexadecylamine as the capping agent to produce Au–Cu bimetallic nanoparticles (Au–Cu NPs). The colloidal Au–Cu NPs were then grafted onto an anodic aluminium oxide (AAO) support through spin coating. The AAO support was fabricated via a two-step anodization method at 80 V by using oxalic acid as the electrolyte. The Au–Cu/AAO catalysts were characterized through field emission scanning electron microscopy–energy dispersive X-ray spectroscopy, Fourier transform infrared spectroscopy and inductive coupled plasma–optical emission spectroscopy. The catalytic activities of the Au–Cu bimetallic catalysts in the reduction of p-nitrophenol (p-NP) were evaluated. Results showed that the rate constant (k) varied in accordance with the pH of the Au precursor. The highest k value of  $4.6 \times 10^{-3}$  s<sup>-1</sup> was obtained with the Au–Cu catalyst prepared at pH 7. The better performance of the investigated bimetallic catalyst than that of the monometallic Au and Cu catalysts demonstrated the promotional role of the second metal in the reduction of p-NP.

Keywords: Au-Cu NPs, pH, anodic aluminium oxide

#### Abstrak

Pemangkin dwilogam Au-Cu dengan prekursor Au pH 3, 5, 7 dan 9 disediakan dengan menggunakan prekursor Cu secara kaedah penurunan kimia dengan heksadesilamin (HDA) sebagai agen penutup untuk penghasilan nanopartikel Au-Cu (NP Au-Cu). Dwilogam NP Au-Cu telah dicantumkan pada sokongan anodik aluminium oxida (AAO) melalui kaedah salutan putaran. Sokongan AAO telah difabrikasi pada 80 V menggunakan asid oksalik sebagai elektrolit melalui kaedah anodisasi dua langkah. Pemangkin Au-Cu/AAO dicirikan oleh mikroskopi elektron pengimbasan pelepasan medan-spektroskopi sinar-X penyerakan tenaga (FESEM-EDX), spektroskopi inframerah transformasi fourier (FTIR) dan spektroskopi pelepasan plasma-optik berganding induktif (ICP-OES). Penurunan *p*-nitrofenol digunakan untuk menilai aktiviti pemangkin bimetal Au-Cu. Keputusan

## Norizwan et al: EFFECT OF pH IN THE SYNTHESIS OF GOLD-COPPER NANOPARTICLES SUPPORTED ON ANODIC ALUMINIUM OXIDE AS CATALYST FOR THE REDUCTION OF p-NITROPHENOL

menunjukkan bahawa pemalar kadar, (k) adalah berbeza bergantung kepada pH prekursor. Nilai k tertinggi iaitu 4.6 x 10<sup>-3</sup> s<sup>-1</sup> telah diperolehi daripada pemangkin Au-Cu yang disediakan pada pH 7. Daripada kajian ini, pemangkin dwilogam menunjukkan prestasi yang lebih baik berbanding pemangkin Au dan Cu logam mono, menunjukkan peranan promosi logam kedua ke arah penurunan p-nitrophenol.

Kata kunci: NP Au-Cu, pH, anodik aluminium oksida

#### Introduction

Gold nanoparticles (Au NPs) are small particles with diameters that range from 1 nm to 100 nm and unique optical and electronic properties. Au NPs can be easily dispersed in water to form colloidal Au, which offers many benefits for various applications. Au NPs are an excellent catalyst for the selective oxidation or hydrogenation of organic substrates. In recent years, interest in using Au NPs as catalysts for the reduction of p-nitrophenol (p-NP) and p-nitroaniline (p-NA) has grown [1-2]. Au NPs have been extensively researched as monometallic or bimetallic NPs. The performance of monometallic Au NPs is limited by particle size and manufacturing technique, but these constraints can be overcome by adding a second metal [3-6]. Au NPs mixed with other transition metals such Au-Pt, Au-Cu, Au-Pd, and Au-Ag have higher catalytic activity than monometallic Au NPs. It is highlighted that Au-Cu NPs are an excellent bimetallic alloy because they are more resistant to oxidation thus have a longer catalytic lifetime [5]. The characteristic of the NPs is highly dependent on their preparation condition such as pH, capping agent and precursor concentration.

However, the Au-Cu NPs tend to agglomerate on their own [6-15]. This can be prevented by introducing the support materials such as metal oxides to stabilize and disperse the Au-Cu NPs. Anodic aluminium oxide (AAO) was chosen as the support as it offers several advantages, such as (i) high surface area and porous structure; the reactants get easy access to the active catalytic site [16-17], (ii) prevent agglomeration of Au-Cu NPs, and (iii) this supported catalyst can easily be separated from the reaction mixture at the end of the reaction by simple filtration.

*p*-NP is a common pollutant that originates from agricultural, pharmaceutical and petrochemical

industries; it is highly carcinogenic and tends to persist in water and soil [2,18]. p-NP causes the irritation and inflammation of the eyes, skin and respiratory tract. The delayed reaction of p-NP in the blood of people exposed to this compound causes methemoglobinemia. The symptoms of methemoglobinemia include cyanosis, confusion and unconsciousness. Therefore, this compound has prompted the development of a wide range of analytical devices by researchers for its determination and eventual removal from contaminated sites. The reduction of p-NP can be monitored easily by using a UV-Vis spectrophotometer at 400 nm. Therefore, in this work, we proposed the preparation of Au-Cu NPs with a Au precursor at different pH values via chemical reduction followed by immobilization on an AAO membrane through spin coating. The activities of these Au-Cu/AAO catalysts were then tested in p-NP reduction. p-NP is a pollutant that is commonly found in most water bodies; it can be upcycled for use in the production of analgesics, such as paracetamol, through reduction into p-aminophenol [1,6].

#### Materials and Methods

#### Preparation of Au-Cu NPs

The bimetallic Au-Cu NPs were synthesized based on the chemical reduction technique. An aqueous solution of CuCl<sub>2</sub>·2H<sub>2</sub>O (50 mM) was mixed with 0.3 mL HAuCl<sub>4</sub>·3H<sub>2</sub>O (50 mM) of various pH of 3, 5, 7, and 9 by using 0.5 M NaOH. The molar ratio of the Au to Cu is 2.5 to 1. The mixture was then added with 0.28 mL of glucose (0.5 M) in a glass vial containing the hexadecylamine (HDA) solution of 22.5 mg in 2 mL distilled water [3]. The vial was magnetically stirred at room temperature overnight followed by heating treatment at 100 °C for 10 mins. After the vial was cooled in an ice bath, 15 mg of HDA was added and the vial was heated again till colour changes observed.

The samples are denoted as Au-Cu pH3, Au-Cu pH5, Au-Cu pH7 and Au-Cu pH9.

#### **Fabrication of AAO membrane**

A 99.99% purity aluminium foil with a thickness of approximately 0.1 mm was cut into (2 cm x 2 cm) pieces, and an AAO membrane was formed on the aluminium foil using a two-step electrochemical anodization procedure that was previously reported [1,16]. The AAO was manufactured in multiple phases. The aluminium foils were cleaned and degreased in the first phase by sonication in acetone for 15 mins. The aluminium foils were then submerged in a chemical polishing solution (15 mL HNO<sub>3</sub> and 85 mL H<sub>3</sub>PO<sub>4</sub>) for 1 min at 70 °C. Then, using 0.3 M oxalic acid as the electrolyte, the initial anodization was performed for 1 minute at 5 °C with a constant voltage of 80 V. The anodic layer was then removed by immersing the foil for roughly 2 hours in a solution of 1.5 wt.% chromic and 6 wt% phosphoric acids. Next, the second anodization procedure was carried out for 2 hours in the conditions described above. Finally, a solution of 5% CuCl<sub>2</sub>.2H<sub>2</sub>O and 15% HCl was used to dissolve the aluminium foils and obtain AAO membrane. The constructed AAO membrane was cleaned multiple times with generous volumes of ethanol and DI water and stored in the desiccator until further used.

#### Immobilization of Au-Cu NPs on AAO

The previously prepared Au-Cu NPs solution was deposited on both sides of the AAO by spin-coating at 1000 rpm for 30 s. Subsequently, the AAO was subjected to calcination at 400 °C for 4 hours at a rate of 10 °C/min. The immobilized Au-Cu NPs are denoted as Au-Cu/AAO pH3, Au-Cu/AAO pH 5, Au-Cu/AAO pH 7 and Au-Cu/AAO pH 9 correspond to the Au-Cu NPs prepared at pH 3, 5, 7, and 9, respectively.

#### Reduction of p-Nitrophenol

The *p*-NP solution was prepared by dissolving solid by *p*-NP (99%, Sigma Aldrich) in distilled water. In a cuvette, 1 mg of Au-Cu/AAO catalyst was added to a solution of NaBH<sub>4</sub> ( $1.5\times10^{-2}$  M, 1.5 mL) and *p*-NP ( $0.05\times10^{-2}$  M, 1.5 mL). The absorbance of the *p*-NP solution was determined at 1-minute intervals using a UV-vis spectrophotometer (Lambda 25, Perkin Elmer)

set at 399 nm. At room temperature and pressure, the catalytic reduction was carried out. Depending on the catalyst, the total reaction time for complete reduction of p-NP would take 5 to 10 mins. Pseudo-first-order kinetics was used to get the value of the rate constant (k) as described by Yazid et al. [6].

#### Characterization

Characterization of the catalysts by Fourier Transform Infrared Spectroscopy was used to assess the surface functionalities of the produced samples (FTIR; Spectrum, Perkin Elmer). Meanwhile, the surface morphology was observed via Field Emission Scanning Electron Microscopy (FESEM: FEI Nova Nanosem 450). The elements of Au and Cu loading on the AAO membrane were determined by using an Inductive Couple Plasma-Optical Emission Spectrometer (ICP-OES: Optima 8000, Perkin Elmer).

#### Results and Discussion Immobilization of Au-Cu NPs on the AAO

Figure 1 shows the photograph of AAO and Au-Cu/AAO. The change of color from yellow to light purple indicates the successful deposition of Au on AAO. The calcination process will vaporize any organic material from the previous steps and leave just the metal and metal oxide species which are Au-Cu NPs and AAO membrane. The calcination step also ensures that the Au-Cu NPs are covalently bonded to the -OH group on the AAO membrane [1,6]. This strong covalent bond prevents aggregation of the particles thus improving their catalytic performance. The spin-coating method provides homogenous distribution of the NPs on the AAO membrane. It is to note that all catalysts prepared at pH 3 to 9 show the same appearance to the naked eyes (Figure 1).

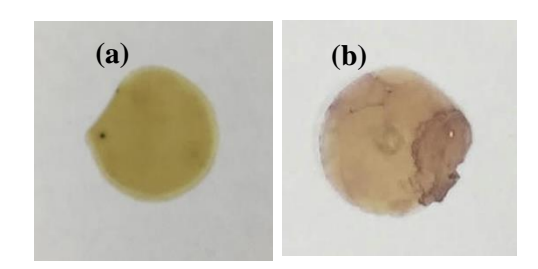


Figure 1. Photograph of (a) bare AAO (b) Au-Cu/AAO pH3

Norizwan et al: EFFECT OF pH IN THE SYNTHESIS OF GOLD-COPPER NANOPARTICLES SUPPORTED ON ANODIC ALUMINIUM OXIDE AS CATALYST FOR THE REDUCTION OF p-NITROPHENOL

The FTIR spectra of the bare AAO (bAAO) and Au-Cu/AAO are presented in Figure 2. Some changes of peaks intensity, particularly O–H vibrations, confirm the attachment of the Au-Cu NPs on the surface of the AAO [7]. The O–H peak in bAAO at 3210 cm<sup>-1</sup> is very

sharp when compared to Au-Cu/AAO O-H peak at 3195 cm<sup>-1</sup>. Even though the FTIR instrumentation was unable to detect the presence of gold and copper in the compound, it could be inferred through the observed peak shifting for O-H from 3210 cm<sup>-1</sup> to 3195 cm<sup>-1</sup>.

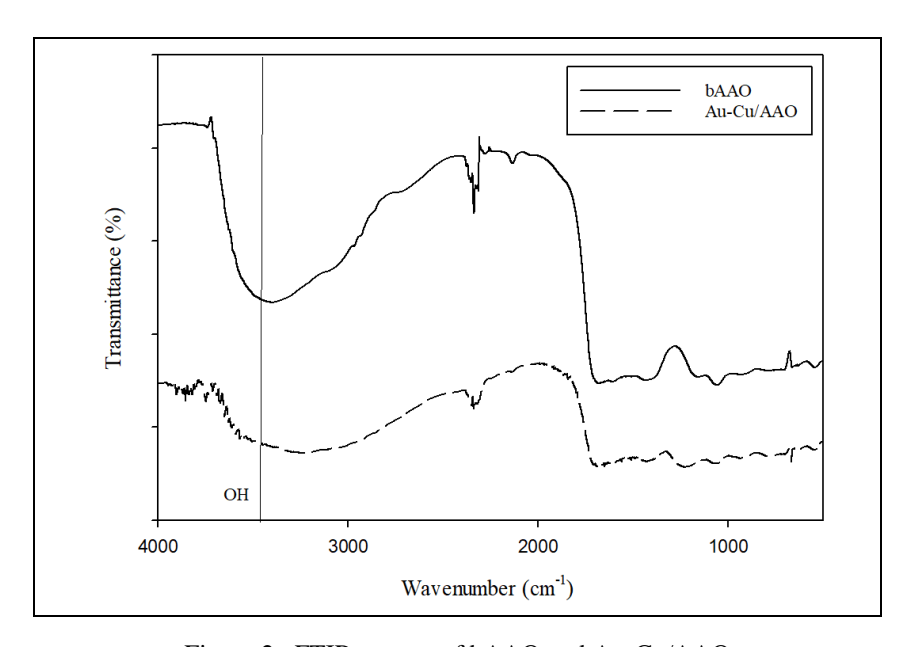


Figure 2. FTIR spectra of bAAO and Au-Cu/AAO

Figure 3 shows FESEM images of synthesized Au-Cu/AAO at pH3 to pH9. FESEM images taken from the top indicated the creation of a hexagonally aligned AAO structure via electrochemical anodization, with typical pore sizes of 100-110 nm. The pores are non-intercrossing and cylindrical in shape resulting in a high surface area. The nanostructure of the as-prepared AAO has a considerable effect on the accessibility (flow) of liquid reactants on both sites of the porous support. A good flow for the reactant to reach the active site is vital for efficient catalytic performance. It is worth noting that exact control of the AAO structure's size and interpore spacing may be accomplished by adjusting the anodization conditions and electrolyte concentration, respectively [16].

The adjustment of pH of the Au precursor has resulted in different sizes and arrangements of the NPs. On Au-Cu/AAO pH3 the size of the NPs is between 113.75  $\pm$  85.20 nm and the NPs are clustered together as shown in Figure 3(a). Whereas, Au-Cu/AAO pH5 and pH7 demonstrated a mix of clustered and individual arrangement of the NPs with a size of 61.54  $\pm$  96.55 nm and 32.33  $\pm$  22.75 nm, respectively. An individually disperse NPs was shown by Au-Cu/AAO pH9 with a size of 34.33  $\pm$  56.47 nm. Noting that the adjustment of pH of the precursor will result in various arrangement and sizes. Table 1 summarizes the characteristic of Au-Cu NPs as observed from FESEM images.

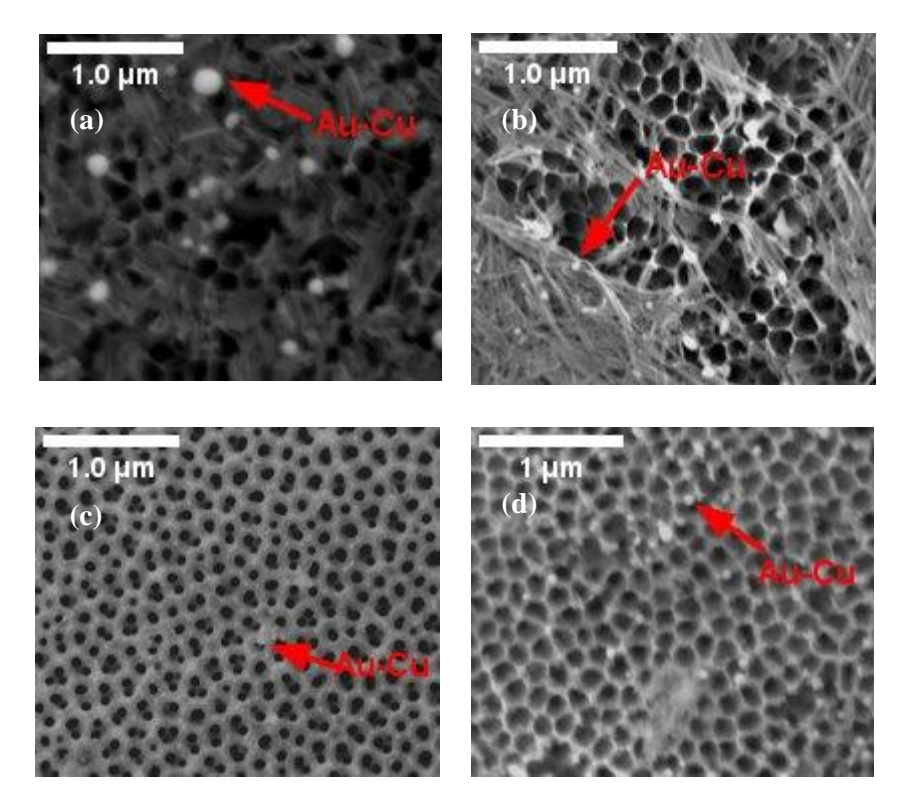


Figure 3. FESEM images of Au-Cu/AAO at different pH of (a) 3 (b) 5 (c) 7 and (d) 9

Table 1. Summary of the characteristic of Au-Cu NPs observed from FESEM images

Catalyst Diameter Size (nm)		Distribution			
Au-Cu/AAO pH3	$113.75 \pm 85.20$	Clustered			
Au-Cu/AAO pH5	$61.54 \pm 96.55$	Mix of Clustered and Individual Dispersal			
Au-Cu/AAO pH7	$32.33 \pm 22.75$	Mix of Clustered and Individual Dispersal			
Au-Cu/AAO pH9	$34.33 \pm 56.47$	Individually Disperse			

The Au-Cu pH 7 was selected for an area scan using EDX analysis (Figure 4). Figure 4(a) shows the area viewed using FESEM. Figure 4(b) depicts only large Au NPs can be detected. Small Au NPs and Cu NPs were also present but cannot be monitored clearly as seen in Figure 4(b) and (c). In contrast, the Al species from the support AAO can be seen clearly. The production of small and highly dispersed NPs on the AAO membrane resulted in reading below the EDX detection limit for small Au and Cu species. The presence of Cu species will be proved when using ICP-OES.

Based on the ICP-OES results presented in Figure 5, the Au to Cu molar ratio were determined to be 1.4: 1, 1.7:1, 2.27:1 and 1.59:1 for the Au-Cu/AAO pH3, pH5, pH7 and pH9 samples, respectively. The Au-Cu/AAO pH 7 is the closest mol to mol ratio from the experimental value of the precursor used which is 2.5 Au to 1 Cu. These results suggest that the deprotonation of the hydroxyl groups at high pH leads to the accumulation of negative charge on the surface of the Au NPs [1,18].

Norizwan et al: EFFECT OF pH IN THE SYNTHESIS OF GOLD-COPPER NANOPARTICLES SUPPORTED ON ANODIC ALUMINIUM OXIDE AS CATALYST FOR THE REDUCTION OF p-NITROPHENOL

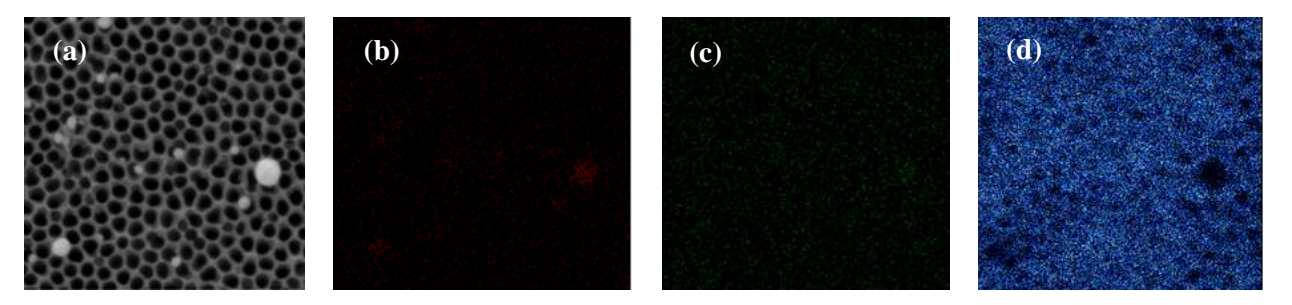


Figure 4. The Au-Cu/AAO pH 7(a) FESEM image and corresponding elemental EDX mapping of (b) Au (c) Cu and (d) Al

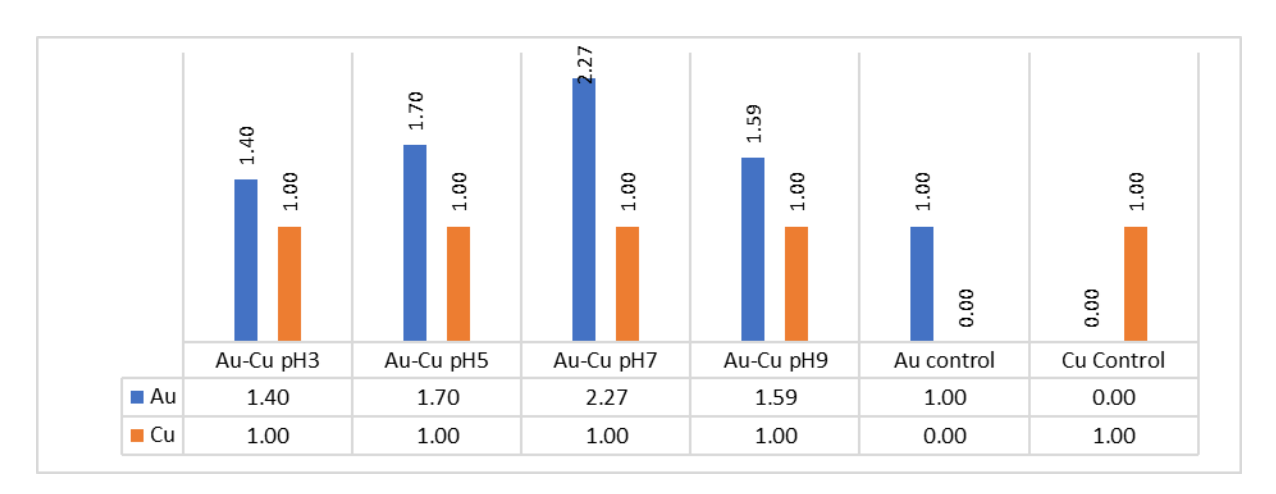


Figure 5. ICP-OES detection of Au to Cu molar ratio

#### Catalytic performance

The efficacy of the prepared Au-Cu/AAO catalysts were tested by catalytic reduction of *p*-NP to *p*-AP. The *p*-NP solution exhibited a high absorption peak at 317 nm under neutral or acidic conditions, but the addition of NaBH<sub>4</sub> increased the alkalinity of the solution, resulting in the creation of *p*-nitrophenolate ions and shifting the absorption peak to 400 nm [2,6]. The appearance and growth of a new peak at 300 nm corresponds to the formation of the product *p*-AP as shown in Figure 6 [1, 6, 18]. The gradual decrease in absorbance at 399 nm with time indicates that the nitro group has been reduced, while the appearance and growth of a new peak at 300 nm corresponds to the

formation of the product p-AP [6,18]. The dark yellow colour of p-NP decreases with the formation of the p-AP, and bubbles are produced by NaBH<sub>4</sub> converting water to H<sub>2</sub> gas. Because the concentration of NaBH<sub>4</sub> in this reaction system far exceeds that of p-NP, its concentration remains constant throughout the reaction. The rate constant (k) for the reaction was calculated using pseudo-first order kinetics in the case of p-NP [6]. The absorbance at 400 nm remains constant over time in the absence of a catalyst, demonstrating that the reduction does not occur. Figure 6 depicts the gradual production of p-AP; two isosbestic spots are visible at 280 and 312 nm, implying that the conversion reaction is carried out by the two main species [1, 6].

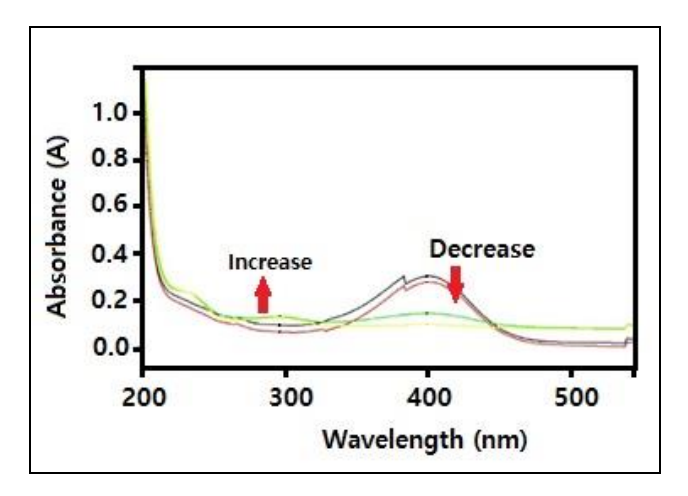


Figure 6: UV-Vis spectra of p-NP over time for Au-Cu/AAO pH 7

For all the studies, the graph of  $\ln(C/C_o)$  vs reaction time is linear (Figure 7), showing that the catalytic reaction followed first-order kinetics. The Au-Cu/AAO pH3, pH, pH7 and pH9 samples were found to have k values of  $4\times10^{-4}$  s<sup>-1</sup>,  $2\times10^{-3}$  s<sup>-1</sup>,  $4.6\times10^{-3}$  s<sup>-1</sup>, and  $6\times10^{-4}$  s<sup>-1</sup>, respectively. A greater k value means that p-NP is reduced more quickly [1,6,18]. The Au control catalyst had the lowest k value, while Cu control had no reaction at all. These findings show that the presence of Cu had an impact in enhancing the catalytic activity of Au NPs in the reduction of p-NP. As previously stated, the Au-Cu/AAO pH7 catalyst possesses smaller Au NPs with a uniform distribution of clustering and

individual NPs, resulting a good impact on catalytic activity. A neutral pH leads to the formation of small and a mix of individual and clustered dispersal arrangements. The various size and arrangement of Au-Cu NPs generated by grafting the NPs onto the AAO is responsible for the various *k*-values. Even though Cu shows zero catalytic activity the presence of it being with Au has increased the catalytic activity of Au when comparing Au control. Table 2 summarizes the *k*-values of all the prepared catalysts for the reduction of *p*-NP. The results indicate that the adjustment of Au precursor at pH 7 and synthesizing it with Cu has a good effect on the catalytic activity.

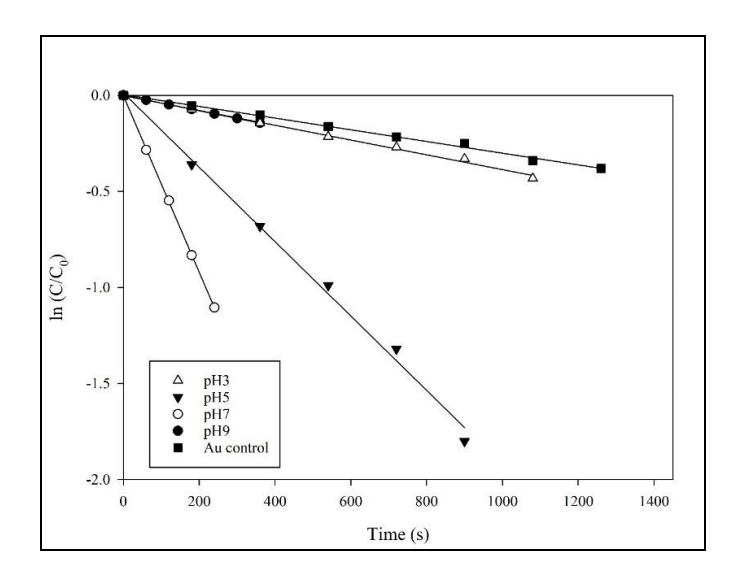


Figure 7. Plot of ln (C/C<sub>o</sub>) versus time (min) for the catalysts Au-Cu/AAO

Norizwan et al: EFFECT OF pH IN THE SYNTHESIS OF GOLD-COPPER NANOPARTICLES SUPPORTED ON ANODIC ALUMINIUM OXIDE AS CATALYST FOR THE REDUCTION OF p-NITROPHENOL

Table 2. Rate of reaction (*k*) of the catalysts

Catalyst	k-value (s <sup>-1</sup> )			
Au-Cu/AAO pH3	4.00×10 <sup>-4</sup>			
Au-Cu/AAO pH5	2.00×10 <sup>-3</sup>			
Au-Cu/AAO pH7	4.60×10 <sup>-3</sup>			
Au-Cu/AAO pH9	6.00×10 <sup>-4</sup>			
Au/AAO pH7 control	3.00×10 <sup>-4</sup>			
Cu/AAO control	no reduction			

#### Conclusion

All synthesized Au-Cu/AAOs were characterized by FESEM-EDX, FTIR, and ICP-OES. The adjustment of pH for the Au precursor during the preparation method has resulted in different Au size and arrangements. The highest activity of  $4.6\times10^{-3}$  s<sup>-1</sup> was obtained for Au-Cu/AAO prepared at pH 7. Furthermore, this bimetallic catalyst exhibited higher catalytic activity than monometallic Au/AAO and Cu/AAO. Further work is underway to extend this concept by using Au NPs at pH 7 with other metals (X) to make another Au-X/AAO catalyst that can be easily recovered from liquid-phase catalytic reactions.

#### Acknowledgment

We would like to thank Universiti Teknologi MARA (UiTM) for providing generous internal financial support under DPPD grant: 600-TNCPI 5/3/DDN (09) (003/2020) in conducting this study and providing all the facilities.

#### References

- Ahmad Zulkifli, F. W., Yazid, H. and Jani, A. M. M. (2021). Immobilization of carbon nanotubes decorated gold nanoparticles on anodized aluminium oxide (Au-CNTs-AAO) membrane for enhanced catalytic performance. *Materials Chemistry and Physics*, 264: 124445.
- Behera, M., Tiwari, N., Basu, A., Rekha Mishra, S., Banerjee, S., Chakrabortty, S. and Tripathy, S. K. (2021). Maghemite/ZnO nanocomposites: A highly efficient, reusable and non-noble metal

- catalyst for reduction of 4-nitrophenol. *Advanced Powder Technology*, 32(8): 2905-2915.
- 3. He, R., Wang, Y.-C., Wang, X., Wang, Z., Liu, G., Zhou, W., Wen, L., Li, Q., Wang, X., Chen, X., Zeng, J. and Hou, J. G. (2014). Facile synthesis of pentacle gold–copper alloy nanocrystals and their plasmonic and catalytic properties. *Nature Communications*, 5: 1-10.
- 4. Heiligtag, F. J. and Niederberger, M. (2013). The fascinating world of nanoparticle research. *Materials Today*, 16: 262-271.
- Odenbrand, C. U. I., Blanco, J., Avila, P. and Knapp, C. (1999). Lean NOx reduction in real diesel exhaust with copper and platinum titania based monolithic catalysts. *Applied Catalysis B: Environmental*, 23: 37-44.
- Yazid, H., Adnan, R., Farrukh, M. A. and Hamid, S. A. (2011). Synthesis of Au/Al<sub>2</sub>O<sub>3</sub> nanocatalyst and its application in the reduction of p-Nitrophenol. *Journal of the Chinese Chemical Society*, 58(5): 593-601.
- 7. Rout, L., Kumar, A., Dhaka, R. S., Reddy, G. N., Giri, S. and Dash, P. (2017). Bimetallic Au-Cu alloy nanoparticles on reduced graphene oxide support: Synthesis, catalytic activity and investigation of synergistic effect by DFT analysis. *Applied Catalysis A: General*, 538: 107-122.
- Sobczak, I. and Wolski, Ł. (2015). Au–Cu on Nb<sub>2</sub>O<sub>5</sub> and Nb/MCF supports – Surface properties and catalytic activity in glycerol and methanol oxidation. *Catalysis Today*, 254: 72-82.

- Sharma, G., Kumar, A., Sharma, S., Naushad, M., Prakash Dwivedi, R., Al Othman, Z. A. and Mola, G. T. (2017). Novel development of nanoparticles to bimetallic nanoparticles and their composites: A review. *Journal of King Saud University-Science*. 31(2): 257-269.
- 10. Zeng, S., Yong, K. T., Roy, I., Dinh, X. Q., Yu, X. and Luan, F. (2011). A review on functionalized gold nanoparticles for biosensing applications. *Plasmonics*, 6(3): 491-506.
- Rocha Rocha, M. Cortez Valadez, A. R. Hernandez Martinez, R. Gamez Cor-rales, R. A. Alvarez, R. Brito Hurtado, M. and Flores Acosta, (2019). Green synthesis of Ag-Cu nanoalloys using opuntia ficus-indica, *Journal of Electronic Material*, 46: 802-807.
- 12. Kumar, V., Singh, D. K., Mohan, S., Bano, D., Gundampati, R. K. and Hasan, S. H. (2017). Green synthesis of silver nanoparticle for the selective and sensitive colorimetric detection of mercury (II) ion. *Journal of Photochemistry and Photobiology* B: Biology, 168: 67-77.
- Chen, H. J., Shao, L., Li, Q. and Wang, J. F. (2013). Gold nanorods and their plasmonic properties, *Chemical Society Reviews*, 42: 2679-2724.
- 14. Brust, M. and Kiely, C. J. (2002). Some recent advances in nanostructure preparation from gold and silver particles: a short topical review,

- Colloids Surf. A, Physicochemical and Engineering Aspect 202 175-186.
- 15. Seo, M. H., Choi, S. M., Seo, J. K., Noh, S. H., Kim, W. B., & Han, B. (2013). The graphene-supported palladium and palladium—yttrium nanoparticles for the oxygen reduction and ethanol oxidation reactions: Experimental measurement and computational validation. *Applied Catalysis B, Environmental*, 129: 163-171.
- 16. Habiballah, A. S., Jani, A. M. M., Mahmud, A. H., Osman, N. and Radiman, S. (2016). Facile synthesis of Ba0.5Sr0.5Co0.8Fe0.2O3-δ (BSCF) perovskite nanowires by templating from nanoporous anodic aluminium oxide membranes. *Materials Chemistry and Physics*, 177: 371-378.
- 17. Chung, C. K., Tsai, C. H., Hsu, C. R., Kuo, E. H., Chen, Y. and Chung, I. C. (2017). Impurity and temperature enhanced growth behaviour of anodic aluminium oxide from AA5052 Al-Mg alloy using hybrid pulse anodization at room temperature. *Corrosion Science*, 125: 40-47.
- Nordin, N., Noor, N. M., Wahab, N. A. A., Yazid, H. and Jani, A. M. (2020). Preparation of bimetallic catalyst: gold-copper (Au-Cu) nanoparticles for catalytic reduction of pnitrophenol. *IOP Conference Series: Materials Science and Engineering*, 957(1): 012036.

## Malaysian Journal of Analytical Sciences (MJAS)





## POTENTIAL OF TEXTILE WASTE AS NITROGEN DOPED POROUS CARBON FOR OXYGEN REDUCTION REACTION

(Potensi Sisa Tekstil Sebagai Karbon Poros Terdop Nitrogen Berliang untuk Tindak Balas Penurunan Oksigen)

Suhaila Mohd Sauid<sup>1, 3</sup>, Siti Kartom Kamarudin<sup>1,2\*</sup>, Loh Kee Shyuan<sup>1</sup>

<sup>1</sup>Fuel Cell Institute

<sup>2</sup>Department of Chemical and Process Engineering, Faculty of Engineering and Built Environment
Universiti Kebangsaan Malaysia, 43600 UKM Bangi, Selangor, Malaysia

<sup>3</sup>School of Chemical Engineering, College of Engineering
Universiti Teknologi MARA, 40450 Shah Alam, Selangor, Malaysia

\*Corresponding author: ctie@ukm.edu.my

Received: 13 December 2021; Accepted: 27 February 2022; Published: 27 June 2022

#### Abstract

Transforming waste into usable materials can protect and conserve the environment, thereby reducing the dependence on landfills, limiting the use of natural resources, and decreasing the carbon footprint. Every year, millions of tons of textile waste are sent to landfills primarily from discarded clothing. Therefore, this waste is worthwhile to convert into functional carbon product. Herein, textile waste from used clothing was converted into nitrogen-doped porous carbons (TNPC) by simple chemical activation followed by carbonisation. Urea and calcium chloride (CaCl<sub>2</sub>) served as nitrogen precursor and pore forming agent, respectively. The surface area and porosity of the prepared TNPCs were affected by the activation temperature. The optimal sample (TNPC900) activated at 900 °C exhibited a large surface area (496 m<sup>2</sup> g<sup>-1</sup>) with appropriate porosity and a reasonable amount of nitrogen doped. Remarkably, the resultant TNPC900 catalyst tested as the electrode material for oxygen reduction reaction in 0.1 M KOH exhibited an outstanding positive onset potential of 0.94 V vs. RHE. TNCP900 catalyst also demonstrated superior stability and tolerance to methanol than Pt/C. Overall, this study showed that the conversion of textile waste through a simple synthesis technique into electrocatalyst could offer a sustainable alternative to Pt for potential applications in fuel cell and energy-storage technology.

Keywords: textile waste, nitrogen-doped porous carbon, oxygen reduction reaction, metal-free catalyst

#### Abstrak

Mengubah sisa menjadi bahan yang boleh digunakan dapat melindungi dan memulihara alam sekitar sekaligus dapat mengurangkan kebergantungan pada tapak pelupusan sampah, mengehadkan penggunaan sumber semula jadi, dan mengurangkan jejak karbon. Setiap tahun, jutaan ton sisa tekstil dihantar ke tapak pelupusan sampah terutama dari pakaian terpakai. Oleh itu, menukar sisa ini menjadi produk karbon berfungsi adalah usaha yang berbaloi. Di sini, sisa tekstil daripada pakaian terpakai telah ditukar kepada karbon berliang terdop nitrogen (TNPC) dengan pengaktifan kimia mudah diikuti dengan langkah karbonisasi. Urea dan kalsium klorida (CaCl<sub>2</sub>) bertindak masing-masing sebagai bahan sumber nitrogen dan ejen pembentukan liang. Keluasan permukaan dan keliangan

### Suhaila et al: POTENTIAL OF TEXTILE WASTE AS NITROGEN DOPED POROUS CARBON FOR OXYGEN REDUCTION REACTION

Sampel optimum (TNPC900) diaktifkan pada 900 ° C mempamerkan keluasan permukaan yang besar (496 m² g⁻¹) dengan keliangan dan jumlah nitrogen terdop yang sesuai. Mangkin TNPC900 yang diuji sebagai bahan elektrod untuk tindak balas penurunan oksigen (ORR) di dalam larutan 0.1 M KOH menunjukkan potensi permulaan positif yang luar biasa iaitu 0.94 V vs RHE. Selain itu, mangkin TNCP900 menunjukkan kestabilan dan toleransi yang unggul terhadap metanol daripada mangkin Pt/C. Oleh itu, kajian ini menunjukkan bahawa penukaran sisa tekstil menggunakan teknik sintesis yang mudah menjadi elektmangkin dapat menawarkan alternatif Pt yang mampan untuk aplikasi di dalam sel bahan api dan teknologi penyimpanan tenaga.

Kata kunci: sisa tekstil, karbon poros terdop nitrogen, tindak balas penurunan oksigen, mangkin bebas metal

#### Introduction

The growing demand of green and efficient energy has driven the exploration for new technologies because of the depletion of fossil fuels and major environmental problems associated with the usage of conventional energy sources. Fuel cells are a competitive energy device for supplying energy with promising efficiency and negligible emission levels through electrochemical reactions into electricity [1]. However, the sluggish oxygen reduction reaction (ORR) at the cathode significantly affects the overall fuel-cell performance and thus requires an efficient catalyst to accelerate the ORR. The scarce platinum (Pt) and its alloy are extensively used as ORR catalysts, but their high price, low stability, and susceptibility to methanol crossover hinder its large-scale application [2, 3]. Extensive researches have been performed for Pt alternatives that are more cost effective and sustainable with high ORR activity [4]. Metal-free nitrogen-doped carbon materials exhibit massive potential as a substitute to costly Pt-based catalysts, where it demonstrates good ORR electrocatalytic activity and durability, even in acidic electrolytes [5, 6]. Furthermore, owing to the absence of metals, these catalysts could significantly reduce the cathode cost [7].

In recent years, biomass-derived nitrogen-doped carbon materials have prompted fascination and huge consideration in various energy-related applications [8]. Since 2010, many types of biomass such as animal and plant biomass, starch, cellulose derivatives, sugar, microorganisms such as fungi and yeast, and human and industrial waste have been converted into nitrogen-doped carbon for ORR [9, 10]. Biomass materials are used because of their adequate source of carbon, relatively low cost, readily available around the world,

and environment friendliness [11, 12]. In particular, the transformation of waste biomass into nitrogen-doped carbon materials reduces the use of natural resources and thus lowers the carbon footprint, eventually leading to less dependence on landfills. Over the past 15 years, the manufacture and use of textile have increased twofold owing to cheaper production cost, more efficient operation, and increasing demand caused by the fast changing fashion industry [13]. Inevitably, more textile waste is created when more textiles are produced. In the U.S only, 11.3 million tonnes of textiles are disposed in landfills, and only 14.7% (2.5 million tonnes) of the total textiles waste generated is being recycled [14]. The reason for the small amount of textiles being recycled is the complexity of segregating the blended fabric materials [15]. Therefore, the conversion of textiles waste into other usable novel materials is worth exploring.

In the present work, we developed metal-free nitrogendoped porous carbon for ORR from discarded clothing. Urea and calcium chloride were used as nitrogen source and pore-forming agent, respectively, during synthesis. Different pyrolysis temperatures were used to explore temperature's effect on the surface characteristics and electrochemical performance of the electrocatalyst. The obtained nitrogen-doped carbon showed a comparable electrocatalytic activity to that of Pt/C, with superior stability and tolerance to methanol.

#### **Materials and Methods**

#### Preparation of nitrogen-doped porous carbon

TNPCs were fabricated following a previously reported procedure [16]. Typically, small textile cuts of polyester blend fabrics were impregnated in solution containing calcium chloride and urea for 12 h. Then, it

was dried at 80 °C for another 12 h prior to pyrolysis at the desired temperature (800, 900, and 1000 °C) for 1 h in  $N_2$  environment. After cooling to room temperature, the pyrolysis products were ground using pestle and mortar into fine powder and then acid etched in 3 M HCl to remove any unstable elements. Multiple rinsing with distilled water was conducted until the eluent reached neutral pH before finally drying at 105 °C overnight. The prepared sample was denoted according to its pyrolysis temperature, i.e., TNPC800, TNPC900, and TNPC1000 for 800, 900, and 1000 °C, respectively.

#### **Surface characterisation**

The surface morphology of the TNPCs was examined by scanning electron microscopy (SEM; CARL ZEISS EVO MA 10). The Brunauer–Emmett–Teller (BET) surface area and porosity of TNPCs were determined from nitrogen adsorption–desorption isotherms evaluated by a Micromeritics 3 Flex instrument. The surface element and binding energy of the prepared TNPCs were analysed by X-ray photoelectron spectroscopy (XPS) by using an Axis Ultra DLD system (Kratos) with a monochromic Al/K-Alpha X-ray source. Background correction were performed for all peaks with carbon peaks (284.8 eV).

#### **Electrochemical characterisation**

Electrochemical tests were performed using an Autolab PGSTAT128N potentiostat (Metrohm-Autolab) with a rotating ring-disk electrode (RRDE). A typical threeelectrode system comprising a platinum rod, 5 mmdiameter glassy carbon, and Ag/AgCl electrodes serving as counter, working, and reference electrodes, respectively, were used. The catalyst ink was prepared by dispersing 4 mg of catalyst powder in the mixture of deionised water, ethanol, and 5wt% Nafion solution. ORR measurements were conducted by cyclic voltammetry (CV) in N2- and O2-saturated 0.1 M KOH solution at a scan rate of 25 mV s<sup>-1</sup>, whereas linear scan voltammetry (LSV) was performed at a sweeping rate of 5 mV s<sup>-1</sup> from 100 to 1600 rotation speeds. CV and LSV were swept within the same potential range from 0.2 V to -0.9 V vs. Ag/AgCl. For comparison, 20wt% Pt/C with the same catalyst loading was used in the electrochemical measurement. Kinetic current density  $(j_K)$  was calculated according to equation (1) where  $j, j_K$ , and  $j_L$  are the measured, kinetic current, and the diffusion-limiting current densities, respectively.

$$j_{K} = \frac{j \cdot j_{L}}{j_{L} - j} \tag{1}$$

The electron-transfer number (n) was calculated from the Koutecky–Levich (K-L) equations (2) [17].

$$\frac{1}{j} = \frac{1}{j_K} + \frac{1}{j_L} = \frac{1}{B}\omega^{-1/2} + \frac{1}{j_K}$$
 (2)

where  $\omega$  is defined as the angular velocity (rad s<sup>-1</sup>), and the proportionality coefficient B is defined as equation (3) [17].

$$B = 0.62D^{2/3}v^{-1/6}nFC^*$$
(3)

where D is the diffusion coefficient of  $O_2$  in 0.1 M KOH (1.9 ×  $10^{-5}$  cm<sup>2</sup> s<sup>-1</sup>), v is the kinematic viscosity of the electrolyte (0.01 cm<sup>2</sup> s<sup>-1</sup>), F is the Faraday constant (96485C mol<sup>-1</sup>), and C\* is the concentration of  $O_2$  in 0.1 M KOH (1.2 ×  $10^{-6}$  mol cm<sup>-3</sup>) [18]. Electrontransfer numbers (n) and  $O_2$  (%) yield were calculated from the RRDE curves using equations (4) and (5), respectively [19].

$$n_{RRDE} = 4 \times \frac{i_d}{i_d + i_r / N_c} \tag{4}$$

$$H_2O_2$$
 (%) = 200 ×  $\frac{i_r/N_c}{i_d+i_r/N_c}$  (5)

where  $i_r$  is the ring current,  $i_d$  is the disk current, and  $N_c$  is the disk-current collection efficiency of ring electrode. ( $N_c$ = 0.256). For stability test, we compared the LSV curves of before and after a continuous 1000 CV cycle of 100 mV s<sup>-1</sup> scan rate in O<sub>2</sub>-saturated 0.1 M KOH of TNPC and Pt/C. The ring potential was set at 1.4 V vs. RHE during the RRDE measurement, which was within the recommended potential window of inducing  $H_2O_2$  oxidation to  $O_2$  [17].

#### **Results and Discussion**

#### **Surface characterisation of TNPCs**

The SEM images of TNPC800, TNPC900, and TNPC1000 are shown in Figure 1, respectively. All three samples had pore-like morphology on the TNPC surface. For TNPC800 and TNPC900, the pores were

more visible and had depth (Figures 1a and 1b, respectively), whereas the pores on TNPC1000 were larger and seemed shallower as if the pores had collapsed (Figure 1c). This finding indicated that the development of pore structures on TNPCs was affected by pyrolysis temperature. An electrocatalyst with porous structure is desirable as it could accommodate abundant active sites and transport channels for ions [20, 21].

 $N_2$  adsorption—desorption isotherm was used to determine the porosity properties of the TNPC samples. As shown in Figure 1(d), all TNPCs demonstrated type-IV isotherm curves with a clear hysteresis loop (parallel adsorption and desorption branches) at  $P/P_o \approx 0.45-1.0$ , signifying the existence of mesopores in all samples [22]. Furthermore, the BJH pore-size distribution plot (Figure 1d inset) also confirmed that all samples contained mesopores within their distribution. The surface areas calculated based on BET for all TNPCs are listed in Table 1. TNPC900 had the largest surface area of 495.97 m<sup>2</sup> g<sup>-1</sup> and the

highest pore volume within the range of the pyrolysis temperature studied. Furthermore, the surface area increased with increased temperature from 800 °C to 900 °C but significantly dropped when the pyrolysis temperature was 1000 °C with decreased surface area to 207.76 m<sup>2</sup> g<sup>-1</sup>. The pore volume also followed the same trend as the surface area. However, the ratio of increased with increased pyrolysis  $S_{meso}/S_{micro}$ temperature. This finding indicated that with increased temperature to 1000 °C, the micropore structures collapsed and created larger pores. Consequently, the surface area decreased, as supported by the higher average pore size obtained at 1000 °C. The increase in pore diameter well agreed with the morphology observed by SEM. Given that ORR occurs at the interfacial/surface of a catalyst, the micro- and mesoporous structure of a catalyst with high surface area and pore volume can serve as abundant active sites influencing the mass-transport properties and diffusion of the electrolyte [23, 24]. Therefore, the porosity structure of these TNPCs is expected to affect ORR performance.

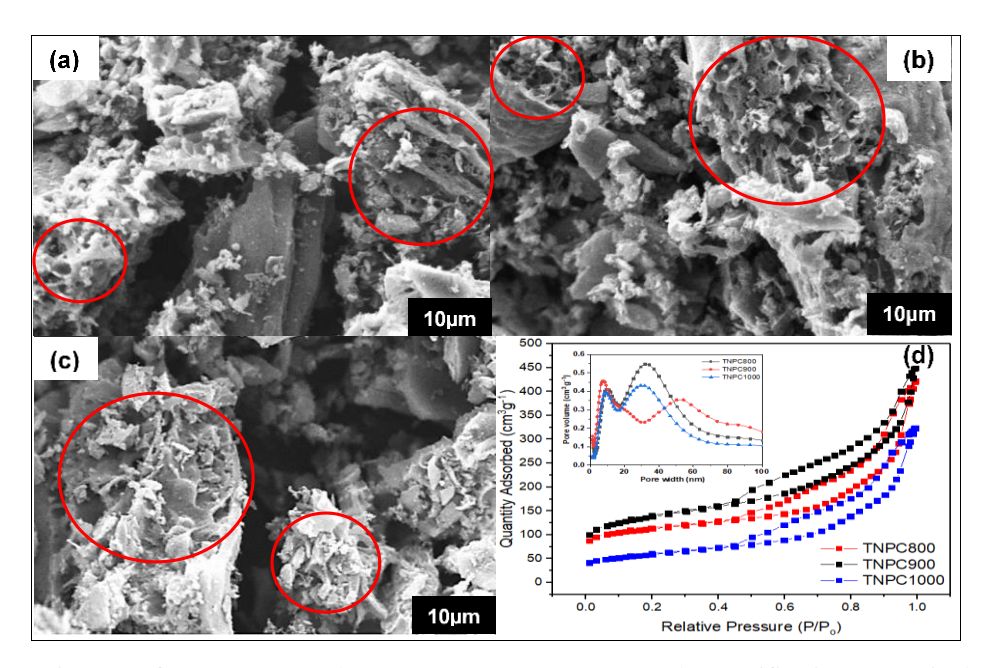


Figure 1. SEM images of (a) TNPC800, (b) TNPC900, (c) TNPC1000 (1k magnification respectively), and (d)  $N_2$  adsorption–desorption isotherms of TNPCs (inset, corresponding pore-size distribution)

N<sub>2</sub> adsorption-desorption isotherm was used to determine the porosity properties of the TNPC samples. As shown in Figure 1 (d), all TNPCs demonstrate type IV isotherm curves with a clear hysteresis loop (parallel adsorption and desorption branches) at  $P/P_0 \sim 0.45 - 1.0$ , signify the existence of mesopores in all samples [22]. Furthermore, the BJH pore size distribution plot (Figure 1d inset) also corroborates that all samples contain mesopores within their distribution. The surface area calculated based on Brunauer-Emmett-Teller (BET) for all TNPCs are tabulated in Table 1. As we can see, TNPC900 has the largest surface area of 495.97 m<sup>2</sup> g<sup>-1</sup> and the highest pore volume in the range of the pyrolysis temperature studied. Furthermore, the surface area enlarge as the temperature was increased from 800 to 900 °C but drop significantly when the temperature of pyrolysis was at 1000 °C as the surface area reduced to 207.76 m<sup>2</sup> g<sup>-1</sup>.

The pore volume also follows the same trend as surface area. However, the ratio of  $S_{\text{meso}}/S_{\text{micro}}$  increase with the increment in pyrolysis temperature. This might indicate that as the temperature raised to 1000 °C, the micropore structures had collapsed which creating larger pores thus decreasing the surface area and this is supported by the higher average pore size obtained at 1000 °C. The increase in pore diameter is in agreement with the morphology observed by SEM. Since ORR occur at the interfacial/surface of a catalyst, the microand mesoporous structure of a catalyst with high surface area and pore volume can serve as abundance active sites that influence the mass transport properties and diffusion of the electrolyte [23,24]. Therefore, it is expected that the porosity structure of these TNPCs will affect the ORR performance.

Table 1. Surface properties of TNPCs

Sample	$S_{BET}$ $(m^2 g^{-1})$	$S_{micro}$ $(m^2 g^{-1})$	$S_{meso}$ $(m^2 g^{-1})$	S <sub>meso</sub> / S <sub>micro</sub> ratio	Pore Volume (cm <sup>3</sup> g <sup>-1</sup> )	Average Pore Size (nm)	C (at%)	N (at%)	O (at%)
TNPC800	416.1	235.55	180.55	0.43	0.64	6.12	92.96	3.54	2.88
TNPC900	495.97	214.77	281.20	0.57	0.67	5.43	91.85	2.80	3.99
TNPC1000	207.76	54.36	153.40	0.74	0.49	9.43	93.39	1.54	3.86

The surface compositions and bonding states of all samples were analysed by XPS. Figure 2(a) displays the survey scans of TNPC samples. C 1s, N 1s, and O 1s were identified at binding energies around 284, 400, and 532 eV. The presence of a small N 1s signal indicated that nitrogen was successfully doped into carbon. The estimated elemental content is listed in Table 1. The nitrogen content can be as high 3.54 at% for TNPC800 and as low as 1.54 at% for TNPC1000, indicating that increased temperature significantly affected nitrogen doping. High-resolution scans of N 1s were further performed to investigate its chemical structure and deconvoluted into three peaks, as exemplified in Figure 2(b). The peaks at 398.4, 400.0, and 401.5 eV corresponded with pyridinic-N, pyrrolic-

N, and graphitic-N, respectively [25, 26]. Pyridinic-N is when two carbon atoms located at the edge of graphitic planes are bound to the nitrogen atom, whereas pyrrolic-N is the nitrogen atom incorporated into the pentagonal ring. Meanwhile, graphitic-N is when a nitrogen atom replaces a carbon atom and bonded with three carbon atoms in the graphene layer [27, 28]. As shown in Figure 2(c), pyridinic-N was the highest for TNPC900 followed by TNPC1000. Furthermore, the rise in temperature from 900 °C to 1000 °C reduced the contents of pyridinic-N slightly but significantly reduced pyrrolic-N. By contrast, the graphitic-N content rose to almost 50 at% at 1000 °C, which was attributed to the transformation of pyrrolic-N and fractional conversion of pyridinic-N into

graphitic-N from the condensation of graphite rings at 1000 °C [29]. Recent studies have reported that pyridinic-N and graphitic-N played important roles in enhancing ORR performance [30, 31]. Pyridinic-N provided active sites and facilitated the dominant 2e<sup>-</sup> to

4e<sup>-</sup> process in the ORR mechanism, whereas graphitic-N promoted the reduction of oxygen to hydrogen peroxide by adsorbing OOH intermediates through a 2e- pathway [32].

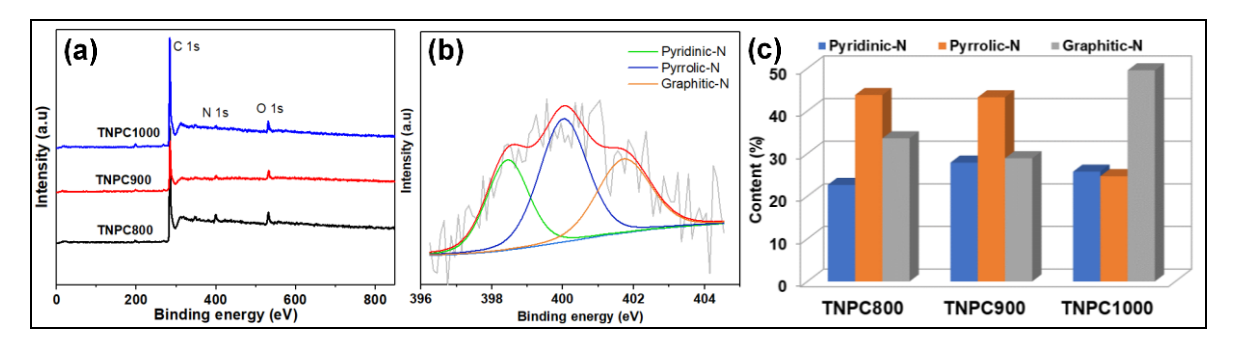


Figure 2. (a) XPS survey spectra; (b) high-resolution XPS of N 1s for TNPC900, and (c) content of nitrogen species of TNPC800, TNPC900, and TNPC1000

#### **Electrochemical performance of TNPCs**

To investigate the possible application of the prepared catalysts for fuel-cell or energy-storage systems, the electrochemical activity of TNPCs was evaluated using a three-electrode system. RRDE or a glassy carbon electrode was loaded with the as-prepared catalyst ink with 0.285 mg cm<sup>-2</sup> loading. As shown in Figure 3 (a), all three catalysts showed no reduction peak observed in N<sub>2</sub>-saturated 0.1 M KOH solution but obvious peaks in a solution of O<sub>2</sub> saturated with the same electrolyte, indicating that these TNPCs were catalytically active towards ORR. However, TNPC900 illustrated a stronger cathodic peak at 0.76 V vs. RHE, and it was more positive than TNPC800 and TNPC1000. Figure 3(b) shows the LSV plots for TNPCs and the commercial Pt/C (20wt%) at 1600 rpm in O2-saturated electrolyte. Amongst the three TNPCs, TNPC900 had the highest ORR activity based on the most positive onset potential E<sub>0</sub> and half-wave potential E<sub>1/2</sub> at 0.94 and 0.78 V vs. RHE, respectively. The E<sub>0</sub> and E<sub>1/2</sub> of TNPC800 (0.92 and 0.74 V, respectively) and TNPC1000 (0.93 and 0.75 V, respectively) were more negative than those of TNPC900. The E<sub>o</sub> of TNPC900 was slightly inferior to that of commercial Pt/C but comparable with values obtained in previous studies using a different biomass, such as coconut mesocarp [26], but higher than those of waste lotus seedpod [12] and cotton stalk [33]. The ORR activity of the TNPCs can also be assessed by their kinetic current densities (j<sub>K</sub>) [34]. The j<sub>K</sub> values at 0.8 V vs. RHE were in the order TNPC900 (1.82 mA cm<sup>-2</sup>) > TNPC1000 (0.55 mA cm<sup>-2</sup>) > TNPC800 (0.46 mA cm<sup>-2</sup>), consistent with  $E_0$  and  $E_{1/2}$ .

To further investigate the kinetic information of ORR for TNPC900, LSV curves were collected at different rotating speeds from 100 rpm to 1600 rpm in O2saturated 0.1 M KOH solution (Figure 3(c)). With increased rotation, the limiting current density increased because of the shorter distance of diffusion [12]. The K-L plot (Figure 3(c) inset) illustrated a linear trend for the potential range of 0.2 V to 0.6 V vs. RHE, signifying similar electron-transfer number (3.5– 3.8) around these potentials. The corresponding electron-transfer number calculated from the ring current and disk current of RRDE (3.55-3.73) curve also agreed with the K-L results (Figure 3d) suggesting a dominant 4e<sup>-</sup> pathway in ORR for TNPC900 catalyst. Conversely, the electron-transfer number calculated for TNPC800 (3.35-3.53) and TNPC1000 (3.48-3.58) was slightly lower than that for TNPC900, indicating that ORR occurred through a combined 2e<sup>-</sup> and 4e<sup>-</sup> transfer pathway. The yield of H<sub>2</sub>O<sub>2</sub> shown in Fig. 3d indicated lesser H<sub>2</sub>O<sub>2</sub> formation on TNPC900, further validating

a higher catalytic efficiency of TNPC900 in 0.1 M KOH solution.

The superior ORR performance of TNPC900 may be largely influenced by the highest surface area, proper ratio of mesopores over micropores, and the role of pyridinic-N. Given that pyridinic-N served as the active sites for the adsorption and dissociation of oxygen [35], TNPC900 exhibited superior ORR activities than the other TNPCs. However, despite TNPC800 having a slightly lower surface area than TNPC900 and the highest nitrogen content (Table 1),

its effect was not as important to ORR as the  $E_{\rm o}$  and  $E_{1/2}$  were the lowest for TNPC800. This finding may be due to the higher proportion of micropores (56.6%) dominating the effect to ORR because the restricted active sites such as micropores were difficult to be wet by liquid electrolyte [36]. This finding was further supported by the higher ORR characteristics of TNPC1000 that even though the surface area and the nitrogen content were the least (Table 1), the larger proportion of mesopores was assumed to facilitate a better ORR activity than TNPC800.

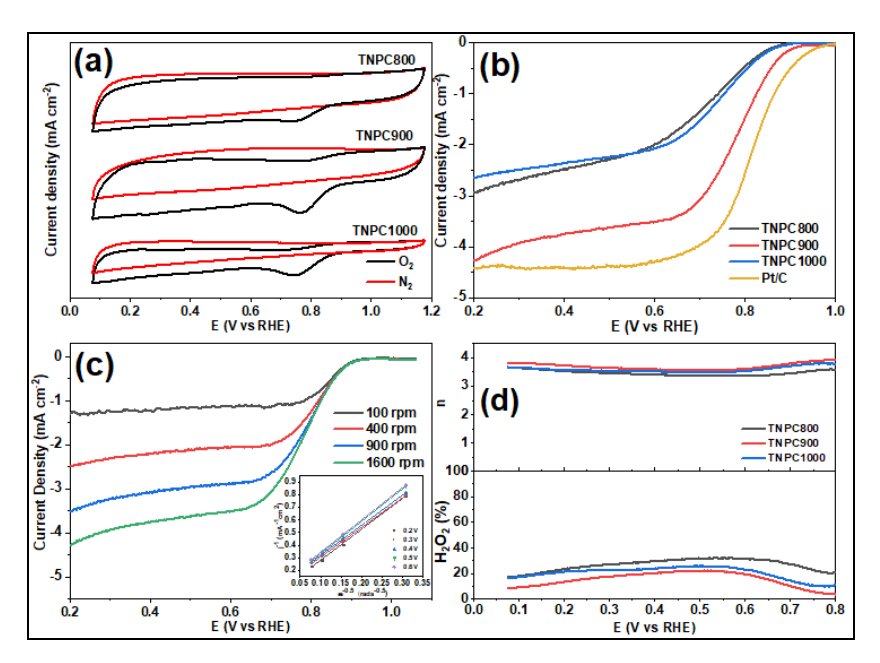


Figure 3. (a) CV curves of TNPCs in  $N_2$ - or  $O_2$ -saturated 0.1 M KOH solution. (b) LSV of samples and Pt/C. (c) LSV of TNPC900 at different rotation speeds (inset, K-L plots of TNPC at 0.2 V to 0.6 V vs. RHE). (d) Plots of number of electron transfer; n and  $H_2O_2$  yield of TNPC900 calculated from RRDE currents

#### Stability of TNPC900

To evaluate the durability of TNPC900, stability test particularly CV was performed in O<sub>2</sub>-saturated 0.1 M KOH at a scan rate of 100 mV s<sup>-1</sup>. After 1000 potential cycles, the E<sub>o</sub> and E<sub>1/2</sub> of TNPC900 remained unchanged (Figure 4a), whereas a significant negative shift was observed for Pt/C (Figure 4(a) inset) under the same condition. Pt/C also experienced 11% loss of the limiting current density. These results indicated TNPC900 had a relatively better stability than Pt/C

under alkaline condition. TNPC900 also showed good tolerance to methanol (Figure 4(b)) as the CV curve was similar before and after adding 3 M methanol. Conversely, a visible oxidation peak emerged for Pt/C (Figure 4(b) inset), which was typical owing to the higher selectivity of Pt for methanol oxidation reaction than ORR [37]. Therefore, the superior stability and methanol tolerance of TNPC900 over Pt/C signified possible application in direct methanol fuel-cell application.

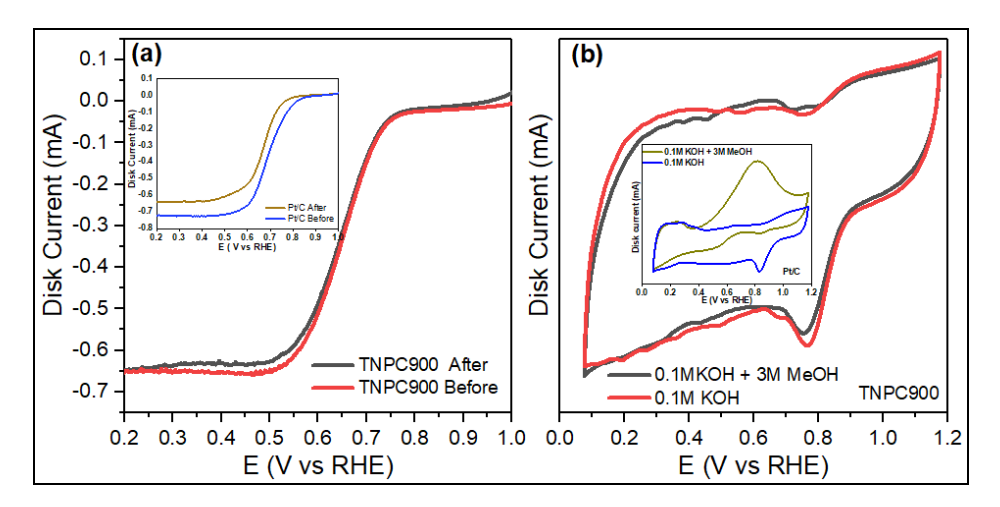


Figure 4. (a) LSV plots for TNPC900 (inset: Pt/C) before and after 1000 CV cycle in O<sub>2</sub>-saturated 0.1 M KOH. (b) CV curves for TNPC900 (inset: Pt/C) before and after 3 M methanol addition

#### Conclusion

We successfully fabricated nitrogen-doped porous carbon from textile waste through chemical activation pyrolysis. Calcium chloride-induced formation and urea served as the nitrogen precursor. Different pyrolysis temperatures (from 800 °C to 1000 °C) impacted the surface characteristics and ORR performance of the TNPCs produced. Among the TNPCs prepared, TNPC900 catalyst exhibited the highest ORR activity with the least H<sub>2</sub>O<sub>2</sub> formation. The excellent electrocatalytic activity may be attributed to the collusion of high surface area, proper ratio of mesopores and micropores, and high pyridinic-N. Although ORR performance was slightly inferior to that of Pt/C, TNPC900 is a good potential Pt substitute because of its abundantly available resource and simple production method. TNPC900 also showed better stability and methanol immunity than commercial Pt/C catalyst, making it potentially suitable for direct methanol fuel-cell application.

#### Acknowledgement

This work is financially supported by the Ministry of Higher Education of Malaysia: TRGS/1/2018/UKM/01/6/2 and Universiti Kebangsaan Malaysia: DIP-2019-021.

#### References

- Steele, B. C. H. and Heinzel, A. (2001). Materials for fuel-cell technologies. *Nature*, 414(6861): 345-352.
- 2. Wang, Y., Li, J. and Wei, Z. (2018). Transition-metal-oxide-based catalysts for the oxygen reduction reaction. *Journal of Materials Chemistry A*, 6(18): 8194-8209.
- Karim, N. A. and Kamarudin, S. K. (2013). An overview on non-platinum cathode catalysts for direct methanol fuel cell. *Applied Energy*, 103(9): 212-220.
- 4. Wu, Z., Song, M., Wang, J. and Liu, X. (2018). Recent progress in nitrogen-doped metal-free electrocatalysts for oxygen reduction reaction. *Catalysts*, 8(5): 196.
- Guo, D., Shibuya, R., Akiba, C., Saji, S., Kondo, T. and Nakamura, J. (2016). Active sites of nitrogen-doped carbon materials for oxygen reduction reaction clarified using model catalysts. *Science*, 351(6271): 361-365.
- 6. Li, J., Wang, S., Ren, Y., Ren, Z., Qiu, Y. and Yu, J. (2014). Nitrogen-doped activated carbon with micrometer-scale channels derived from luffa sponge fibers as electrocatalysts for oxygen reduction reaction with high stability in acidic media. *Electrochimica Acta*, 149: 56-64.

- Quílez-Bermejo, J., Morallón, E. and Cazorla-Amorós, D. (2020). Metal-free heteroatom-doped carbon-based catalysts for ORR. A critical assessment about the role of heteroatoms. *Carbon*, 165: 434-454.
- 8. Gao, Z., Zhang, Y., Song, N. and Li, X. (2017). Biomass-derived renewable carbon materials for electrochemical energy storage. *Materials Research Letters*, 5(2): 69-88.
- Borghei, M., Lehtonen, J., Liu, L. and Rojas, O. J. (2018). Advanced biomass-derived electrocatalysts for the oxygen reduction reaction. *Advanced Materials*, 30(24): 1703691.
- Kaur, P., Verma, G. and Sekhon, S. S. (2019).
   Biomass derived hierarchical porous carbon materials as oxygen reduction reaction electrocatalysts in fuel cells. *Progress in Materials Science*, 102: 1-71.
- 11. Zhou, H., Zhang, J., Zhu, J., Liu, Z., Zhang, C. and Mu, S. (2016). A self-template and KOH activation co-coupling strategy to synthesize ultrahigh surface area nitrogen-doped porous graphene for oxygen reduction. *RSC Advances*, 6(77): 73292-73300.
- Zheng, B., Wang, J., Pan, Z., Wang, X., Liu, S., Ding, S. and Lang, L. (2020). An efficient metalfree catalyst derived from waste lotus seedpod for oxygen reduction reaction. *Journal of Porous Materials*, 27(3): 637-646.
- 13. Polajnar Horvat, K. and Šrimpf Vendramin, K. (2021). Issues surrounding behavior towards discarded textiles and garments in Ljubljana. *Sustainability (Switzerland)*, 13(11): 1-11.
- USEPA (2019). Textiles: Material-specific data. Available from https://www.epa.gov/facts-and-figures-about-materials-waste-and-recycling/textiles-material-specific-data#TextilesOverview. [Accessed online: 16-Dec-2019].
- 15. Ramamoorthy, S. K., Skrifvars, M., Alagar, R. and Akhtar, N. (2018). End-of-life textiles as reinforcements in biocomposites. *Journal of Polymers and the Environment*, 26(2): 487-498.
- Sauid, S. M., Kamarudin, S. K., Karim, N. A. and Shyuan, L. K. (2021). Superior stability and methanol tolerance of a metal-free nitrogen-doped

- hierarchical porous carbon electrocatalyst derived from textile waste. *Journal of Materials Research* and *Technology*, 11: 1834-1846.
- Ge, X., Sumboja, A., Wuu, D., An, T., Li, B., Goh, F. W. T., ... and Liu, Z. (2015). Oxygen reduction in alkaline media: from mechanisms to recent advances of catalysts. ACS Catalysis, 5(8): 4643-4667.
- Ratso, S., Kruusenberg, I., Käärik, M., Kook, M., Saar, R., Kanninen, P., ... and Tammeveski, K. (2017). Transition metal-nitrogen co-doped carbide-derived carbon catalysts for oxygen reduction reaction in alkaline direct methanol fuel cell. *Applied Catalysis B: Environmental*, 219: 276-286.
- Zhou, R., Zheng, Y., Jaroniec, M. and Qiao, S. Z. (2016). Determination of the electron transfer number for the oxygen reduction reaction: From theory to experiment. ACS Catalysis, 6(7): 4720-4728.
- Tang, J., Wang, Y., Zhao, W., Zeng, R. J., Liu, T. and Zhou, S. (2019). Biomass-derived hierarchical honeycomb-like porous carbon tube catalyst for the metal-free oxygen reduction reaction. *Journal of Electroanalytical Chemistry*, 847: 113230.
- Shi, J., Lin, N., Lin, H. B., Yang, J. and Zhang, W. L. (2020). A N-doped rice husk-based porous carbon as an electrocatalyst for the oxygen reduction reaction. *Xinxing Tan Cailiao/New Carbon Materials*, 35(4): 401-409.
- Thommes, M., Smarsly, B., Groenewolt, M., Ravikovitch, P. I. and Neimark, A. V. (2006). Adsorption hysteresis of nitrogen and argon in pore networks and characterization of novel microand mesoporous silicas. *Langmuir*, 22(2): 756-764.
- 23. Jiang, M., Yu, X., Yang, H. and Chen, S. (2020). Optimization strategies of preparation of biomass-derived carbon electrocatalyst for boosting oxygen reduction reaction: A minireview. *Catalysts*, 10(12): 1-17.

- 24. Mao, X., Cao, Z., Yin, Y., Wang, Z., Dong, H. and Yang, S. (2018). Direct synthesis of nitrogen and phosphorus co-doped hierarchical porous carbon networks with biological materials as efficient electrocatalysts for oxygen reduction reaction. *International Journal of Hydrogen Energy*, 43(22): 10341-10350.
- 25. Zhao, Q., Ma, Q., Pan, F., Wang, Z., Yang, B., Zhang, J. and Zhang, J. (2016). Facile synthesis of nitrogen-doped carbon nanosheets as metal-free catalyst with excellent oxygen reduction performance in alkaline and acidic media. *Journal of Solid State Electrochemistry*, 20(5): 1469-1479.
- 26. Zhang, W., Qi, J., Bai, P., Wang, H. and Xu, L. (2019). High-level nitrogen-doped, micro/mesoporous carbon as an efficient metal-free electrocatalyst for the oxygen reduction reaction: Optimizing the reaction surface area by a solvent-free mechanochemical method. *New Journal of Chemistry*, 43(27): 10878-10886.
- 27. Lazar, P., Mach, R. and Otyepka, M. (2019). Spectroscopic fingerprints of graphitic, pyrrolic, pyridinic, and chemisorbed nitrogen in N-doped graphene. *Journal of Physical Chemistry C*, 123(16): 10695-10702.
- 28. Zainul Abidin, A. F., Loh, K. S., Wong, W. Y. and Mohamad, A. B. (2019). Nitrogen-doped carbon xerogels catalyst for oxygen reduction reaction: Improved structural and catalytic activity by enhancing nitrogen species and cobalt insertion. *International Journal of Hydrogen Energy*, 44(54): 28789-28802.
- 29. Sharifi, T., Hu, G., Jia, X. and Wågberg, T. (2012). Formation of active sites for oxygen reduction reactions by transformation of nitrogen functionalities in nitrogen-doped carbon nanotubes. *ACS Nano*, 6(10): 8904-8912.
- Liu, R., Zhang, H., Liu, S., Zhang, X., Wu, T., Ge, X., ... and Wang, G. (2016). Shrimp-shell derived carbon nanodots as carbon and nitrogen sources to fabricate three-dimensional N-doped porous carbon electrocatalysts for the oxygen reduction reaction. *Physical Chemistry Chemical Physics*, 18(5): 4095-4101.
- 31. Zheng, F. Y., Li, R., Ge, S., Xu, W. R. and Zhang, Y. (2020). Nitrogen and phosphorus co-doped

- carbon networks derived from shrimp shells as an efficient oxygen reduction catalyst for microbial fuel cells. *Journal of Power Sources*, 446: 227356.
- 32. Lai, L., Potts, J. R., Zhan, D., Wang, L., Poh, C. K., Tang, C. and Ruoff, R. S. (2012). Exploration of the active center structure of nitrogen-doped graphene-based catalysts for oxygen reduction reaction. *Energy and Environmental Science*, *5*(7): 7936-7942.
- 33. Xu, S. S., Qiu, S. W., Yuan, Z. Y., Ren, T. Z. and Bandosz, T. J. (2019). Nitrogen-containing activated carbon of improved electrochemical performance derived from cotton stalks using indirect chemical activation. *Journal of Colloid and Interface Science*, 540: 285-294.
- 34. Akula, S. and Sahu, A. K. (2019). Heteroatoms codoping (N, F) to the porous carbon derived from spent coffee grounds as an effective catalyst for oxygen reduction reaction in polymer electrolyte fuel cells. *Journal of The Electrochemical Society*, 166(2): F93-F101.
- 35. Li, D., Fan, Y., Yuan, H., Deng, L., Yang, J., Chen, Y. and Luo, B. (2020). Renewable and metal-free carbon derived from aquatic scindapsus affording meso–microporosity, large interface, and enriched pyridinic-N for efficient oxygen reduction reaction catalysis. *Energy & Fuels*, 34(10): 13089-13095.
- 36. Fan, Z., Li, J., Zhou, Y., Fu, Q., Yang, W., Zhu, X. and Liao, Q. (2017). A green, cheap, high-performance carbonaceous catalyst derived from *Chlorella pyrenoidosa* for oxygen reduction reaction in microbial fuel cells. *International Journal of Hydrogen Energy*, 42(45): 27657-27665.
- 37. Cao, C., Wei, L., Zhai, Q., Wang, G. and Shen, J. (2017). Biomass-derived nitrogen and boron dual-doped hollow carbon tube as cost-effective and stable synergistic catalyst for oxygen electroreduction. *Electrochimica Acta*, 249: 328-336.

# Malaysian Journal of Analytical Sciences (MJAS)



Published by Malaysian Analytical Sciences Society

## PHOTOCATALYTIC HYDROGEN GENERATION FROM WATER BY TiO<sub>2</sub>/Co<sub>3</sub>O<sub>4</sub> COMPOSITE PHOTOCATALYSIS

(Penjanaan Hidrogen Fotokatalitik dari Molekul Air Mengunakan Komposi Fotomangkin TiO<sub>2</sub>/Co<sub>3</sub>O<sub>4</sub>)

Siti Nurul Falaein Moridon<sup>1</sup>, Dian Anggraini<sup>2</sup>, Khuzaimah Arifin<sup>1</sup>\*, Lorna Jeffery Minggu<sup>1</sup>, Mohammad B. Kassim<sup>1,3</sup>

<sup>1</sup>Fuel Cell Institute,

Universiti Kebangsaan Malaysia, 43600 UKM Bangi, Selangor, Malaysia

<sup>2</sup>Department of Chemistry, Faculty of Mathematic and Natural Science,
Universitas Riau, Kampus Binawidya, Km 12.5 Simpang Baru, Pekan baru, Riau, Indonesia,

<sup>3</sup>Faculty of Science and Technology,
Universiti Kebangsaan Malaysia, 43600 UKM Bangi, Selangor, Malaysia

\*Corresponding author: khuzaim@ukm.edu.my

Received: 28 November 2021; Accepted: 6 March 2022; Published: 27 June 2022

#### Abstract

Titanium dioxide ( $TiO_2$ ) is one of the most studied materials as photocatalyst of water splitting for hydrogen generation. However,  $TiO_2$  has a large band gap of around 3.2 eV, limits its absorption energy to visible light, and the photoexcitation products, such as electron and hole, are recombined rapidly. One method to overcome this problem is by creating a composite heterojunction with other semiconductor materials. In this study, the photocatalytic hydrogen generation of water splitting by  $TiO_2/Co_3O_4$  composite photocatalyst was evaluated. The composite was prepared through hydrothermal synthesis assisted by ball mill crushing, and the powder was annealed at 550 °C. The percentage of  $Co_3O_4$  loading on the  $TiO_2$  varied at 0.5% w/w (TC-05), 1% w/w (TC-1), and 2% w/w (TC-2) to study the suitable amount of  $Co_3O_4$ . The surface morphology of the composites was investigated through field emission scanning electron microscopy (FESEM) analyses. Results showed that nanosphere and cubic—shaped morphologies were obtained. For the hydrogen performance analysis, two different conditions of photocatalytic hydrogen generation, which are in pure water and water with addition of 10 vol% of methanol solution as the sacrificial reagent, were measured by using a hydrogen sensor (UNISENSE). TC-1 showed the highest hydrogen production in the pure water, which is 6.75  $\mu$ mol h<sup>-1</sup> g<sup>-1</sup> compared with others. The addition of 10% methanol enhanced the hydrogen production by three times compared with pure water (20.22  $\mu$ mol h<sup>-1</sup> g<sup>-1</sup>. The superior heterojunction of  $TiO_2$  and  $Co_3O_4$  performance can be used in practical applications to enhance the photocatalytic properties of  $TiO_2$ .

Keywords: cobalt oxide, hydrogen production, PEC, titanium dioxide

#### **Abstrak**

Titanium dioksida (TiO<sub>2</sub>) adalah salah satu bahan yang paling banyak dikaji sebagai fotomangkin pembelahan molekul air untuk penjanaan hidrogen. Walau bagaimanapun, TiO<sub>2</sub> mempunyai jurang jalur yang besar sekitar 3.2 eV, yang mengehadkan tenaga

### Siti Nurul Falaein: PHOTOCATALYTIC HYDROGEN GENERATION FROM WATER BY TiO<sub>2</sub>/Co<sub>3</sub>O<sub>4</sub> COMPOSITE PHOTOCATALYSIS

penyerapannya kepada cahaya nampak, dan hasil fotopengujaan, iaitu, elektron dan lubang mengakibatkan bergabung semula dengan cepat. Salah satu cara untuk mengatasi masalah tersebut ialah dengan mencipta gabungan komposit dengan bahan semikonduktor lain. Dalam kajian ini, untuk penjanaan hidrogen bagi pembelahan molekul air fotomangkin gabungan komposit TiO<sub>2</sub>/Co<sub>3</sub>O<sub>4</sub> telah dinilai. Kaedah sintesis hidroterma dibantu oleh proses penghancuran penggilingan bebola yang digunakan untuk menyediakan komposit berikutan penyepuhlindapan serbuk pada 550 °C. Peratusan pengabungan Co<sub>3</sub>O<sub>4</sub> pada TiO<sub>2</sub> telah divariasi pada 0.5% w/w (TC-05), 1% w/w (TC-1), dan 2% w/w (TC-2) untuk mengkaji kadar Co<sub>3</sub>O<sub>4</sub> yang sesuai. Morfologi permukaan komposit telah disiasat menggunakan analisis FESEM. Berdasarkan FESEM menunjukkan nanosfera dan berbentuk kubik. Untuk analisis prestasi hidrogen, dua keadaan berbeza penjanaan hidrogen fotokatalitik iaitu dalam air tulen dan air ditambah 10 vol % larutan metanol sebagai reagen, dan telah diukur menggunakan sensor hidrogen (UNISENSE). Hasilnya, TC-1 menunjukkan pengeluaran hidrogen tertinggi dalam air tulen iaitu 6.75 μmol h<sup>-1</sup> g<sup>-1</sup> berbanding yang lain. Penambahan 10% metanol meningkatkan pengeluaran hidrogen 3 kali lebih tinggi berbanding dengan air tulen 20.22 μmol h<sup>-1</sup> g<sup>-1</sup>. Gabungan komposit TiO<sub>2</sub> dan Co<sub>3</sub>O<sub>4</sub> boleh digunakan dalam aplikasi praktikal meningkatkan sifat fotomangkin TiO<sub>2</sub>.

Kata kunci: kobalt oksida, pengeluaran hidrogen, PEC, titanium dioksida

#### Introduction

The growth in global population and quality of life has caused a remarkably increase in energy consumption, where fossil-based fuels are the primary energy contributors to date. Given the nonrenewable nature of fossil fuels, they will be depleted if humans do not undertake steps to safeguard these resources. Alternative fuels are necessary to fulfil future energy demands if fossil fuels are no longer available, particularly for the transportation sector, which consumes around 60% of global energy [1, 2]. Hydrogen was identified four decades ago as a fundamental element of a feasible future energy framework for giving safe, savvy, and ecologically harmless energy. The Energy Policy Act of 1992 classifies hydrogen as an alternative fuel. The ability to power fuel cells in zero-emission cars and the fuel cell's rapid filling time and high efficiency have sparked interest in hydrogen as an alternative transportation fuel. A fuel cell with an electric motor is two to three times more efficient than a gasolinepowered internal combustion engine. Internal combustion engines may use hydrogen as a fuel [3, 4].

The availability of H<sub>2</sub> has become a new barrier because it is not naturally accessible on earth. Hydrogen may be found in a variety of forms, including hydrocarbons, water molecules, and acid and base molecules. Thus, H<sub>2</sub> must be eliminated from all of the abovementioned sources [5]. Coal gasification, steam reforming of natural gas, cryogenic distillation, and water splitting are the methods used for producing

commercial hydrogen [6]. Coal gasification and steam reforming of natural gas processes can produce significant quantities of hydrogen. However, these approaches need a strong and safe system due to the tremendous energy consumption (temperatures > 1000 °C) necessary to perform reactions [7]. Electricity generated from renewable energy sources, such as hydropower, wind power, and solar power, might be used to electrolyze water molecules. However, these procedures are inefficient and costly [8]. Photocatalytic water splitting technologies have gained considerable interest for producing green and sustainable hydrogen energy from water. The intrinsic features and architectures of semiconductor-based photocatalysts and photoelectrodes have a large influence on the efficiency of solar-to-hydrogen conversion photocatalytic and/or PEC catalysis [9].

Titanium dioxide (TiO<sub>2</sub>) became the most widely used photocatalyst in the 1970s when water splitting drew the attention of researchers. This condition is due to the low cost, chemical stability, Earth abundance, and nontoxicity of TiO<sub>2</sub>. Unfortunately, the potential of TiO<sub>2</sub> is limited because of its high band gap width, poor conductivity, and problematic excited dissociation and electron transport. Thus, many studies have focused on improving the TiO<sub>2</sub>'s photocatalytic efficacy by changing its surface and microstructure, adding cocatalysts, and creating heterojunctions with metals or other semiconductors [10]. Engineered heterojunctions in photocatalysts were revealed to be a viable approach for increasing catalyst activity by allowing

photogenerated electron-hole pairs to be separated spatially. Co<sub>3</sub>O<sub>4</sub> is a good choice for fabricating TiO<sub>2</sub>based hybrids for water splitting because Co<sub>3</sub>O<sub>4</sub> is one of the most well-known p-type semiconductors, with incredible substance dependability, low solvency, and solid electrical, attractive, and reactant attributes. The cost-effectiveness and availability of Co-based chemicals may simplify large-scale applications [11-13]. Compared with the typical hydrogen electrode, Co<sub>3</sub>O<sub>4</sub> has conduction band (CB) and valence band (VB) areas of 0.97 and 1.23 eV, respectively, thereby resulting in a p-n heterointersection with TiO2. The performance of a combination of varying weight percent of TiO2/Co3O4 thin films in PEC and photocatalytic water splitting was investigated in this work. TiO<sub>2</sub> P25 was used to make a heterojunction with Co<sub>3</sub>O<sub>4</sub> by using a hydrothermal technique.

#### **Materials and Methods**

#### Materials

Cobalt nitrate hexahydrate Co (NO<sub>3</sub>)<sub>2</sub>.6H<sub>2</sub>O and TiO<sub>2</sub> P25 were obtained from Sigma-Aldrich. Urea (analytical grade), polyethylene glycol, and ethanol were purchased from Chem-Supply. All chemicals were used without further purification.

#### Preparation of TiO<sub>2</sub>

Ethanol (1 mL) was mixed with 0.2 g of TiO<sub>2</sub> P25 and 0.05 g of polyethylene glycol, and the mixture was crushed. Blade coating was used to coat the slurry on the fluorine-doped tin oxide (FTO) surface at 0.5 mm thickness, which was then annealed at 500 °C for 2 h.

#### Synthesis of cobalt oxide

In accordance with prior research, cobalt oxide was produced by using a hydrothermal technique [11]. Cobalt nitrate hexahydrate (1.74 g) and urea (0.72 g) were dissolved in 50 mL deionized water. A stainless-steel autoclave was used to transfer the homogenous solution. The autoclave was placed in a furnace for 6 h at 100 °C. The autoclave was turned off and allowed to cool to ambient temperature. The sample was washed with deionized water before being dried in an oven. Cobalt oxide produced by hydrothermal technique was ball milled for 2 h before being mixed with TiO<sub>2</sub>.

### Synthesis of the composite heterojunction of $TiO_2$ and $Co_3O_4$ as a sample

 $TiO_2$ ,  $Co_3O_4$ , polyethylene glycol, and ethanol were ball milled for 20 min, coated over the FTO surface, and annealed for 2 h at 550 °C. TC-05 (0.5%  $Co_3O_4$ .TiO<sub>2</sub>), TC-1 (1%  $Co_3O_4$ .TiO<sub>2</sub>), and TC-2 (2%  $Co_3O_4$ .TiO<sub>2</sub>) were the three weight variants of  $TiO_2$ : $Co_3O_4$ . The sample was characterized and used as a working electrode.

#### Characterization

A field emission scanning electron microscopy (FESEM) model of ZEISS MERLIN was used to examine the surface morphology with 10k magnification and signal A intense duo.

#### **Electrochemical study**

In a three-electrode setup with 0.5 M  $Na_2SO_4$  electrolyte solution, linear sweep voltammetry (LSV) analysis was performed by using an Ametek Versastat 4 under a  $100 \text{ mW/cm}^2$  xenon light. The working electrodes were  $TiO_2/Co_3O_4$  thin films, the counter electrodes were platinum wires, and the reference electrodes were Ag/AgCl electrodes.

#### Photocatalytic H<sub>2</sub> generation measurements

The sample (100 mg) was weighed and placed in a reactor to conduct the photocatalytic  $H_2$  generation measurements. The sample was added with 100 mL of sodium sulfate and placed under solar AM 1.3 illumination (100 mW cm $^{-2}$ ) using 75 W Xenon light at 500 nm bandwidth for 2 h, and hydrogen readings were taken every 20 min. The steps were repeated by adding methanol as scavenger, and the readings were taken. In this study, a hydrogen sensor was used to measure the hydrogen produced through a photochemical process.



Figure 1. Photoreactor set up for the photocatalytic H<sub>2</sub> generation measurements

#### **Results and Discussion**

#### **Characterizations of catalysts**

Figure 2 displays the FESEM images of the asprepared (a)  $TiO_2$  (b) TC-05, (c) TC-1, and (d) TC-2 samples. From Figure 2a, the  $TiO_2$  shows well-defined nanocubic morphology, with the width of 1.011  $\mu$ m. Figures 2b–c shows that the loaded  $Co_3O_4$  is finely dispersed on the  $TiO_2$  surface with a diameter of approximately 7.14 nm. Figure 2d shows that an obvious agglomeration occurs during the introduction of  $Co_3O_4$  species. The result is mostly similar to a previous study [12]. However, the different weight percentages of composite heterojunction show different sizes of loaded  $Co_3O_4$  [12].

LSV analysis was used to study the potential of the photocatalyst, and the overpotentials of TC-05, TC-1, and TC-2 were calculated. Figure 3a shows the photocurrent responses of (a)  $TiO_2$ , (b) TC-05, (c) TC-1, and (d) TC-2 samples. TC-1 had the highest photocurrent density (70  $\mu$ A cm<sup>-2</sup>) among the

composites, implying that coating TiO2 with Co3O4 nanoparticles (NPs) improved the photogeneration performance. However, the photocurrent decreased when the Co<sub>3</sub>O<sub>4</sub> composites increased to 2 wt.%. This condition occurred because of the agglomeration of the photocatalyst, as shown in the FESEM image (Figure 2d). The agglomeration of the photocatalyst decreased the active site and surface area. EIS analysis was used to test the charge carrier transport capabilities of the composites (Figure 3b), The Nyquist plot of TC-1 was less than that of TC-05 and TC-2. This finding revealed that the TC-1 sample had the lowest electron migration resistance among the samples, indicating that it had a high photocatalytic hydrogen evolution reaction (HER) performance. These findings suggested that the TC-1 sample had the best charge detachment behavior of photogenerated carriers among the photocatalyst samples. The amount of active free radicals available for photocatalytic H<sub>2</sub> creation will rise if charge carrier separation was effective [14].

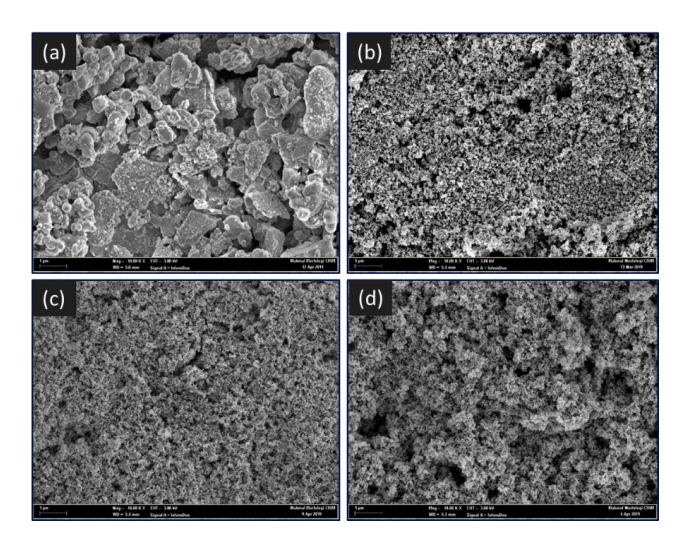


Figure 2. FESEM image of (a)  $TiO_2$  (b) TC-05, (c) TC-1, and (d) TC-2

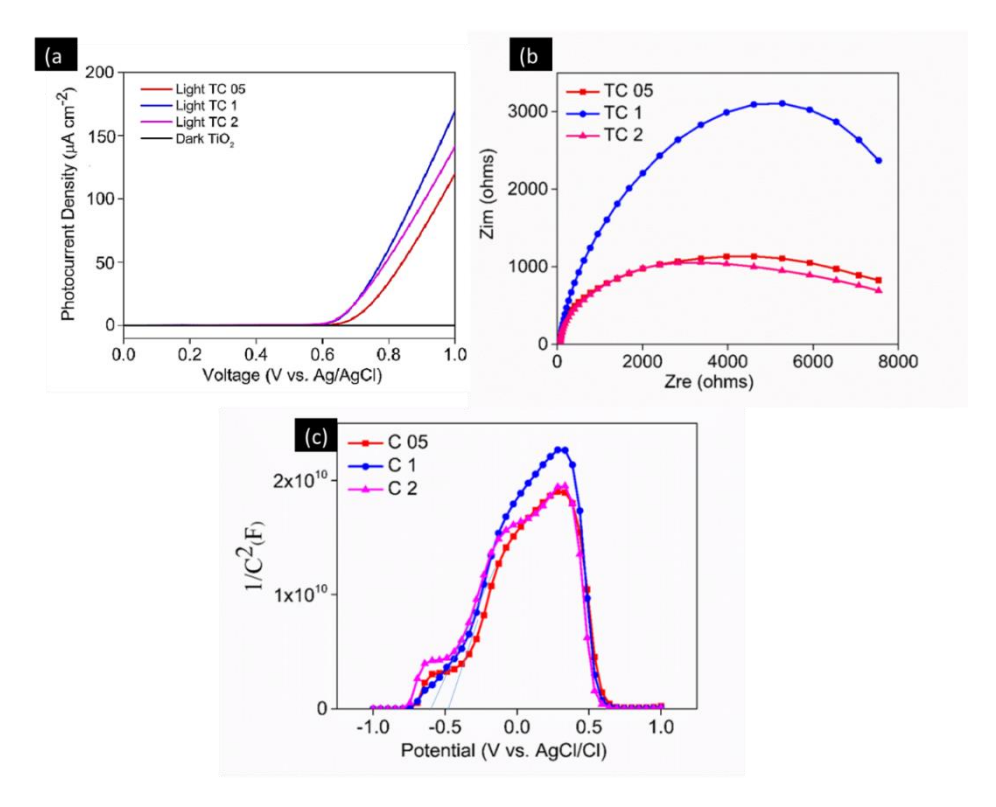


Figure 3. (a) Photocurrent density (b) Electrochemical impedance spectroscopy (EIS), and (c) Mott–Schottky plot of TC-05, TC-1 and TC-2

#### Photocatalytic hydrogen generation

The photocatalytic hydrogen evolution of the prepared samples was evaluated under artificial sunlight irradiation by using a hydrogen sensor. The photocatalytic hydrogen evolution was tested in two different solutions, and the results were compared. The first analysis (Figure 3a) was tested by using only pure water, and the second analysis (Figure 4b) was tested by using pure water with the addition of 10 vol% of methanol solution as the sacrificial reagent. The comparison of Figures 4a and b showed that the sample with methanol exhibited three times excellent photocatalytic hydrogen evolution as compared without methanol. As shown in Figures 4a and b, the TC-1 sample exhibited the highest H<sub>2</sub> advancement rate (6.75  $\mu$ mol g<sup>-1</sup>h<sup>-1</sup>) in pure water and (20.22  $\mu$ mol g<sup>-1</sup>h<sup>-1</sup>) in methanol among all the prearranged Co<sub>3</sub>O<sub>4</sub>/TiO<sub>2</sub> tests. The H<sub>2</sub> production in methanol is higher compared with pure water because methanol effectively separates the hole charges, and the hole-electron pair

recombination is reduced [15]. The  $H_2$  advancement rate of TC-2 diminished to 5.70  $\mu$ mol  $g^{-1}h^{-1}$  in pure water and 16.71  $\mu$ mol  $g^{-1}h^{-1}$  in methanol.

The photocatalytic HER of the proposed TiO<sub>2</sub>/Co<sub>3</sub>O<sub>4</sub> heterojunctions is shown in Figure 5 to analyze the composite heterojunction of TiO<sub>2</sub>/Co<sub>3</sub>O<sub>4</sub>. A previous study [11] provided the specifics of the Co<sub>3</sub>O<sub>4</sub> band structure. TiO<sub>2</sub> has a higher Fermi level than Co<sub>3</sub>O<sub>4</sub> before they come into contact in the heterojunction. Negative charges migrated from TiO<sub>2</sub> to Co<sub>3</sub>O<sub>4</sub> after the heterojunction because p-type Co<sub>3</sub>O<sub>4</sub> NPs developed on the surface of n-type TiO<sub>2</sub>. This condition caused the Fermi level alignment between  $TiO_2$  and  $Co_3O_4$ , resulting in a p-n  $Co_3O_4/TiO_2$ junction. According to Wang et al. (2022), a space charge region with a strong built-in electric field in the TiO<sub>2</sub> to Co<sub>3</sub>O<sub>4</sub> direction occurs at the TiO<sub>2</sub>/Co<sub>3</sub>O<sub>4</sub> interface when the energy bands of TiO2 and Co3O4 are bent up and down, resulting in a drift of the

photogenerated charge carrier for heat transfer until a balance thermal equilibrium is reached [16]. The charge transfer mechanism is shown in Figure 5. Under solar AM 1.3 illumination, photogenerated electrons migrated from TiO<sub>2</sub> and Co<sub>3</sub>O<sub>4</sub> VBs to the corresponding CBs. The photogenerated electrons were guided from the p-type Co<sub>3</sub>O<sub>4</sub> CB to the n-type TiO<sub>2</sub> CB by the induced built-in electric field, resulting in

the spatial detachment of photogenerated electron–hole sets. Similarly,  $\text{Co}_3\text{O}_4$  NPs filled in as a cocatalyst in this p-n  $\text{Co}_3\text{O}_4/\text{TiO}_2$  intersection, assisting in expanding the charge partition. Therefore, more photogenerated electrons might focus on  $\text{TiO}_2$ , which can then be used in the water reduction cycle to produce  $\text{H}_2$ .

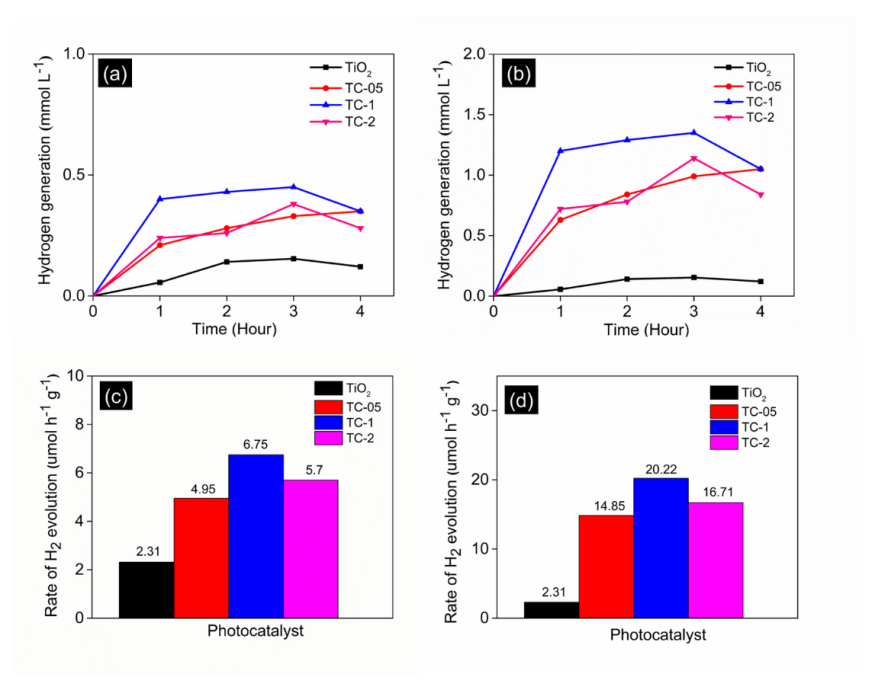


Figure 4. Photocatalytic hydrogen evolution of sample with (a) pure water (b) pure water and methanol, and hydrogen evolution rate of sample with (c) pure water and (d) pure water and methanol.

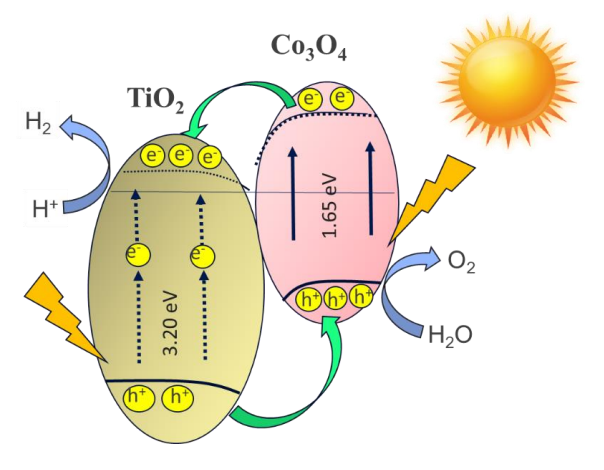


Figure 5. Schematic of the photocatalytic HER mechanism and photogenerated electron–hole separation route of Co<sub>3</sub>O<sub>4</sub>/TiO<sub>2</sub> *p*–*n* junction.

#### Conclusion

In this study, hydrothermal synthesis was used to efficiently construct a  $Co_3O_4/TiO_2$  p-n heterojunction. With a photocatalytic  $H_2$  development pace of 20.22 mol  $g^{-1}h^{-1}$ , the enhanced  $Co_3O_4/TiO_2$  heterojunction had the best photocatalytic  $H_2$  advancement rate. This study used the catalytic effect of  $Co_3O_4$  to distinguish photogenerated electron-hole pairs. A unique  $Co_3O_4/TiO_2$  contact interface and a p-n heterojunction was utilized for fast charge carrier transport pathways to enhance the photocatalytic performance. This study may help in the future development and production of p-n heterojunction photocatalyst with high visible light-driven energy conversion efficiency.

#### Acknowledgment

This work was supported by the Malaysia's Ministry of Education through the FRGS/1/2019/STG01/UKM/03/2 research grant.

#### References

- 1. Acar, C. and Dincer, I. (2020). The potential role of hydrogen as a sustainable transportation fuel to combat global warming. *International Journal of Hydrogen Energy*, 45(5): 3396-3406.
- Rath, B. N., Akram, V., Bal, D. P. and Mahalik, M. K. (2019). Do fossil fuel and renewable energy consumption affect total factor productivity growth? Evidence from cross-country data with policy insights. *Energy Policy*, 127: 186-199.
- 3. Griffiths, S., Sovacool, B. K., Kim, J., Bazilian, M. and Uratani, J. M. (2021). Industrial decarbonization via hydrogen: A critical and systematic review of developments, sociotechnical systems and policy options. *Energy Research & Social Science*, 80: 102208.
- Zhao, F., Mu, Z., Hao, H., Liu, Z., He, X., Victor Przesmitzki, S. and Ahmad Amer, A. (2020). Hydrogen fuel cell vehicle development in China: An industry chain perspective. *Energy Technology*, 8(11): 2000179.
- Hosseini, S. E. and Wahid, M. A. (2020). Hydrogen from solar energy, a clean energy carrier from a sustainable source of energy. *International Journal of Energy Research*, 44(6): 4110-4131.

- 6. Mah, A. X. Y., Ho, W. S., Bong, C. P. C., Hassim, M. H., Liew, P. Y., Asli, U. A., ... and Chemmangattuvalappil, N. G. (2019). Review of hydrogen economy in Malaysia and its way forward. *International Journal of Hydrogen Energy*, 44(12): 5661-5675.
- 7. Ahmad, H., Kamarudin, S. K., Minggu, L. J. and Kassim, M. (2015). Hydrogen from photo-catalytic water splitting process: A review. *Renewable and Sustainable Energy Reviews*, 43: 99-610.
- 8. Acar, C. and Dincer, I. (2019). Review and evaluation of hydrogen production options for better environment. *Journal of Cleaner Production*, 218: 835-849.
- 9. Qureshy, A. M., Ahmed, M. and Dincer, I. (2019). Performance assessment study of photo-electrochemical water-splitting reactor designs for hydrogen production. *International Journal of Hydrogen Energy*, 44(18): 9237-9247.
- Arifin, K., Yunus, R. M., Minggu, L. J. and Kassim, M. B. (2021). Improvement of TiO<sub>2</sub> nanotubes for photoelectrochemical water splitting. *International Journal of Hydrogen Energy*, 46(7): 4998-5024.
- Moridon, S. N. F., Salehmin, M. I., Mohamed, M. A., Arifin, K., Minggu, L. J. and Kassim, M. B. (2019). Cobalt oxide as photocatalyst for water splitting: Temperature-dependent phase structures. *International Journal of Hydrogen Energy*, 44(47): 25495-25504.
- Anggraini, D., Wardani, P. K., Agustina, M., Awaluddin, A.and Arifin, K. (2019). TiO<sub>2</sub>/Co<sub>3</sub>O<sub>4</sub> Composite as photoanode of photoelectrochemical water splitting. *In Journal of Physics: Conference Series*, 1351: 012032.
- 13. Moridon, S. N. F., Salehmin, M. N. I., Arifin, K., Minggu, L. J. and Kassim, M. B. (2021). Synthesis of cobalt oxide on FTO by hydrothermal method for photoelectrochemical water splitting application. *Applied Sciences*, 11(7): 3031.

### Siti Nurul Falaein: PHOTOCATALYTIC HYDROGEN GENERATION FROM WATER BY TiO<sub>2</sub>/Co<sub>3</sub>O<sub>4</sub> COMPOSITE PHOTOCATALYSIS

- 14. Kumar, S.G. and Rao, K. K. (2017). Comparison of modification strategies towards enhanced charge carrier separation and photocatalytic degradation activity of metal oxide semiconductors (TiO<sub>2</sub>, WO<sub>3</sub> and ZnO), *Applied Surface Science*, 2017: 391124-148.
- Alenzi, N., Liao, W. S., Cremer, P. S., Sanchez-Torres, V., Wood, T. K., Ehlig-Economides, C. and Cheng, Z. (2010). Photoelectrochemical hydrogen production from water/methanol
- decomposition using Ag/TiO<sub>2</sub> nanocomposite thin films. *International Journal of Hydrogen Energy*, 35(21): 11768-11775.
- Wang, L., Tang, G., Liu, S., Dong, H., Liu, Q., Sun, J. and Tang, H. (2022). Interfacial active-siterich 0D Co<sub>3</sub>O<sub>4</sub>/1D TiO<sub>2</sub> pn heterojunction for enhanced photocatalytic hydrogen evolution. *Chemical Engineering Journal*, 428: 131338.

# Malaysian Journal of Analytical Sciences (MJAS)



Published by Malaysian Analytical Sciences Society

# THE THERMAL STABILITY AND PRELIMINARY PERFORMANCE OF SODIUM ALGINATE AND POLYVINYL ALCOHOL-BASED MEMBRANE IN DMFC: MONTMORILLONITE AS A FILLER

(Kestabilan Haba dan Prestasi Awal Membran Berasaskan Natrium Alginat dan Polivinil Alkohol untuk DMFC: Montmorillonit sebagai Pengisi)

Maryam Taufiq Musa and Norazuwana Shaari\*

Fuel Cell Institute, Universiti Kebangsaan Malaysia, Bangi,43600, Selangor, Malaysia

\*Corresponding author: norazuwanashaari@ukm.edu.my

Received: 15 December 2021; Accepted: 24 March 2022; Published: 27 June 2022

#### Abstract

Biopolymer-based membranes have emerged vastly in recent years for fuel cell applications. Polymer electrolyte membranes (PEM) have become a major component in DMFC stacks that have gone through many studies beforehand. An improvement has been made to PEM, especially using biopolymers like alginate based. Sodium alginate (SA) has significant characteristics such as being too hydrophilic, which is its biggest weakness as a PEM. Blending it with another polymer of polyvinyl alcohol (PVA) and adding a clay filler of montmorillonite (MMT) would be a great solution, in this work. From TGA-DSC analysis, SA/PVA-MMT achieved different thermal stability as the filler content differed. The glass transition temperature of the membrane had increased as the MMT content increased, at a maximum range of 240-260 °C at 15 wt.% of MMT content. The membrane's thermal stability ranking was then followed by 10 wt.% (250 °C) and 2 wt.% (240 °C) of filler content. The higher the glass transition temperature, the greater the thermal stability due to the greater mass loss after being exposed to a later heating. Meanwhile, for the proton conductivity test, a hybrid membrane of SA/PVA-MMT with SVM 20 (20 wt.% MMT) obtained the highest value of 8.0510 mS/cm, followed by SVM 10, SVM 2, SVM 15 and SVM 5 with values of 6.5025, 2.6429, 2.0332 and 1.6083 mS/cm respectively. Higher proton conductivity enables the potential of the hybrid to conduct electricity in DMFC. The lowest methanol uptake was shown by the membrane with 20 wt.% MMT content, with a value of 53.00%, followed by 15 wt.% (97.46%), 10 wt.% (121.59%), 5 wt.% (132.23%) and 2 wt.% (203.30%), respectively. Low methanol uptake of the membrane indicated that the DMFC stack could operate with high efficiency. This study showed that SA/PVA-MMT could be a promising choice of PEM with an optimum MMT content of 10 wt.% for a better performance produced by a cheaper hybridized membrane.

Keywords: alginate, polyvinyl alcohol, montmorillonite, copolymer membrane, thermal stability

#### **Abstrak**

Membran berasaskan biopolimer telah muncul secara meluas sejak kebelakangan tahun ini, dalam aplikasi sel fuel. Membran polimer elektrolit (PEM) telah menjadi komponen utama dalam tindanan DMFC, yang mana telah menjadi objek kajian berkali ganda sebelumnya. Satu penambahbaikan PEM telah dibuat khususnya menggunakan biopolimer alginat. Natrium Alginat (SA)

#### Maryam & Norazuwana: THE THERMAL STABILITY AND PRELIMINARY PERFORMANCE OF SODIUM ALGINATE AND POLYVINYL ALCOHOL-BASED MEMBRANE IN DMFC: MONTMORILLONITE AS A FILLER

mempunyai sifat signifikan iaitu terlalu hidrofili, yang mana ianya merupakan kelemahan terbesar sebagai PEM. Di dalam kajian ini, Natrium alginat (SA) akan dicampur bersama polivinil alkohol (PVA) dan montmorillonit (MMT), sejenis pengisi berasaskan tanah liat. Campuran ini telah menghasilkan prestasi yang amat baik. Daripada analisis TGA-DSC, SA/PVA-MMT telah mencapai kestabilan haba yang berbeza apabila kandungan pengisi turut berbeza. Suhu peralihan kaca membran tersebut bertambah apabila kandungan MMT dalam sampel juga bertambah, pada 15 wt.% MMT, maksima julat suhu dicapai ialah 240-260 °C. Kestabilan haba membran ini kemudiannya diikuti dengan 10 wt.% (250 °C) dan 2 wt.% (240 °C) konten pengisi. Semakin tinggi suhu peralihan kaca, semakin tinggi kestabilan haba membran disebabkan jisim mula berkurang banyak pada suhu pemanasan yang tinggi (lebih lewat). Manakala untuk kekonduksian proton, SVM 20 (20 wt.% MMT) mendapat nilai tertinggi iaitu, 8.0510 mS/cm, diikuti dengan SVM 10, SVM 2, SVM 15 dan SVM 5 dengan nilaian 6.5025, 2.6429, 2.0332 dan 1.6083 mS/cm masing-masing. Tingginya nilai kekonduksian proton, semakin besarlah potensi membran hibrid tersebut untuk mengalirkan elektrik dalam DMFC. Ambilan metanol terendah dibuktikan oleh SVM 20 (20 wt.% MMT) dengan nilaian 53.00%, diikuti dengan 15 wt.% (97.46%), 10 wt.% (121.59%), 5 wt.% (132.23%) dan 2 wt% (203.30%) masing-masing. Hasil ambilan metanol yang rendah menunjukkan tindanan DMFC boleh beroperasi pada tahap keberkesanan yang tinggi. Kajian ini menyimpulkan bahawa SA/PVA-MMT boleh menjadi pilihan PEM yang terbaik, dengan kandungan MMT optimum pada 10 wt% beserta kos yang rendah untuk prestasi yang lebih baik.

Kata kunci: alginat, polivinil alkohol, montmorillonit, membran dwipolimer, kestabilan haba

#### Introduction

A polymer electrolyte membrane (PEM) that contains additives is normally able to enhance performance when operating in a fuel cell system. There are many polymers, such as sulfonated poly(ether ether) ketone [1], polybenzimidazole [2], polyvinyl alcohol [3], sulfonated polyimide [4] and polyether sulfone [5], that have been utilized in previous studies to develop non-Nafion based membranes. These polymers are claimed to be capable of replacing Nafion owing to their polysaccharide backbone, which is able to act as both hydrophilic and hydrophobic domains. However, with the high production costs needed for polymer materials, an alternative innovation has been constructed, using biopolymers that are PEM-based.

Recent studies have discovered that chitosan [6], carrageenan [7] and alginate [8] are PEM-based. These biopolymers have the potential to conduct protons as they are mostly in an amorphous state. The highly amorphous condition of the materials resulted in high proton conductivity as there are more proton pathways in amorphous mediums [9]. Charradi et al. worked on SiO<sub>2</sub>-montmorillonite filled membranes (9% content) for PEMFC and obtained 0.158 S/cm proton conductivity, which was higher than the pristine polymer at 120 °C and 100% relative humidity [10]. Sainul Abidin et al. achieved the highest proton

conductivity of 0.0706 S/cm by using modified montmorillonite at 10 wt.% loading, under 70 °C conditions, using a polyimide based PEM [11]. Wang et al. synthesized chitosan-based PEM that was filled with solvent-free carbon nanotube fluids and was able to perform maximum proton conductivity at a value of 0.044 S/cm at 80 °C [12]. Since biopolymers are highly amorphous, by blending them with other semicrystalline polymers such as PVA, the resulting membrane could have better flexibility and a firmer structure. Zakaria et al. and Yang et al. worked on PVA-based membranes, each achieving the highest proton conductivity of 0.0095 S/cm and 0.0368 S/cm respectively, both at 30 °C [13, 14]. Nevertheless, these works were unable to figure out the hidden potential of blending membrane composites of sodium alginate and polyvinyl alcohol together with an inorganic filler montmorillonite. Montmorillonite is a clay-type filler, that contains silica tetrahedral, an octahedral layer of aluminum, and exchangeable cations like magnesium and potassium.

Montmorillonite (MMT) has been studied previously, modified with additional protons like H+, Na+, Mg2+ Ca<sup>2+</sup> and K<sup>+</sup>. Wu et al. achieved high proton conductivities at 38.5 mS/cm with balanced water uptake, 24.26% when developed cloisite sodium montmorillonite [15]. Wang et al. reported 5wt% of MMT-PBI-O exhibited 0.5 mS/cm proton conductivities at 80 °C and losing weight easily (under TGA analysis) compared to pure PBI-O membrane [16]. This was because the insertion of MMT facilitates water absorption thus allowing proton channel formation; 5 wt.% was better than 3wt% MMT. When blending MMT with SPEEK polymer, the water uptake reached 35% which was lower than pure SPEEK, contributing to 0.057 S/cm of ionic conductivity at ambient condition, which was a good finding from Ata et al. [17].

These reports potentially bring up this study to show how MMT involvements can improve proton conductivity of polymer matrix besides its thermal stability could be maintained as well. To distinguish, additional polymer – PVA was included together with biopolymer sodium alginate for developing a novel hybrid membrane electrolyte for direct methanol fuel cell application. This work highlighted on membrane performance tests relating to the thermal degradation analysis.

#### **Materials and Methods**

The membranes comprising of sodium alginate, polyvinyl alcohol and montmorillonite as the hybridized membrane of SA/PVA-MMT, were simply named as SVM in this work. The variation of MMT loadings in each sample were differentiated as shown in Table 1.

Table 1. The notation for each sample

MMT Loadings (wt.%)	Notation
0	SV0
2	SVM2
5	SVM5
10	SVM10
15	SVM15
20	SVM20

#### Membrane preparation

The SVM blended solution was prepared using the solution casting method. Sodium alginate (SA, Acros Belgium) and polyvinyl alcohol (PVA, R & M

Chemicals) were mixed together at a concentration ratio of 40:60. The SA and PVA solutions were prepared separately, then dispersed in deionized (DI) water, at 70 °C and 90 °C respectively. Both polymer solutions were mixed in a beaker and stirred for 1 hour, adding 1 mL of 10% glutaraldehyde (GA, Nacalai Tesque Japan) for internal crosslinking, dropwise, until homogenized. Then solutions of 2 wt.%, 5 wt.%, 10 wt.%, 15 wt.% and 20 wt.% Montmorillonite (MMT, Acros Belgium) were prepared in 5 mL DI water each, were dispersed overnight at ambient temperature. The SA/PVA solutions and MMT solutions were blended altogether, stirring for 5 hours, to create a homogenized mixture. The mixture was then cast in a petri dish and dried for 12 hours at 60 °C, followed by 1 hour at 80 °C using a box furnace (Carbolite chamber) to become a membrane film. The membrane film was externally crosslinked with 1.5 wt.% CaCl<sub>2</sub> and 10% GA by soaking it for 30 minutes under ambient conditions, before further testing.

#### Thermal analysis

The film samples were characterized using the Simultaneous Thermal Analyzer-Differential Scanning Calorimetry (STA-DSC), NETZSCH Proteos Software, to determine their thermal stability based on the glass transition temperature (T<sub>g</sub>). The analysis was run under a nitrogen atmosphere, within the temperature range of 30-800 °C, with a heating rate of 10 °C/min.

#### Membrane performance tests

The membrane film was proceeded to the liquid uptake performance test and proton conductivity test. The membrane film was cut according to a 2 cm x 2 cm dimension for both water and methanol uptake. The film was weighed after 24 hours of being soaked in DI water and 10 % methanol for respective tests, which is denoted as  $W_{\rm wet}$  (g). The films were weighed again after drying for 24 hours at room temperature, denoted as  $W_{\rm dry}$ (g). The weights recorded were calculated using the liquid uptake equation formula (1) to obtain the percentage of water uptake and methanol uptake.

$$\frac{W_{wet} - W_{dry}}{W_{dry}} \times 100 \tag{1}$$

For proton conductivity testing, the membrane film (4 cm x 1 cm dimension) must be in a fully hydrated

state; it was immersed in DI water for an hour before being placed in a four-electrode conductivity cell that was connected to a potentiostat/galvanostat (WonATech) for 60 seconds, over a frequency range of 1 MHz–50 Hz. This potentiostat would produce a linear trend of voltage versus the current graph, producing a membrane resistance from the slope. The in-plane proton conductivity value ( $\sigma$ ) can be calculated by using the in-plane proton conductivity equation (2) [5]:

$$\sigma = \frac{L}{RWT} \tag{2}$$

where L is the length of the film in cm, R is the average resistance  $(\Omega)$ , W is the film width (cm) and T is the thickness of the film (cm).

#### **Results and Discussion**

#### **FESEM**

For micrographs images, only four samples were observed, because the morphology analysis demand was required just to emphasized on the homogeneity of the surfaces as clay loadings increased – SV0, SVM5,

SVM10, SVM20. These desired membranes were proven having carbon, oxygen and sodium elements as observed in EDX in Figure 1(c), (f), (i), (l). Figure 1 (a), (d), (g), (j) were the surface morphology of the membranes while Figure 1 (b), (e), (h), (k) were showing the cross sectional of the membranes. based on Figure 1 (a), which resembling SV0, the present surface image seemed to have pores, as well as could be seen in the cross-section image (Figure 1(b)). Too many porosities were undesirable because it creates channel for water absorption which then leading to excessive membrane swelling. When introduce a little amount of MMT, the surface image for SVM5 looked rougher than SV0, as illustrated in Figure 1(d). The cross-sectional image for SVM2 looked rougher as well, implying the successful intercalation of MMT, with proven EDX elemental peak based on the rising of Mg, Al, Si, K peaks. However, the declining peak of Na, was due to the well-blend of MMT with the polymer chain, interrupting the structure of polymer consisting Na.

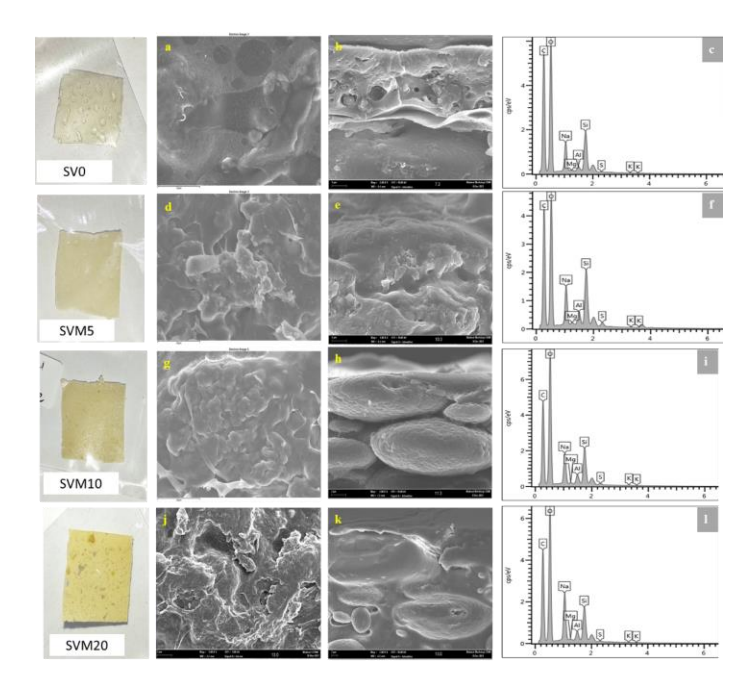


Figure 1. FESEM images of membrane samples, followed by the physical sample on the left-handside, surface images, cross-sectional images and elemental peaks EDX on the right-handside. SV0 (a, b, c), SVM5 (d, e, f), SVM10 (g, h, i) and SVM20 (j, k, l)

As MMT increased higher, SVM10 membrane surface looked much rougher and compact cross-sectional area as shown in Figure 1(g, h). This indicating that water molecules had fully evaporated from the polysaccharide matrix [18], as white tiny particle were visible in Figure 1(h) depicting the successful intercalation of MMT into the SA/PVA copolymer matrix. Nevertheless, the agglomeration presented in SVM20 because of excessive MMT addition resulting it to concentrate at one point, that further discussed in liquid uptake part.

#### **TGA-DSC**

For thermal stability analysis, only four samples were involved since we just insisted to compare the obvious trend among the expected significant MMT loadings in the membranes - SV0, SVM2, SVM10, SVM15. The membrane film obtained good thermal stability, with an increased temperature phase of degradation as MMT loadings increased. Referring to Figure 2, the polymer blend started to degrade at 220-240 °C and proved to be better than previous studies, which indicated that the first stage began at 80 °C [19] and 198 °C [20] with only PVA and SA. This first degradation phase was attributed to solvent evaporation [21]. By adding MMT, the membrane has a combination of amorphous and crystalline phases, making the degradation phases a bit slower. The polymer must have a semi-crystalline phase since high amorphous properties might result in a low strength structure of the film. The presence of semi-crystalline properties of the PVA could strengthen the interaction bond between the polymer chain and the filler bond. The interaction bond involved was a strong hydrogen bond, which is difficult to break apart. The weight loss of the membranes was around 50.4-55.2%, which began at a range of 259.8-263.5 °C, which was dominated by SVM 15. In comparison, the second degradation phase of these MMT-filled membranes had slightly lower thermal stability than the SP/PVA membrane at 307 °C [19]. This was due to the presence of MMT, which has hydrophilic properties that cause it to easily degrade. The hydrophilicity enables the membrane to retain water molecules in the matrix, thus degrading at lower temperatures [20, 22]. However, the presence of PVA and MMT in a sodium alginate-based membrane was much better as this blended membrane took higher ranges of the third degradation phase (470–800 °C) to fully depolymerize the polysaccharide backbone owing to the interfacial connections and improvised crystallinity.

The thermograms of DSC shown in Figure 3, indicating that the glass transition phase changed as MMT loading increased. The glass transition temperature increased from SV0 to SVM10 which was owing to the dipole interaction declining that happened within the homopolymers [23]. This is simultaneous phase to the TGA thermogram whereby the hybridized membranes facing phase changes to rubbery state at a later temperature as the clay fillers added. However, when reaching 15 wt.% of MMT in the hybridized membrane, the glass transition temperature decreased to complex peak value of 123.6 °C, which could be seen overlapping peak with the control membrane, SV0 in the thermogram. This indicating that backbone polymers became soften at certain higher loading point. In relation to the water uptake performance, SVM15 absorb more water molecules than SVM10 by 10.84%, deducing it has voids for water binding. The voids presence turned up SVM15 membrane to be easily degraded and change phase. Therefore, SVM10 was much preferable type of membrane in this case because it possessed the greater thermal stability with peak value glass transition temperature at 196.7 °C.

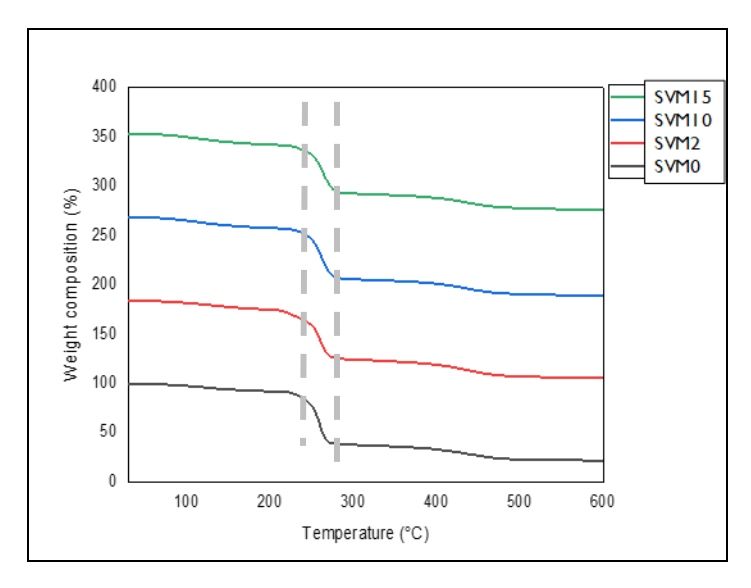


Figure 2. The thermogram of the membranes

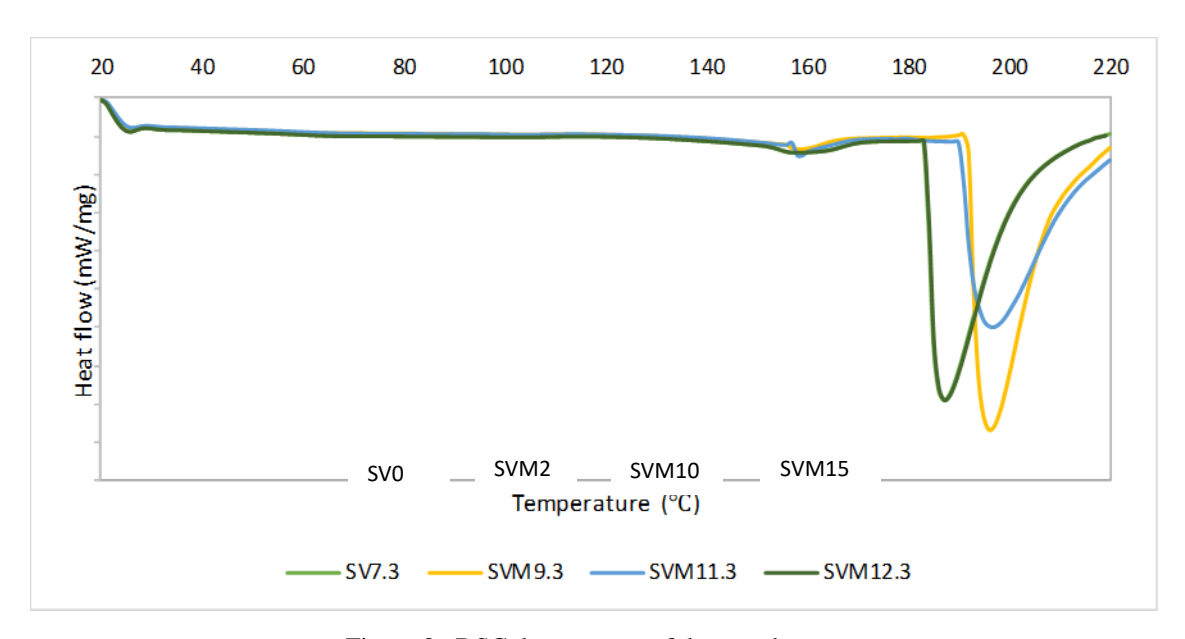


Figure 3. DSC thermogram of the membranes

#### Membrane performance tests

From Figure 4, the graph trend fluctuated as the MMT content increased. The maximum value of proton conductivity was achieved at 8.0510 mS/cm by using SVM20 (at 20 wt.% MMT loadings). During the conductivity testing, the prominent functional groups involved were H+, H3O+ and OH ions, where H+ dissociated from the water molecules, hopping from one molecule to another. The insufficiency of single electrons causes the H+ to react actively with the OH free ions from the MMT, which also contributes to transporting the protons throughout the medium. The hydration state of the membrane was crucial as it would produce more H<sup>+</sup> to actively bind with lone pairs of electrons in H<sub>2</sub>O, thus forming a highly reactive ion, H<sub>3</sub>O<sup>+</sup>. The cycle of transporting protons through

negatively charged ions was repeated simultaneously with the protons hopping. In this study, both mechanisms could potentially occur - the proton hopping mechanism, namely, the Grotthuss mechanism, and the proton being transported, namely the Vehicular mechanism [24]. As shown by SVM15, the existence of free volumes in the membrane decreased when a higher MMT filling was introduced, which resulted in difficulties for the protons to be transferred. The tendency of the proton conductivity to increase at 20 wt.% MMT was due to the presence of active sites at the MMT, which enabled the transport of the proton to pass through. The values were lower at SVM5 and SVM15, most probably caused by the activation of the inhibition properties of MMT when extra loading produced an aggregated effect on the membrane [25, 26].

For water uptake performance, according to Figure 5, the membrane began to reduce absorbing water at 2 wt.% MMT. Then, the trend started to decline again at 15 wt.% MMT after a slight increase at 10 wt.% MMT. The increment of water absorption was due to the introduction of MMT to the pure SAPVA membrane, slightly induced by the hydrophilicity of MMT, which provides a high water content to the membrane [22].

This hydrophilic property, owing to its oxygenated functional group (-OH) [27], through the abundance of water, creates a continuous transferring channel and facilitates ion movement [22]. These functional groups interact with each other (polymer and fillers) via strong hydrogen bonding or polar-polar interaction [27]. The lowest water uptake point was at 20 wt.% (SVM20), after 10 wt.% (SVM10) of MMT. The water uptake level dropped from 162.46% to a value of 129.65% at 10 wt.%, before it decreased even further to 74.89%, with the addition of SVM20.

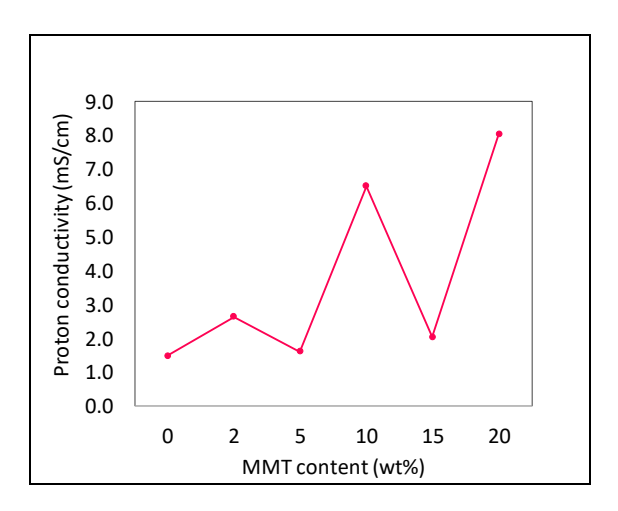


Figure 4. Proton conductivity for SVM2 (2 wt.%), SVM5 (5 wt.%), SVM10 (10 wt.%), SVM15 (15 wt.%) and SVM20 (20 wt.%)

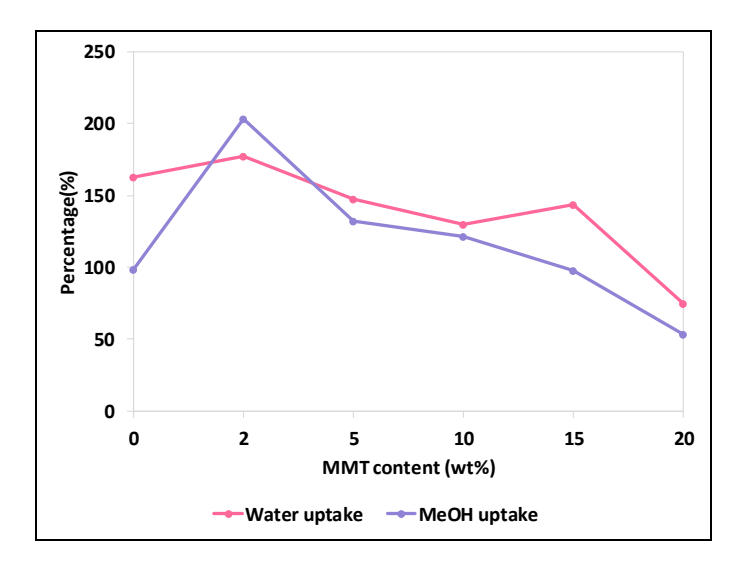


Figure 5. Water uptake and methanol uptake performances for SVM2-20

Table 2. The comparison of previous membrane hybridized studies

Membrane Composite	Filler Loadings (wt.%)	Proton Conductivity (mS/cm)	References
Pure SA	0	0.48	[18]
PVA/SA(6/4)	0	91.0	[19]
PVA/TiO <sub>2</sub>	15	48.0	[28]
SA/TiO <sub>2</sub>	25	17.3	[8]
SA/Alumina	15	13.0	[20]
PVA/MMT	10	36.8	[14]

The additional MMT filler had partially reduced the size of the ion channels because of agglomeration, hence blocking the absorption of water. Figure 6 and Figure 7 illustrate the plausible figures of how MMT filled up the polymers' matrix. The matrix inside the membranes was homogenously distributed, thus decreasing the free voids of the resultant matrix [27]. The mobility of the SA/PVA chains was reduced then, thus leading to a decrement of water content. Based on

the experimental results as shown in Table 3 and Figure 5, the methanol uptake value dropped after reaching its peak at 2 wt.% MMT, from 203.30%, to 53% at 20 wt.% MMT. The explanation for methanol uptake was similar, since the graph trend also decreased as MMT loading increased. The same trend showed that there was good networking and bonding between the alginate polymer and MMT, which prevented fuel crossing [22].

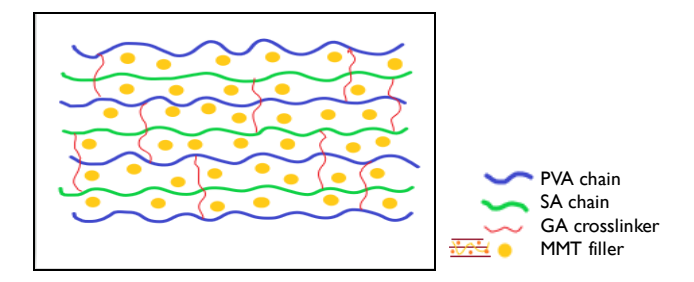


Figure 6. The plausible figures for blended SVM membranes [29]

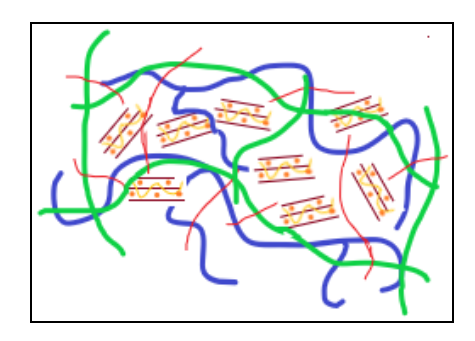


Figure 7. The another version of plausible figures [3]

Table 3. Proton conductivity and liquids uptake of the membranes according to the MMT loadings

Sample	MMT Loadings (wt.%)	Proton Conductivity (mS/cm)	Water Uptake (%)	Methanol Uptake (%)
SV 0	0.0	1.4828	162.46	98.55
SVM 2	2.0	2.6429	177.50	203.30
SVM 5	5.0	1.6083	147.10	132.23
SVM 10	10.0	6.5025	129.65	121.59
SVM 15	15.0	2.0332	143.70	97.46
SVM 20	20.0	8.0510	74.89	53.00

#### Conclusion

Sodium alginate-based membranes are biopolymers that have a high potential to be used in conducting protons. By blending it with semi-crystalline PVA, the membrane is more thermally stable when the depolymerization phase occurs at a higher temperature. The addition of the inorganic filler, MMT, to the PEM could have a more powerful impact in terms of the liquid uptake. The study proves that 10 wt.% of MMT is the most preferable to obtain a balanced water uptake and reduce methanol uptake, hence suggesting SVM10 as the best composite PEM with improved proton

conductivity. Overall, further research might require functionalizing MMT or PVA to enhance the conductivity value in order to be the most promising alternative PEM.

#### Acknowledgement

The authors would like to give their heartiest gratitude to Universiti Kebangsaan Malaysia for the research funding received through GGPM-2019-002 that has financially supported this work.

#### References

- R., Chirachanchai, S., Shishatskiy, S. and Nunes, S. P. (2008). Sulfonated montmorillonite/sulfonated poly(ether ether ketone) (SMMT/SPEEK) nanocomposite membrane for direct methanol fuel cells (DMFCs). *Journal of Membrane Science*, 323(2), 337-346.
- Singha, S., Koyilapu, R., Dana, K. and Jana, T. (2019). Polybenzimidazole-clay nanocomposite membrane for PEM fuel cell: Effect of organomodifier structure. *Polymer*, 167: 13-20.
- 3. Yang, C. C. (2011). Fabrication and characterization of poly(vinyl alcohol)/montmorillonite/ poly(styrene sulfonic acid) proton-conducting composite membranes for direct methanol fuel cells. *International Journal of Hydrogen Energy*, 36(7): 4419–4431.
- 4. You, P. Y., Kamarudin, S. K. and Masdar, M. S. (2019). Improved performance of sulfonated polyimide composite membranes with rice husk ash as a bio-filler for application in direct methanol fuel cells. *International Journal of Hydrogen Energy*, 44(3): 1857-1866.
- 5. Xing, D., He, G., Hou, Z., Ming, P. and Song, S. (2011). Preparation and characterization of a modified montmorillonite/sulfonated polyphenylether sulfone/PTFE composite membrane. *International Journal of Hydrogen Energy*, 36(3): 2177-2183.
- Rosli, N. A. H., Loh, K. S., Wong, W. Y., Mohamad Yunus, R., Lee, T. K., Ahmad, A. and Chong, S. T. (2020). Review of chitosan-based polymers as proton exchange membranes and roles of chitosan-supported ionic liquids. *International Journal of Molecular Sciences*, 21(632): 1-52.
- Mohy Eldin, M. S., Farag, H. A., Tamer, T. M., Konsowa, A. H. and Gouda, M. H. (2020). Development of novel iota carrageenan-gpolyvinyl alcohol polyelectrolyte membranes for direct methanol fuel cell application. *Polymer Bulletin*, 77(9), 4895-4916.
- 8. Shaari, N., Kamarudin, S. K. and Zakaria, Z. (2019). Potential of sodium alginate/titanium oxide biomembrane nanocomposite in DMFC application. *International Journal of Energy Research*, 43(14): 8057-8069.

- 9. Yang, C. C. and Lin, S. J. (2002). Preparation of composite alkaline polymer electrolyte. *Materials Letters*, *57*(4): 873-881.
- Charradi, K., Ahmed, Z., Aranda, P. and Chtourou, R. (2019). Silica / montmorillonite nanoarchitectures and layered double hydroxide-SPEEK based composite membranes for fuel cells applications. *Applied Clay Science*, 174: 77-85.
- Sainul Abidin, K., Kannan, R., Bahavan Palani, P. and Rajashabala, S. (2017). Role of structural modifications of montmorillonite, electrical properties effect, physical behavior of nanocomposite proton conducting membranes for direct methanol fuel cell applications. *Materials Science-Poland*, 35(4): 707-716.
- Wang, J., Gong, C., Wen, S., Liu, H., Qin, C., Xiong, C. and Dong, L. (2018). Proton exchange membrane based on chitosan and solvent-free carbon nanotube fluids for fuel cells applications. *Carbohydrate Polymers*, 186: 200-207.
- 13. Zakaria, Z., Kamarudin, S. K., Timmiati, S. N. and Masdar, M. S. (2019). New composite membrane poly(vinyl alcohol)/graphene oxide for direct ethanol–proton exchange membrane fuel cell. *Journal of Applied Polymer Science*, 136(2): 1-13.
- 14. Yang, C. C. and Lee, Y. J. (2009). Preparation of the acidic PVA/MMT nanocomposite polymer membrane for the direct methanol fuel cell (DMFC). *Thin Solid Films*, 517(17): 4735-4740.
- Wu, X.-W., Wu, N., Shi, C.-Q., Zheng, Z.-Y., Qi, H.-B. and Wang, Y.-F. (2016). Proton conductive montmorillonite-Nafion composite membranes for direct ethanol fuel cells. *Journal of Applied Surface Science*, 2016: 1-6.
- Wang, F., Wang, D. and Zhu, H. (2018). Montmorillonite-polybenzimidazole inorganic-organic composite membrane with electric field-aligned proton transport channel for high temperature proton exchange membranes. *Polymer-Plastics Technology & Engineering*, 2018: 1-8.
- 17. Ata, K. C., Kadioglu, T., Turkmen, A. C., Celik, C. and Akay, R. G. (2020). Investigation of the effects of SPEEK and its clay composite membranes on the performance of direct borohydride fuel cell. *International Journal of*

- Hydrogen Energy, 45(8): 5430-5437.
- Shaari, N., Kamarudin, S. K., Basri, S., Shyuan, L. K., Masdar, M. S. and Nordin, D. (2018).
   Enhanced mechanical flexibility and performance of sodium alginate polymer electrolyte biomembrane for application in direct methanol fuel cell. *Journal of Applied Polymer Science*, 135(37): 46666.
- 19. Yang, J. M., Wang, N. C. and Chiu, H. C. (2014). Preparation and characterization of poly(vinyl alcohol)/sodium alginate blended membrane for alkaline solid polymer electrolytes membrane. *Journal of Membrane Science*, 457: 139-148.
- 20. Shaari, N. and Kamarudin, S. K. (2020). Sodium alginate/alumina composite biomembrane preparation and performance in DMFC application. *Polymer Testing*, 81: 106183.
- 21. Yang, C. C., Lee, Y. J. and Yang, J. M. (2009). Direct methanol fuel cell (DMFC) based on PVA/MMT composite polymer membranes. *Journal of Power Sources*, 188(1): 30-37.
- 22. Shaari, N., Kamarudin, S. K., Basri, S., Shyuan, L. K., Masdar, M. S., & Nordin, D. (2018). Enhanced Proton Conductivity and Methanol Permeability Reduction via Sodium Alginate Electrolyte-Sulfonated Graphene Oxide Bio-membrane. Nanoscale Research Letters, 13(1): 1-16.
- Hemalatha, R., Alagar, M., Selvasekarapandian, S., Sundaresan, B. and Moniha, V. (2019). Studies of proton conducting polymer electrolyte based on PVA, amino acid proline and NH<sub>4</sub>SCN. *Journal of Science: Advanced Materials and Devices*, 4(1): 101-110.
- Kreuer, K. D. (2001). On the development of proton conducting polymer membranes for hydrogen and methanol fuel cells. *Journal of Membrane Science*, 185: 29-39.

- Radmanesh, F., Rijnaarts, T., Moheb, A., Sadeghi, M. and de Vos, W. M. (2019). Enhanced selectivity and performance of heterogeneous cation exchange membranes through addition of sulfonated and protonated Montmorillonite.
   Journal of Colloid and Interface Science, 533: 658-670.
- 26. Uddin, F. (2018). Montmorillonite: An introduction to properties and utilization. IntechOpen Web of Science, Pakistan: pp. 1-23.
- 27. Kakati, N., Maiti, J., Das, G., Lee, S. H. and Yoon, Y. S. (2015). An approach of balancing the ionic conductivity and mechanical properties of PVA based nanocomposite membrane for DMFC by various crosslinking agents with ionic liquid. *International Journal of Hydrogen Energy*, 40(22): 7114-7123.
- Yang, C.-C., Chiu, S. J., Lee, K.-T., Chien, W.-C., Lin, C.-T. and Huang, C.-A. (2008). Study of poly(vinyl alcohol)/titanium oxide composite polymer membranes and their application on alkaline direct alcohol fuel cell. *Journal of Power Sources*, 184(1): 44-51.
- 29. Kamjornsupamitr, T., Sangthumchai, T., Saejueng, P., Sumranjit, J., Hunt, A. J. and Budsombat, S. (2021). Composite proton conducting membranes from chitosan, poly(vinyl alcohol) and sulfonic acid-functionalized silica nanoparticles. *International Journal of Hydrogen Energy*, 46(2): 2479-2490.

# Malaysian Journal of Analytical Sciences (MJAS)



Published by Malaysian Analytical Sciences Society

### FORMULATION AND CHARACTERISATION OF LSCF/YSZ-SDC AND LSCF/YSZ-SDCC DUAL COMPOSITE CATHODES FOR INTERMEDIATE-TEMPERATURE SOLID OXIDE FUEL CELL

(Formulasi dan Ciri Dwi-Komposit Katod LSCF/YSZ-SDC dan LSCF/YSZ-SDC Karbonat untuk Sel Bahan Api Oksida Pepejal Bersuhu Pertengahan)

Nurul Farhana Abdul Rahman, Umira Asyikin Yusop, Yohannes Nyambong Lowrance, Hamimah Abd. Rahman\*, Mohd Azham Azmi, Shahruddin Mahzan, Azzura Ismail

Faculty of Mechanical and Manufacturing Engineering, Universiti Tun Hussein Onn Malaysia, 86400 Parit Raja, Batu Pahat, Johor, Malaysia

\*Corresponding author: hamimah@uthm.edu.my

Received: 28 November 2021; Accepted: 27 February 2022; Published: 27 June 2022

#### Abstract

A cathode component solid oxide fuel cell (SOFC) is important in the manufacturing of the cells. This study evaluated two dual composite cathodes, namely, (La<sub>0.6</sub>Sr<sub>0.4</sub>)<sub>0.97</sub>Co<sub>0.2</sub>Fe<sub>0.8</sub>O<sub>3</sub> (LSCF)/Y<sub>0.8</sub>Zr<sub>0.92</sub>O<sub>1.96</sub> (YSZ)-Sm<sub>0.2</sub>Ce<sub>0.8</sub>O<sub>1.9</sub> (SDC) and LSCF/YSZ-SDC carbonate (SDCC). The dual composite cathodes with different compositions were developed through high-energy ball milling (HEBM) for the production of dual composite powder and screen-printing method for the fabrication of symmetrical cells. The properties of the dual composite cathodes were studied. Phase identification was carried out via X-ray diffractometry (XRD), and the electrochemical performance of the symmetrical cells was measured by impedance test. The physical morphologies of LSCF/YSZ-SDC and LSCF/YSZ-SDCC were slightly different. The XRD patterns of the LSCF/YSZ-SDC cathode powder showed no secondary peak, whereas the LSCF/YSZ-SDCC cathode powder had SrCO<sub>3</sub> as an impurity. Microstructure and powder homogeneity are considered essential in addition to the good formulation of the dual composite's cathodes. The particle sizes of LSCF/YSZ-SDC and LSCF/YSZ-SDCC as analyzed by ImageJ software were in the range of 130–160 nm. The printed cathode was investigated under heat treatment from 700 °C to 500 °C. The electrochemical performance of LSCF/YSZ-SDCC was slightly better compared with that of LSCF/YSZ-SDC because of the addition of the carbonate; however, the polarization resistance obtained did not meet the standard range. The electrochemical performance obtained from this study was not favorable because of severe problems, such as the technique applied during cell fabrication and the presence of impurity after the HEBM process.

Keywords: dual composite cathodes, intermediate temperature, screen printing, solid oxide fuel cell

#### **Abstrak**

Komponen katod untuk sel bahan api oksida pepejal (SOFC) adalah penting dalam pembuatan sel. Dalam kajian ini, penilaian katod komposit dwi (LSCF)/(YSZ)-(SDC) and (LSCF)/(YSZ)-Karbonat (SDCC) dibentangkan. Komposisi yang berbeza bagi katod komposit dwi telah dibangunkan melalui teknik pengisaran bebola tenaga tinggi untuk penghasilan serbuk komposit dwi dan kaedah percetakan skrin telah digunakan untuk fabrikasi sel simetri. Pencirian sifat katod komposit dwi telah dikaji. Pengenalpastian fasa melalui kaedah pembelauan sinaran-X telah dijalankan dan prestasi electrokimia sel simetri diukur dengan

Nurul Farhana et al: FORMULATION AND CHARACTERISATION OF LSCF/YSZ-SDC AND LSCF/YSZ-SDCC DUAL COMPOSITE CATHODES FOR INTERMEDIATE-TEMPERATURE SOLID OXIDE FUEL CELL

menggunakan ujian impedans. Perbandingan antara morfologi fizikal LSCF/YSZ-SDC and LSCF/YSZ-SDCC menunjukkan sedikit perbezaan dengan penambahan karbonat. Corak sinar-X untuk komposit dwi campuran LSCF/YSZ-SDC katod serbuk tidak memaparkan puncak sekunder. Bagaimanapun, Komposit dwi campuran LSCF/YSZ-SDCC katod serbuk memaparkan kehadiran sebagai bendasing. Kehomogenan struktur mikro dan serbuk dianggap pentiing sebagai tambahan kepada perumusan katod dwi komposit yang baik. Purata saiz zarah purata bagi LSCF/YSZ-SDC and LSCF/YSZ-SDCC dwi komposit selepas dianalisis oleh perisian Image J didedahkan berada dalam julat antara 130-160. Filem bercetak katod telah disiasat di bawah suhu rawatan haba dari 700 °C hingga 500 °C. Prestasi elektrokimia LSCF/YSZ-SDCC menunjukkan lebih baik sedikit berbanding LSCF/YSZ-SDC kerana penambahan karbonat namun keputusan yang diperoolehi tidak mencapai julat piawai rintangan polarisasi. Prestasi elektokimia yang diperoleh daripada kajian ini adalah tidak memberangsangkan kerana masalah yang teruk seperti teknik yang digunakan semasa fabrikasi sel dan kehadiran bendasing selepas proses HEBM.

Kata kunci: katod komposit dwi, suhu pertengahan, percetakan skrin, sel bahan api oksida pepejal

#### Introduction

Solid oxide fuel cells (SOFCs) are still highly investigated because they have the highest potential for future power-generating devices in fuel cell technology. The capability of SOFCs to convert chemical energy from hydrogen or versatile fuels, particularly hydrocarbon fuels, into electrical or thermal energy made SOFCs a potential renewable energy source. Recent developments in SOFCs have focused on limiting the operating temperature and selecting a stable material for SOFC components. Although many cathodes have been developed and studied in detail, dual composite cathodes are barely reported. Dual composite cathodes are introduced to create an ideal cathode microstructure that can help improve phase contiguity and interfacial coherence by selecting suitable materials as cathode components [1-4]. Several studies have development of dual composite cathode investigated. According to Ko [3],  $(La_{0.6}Sr_{0.4})_{0.97}Co_{0.2}Fe_{0.8}O_3$  (LSM)- $Y_{0.8}Zr_{0.92}O_{1.96}$  (YSZ) composite cathodes struggle to achieve a high electrochemical performance because their effective surface area is small for electrocatalytic reactions. As a solution, an LSM/YSZ-YSZ dual composite cathode was created with LSM and YSZ particles conjugated together on YSZ-based particles. Based on the reported analysis, the LSM/YSZ-YSZ dual composite cathode had improved cathodic performance and also improved the durability of the cell by enhancing the phase contiguity and interfacial coherence between cells. Several dual composite cathodes were created for the further investigation of dual composite cathode materials. For example, LSM/YSZ-gadolinium-doped

ceria (GDC), LSCF/YSZ-GDC and LSCF/GDC-YSZ were developed. The cell performances of these dual composite cathodes were investigated by comparing with a single composite cathode (LSCF-GDC), and the results showed that LSCF/GDC-YSZ had a lower polarization resistance (0.075  $\Omega$ cm²) than LSCF-GDC (0.195  $\Omega$ cm²) [3-4]. However, the operating temperatures of previously developed dual composite cathodes for SOFCs are high.

In this study, two new dual composite cathodes, namely, LSCF/YSZ-Sm<sub>0.2</sub>Ce<sub>0.8</sub>O<sub>1.9</sub> (SDC) and LSCF/YSZ-SDC carbonate (SDCC), were developed in an attempt to investigate their electrochemical performances in limited operating temperatures. Previous research developed and evaluated two different dual composite cathodes, namely, LSM/GDC-YSZ and LSCF/YSZ-GDC. The electrochemical performances of these cathodes were investigated at high operating temperatures [3-4]. In the present study, the operating temperature was limited to 700-500 °C. YSZ was added to the LSCF-SDC composite cathode as an electrolyte material because YSZ can help increase the performances of cell components [5]. Moreover, SDC was used instead of GDC in this research. Both doped ceria are good oxygen ion conductors [6], but SDC is preferred because of its excellent ionic conductivity, which is related to oxygen vacancy [6]. Samarium causes a remarkable increase in oxygen vacancies, which help increase ionic conductivity [6]. Additionally, incorporating carbonate salts (Li<sub>2</sub>CO<sub>3</sub> and Na<sub>2</sub>CO<sub>3</sub>) can improve ionic conductivity [7]. For these reasons, two new dual composite cathodes were developed and examined in this study.

The present work aimed to investigate the electrochemical performances of dual composite cathodes in an operating temperature between 700 °C and 500 °C. The dual composite cathodes were prepared by mixing LSCF with YSZ-SDC and YSZ-SDCC with different weight percentages. The symmetrical cells were prepared by screen printing method using LSCF/YSZ-SDC and LSCF/YSZ-SDCC as the inks. Moreover, the phase microstructure and electrochemical performances of the dual composite cathode symmetrical cells were evaluated in depth in this study.

#### **Materials and Methods**

### Preparation and characterization of dual composite powders

YSZ-SDC and YSZ-SDCC composite powders were prepared using high-speed ball milling technique. SDCC electrolyte was prepared using low-speed ball milling method with 80 wt.% raw SDC powder (Kceracell, South Korea) mixed with 20 wt.% binary carbonates, which comprise 67 mol.% Li<sub>2</sub>CO<sub>3</sub> and 33 mol.% Na<sub>2</sub>CO<sub>3</sub> (Sigma Aldrich, USA) [7]. YSZ-SDC and YSZ-SDCC composite powders were prepared by mixing commercial YSZ powder (Kceracell, South Korea) with commercial SDC and SDCC electrolyte powders, respectively, via high-energy ball milling (HEBM)

(Fritsch Pulveristte, Germany) at 550 rpm for 2 h in zirconia jars. Three different weight ratios (50 wt.%:50 wt.%, 60 wt.%:40 wt.% and 70 wt.%:30 wt.%) for YSZ-SDC and YSZ-SDCC were selected as inspired from a previous research [8]. The resultant YSZ-SDC and YSZ-SDCC wet mixtures were dried and calcined.

In the second step, a commercial LSCF powder (Kceracell, South Korea) was added into the obtained YSZ-SDC and YSZ-SDCC composite powders with a 50:50 ratio to form dual composite cathode powders. HEBM was applied to produce homogenous mixtures of the dual composite cathode powders. Lastly, both dual composite cathode powders were dried overnight and heat treated at 750 °C for 1 h [8]. Table 1 shows the compositions of the prepared composite powders and dual composite powders.

All the fabricated powders were characterized by X-ray diffractometry (XRD; D8 Advanced Bruker, Germany) to identify the crystalline phases and the formation of any secondary phases. Then, the microstructure and element composition distribution were characterized using field-emission scanning electron microscopy (FESEM) with electron-dispersive spectroscopy (EDS; JSM 6380-Jeol, Japan). The particle sizes of all the resultant powders were estimated through the ImageJ software using the micrographs obtained by FESEM.

Table 1. Weight ratio compositions of c	composite and dual	composite powders
---	--------------------	-------------------

Composite Powder	Weight Ratio Composition (wt.%)	Dual Composite Powder	Designated samples	Weight Ratio Composition (wt.%)
YSZ-SDC	50:50	LSCF/YSZ-SDC	LYS1	50/50:40
YSZ-SDC	60:40	LSCF/YSZ-SDC	LYS2	50/60:40
YSZ-SDC	70:30	LSCF/YSZ-SDC	LYS3	50/70:30
YSZ-SDCC	50:50	LSCF/YSZ-SDCC	LYSC1	50/50:50
YSZ-SDCC	60:40	LSCF/YSZ-SDCC	LYSC2	50/60:40
YSZ-SDCC	70:30	LSCF/YSZ-SDCC	LYSC3	50/70:30

### Electrical performance analysis of LSCF/YSZ-SDC and LSCF/YSZ-SDCC dual composite cathodes

The dual composite symmetrical cells (LSCF/YSZ-SDC//YSZ electrolyte//LSCF/YSZ-SDC and LSCF/YSZ-SDCC//YSZ electrolyte// SCF/YSZ-SDCC) were prepared for the evaluation of the electrical performances of the dual composite cathodes. YSZ electrolyte pellet was prepared using a uniaxial press (Bench Top 3851, Carver, USA). Commercial YSZ powder (0.5 g) was mixed with a drop of polyethylene glycol to produce 13 mm-thick YSZ pellets. LSCF/YSZ-SDC and LSCF/YSZ-SDCC were screen printed on both sides of the YSZ electrolyte pellet. The dual composite powder was merged with terpineol (solvent; Merck kGaA, Germany), ethyl cellulose (binder; Sigma Aldrich, USA) and oleic acid (dispersant; Sigma Aldrich, USA) to create the screenprinting ink [9]. All the chemicals were mixed and agitated for several hours in an agate mortar until the suitable ink viscosity was achieved. Samples of the dual composite cathode symmetrical cells were placed in alumina boats and sintered at 600 °C for 90 min at a heating rate of 5 °C/min using a furnace (PLF 130, Protherm, Turkey) [10]. The surface morphologies of the dual composite cathodes were examined by scanning electron microscopy (SEM; Jeol, Japan). The electrical performances of symmetrical cells were tested using AC impedance spectroscopy (Metroahm Autolab Potentiostat and Galvanostat) in the frequency range of 0.1-1 MHz and AC voltage amplitude of 500-700 °C. Figure 1 shows the schematic diagram for the dual composite cathode symmetrical cell with characterization, which will be discussed later in this paper.

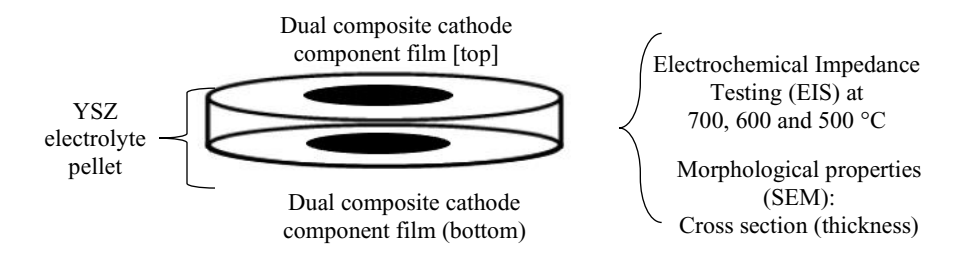


Figure 1. Schematic diagram of the dual composite cathode symmetrical cell

#### **Results and Discussion**

#### Characterization of dual composite powders

The XRD patterns of LSCF/YSZ-SDC and LSCF/YSZ-SDCC powders with different electrolytes and electrolyte contents (YSZ-SDC and YSZ-SDCC) are shown in Figures 2(a) and (b), respectively. Both dual composites cathodes were compared with commercial LSCF, YSZ, SDC and SDCC. As shown in Figure 2, only three primary phases of the standard peaks of LCSF perovskite (JCPDS No 01-089-5720), SDC (JCPDS No 01-075-0157) and YSZ (JCPDS No 00-030-1468) were detected. The carbonate (Li/Na) peaks in the SDCC composite shown in Figure 2(b) yielded the crystallite peak of the pure fluorite structure of SDC, which is

equivalent to the pure SDC structure. This result indicates that carbonates form an amorphous form, whereas SDC forms a well-defined fluorite crystal structure [8]. The SDCC peak was similar to the SDC pattern, as the addition of binary carbonates did not affect the shape and size of the original structures of the SDC particles. Li<sub>2</sub>CO<sub>3</sub> and Na<sub>2</sub>CO<sub>3</sub> were in molten amorphous states because the calcination temperature was over their melting temperatures [10]. Secondary phases were detected in the LSCF/YSZ-SDCC dual composite. Figure 2(c) shows the enlarged XRD pattern of the secondary phase identified as strontium carbonate (SrCO<sub>3</sub>, JCPDS No. 00-005-0418). According to Rahman et al. (2020), this phenomenon is normally due

to excessive power generated during the milling process of commercial LSCF powders, which caused the minor phase of SrCO<sub>3</sub> to form [11]. The formation of SrCO<sub>3</sub> impurity might be one of the reasons that caused the degradation of the electrochemical performances of the dual composite cathode cells owing to its

incompatibility with the electrolyte material. A further analysis between the formation of impurities and the performances of dual composite cells need to be addressed more in the future.

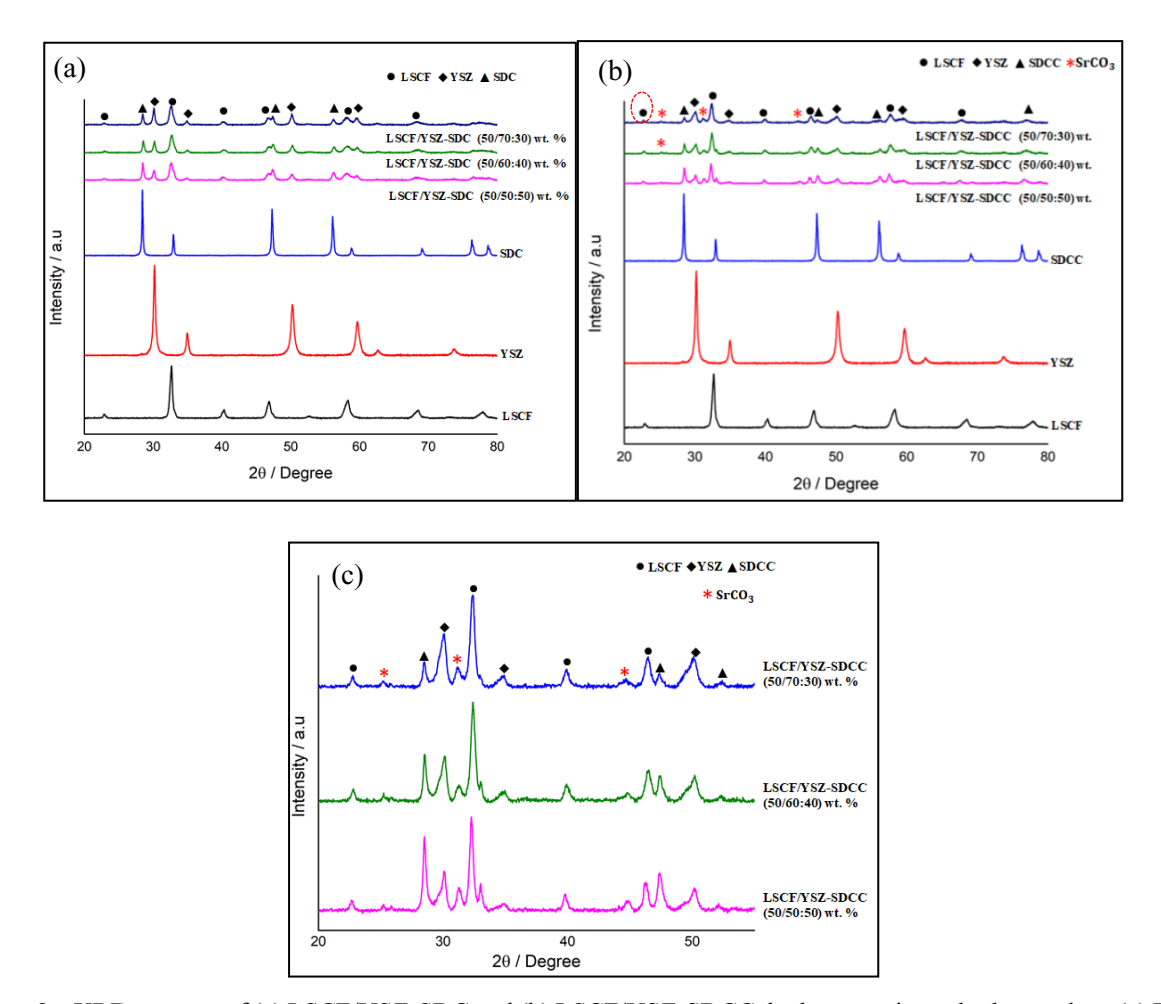


Figure 2. XRD patterns of (a) LSCF/YSZ-SDC and (b) LSCF/YSZ-SDCC dual composite cathode powders. (c) Peak enlargement for LSCF/YSZ-SDCC dual composite cathode powder

### Microstructure analysis of dual composite cathode powders

The effect of various weight compositions (YSZ-SDC and YSZ-SDCC) on powder morphology after the incorporation with LSCF were further investigated via FESEM. Figures 3 and 4 show the FESEM micrographs of the LSCF/YSZ-SDC and LSCF/YSZ-SDCC dual

composite cathodes. Well-distributed and fine particles were obtained in all dual composite cathode powders after HEBM. Fine particles in the range of 130–160 nm were observed. HEBM is a well-known technique used to synthesise nanocrystalline perovskites that exhibit an improvement in response ratios at low operating temperatures [12]. The particle sizes of the commercial

Nurul Farhana et al: FORMULATION AND CHARACTERISATION OF LSCF/YSZ-SDC AND LSCF/YSZ-SDCC DUAL COMPOSITE CATHODES FOR INTERMEDIATE-TEMPERATURE SOLID OXIDE FUEL CELL

powders of LSCF,YSZ and SDC, as well as those of the developed dual composite cathodes, are tabulated in Table 2. LYSC1 (159 nm) had the largest particle size, followed by LYSC2 (145 nm) and LYSC3 (135 nm). Similarly, amongst the LSCF/YSZ-SDC dual composites, LYS1 (147 nm) displayed a slightly larger particle size compared with LYS2 (138 nm) and LYS3 (126 nm). The prepared LSCF/YSZ-SDC and LSCF/YSZ-SDCC dual composite powders had smaller particles compared with commercial LSCF, YSZ and SDC powders. The decrease in size can be affected by the calcination process, as the calcination temperature directly influences the parameters [14]. The decrease in

the average particle size of the dual composite powders was expected because the milling process creates mechanical energy to breakdown the particles into smaller size and creates a uniform mixture of solid contents [15]. However, a slight agglomeration was seen in the LYS3 dual composite powders. This finding indicates that the composition 70YSZ:30SDC is not suitable for the development of dual composite cathodes. As a result, the total polarisation resistance of LYS3 was the highest amongst the compounds. Parwaiz et al. reported that the improper selection of a sample parameter will induce unwanted phase transformation and undesirable material properties [16].

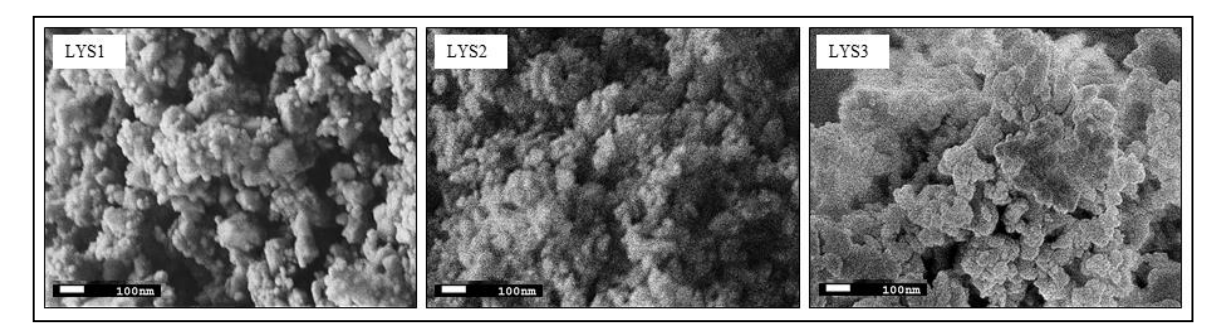


Figure 3. FESEM micrographs of the LSCF/YSZ-SDC dual composite cathode after HEBM and calcination at  $50,000 \times \text{magnification}$ 

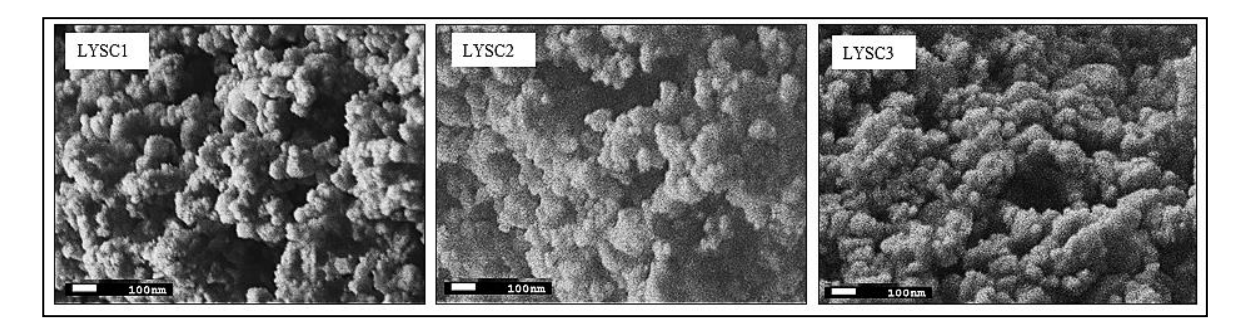


Figure 4. FESEM micrographs of the LSCF/YSZ-SDCC dual composite cathode after HEBM and calcination at 50,000× magnification

Table 2. Average particle sizes of the commercial and prepared dual composite powders

Powders	Average Particle Size (nm)
Commercial Powder LSCF	567
Commercial Powder YSZ	379
Commercial Powder SDC	130
Prepared LSCF/YSZ-SDC (50/50:50 wt.%)	147
Prepared LSCF/YSZ-SDC (50/60:40 wt.%)	138
Prepared LSCF/YSZ-SDC (50/70:3 0wt.%)	126
Prepared LSCF/YSZ-SDCC (50/50:50 wt.%)	159
Prepared LSCF/YSZ-SDCC (50/60:40 wt.%)	145
Prepared LSCF/YSZ-SDCC (50/70:30 wt.%)	135

### Microstructure analysis of dual composite cathode symmetrical cells

The printed surfaces and cross-sections of the LSCF/YSZ-SDC and LSCF/YSZ-SDCC pellets were observed through SEM and EDS as illustrated in Figure 5, Figure 6 and Figure 7. Figure 5 shows the secondary (SE) SEM images of the printed surfaces of the dual composite cathodes in the same magnification. Small pores were seen in all LSCF/YSZ-SDCs, whereas large pores were detected in the LSCF/YSZ-SDCCs. This outcome was probably because the binary carbonate reached the melting point as the sintering temperature (600 °C) during the preparation of the symmetrical cells was fixed. In addition, the porosity of the cathode should lie in the range of 20%-40% to achieve a better electrochemical performance [17]. The estimated average porosity for both dual composite cathodes was determined using SEM. The maximum porosity percentages of all LSCF/YSZ-SDC and LSCF/YSZ-SDCC dual composite cathodes were kept within the acceptable range. Table 3 shows the estimated averages porosity for the different compositions of the dual composite cathodes. The morphology of the pellets showed a regular distribution; however, the addition of carbonate as the solid content increased the roughness of the printed surface. The addition of a solid content helps increase the surface roughness by improving the elastic properties of the screen-printing ink [18]. As shown in Figure 5, a small crack was observed on the surface of the printed cathode films in the LYS3 and LYSC3 dua1 composite cathodes. Carbonate degradation might have led to the cracking phenomenon. Besides, a weak adhesion to the surface of the substrate during the deposition of the printed material is perhaps one of the reasons that caused the cracking surface [19].

Nurul Farhana et al: FORMULATION AND CHARACTERISATION OF LSCF/YSZ-SDC AND LSCF/YSZ-SDCC DUAL COMPOSITE CATHODES FOR INTERMEDIATE-TEMPERATURE SOLID OXIDE FUEL CELL

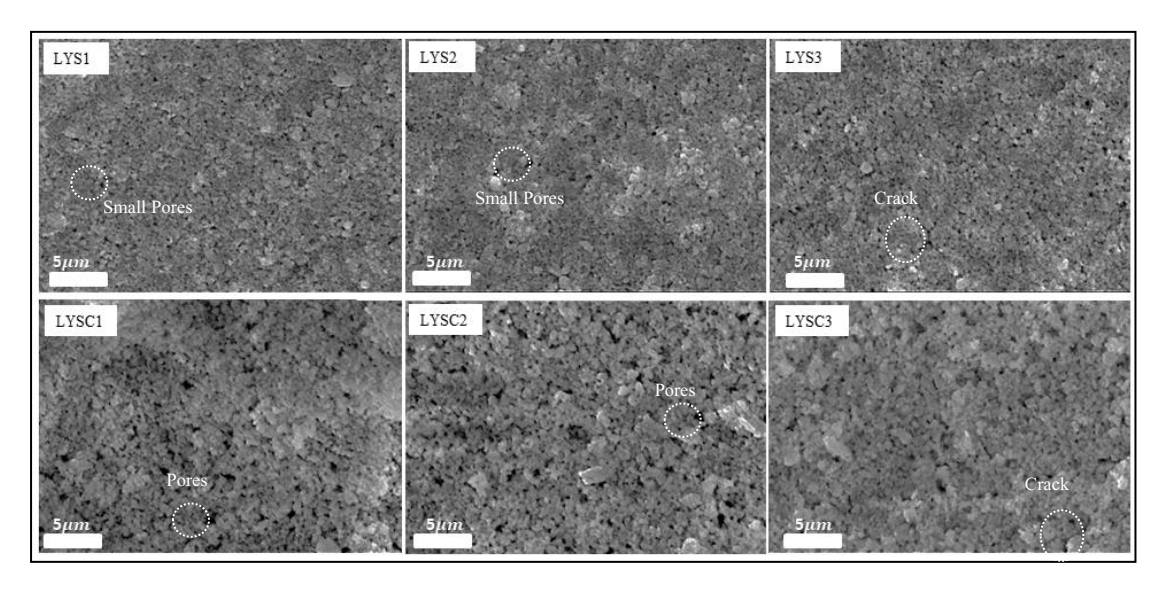


Figure 5. SEM micrographs for of the printed surfaces of (above) LSCF/YSZ-SDC and (below) LSCF/YSZ-SDCC at 10,000× magnification

Table 3. Average porosity of dual composite cathode symmetrical cells

<b>Dual Composite Cathode</b>	le Average Poros		ity (%)	
•	50/50:50	50/60:40	50/70:30	
LSCF/YSZ-SDC	20.22	25.91	25.07	
LSCF/YSZ-SDCC	23.85	26.29	25.86	

Figure 6 and Figure 7 show the cross-section micrograph view and EDS spectra of LSCF/YSZ-SDC and LSCF/YSZ-SDCC dual composite cathode layer on YSZ electrolyte pellet by 10 times repetition using screen printing method. The EDS spectra presented all the elements consist of La, Sr, Co, Fe, Sm, Ce, Y, Zr, O and C from LSCF/YSZ-SDC dual composite cathode. Na element was detected from LSCF/YSZ-SDCC as the addition of the  $Na_2Co_3$  carbonate existing in melting amorphous state however due to a very low energy characteristics radiation, element Li were not detected in EDS spectra analysis region

The screen-printing thickness of the dual composite cathode layer was uniform thickness for 10 times repetition for each layer. Table 4 shows the total thickness of each LSCF/YSZ-SDC and LSCF/YSZ-SDCC after the printing of 10 layers. The average

thicknesses of the dual composite cathodes per printing are presented in Table 4. The thickest screen-printed layer was 45.6 µm for the LYSC3 composition. The thickness of the cathode layer using the LSCF/YSZ-SDCC ink seen wider compared with that of the LSCF/YSZ-SDC ink. The increase in thickness using the LSCF/YSZ-SDCC inks may be related to the improved elastic properties caused by the addition and increase in solid content [18]. The formulations for dual composite cathode ink are non-identical for each composition as the weight compositions (YSZ-SDC and YSZ-SDCC) are different. The powder volume of the final dual composite ink was <30 vol.% as suggested from a previous research to obtain good quality cathode inks [18]. Thus, the thickness of the screen-printing layer and the production of cathode inks are important as it can help improve cell performance [20].

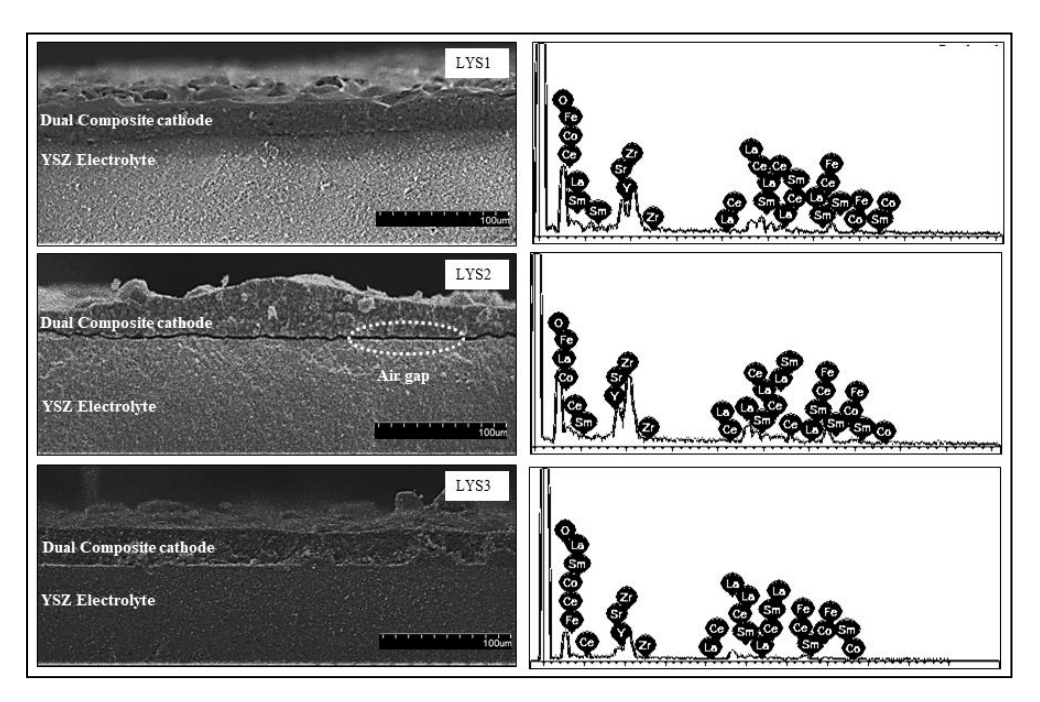


Figure 6. Cross-sectional micrographs and EDS spectra of screen-printed LSCF/YSZ-SDC cathode films

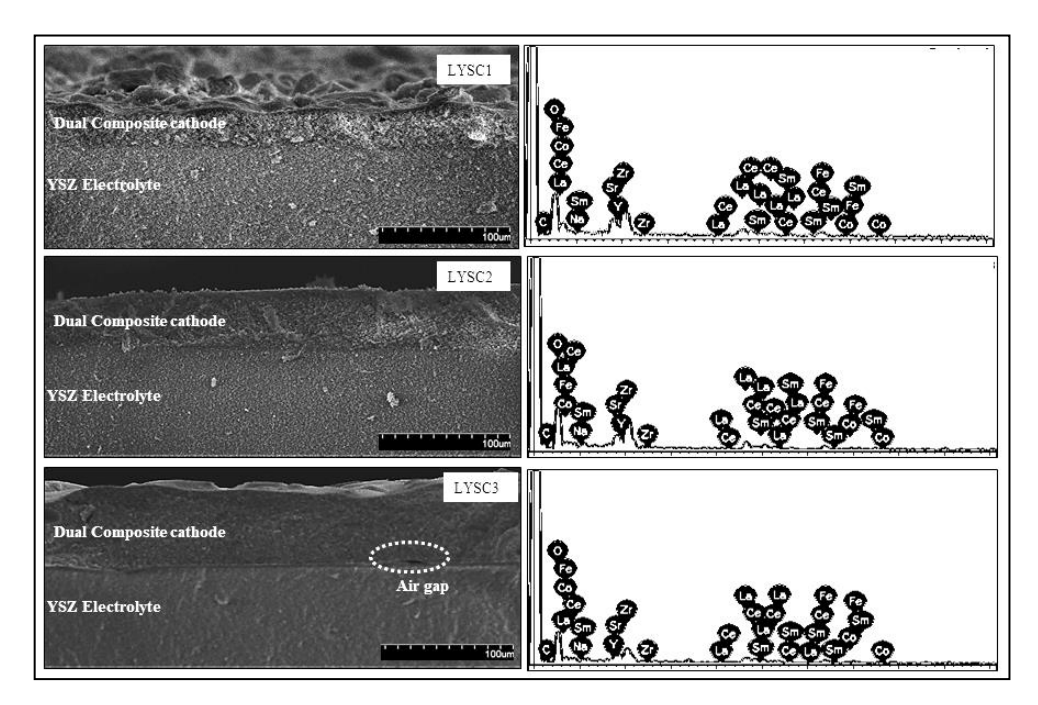


Figure 7. Cross-sectional micrographs and EDS spectra of screen-printed LSCF/YSZ-SDCC cathode films

Nurul Farhana et al: FORMULATION AND CHARACTERISATION OF LSCF/YSZ-SDC AND LSCF/YSZ-SDCC DUAL COMPOSITE CATHODES FOR INTERMEDIATE-TEMPERATURE SOLID OXIDE FUEL CELL

Table 4	Screen	nrinting	thickness	of the	cathode layer	-
I auto T.	SCICCII	priming	unckness	or the	cathout layer	

<b>Dual Composite Cathode</b>	Total Thickness (μm)	Average Thickness per Printing (µm)
LYS1	17.9	1.79
LYS2	16.3	1.63
LYS3	15.1	1.51
LYSC1	23.8	2.38
LYSC2	32.5	3.25
LYSC3	45.6	4.56

### Electrochemical performance of the dual composite cathodes

The ionic conductivities of the symmetrical cells of LSCF/YSZ-SDC and LSCF/YSZ-SDCC were measured. Figures 8 and 9 show the impedance spectra of LSCF/YSZ-SDC and LSCF/YSZ-SDCC in an open circuit condition with a firing temperature from 700 °C to 500 °C in air. The impedance spectra were fitted, and the fitting results are shown in Table 5. The total polarization resistance of all cells showed a decrement with the increment in operating temperature (500–700 °C). In addition, the ionic conductivities of the dual composite cathodes were calculated using equation below.

Ionic conductivity formula:

$$\sigma = \frac{1}{\rho} = \left(\frac{1}{R}\right) x \left(\frac{A}{d}\right) \tag{1}$$

where:  $\sigma$ : Conductivity, d: Thickness of the sample (cm), R: Resistance ( $\Omega$ ), A: Effective area (cm<sup>2</sup>), and  $\rho$ : Resistivity ( $\Omega$ m).

LYS2 (0.080×10<sup>-5</sup> S cm<sup>-1</sup>) yielded the highest ionic conductivity for the LSCF/YSZ-SDC parameter, whereas LYSC1 (0.410×10<sup>-5</sup> S cm<sup>-1</sup>) attained the greatest ionic conductivity for the LSCF/YSZ-SDCC parameter. Both dual composite cathodes yielded the best ionic conductivity at 700 °C. LYSC1 (307 kΩ) showed the lowest polarization resistance, followed by LYSC2 (37.90 k $\Omega$ ) and LYSC3 (39.20 k $\Omega$ ), at 700 °C. Unfortunately, the recorded polarization resistance values were not favorable, as the resistance was too high, and the ionic conductivity was extremely low. Nonetheless, this finding proved that the conductivity and polarization resistance of LSCF/YSZ-SDCC was slightly better compared with those of the dual composite cathodes without the addition of binary carbonate. This finding was also coherent with the findings of previous research, which reported that binary carbonates are able to enhance the electrochemical performances. [11-12].

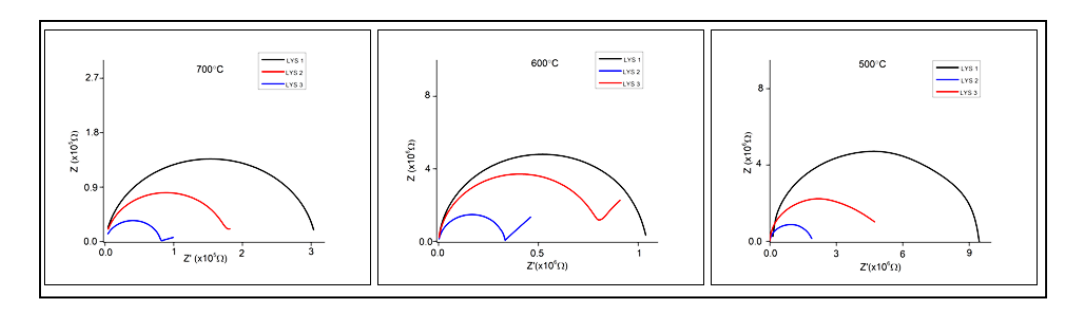


Figure 8. Impedance spectra of LSCF/YSZ-SDCC at 700, 600 and 500 °C

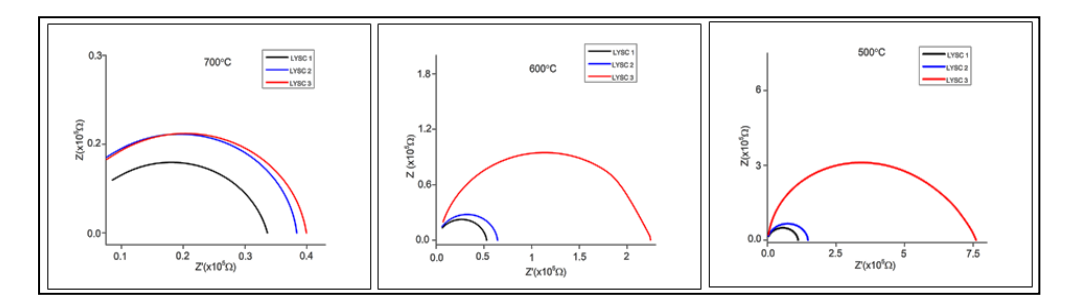


Figure 9. Impedance spectra of LSCF/YSZ-SDCCC at 700, 600 and 500 °C

Table 5. Polarization resistance and conductivity of the dual composite cathodes from 700 °C to 500 °C

Temperature	Samples	Total Resistance, ( $R_{total}$ ) [k $\Omega$ ]	Conductivity, (σ) [×10 <sup>-5</sup> S cm <sup>-1</sup> ]
	LYS1	307.0	0.042
	LYS2	159.90	0.080
700 °C	LYS3	$3.61 \times 10^{3}$	0.004
	LYSC1	31.10	0.410
	LYSC2	37.90	0.336
	LYSC3	39.20	0.325
	LYS1	$1.04 \times 10^{3}$	0.012
	LYS2	666.0	0.019
600 °C	LYS3	$8 \times 10^{3}$	0.0016
000 C	LYSC1	52.50	0.2426
	LYSC2	63.60	0.2003
	LYSC3	222.0	0.0574
	LYS1	$9.31 \times 10^{3}$	0.0014
	LYS2	$6.39 \times 10^{3}$	0.0020
500 °C	LYS3	$16.1 \times 10^3$	0.0008
	LYSC1	111.0	0.1148
	LYSC2	148.0	0.0861
	LYSC3	759.0	0.0168

The high ionic conductivity for excellent fuel cell performance at the intermediate- to low-temperature region is in the range of 0.01–1 S cm<sup>-1</sup>[21]. The data gathered in this study show that the obtained ionic conductivity is not within the acceptable range. Some

factors possibility affected the performances of the LSCF/YSZ-SDC and LSCF/YSZ-SDCC cells. The first factor was the selection of sintering temperature during the preparation of the symmetrical cells. The sintering temperature for a YSZ material is 1300–1600 °C;

therefore, 1400 °C was chosen as the sintering temperature for SOFC application [22]. In addition, selecting the appropriate temperature for a material is crucial, as high conductivity is achieved when the operating temperature is above the melting point of the material [23]. Besides the selection of sintering temperature, the development of symmetrical cells is considered one of the reasons for the low ionic conductivity. For example, during the cross-sectional analysis, the dual composite ink was not well screen printed on the surface of the YSZ pellet. This poor application may trap air between the cathode and electrolyte layers. During the printing process, parameters, including printing repetition layer, squeegee-related parameters, printing angle and forces exerted during the screen-printing process, influence the quality of the printed layer [20].

#### Conclusion

The current study presented the development of new dual composite cathodes, namely, LSCF/YSZ-SDC and LSCF/YSZ-SDC carbonate, for use in intermediate-temperature SOFC application. The main objective was to enhance the electrochemical performances of LSCF/YSZ-GDC and LSM/GDC-YSZ, which remains a challenge owing to the poor ionic conductivities of LSCF/YSZ-SDC and LSCF/YSZ-SDCC. However, this study proved that the addition of the Li/Na binary carbonate helped increase the ionic conductivity and showed a better electrochemical performance compare with LSCF/YSZ-SDC.

#### Acknowledgement

The research was supported by the Ministry of Higher Education of Malaysia through funding under the Fundamental Research Grant Scheme (FRGS/1/2020/TK0/UTHM/02/15) and partially funded by Universiti Tun Hussein Onn Malaysia under the Collaborative Research Grant (CRG K260) and Postgraduate Research Grant (GPPS H577).

#### References

 Udomsilp, D., Thaler, F., Menzler, N. H., Bischof, C., de Haart, L. G. J., Opitz, A. K. and Bram, M.(2019). Dual-phase cathodes for metalsupported solid oxide fuel cells: Processing

- performance, durability. *Journal of the Electrochemical Society*, 166(8): F506.
- Rahman, N. F. A., Rahman, H. A and Azmi, M. A. (2021). Perovskite-type oxide-based dual composite cathode for solid oxide fuel cells: A short review. *Solid State Phenomena*, 317: 417-425.
- 3. Ko, H. J., Myung, J. H., Hyun, S. H. and Chung, J. S. (2012). Synthesis of LSM-YSZ-GDC dual composite SOFC cathodes for high-performance power-generation systems. *Journal of Applied Electrochemistry*, 42(4): 209-215.
- Ko, H. J., Myung, J. H., Lee, J. H., Hyun, S. H. and Chung, J. S. (2012). Synthesis and evaluation of (La<sub>0.6</sub>Sr<sub>0.4</sub>)(Co<sub>0.2</sub>Fe<sub>0.8</sub>)O<sub>3</sub> (LSCF)-Y<sub>0.08</sub>Zr<sub>0.92</sub>O<sub>1.96</sub> (YSZ)-Gd<sub>0.1</sub>Ce<sub>0.9</sub>O<sub>2-δ</sub> (GDC) dual composite SOFC cathodes for high performance and durability. *International Journal of Hydrogen Energy*, 37(22): 17209-17216.
- Railsback, J., Choi, S. H. and Barnett, S. A. (2019). Effectiveness of dense Gd-doped ceria barrier layers for (La,Sr)(Co,Fe)O<sub>3</sub> cathodes on Yttriastabilized zirconia electrolytes. Solid State Ionics, 335: 74-81.
- 6. Fergus, J., Hui, R., Li, X., Wilkinson, D. P and Zhang, J. (2016). Solid oxide fuel cells: Materials properties and performance. CRC press.
- Rahman, H. A., Ng, K. H., Ahmad, S., Taib, H., Mahzan, S., Salleh, S. M. and Muchtar, A. (2019, March). Influence of microstructure on the electrochemical behaviour of LSCF-SDCC. In *IOP* Conference Series: Materials Science and Engineering, 494(1): 012062.
- 8. Mohammad, S. F., Ahmad, S., Rahman, H. A. and Muchtar, A. (2019). Effect of SSC Loading on the microstructural stability SSC-SDCC composite cathode as new potential SOFC. *International Journal of Integrated Engineering*, 11(7): 162-168.
- 9. Somalu, M. R., Muchtar, A., Daud, W. R. W. and Brandon, N. P. (2017). Screen-printing inks for the fabrication of solid oxide fuel cell films: a review. *Renewable and Sustainable Energy Reviews*, 75: 426-439.

- 10. Huang, J., Gao, Z. and Mao, Z. (2010). Effects of salt composition on the electrical properties of samaria-doped ceria/carbonate composite electrolytes for low-temperature SOFCs. *International Journal of Hydrogen Energy*, 35(9): 4270-4275.
- 11. Abd Rahman, H., Agun, L., Hoa, N. K., Ahmad, S. and Nordin, N. A. (2020). Effects of binary (lithium/natrium)<sub>2</sub> carbonates on the phase and microstructural stability of LSCF-SDC for low temperature solid oxide fuel cells. *Sains Malaysiana*, 49(12): 3155-3167.
- 12. Mohammad, S. F., Ahmad, S., Rahman, H. A. and Muchtar, A. (2019). Effect of SSC loading on the microstructural stability SSC-SDCC composite cathode as new potential SOFC. *International Journal of Integrated Engineering*, 11(7): 162-168.
- 13. Ghasdi, M. and Alamdari, H. (2010). CO sensitive nanocrystalline *LaCoO*<sub>3</sub> perovskite sensor prepared by high energy ball milling. *Sensors and Actuators B: Chemical*, 148(2): 478-485.
- 14. Baharuddin, N. A., Abd Rahman, H., Muchtar, A., Sulong, A. B. and Abdullah, H. (2013). Development of lanthanum strontium cobalt ferrite composite cathodes for intermediate-to lowtemperature solid oxide fuel cells. *Journal of Zhejiang University Science A*, 14(1): 11-24.
- 15. Gao, D., Zhao, J., Zhou, W., Ran, R. and Shao, Z. (2011). Influence of high-energy ball milling of the starting powder on the sintering; microstructure and oxygen permeability of  $Ba_{0.5}Sr_{0.5}Fe_{0.5}O_{3-\delta}$  membranes. *Journal of Membrane Science*, 366(1-2): 203-211.
- 16. Parwaiz, S., Khan, M. M. and Pradhan, D. (2019). *CeO*<sub>2</sub>-based nanocomposites: An advanced alternative to TiO<sub>2</sub> and ZnO in sunscreens. *Materials Express*, 9(3): 185-202.
- 17. Lu, X., Heenan, T. M., Bailey, J. J., Li, T., Li, K.,

- Brett, D. J. and Shearing, P. R. (2017). Correlation between triple phase boundary and the microstructure of solid oxide fuel cell anodes: The role of composition, porosity and Ni densification. *Journal of Power Sources*, 365: 210-219.
- Somalu, M. R., Muchtar, A., Daud, W. R. W. and Brandon, N. P. (2017). Screen-printing inks for the fabrication of solid oxide fuel cell films: a review. Renewable and Sustainable Energy Reviews, 75: 426-439.
- Zhang, J. and Jung, Y. G. (2018). Advanced ceramic and metallic coating and thin film materials for energy and environmental applications Berlin: Springer: pp. 20.
- Baharuddin, N. A., Abdul Rahman, N. F., Abd. Rahman, H., Somalu, M. R., Azmi, M. A. and Raharjo, J. (2020). Fabrication of high-quality electrode films for solid oxide fuel cell by screen printing: a review on important processing parameters. *International Journal of Energy Research*, 44(11): 8296-8313.
- 21. Chen, Y., Lin, Y., Zhang, Y., Wang, S., Su, D., Yang, Z. and Chen, F. (2014). Low temperature solid oxide fuel cells with hierarchically porous cathode nano-network. *Nano Energy*, 8: 25-33.
- 22. Talebi, T., Haji, M. and Raissi, B. (2010). Effect of sintering temperature on the microstructure, roughness and electrochemical impedance of electrophoretically deposited YSZ electrolyte for SOFCs. *International Journal of Hydrogen Energy*, 35(17): 9420-9426.
- Ali, S. M., Muchtar, A., Sulong, A. B., Muhamad, N. and Majlan, E. H. (2013). Influence of sintering temperature on the power density of samariumdoped-ceria carbonate electrolyte composites for low-temperature solid oxide fuel cells. *Ceramics International*, 39(5): 5813-5820.

# Malaysian Journal of Analytical Sciences (MJAS)



Published by Malaysian Analytical Sciences Society

#### PtRu SUPPORTED ON POROUS 3D TITANIUM DIOXIDE-GRAPHENE AEROGEL AS A POTENTIAL ELECTROCATALYST FOR DIRECT METHANOL FUEL CELLS

(PtRu disokong pada 3D Titanium Dioksida-Grafin Aerogel Berliang Sebagai Potensi Elektromangkin untuk Sel Bahan Bakar Metanol Langsung)

Siti Hasanah Osman<sup>1\*</sup>, Siti Kartom Kamarudin<sup>1,2</sup>, Sahriah Basri<sup>1</sup>, Nabila A.Karim<sup>1</sup>

<sup>1</sup>Fuel Cell Institute

<sup>2</sup>Department of Chemical and Process Engineering, Faculty of Engineering and Built Environment Universiti Kebangsaan Malaysia, 43600 UKM Bangi, Selangor, Malaysia

\*Corresponding author: ctie@ukm.edu.my

Received: 9 November 2021; Accepted: 27 February 2022; Published: 27 June 2022

#### Abstract

The catalyst support is typically implemented to improve the catalytic activity in direct methanol fuel cells (DMFCs). Thus, this study focused on the novel support of 3D hierarchical porous TiO<sub>2</sub>-graphene aerogel which was established via a combination of hydrothermal method and freezing drying method. XRD, Raman spectra, and FESEM were used to study the PtRu/TiO<sub>2</sub>-GA. The estimated particle size of PtRu/TiO<sub>2</sub>-GA determined from the XRD analysis was less than composite TiO<sub>2</sub>-GA. The existence of the carbon support material was confirmed by the Raman spectra in all generated samples. Within the electrocatalyst and TiO<sub>2</sub>-GA, the ratio value of the D band to the G band (I<sub>D</sub>/I<sub>G</sub>) was not significantly different. The computed I<sub>D</sub>/I<sub>G</sub> values for TiO<sub>2</sub>-GA and PtRu/TiO<sub>2</sub>-GA electrocatalysts were 0.99 and 1.02, respectively. The best TiO<sub>2</sub>-GA was doped with PtRu catalyst for the electrochemical test and DMFC performance based on FESEM characterization. PtRu/TiO<sub>2</sub>-GA exhibited better electrocatalytic activity, as well as improved PtRu usage efficiency stability and methanol oxidation reaction. Notably, the ECSA value was around 76.01 m<sup>2</sup>g<sup>-1</sup>, and the mass activity (957.15 mAmg<sup>-1</sup>) was higher than commercial with the same loading (20%) PtRu/C (110.79 mAmg<sup>-1</sup>). Interestingly after the 2000s, the current density of PtRu/TiO<sub>2</sub>-GA was consistently higher than that of PtRu/C. The superior electrocatalytic performance of PtRu/TiO<sub>2</sub>-GA towards methanol oxidation demonstrates its use in practical application as a promising anode material for DMFCs

Keywords: 3D titanium dioxide-graphene aerogel, platinum-ruthenium nanoparticles, electrocatalysis, methanol electro-oxidation

#### Abstrak

Sokongan mangkin biasanya dilaksanakan untuk meningkatkan aktiviti pemangkin dalam sel bahan api metanol langsung (SFML). Oleh itu, kajian ini memberi tumpuan kepada novel sokongan pada TiO<sub>2</sub>-grafin aerogel berliang hierarki 3D telah ditubuhkan dengan gabungan kaedah hidroterma dan kaedah pengeringan beku. XRD, spektrum Raman dan FESEM digunakan untuk mengkaji PtRu/TiO<sub>2</sub>-GA. Anggaran saiz zarah PtRu/TiO<sub>2</sub>-GA yang ditentukan daripada analisis XRD adalah kurang daripada komposit TiO<sub>2</sub>-GA. Kewujudan bahan sokongan karbon telah disahkan oleh spektrum Raman dalam semua sampel yang dihasilkan. Dalam elektromangkin dan TiO<sub>2</sub>-GA, nilai nisbah jalur D kepada jalur G (I<sub>D</sub>/I<sub>G</sub>) tidak berbeza dengan ketara. Nilai

I<sub>D</sub>/I<sub>G</sub> yang dikira untuk elektromangkin TiO<sub>2</sub>-GA dan PtRu/TiO<sub>2</sub>-GA ialah 0.99 dan 1.02, masing-masing. TiO<sub>2</sub>-GA terbaik akan didop dengan mangkin PtRu untuk ujian elektrokimia dan prestasi SFML berdasarkan pencirian FESEM. PtRu/ TiO<sub>2</sub>-GA mempamerkan aktiviti elektrokatalitik yang lebih baik, serta peningkatan kestabilan kecekapan penggunaan PtRu dan tindak balas pengoksidaan metanol. Terutama, nilai ECSA adalah sekitar 76.01 m<sup>2</sup>g<sup>-1</sup>, aktiviti jisim (957.15 mAmg<sup>-1</sup>) adalah lebih tinggi daripada komersial dengan pemuatan yang sama (20%) PtRu/C (110.79 mAmg<sup>-1</sup>). Menariknya selepas minit ke-2000 saat, ketumpatan semasa PtRu/TiO<sub>2</sub>-GA sentiasa lebih tinggi daripada PtRu/C. Prestasi elektrokatalitik unggul PtRu/TiO<sub>2</sub>-GA terhadap pengoksidaan metanol boleh digunakan dalam aplikasi praktikal sebagai bahan anod yang menjanjikan untuk DMFC.

**Kata kunci:** 3D titanium dioksida-grafin aerogel, nanopartikel platinum-ruthenium, elektromangkin, elektro-pengoksidaan metanol

#### Introduction

Direct methanol fuel cells (DMFCs) have gained traction recently due to their technological advances through a variety of characteristics: low emissions, excellent energy conversion efficiency, liquid fuel handling convenience, and low operating temperature. These are the results of the increasing use of mobile devices and the prerequisite of affording sufficient energy and power for the application [1, 2]. The electrochemical reaction in a direct methanol fuel cell is represented as follows:

 $CH_3OH + H_2O \rightarrow CO_2 + 6H^+ + 6e^ E^{\circ} = 0.016V \text{ (vs. SHE) (Anode reaction)}$ 

 $3/2O_2 + 6H^+ + 6e^- \rightarrow 3H_2O$ E° = 1:229V (vs: SHE) (Cathode reaction)

 $CH_3OH + H_2O \rightarrow CO_2 + 6H^+ + 6e^ E^\circ = 1:245V$  (vs: SHE) (Overall reaction)

The need for highly active catalysts for the oxidation process of hydrogen-rich liquid fuels is one of the major driving forces behind the development of DMFC technology. The electrocatalyst selection is critical for DMFC because the quality of the reaction kinetics of catalyst influences current density and cell lifespan. Improved catalyst activity and durability can be achieved through the development of novel support materials or the use of innovative catalytic metals [3]. Due to their increased catalytic activity in the electrooxidation of methanol, platinum group metals (PGMs) are the most used anode catalysts in DMFCs [4-8]. Platinum is costly, thus finding a replacement catalyst will necessitate further research. The best catalyst for DMFCs right now is bimetallic platinumruthenium (PtRu). Pt loading can be lowered by reducing the electrocatalyst costs in DMFC using only

the corresponding ratio of 1:1. Additionally, bimetallic Ru catalyst works in catalytic operations by eliminating carbon monoxide (CO) from the active site for HOR, where this catalyst can reduce CO poisoning [11, 12]. PtRu demonstrated a higher catalytic activity in the DMFC according to research by Bock et al. [4], and it was evident that the catalytic performance was significantly dependent on the distribution of Pt and Ru sites at the atomic level. However, the PtRu catalyst cannot solve the problem of low methanol oxidation. Further catalyst modifications are required to help the fuel cell sector.

The DMFC has been in progress for a decade with the creation of several catalyst-based solutions. Alternative support materials are stable and cost-effective, and they have been identified and developed with great effort [28-30]. Novel carbon supports, for example carbon nanotubes [5], mesoporous carbon [6], graphene [7], noncarbon materials, and nonconductive whiskers, due to their strong corrosion-resistance, have been explored as carbon alternatives. Graphene is the best candidate for catalyst support in fuel cells because of its chemical resistance, large and sufficient porosity, high conductivity, and diversity of topologies (network, aerogel, foam, etc.) [8, 9]. In general, the graphene aerogel (GA), which has a three-dimensional (3D) structure, has received a lot of attention due to its extensive macroporosity and multidimensional electron transport pathways, making it ideal for catalysis and energy storage devices [10, 11]. In the advancement of DMFCs, applying additional materials to the catalyst, including the formation of new hybrid catalysts, has become a trend [4-6]. However, issues such as electronic and protonic functioning, poor catalytic activity, stability, and conductivity are still persistent.

The most used materials to improve the electrocatalysis of DMFCs are metal oxides. Titanium dioxide (TiO2) is a type of inorganic substance, non-flammable, and corrosion-resistant, fundamentally stable. Furthermore.  $TiO_2$ crystal structures are thermodynamically stable, contributing the production of a composite material that is thermally and electrochemically stable [12]. Anatase stimulates charge carriers deeper within the bulk material, leading more in surface reactions and rising catalytic activity with time [13]. Additionally, when the TiO<sub>2</sub> metal oxide interacts with another component, the electrical behaviour of the materials improves as well. Instead of lowering CO oxidation potentials, this material can also support to increase oxidation activity [14]. The metal catalyst is supported by TiO2, which impacts the reaction kinetics and mechanism [15]. TiO<sub>2</sub> has all the advantages recorded above and it can be used in a variety of industries. Despite these benefits, the low conductivity of material prevents it from being widely used in fuel cell applications.

Significant loading of a Pt catalyst on TiO<sub>2</sub> made from an electrically conductive substance like N-doped carbon, as well as the use of sub-stoichiometric TiO<sub>2</sub>, is necessary to overcome this obstacle [16]. In 2018, Abdullah et al. [16] developed PtRu alloys on a nanofiber catalyst structure with metal oxide as the catalyst support; PtRu/TiO2-embedded carbon nanofiber (CNF) (PtRu/TECNF) was designed by Ito et al. [17], and Ercelik et al. [18] demonstrated PtRu/C-TiO2 as an electrocatalyst in DMFC technology; the result indicated that the performance of this new composite electrocatalyst was superior to PtRu catalyst. The abovementioned performance is due to the homogeneous dispersion of PtRu nanoparticles on the support material. Consequently, combining a powerful PtRu catalyst with a rational TiO2 and graphene aerogel structure has unique properties and high surface area, it has developed as the latest support material, with the possibility to increase electrocatalytic activity in MOR.

#### Materials and Methods Preparation of TiO<sub>2</sub>-GA and electrocatalyst

TiO<sub>2</sub>-GA was produced hydrothermally, then freezedried in a typical experiment. Firstly, 20 mg of TiO<sub>2</sub> were homogeneously disseminated into 10 mL of GO solution (2 mg/mL) using moderate ultrasonication for 2 hours. After that, the solution was placed in a 50mL of Teflon-lined autoclave and kept at 200°C for 12 hours. To make a TiO<sub>2</sub>-GA composite, the produced TiO<sub>2</sub>-graphene hydrogel was thoroughly rinsed with deionized water before being freeze-dried for 24 hours. The steps of TiO<sub>2</sub>-GA production are depicted schematically in Figure 1.

For electrocatalyst synthesis, a microwave-assisted alcohol reduction approach was used. The optimal TiO<sub>2</sub>-GA support doped with PtRu catalyst was chosen specifically for this study. On TiO<sub>2</sub>-GA support, 20 wt.% Pt-Ru with an atomic ratio of 1:1 was loaded. To begin, Ethylene Glycol (EG) solutions were combined with ruthenium chloride precursors and chloroplatinic acid precursors, and were homogenized for 15 minutes. After that, the TiO2-GA powder that had been produced was mixed into the cooperation precursor solutions and agitated for 30 minutes to ensure that everything was well mixed. After that, the pH of the solution was adjusted to 10 using a 1 M NaOH solution. In addition, the mixture was microwaved for 1 minute, and was left to accomplish the reduction process for 1 minute twice. Finally, before being dried in a 120 °C oven for 3 hours, the sample was filtered and rinsed a few times with ethanol and DI water to remove the impurities.

#### Characterizations

To prove crystallinity in the manufactured tests for characterization uses, X-ray Diffraction (XRD) is a powerful physical description method. Using a D8 Advance/Bruker, AXS Germany model, all fabricated tests were examined at  $2\theta$  from  $5^{\circ}$  to  $100^{\circ}$ . Moreover, the degree of graphitization was described using Raman spectrum analysis. The surface morphology and forms of the samples were explored using a Field Emission Scanning Electron Microscope (FESEM).

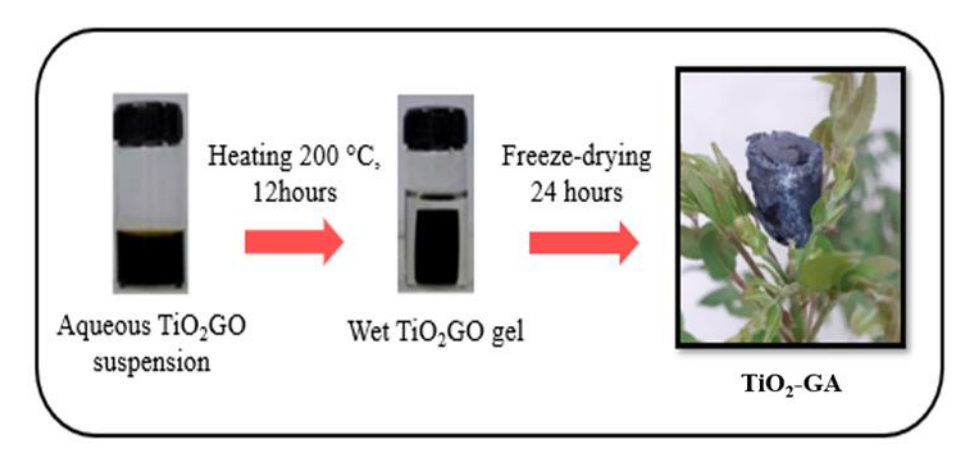


Figure 1. Design of the preparation of TiO<sub>2</sub>-GA composite

### Electrochemical characterization and performance test

In a 0.5 M H<sub>2</sub>SO<sub>4</sub> the electrocatalyst performance was estimated by determining the electrochemical surface area, ECSA, cyclic voltammetry (CV), and catalyst stability measured with a chronoamperometry (CA) test. Three-electrode cell systems were used at room temperature: a working electrode with a glassy carbon electrode (3 mm Ø), reference electrodes noted as Ag/AgCl electrodes, and counter platinum-based electrode. Furthermore, 3 mg of electrocatalyst of PtRu/TiO2-GA and commercial catalyst were dispersed in 150 mL DI water, 150 mL IPA, and 50 mL Nafion (5 wt.%) solution to make the electrocatalyst ink for the working electrode. On the glassy electrode, there was a catalyst loading of 0.0503 mg cm<sup>-2</sup>. The CV was measured at a 50 mVs<sup>-1</sup> scan rate with potentials ranging from -0.2 to 1.0 V vs. Ag/AgCl. Note that in this analysis, the potentials ranged from -0.2 to 1.0 V vs. Ag/AgCl, while CV was recorded at a 50 mVs<sup>-1</sup> scan rate. The long- term performance of all electrocatalysts was assessed using chronoamperometry (CA) in the electrolyte solution at a potential of 0.6 V for 2000 s.

#### **Results and Discussion**

The crystal structure and pattern of the built catalyst support and electrocatalyst were investigated using XRD analysis. As a result, the TiO<sub>2</sub>-GA support was synthesized by hydrothermal at 200 °C. The microwave-assisted alcohol reduction approach was used to make the PtRu/TiO<sub>2</sub>-GA and PtRu/C marketable. The analysis

of the diffraction peak for the associated sample and comparative samples of XRD pattern for PtRu/TiO2-GA electrocatalyst is shown in Figure 2(a). Peaks at 25.3°,  $37.8^{\circ}$ ,  $48.0^{\circ}$ ,  $53.9^{\circ}$ ,  $55.1^{\circ}$ ,  $62.7^{\circ}$ ,  $68.8^{\circ}$ ,  $70.3^{\circ}$ , and  $75.0^{\circ}$ are indexed to (101), (004), (200), (105), (211), (204), (116), (220), and (215) crystal planes of TiO<sub>2</sub> anatase, respectively based on XRD examination for TiO2-GA support sample [19, 20]. The TiO<sub>2</sub>-GA hydrothermal at 200 °C was chosen as the best-produced TiO2-GA and was doped with PtRu catalyst. The XRD results for the synthesized PtRu/TiO2-GA showed the presence of all particles, PtRu, and C support. The Pt particles peaked at  $39.7^{\circ}$  (111),  $46.2^{\circ}$  (200),  $67.5^{\circ}$  (220), and  $81.3^{\circ}$  (311). The diffraction peaks for Ru were 40.7° (111), 47° (200), 69° (220), and 83.7° (311). The structure of both metals was cubic, and in the electrocatalyst sample, high Bragg angles were detected in the range of 25°-60°, indicating that the catalyst possessed bimetallic or alloy interaction [21]. Additionally, the estimated crystallite size of PtRu was computed using Scherrer's equation, which revealed that PtRu/TiO2-GA particles were smaller than PtRu/C particles [22]. As shown in Table 1, the particle size of Pt and Ru can also be predicted using the crystallite size. In general, smaller particles perform better in MOR electrocatalysis reactions than larger particles, since smaller catalyst particles contribute to a higher particle surface area. Furthermore, the smaller catalyst particle size may allow for a reduction in the use of Pt in electrocatalyst, as well as a reduction in the overall cost of DMFC production. The decreased size of PtRu particles found in the

electrocatalyst sample could potentially be due to the lower crystalline structure.

In terms of the chemical and structural information offered by the shift in wavelength of inelastically scattered radiation, the D and G bands were 1350 and 1590 cm<sup>-1</sup>. The two separate peaks in the Raman spectra for the samples in Figure 2(b) indicated that the D band was linked to crystal boundary vibrations and the G band reflected perfect sp2 vibrations of graphitic crystals. From the Raman spectrum analysis, the intensity ratio of the D to G band (I<sub>D</sub>/I<sub>G</sub>) had a descending order: TiO<sub>2</sub>-GA (1.02), PtRu/ TiO<sub>2</sub>-GA (0.99) and PtRu/C (0.98). The band fluctuated depending on the relative intensity of the D and G bands on the type of graphite material, and it could be used to estimate the degree of graphitization. The I<sub>D</sub>/I<sub>G</sub> ratio observed in this work showed that the aerogel was successfully achieved after the catalyst was disseminated at TiO<sub>2</sub>-GA [23], [24]. Ultimately, in the disintegrated region and structure of TiO2-GA, the carbon layer in these electrocatalysis samples was not significantly different. The weak

Raman shift bands at  $152 \text{ cm}^{-1}$  and  $154 \text{ cm}^{-1}$  were identified in  $\text{TiO}_2\text{-GA}$  and  $\text{PtRu/TiO}_2\text{-GA}$ , respectively, and were linked to unique characteristics of  $\text{TiO}_2$  anatase [25].

FESEM was used to analyze the dispersion surface, morphologies, and sizes of PtRu/TiO2-GA and PtRu/C produced using a microwave-assisted alcohol-reduction technique. PtRu/TiO2-GA had a 3D-porous cellular structure, exhibiting constant porosity of sizes ranging from micrometres to sub micrometres as seen in Figure 3. Furthermore, the tight inspection revealed an evenly adorned PtRu nanoparticles in a 3D porous cellular structure, demonstrating a strong interaction among the PtRu-carbon building block. Interestingly, the PtRu/C images revealed that these carbon-supporting materials were spherical. [26]. The findings indicated that the samples were agglomerated with a diameter of 120-150 nm, which was available in the nanoscale range. The Van der Waals interaction surrounded by the particles could be causing the aggregation [27].

Table 1. Estimated crystallite size of TiO2-GA and PtRu/TiO2-GA on XRD analysis

Samples	XRD/Crystallite Size (nm)		
TiO <sub>2</sub> -GA	7.9		
PtRu/TiO <sub>2</sub> -GA	3.8		
PtRu/C	3.9		

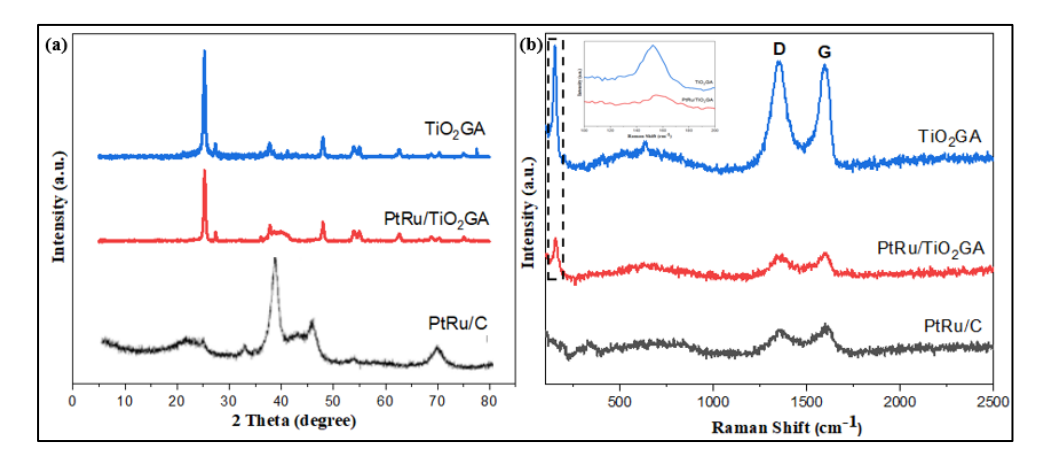


Figure 2. (a) XRD patterns of TiO<sub>2</sub>-GA composite and PtRu/TiO<sub>2</sub>-GA electrocatalyst (b) Raman spectra of TiO<sub>2</sub>-GA composite and PtRu/TiO<sub>2</sub>-GA electrocatalyst

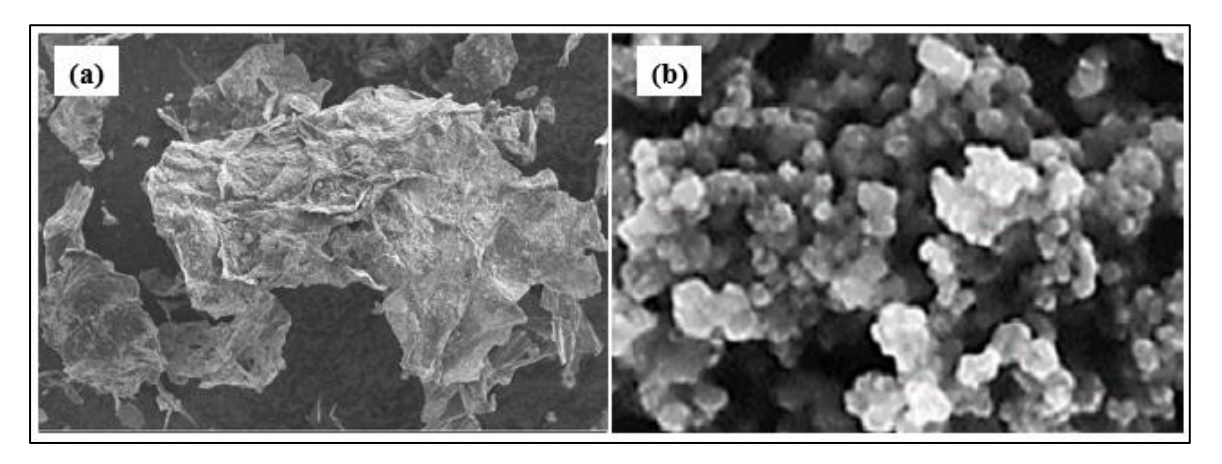


Figure 3. FESEM image of the prepared (a) PtRu/TiO2-GA and (b) PtRu/C Electrocatalytic performance

In recent decades, DMFCs have been intensively explored and gained increasing attention in the electrooxidation by methanol. For the methanol oxidation in acid media, the electrochemical efficiency of the PtRu/TiO2-GA catalyst has been explored. The PtRu/TiO2-GA CV curves and PtRu/C catalysts in N2 with 0.5M H<sub>2</sub>SO<sub>4</sub> saturated solutions are displayed in Figure 4(a). In the area from -0.2 V to 1.0 V vs Ag/AgCl, both electrics demonstrated the characteristics of hydrogen adsorption-desorption. The ECSAs computed for PtRu/TiO2-GA and PtRu/C amount was about 68.44 m<sup>2</sup> g<sup>-1</sup> and 20.44 m<sup>2</sup> g<sup>-1</sup>, respectively. The ECSA for PtRu/TiO2-GA was 3 times that of PtRu/C and 30 % greater than that for commercial PtRu/C. This finding demonstrates that retaining a bimetallic 3D structure in TiO2-GA helps to increase the ECSA of PtRu nanoparticles and improve catalyst utilization. This is owing to the differences in crystallite size between PtRu/TiO<sub>2</sub>-GA and PtRu/C as shown in Table 1 from the XRD analysis: the PtRu/TiO2-GA crystallite size for TiO<sub>2</sub>-GA was the lowest and it had a superior ECSA value. Hence, the catalyst and reaction surface area can be increased by using the smallest crystallite size.

Figure 4(b) illustrates that the peak mass activity PtRu/TiO<sub>2</sub>-GA is greater than PtRu/C. The CV values

are indicated in Table 2 for the PtRu/TiO<sub>2</sub>-GA and PtRu/C electrocatalyst. For PtRu/TiO<sub>2</sub>-GA catalyst, the value for mass activity was 957.15 mA mg<sup>-1</sup> PtRu, 12 times greater than that of the commercial PtRu/C catalyst. This reveals that the support for TiO<sub>2</sub>-GA is a superior replacement for carbon catalyst support. Throughout the carbonization process, the aerogel mixture can boost the electrical and thermal leads of the catalyst [28].

In a composite electrocatalyst, using an aerogel structure can increase the overall surface area as well as the active reaction site on the surface of the electrocatalyst. An additional benefit is the high anatase TiO<sub>2</sub> composition, as determined by the XRD measurements. Anatase has a higher electrocatalytic activity than rutile TiO<sub>2</sub>. Besides increasing peak current density, the metalsupport interaction also shows a favourable effect, and the material combination of PtRu and TiO2-GA is an effective electrocatalyst in DMFCs. The performance of PtRu/C is significantly poorer than that of PtRu agglomeration, where the ECSA value as well as the crystallite size as determined by XRD are emphasized. Such state reduces the possibility of the electrocatalyst surface to be an active site and lowers the performance of the electrocatalysts.

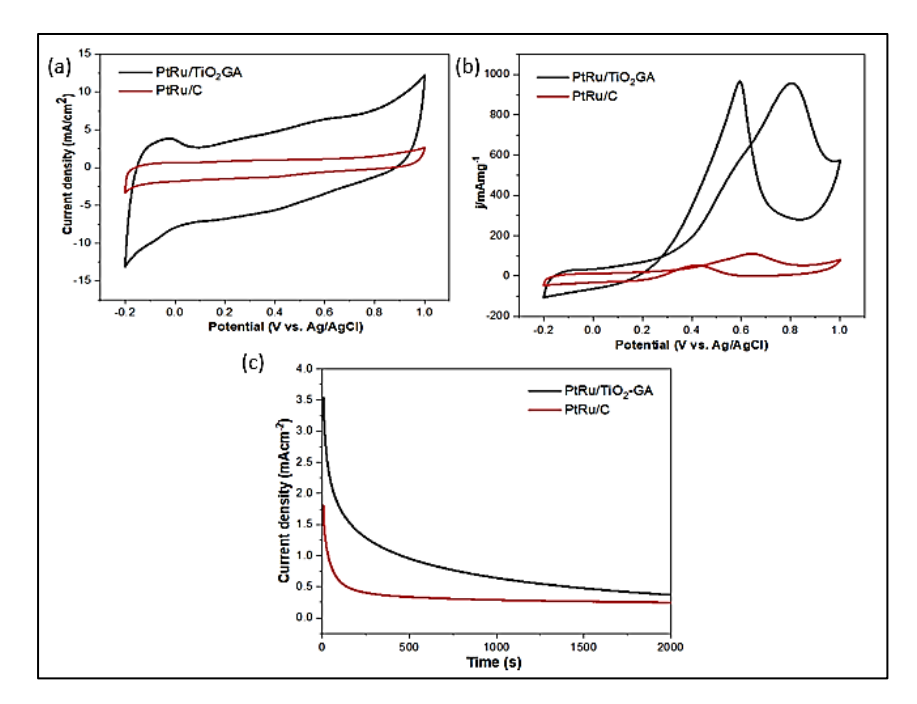


Figure 4. (a) CVs of PtRu/TiO<sub>2</sub>-GA and PtRu/C in N<sub>2</sub> saturated 0.5 M H<sub>2</sub>SO<sub>4</sub> solution at scan rate 50 mVs<sup>-1</sup>, (b) CVs of PtRu/TiO<sub>2</sub>-GA and PtRu/C in N<sub>2</sub> saturated 0.5 M H<sub>2</sub>SO<sub>4</sub> solution containing 1 M CH<sub>3</sub>OH at scan rate 50 mVs<sup>-1</sup>, and (c) Chronoamperometric curves of H<sub>2</sub>SO<sub>4</sub> in N<sub>2</sub> saturated containing 1 M CH<sub>3</sub>OH

Table 2. Assessment of the performance outcomes with the previous research

Research	Type of Catalyst	ECSA (m <sup>2</sup> /g <sub>PtRu</sub> )	Mass ativity (mA/mg <sub>PtRu</sub> )
This study	PtRu/TiO <sub>2</sub> -GA	68.44	957.15
This study	PtRu/C	20.44	79.11
Abdullah et al. [16]	PtRu/TiO <sub>2</sub> -CNF	10.4	345.64
Basri et al. [29]	PtRuNiFe/MWCNT	-	151.47
Ramli et al. [30]	PtRu/CNC	16.23	427.00

CA tests were carried out to verify the stability of electrocatalyst and endurance for long-term MOR performance in a 1M methanol solution containing 0.5 M H<sub>2</sub>SO<sub>4</sub> for 2000 seconds. At 0.6 V, the potential was kept constant. The CA curves electrocatalysts for the PtRu/TiO<sub>2</sub>-GA and PtRu/C are shown in Figure 4(c). The current density of electrocatalysts indicates a dramatic decline at the beginning of the experiment probably due to methanol oxidation mediation poisoning. The limiting current PtRu/TiO<sub>2</sub>-GA was higher than PtRu/C across the entire duration, indicating

better stability. The result demonstrated that the PtRu/TiO<sub>2</sub>-GA catalyst showed higher stability than PtRu/C. Consequently, it is assumed that the synergistic effects of combining Pt and Ru help to reduce poisoning rates [16]. Hence, the 3D hierarchical porous TiO<sub>2</sub>-graphene aerogel encapsulation structure is important in enhancing the durability. This unique structure can be extensively applicable to commercial catalytic products. It was also shown that TiO<sub>2</sub>-GA as support was a better alternative to bimetallic support since the mesoporous

structure of TiO<sub>2</sub>-GA could improve the total surface area on the electrocatalyst surface area.

#### Conclusion

The novel 3D hierarchical porous TiO<sub>2</sub>-graphene aerogel (TiO<sub>2</sub>-GA) was synthesized using hydrothermal technique and then freeze-dried before being used as a catalytic support for an anodic catalyst in the DMFC. Therefore, the catalytic activity of electrocatalyst was determined by comparing it to that of commercial PtRu/C. The maximal mass activity of the manufactured electrocatalyst PtRu/TiO<sub>2</sub>-GA was 12 times that of the PtRu/C commercial electrocatalyst. The catalyst support of TiO<sub>2</sub> and the graphene aerogel catalyst structure resulted in the maximum catalytic activity. The reaction between the PtRu and TiO<sub>2</sub>-GA catalysts at the metal-support interface serves to advance the characteristics of catalyst layers. Therefore, PtRu/TiO<sub>2</sub>-GA is a viable choice for anode catalyst support in DMFCs.

#### Acknowledgement

The authors gratefully acknowledge the financial support for this work by The Ministry of Higher Education (MOHE) MALAYSIA and Universiti Kebangsaan Malaysia under Grant No: KKP/2020/UKM-UKM/3/1.

#### References

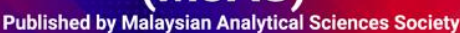
- Rashidi, R., Dincer, I., Naterer, G. F. and Berg, P. (2009). Performance evaluation of direct methanol fuel cells for portable applications. *Journal of Power Sources*, 187(2): 509-516.
- 2. Achmad, F., Kamarudin, S. K., Daud, W. R. W. and Majlan, E. H. (2011). Passive direct methanol fuel cells for portable electronic devices. *Applied Energy*, 88(5): 1681-1689.
- Zhao, L., Wang, Z. B., Li, J. L., Zhang, J. J., Sui, X. L. and Zhang, L. M. (2016). Hybrid of carbon-supported Pt nanoparticles and three dimensional graphene aerogel as high stable electrocatalyst for methanol electrooxidation. *Electrochimica Acta*, 189: 175-183.
- 4. Bock, C., Paquet, C., Couillard, M., Botton, G. A. and MacDougall, B. R. (2004). Size-selected synthesis of PtRu nano-catalysts: reaction and size control mechanism. *Journal of the American*

- Chemical Society, 126(25): 8028-8037.
- Zhang, X., Ma, J., Yan, R., Cheng, W., Zheng, J. and Jin, B. (2021). Pt-Ru/polyaniline/carbon nanotube composites with three-layer tubular structure for efficient methanol oxidation. *Journal of Alloys and Compounds*, 867: 159017.
- Li, W., Wang, Q., Wang, L., Fu, X. Z. and Luo, J. L. (2021). Mesoporous CeO<sub>2</sub>—C hybrid spheres as efficient support for platinum nanoparticles towards methanol electrocatalytic oxidation. Journal of Rare Earths, 39(6): 674-681.
- 7. Yang, Y., Guo, Y. F., Fu, C., Zhang, R. H., Zhan, W., Wang, P., ... & Zhou, X. W. (2021). In-situ loading synthesis of graphene supported PtCu nanocube and its high activity and stability for methanol oxidation reaction. *Journal of Colloid and Interface Science*, 595: 107-117.
- 8. Ren, X., Lv, Q., Liu, L., Liu, B., Wang, Y., Liu, A. and Wu, G. (2020). Current progress of Pt and Pt-based electrocatalysts used for fuel cells. *Sustainable Energy & Fuels*, 4(1): 15-30.
- 9. Karuppanan, K. K., Raghu, A. V., Panthalingal, M. K., Thiruvenkatam, V., Karthikeyan, P. and Pullithadathil, B. (2019). 3D-porous electrocatalytic foam based on Pt@ N-doped graphene for high performance and durable polymer electrolyte membrane fuel cells. Sustainable Energy & Fuels, 3(4): 996-1011.
- 10. Gorgolis, G. and Galiotis, C. (2017). Graphene aerogels: a review. *2D Materials*, 4(3): 032001.
- 11. Mao, J., Iocozzia, J., Huang, J., Meng, K., Lai, Y. and Lin, Z. (2018). Graphene aerogels for efficient energy storage and conversion. *Energy & Environmental Science*, 11(4): 772-799.
- Siwińska-Stefańska, K. and Jesionowski, T. (2017).
   Advanced hybrid materials based on titanium dioxide for environmental and electrochemical applications. In Titanium Dioxide. IntechOpen.
- 13. Odling, G. and Robertson, N. (2015). Why is anatase a better photocatalyst than rutile? The importance of free hydroxyl radicals. *ChemSusChem*, 8(11): 1838-1840.

- Dey, S. and Mehta, N. S. (2020). Synthesis and applications of titanium oxide catalysts for lower temperature CO oxidation. *Current Research in Green and Sustainable Chemistry*, 3: 10002.
- Bagheri, S., Muhd Julkapli, N. and Bee Abd Hamid, S. (2014). Titanium dioxide as a catalyst support in heterogeneous catalysis. *The Scientific World Journal*, 2014: 727496.
- Abdullah, N., Kamarudin, S. K. and Shyuan, L. K. (2018). Novel anodic catalyst support for direct methanol fuel cell: characterizations and single-cell performances. *Nanoscale Research Letters*, 13(1): 1-13.
- Ito, Y., Takeuchi, T., Tsujiguchi, T., Abdelkareem, M. A. and Nakagawa, N. (2013). Ultrahigh methanol electro-oxidation activity of PtRu nanoparticles prepared on TiO<sub>2</sub>-embedded carbon nanofiber support. *Journal of Power Sources*, 242: 280-288.
- Ercelik, M., Ozden, A., Seker, E. and Colpan, C. O. (2017). Characterization and performance evaluation of PtRu/CTiO<sub>2</sub> anode electrocatalyst for DMFC applications. *International Journal of Hydrogen Energy*, 42(33): 21518-21529.
- Liu, R., Guo, W., Sun, B., Pang, J., Pei, M. and Zhou, G. (2015). Composites of rutile TiO<sub>2</sub> nanorods loaded on graphene oxide nanosheet with enhanced electrochemical performance. *Electrochimica Acta*, 156: 274-282.
- Xiang, C., Guo, R., Lan, J., Jiang, S., Wang, C., Du, Z. and Cheng, C. (2018). Self-assembling porous
   3D titanium dioxide-reduced graphene oxide aerogel for the tunable absorption of oleic acid and RhodamineB dye. *Journal of Alloys and Compounds*, 735: 246-252.
- Cordero-Borboa, A. E., Sterling-Black, E., Gómez-Cortés, A. and Vázquez-Zavala, A. (2003). X-ray diffraction evidence of the single solid solution character of bi-metallic Pt-Pd catalyst particles on an amorphous SiO<sub>2</sub> substrate. *Applied Surface Science*, 220(1-4): 169-174.
- Vorokh, A. S. (2018). Scherrer formula: estimation of error in determining small nanoparticle size. *Nanosystem Physics Chemistry Mathematics*, pp. 364-369.

- Stankovich, S., Dikin, D. A., Piner, R. D., Kohlhaas, K. A., Kleinhammes, A., Jia, Yue, W., SonBinh, T. N., and Ruoff, R. S. (2007). Synthesis of graphene-based nanosheets via chemical reduction of exfoliated graphite oxide. carbon, 45(7): 1558-1565.
- Zhu, Y., Murali, S., Cai, W., Li, X., Suk, J. W., Potts, J. R. and Ruoff, R. S. (2010). Graphene and graphene oxide: synthesis, properties, and applications. *Advanced Materials*, 22(35): 3906-3924.
- 25. Li, Y., Cai, Q., Wang, L., Li, Q., Peng, X., Gao, B., ... and Chu, P. K. (2016). Mesoporous TiO<sub>2</sub> nanocrystals/graphene as an efficient sulfur host material for high-performance lithium–sulfur batteries. ACS Applied Materials & Interfaces, 8(36): 23784-23792.
- Norilhamiah, Y., Kamaruddin, S. K., Karim, N. A., Masdar, M. S. and Loh, K. S. (2017). Gliserol, P. E. (2017). Preliminary study on pd-based binary catalysts supported with carbon nanofiber for the electrooxidation of glycerol. *Malaysian Journal of Analytical Sciences*, 21(3): 700-708.
- 27. Ibrahim, S. A., Anwar, M. K., Ainuddin, A. R., Hariri, A., Rus, A. Z. M., Kamdi, Z., Yunos, M. Z., and Harun, Z. (2019). Synthesis and characterization of visible light active Fe-TiO<sub>2</sub> using hydrothermal method. *International Journal of Integrated Engineering*, 11(5): 80-85.
- 28. Shaari, N. and Kamarudin, S. K. (2019). Current status, opportunities, and challenges in fuel cell catalytic application of aerogels. *International Journal of Energy Research*, 43(7): 2447-2467.
- Basri, S., Kamarudin, S. K., Daud, W. R. W., Yaakob, Z. and Kadhum, A. A. H. (2014). Novel anode catalyst for direct methanol fuel cells. *The* Scientific World Journal, 2014: 547604.
- 30. Ramli, Z. A., Kamarudin, S. K., Basri, S. and Zainoodin, A. M. (2020). The potential of novel carbon nanocages as a carbon support for an enhanced methanol electro oxidation reaction in a direct methanol fuel cell. *International Journal of Energy Research*, 44(13): 10071-10086.

## Malaysian Journal of Analytical Sciences (MJAS)





# A REVIEW ON PREPARATION, MODIFICATION AND FUNDAMENTAL PROPERTIES OF SPEEK NANOCOMPOSITE PEM FOR DIRECT METHANOL FUEL CELL APPLICATIONS

(Satu Ulasan tentang Penyediaan, Pengubahsuaian dan Ciri Asas Komposit Nano Membran Elektrolit Polimer SPEEK untuk Aplikasi Sel Bahan Api)

Nor Fatina Raduwan and Norazuwana Shaari\*

Fuel Cell Institute, Universiti Kebangsaan Malaysia, Bangi, 43600 Selangor, Malaysia

\*Corresponding author: norazuwanashaari@ukm.edu.my

Received: 14 December 2021; Accepted: 3 February 2022; Published: xx June 2022

#### Abstract

Various types of promising proton exchange membrane (PEM) are based on thermoplastics due to their excellent conductivity, good thermal and chemical stability, high durability as well as low fabrication and material cost. Sulfonated poly (ether ether ketone) or SPEEK is one of the examples of thermoplastic polymer that has been sulfonated to enhance its fundamental properties. These properties can be altered and improved through the fabrication process and modifications of the membranes. Thus, current researches on combining SPEEK with other polymers and inorganic particles through various fabrication methods are discussed in this review. The characterization of SPEEK-based membrane in terms of its water uptake, methanol permeability, proton conductivity, thermal and mechanical stability are also included in the discussion. The impact of membrane modifications on the fundamental properties and comparison of different membrane preparation methods are addressed. In addition, the advantages and drawbacks of modified membranes are summarized.

Keywords: SPEEK; polymer electrolyte membrane; fuel cell

#### Abstrak

Pelbagai jenis polimer elektrolit membran yang diyakini adalah daripada termoplastik disebabkan oleh kekonduksian yang cemerlang, kestabilan terma dan kimia yang baik, ketahanan yang tinggi dan kos bahan dan pembuatan yang rendah. Poli (eter eter keton) tersulfonat atau SPEEK adalah satu contoh polimer termoplastik yang telah disulfonasi untuk mempertingkatkan ciri asas seperti pengambilan air dan ketertelapan metanol yang rendah, meningkatkan kekonduksian proton dan mempunyai ketahanan dan kestabilan yang tinggi. Ciri-ciri ini boleh diubahsuai dan dipertingkat melalui proses fabrikasi dan pengubahsuaian ke atas membran. Oleh yang demikian, para penyelidik menggabungkan SPEEK dengan polimer jenis lain dan bahan tak organik melalui pelbagai cara fabrikasi telah dibincangkan dalam ulasan ini. Kesan daripada pengubahsuaian membrane k etas ciri-ciri asanya dan perbandingan cara penyediaan membrane turut dibincangkan. Seterusnya, kelebihan dan kekurangan membran terubahsuai turut diringkaskan.

Kata kunci: SPEEK, membran elektrolit polimer, sel fuel

#### Introduction

As of September 2021, the current world population is 7.9 billion, according to the most recent United Nations estimates as elaborated by Worldometer. It is estimated that the population will reach up to 10 billion in another 30 years [1]. In line with the increase in the world population, the demand for energy also increases. Conventional fossil fuels are the primary sources of power to meet the world's energy demands. However, the depletion of fossil fuel sources and the rise of environmental issues, i.e., global warming due to the excessive releases of greenhouse gases have shifted the interest into the environmentally sustainable energy research [2]. One of the alternative energies that can solve this issue is through the utilization of natural sources such as hydrogen.

Hydrogen is one of the most abundant elements in the universe. For instance, the sun consists mainly of hydrogen. While on earth, hydrogen combines with other elements either in liquid, gas, or solid form as it does not exist freely in nature. As it only exists in a compound form, specific processes are required to split and obtain hydrogen, such as reforming, hydrolysis, and electrolysis [3]. Hydrogen can be utilized in many applications such as petroleum refining and fertilizer production, and for the past decades it has been widely used in fuel cell to generate electricity.

#### Fuel cell technology

Fuel cell is an electrochemical device that converts fuel and oxidant into electricity [4]. Basically, hydrogen is supplied as fuel at the anode and oxygen (oxidant) at the cathode. At the cathode, oxygen is reduced, and oxygen ions are produced. These oxygen ions will pass through the electrolyte and move towards the anode. When reaching the anode, they react with the protons that are broken down from hydrogen [5]. Electrons that are obtained from hydrogen molecules travel at the outer circuit and generate electricity. The half-reactions of this process at both sides are shown by the following equation:

Cathode :  ${}^{1}/_{2} O_{2} + 2H^{+} + 2e^{-} \rightarrow H_{2}O$  (1)

Anode :  $H_2 \rightarrow 2H^+ + 2e^-$  (2)

Overall reaction :  $H_2 + \frac{1}{2} O_2 \rightarrow H_2O$  (3)

As it generates electricity through an electrochemical reaction, the by-products from the reaction are basically water and heat, which do not contribute to the environmental pollution. In fact, the water can be reused in the system, and the heat that is generated can be recycled into another system, such as a water heater system. These reused and recycled processes eliminate energy wastes and yield high energy efficiency of fuel cells up to 90% [6]. Correspondingly, there are various types of fuel cells depending on the types of electrolytes that are used. They are further sub-categorized by the types of fuel (hydrogen, reforming hydrogen-rich fuels, i.e., methanol, ethanol, and hydrocarbon), and operating temperature low temperature (LT), intermediate temperature (IT), high temperature (HT). For example, direct methanol fuel cell (DMFC) and direct ethanol fuel cell (DEFC), also known as direct liquid fuel cell (DLFC), are the extension study to the proton exchange membrane fuel cell (PEMFC). While for microbial fuel cell (MFC), some improvements are being made where glucose is employed on-non enzymatic noble metal electrode to overcome certain drawbacks of the conventional MFC, which is known as direct glucose fuel cell (DGFC). Whereas a direct borohydride fuel cell (DBFC) is a sub-category of an alkaline fuel cell (AFC), and the latest research has reported that the anionic exchange membrane fuel cell (AEMFC) possesses great potential in replacing the traditional liquid electrolyte AFC [7]. In SOFC, there are three sub-categories, which are differentiated by the range of operating temperature, i.e., LT-SOFC, IT-SOFC and HT-SOFC. Each temperature range requires different types of material to be used as electrolytes. All existing fuel cells and their characteristics, including the efficiency, are summarized in Table 1.

		31			
Electrolyte	Types of Fuel Cells	Sub-Category	Operating Temperature (°C)	Fuel/Oxidant	Efficiency (%)
Phosphate buffer	MFC	DGFC	25-30	Organic load/Oxygen	-
Alkaline solution	AFC	DBFC AEMFC	50-90	Sodium or potassium borohydride/Oxygen or hydrogen peroxide Hydrogen/Oxygen	50-70
Solid polymer membrane	PEMFC	DMFC DEFC	50-120	Methanol/Oxygen Ethanol/Oxygen	40-50
Acidic solution	PAFC		175-220	Hydrogen/Oxygen	40-45
Molten mixture	MCFC		600-650	Hydrogen/Oxygen	50-60
Ceramic oxides	SOFC	LT-SOFC IT-SOFC HT-SOFC	400-600 600-800 800-1000	Hydrogen or hydrocarbon/Oxygen	60-90

Table 1. Types of fuel cells and their characteristics

Among the types of fuel cells, DMFC which is the subcategory of PEMFC has been widely used in various applications- covering small-scale appliances to mobile usage such as transportation. These broad applications are due to the advantages of low operating temperature, which lead to rapid start-up and a long-life span. Besides that, the DMFC system yields high power density and through its compact design, provides superior transportation facilities compared to other existing fuel cells. Although it has a compact design, complex heat and water management are unavoidable. Also, it uses expensive materials as a catalyst, such as Platinum, Pt, and Palladium, Pd to speed up the chemical reaction, and Nafion® for membrane materials. However, owing to its vast advantages, DMFC has generated an interest among researchers to find a way to overcome the drawbacks.

### Development of proton exchange membrane (PEM) for DMFC

DMFC is a type of fuel cell that uses methanol as fuel to replace hydrogen in a typical fuel cell. As methanol is a non-volatile liquid fuel, it does not easily evaporate into gas at room temperature. In fact, this type of fuel cell does not require any fuel processing equipment as the mixture of methanol and water are directly fed into the cell. Therefore, it is easy to store and handle compared to the volatile hydrogen gas. Other advantages of using methanol in fuel cell systems are the high energy density that is obtained; due to its abundant resources, the price of methanol is relatively cheap and affordable. The reactions that take place in both electrodes are as follows:

Anode : 
$$CH_3OH + H_2O \rightarrow CO_2 + 6H^+ + 6e^-$$
 (4)

Cathode : 
$$3/2 O_2 + 6H^+ + 6e^- \rightarrow 3H_2O$$
 (5)

Accordingly, the overall cell reaction is

Overall : 
$$3/2 O_2 + CH_3OH \rightarrow CO_2 + 2H_2O$$
 (6)

One of the key components in fuel cells, especially for DMFC, is the proton exchange membrane (PEM). PEM is needed to complete the electrochemical reaction to fulfill the energy requirement in which it serves to transfer H<sup>+</sup> within itself from anode to cathode [8]. The high and outstanding PEM must meet specific criteria such as having good oxidative and hydrolytic stability, possessing high mechanical and thermal stability, and

yield a high proton conductivity as well as being cost effective in the fabrication of membrane electrode assembly (MEA). As it is located between the electrodes, the PEM must also have good barrier properties to avoid the mixing of fuel (methanol) from the anode and oxidant (oxygen) coming from the cathode. The permeability of the membrane is an unresolved issue that is still under ongoing research. The

high permeability membrane or leakage of the MEA (consisting of PEM) can contribute to a serious methanol crossover issue, which eventually will deteriorate the performance of fuel cell. Therefore, a high durability membrane is needed to overcome this issue.

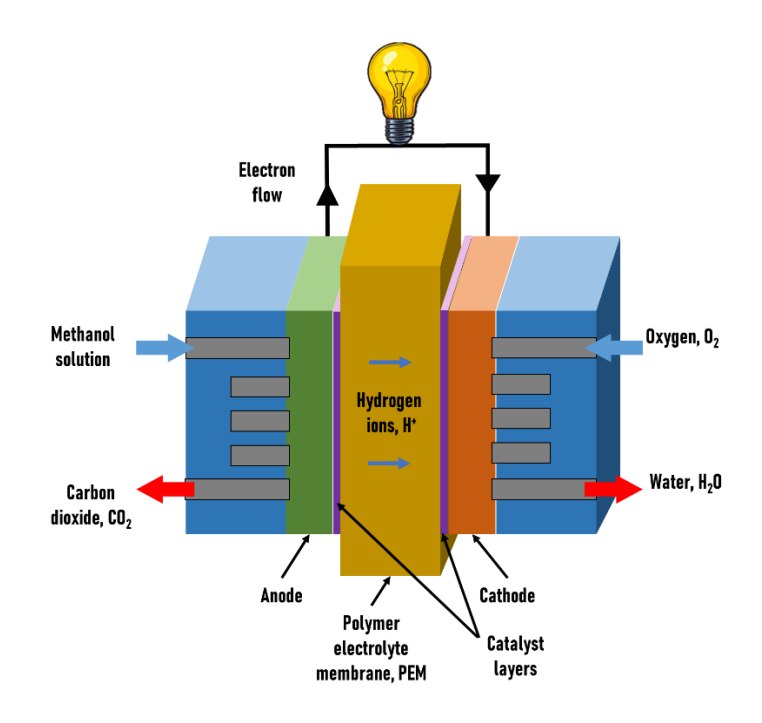


Figure 1. Working principle of DMFC

Table 2. Target requirement for an ideal PEM [9]

Criteria	Target Requirement
Proton conductivity	$0.1 - 1 \text{ S cm}^{-1}$
Oxygen crossover	2 mA cm <sup>-2</sup>
Fuel crossover	2 mA cm <sup>-2</sup>
Electrical resistance	$1000~\Omega~\text{cm}^{\text{-}2}$
Durability	20,000 cycles
Chemical stability	More than 500 h

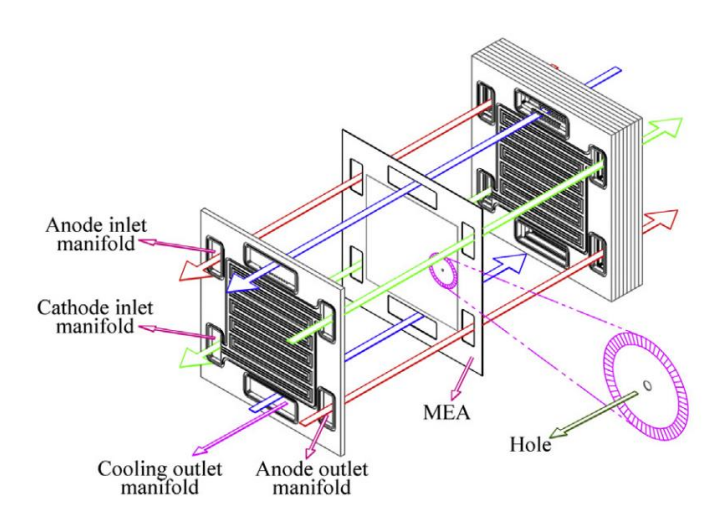


Figure 2. The leakage passing through the PEM [10]

#### Classification of polymeric membranes

Polymeric membranes can be classified into fluorinated and non-fluorinated polymers. Fluorocarbon-based ionexchange membrane or Nafion® is the most common and readily available membrane in the market. Nafion® possesses unique structures that contribute to stability in terms of mechanical and chemical aspects as well as imparts high proton conductivity [11]. However, the presence of (approximately 4 nm) ionic clusters which are considerably large in size compared to methanol molecules, make them penetrate easily from anode to cathode. The methanol crossover is also being contributed by the separated nanophase of hydrophobic and hydrophilic domains of Nafion®. This methanol crossover will create a mixed potential that includes methanol and performance loss at cathode and anode, respectively. It will simultaneously affect the oxygen reduction reaction (ORR) and methanol oxidation reaction (MOR), which lead to a lower cathode potential and decrease in the cell voltage (as much as 0.15-0.2V)[12]. Besides that, electrocatalyst poisoning might occur at the cathode due to methanol oxidation from the crossover [13].

The ways to overcome these problems are (a) synthesizing new polymeric membranes (non-fluorinated polymers) such as poly ether sulfone (PES),

polyphenyl sulfone (PPSU), poly benzimidazole (PBI)[14, 15], poly ether ether ketone (PEEK), polyvinyl alcohol (PVA)[16] and polyimide (PI); (b) sulfonation of aromatic polymers; and (c) incorporating the existing polymer membrane with other materials which are also known as filler. Filler can consist of inorganic particles such as titanium dioxide, iron titanate, zirconium phosphate, silica, heteropolyacid, and zeolites. The incorporation of this filler into the polymer produces a composite or hybrid membrane. This composite or hybrid membrane with control structure and outstanding properties for DMFC is attracting significant attention among researchers. This is proven by the number of papers that have been published in high-impact journals for the past ten years. Using the keywords search of 'composite membrane' or 'hybrid membrane' and 'direct methanol fuel cell' in the ScienceDirect website, the increasing trend of published papers that are related to the keywords is observed in Figure 3.

Due to the shortcomings and drawbacks of the perfluorosulfonic acid membrane as stated, non-fluorinated polymers, specifically poly arylene ether ether type-polymers such as PEEK, PES, PS, PI, PBI, and their derivatives have the potential to replace it. Besides having good thermal and mechanical stability, these alternative polymers also possess good cost-effective properties as well as high proton conductivity.

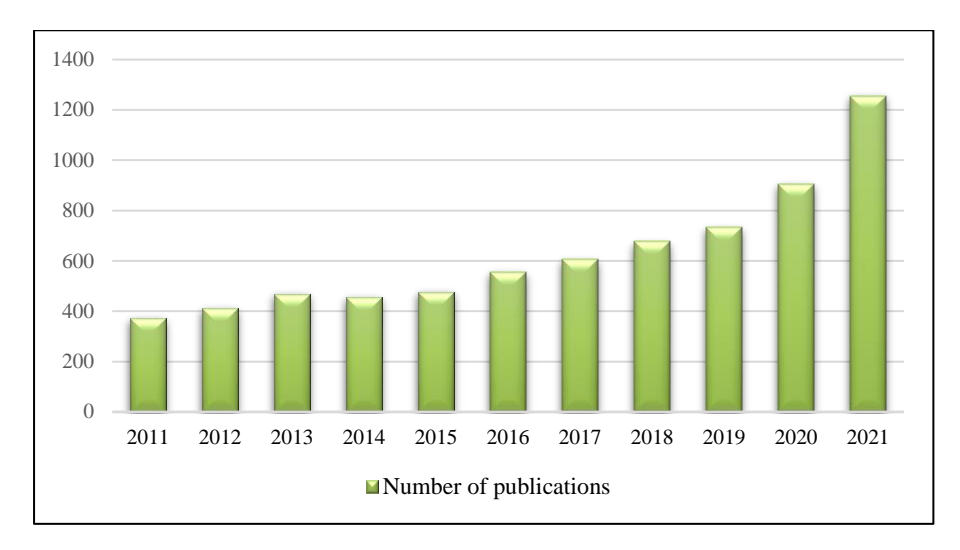


Figure 3. The trend of publication of composite membrane in high impact journals for the past 10 years

#### Sulfonated and modified PEEK as PEM

Polyether ether ketone or PEEK is a semi-crystalline thermoplastic polymer that belongs to the polyketone family of polymers (PEK, PEEK, PEEKK, PEKK, PEKKK). Amongst them, PEEK is the most commonly used and produced in bulk production. The key properties of PEEK that make it widely used in various fields such as aerospace, automotive, electrical, and biomedical application are its good solvent resistance, dimensional stability, biocompatible, long life, and it exhibits exceptional mechanical properties [17, 18].

In order to improve the hydrophilicity and transportation of ions in PEEK material, sulfonation is carried out. Sulfonation is the process of either introducing sulfonic acid groups using sulfuric acid directly into the polymer chains as shown in Figure 4, by polymerizing functionalized sulfonated monomers or by grafting the sulfonic acid onto the aromatic backbone to produce random copolymers [9, 19]. However, the last method does not seem to be suggested as it leads to chemical degradation of the polymer chain [20].

The charged groups are important as they separate the protons from each other by water molecules and provide proton transport. Their addition depends on the substituents present in the ring [18]; substitution occurs

on the aromatic ring between two ether (-O-) links. Many other polymers have also been sulfonated to enhance their properties in terms of wettability, water flux, perm selectivity, and solubility in solvents for processing. The solubility of PEEK enables it to be easily cast from organic solution and to eliminate complicated processes rather than when to fabricate perfluorosulfonic acid membranes. Other polymers, sulfonated polyarylene ether ketones (SPAEKs) with 60% of sulfonation degree, showed the best performance in terms of conductivity and methanol permeability [19].

At the same time, sulfonation also increased the proton conductivity of the polymer due to the improved hydrophilicity [21]. The proton conductivity is increased by increasing the degree of sulfonation. However, a higher sulfonation degree will increase the water uptake and raise another swelling issue. Swelling can make the membrane fragile, and changes of dimensions that lead to mechanical failures. Therefore, an optimum and moderate degree of sulfonation is crucial when undergoing the SPEEK sulfonation process. Based on the research by Li et al., it is advisable that for DMFC application, the degree of sulfonation for SPEEK is in the range of 30% to 60%. This is because too low a sulfonation degree will give poor conductivity. Otherwise, the polymers are highly swollen in methanol

water solution (1 M) when the degree of sulfonation is above 60% [22].

In the recent past, researchers have incorporated SPEEK with fillers to further enhance its properties, in addition to overcoming some limitations of having SPEEK alone

as the membrane. This is due to the presence of significant numbers of dead-end channels in SPEEK limits, the conductivity thus affecting the overall performance [24]. Therefore, in order to not sacrifice the mechanical strength in the higher degree of sulfonation, fillers are added into an organic polymeric matrix.

Figure 4. Process of PEEK sulfonation [23]

#### Preparation methods of composite PEM

As polymer SPEEK owns many of the dead channels, it limits the flow of effective ionic conductivity. These ionic conductive channels can be built by incorporating organic polymers with inorganic backbones. Different ways of incorporating them are illustrated in Figure 5. Organic-inorganic composite membrane can benefit in mechanical and thermal stability from inorganic backbone, while the organic polymer gives advantages in terms of chemical reactivity, ductility and flexibility of processing.

The composite of ionically conductive polymer and inorganic material can be varied, as shown in Figure 6. Usually, an inorganic precursor such as a monomer or oligomer is blended with a linear or network polymer matrix. The preparation methods of the nanocomposite materials include mixing or blending, *in-situ* polymerization or infiltration, and sol-gel.

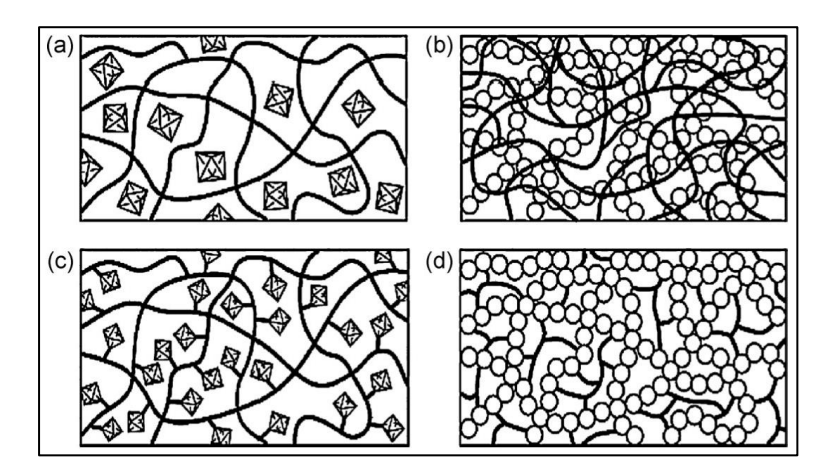


Figure 5. Different ways of incorporating the inorganic system in organic polymers: (a) inorganic moiety embedded into an organic polymer (b) interpenetrating networks with chemical bonds (c) inorganic groups incorporated by bonding to the backbone and (d) dual organic-inorganic hybrid polymer [25]

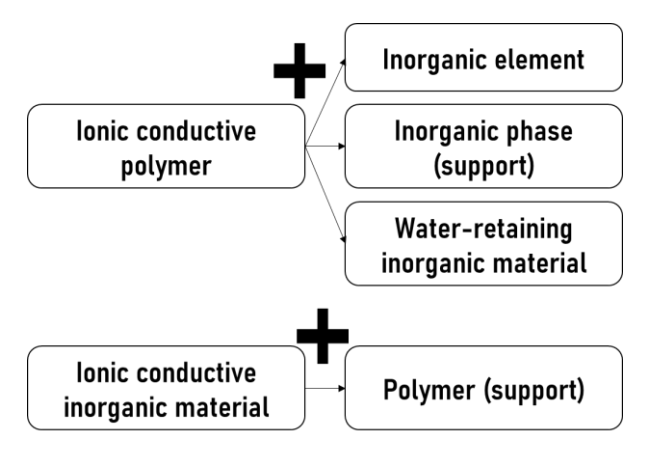


Figure 6. Different ways of organic-inorganic composite membranes arrangements [26]

#### Mixing or blending method.

The simplest method to prepare composite PEM is by direct mixing or blending of inorganic materials into the organic polymer matrix. There are two ways of blending the composite, which are melt blending and liquid-state blending. In both ways, it is important to ensure the desired composite components can be dispersed in a common solvent or melt at a high temperature.

Salarizadeh et al. [27] prepared blend nanocomposite SPEEK/perfluorosulfonic acid (PFSA)/barium strontium titanate (BST) membranes by dissolving SPEEK in N,N-dimethylacetamide (DMAC) followed by mixing with the BST dispersion and PFSA solution. The experimental procedure is shown in Figure 7.

Although melt blending is more common due to its efficiency and prevention from the dispersing of hazardous material into the environment, the filler agglomeration tends to occur when the inorganic nanoparticles are dispersed in polymer matrix. In order to overcome the limitation, the surface of the nanoparticles is being modified to produce nanostructural composites.

Composite of nanosilica and polymer is the common example of membrane that is prepared by solution blending due to its simplicity in preparation. This membrane is widely being researched for gas separation, pervaporation and PEM in fuel cell application [28].

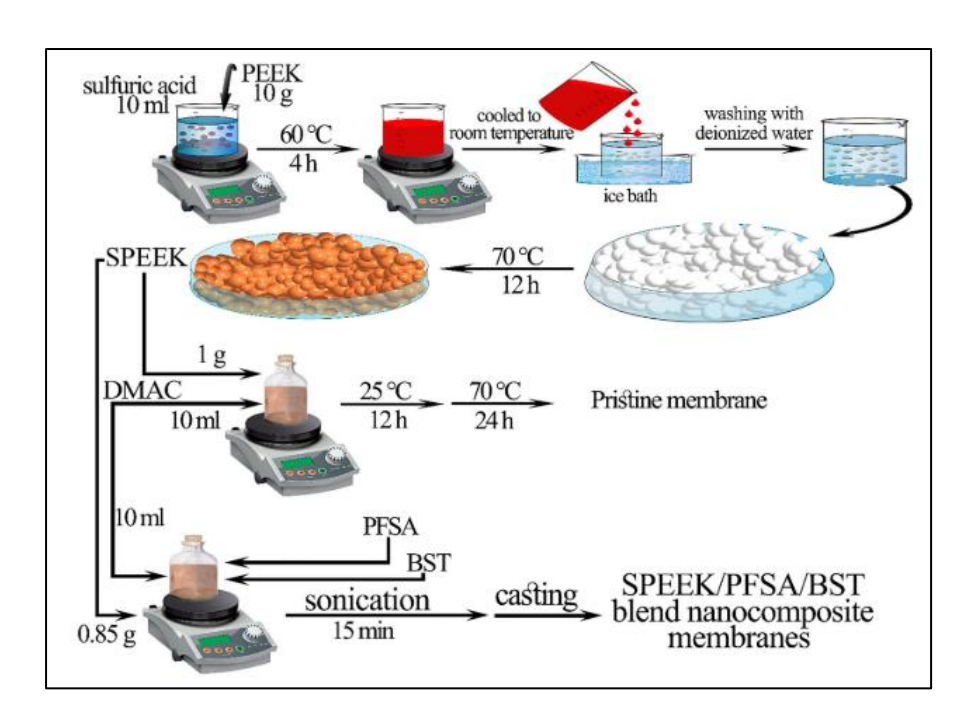


Figure 7. The steps involved in preparing the blend nanocomposite membrane SPEEK/PFSA/BST [29]

#### In-situ polymerization or infiltration method

In this method, inorganic nanoparticles are introduced in the polymer membrane to modify the transport properties. Firstly, the preformed membrane will be immersed in a solvent, allowing it to swell in order to increase the pore or void volume before the inorganic particle is doped or infiltrated. After the inorganic particle is infiltrated, the composite is cured by heat, radiation, or chemical grafting to gain covalent bonding inside the matrix. The drawback of this method is the leaching of inorganic materials from the membrane matrix [30].

#### Sol-gel method

This method is favorable as it is an environmentally friendly way and is conducted in low temperature. Briefly, sols are dispersions of colloidal particles in a liquid, while gels may be classified into four categories: (i) well-ordered lamellar structures of inorganics with organics (i.e., organopolysilsesquioxanes; (ii) covalent disordered polymeric networks; (iii) polymer networks formed through physical aggregation; (iv) disordered structures of inorganic and organic networks. There are two consecutive steps in sol-gel reactions, which are hydrolysis of metal alkoxides to produce hydroxyl groups and polycondensation of the hydroxyl groups to form a three-dimensional network. The process is started with solvents (low molecular weight) with alkoxide precursors M(OR)<sub>n</sub>, (M is a network-forming element: Si, Ti, Zr, Al, B, etcetera, and R is an alkyl group (C<sub>x</sub>H<sub>2x+1</sub>)) and water. Later, low molecular weight byproducts (alcohol or water) are produced during hydrolysis and condensation. They must be removed, resulting in shrinkage during the sol-gel process.

#### **Modification of SPEEK membrane**

Sulfonated PEEK is an organic thermoplastic polymer that possesses outstanding thermal and mechanical properties. As mentioned in the previous section, fillers are needed to overcome some of the drawbacks of SPEEK that can limit its potential to emerge as high-performance membrane. The introduction of nanostructures fillers can overcome the thermal and mechanical instability of SPEEK polymer. The inorganic materials as additives such as hygroscopic

oxides (silicon oxide, zirconium oxide, titanium dioxide, iron-titanates, zeolites, and boron phosphate), solid acids and heteropolyacids (HPAs), clay, graphene oxide (GO), carbon nanotubes (CNTs), fullerene and perovskite oxides have shown improved performance for SPEEK membrane [31–33]. Besides overcoming the instability in thermal and mechanical properties, the modifications to SPEEK membrane through inorganic filler also improve methanol permeability in DMFC.

Zhang et al. [34] synthesized nanocomposite membrane by incorporating sulfonated hallyosite nanotubes (SHNTs) into the SPEEK matrix. The well-dispersed SHNTs in the SPEEK matrix bring advantages in terms of the thermal and mechanical stabilities of the membrane. Besides that, the water uptake, ionic exchange capacity, and proton conductivity have been improved tremendously due to the construction of ionic channels that are interconnected by the SHNTs in the SPEEK matrix. Figure 8 shows the improved proton pathways that will allow efficient proton transfer and lead to the enhancement of proton conductivity.

Bagheri et al. [35] prepared SPEEK, sulfonated poly (vinilidinfluoride-co-hexaflourpropylen) (SPVDF-co-HFP), and lanthanum chromite (LaCrO<sub>3</sub>) as nanocomposite blend membrane using solvent casting method. The increasing in proton conductivity is observed at the nanoparticle content of 1.5 wt.%, and the addition of 1.5 wt.% LaCrO<sub>3</sub> nanoparticles managed to make this membrane as effective barrier against methanol permeation. Figure 9 shows the performance of the composite membrane with different content.

Later, Salarizadeh et al. [29] prepared another blend nanocomposite membrane of SPEEK with two different types of additives, namely perfluorosulfonic acid (PFSA) and Ba<sub>0.9</sub>Sr<sub>0.1</sub>TiO<sub>3</sub> (BST) doped-perovskite nanoparticles. The addition of both additives has indicated that proton conductivity is improved while methanol permeability is decreased compared to pristine SPEEK membrane. The increase in proton conductivity is contributed by the high specific surface area of perovskite nanoparticles

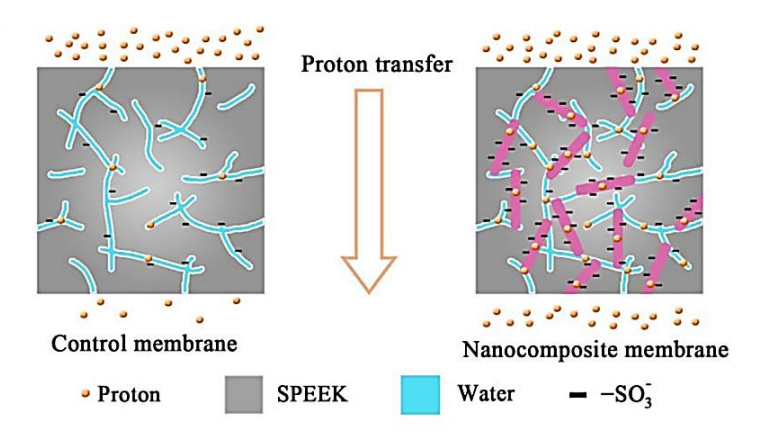


Figure 8. SHNTs interconnect the ionic channels within SPEEK matrix via -SO<sub>3</sub>H groups [34]

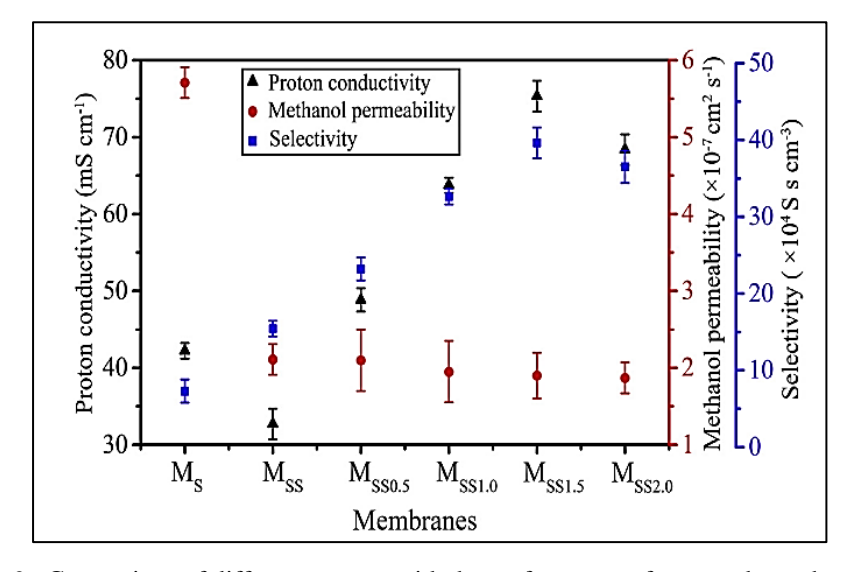


Figure 9. Comparison of different content with the performance of prepared membrane [35]

Composite	Improvement	Ref.
SPEEK/SnO <sub>2</sub> /sBH	Water retention properties increase, which consequently enhance the ionic conductivity of the composite membrane.  Methanol diffusion channels decrease and demonstrate the high power density as well as excellent durability	[36]
SPEEK/QDs/CS	Enhanced through-plane conductivity and decreased transfer anisotropy	[37]
sPEEK/sGNR-sGQD	Improved physico-chemical properties resulting in enhanced electrochemical selectivity. Significant enhancement in DMFC performance and better durability can be observed	[38]
SPEEK/CNFs	Improved mechanical strength and water uptake of the composite membranes and low methanol permeability	[39]
SPEEK/PVA/TEOS	The proton transport and fuel cells performance increased	[40]
SPEEK/PFSA/BST	Improved proton conductivity and methanol barrier. Enhanced mechanical stability	[29]

Table 3. Influence on membrane performances during the SPEEK modification

#### Properties of SPEEK composite membrane

## Water uptake, swelling ratio, ion-exchange capacity, mechanical properties

The water uptake (WU) and membrane swelling (SW) are essential parameters in DMFC application as they directly affect the proton conductivity and mechanical stability of the membrane. Controlling the WU of the membrane is quite necessary for high WU can lead to mechanical and dimensional stability while low WU decreases the proton transferring rate within the membrane. They are calculated from the following equations:

$$WU (\%) = \frac{m_{wet} - m_{dry}}{m_{dry}} \times 100 \tag{7}$$

$$SW (\%) = \frac{L_{wet} - L_{dry}}{L_{dry}} \times 100$$
 (8)

To determine the water uptake (WU) and membrane swelling (SW), the membranes are dried and then their weights ( $M_{dry}$ ) and the thickness ( $L_{dry}$ ) are measured. After that, they are soaked in deionized water. Finally, the surface water of membranes is blotted with a clean paper, and immediately weights ( $M_{wet}$ ) and thickness ( $L_{wet}$ ) of membranes are measured.

The ion-exchange capacity (IEC) value is defined as the molar number of fixed sulfonate sites per gram polymer. It is decided by the concentration of exchangeable ions in membranes and determined by an acid-base titration method[41]. It is very closely related to water uptake as increasing the water uptake will increase the value of IEC. The value of IEC was calculated based on the following formula:

$$IEC = \frac{(N_{NaOH} \times V_{NaOH})}{mass_{dry}} \times 100\%$$
 (9)

The dried membrane is soaked in a saturated NaCl solution for a certain time and later is titrated with a NaOH solution using phenolphthalein as an indicator. The  $N_{\text{NaOH}}$  is the concentration of NaOH solution, while  $V_{\text{NaOH}}$  is the volume of NaOH solution consumed. The mechanical properties of the membrane are investigated using a universal tensile testing machine. It is evaluated with tensile stress-strain tests. Typically, the value of Young's modulus is calculated from the slope of the initial linear part of the stress-strain curve. The maximum stress value of the entire curve was taken as the tensile strength [42].

#### Thermal and chemical stability

The thermal stability of the membrane is measured by its degradation of decomposition at a specific temperature. The membrane that has a good thermal stability should withstand a required temperature for a longer time before it degrades or decomposes [43]. It is usually investigated by a thermogravimetric analyzer (TGA) where the weight loss of the samples is determined.

The thermal stability study of the composite membrane SPEEK with inorganic additive, clay and electrospun fibers is carried out by Awang et al. [43]. The thermogravimetric analysis indicated that SPEEK with added inorganic filler (i.e., Cloisite) gives a higher degradation temperature compared to pristine SPEEK. It shows that the composite organic-inorganic membrane is thermally stable, especially when the amounts of Cloisite is increased as shown in Figure 10. The Cloisite acts as a mass transport barrier and insulator against the colatile compound when the heat is applied [44].

The chemical stability of the membrane is usually being tested by Fenton's reagent. The experiment subjects the membrane to a very large excess of <a href="https://example.com/hydroxyl">hydroxyl</a> radicals between 60 and 80 °C to assess chemical durability. The reagent is made when ferrous sulfate is dissolved in

hydrogen peroxide (H<sub>2</sub>O<sub>2</sub>) aqueous solution. This is to mimic the real situation during DMFC operation where H<sub>2</sub>O<sub>2</sub> is formed at the cathode side due to the partial reduction of O<sub>2</sub> and the iron ion (Fe<sup>2+</sup>) that is formed from the corrosion of the iron back plate. The migration of Fe<sup>2+</sup> to the cathode side will react with H<sub>2</sub>O<sub>2</sub> and produces a free radical similar to the Fenton reagent. Then the prepared membrane is immersed in the reagent under stirring at a specific temperature. Carbon dioxide (CO<sub>2</sub>) will be produced as a by-product when free radicals react with organic polymer. As CO<sub>2</sub> gas forms bubbles, the membrane structures tend to break if they cannot withstand the bubbles' pressure. Oxidative stability of the membrane is recorded by the time the membrane begins to break [35].

From the chemical stability test conducted by Salleh et al. [45] on composite membrane SPEEK/Cloisite/triaminopyrimidine (SP/CL/TAP), it is proven that the presence of inorganic particles in nanocomposite membrane increased its resistance towards radical attack. The nanocomposite membrane can maintain its weight up to 48 hours. From the FESEM image, as shown in Figure 10, the surface deformation of SP/CL/TAP membrane started to occur after being exposed to Fenton reagent solution for 24h (Figure 11(h)).

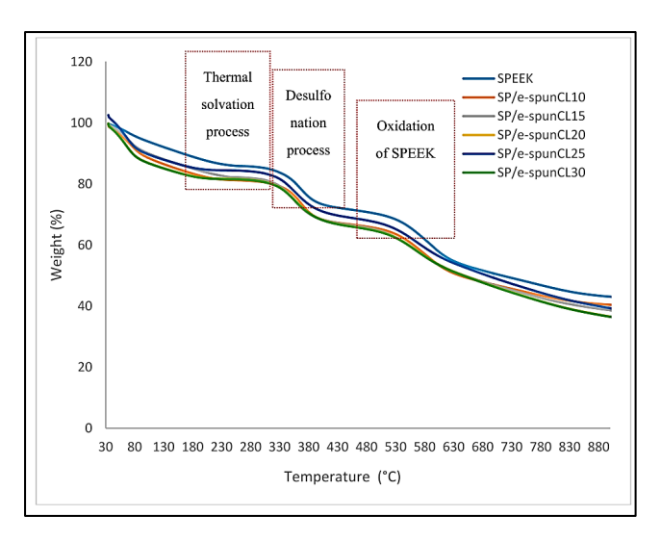


Figure 10. TGA of the SPEEK and composite SPEEK membrane with different amounts of Cloisite [43].

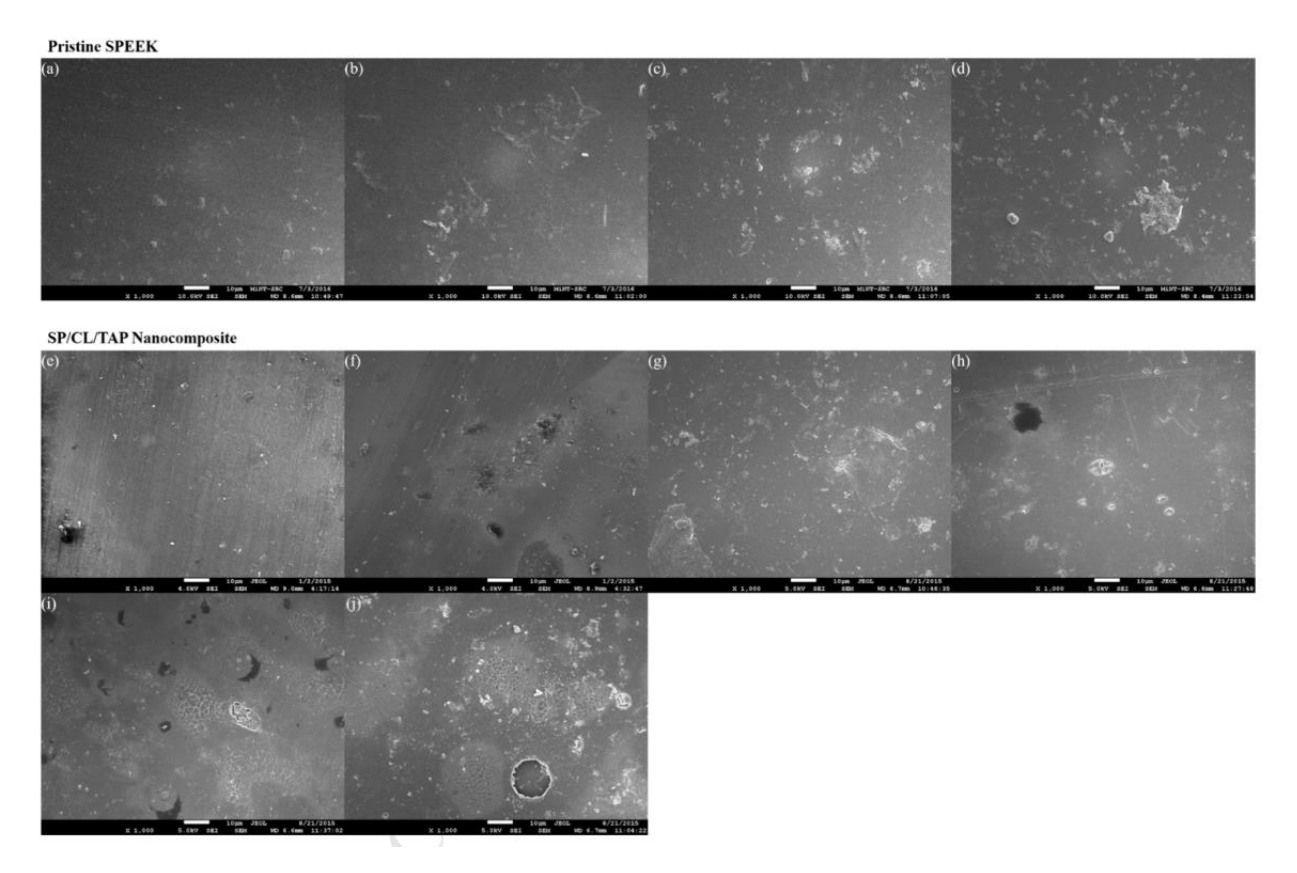


Figure 11. FESEM micrographs of pristine SPEEK and nanocomposite membrane SP/CL/TAP surface before (a,e) and after exposed to Fenton reagent solution for 6h (b,f), 12h (c,g) and 24h (d,h), 48h (i) and 96h (j) [45]

#### Methanol permeability

The methanol permeability (P, cm<sup>2</sup> s<sup>-1</sup>) can be determined by different techniques such as potentiometry, gas chromatography technique (GC), and densimetry method. Each and every technique have its respective advantages and drawbacks, as summarized in Table 4. These three different experimental methods, however, provided very comparable results.

The cell was separated into two equal-sized compartments by a membrane. The compartment in the left side was filled with methanol solution while the compartment in the right was filled with deionized water and both part had equal volume. The prepared membranes with certain areas are located vertically between the two compartments after keeping them in deionized water. The schematic experimental set-up is

illustrated in Figure 12 [46]. As there is a methanol concentration gradient between these two parts, methanol can diffuse from the left to the right compartment, and methanol permeability was measured as a function of time. It is calculated from the following equation:

$$C_R(t) = \frac{AP}{LV_R}C_L(t - t_0) \tag{10}$$

where,  $C_L$  and  $C_R$  are the concentration of methanol in methanol and water compartment (mol  $L^{-1}$ ) respectively; L is the thickness of the membranes (cm), A is the diffusion area (cm<sup>2</sup>), and  $V_R$  is the volume of deionized water in water compartment (mL). Methanol concentration in the water compartment was examined with time using a density meter.

FUEL CELL APPLICATIONS

Table 4. Summar	v of different technic	mes used to measure	methanol permeability
-----------------	------------------------	---------------------	-----------------------

Techniques	Advantages	Drawbacks
Potentiometry	<ul><li>Simplest method</li><li>Cheapest</li></ul>	<ul> <li>Limited for certain parameters</li> <li>Absolute values of concentration at a given time cannot be measured</li> <li>Time-consuming</li> </ul>
Gas chromatography technique	Highly precise	• Very expensive
Densimetry	<ul> <li>Most efficient in terms of accuracy, simplicity, experimental time, and cost</li> </ul>	-

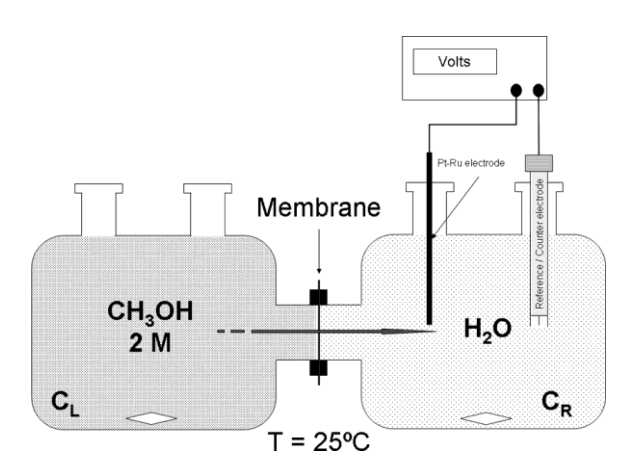


Figure 12. Schematic diagram of experimental set up to determine methanol permeability across the membrane [46]

#### **Proton conductivity**

The electrochemical performance of the composite membrane is often indicated by the value of proton conductivity. The proton conductivity heavily relied on the degree of sulfonation, water uptake, and methanol permeation. A summary of fundamental properties that contributed to proton conductivity of SPEEK based membrane is tabulated in Table 5. The proton conductivity is determined from the following equation:

$$\sigma = L/RA \tag{11}$$

where,  $\sigma$  is the proton conductivity of the membrane (S cm<sup>-1</sup>), L is the thickness of the membrane (cm), R is the

resistance of the membrane  $(\Omega)$ , and A is the surface area of the two electrodes (cm<sup>2</sup>).

Gong et al. [42] illustrated proton conduction in composite membrane SPEEK/BPO<sub>4</sub>@CNT in Figure 13. The composite membrane has higher proton conductivity compared to the pure SPEEK membrane. It could be primarily attributed to the dissociation of the absorbed water molecules on the BPO<sub>4</sub>. The fundamental properties that contribute to the performance of composite SPEEK-based membranes that have been discussed in the earlier section are summarized in Table 5.

Table 5. Summary	of fundamental	properties of com	nosite mem	brane SPEEK
Table 5. Buillian	or rundamentar	properties of com	posite mem	Drane of LLIX

Composite SPEEK-Based Membrane	Water Uptake (%)	Methanol Permeability (×10 <sup>-7</sup> cm <sup>2</sup> s <sup>-1</sup> )	Proton Conductivity @RT (Scm <sup>-1</sup> )	Ref
SPEEK/SPVDF-co-HFP	~25	2.11	0.0327	[35]
SPEEK/SPVDF-co-HFP (0.5 wt.%)	~30	2.10	0.0488	
SPEEK/SPVDF-co-HFP (1.0 wt.%)	~35	1.95	0.0638	
SPEEK/SPVDF-co-HFP (1.5 wt.%)	41.23	1.90	0.0753	
SPEEK/SPVDF-co-HFP (2.0 wt.%)	~35	1.87	0.0684	
sPEEK	29.3	$9.24 \pm 0.02$	0.0102	[38]
$sPEEK/^{1}sGNR$ (1.5 wt.%)	30.4	$6.25 \pm 0.28$	0.0150	
sPEEK/sGNR- <sup>2</sup> sGQD (1.0 wt.%)	33.9	$6.76 \pm 0.20$	0.0135	
sPEEK/sGNR-sGQD (1.0 wt.%) sPEEK/sGNR-sGQD (1.5 wt.%)	37.1	$4.35 \pm 0.17$	0.0195	
sPEEK/sGNR-sGQD (1.5 wt.%) sPEEK/sGNR-sGQD (2.0 wt.%)	33.6	$5.24 \pm 0.17$	0.0147	
<sup>3</sup> CS/ <sup>4</sup> SP	52	-	0.158*	[37]
CS/SP/ <sup>5</sup> PQD-10%	-	-	0.327*	
CS/SP/PQD-10% CS/SP/PQD-20%	-	-	0.375*	
CS/SP/PQD-20% CS/SP/PQD-30%	85	=	0.456*	
CS/SP/ <sup>6</sup> GQD-20%	-	-	0.309*	
SPEEK/ <sup>7</sup> BH	25.05	1.58	0.0570**	[36]
	38.62	2.52	0.0586**	[50]
SPEEK/sBH (1 wt.%)	45.01	2.90	0.0728**	
SPEEK/sBH(3 wt.%)	44.73	2.87	0.0618**	
SPEEK/sBH (5 wt.%) SPEEK/SBH/SnO <sub>2</sub> (3 wt.%)	50.34	1.28	0.0920**	
SPEEK/8rGONR@TiO <sub>2</sub>		-	1.78	[47]

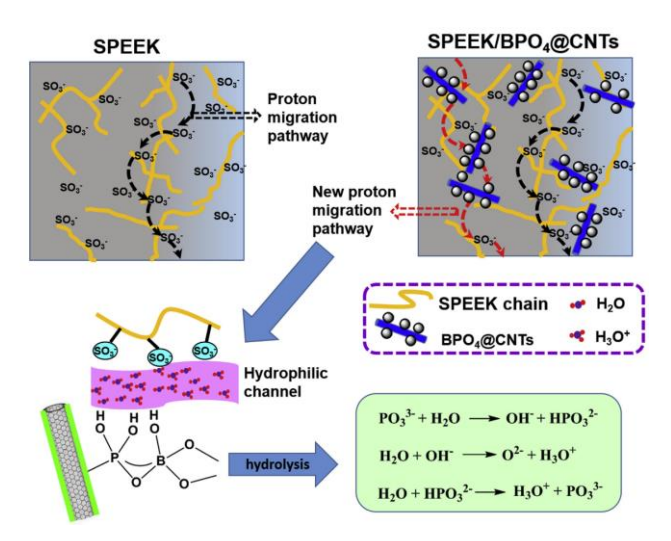


Figure 13. Schematic illustration of proton conduction in SPEEK and composite membrane SPEEK [42]

#### Future perspective and conclusions

The potential of composite SPEEK membrane as highperformance PEM is undeniable based on the past research. The properties such as water uptake and methanol permeation are closely linked to the performance of the membrane in terms of mechanical, thermal, chemical stability, and proton conductivity. With the results that have been obtained in literatures, the composite SPEEK membrane will be a strong competitor that has a big chance to replace the Nafion membrane. However, further investigations are needed i) to find optimum parameters and cost-effective methods in preparing the membrane, ii) to improve the distribution and proportion of inorganic particles in the polymer matrix, iii) to optimize the water uptake and methanol permeation in the membrane, iv) to produce a membrane that is suitable for higher temperature, humidity, and pressure.

In conclusion, the role of filler in improving the performance and properties of the SPEEK membrane is significant in comparison to the properties of either component in isolation.

#### References

- Worldometer. (2021). Current World Population. Access from https://www.worldometers.info/world-population/ [Retrieved September 8, 2021]
- Haiges, R., Wang, Y. D., Ghoshray, A. and Roskilly, A. P. (2017). Optimization of Malaysia's Power generation mix to meet the electricity demand by 2050. *Energy Procedia*, 142: 2844-2851.
- 3. Laguna-Bercero, M. A. (2012). Recent advances in high temperature electrolysis using solid oxide fuel cells: a review. *Journal of Power Sources*, 203: 4-16.
- 4. Dai, H., Jiang, B., Hu, X., Lin, X., Wei, X. and Pecht, M. (2020). Advanced battery management strategies for a sustainable energy future: multilayer design concepts and research trends. *Renewable and Sustainable Energy Reviews*, 8: 110480.
- 5. Bahru, R., Shaari, N. and Mohamed, M. A. (2020). Allotrope carbon materials in thermal interface

- materials and fuel cell applications: A review. *International Journal of Energy Research*, 44(4): 2471-2498.
- 6. Raduwan, N. F., Muchtar, A., Somalu, M. R., Baharuddin, N. A. and Muhammed Ali, S. A. (2018). Challenges in fabricating solid oxide fuel cell stacks for portable applications: A short review. *International Journal of Integrated Engineering*, 10(5): 80-86.
- Ferriday, T. B. and Middleton, P. H. (2021). Alkaline fuel cell technology - a review. International Journal of Hydrogen Energy, 46(35): 18489-18510.
- 8. Junoh, H., Jaafar, J., Mohd Norddin, M. N. A., Ismail, A. F., Othman, M. H. D., Rahman, M. A., ... and Ilbeygi, H. (2015). A review on the fabrication of electrospun polymer electrolyte membrane for direct methanol fuel cell. *Journal of Nanomaterials*, 4: 4.
- 9. Esmaeili, N., Gray, E. M. A. and Webb, C. J. (2019). Non-fluorinated polymer composite proton exchange membranes for fuel cell applications a review. *ChemPhysChem*, 20(16): 2016-2053.
- Asghari, S., Fouladi, B., Masaeli, N. and Imani, B.
   F. (2014). Leak diagnosis of polymer electrolyte membrane fuel cell stacks. *International Journal of Hydrogen Energy*, 39(27): 14980-14992.
- Wu, H., Hou, W., Wang, J., Xiao, L. and Jiang, Z. (2010). Preparation and properties of hybrid direct methanol fuel cell membranes by embedding organophosphorylated titania submicrospheres into a chitosan polymer matrix. *Journal of Power Sources*, 195(13): 4104-4113.
- 12. Jiang, S. P., Liu, Z. and Tian, Z. Q. (2006). Layer-by-layer self-assembly of composite polyelectrolyte-nafion membranes for direct methanol fuel cells. *Advanced Materials*, 18(8): 1068-1072.
- Kim, H. J., Kim, D. Y., Han, H. and Shul, Y. G. (2006). PtRu/C-Au/TiO<sub>2</sub> Electrocatalyst for a direct methanol fuel cell. *Journal of Power Sources*, 159: 484-490.

- 14. Taherkhani, Z., Abdollahi, M., Sharif, A. and Barati, S. (2021). Poly(benzimidazole)/ poly(vinylphosphonic acid) blend membranes with enhanced performance for high temperature polymer electrolyte membrane fuel cells. *Solid State Ionics*, 364: 115635.
- 15. Zarrin, H., Jiang, G., Lam, G. Y. Y., Fowler, M. and Chen, Z. (2014). High performance porous polybenzimidazole membrane for alkaline fuel cells. *International Journal of Hydrogen Energy*, 39(32): 18405-18415.
- Herranz, D., Escudero-Cid, R., Montiel, M., Palacio, C., Fatás, E. and Ocón, P. (2018). Poly (vinyl alcohol) and poly (benzimidazole) blend membranes for high performance alkaline direct ethanol fuel cells. *Renewable Energy*, 127: 883-895.
- 17. Gao, X., Liu, Y. and Li, J. (2015). Review on modification of sulfonated poly (-ether-ether-ketone) membranes used as proton exchange membranes. *Medziagotyra*, 21(4): 574-582.
- 18. Yee, R. S. L., Zhang, K. and Ladewig, B. P. (2013). The effects of sulfonated poly(ether ether ketone) ion exchange preparation conditions on membrane properties. *Membranes*, 3(3): 182-195.
- Xiang, Z., Zhao, X., Ge, J., Ma, S., Zhang, Y. and Na, H. (2016). Effect of sulfonation degree on performance of proton exchange membranes for direct methanol fuel cells. *Chemical Research in Chinese Universities*, 32(2): 291-295.
- Hasani-Sadrabadi, M. M., Dashtimoghadam, E., Sarikhani, K., Majedi, F. S. and Khanbabaei, G. (2010). Electrochemical investigation of sulfonated poly(ether ether ketone)/clay nanocomposite membranes for moderate temperature fuel cell applications. *Journal of Power Sources*, 195(9): 2450-2456.
- Chang, J. H., Park, J. H., Park, G. G., Kim, C. S. and Park, O. O. (2003). Proton-conducting composite membranes derived from sulfonated hydrocarbon and inorganic materials. *Journal of Power Sources*, 124(1): 18-25.
- 22. Li, L., Zhang, J. and Wang, Y. (2003). Sulfonated Poly(ether ether ketone) membranes for direct methanol fuel cell. *Journal of Membrane Science*, 226(1–2): 159-167.

- 23. Ata, K. C., Kadıoğlu, T., Türkmen, A. C., Çelik, C. and Akay, R. G. (2020). Investigation of the effects of SPEEK and its clay composite membranes on the performance of direct borohydride fuel cell. *International Journal of Hydrogen Energy*, 45(8): 5430-5437.
- Rambabu, G. and Bhat, S. D. (2015). Sulfonated fullerene in SPEEK matrix and its impact on the membrane electrolyte properties in direct methanol fuel cells. *Electrochimica Acta*, 176: 657-669.
- Kickelbick, G. (2003). Concepts for the incorporation of inorganic building blocks into organic polymers on a nanoscale. *Progress in Polymer Science*, 28(1): 83-114.
- Peighambardoust, S. J., Rowshanzamir, S. and Amjadi, M. (2010). Review of the proton exchange membranes for fuel cell applications. *International Journal of Hydrogen Energy*, 35(17): 9349-9384.
- Balazs, A. C., Emrick, T. and Russell, T. P. (2006).
   Nanoparticle polymer composites: Where two small worlds meet. *Science*, 314(5802): 1107-1110.
- Zou, H., Wu, S. and Shen, J. (2008). Polymer/silica nanocomposites: Preparation, characterization, propertles, and applications. *Chemical Reviews*, 108(9): 3893-3957.
- 29. Salarizadeh, P., Bagheri, A., Beydaghi, H. and Hooshyari, K. (2019). Enhanced properties of SPEEK with incorporating of PFSA and barium strontium titanate nanoparticles for application in DMFCs. *International Journal of Energy Research*, 43(9): 4840-4853.
- Tripathi, B. P. and Shahi, V. K. (2011). Organic-inorganic nanocomposite polymer electrolyte membranes for fuel cell applications. *Progress in Polymer Science (Oxford)*, 36(7): 945-979.
- 31. Wong, C. Y., Wong, W. Y., Ramya, K., Khalid, M., Loh, K. S., Daud, W. R. W., ... and Kadhum, A. A. H. (2019). Additives in proton exchange membranes for low- and high-temperature fuel cell applications: A review. *International Journal of Hydrogen Energy*, 44(12): 6116-6135.

- 32. Rambabu, G., Bhat, S. D. and Figueiredo, F. M. L. (2019). Carbon nanocomposite membrane electrolytes for direct methanol fuel cells—a concise review. *Nanomaterials*, 9(9): 1292.
- 33. Taufiq Musa, M., Shaari, N. and Kamarudin, S. K. (2020). Carbon nanotube, graphene oxide and montmorillonite as conductive fillers in polymer electrolyte membrane for fuel cell: An overview. *International Journal of Energy Research*, 45(2): 1309-1346.
- 34. Zhang, H., Ma, C., Wang, J., Wang, X., Bai, H. and Liu, J. (2014). Enhancement of proton conductivity of polymer electrolyte membrane enabled by sulfonated nanotubes. *International Journal of Hydrogen Energy*, 39(2): 974-986.
- 35. Bagheri, A., Javanbakht, M., Hosseinabadi, P., Beydaghi, H. and Shabanikia, A. (2018). Preparation and characterization of SPEEK/SPVDF-Co-HFP/LaCrO<sub>3</sub> nanocomposite blend membranes for direct methanol fuel cells. *Polymer*, 138: 275-287.
- 36. Ranjani, M., Al-Sehemi, A. G., Pannipara, M., Aziz, M. A., Phang, S. M., Ng, F. L. and Kumar, G. G. (2020). SnO<sub>2</sub> nanocubes/bentonite modified SPEEK nanocomposite composite membrane for high performance and durable direct methanol fuel cells. *Solid State Ionics*, 353(3): 115318.
- 37. Li, P., Dang, J., Wu, W., Lin, J., Zhou, Z., Zhang, J. and Wang, J. (2020). Nanofiber composite membrane using quantum dot hybridized SPEEK nanofiber for efficient through-plane proton conduction. *Journal of Membrane Science*, 609(5): 118198.
- 38. Shukla, A., Dhanasekaran, P., Nagaraju, N., Bhat, S. D. and Pillai, V. K. (2019). A facile synthesis of graphene nanoribbon-quantum dot hybrids and their application for composite electrolyte membrane in direct methanol fuel cells. *Electrochimica Acta*, 297: 267-280.
- Liu, X., Yang, Z., Zhang, Y., Li, C., Dong, J., Liu, Y. and Cheng, H. (2017). Electrospun multifunctional sulfonated carbon nanofibers for design and fabrication of SPEEK composite proton exchange membranes for direct methanol fuel cell

- application. *International Journal of Hydrogen Energy*, 42(15): 10275-10284.
- 40. Sahin, A. (2018). The development of SPEEK/PVA/TEOS blend membrane for proton exchange membrane fuel cells. *Electrochimica Acta*, 271, 127–136.
- 41. Jiang, Z., Zhao, X. and Manthiram, A. (2013). Sulfonated poly(ether ether ketone) membranes with sulfonated graphene oxide fillers for direct methanol fuel cells. *International Journal of Hydrogen Energy*, 38(14): 5875-5884.
- 42. Gong, C., Zheng, X., Liu, H., Wang, G., Cheng, F., Zheng, G., ... and Tang, C. Y. (2016). A new strategy for designing high-performance sulfonated poly(ether ether ketone) polymer electrolyte membranes using inorganic proton conductor-functionalized carbon nanotubes. *Journal of Power Sources*, 325: 453-464.
- 43. Awang, N., Jaafar, J. and Ismail, A. F. (2018). Thermal stability and water content study of void-free electrospun SPEEK/cloisite membrane for direct methanol fuel cell application. *Polymers*, 10(2): 1-15.
- 44. Yamaguchi, T., Miyata, F. and Nakao, S. I. (2003). Pore-filling type polymer electrolyte membranes for a direct methanol fuel cell. *Journal of Membrane Science*, 214(2): 283-292.
- 45. Salleh, M. T., Jaafar, J., Mohamed, M. A., Norddin, M. N. A. M., Ismail, A. F., Othman, M. H. D., ... and Salleh, W. N. W. (2017). Stability of SPEEK/Cloisite®/TAP nanocomposite membrane under fenton reagent condition for direct methanol fuel cell application. *Polymer Degradation and Stability*, 137: 83-99.
- 46. Mollá, S., Compañ, V., Lafuente, S. L. and Prats, J. (2011). On the methanol permeability through pristine Nafion® and /PVA membranes measured by different techniques. A comparison of methodologies. *Fuel Cells*, 11(6): 897-906.
- 47. Roy, T., Wanchoo, S. K. and Pal, K. (2020). Novel sulfonated poly (ether ether ketone)/rGNOR@TiO<sub>2</sub> nanohybrid membrane for proton exchange membrane fuel cells. *Solid State Ionics*, 349: 115296.

## Malaysian Journal of Analytical Sciences (MJAS)



Published by Malaysian Analytical Sciences Society

# PHYSICAL AND ELECTROCHEMICAL CHARACTERISTICS OF LiCo $_{0.6}$ Sr $_{0.4}$ O $_2$ CATHODE INK FOR INTERMEDIATE-LOW TEMPERATURE SOLID OXIDE FUEL CELL

(Pencirian Fizikal dan Elektrokimia Terhadap Dakwat Katod LiCo<sub>0.6</sub>Sr<sub>0.4</sub>O<sub>2</sub> bagi Sel Fuel Oksida Pepejal Bersuhu Sederhana Rendah)

Nur Nadhihah Mohd Tahir<sup>1</sup>, Nurul Akidah Baharuddin<sup>1\*</sup>, Wan Nor Anasuhah Wan Yusoff<sup>1</sup>, Azreen Junaida Abd Aziz<sup>1</sup>, Mahendra Rao Somalu<sup>1</sup>, Andanastuti Muchtar<sup>1,2</sup>

#### <sup>1</sup>Fuel Cell Institute

<sup>2</sup>Department of Mechanical and Manufacturing Engineering, Faculty of Engineering and Built Environment Universiti Kebangsaan Malaysia, 43600 UKM Bangi, Selangor, Malaysia

\*Corresponding author: akidah@ukm.edu.my

Received: 30 November 2021; Accepted: 27 February 2022; Published: 27 June 2022

#### Abstract

Solid oxide fuel cell (SOFC) is a technology used to generate electricity with less emission. Selection of a suitable, compatible cathode material that will be used with the ionic and protonic electrolyte is crucial in achieving an excellent performance of intermediate-low temperature SOFC. LiCo<sub>0.6</sub>Sr<sub>0.4</sub>O<sub>2</sub> (LCSO) is stoichiometrically prepared via glycine nitrate combustion followed by ball milling and triple roll mill (TRM) machine to produce a homogeneous LCSO cathode ink. The prepared sample powder of LCSO is initially characterised by X-ray diffraction (XRD) and scanning electron microscope (SEM) fitted with energy-dispersive X-ray spectroscopy. The XRD demonstrated that the prepared LCSO powder calcined at 800 °C shows a phase structure of rhombic lattice and space group of R-3m. The prepared ink is then layered on both sides of the samarium-doped-ceria (SDC) electrolyte to produce LCSO | SDC | LCSO symmetrical cell. The prepared ink has varied gap sizes on the TRM machine. The electrochemical performance of electrochemical impedance spectroscopy reports that the best gap size is at 40  $\mu$ m with the lowest polarisation resistance (R<sub>p</sub>), of 8.32  $\Omega$ . In conclusion, this work confirms the importance of a high-quality lithium-based cathode ink in SOFC applications.

Keywords: solid oxide fuel cell, cathode, ink, lithium, triple roll mill

#### Abstrak

Sel fuel oksida pepejal (SOFC) boleh dikategorikan sebagai teknologi pembebasan karbon rendah dalam menjana tenaga elektik. Pemilihan bahan katod yang sesuai dan serasi untuk digunakan bersama dengan elektrolit ionik dan protonik adalah penting dalam mencapai prestasi SOFC bersuhu sederhana-rendah (IT-LT SOFC) yang baik. LiCo<sub>0.6</sub>Sr<sub>0.4</sub>O<sub>2</sub> (LCSO) telah disediakan mengikut stoikiometri menggunakan pembakaran glisin nitrat diikuti dengan pengisaran bebola dan pengisaran tiga penggelek untuk menghasilkan dakwat katod LCSO yang homogen. Serbuk sampel LCSO yang disediakan pada mulanya dicirikan menggunakan pembelauan sinar-X (XRD) dan mikroskop elektron pengimbasan (SEM) yang dipasang dengan spektroskopi sinar-X penyebaran tenaga (EDX). Hasil dapatan XRD menunjukkan kalsin serbuk katod LCSO yang disediakan pada 800 °C menunjukkan struktur

fasa kekisi Rhombo dan kumpulan ruang R-3m Dakwat yang disediakan kemudiannya disapukan pada kedua-dua belah elektrolit samarium terdop seria (SDC) untuk menghasilkan sel simetri LCSO | SDC | LCSO. Dakwat yang disediakan dipelbagaikan saiz celah mesin gulung tiga. Daripada prestasi elektrokimia spektroskopi impedans elektrokimia (EIS) melaporkan bahawa saiz celah terbaik adalah pada 40  $\mu$ m dengan rintangan polarisasi terendah,  $R_p$  8.32  $\Omega$  Kesimpulannya, kajian ini mengesahkan kepentingan dakwat katod berasaskan litium berkualiti tinggi dalam aplikasi SOFC.

Kata kunci: sel fuel oksida pepejal, katod, dakwat, litium, pengisar tiga penggelek

#### Introduction

Fuel cells are currently receiving great attention worldwide due to their claim of being the safest and cleanest technology [1]. A fuel cell can also be considered an efficient power generator due to lesser emission and a higher rate of energy conversion efficiency compared with conventional internal combustion engines. Lina et al. stated that a fuel cell is a clean power generator with less noise pollution [2]. Fuel cells have several types, and this work explains solid oxide fuel cell (SOFC) in detail. Nowadays, SOFC is well-known in the technological and industrial fields. The only identification that distinguishes SOFC from other types of fuel cells is that they operate at a high temperature, ranging from 400 °C to 1000 °C [3-5]. SOFC is an energy conversion device that can convert chemical energy derived from the fuel into electrical and thermal energy [6,7].

SOFC consists of three main components: anode, cathode and electrolyte. The anode and the cathode are known as an electrode–electrolyte layer that is sandwiched between the anode and cathode electrodes [8]. The schematic of the SOFC is shown in Figure 1.

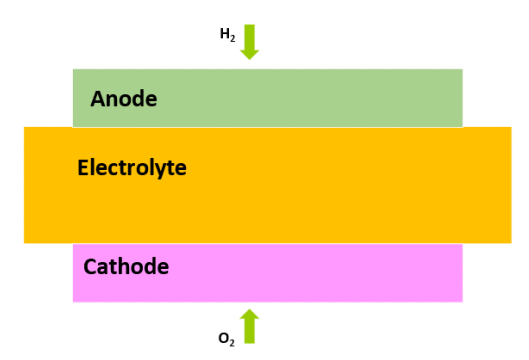


Figure 1. Schematic of SOFC

SOFC has a high energy efficiency when operating at a high temperature of 1000 °C [9, 10]. Studies show that SOFC can achieve an efficiency of 60%-65%. On the one hand, SOFC has been declared as the most promising power generation technology due to its variety of advantages. On the other hand, the high operating temperature which causes material degradation and an increase in manufacturing cost, also results in poor durability of SOFC and limits its application [11]. Accordingly, selection of an intermediate-low temperature is crucial to overcome these arising issues on high operating temperature. The temperature range of intermediate-low temperature is 400 °C-700 °C [12]. The operating cost of this device will be reduced by lowering its temperature, thereby enhancing its commercialisation. SOFC has two types of environments: oxide-conducting SOFC (O<sup>2-</sup>-SOFC), which is the pioneer or conventional type, and protonconducting SOFC (H<sup>+</sup>-SOFC). Figure 2 (a) and (b) show the O<sup>2</sup>—SOFC and H<sup>+</sup>-SOFC, respectively.

Currently, the focus of SOFC development is on intermediate-low temperature SOFC (IT-LT SOFC). However, the high operating temperature of SOFC causes cell degradation issues. To overcome this problem, the operating temperature of SOFC should be reduced to 400-800 °C. Existing materials that have been traditionally operated at elevated temperatures have electrochemical performance under intermediate-low temperature environment. Accordingly, selection of a suitable and compatible cathode material is crucial for IT-LT SOFCs. Lithiatedbased materials are one of the strong candidates for the cathode component of IT-LT SOFCs. The lithiatedbased cathode has been widely used in many batteries, electrochemical applications, such as capacitors and O<sub>2</sub> metal batteries [13-22]. The lithiatedbased material in SOFC provides a free moving lithiumion (Li<sup>+</sup>) cation pathway [23]. The lithium-based cathode can be categorised as a triple (H<sup>+</sup>/O<sup>2-</sup>/e<sup>-</sup>) conducting cathode material, indicating that it can allow those three conducting elements to pass through the cathode boundary or cathode active site [24]. Liu et al. stated that lithium cobaltite, LiCoO2 is one of the promising lithiated-based materials to be used in SOFC applications with triple conducting mechanism capabilities [25,26]. Wan Yusof [27] reported that LiCoO2 or lithium-based material shows a reasonable perspective in intermediate to low temperature for proton- and oxide-conducting SOFC applications [28]. Moreover, strontium (Sr) is widely used as a cathode dopant for most cathode materials to achieve high electrocatalytic activity, especially at the oxygen reduction reaction (ORR) that occurs only in the cathode [29]. Jamil et al. adopted a broad perspective, in which the existence of an Li compound may uplift oxygen concentration, especially at the grain boundary, resulting in high ionic conductivity [30]. Li<sup>+</sup> promotes proton transfer, which makes Li-based cathode materials viable for proton-conducting IT-LT SOFC. Improving the performance of this material requires an in-depth study of the powder and ink preparation aspects. Meanwhile, numerous studies have been conducted on the powder synthesis-related parameters. As previously discussed, a huge gap was observed on the ink production-related parameters. Hence, this study aims to produce a highquality lithiated-based cathode ink (LiCo<sub>0.6</sub>Sr<sub>0.4</sub>O<sub>2</sub>) by altering the gap size of roller in triple-roll mills and to characterize the physical properties and electrochemical performance of the cathode inks for IT-LT SOFC application. The high-quality cathode ink will be produced with a triple roll mill machine, which has been proven to be the optimum method for ink production.

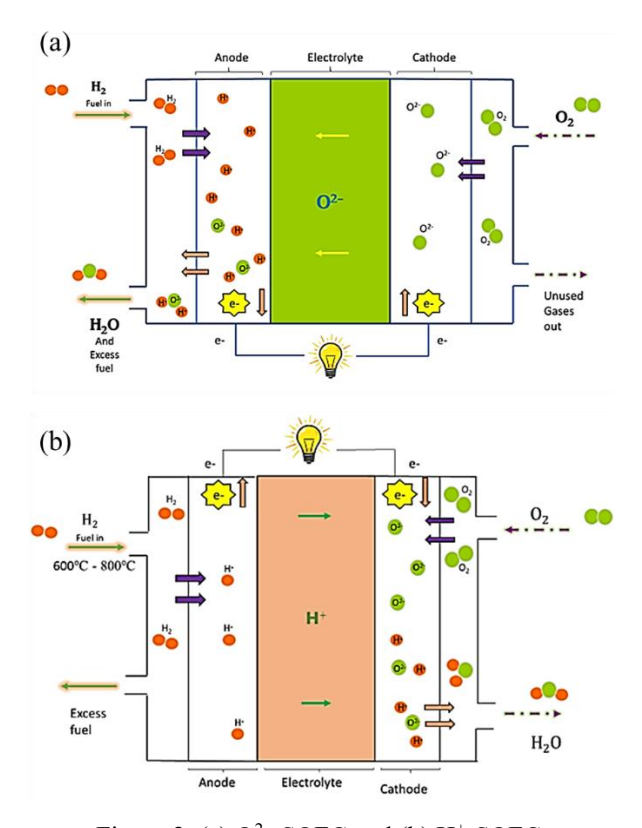


Figure 2. (a) O<sup>2</sup>—SOFC and (b) H<sup>+</sup>-SOFC

#### Materials and Methods

#### Preparation of cathode sample powder LiCoSrO

In this work, LiCo<sub>0.6</sub>Sr<sub>0.4</sub>O<sub>2</sub> precursor powders were produced through the glycine nitrate combustion method. The precursor materials were Lithium Nitrate ReagentPLus, LiNO<sub>3</sub> (Sigma Aldrich, Germany), Strontium Nitrate (ACS Reagent, >99%) Sr(NO<sub>3</sub>)<sub>2</sub> (Sigma Aldrich, Germany) and Cobalt (II) Nitrate Hexahydrate Reagent Grade, 98%, Co(NO<sub>3</sub>)<sub>2</sub>.6H<sub>2</sub>O (Merck Chemicals, Germany). A stoichiometric amount of the precursor materials was dissolved in 100 mL deionised water and stirred for 40 min on a hotplate with a magnetic stirrer at room temperature. Afterwards, a calculated amount of glycine (Sigma-Aldrich, Germany) was added to the precursor material solution as fuel. The mixture was continuously stirred on the hotplate at room temperature for 18 h. Subsequently, the solution was continuously stirred whilst the temperature of the hotplate was slowly increased to between 250 °C to 300 °C to achieve the combustion of the materials and all the nitrates. Thereafter, the obtained black ash precursor powder was further dried at 120 °C for 12 h in

a drying oven. The raw powder was then ground using a mortar agate to obtain a fine, smooth powder. Finally, the dried fine precursor powder was calcined at 800 °C in a high-temperature furnace (Berkeley Scientific, USA) for 5 h holding time. The TGA graph of the previous study [27] on the same material shows that LCSO materials were decomposed at temperatures ranging from 700 – 1000 °C. After the LCSO powder was calcined, it was subjected to X-ray diffraction (XRD) testing and scanning electron microscope (SEM) analysis for LCSO its characterisation.

#### **Material characterisation**

Wan Yusoff et al. [27] investigated the thermal decomposition behaviour of the LCSO powder in 2020, via thermogravimetric analysis/differential scanning calorimetry (TGA/DSC, SING Mettler Toledo, United States) to determine the optimal calcination temperature. The analysis was conducted on the LCSO precursor powder synthesised from room temperature to 1000 °C at a heating rate of 10 °C/min<sup>-1</sup> under air with a flow rate

of 50 mL/min<sup>-1</sup>. Then, the precursor LCSO powder was further analysed via XRD (Bruker AXS D8 Advance, Germany) with a CuK $\alpha$  ( $\lambda$  = 0.15406 nm) radiation source to confirm its phase and structure. An X-ray diffractometer was operated at 40 kV and 40 mA, and fitted with a 1-D fast detector (Lynx-Eye). The XRD spectrum was recorded for 2 $\theta$  ranging from 20° to 70° with a step size of 0.025°. The morphology of the LCSO particles was examined via SEM (Carl Zeiss EVO MA10, Germany). From the material characterisation, the optimal calcination temperature was selected to produce another batch of LCSO cathode powder, which was used to synthesise the LCSO cathode ink.

#### Ink preparation

The cathode ink was produced using several methods and techniques that have been utilized by other researchers. The common methods used for synthesizing the ink are triple roll mill (TRM) machine, ball milling and manual mixing (hands-on). The methods used by other researchers are summarised in Table 1.

Table 1. Summary of methods used to produce ink

Method	Element	Performance	Reference
Ball Milling	Iron and nitrogen dope carbide-derived carbon (SiCDC)	The grain size decreases from 1 μ to 200 nm.	Ratso et al. 2021[31]
	Multiwalled carbon nanotubes/epoxy suspensions	A better-quality texture of the material is produced.	Olowojoba et al. [32]
TRM Machine	Soda lime glass	Fast response and process can be broken down into phases. The particle size breakage yields a good result.	Böttcher et al. [33]
	$La_{0.6}Sr_{0.4}CoO_{3-\delta}$ (LSC)	High porosity and good electrochemical performance are achieved with a TRM machine.	Samat et al. [10]
Manual Mixing	$La_{0.6}Sr_{0.4}CoO_{3-\delta} (LSC)$	The porosity is lower, and the value of ASR is higher compared with other methods.	Samat et al. [34]

Table 1 shows that using the TRM machine as the medium in synthesising the cathode is the best option because if the better quality and outstanding electrochemical performance. Several parameters in the ink production process are maintained variable during the research. Determining and varying the parameters is

crucial to producing a high-quality cathode ink. Table 2 shows the parameters considered and previously studied. The parameters studied by the researchers include roller speed, frequency of rotation, roller gap size, ink thickness, feed rate and breakage behaviour.

Table 2. Parameter study related to the TRM machine

Parameter study related to the TRM	Reference
Roller gap size	Wan Yusoff et al. [27]
Roller speed and rotation frequency	Olowojoba et al. [32]
Roller speed, roller gap size, feed rate and breakage behaviour	Böttcher et al. [33]
Ink thickness	Samat et al. [34]
Roller speed and roller gap size	Somalu et al. [35]

TRM is essential in the production of homogenous screen-printing inks because it breaks down most particle agglomerates during milling. The difference in roller speeds produces shear stress between the rollers, which pull agglomerates apart when the material passes between the gaps. The working principle of the TRM machine is shown in Figure 3. The resulting shear rates between the gaps are provided in the following equation:

Shear rate= 
$$\frac{\Delta v}{x}$$
, (1)

 $\Delta v$ : speed difference, and x: gap between rollers.

The LCSO ink was prepared with EXAKT 50 I, Germany TRM machine in the SOFC Laboratory at Institute Fuel Cell UKM. The produced LCSO powder was ball-milled for 24 h with a 10-rpm rotating rate. The ink was prepared by using the right composition to produce a good-quality cathode ink. The ink composition is tabulated in Table 3. The postball milled LCSO powder was mixed with a vehicle buffer solution, dispersant and solvent. The premixed ink was manually ground before producing a smooth, fine ink with the TRM machine. Then, all the premixed ink was mixed well. The LCSO with various ink parameters were formed, and the parameters produced throughout this work are listed in Table 4.

Table 3. LCSO ink composition

Solid Content	Weigh (wt.%)
LCSO powder (ball milled)	67.33
Solvent (Terpineol)	29.98
Binder (Ethylcelulose N7 grade (0.25%–0.5 wt.%)	1.35
Dispersant (Hypermer KD15)	1.35

Table 4. LCSO ink parameter

Variable Parameter	Gap Size (µm)
1	g <sub>1</sub> - 10
2	g <sub>2</sub> - 20
3	g <sub>3</sub> - 30
4	g <sub>4</sub> - 40
5	g <sub>5</sub> - 50

#### Fabrication of symmetrical cell LCSO|SDC|LCSO

The fabrication of symmetrical cell started with the production of an electrolyte pellet of Sm<sub>0.2</sub>Ce<sub>0.8</sub>O<sub>1.9</sub> (SDC). Then, the prepared LCSO cathode ink was layered on both sides of the electrolyte pellet. Prior to the half and symmetrical cell production for electrical conductivity electrochemical and impedance spectroscopy (EIS) analysis, the SDC powders (Sigma-Aldrich) were pressed into a coin-shaped structure to form an electrolyte substrate at 52 MPa. The SDC electrolyte was sintered at 1400 °C for 6 h. Then, the asprepared cathode inks were screen printed two layers on one side (half-cell) and both sides (symmetrical cell) of the electrolyte surface with an active area, A, of 1 cm<sup>2</sup> prior to sintering at 800 °C for 2 h. The prepared symmetrical cell LCSO|SDC|LCSO is shown in Figure 3.

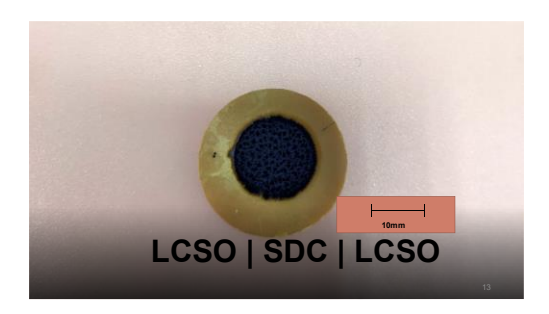


Figure 3. Prepared symmetrical cell LCSO|SDC|LCSO

## Electrochemical analysis of the LCSO|SDC|LCSO symmetrical cell

The electrochemical performance was measured using EIS with a potentiostat (PGSTAT302 N, Metrohm Autolab, Netherlands) operating at 106–0.1 Hz with a sinusoidal voltage amplitude of 10 mV. Symmetrical cells were evaluated in the air at 500 °C–800 °C under typical IT-SOFC operating conditions, with a constant air flow rate of 0.2 Lmin<sup>-1</sup>. EIS was performed on all symmetrical cells with a constant active area of 1 cm<sup>2</sup>, and the data were processed with NOVA software (version 1.10) to determine the ASR values of the LCSO cathode.

#### Results and Discussion

#### Properties of prepared powder

The XRD spectrum of the as-synthesised powder cathode calcined at 800 °C and 900 °C for 5 h is shown in Figure 4. The data base cannot provide the full spectrum of LiCoSrO because this material is new. Accordingly, the XRD was compared with LiCoO2 and SrCO<sub>3</sub>. The calcined LCSO powders exhibited merely a single phase, as confirmed by the XRD measurement. The plotted results showed a peak almost similar to the reference LiCoO<sub>2</sub> with SrCO<sub>3</sub>. All the prominent peaks in the XRD spectrum of the calcined powder were matched with the reference code PDF 00-050-0653 lithium cobalt oxide (LiCoO<sub>2</sub>) of rhombic lattice structure and space group of R-3m and PDF 01-084-1778 strontium carbonate (SrCO<sub>3</sub>) of orthorhombic lattice structure with space group of R-3m. Thus, the highest peaks were indexed to their Miller indices (hkl) of (111) and (104) for LiCoO<sub>2</sub> and SrCO<sub>3</sub>, respectively.

The morphological analysis was conducted on the LCSO powders calcined at temperatures of 800 °C and 900 °C by SEM and EDX. The results for both microstructures are illustrated in Figures 5 and 6. The results show that the microgram has a random fragment structure, whereas EDX confirms that all the components of LCSO are in the cathode powders. The EDX graph in Figure 6 clearly shows that all the components of Li, cobalt (Co), strontium (Sr) and oxide (O<sub>2</sub>) are present in the LCSO powder for both temperatures of calcined LCSO. However, the LCSO precursor powder calcined at a temperature of 800 °C shows less impurities than that calcined at 900 °C.

After analysing the calcined powder and producing a high-quality ink, the best composition was considered. Based on the LCSO ink composition in Table 3, the smooth, fine-texture ink was successfully produced using the in-house TRM machine. The produced LCSO cathode ink is shown in Figure 7.

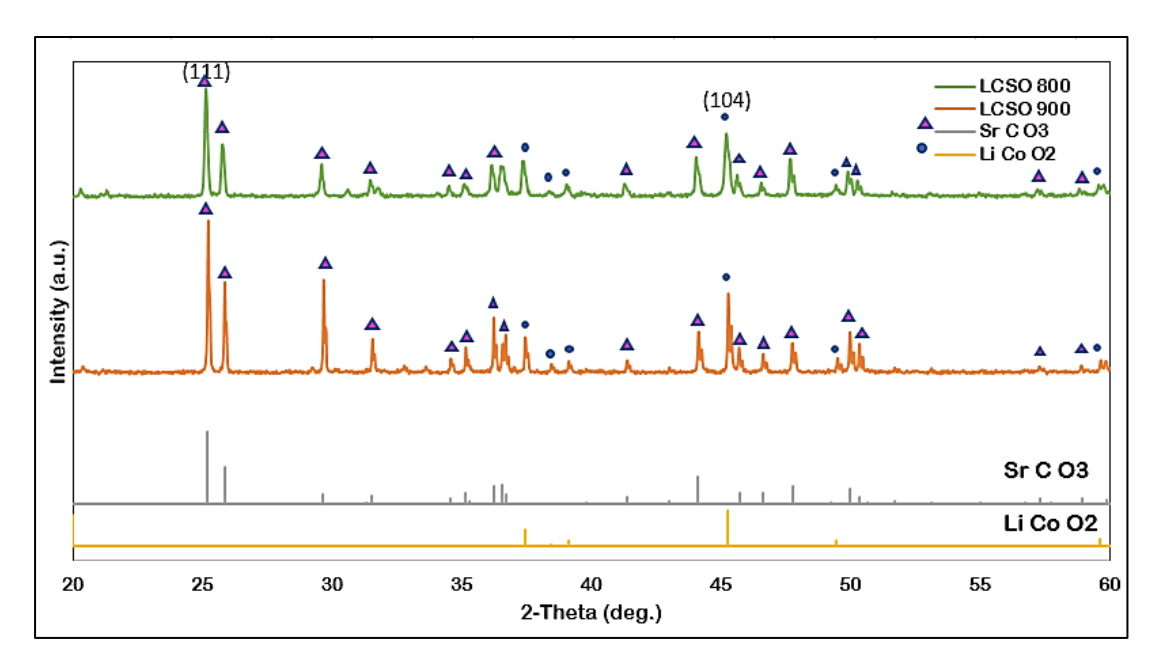


Figure 4. XRD spectrum obtained by this research



Figure 5. SEM of the LCSO powder calcined at temperatures of 800 °C and 900 °C

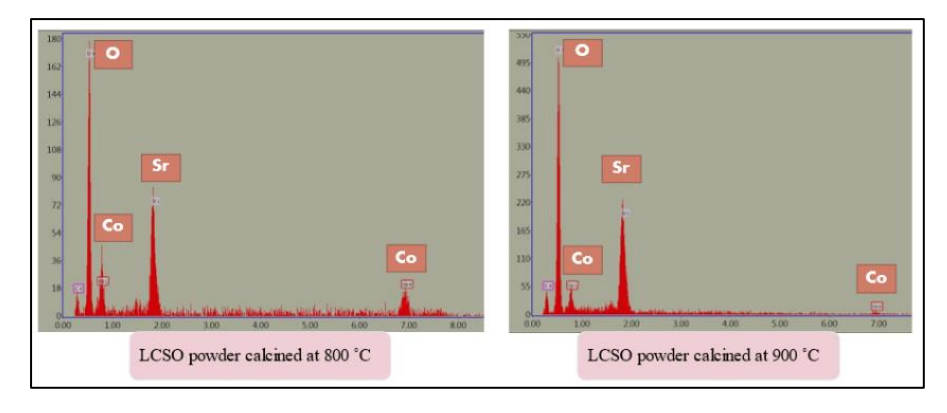


Figure 6. EDX analysis of the calcined LCSO powder

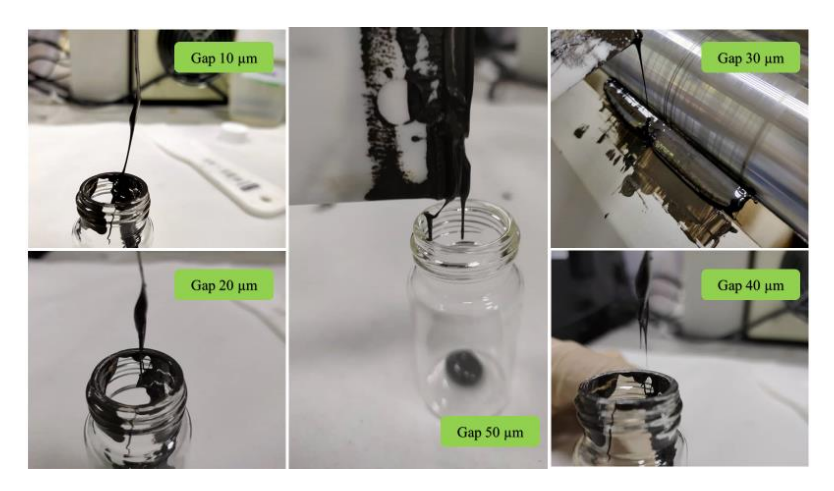
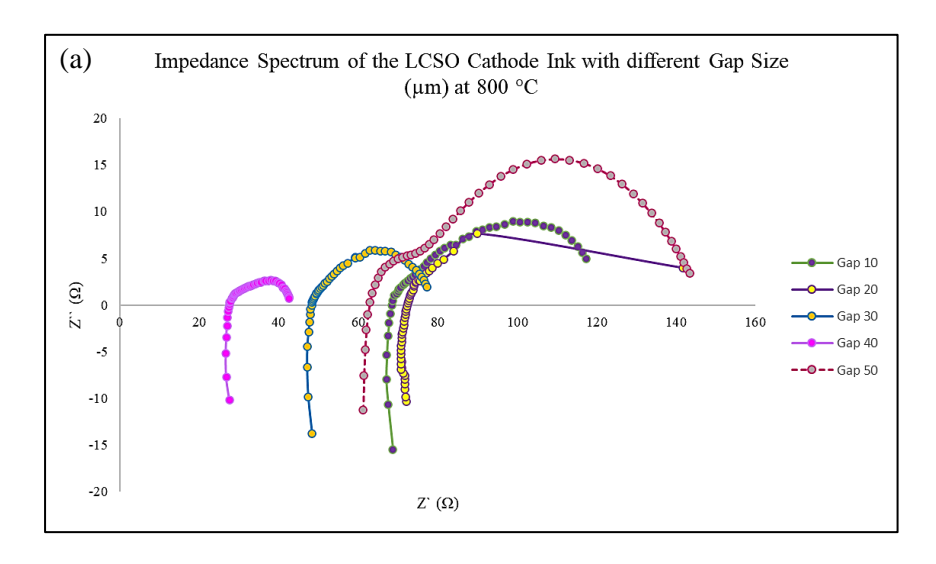


Figure 7. Produced LCSO cathode ink

#### Electrochemical performance analysis

Figure 8 shows the electrochemical impedance spectrum of the LCSO|SDC|LCSO symmetrical cells with different cathode ink parameters of the gap size of the TRM. The spectra are fitted via electrical circuit fitting composed of resistance (R) and constant phase element (CPE). Resistances and constant phase elements are illustrated by R<sub>S</sub>, R<sub>1</sub>, R<sub>2</sub>, CPE<sub>1</sub> and CPE<sub>2</sub> for high- and low-frequency arcs. The impedance are was analysed using an electric equivalent circuit, as shown in Figure 8(b). All the measured and calculated values of polarisation resistance and area specific resistance

(ASR) at 800 °C of each symmetrical cell with different gap size are listed in Table 5. The impedance spectra in Figure 8(a) show that gap size of 40  $\mu$ m is the lowest amongst the other gap sizes, and this is proven by the measured and calculated polarisation resistance,  $R_p$ , value in Table 5 that shows the gap sizes of 10, 20, 30, 40 and 50  $\mu$ m of 32.35, 39.63, 17.07, 8.32 and 43.36  $\Omega$ , respectively. The LCSO cathode ink produced with the TRM shows that the best gap size is 40  $\mu$ m with proven electrochemical performance of 8.32  $\Omega$ .



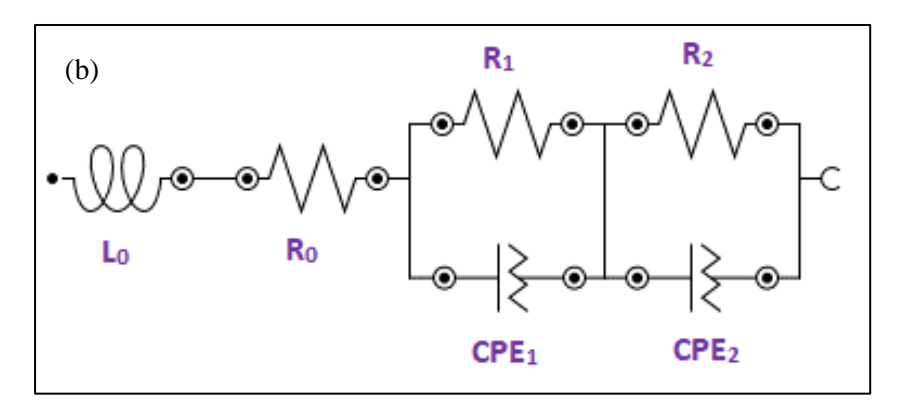


Figure 8. (a) Impedance spectra of the different gap sizes; (b) adopted an electrical equivalent circuit to analyse the impedance data

Table 5. Values of the polarisation resistance and ASR of LCSO|SDC|LCSO symmetrical cells of different gap sizes of the ink produced

Gap Size (µm)	Polarisation Resistance, Rp (Ω)	ASR at 800 °C (Ω cm²)
10	32.35	16.175
20	39.63	19.815
30	17.07	8.535
40	8.32	4.160
50	43.36	21.680

#### Conclusion

The LCSO cathode ink is synthesised via glycine nitrate combustion. Subsequently, the cathode ink was produced using the TRM machine method, and the gap size of the TRM varied at 10, 20, 30, 40 and 50 µm. Amongst the different gap sizes, the best gap size is 40 µm with proven electrochemical performance of EIS with polarisation resistance,  $R_p$  value of 8.32  $\Omega$  and ASR of 4.160  $\Omega$ cm<sup>2</sup>. This work benchmarks the attempt of a compatibility of an Li-based cathode ink in the application of IT-LT SOFCs. Moreover, this work is involved in and will compete in the production of a durable SOFC system to enhance its viability in actual applications. In the future, the production of the LCSO cathode ink under various IT-LT SOFC environments, such as proton conducting SOFC (H+-SOFC) and oxide conducting SOFC (O<sup>2</sup>—SOFC) will be conducted to find the optimal environment for LCSO cathode ink to work for.

#### Acknowledgement

The authors gratefully acknowledge the financial support provided by the Ministry of Higher Education, Malaysia and the funding support via the research sponsorship under Fundamental Research Grant Scheme grant number FRGS/1/2019/TK07/UKM/02/1 and Universiti Kebangsaan Malaysia through Research Grant DIP-2010-011.

#### References

 Ali, S. M., Anwar, M., Abdalla, A. M., Somalu, M. R. and Muchtar, A. (2017). Ce0.80Sm0.10Ba0.05Er0. 05O2-δ multi-doped ceria electrolyte for intermediate temperature solid oxide fuel cells. *Ceramics International*, 43(1): 1265-1271.

- Rashid, N. L. R. M., Samat, A. A., Jais, A. A., Somalu, M. R., Muchtar, A., Baharuddin, N. A. and Isahak, W. N. R. W. (2019). Review on zirconatecerate-based electrolytes for proton-conducting solid oxide fuel cell. *Ceramics International*, 45(6): 6605-6615.
- 3. Baharuddin, N. A., Abdul Rahman, N. F., Abd. Rahman, H., Somalu, M. R., Azmi, M. A. and Raharjo, J. (2020). Fabrication of high-quality electrode films for solid oxide fuel cell by screen printing: a review on important processing parameters. *International Journal of Energy Research*, 44(11): 8296-8313.
- 4. Abd Aziz, A. J., Baharuddin, N. A., Somalu, M. R. and Muchtar, A. (2020). Review of composite cathodes for intermediate-temperature solid oxide fuel cell applications. *Ceramics International*, 46(15): 23314-23325.
- Tahir, N. N. M., Baharuddin, N. A., Samat, A. A., Osman, N. and Somalu, M. R. (2022). A review on cathode materials for conventional and protonconducting solid oxide fuel cells. *Journal of Alloys* and Compounds, 894: 162458.
- Kim, M., Kim, D. H., Han, G. D., Choi, H. J., Choi, H. R. and Shim, J. H. (2020). Lanthanum strontium cobaltite-infiltrated lanthanum strontium cobalt ferrite cathodes fabricated by inkjet printing for high-performance solid oxide fuel cells. *Journal of Alloys and Compounds*, 843: 155806.
- 7. Rainwater, B. H., Liu, M. and Liu, M. (2012). A more efficient anode microstructure for SOFCs based on proton conductors. *International Journal of Hydrogen Energy*, 37(23): 18342-18348.
- 8. Dwivedi, S. (2020). Solid oxide fuel cell: Materials for anode, cathode and electrolyte. *International Journal of Hydrogen Energy*, 45(44): 23988-24013.
- Rosli, A. Z., Somalu, M. R., Osman, N. and Hamid, N. A. (2021). Physical characterization of LSCF-NiO as cathode material for intermediate temperature solid oxide fuel cell (IT-SOFCs). *Materials Today: Proceedings*, 46:1895-1900.
- Samat, A. A., Somalu, M. R., Muchtar, A. and Osman, N. (2019, June). Electrochemical performance of La0. 6Sr0. 4CoO3-δ cathode in air and wet air for BaCe0.54Zr0.36Y0.1O3-based proton-conducting solid oxide fuel cell. *In IOP*

- Conference Series: Earth and Environmental Science, 268(1): 012136.
- 11. Lv, H., Jin, Z., Peng, R., Liu, W. and Gong, Z. (2019). BaCoxFe0. 7-xZr0. 3O3-δ (0.2≤ x≤ 0.5) as cathode materials for proton-based SOFCs. *Ceramics International*, 45(18): 23948-23953.
- Huan, D., Shi, N., Xie, Y., Li, X., Wang, W., Xue, S., ... and Lu, Y. (2020). Cathode materials for proton-conducting solid oxide fuel cells. *Intermediate Temperature Solid Oxide Fuel Cells*: pp. 263-314.
- 13. Le, S., Zhu, S., Zhu, X. and Sun, K. (2013). Densification of Sm0. 2Ce0.8O1.9 with the addition of lithium oxide as sintering aid. *Journal of Power Sources*, 222: 367-372.
- Yuan, L. X., Wang, Z. H., Zhang, W. X., Hu, X. L., Chen, J. T., Huang, Y. H. and Goodenough, J. B. (2011). Development and challenges of LiFePO<sub>4</sub> cathode material for lithium-ion batteries. *Energy & Environmental Science*, 4(2): 269-284.
- 15. Hofmann, T., Westhoff, D., Feinauer, J., Andrä, H., Zausch, J., Schmidt, V. and Mueller, R. (2020). Electro-chemo-mechanical simulation for lithium ion batteries across the scales. *International Journal of Solids and Structures*, 184: 24-39.
- Janowitz, K., Kah, M. and Wendt, H. (1999).
   Molten carbonate fuel cell research: Part I.
   Comparing cathodic oxygen reduction in lithium/potassium and lithium/sodium carbonate melts. *Electrochimica Acta*, 45(7): 1025-1037.
- 17. Accardo, G., Kim, G. S., Ham, H. C. and Yoon, S. P. (2019). Optimized lithium-doped ceramic electrolytes and their use in fabrication of an electrolyte-supported solid oxide fuel cell. *International Journal of Hydrogen Energy*, 44(23): 12138-12150.
- Preethi, S., Abhiroop, M. and Babu, K. S. (2019). Low temperature densification by lithium codoping and its effect on ionic conductivity of samarium doped ceria electrolyte. *Ceramics International*, 45(5): 5819-5828.

- Kanthachan, J., Khamman, O., Intatha, U. and Eitssayeam, S. (2021). Effect of reducing calcination processing on structural and electrochemical properties of LiNi0.5Mn0.3Co0.2O2 cathode materials for lithium battery. *Materials Today: Proceedings*, 47: 3600-3603.
- Hu, X., Qiang, W. and Huang, B. (2017). Surface layer design of cathode materials based on mechanical stability towards long cycle life for lithium secondary batteries. *Energy Storage Materials*, 8: 141-146.
- Peng, Y., Tan, R., Ma, J., Li, Q., Wang, T. and Duan, X. (2019). Electrospun Li<sub>3</sub>V<sub>2</sub>(PO<sub>4</sub>)<sub>3</sub> nanocubes/carbon nanofibers as free-standing cathodes for high-performance lithium-ion batteries. *Journal of Materials Chemistry A*, 7(24): 14681-14688.
- 22. Yan, R., Oschatz, M. and Wu, F. (2020). Towards stable lithium-sulfur battery cathodes by combining physical and chemical confinement of polysulfides in core-shell structured nitrogen-doped carbons. *Carbon*, 161, 162-168.
- 23. Zhang, L., Lan, R., Kraft, A., Wang, M. and Tao, S. (2010). Cost-effective solid oxide fuel cell prepared by single step co-press-firing process with lithiated NiO cathode. *Electrochemistry Communications*, 12(11): 1589-1592.
- 24. Hussain, S. and Yangping, L. (2020). Review of solid oxide fuel cell materials: Cathode, anode, and electrolyte. *Energy Transitions*, 4(2): 113-126.
- Hou, J., Miao, L., Hui, J., Bi, L., Liu, W. and Irvine, J. T. (2018). A novel in situ diffusion strategy to fabricate high performance cathodes for low temperature proton-conducting solid oxide fuel cells. *Journal of Materials Chemistry A*, 6(22): 10411-10420.
- Yuan, K., Yu, Y., Wu, Y., Ji, X., Xu, Z. and Shen, J. (2018). Plasma sprayed coatings for low-temperature SOFC and high temperature effects on Lix (Ni, Co) yO<sub>2</sub> catalyst layers. *International Journal of Hydrogen Energy*, 43(28): 12782-12788.
- Wan Yusoff, W. N. A., Somalu, M. R., Baharuddin, N. A., Muchtar, A. and Wei, L. J. (2020). Enhanced performance of lithiated cathode materials of LiCo0.6X0.4O<sub>2</sub> (X= Mn, Sr, Zn) for proton-

- conducting solid oxide fuel cell applications. *International Journal of Energy Research*, 44(14): 11783-11793.
- 28. Yusoff, W. N. A. W., Norman, N. W., Samat, A. A., Somalu, M. R., Muchtar, A. and Baharuddin, N. A. (2019). Performance of LiCo0.6Zn0.4O<sub>2</sub> as a potential cathode material candidate for intermediate solid oxide fuel cell application. *In IOP Conference Series: Earth and Environmental Science*, 268(1): 012139.
- 29. Zhang, Y., Yang, G., Chen, G., Ran, R., Zhou, W. and Shao, Z. (2016). Evaluation of the CO<sub>2</sub> poisoning effect on a highly active cathode SrSc0.175Nb0.025Co0.8O3-δ in the oxygen reduction reaction. ACS Applied Materials & Interfaces, 8(5): 3003-3011.
- Jamil, S. M., Othman, M. H. D., Rahman, M. A., Jaafar, J., Mohamed, M. A., Yusop, M. Z. M., ... and Tanemura, M. (2017). Dual-layer hollow fiber MT-SOFC using lithium doped CGO electrolyte fabricated via phase-inversion technique. *Solid State Ionics*, 304: 113-125.
- 31. Ratso, S., Zitolo, A., Käärik, M., Merisalu, M., Kikas, A., Kisand, V., ... and Tammeveski, K. (2021). Non-precious metal cathodes for anion exchange membrane fuel cells from ball-milled iron and nitrogen doped carbide-derived carbons. *Renewable Energy*, 167: 800-810.
- 32. Olowojoba, G., Sathyanarayana, S., Caglar, B., Kiss-Pataki, B., Mikonsaari, I., Hübner, C. and Elsner, P. (2013). Influence of process parameters on the morphology, rheological and dielectric properties of three-roll-milled multiwalled carbon nanotube/epoxy suspensions. *Polymer*, 54(1): 188-198.
- Böttcher, A. C., Thon, C., Fragnière, G., Chagas, A., Schilde, C. and Kwade, A. (2021). Rigidly-mounted roll mill as breakage tester for characterizing fine particle breakage. *Powder Technology*, 383: 554-563.

- 34. Abdul, S. A., Yusoff, W. N. A. W., Baharuddin, N. A., Somalu, M. R., Muchtar, A. and Osman, N. (2018). Electrochemical performance of sol-gel derived La0.6S0.4CoO3-δ cathode material for proton-conducting fuel cell: A comparison between simple and advanced cell fabrication techniques. Processing and Application of Ceramics, 12(3): 277-286.
- 35. Somalu, M. R., Muchtar, A., Daud, W. R. W. and Brandon, N. P. (2017). Screen-printing inks for the
- fabrication of solid oxide fuel cell films: a review. *Renewable and Sustainable Energy Reviews*, 75: 426-439.
- 36. Sun, G., Yu, F. D., Zhao, C., Yu, R., Farnum, S., Shao, G., ... and Wang, Z. B. (2021). Decoupling the voltage hysteresis of Li-rich cathodes: electrochemical monitoring, modulation anionic redox chemistry and theoretical verifying. *Advanced Functional Materials*, 31(1): 2002643.

# **Malaysian Journal of Analytical Sciences** (MJAS) Published by Malaysian Analytical Sciences Society



## CHEMICAL OXYGEN DEMAND AND TURBIDITY REMOVAL OF LANDFILL LEACHATE USING ELECTROCOAGULATION TECHNIQUE WITH Al ELECTRODE

(Penyingkiran Permintaan Oksigen Kimia dan Kekeruhan daripada Larut Resap Tapak Pelupusan dengan Menggunakan Elektrod Al)

Norilhamiah Yahya<sup>1\*</sup>, M. Firdaus Mamat<sup>1</sup>, Suhaini Mamat<sup>1</sup>, Nabila A. Karim<sup>2</sup>

<sup>1</sup>Malaysian Institute of Chemical and Bioengineering Technology, Universiti Kuala Lumpur, 78000 Alor Gajah, Malacca, Malaysia <sup>2</sup>Fuel Cell Institute, Universiti Kebangsaan Malaysia, 43600 Bangi, Malaysia

\*Corresponding author: norilhamiah@unikl.edu.my

Received: 2 December 2021; Accepted: 6 March 2022; Published: 27 June 2022

### Abstract

The electrocoagulation process is classified as green technology to treat landfill leachates. A 16 full factorial experimental design evaluated and optimized the electrocoagulation method and compromised efficiency and operational costs. This study assessed three factors: operation time, voltage, and electrode size, to determine the most influencing parameters and describe the interaction between chemical oxygen demand (COD) and turbidity removal. Statistical analysis results using a half-normal plot demonstrated that all main factors significantly affected the removal efficiency of COD and turbidity. The Pareto chart reveals that the order of significance for COD and turbidity removal efficiency was voltage > operation time > electrode size> interaction between voltage and electrode. The best regression coefficients (R<sup>2</sup>) were obtained for COD and turbidity, which reached 0.9597 and 0.9908, respectively, confirming that the predicted values complied with the experimental values. This implied the appropriateness of the employed regression model. The optimization process results showed that for maximizing the removal efficiency of COD and turbidity, the optimal level of operation time was 30 min, voltage 30 V and electrode 10 cm2 by using a batch reactor.

Keywords: electrocoagulation, landfill leachate, chemical oxygen demand, turbidity

#### **Abstrak**

Proses elektrokoagulasi diklasifikasikan sebagai teknologi hijau untuk merawat tapak pelupusan larut lesap. Reka bentuk eksperimen 16 faktorial penuh telah digunakan untuk menilai dan mengoptimumkan kaedah elektrokoagulasi dan untuk mencapai kompromi antara kecekapan dan kos operasi. Kajian ini menilai tiga faktor: masa operasi, voltan dan saiz elektrod untuk menentukan parameter yang paling mempengaruhi dan menerangkan interaksi antara parameter untuk permintaan oksigen kimia (COD) dan penyingkiran kekeruhan. Keputusan analisis statistik menggunakan plot separa normal menunjukkan bahawa semua faktor utama mempunyai kesan yang ketara ke atas kecekapan penyingkiran COD dan kekeruhan. Carta Pareto mendedahkan, untuk COD dan kecekapan penyingkiran kekeruhan, urutan kepentingan ialah voltan > masa operasi > saiz elektrod > interaksi antara voltan dan saiz elektrod.. Pekali regresi terbaik (R2) diperoleh untuk COD dan kekeruhan mencapai nilai masing-masing 0.9597 dan 0.9908 mengesahkan bahawa nilai yang diramalkan adalah mematuhi nilai eksperimen yang membayangkan kesesuaian model regresi yang digunakan. Hasil proses pengoptimuman menunjukkan bahawa untuk memaksimumkan kecekapan penyingkiran COD dan kekeruhan, tahap masa operasi yang optimum adalah 30 minit, voltan 30 V dan elektrod 10 cm² dengan menggunakan reaktor batch.

Kata kunci: elektrokoagulasi, larut lesap tapak pelupusan, permintaan oksigen kimia, kekeruhan

#### Introduction

Malaysia produces about 42,672 metric tons of solid waste every day, and the value may be increased every year due to urbanization, increase in population, and per capita waste generation [1]. Generally, organic wastes constitute 40 – 60 % of the overall weight in most developing countries. Despite several advantages of landfilling, the resulting heavily polluted leachate has caused an urgent concern because landfilling is a widely used method for solid waste disposal. Various factors influence leachate quality and quantity, such as landfilling technique, seasonal weather variation, waste type and composition, and landfill structure [2]. Therefore, environmental specialists are determined to develop effective treatments for vast quantities of heavily polluted leachates.

The EC process is a process to form floc with the help of oxidized metal in wastewater, whereby it needs to be cleaned by the electro-dissolution anode [3]. EG can also be defined as a process of removing the suspended solids from wastewater by using electricity to neutralize the harmful particles through hydroxide complexes formation in water to gather the suspended solid, help bridge, bind, and strengthen floc sedimentation due to gravity force. This process collects the suspended solids in water without coagulants, and then coagulation occurs when a direct current is applied, thus capable of removing small particles and setting them into motion. Several factors that influence the EC process's efficiency are electrode types, the gap between electrodes, electrode size, the configuration of metals, current density, charge loading, pH value of the sample, the addition of supporting electrolyte, and operation time. The electrodes that are usually used are iron, aluminum, and stainless steel. This metal sheet pair is anode and cathode [4].

Nowadays, most treatment methods widely used worldwide to treat wastewater are physical-chemical and biological processes, but the treatment of leachates by using these methods is complex due to low biodegradability and high toxicity. The biological process is a method that uses natural methods that depend on microorganisms, nematodes, and tiny creatures. At the same time, physical-chemical processes require added synthetic substances [5]. For example, Castillo-Suárez [6] used peroxicoaguation and solar peroxicoagulation in a batch electrolytic reactor in the presence of solar ultraviolet light and studied three main parameters to treat the leachates, which are pH value, current density, and treatment time. The use of these three parameters gives the optimal value of biochemical oxygen and COD removed at 55.5% and 62.3%, respectively. Jang et. al [7] studied the effect of adding lithium manganese oxide and activated carbon electrodes in the electrochemical sorption of the lithiumion battery leachate. The authors found that increased capacity, selectivity, and purity depended on the reaction time and applied current. The same parameters; time, and current density, were also studied by Galvão [8] in the EC process treatment. Five responses were recorded: ultraviolet absorbance, biological oxygen demand, COD, turbidity, and color, while the percentage values of removal when applied with 128 Am<sup>-2</sup> for 90 min were 40%, 90%, 40%, 82%, and 82%, respectively. The removal efficiency was increased to a maximum by increasing the electrolysis time, leading to a constant rate. The number of generated metal hydroxides increased with the electrolysis time.

In this regard, a group of researchers used the EC process to remove cefazolin and COD from hospital wastewater [9]. The tests were performed in three specific voltages (15V, 30 V, 50 V) and periods (10 min, 30 min, 50 min). The result showed that the maximum

efficiency of contamination removal in 50 min was more than 92%. Chairunnisak et al. [10] reported that the electrocoagulation method resulted in the optimum COD reduction of 94.53% from operating time of 39.28 min, 20 V, and without electrolyte concentration. A study conducted by Amarine et al. [11] showed that the removal efficiency depended on the electrodes' applied voltage and immersed surface. This removal efficiency was 94.41% after 150 min, the electrical voltage of 30 V, and the immersed surface of 33.75 cm<sup>2</sup>. Another research by Bajpai et al. [12] found that an optimum condition (14 V and 47 min) at a pH value of 7.35, which provided experimental removal efficiency (75.6% COD, 78.7% total dissolved solids, 93.4% turbidity, and 63.2% chloride).

There is in situ generation of coagulants by the dissolution of sacrificial anodes due to direct current flow. Different studies have proven that the aluminum electrode was the most effective and successful. Therefore, aluminum was used as the electrode material in this study. The anode produces metal cations after its oxidation process by applying direct current; this cation involves further reactions and produces different polymeric hydroxides of metal, similar to salts used in conventional coagulation.

The reactions when using aluminum electrodes can be summarized as follows;

#### **Anode reactions:**

$$Al(s) \rightarrow Al_{(aq)}^{3+} + 3e \tag{1}$$

$$Al_{(aq)}^{3+} + 30H^{-} \rightarrow Al(0H)_{3}$$
 (2)

#### **Alkaline reactions:**

$$Al_{aq}^{3+} + 3H_2O \rightarrow Al(OH)_3 + 3H^+$$
 (3)

#### Acidic pH range

Cathode reactions leads to mainly hydrogen evolution:

$$3H_2O + 3e \leftrightarrow \frac{3}{2}H_2 \uparrow + OH^-$$
 (4)

As seen in the above reactions, EC combines oxidation, flocculation and flotation. The EC occurs in three steps. In the first step, a coagulant is formed due to oxidation of the anode. In the second step, pollutants get

destabilized, while in the last step, the destabilized matters get united and removed.

EC is an exceptional strategy for water and wastewater treatment. While the EC has been applied to different modern gushing, for example, nourishment businesses, tannery, mechanical shops (dissolvable polymerization production, and wastewater material industry. Naje & Abbas [13] limited studies were carried out on the effective voltage, operation time and electrode side in the electrocoagulation process time in the COD and turbidity removal. Simple, affordable, and efficient leachate treatment systems are urgently needed in developing countries because most conventional technologies in industrialized nations are too expensive and complex. Rusdianasari et al. [14]. EC is a simple method to treat wastewater efficiently, and it seems to be a promising treatment method due to its high effectiveness, lower maintenance cost, less need for labor, and rapid achievement of results. In this study, statistical analysis via factorial design was used to investigate factors that influence the reduction of two primary contaminants in leachate, which were COD and turbidity.

#### Materials and Methods

#### Sample collection

A close landfill that was shut down for over five years was selected to collect the leachate samples. Even though the landfill was shut down, the leachate was still being produced in the landfill. The amount of leachate produced was 200 m³ per day, while the volume of leachate discharged was 190 m³. The grab sampling technique was used for collecting the samples. Samples were kept at a temperature of 4 °C in an icebox to preserve the original circumstances of the sample. The main characteristics of the studied leachate samples are shown in Table 1.

Table 1. Characteristics of the leachate sample used in this study

Parameters	Units	Value
Chemical Oxygen Demand (COD)	mg/L	675
Turbidity	NTU	705

#### **Experimental set-up**

The batch experimental was set up the electrochemical unit, which consisted of an electrocoagulation cell, a DC power supply, and aluminum electrodes. In this study, EC cell was made from aluminum anodes, and cathodes with 2 cm spacing were placed vertically on the cell floor. The electrodes had dimensions of 5.65 cm × 13.9 cm, with a functional area of 28.76 cm<sup>2</sup> (anode). The stirrer was set at 100 rpm to maintain the composition and avoid flocs in the solution. The electrodes were soaked in 0.4 M of HCl (hydrochloric acid) for 10 min and then rinsed with deionized or distilled water to remove any organic proteins from the surface of the electrodes. The procedure started with an electrocoagulation cell cleaned with distilled water and dried using a dryer. The experiments were carried out in batches. In each experiment, a 500 ml leachate sample was filled into the electrochemical cell with the Al electrodes dipped into the sample at room temperature. The electrodes (anode and cathode) were clamped at the electrode stand. The circuit was completed by connecting wires to the electrodes (anode and cathode) and the DC power supply.

#### **Analysis**

The removal efficiency of COD and turbidity was determined according to the following formulas:

$$COD (\%) = \frac{CODo - CODt}{CODo} \times 100$$
 (5)

where  $COD_0$  and CODt are the chemical oxygen demand (COD) at time = 0 (initial) and at t (reaction time, t), respectively.

Turbidity (%) = 
$$\frac{\text{Co-Ct}}{\text{Co}} \times 100$$
 (6)

where  $C_0$  and  $C_t$  are turbidity registered (in NTU) at time t=0 (initial) and at t (reaction time), respectively.

#### Full factorial design of experiments

The three independent factors used in the full factorial design were the voltage, operation time, and electrode size. In contrast, the responses used were the removal

percentage of COD and turbidity to achieve the optimum conditions in the experimental design method approach. The input factor variables with their range and levels are shown in Table 2. In this work, 16 experiments were run wholly, including the combination of all levels of other factors, and performed randomly to reduce experimental errors. As the output of factorial screening tests, the critical interactions between all variables were given. The model's validity is verified by analyzing values in the analysis of variance (ANOVA) table. The interactive statistical data analysis tool software in the analysis design was used to construct the model for factorial screening design.

Table 2. Factors and levels used in this experimental design

Parameter	Low Level (-)	High Level (+)
Operation Time (min)	10	30
Voltage (v)	10	30
Size of electrode (m <sup>2</sup> )	10	30

#### **Results and Discussion**

#### The effect of the voltages

The initial concentration is one of the remarkable factors in the electrocoagulation process. The influence of this factor on the COD and turbidity removal efficiency is depicted in Figures 1(a) and 1(b). As demonstrated in both figures, the COD and turbidity removal efficiency increased by increasing the voltages for the electrocoagulation process from 5V to 30V. However, more voltage increments caused a descending trend in the removal efficiency. The descending trend can be attributed to the fact that there is a threshold limit for the elimination. The decaying of COD and turbidity removal efficiencies due to the increase in electrical power reduced the lifespan of the electrodes.

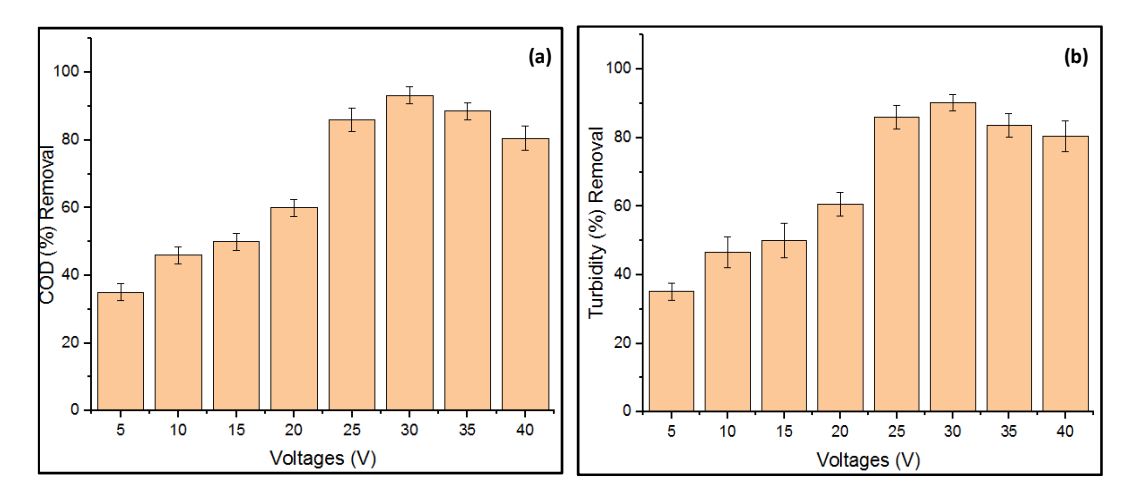


Figure 1. Removal percentages for (a) COD and (b) turbidity removal after 30 min of the mode of operation at different voltages

#### The effect of the operation time

Figure 2(a) and Figure 2(b) depict the effect of operating time on COD and turbidity removal efficiency. By changing the operating time from 5 min to 30 min, the removal percentages of COD and turbidity increased in the same trend of increment. In this process, EC involved two stages: destabilization and aggregation. The first stage is usually short, whereas the second stage is relatively long. Metal ions, as destabilization agents,

are produced at the anode through electrochemical reactions. For 30 min, they indicated an increase in electrolysis duration and increased destabilization of colloidal particles. Both graphs demonstrated that the maximum efficiency of the EC process is obtained at a treatment time of 30 min, and a further increase in treatment time to 40 min did not result in any significant improvement in the removal efficiency of the studied parameters.

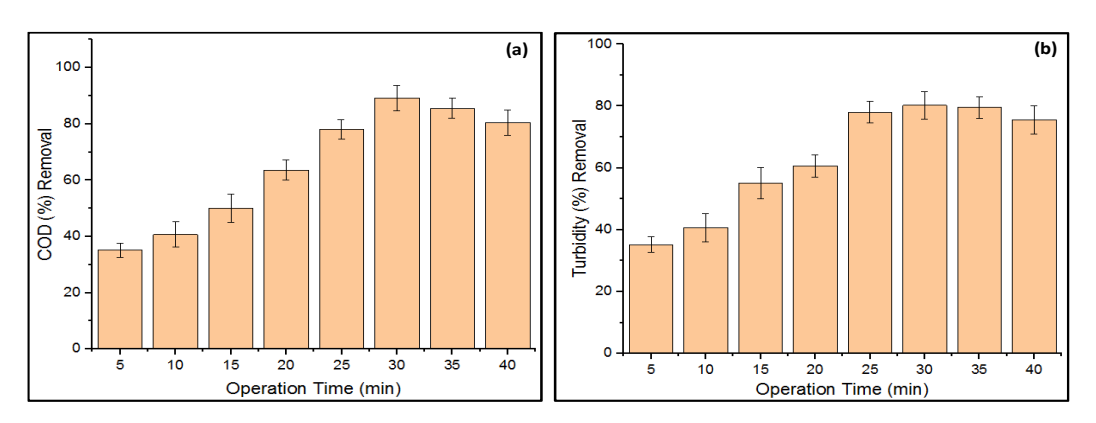


Figure 2. Removal percentages for (a) COD and (b) turbidity removal for 30 voltages for different operation time

#### The effect of the size of electrodes

Figures 3(a) and 3(b) shows that larger electrodes contribute to high COD and turbidity removal efficiencies. A larger surface area electrode has more area for this oxidation process. However, larger electrodes will incur higher costs and worsen portability.

This study aims to preliminarily ascertain the effect of the electrode size on COD and turbidity removal and provide optimal electrode size for electrocoagulation

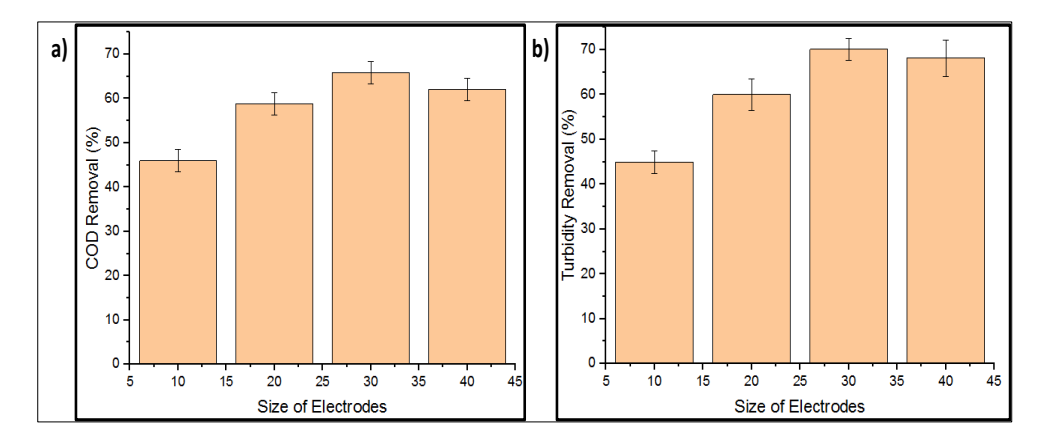


Figure 3. Removal percentages for (a) COD and (b) turbidity removal at the different sizes of electrodes for 30 min operation time and 40 volt

#### Statistical validity of the model

A matrix of full-factorial design from the two levels (24) is shown in Table 3. Each combination is experimentally carried out in a randomized sequence to meet the

statistical requirement for independence of observations. As a result, two responses are examined in the leachate treatment: the COD and turbidity removal.

Table 3. The 3-factor full factorial design matrix and the response function

Exp	<b>Factors</b>			Removal Efficiencies		
EAP _	<b>Operation Time</b>	Voltage	Electrode Size	COD (mg/l)	Turbidity (NTU)	
1	10	30	10	96	100	
2	10	10	10	200	209	
3	10	30	10	98	97	
4	30	30	30	65	60	
5	30	10	30	92	95	
6	30	10	30	97	100	
7	10	10	30	140	141	
8	30	10	10	156	151	
9	10	30	30	49	51	
10	30	10	10	150	152	
11	10	30	30	87	90	
12	10	10	10	170	190	
13	30	30	10	56	60	
14	30	30	10	40	42	
15	30	30	30	70	75	
16	10	10	30	138	140	

# Analysis of variance (ANOVA) Effect of variables on COD removal

The ANOVA for the correlative model development step is presented in Table 4 to describe the removal efficiency of COD as a function of the studied variables. It demonstrated that all the above factors are significant, and the (B) voltage is a highly remarkable variable. The ANOVA shows that the p-value for the model is less than 0.0001, and an F value of 27.22 is obtained for the model, demonstrating the significance of the developed correlation. Besides the main factors A, B, and C, which refer to the operation time, voltage, and electrode size, the model also suggested the interactions of AB, AC, BC, and ABC. Those interactions in the model are less than 0.05, except for the interactions of AB and AC. Nevertheless, these higher values of AB and AC did not affect the total p-value of the model.

Furthermore, the ANOVA table displays supplementary pieces of beneficial information. For instance, the quantity "R-squared" is defined as [15];

$$R^2 = \frac{\text{model sum of squares}}{\text{total sum of squares}}$$
 (7)

The coefficient of determination (R<sup>2</sup>), which shows proportional variation in the response explained by the independent variables in the linear regression model, is 0.9597, which means that the model could describe 95.97% of the variations in the response. The adjusted coefficient of determination (R<sup>2</sup>adj) is 0.9244. The value of R<sup>2</sup>, which is close to 1, revealed a significant linear relationship between the factors and response. There is a slight difference between R<sup>2</sup> and R<sup>2</sup>adj values, which shows that some insignificant conditions (error) are included in the model. The final empirical models in terms of actual parameters are determined as follow

$$COD = +106.50 - 15.75 *A - 36.38 *B - 14.25 *C + 3.38 *AB + 4.50 *AC + 11.88 *BC + 7.62 *ABC$$
(8)

Source	Sum of Squares	df	Mean Square	F-Value	P-Value	
Model	32081	7	4583	27.21901	< 0.0001	significant
A-Operation time	3969	1	3969	23.57238	0.001	
B-Voltage	21170.25	1	21170.25	125.7327	< 0.0001	
C-Size electrode	3249	1	3249	19.29621	0.002	
AB	182.25	1	182.25	1.082405	0.3286	
AC	324	1	324	1.924276	0.203	
BC	2256.25	1	2256.25	13.40015	0.0064	
ABC	930.25	1	930.25	5.52487	0.0466	
Pure Error	1347	8	168.375			
Cor Total	33428	15				
		Mod	del Summary			
S	R-sq		R-sq(Adj)		R-sq(Pre)	
12.98	95.97%		92.44%		83.88%	

Table 4. ANOVA test for the removal of COD

Figure 4 depicts the half-normal plot and Pareto chart, which shows that the primary factors and interaction factors might positively or negatively affect electrocoagulation process COD and turbidity removal efficiencies. A half-normal plot (Figure 4a) shows that the non-significant ones fell along with a straight line

normal distribution and centered near 0. Meanwhile, the essential factors contributed to COD removal efficiencies away from the straight line. Therefore, in order of significance, B (voltage), A (operation time), and C (size of the electrode) have the effects of the most critical factors in COD removal efficiency. Other

significant factors included interaction between (BC) voltage and size of electrodes and (ABC) interaction between three factors, which are operation time, voltage, and size of electrodes (ABC). Factors with the tallest bars significantly affected the process in the Pareto chart. As depicted in Figure 4b, the Pareto chart had two lines: Bonferroni (3.584) and t value limit lines (2.306).

The factors with t values above the Bonferroni line are essential. Also, the factors with t values between the Bonferroni and t value lines are significant. However, those with t values below the t value-line are not remarkable.

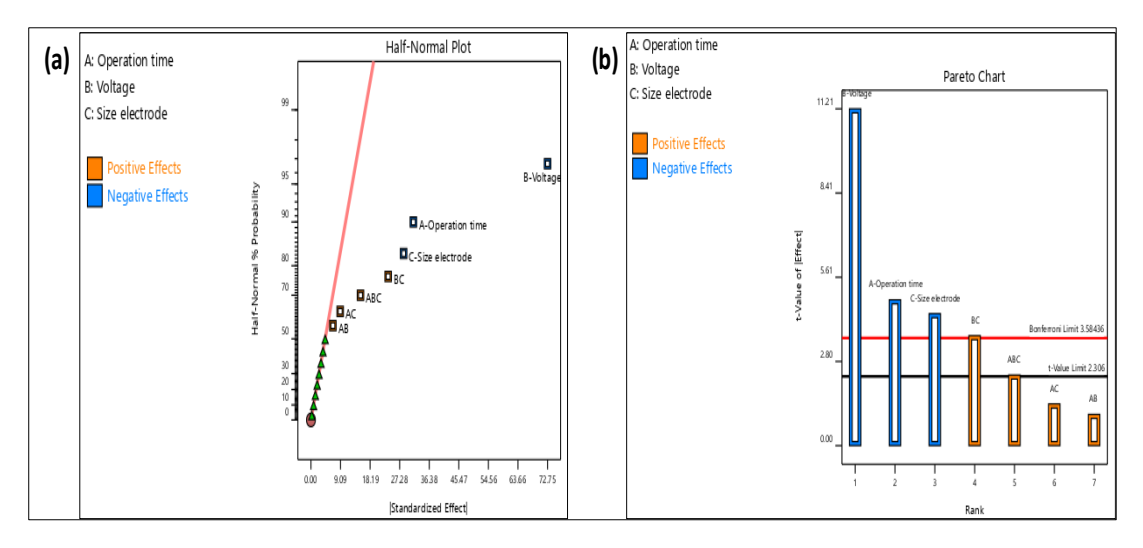


Figure 4. (a) Half-normal probability plot of the effects for the removal of COD and (b) standardized Pareto chart for COD

#### Effect of variables on turbidity removal

Table 5 shows the ANOVA test for the removal of turbidity. The models or variables with a p-value < 0.05 are considered significant with a 95% confidence level. Therefore, the result of ANOVA in Table 4 showed that all variables A, B, and C and the interactions of AB, AC, and BC are significant model terms in terms of turbidity, except for the ABC interaction. The model obtained a p-value of 0.0001, implying that the model is significant. The ANOVA result shows that the coefficient of

determination, R<sup>2</sup>, for the model was 0.9908, which means that the quality of the model is 99.08%. The adjusted R<sup>2</sup> for the model is 0.9522, which shows a good agreement between the results predicted by the regression design and experimental data. A reasonable agreement between the adjusted R<sup>2</sup> and predicted R<sup>2</sup> indicated an adequate model, as shown in Table 5. The final empirical models in terms of actual parameters are determined as follows.

Turbidity = 
$$+109.56 - 17.69 *A - 37.69 *B - 15.56 *C + 5.06 *AB + 6.19 *AC + 12.69 *BC + 4.94 *ABC$$
 (9)

Source	Sum of Squares	df	Mean Square	F-Value	<i>P</i> -Value		
Model	35594.44	7	5084.92	32.98	< 0.0001	significant	
A-Operation time	5005.56	1	5005.56	32.46	0.0005		
B-Voltage	22725.56	1	22725.56	147.39	< 0.0001		
C-Size electrode	3875.06	1	3875.06	25.13	0.0010		
AB	410.06	1	410.06	2.66	0.1416		
AC	612.56	1	612.56	3.97	0.0814		
BC	2575.56	1	2575.56	16.70	0.0035		
ABC	390.06	1	390.06	2.53	0.1504		
Pure Error	1233.50	8	154.19				
Cor Total	36827.94	15					
Model Summary							
S	R-sq		R-sq(Adj)		R-sq(Pre)		
12.42	96.65%		93.72%		86.60%		

Table 5. ANOVA test for the removal of turbidity

The factorial design plot, including the half-normal plot and Pareto chart of effects, are shown in Figure 5. The half-normal probability plot of the effects in Figure 5a shows the absolute values of the estimated effects from the largest effect to the smallest effect. From this analysis, it could be observed that the largest effect on turbidity removal efficiencies that is well displaced in the plot was the AB interaction (operation time and voltage), followed by B (voltage), AC interaction (operation time and size of electrode), BC interaction (voltage and size of electrode), A (operation time) and (C) size of the electrode. The sequence of the significant main effects with respect to decreasing influence on turbidity removal is found to be AB > B > AC > BC > A

> C > ABC. The half-normal plot of the effects indicated that the single factor has a negative effect. By increasing the level, there is a significant reduction in turbidity in landfill leachates - another quick way to screen the significant factors is by analyzing the Pareto chart of the estimated effects. The Pareto chart is generated and tabulated, as shown in Figure 5b, to validate the results obtained from the half-normal probability plot of effects in Figure 5a. Pareto chart analyses revealed that all factors and interaction factors are statistically significant, and none of them was below the limit of Benferroni (3.46).

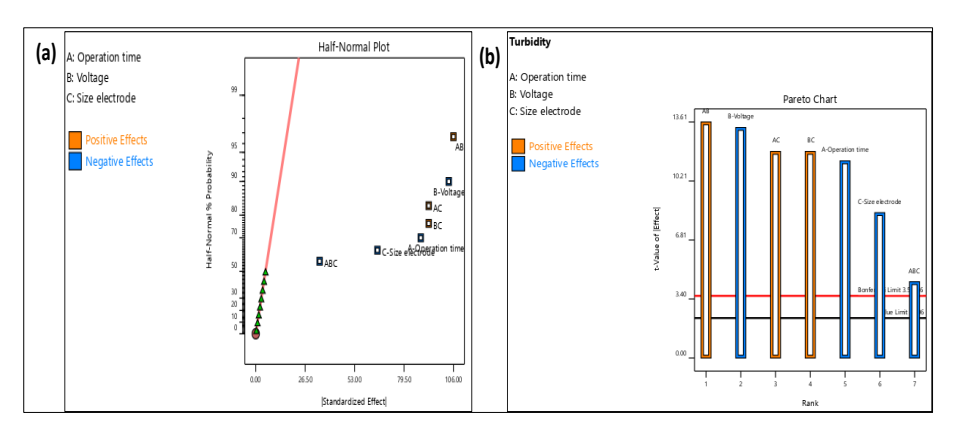


Figure 5. (a) Half-normal probability plot of the effects for the removal of turbidity and (b) standardized Pareto chart for turbidity

#### Model validation and multiple response optimization

An additional experiment is performed for each set of experiments to validate the models further. Optimized conditions and corresponding maximum COD removal are depicted using the ramp graph shown in Figure 6. Under the optimum conditions, three replicate experiments are conducted. The conditions with predicted and measured results are listed in Table 6. The table shows that the three responses are close to those estimated using factorial design. The model's validity is confirmed as the variation coefficients were around 5% for COD and turbidity removals. This method provided savings in terms of the time and size of electrodes.

Electrolysis time also significantly affects the efficiency of electrochemical coagulation methods in removing pollutants. It determines how much coagulant is produced and how much the cycle costs [16]. Increasing electrolysis time up to the optimum level increases pollutant removal efficiency but does not increase it beyond the optimum level. The fact is that the formation of coagulants at constant current voltage increases with an increase in electrolysis time, resulting in increased efficiency for removal [17]. The voltage applied to the electrodes is one of the most critical parameters that affect the efficiency and economy of electrocoagulation cycle [18]. Figure 7 shows a sample leachate landfill before and after electrocoagulation process. A clear solution is obtained after using the electrocoagulation process by using parameters in this experime

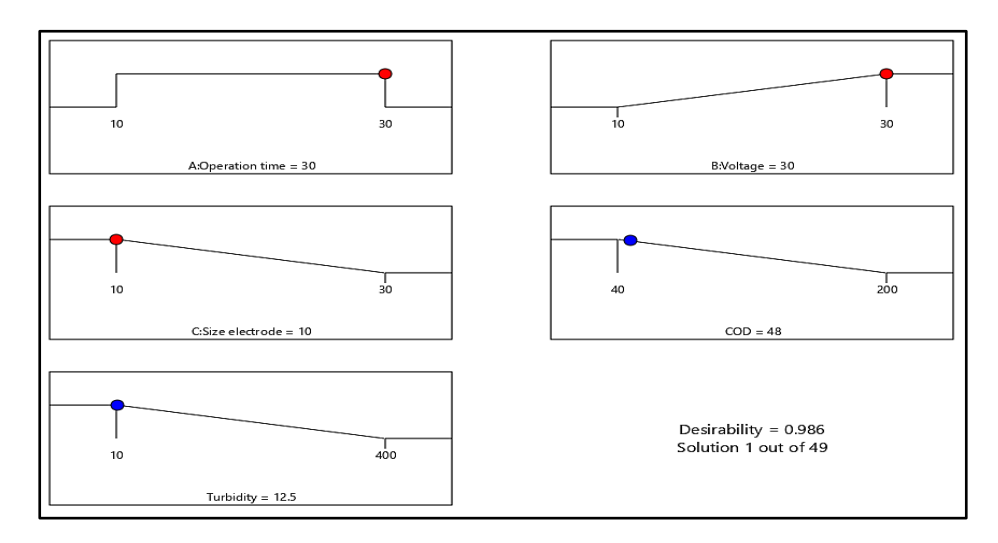


Figure 6. Suggestion value for optimization model

Table 6. Validation of the model

		Factors		<b>A</b>		
Removal Efficiencies	Operation Time (min)	Voltage (V)	Electrode Size (m²)	Predicted	Average Experimental Results	
COD (mg/l)	30	30	10	48.00	45.72	
Turbidity (NTU)	30	30	10	12.5	11.87	

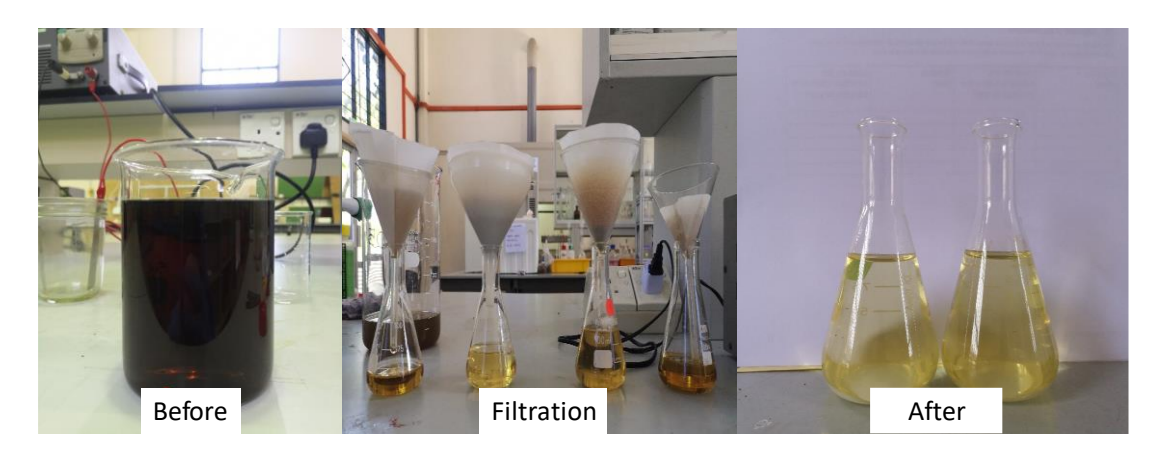


Figure 7. Sample leachate landfill before and after electrocoagulation

#### Conclusion

In this study, the FFD design of the experiment was used to observe the impact of voltage, operation time, and size of electrodes for the removal of COD and turbidity from landfill leachates by the electrocoagulation process. The screening experiment for the EC process was obtained by running 16 combinations of experiments provided by FFD design in the design of experiment software. The optimum condition was achieved by keeping the goal of operating time maximum, voltage maximum, size of electrode minimum, COD, and turbidity pollutant removal efficiencies in the "maximized" condition. The statistical analysis showed that the relevant p-value of each model was less than 0.001 (p-value < 0.001), indicating the corresponding significance of the model for all responses. The predicted values of COD and turbidity were 48 mg/l and 12.5 NTU, respectively. The maximum COD and turbidity removal experimental values were 45.72 mg/l and 11.87 NTU, respectively, at 30V, 30 min, and 10 cm electrode sizes. Therefore, this indicated that the electrocoagulation process gave good response for the treatment of leachate samples and agreed with the predicted values with less than 5% deviation.

#### Acknowledgments

The authors gratefully acknowledge the financial support for this work by Universiti Kebangsaan Malaysia under Grant GUP-2021-075.

#### References

- Adhikari, B., Dahal, K. R. and Nath Khanal, S. (2014). A review of factors affecting the composition of municipal solid waste landfill leachate. *International Journal of Engineering* Science and Innovative Technology, 3(5): 273-281.
- 2. Hoai, S. T., Nguyen Lan, H., Thi Viet, N. T., Nguyen Hoang, G. and Kawamoto, K. (2021). Characterizing seasonal variation in landfill leachate using leachate pollution index (LPI) at nam son solid waste landfill in Hanoi, Vietnam. *Environments*, 8(3): 17.
- 3. Zailani, L. M. and Zin, N. S. M. (2018). Application of electrocoagulation in various wastewater and leachate treatment-A review. In *IOP Conference Series: Earth and Environmental Science*, 140(1): 012052.
- Makde, K. N. and Hedaoo, M. N. (2018). Application of electrocoagulation in wastewater treatment: A general review. *International Research Journal of Engineering and Technology*, 5(12): 1567-1572.
- 5. Musa, M. A. and Idrus, S. (2021). Physical and biological treatment technologies of slaughterhouse wastewater: A review. *Sustainability*, 13(9): 4656.
- Castillo-Suárez, L. A., Bruno-Severo, F., Lugo-Lugo, V., Esparza-Soto, M., Martínez-Miranda, V. and Linares-Hernández, I. (2018). Peroxicoagulation and solar peroxicoagulation for landfill leachate treatment using a Cu–Fe system. Water, Air, & Soil Pollution, 229(12): 1-17.

# Norilhamiah et al: CHEMICAL OXYGEN DEMAND AND TURBIDITY REMOVAL OF LANDFILL LEACHATE USING ELECTROCOAGULATION TECHNIQUE WITH AI ELECTRODE

- Jang, Y., Hou, C. H., Park, S., Kwon, K. and Chung, E. (2021). Direct electrochemical lithium recovery from acidic lithium-ion battery leachate using intercalation electrodes. *Resources, Conservation* and Recycling, 175: 105837.
- 8. Gatsios, E., Hahladakis, J. N. and Gidarakos, E. (2015). Optimization of electrocoagulation (EC) process for the purification of a real industrial wastewater from toxic metals. *Journal of Environmental Management*, 154: 117-127.
- Pirsaheb, M., Mohamadisorkali, H., Hossaini, H., Hossini, H. and Makhdoumi, P. (2020). The hybrid system successfully to consisting of activated sludge and biofilter process from hospital wastewater: Ecotoxicological study. Journal of Environmental Management, 276: 111098.
- Chairunnisak, A., Arifin, B., Sofyan, H. and Lubis, M. R. (2018, March). Comparative study on the removal of COD from POME by electrocoagulation and electro-Fenton methods: Process optimization. *In IOP Conference Series: Materials Science and Engineering*, 334(1): 012026.
- 11. Amarine, M., Lekhlif, B., Sinan, M., El Rharras, A. and Echaabi, J. (2020). Treatment of nitrate-rich groundwater using electrocoagulation with aluminum anodes. *Groundwater for Sustainable Development*, 11: 100371.
- Bajpai, M., Singh Katoch, S. and Singh, M. (2020).
   Optimization and economical study of electrocoagulation unit using CCD to treat real graywater and its reuse potential. *Environmental Science and Pollution Research*, 27(33): 42040-42050.
- 13. Naje, A. S. and Abbas, S. A. (2013). Electrocoagulation technology in wastewater

- treatment: a review of methods and applications. *Civil and Environmental Research*, 3(11): 29-42.
- 14. Rusdianasari, R., Taqwa, A., Jaksen, J. and Syakdani, A. (2017). Treatment of landfill leachate by electrocoagulation using aluminum electrodes. *In MATEC Web of Conferences*, 101: 02010.
- Shadmehr, J., Mirsoleimani-azizi, S. M., Zeinali, S. and Setoodeh, P. (2019). Electrocoagulation process for propiconazole elimination from wastewater: experimental design for correlative modeling and optimization. *International Journal of Environmental Science and Technology*, 16(10): 5409-5420.
- 16. Akhter, F., Soomro, S. A., Siddique, M. and Ahmed, M. (2021). Pollutant Removal efficiency of electrocoagulation method from industrial wastewater: Comparison with other treatment methods and key operational parameters—a comparative study review. Water, Air, & Soil Pollution, 232(3): 1-13.
- Mallesh, B. (2018). A review of electrocoagulation process for wastewater treatment. *International Journal Chemical Technology Research*, 11: 289-320.
- 18. Graça, N. S., Ribeiro, A. M. and Rodrigues, A. E. (2019). Removal of fluoride from water by a continuous electrocoagulation process. *Industrial & Engineering Chemistry Research*, 58(13): 5314-5321.

# Malaysian Journal of Analytical Sciences (MJAS)



Published by Malaysian Analytical Sciences Society

## ENHANCING THE OXYGEN REDUCTION REACTION OF LOW-PLATINUM AND NON-PLATINUM CATALYSTS FOR FUEL CELL APPLICATIONS

(Peningkatan Tindak Balas Penurunan Oksigen Mangkin Platinum Bermuatan Rendah dan Bebas Platinum Untuk Aplikasi Sel Bahan Api)

Kazi Rumanna Rahman<sup>1</sup>, Kuan Ying Kok<sup>2</sup>, Nor Azillah Fatimah Othman<sup>3</sup>, Wai Yin Wong<sup>1</sup>, Kean Long Lim<sup>1\*</sup>

<sup>1</sup>Fuel Cell Institute,
Universiti Kebangsaan Malaysia, 43600 UKM Bangi, Selangor, Malaysia

<sup>2</sup> Industrial Technology Division

<sup>3</sup>Radiation Processing Technology Division

Malaysia Nuclear Agency, 43000, Kajang, Selangor, Malaysia

\*Corresponding author email: kllim@ukm.edu.my

Received: 13 December 2021; Accepted: 6 March 2022; Published: 27 June 2022

#### **Abstract**

Nowadays, research efforts are focused on developing low-Pt and non-Pt catalysts for ORR. The addition of Pt-group metal (PGM) in pure Pt to form Pt-PGM catalysts exhibits better ORR performance than pure PGM catalysts and Pt/C. More than 20 wt.% of Pt loading is required in Pt-PGM alloys for improving catalytic activity. Studies have also shown that the addition of transition metal (TM), which has a smaller atomic size, into PGM reduced the bond distance between two metallic atoms and geometric parameters, thus remarkably improving the catalytic stability and ORR activity. However, TM based catalysts should be supported on nitrogendoped carbon with high surface area to attain high ORR activity. A large surface area and high electronic conductivity of carbon support also facilitate the ORR activity. Performances of alloy catalysts are directly related to their synthesis temperature and structural properties. Designing the core-shell combinations and controlling the shell thickness is one of the structural strategies in enhancing mass activity and durability. Lately, irradiation techniques are used to modify the physicochemical properties. Nevertheless, TM-based catalysts are usually stable in alkaline solutions but not in acidic solutions. This review focuses on the strategies to develop cost-effective catalysts from low-platinum and non-platinum catalysts with enhanced ORR activity.

Keywords: oxygen reduction reaction, platinum group metal alloys, transition metal catalysts, synthesis techniques

#### Abstrak

Pada masa kini, usaha penyelidikan tertumpu kepada pembangunan mangkin platinum (Pt) bermuatan rendah dan bebas platinum untuk tindak balas penurunan oksigen (ORR). Penambahan logam kumpulan Pt (PGM) dalam Pt tulen untuk membentuk Pt-PGM menunjukkan prestasi ORR yang lebih baik daripada prestasi mangkin PGM tulen dan Pt/C. Sebanyak lebih daripada 20 wt.% muatan Pt adalah diperlukan dalam aloi Pt-PGM untuk meningkatkan aktiviti pemangkinan. Kajian telah menunjukkan penambahan logam peralihan (TM) yang mempunyai saiz atom yang lebih kecil ke dalam PGM mengurangkan jarak antara dua atom logam dan parameter geometri sekali gus meningkatkan kestabilan pemangkinan dan aktiviti ORR. Namun demikian,

mangkin berasakan TM perlu disokong dengan karbon terdop nitrogen yang berpermukaan yang luas untuk mencapai aktiviti ORR yang tinggi. Penyokong karbon yang berpemukaan luas dan mempunyai kekonduksian elektronik yang tinggi juga memudahkan aktiviti ORR. Prestasi mangkin aloi adalah berkait langsung dengan suhu sintensi dan sifat strukturnya. Mereka bentuk gabungan teras-cangkerang dan mengawal ketebalan cangkerang adalah salah satu strategik penstrukturan dalam meningkatkan aktiviti jisim dan ketahanan. Akhir-akhir ini, teknik-teknik penyinaran digunakan ubah mengubahsuai sifat fizikokimia. Namun demikian, mangkin berasaskan TM biasanya stabil dalam larutan alkali tetapi tidak dalam larutan asid. Ulasan ini berfokus pada strategik untuk membangunkan magkin berkos efektif daripada mangkin Pt bermuatan rendah dan bebas platinum dengan aktitiviti ORR yang dipertingkatkan.

Kata kunci: tindak balas penurunan oksigen, logam aloi kumpulan platinum, mangkin logam peralihan, kaedah sintesis

#### Introduction

A fuel cell is an energy conversion device that converts chemical energy into electric energy through an oxidation reaction at the anode and a reduction reaction at the cathode. The cathode reaction, known as oxygen reduction reaction (ORR), is a fundamental reaction to various disciplines, such as energy conversion, material dissolution, or biology. The performance of fuel cells depends on the rate of ORR [1, 2]. Difficulties in O<sub>2</sub> adsorption, O-O bond cleavage and oxide removal are the main reasons for the sluggish reaction kinetics of ORR [3]. The state-of-the-art Pt/C (platinum/carbon black) catalyst and Pt-based alloy catalysts are used for the cathode reaction in aqueous electrolytes, and these catalysts are considered the best for ORR. All Pt or Ptbased catalysts still suffer from CO and S poisoning on Pt, loss of active surface area, corrosion of carbon support, low durability and limited supply, high cost, and use of a high amount of Pt [4-6]. So, non-Pt based catalysts with improved catalytic activity are required to overcome these limitations of Pt [7]. The main characteristic of an effective fuel cell catalyst is its capability to facilitate the rate of ORR [8]. Transition metal (TM) alloys, chalcogenides, carbides, nitrides, and metal-N4 macrocyclic compounds instead of Pt/C and PGM catalysts, are potential electrocatalysts for ORR [9]. Composition, particle size, crystallographic orientation, etc contribute to the enhancement in catalytic activity and d-band vacancy is considered as an important factor for enhancing catalytic behavior towards ORR. For developing a cost effective catalyst with improving ORR activity, the current research follows four different trends: 1) to reduce the wt% of Pt in alloy catalysts, 2) to develop the PGM free catalyst named M-N-C, where M for transition metal, nitrogen,

and carbon, 3) to utilize the carbon with large surface area as catalyst support and 4) synthesis technique for designing cost-effective ORR cathode catalysts[10–13]. In the following section, we describe the general mechanism of ORR cathode in acidic and alkaline solutions, which gives a clear idea of the reaction paths.

#### General mechanism of ORR cathode

In general, anode and cathode reactions occur on a metal surface. The reaction that occurs at the cathode site is known as the ORR reaction. Usually, the ORR reaction is the limiting reaction step of the overall reaction because of its sluggish kinetic, hence it is essential to understand the ORR mechanisms to design an effective catalyst.

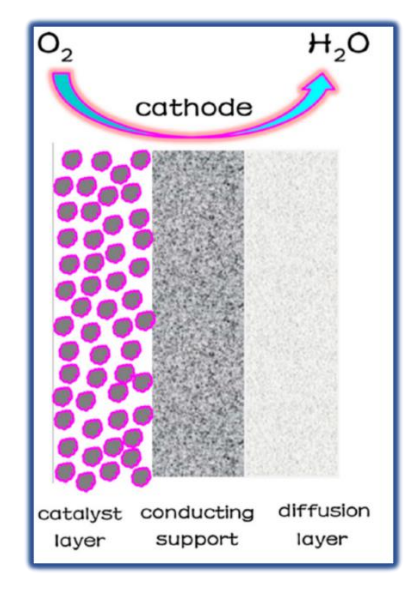


Figure 1. The structure of PEMFC cathode with catalyst layer [14]

The ORR mechanism involves a direct four-electron (4e-) or a series of two-electron (2e-) pathways. A one-step 4e- transfer mechanism is more efficient than a 2e-transfer mechanism. Thus, catalysts that facilitate the 4e- pathway reaction are more favorable. In the 4e-transfer pathway, O<sub>2</sub> is converted into either H<sub>2</sub>O (acidic medium) or OH<sup>-</sup> (alkaline medium) on a single catalytic site. This process depends completely on the electrolytes [14–17].

In an acidic electrolyte, the 4e<sup>-</sup> transfer pathway can be written as in Eq. (1):

$$O_2(g) + 4H^+(aq) + 4e^- \rightarrow 2H_2O(1)$$
 (1)

and 2e<sup>-</sup> transfer pathway can be expressed as Eqs. (2, 3, and 4):

$$O_2(g) + 2H^+(aq) + 2e^- \rightarrow H_2O_2(1)$$
 (2)

 $H_2O_2$  is produced in the intermediate step of the Eq.(2) pathway.  $H_2O_2$  is finally reduced to water:

$$H_2O_2(aq) + 2H^+(aq) + 2e^- \rightarrow 2H_2O(1)$$
 (3)

or is decomposed as follows:

$$H_2O_2(aq) + 2H(aq) + 2e^- \rightarrow 2H_2O(l) + O_2(g)$$
 (4)

On the other hand, O<sub>2</sub> is converted into OH<sup>-</sup> by 4e<sup>-</sup> pathway, which is written as Eq. (5), and forms HO<sub>2</sub><sup>-</sup> via 2e<sup>-</sup> pathway in an alkaline medium,

$$O_2(g) + 2H_2O(aq) + 4e^- \rightarrow 4OH^-(1)$$
 (5)

Eqs. (6,7 and 8) express the step of the 2e<sup>-</sup> transfer pathway alkaline solutions.

$$O_2(g) + H_2O(aq) + 2e^- \rightarrow HO_2^-(l) + HO^-$$
 (6)

Peroxide is also unstable

$$HO_2^-(aq) + H_2O(1) + 2e^- \rightarrow 3OH^-(aq)$$
 (7)

and decomposes into the following:

$$2HO_2^-(aq) \to 2HO^-(aq) + O_2(g)$$
 (8)

#### Pt-group alloy catalysts

Pt is the best monometallic catalyst for ORR in acidic and alkaline solutions. The fuel cell stack needs almost 80%–90% Pt, which increases the cost of the entire stack. Moreover, Pt has some drawbacks, such as CO poisoning, short life span, low durability, etc. So, the current research trend emphasizes reducing Pt use and

the development of bimetallic and trimetallic alloy catalysts to overcome the stumbling block of Pt [18-20]. Some researchers used several noble metals like Pd, Ir, Rh, Ag, and Ru as cathode catalysts. All single noble metal catalysts followed the 4e- pathway but exhibited lower catalytic activity than Pt. Improvement of catalytic activity depends on the optimization of particle size and shape, surface structure, support metal, and synthesis process [21]. It also revealed that combinations of two Pt-group metals can tune the ability of oxygen adsorption due to constructing a hetero-metalmetal bond by altering the electronic configurations. Coupled metals also generate a new active site. The mutual effect of changing electronic and geometric structure encourages a 4e<sup>-</sup> reaction pathway towards ORR [17]. The d band vacancies which consider as important parameters increase due to the existence of Pt atom, d band vacancies boosted  $2\pi$  electron donation from O<sub>2</sub> to the catalyst surface. Finally, O<sub>2</sub> reacted with donated electrons and protons to yield desirable H<sub>2</sub>O molecules [22].

Due to the similar crystal structure of Pt, palladiumbased catalysts have stimulated extensive concern among researchers [23]. Zhou et al. reported that Pt-Pd/C exhibited higher durability than commercial Pt/C as a cathode catalyst. They also concluded that particle size and electrochemical surface area (ECSA) loss are associated with durability, and larger particles are more stable in alkaline solution [24]. Wang et al. established the relationship between weight ratio and particle size. They reported that ORR activity was controlled by the size of Pt nanoparticles, and 30% of Pt-Pd/C exhibited remarkable performances, whereas the weight ratio of Pt: Pd was 1:1. The mass activity (MA) and the ECSA value of this Pt-Pd/C catalyst (MA= 0.488 mA μg<sup>-1</sup> and ECSA=107.7 m<sup>2</sup> g<sup>-1</sup>) are four times and 1.69 times higher than those of commercial 10% Pt/C (MA=0.123 mA μg<sup>-1</sup> and ECSA=63.6 m<sup>2</sup> g<sup>-1</sup>) in acidic solution[25, 26]. The ratio of Pt-Pd has a great impact on surface morphology and catalytic activity. In the presence of Pd, Pt-Pd/C exhibits larger ECSA, higher mass activity, and larger particle size.

The impact of Pt-Pd/C with different atomic ratios on the particle size, mass activity (MA), and ECSA values are depicted in Figure 2. From the graph, it is clear that smaller particle size is expected for better ORR activities. A relationship is observed between ECSA and the particle size and ratio. Particle size shows an increasing trend with an increasing Pt: Pd in compositions, and ECSA shows a decreasing trend with the increasing Pt: Pd. A higher amount of Pd, i.e. above 1:2 (Pt: Pd), causes a lower dispersion rate, which is the

key reason for the decrease in catalytic activity and mass activity [27]. Pd increases overall ORR performance, especially stability in both acidic and alkaline-aqueous electrolytes. A low particle dispersion rate still occurs if the ratio of Pt: Pd is more significant than 1:2. So, it is a major question of which ratio will be taken into consideration.

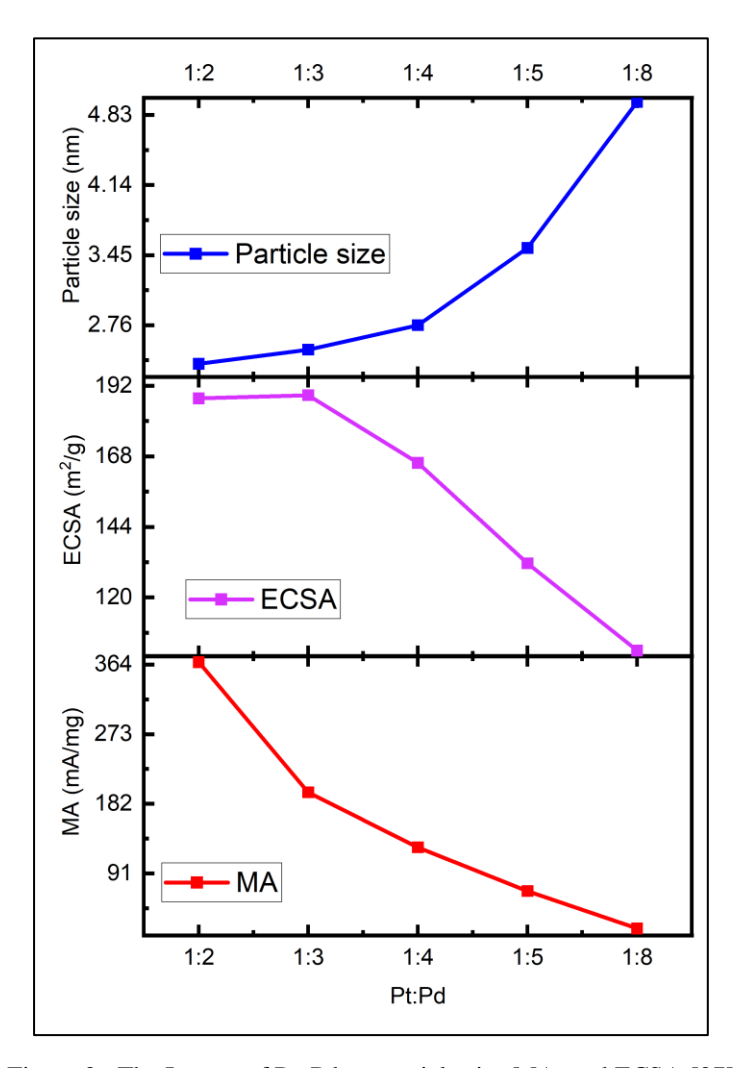


Figure 2. The Impact of Pt: Pd on particle size MA, and ECSA [27]

Ru is another alternative metal for reducing the use of Pt and improving catalytic activity. Small particles show better CO tolerance than large particles for Pt-Ru alloys. The Pt: Ru ratio of 1:1 exhibits an enhanced ORR activity, and the morphological change induces several

active sites for CO oxidation, but the oxidation state of Ru is gradually decreased by increasing particle size [28]. In both types of electrolytes. Pt-Ru alloy exhibited better mass activity and stability than state of art Pt/C. Ru surface facilitates the break of O-O bond and

supports the proton transport at the same time. As a result, Pt nanoparticles exhibited enhanced ORR catalytic activity [29, 30]. The ECSA, mass activity, and Pt-Ru particle size vary with Pt atom in alloys[31]. According to the literature, the degree of alloying Pt-Ru strongly depends on the nature of the electrolyte. The particle size of the Pt-Ru catalyst decrease with increasing pH of solution[32]. The main drawback of Pt-Ru alloy is that it needs more Pt than Pt-Pd, and as a single metal catalyst, Ru/C exhibits lower catalytic activity compared with Pd/C, Ir/C, and Rh/C in acidic media [33].

In acidic solution, Pt-Pd/C and Pt-Ir/C both catalysts exhibited almost the same ECSA and both catalysts performed better than Pt/C. In terms of stability, Pt-Ir/C was better than Pt-Pd/C and Pt/C. Pt and Ir's nucleation helps to improve the durability and catalytic activity. Crystallite size could be able to tune the performance of Pt-Ir [34, 35]. The mass ratio is the most important factor for the Pt-Ir catalyst. The Pt-Ir/C (16:84) presents a larger ECSA value, which is 28.7 m<sup>2</sup> g<sup>-1</sup>, and its mass activity is 373.3 mA mg<sub>pt</sub>-1, which is greater than Pt/C  $(ECSA=18.3 \text{ m}^2 \text{ g}^{-1} \text{ and } MA=142.9 \text{ mA } mg_{pt}^{-1}).$ However, Pt-Ir/C (4:96) and Pt/C possess the same ECSA value, but Pt-Ir/C (4:96) exhibits lower catalytic activity than Pt/C [36]. Like other Pt group metal alloys, Pt-Ir follows the 4e- pathway and exhibits improved ORR activity. Catalytic performances of this catalyst are strongly influenced by the synthesis technique, treatment temperature, catalyst support, and the presence of Pt [37].

Pt-Rh alloy also exhibits better durability than a single Pt catalyst. Rh itself does not participate in the activity of the catalyst, but the existence of Rh plays a crucial role[38]. Rh covers only 15%–20% of the surface because Pt suppresses it. Both metals possess a similar

crystal structure and similar-sized cells. So, it is difficult to determine the active phase that belongs to Rh. A small amount of Rh is needed to make a Pt-Rh alloy and acts as a bimetallic catalyst[39]. Narayanamoorthy et al[40] reported that supportless Pt-Rh alloy is better than Pt-Rh catalyst with Vulcan carbon (VC) and Pt/C (CB). Supportless Pt-Rh (154.4 m²g⁻¹) possesses a higher ECSA value than Pt-Rh/C (103.5 m²g⁻¹) and is 2.5 times higher than Pt-Rh/VC (61.76 m²g⁻¹). The cluster morphology depends on the availability of Pt surface[40]. Several studies concluded that smaller particle sizes presented larger ECSA, which exhibit higher mass activity and stability. All PGM alloys follow the 4e⁻ pathway and exhibit comparable catalytic activity in both electrolytes.

Making alloys with low-cost materials is a good strategy for reducing Pt use. TMs are the most acceptable metals for changing the electronic configuration in the cluster [41]. The addition of PGM increases the particle size, whereas Ag reduces the particle size due to its small diameter (<5 nm), facilitating ECSA and ORR activity. Many investigations have been performed on Ag to overcome the limitation of Pt/C [42]. The catalytic activity of Pt-Ag/rGO is slightly higher than that of Pt/C in acidic solution with a Pt: Ag ratio of 1:3. This catalyst exhibits a larger ECSA value (67.8 m<sup>2</sup> g<sup>-1</sup>) than Pt/C (39.2 m<sup>2</sup> g<sup>-1</sup>) [43]. Pt-M/C (M=Fe, Co, Ni) presents a larger particle size compared with Pt/C. The particle size of Pt-M/C is calculated to be 2.5 nm to 2.8 nm, whereas that of Pt/C is 2.1 nm when the ratio of Pt: M is 50:50. Pt-Fe/C (100 m<sup>2</sup> g<sup>-1</sup>) exhibits the highest ECSA value among Pt-M/C, which is lower than 50 wt% of Pt/C (119 m<sup>2</sup> g<sup>-1</sup>). All Pt-M/C show improved mass activity compared with Pt/C. The variable electron state of TM atoms induces a strong interaction between TM-O, which encourages the slower loss rate of ECSA than PGM [44, 45].

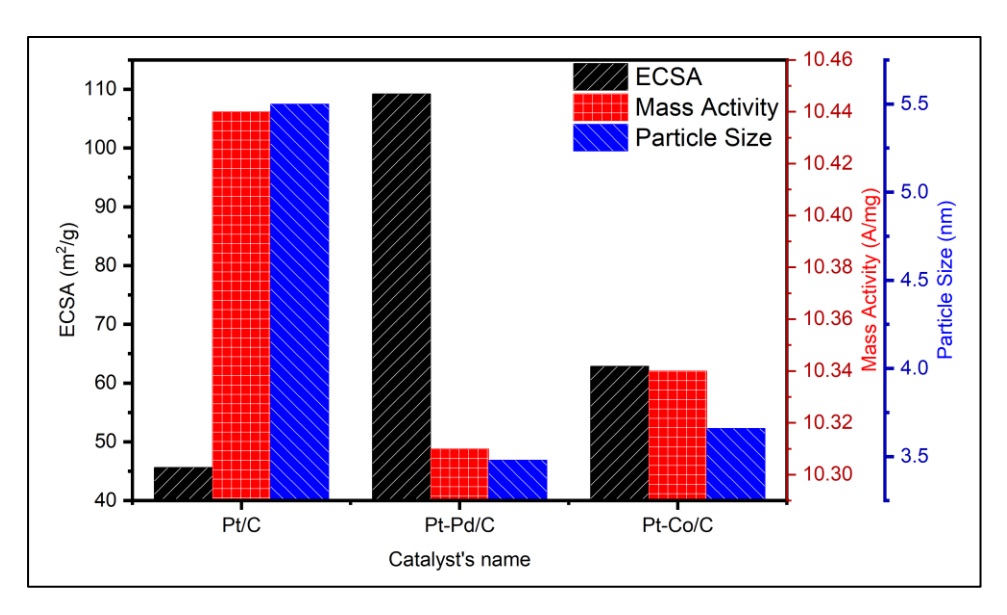


Figure 3. Effect of making alloy with platinum group metal (PGM) and transition metal (TM) [46]

From Figure 3, it has been seen that Pt-Pd/C increases the ECSA and decreases the particle size. On the other hand, Pt-Co/C reduces the ECSA, and particle size was a little larger than Pt-Pd/C. In the case of MA, TM exhibited better performance than PGM. Catalytic activity increased due to lattice compression, resulting from the downward shift of the d-band center of Pt and Pd. ORR activity showed a decreasing trend with an increasing amount of Co. Compare with Pt-Pd/C and Pt/C, Pt-Co/C showed better stability in acidic solution. However, it has been suffering from low stability while using in Toyota Mirai Fuel Cell Vehicles [46-49]. To overcome the stability problem, Pt-Fe/C is a good substitute for Pt/C. Fe can tune the electronic structure of Pt that enhanced the durability of Pt-Fe/C in an acid medium [50, 51]. PGM sites' surface activity has been influenced by the small atomic size of TM and the reduction in the PGM-TM bond, which serves better catalytic activities of PGM-TM alloys. The study revealed that the enhancement of ORR performance depends on the density of PGM [52].

According to literature, the observed improvement in catalytic activity reveals several issues that should be considered in future studies to develop a better catalyst, as follows: (i) increase in the resistance to particle sintering; (ii) surface roughening due to the removal of

some alloying metal that increases the electrochemical surface area; and (iii) preferential crystal orientation [52–55]. High durability and catalyst activity are the keys to solving the current problem of Pt. PGM and PGM-TM alloy catalysts exhibit excellent activity and stability compared with traditional Pt/C catalysts. All types of mixed metal alloys are suitable substitutes for commercial Pt/C in alkaline electrolytes. In acidic electrolytes, these catalysts show poor performances without Pt in their composition. PGM-TM bond helps increase durability and stability, but a large amount of PGM is needed to exhibit better catalytic activity.

#### TM alloy catalysts for ORR

Many experimental studies proved that nitrogen-doped carbon support increases the concentrations of ORR active sites and stability by associating two adjacent carbon crystallites of TM catalyst; the configuration of TM active sites changes completely according to C-N species [56–58]. Here, we discuss some promising TM catalysts that exhibit improved ORR activity in the presence of N.

Fe-N-C has drawn much attention due to its catalytic performances. N coordinated Fe atom has been a highly active center for ORR [59]. Fe-N-C nanoparticles show outstanding stability in both acidic and alkaline

solutions. Only 0.5 wt% of the Fe-contained Fe-N-C catalyst possesses a high surface area (1501 m<sup>2</sup>g<sup>-1</sup>) and exhibits superior durability to Pt/C. Half wave potential

 $(E_{1/2})$  of Fe-N-C and commercial Pt/C is presented in Figure 4.

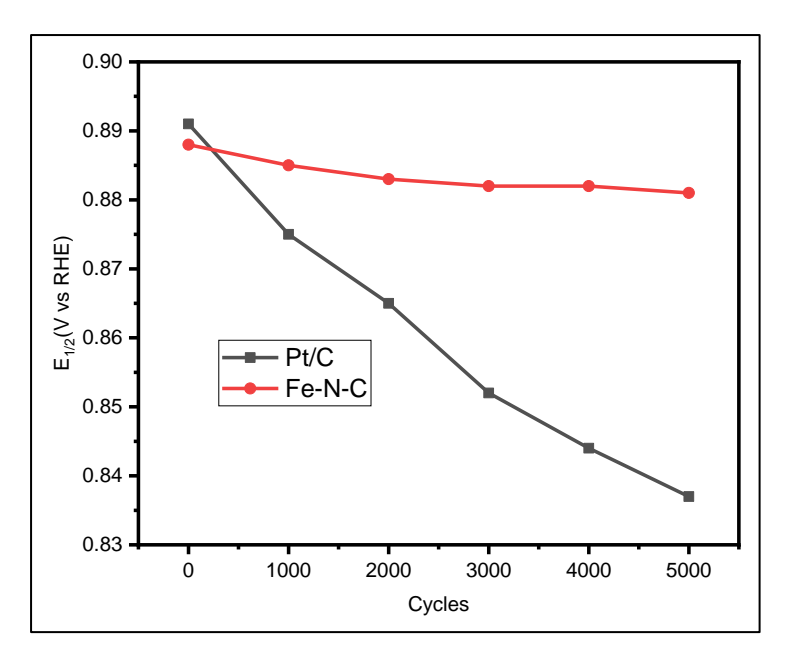


Figure 4. E<sub>1/2</sub> of Fe-N-C and Pt/C at every 1000 cycles in the durability test [60]

From Figure 4, it is clearly observed that after 5000 potential cycles, Fe-N-C remains unchanged whereas Pt/C gradually decreases under the same condition [60, 61]. The formation of Fe-N is powerfully demonstrated by carbon chemistry. Fe-N active sites are also an essential issue for ORR activity. The Fe-N/C/rGO (10% to 20% of Fe) exhibits improved ECSA and ORR activity, which are comparable with those of Pt/C and are higher in comparison with those of Fe-N/C/rGO (5%-10% of Fe), Fe-N/C, and Fe-N/rGO [62, 63]. Fe-N-based catalyst follows the 4e<sup>-</sup> reaction pathway in both types of electrolytes. The weight percentage of Fe plays an important role in the composition. This percentage depends on the presence of inducing elements, such as N, P, and S [64]. The gap between the valence and conduction bands of Fe atom (-0.82 eV) enhances catalytic stability and a small amount of metal doping can increase conductivity, and durability [65]. Jiang et al reported that the binding energy of O<sub>2</sub> that presents in the Fe-N<sub>x</sub> site helps the adsorption of O<sub>2</sub> on Fe-N<sub>x</sub> sites, which promotes ORR activity of Fe-N-C. 20wt% to 35wt% ionomer concentration increases the ionic conductivity of the cathode site. Above 35 wt.% concentration, active sites gradually decrease. However, unsaturated Fe can change the charge density of N-doped carbon support and the central Fe atom in Fe- $N_x$ . Some researchers replaced Fe with Co or Ni [66–68].

Co is the most widely used substitute and partial substitute metal in compositions due to its low price, high durability, and 4e<sup>-</sup> reaction selectivity [69]. The Co-based catalyst exhibited superior stability to that of Fe. Like Fe, the bimetallic atom-doped Co catalyst shows better ORR performance by forming dual sites than a single metal Co catalyst. Double active sites facilitate electron transfer [70]. Partially substituted Co-Te/C (1:1.93) and Co-Se/C (1:1.25) are catalysts that follow the 4e<sup>-</sup> reaction pathway in acidic solution, but the catalytic activity is not comparable with that of Pt/C [71]. Support metal has an impact on Co-based catalytic activity. Co<sub>2</sub>P/NRC nanorods enhance durability and catalytic action to a level comparable to Pt/C in alkaline media [72]. The performance of the Co-N-C-based catalyst depends on the active site of Co-N<sub>x</sub> and

nitrogen-containing functional groups and the effect of mutual interaction between Co-O-C and Co-N-C bond formations. Co-N/C catalyst follows the 4e<sup>-</sup> reaction pathway and exhibits high durability and current density. High amounts of Co<sup>2+</sup> oxidation states are associated with increasing ORR activity [41, 57, 73]. Co-Fe alloy is among the prominent non-PGM catalysts for ORR. It has been reported that charge redistribution between Fe-Co alloy and N-supported graphitic carbonnanotube enhances the catalysts' behavior. The corrosion resistance and electronic conductivity increase with the amount of Co increase in alloy [74, 75].

Ni-based catalyst is another good alternative to most active Pt-group metal catalysts. Ni or Ni alloys are not easily oxidizable, and the Ni structure facilitates the transportation of ions and the charge conductivity[76]. N-doped Ni-Co and Fe-Ni catalysts showed comparable ORR performance with Pt/C and exhibited superior stability [77, 78]. The enhancement of catalytic activity completely depends on the mutual effect of Ni and the N-carbon metal's electronic structures. The edge N atom and the geometric effect of support metal regulate the electronic configuration of Ni [79, 80]. Ni-Mo catalyst showed the highest mass activity among Pt free catalysts used in the present time due to the high dispersion of Ni particles, and Mo facilitates mass activity[81]. In an alkaline aqueous solution, the N-C structure works as a support of the Ni nanoparticles and enhances the catalytic activity towards ORR [79].

As a 3d transition metal, Cu shows high electro-catalytic activity towards ORR due to its valence electron configuration, which is closest to Pt. It has a very strong complex ability to generate Cu-N bonds and exhibits the highest stability in an aqueous solution among 3d transition metals [82]. Cu metal works as an active component for ORR, and this metal is used for constituting active sites. Cu enlarges the surface area of the catalyst. Cu<sup>2+</sup> ions have a great affinity to form a stable complex with N-based ligands. Cu-N interaction speeds up the peroxide reduction and oxygen activation [83, 84]. The CuFe/C (1.5wt.% Fe and 1.7 wt.% Cu) alloy catalyst and Pt/C (30%) exhibit the same catalytic activity. Fe<sup>3+</sup>-N works as an active site for ORR, and Cu<sup>2+</sup>/Cu<sup>+</sup> plays the role of a redox mediator that shuttles

the electron from the electrode to FeN- $O_2$  [85]. During ORR, the Fe atom in Cu alloy facilitates the desorption of oxygenated intermediates, which increases the rate of ORR kinetics. The electronic structure of catalyst metals has been changed by the interaction between the metal catalyst and the support metal. N particularly helps donate electrons to the O-O bond, thereby increasing stability [86]. Cu ascribes to high redox potentials, and the current densities of the d-orbital of Cu lead to a weaker O-O bond [87].

Among the transition metals, manganese oxides became the focus of research due to their variable oxidation states and high stability in alkaline media. Mn<sup>3+</sup> species modifies the crystallinity, surface area, and pore size of catalysts [88]. Liu and co-workers identified the two types of Mn coordination, octahedral Mn<sup>4+</sup> (i.e. partial d-orbital filling Mn) and pyramidal Mn<sup>3+</sup> and Mn<sup>3+</sup> coordination is essential for ORR activity [89]. The N-C structure helps reduce electron cloud densities on a carbon atom by inducing N. The active site of the Mn-N-C catalyst is the combined structure of N-C and Mn-N [90]. The covalency of the Mn-O bond is responsible for specific ORR activity and works as an electron transfer mediator to O. The existence of Mn<sup>3+</sup> on the active site facilitates the ORR activity, whereas Mn<sup>4+</sup> encourages the 4e<sup>-</sup> reaction pathway [91].

However, TM based catalysts exhibit higher levels of ORR activity in alkaline media that indicate the exchange of electrons and the change of oxidation state during ORR, the exact role of TM is not clear[57]. Transition metals (TM) have been recognized as alternatives due to their high corrosion resistance and stabilities, electrical conductivities, and mechanical strengths. N-doped carbon-supported TM catalyst exhibits better ORR activity in alkaline solution. Formation of C-N increases the concentration of active sites.

#### **Benefits of the carbon support**

Carbon support helps increase the electronic behavior of catalysts and enhances ORR performance. ECSA, durability, reaction pathway, and electrical conductivity have been influenced by support materials [92]. Corrosion of metal is an important factor in fuel cell

operations. Carbon support metal helps overcome corrosion problems by making a strong bond between nanoparticles and support materials [93]. Carbon nanomaterials are considered good catalyst support due to their excellent properties, which ensure the following parameters: 1) high electrical conductivity; 2) large surface area; 3) strong interaction between support and catalyst; 4) high electrical stability under the fuel cell condition, and 5) low cost [94-96]. Large surface areas of support suppress the particle size. This criterion helps make a highly concentrated catalyst particle that increases the efficiency of the electrode by reducing embedded sites and shortening the reactant pathway [97, 98]. C(Carbon black) is widely used for commercial Pt catalysts. Poor durability and low catalyst metal utilization are the main weaknesses of C. GO (graphene oxide), rGO (reduced graphene oxide, MWCNT(multiwall carbon nanotube), and so on are considered a better substitute for C. [99, 100]. Nowadays, GO and rGO are widely used because of the partial transition from sp<sup>2</sup> to sp<sup>3</sup>carbon atoms. Both GO and rGO derivatives of graphene are easy to produce on a large scale using graphene sheets, catalyst metal is located between pores, thereby reducing the aggregation of catalyst metals, and this behavior helps enhance catalyst efficiency [101, 102]. Studies revealed that in rGO, oxygen groups participate in the transfer of electrons, which causes the reduction of catalytic activity. Electric contact efficiency plays an important role between two catalyst particles. rGO has higher thermal stability than GO due to lower defect density [103, 104].

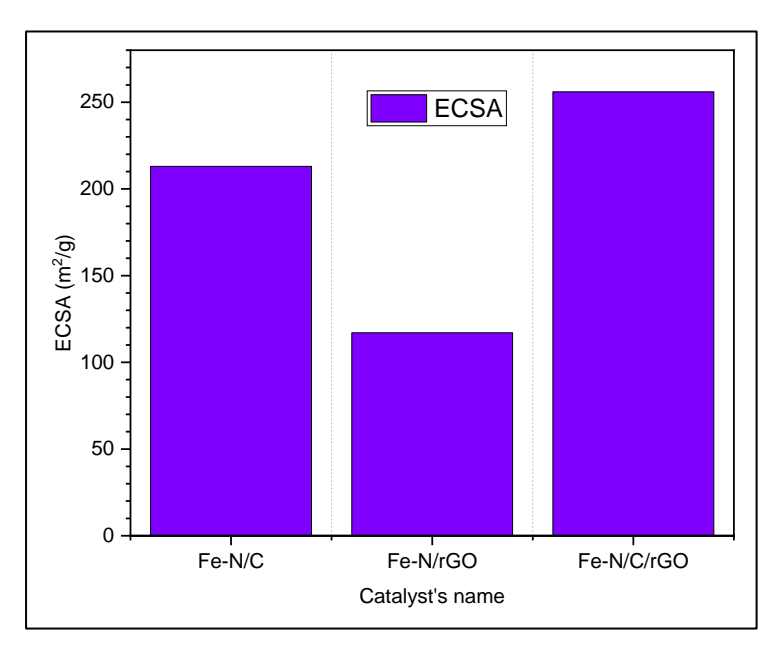


Figure 5. Effect of carbon support on ECSA [63]

It has been seen from Figure 5, ECSA of catalysts changes with the change of support metal, carbon black (C) supported Fe catalyst exhibited larger ECSA than reduced graphene oxide (rGO). Fe catalyst presented the largest ECSA while C and rGO were used together [63] Surface modification of the graphene sheet is conducted by inducing the heteroatom to boost the interaction with a metal catalyst; graphene aggregation is avoided by changing the interfacial properties [105]. The

electrochemical activity of the non-PGM catalyst depends on the doped element (N, S, and P) that supports carbon. The edge plane sites contribute to the improvement of catalytic performances, and spin densities on adjoining carbon atoms induce different ORR sites [64, 106–109]. Based on the above discussion, we summarise the properties of different carbon forms in Table 1, that influence the ORR activity.

Table 1. Represents the ECSA, conductivity, advantages, and disadvantages of widely used carbon forms as support

Carbon Materials	ECSA (m <sup>2</sup> g <sup>-1</sup> )	Conductivity (S cm <sup>-1</sup> )	Advantages	Disadvantages	Ref.
Vulcan XC-72	250	2.77	The catalytic activity can be increased by surface modification and pre-heat treatment.	Low utilization of metal catalysts and poor durability.	[110, 111]
CNT	50-1000	200-900	Excellent electrochemical stability and high hydrophilicity produce better ORR reactions.	Highly sensitive to different gas and synthesis methods.	[52, 112, 113]
GO	2630	~104	Easy to synthesis on an industrial scale and functionalized as well.	Catalytic properties change with changing synthesis tech.	[114–116]
Ordered porous carbon(OPC)	600-2800	3.28x10 <sup>-4</sup> - 2.2x10 <sup>-3</sup>	Stability increases with increasing annealing temperature	Electrochemical activities strongly depend on pore size and the diameter less than 10nm.	[117–120]
Graphene nanosheets (GNS)	56	10 <sup>3</sup> -10 <sup>4</sup>	Highly stable than MWCNT, SWCNT, CB, and GO	Highly sensitive to the synthesis process. During preparation, it losses many properties due to aggregate.	[98, 121, 122]

#### Promising synthesis technique for ORR catalysts

The synthesis condition influences the catalyst compositions and structure of active sites. Several strategies are used to establish a catalyst that is comparable to Pt/C in both acid and base solutions. Among the improvement techniques, pyrolysis and core-shell techniques are widely used for developing alloy catalysts. Most recently, the irradiation method utilizes for obtaining a higher degree of alloying.

#### **Pyrolysis**

Different types of metal alloys help reduce PGM use and help modify the surface structure and reactivity within alloying elements through the change of electronic and geometric structure [11, 111]. Alloying PGM with transition metals declines the OH adsorption due to the existence of PGM-TM bond distance in lattice contraction, which promotes higher ORR activity than pure PGM. The durability of PGM-TM alloys depends

on the degree of alloy homogeneity [52, 123]. Performances of alloy catalysts are directly related to pyrolysis treatment. The effect of pyrolysis temperature has been illustrated in Figure 6(a-f).

From the TEM image of FeCN/GN(graphene nanosheets), it is clear that below 700° C, only a few FeCN particles have been observed, marked by the white circle in Figure 6(a) and 6(b) which were pyrolyzed at 500° C and 600° C respectively. Figure 6(d-f) represents FeCN samples that pyrolyzed at 800 °C, 900 °C, and 1000 °C respectively. FeCN particles were uniformly distributed on GN(graphene nanosheets) above 700 °C. Figure 6(c) represents the sample

pyrolyzed at 700 °C. At 700 °C, FeCN/GN exhibited the highest electron transfer (3.94) and ORR activity in acidic solutions. In general, a pyrolysis temperature below 700 °C is not enough to induce stable and active ORR sites [112, 124, 125]. The formation of Fe-N<sub>x</sub> active sites strongly depends on pyrolysis, which contributes to ORR activity. N atoms have been successfully united into a carbon matrix, and the proportion of N touches the maximum level at 900 °C [53,119]. The pyrolysis treatment approach helps increase the concentration of ORR sites by modifying the M-N<sub>x</sub>/C structure. Heat treatment also controls metal-N bonding [76,120].

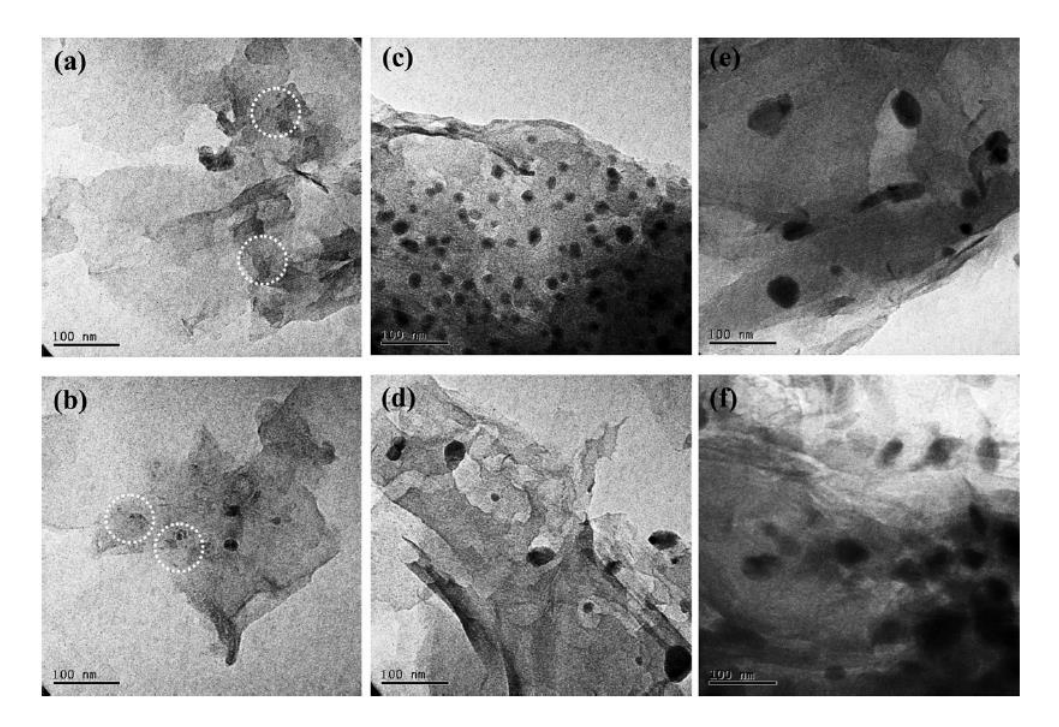


Figure 6. TEM image of FeCN/GN at 500 °C (a), 600 °C (b), 700 °C (c),800 °C (d), 900 °C (e), and 1000 °C (f) [124]

#### **Core-shell structure**

Mutual interaction of core metal and shell facilitates the mass activity and durability of ORR in both acidic and alkaline electrolytes. Generally, a core-shell-structured catalyst is designed by capturing the catalyst metal in carbon materials. This structure provides an exclusive electronic interaction between confined nanomaterials and carbon shells, thereby playing the main role in the enhancement of catalytic activity. Both single metal particles and metal alloy materials can serve as shells or core [105, 108]. This approach leads to a change in the d-band positions, which help provide higher activation energies. Ligand performances enhance catalytic activity and improve charge transfer [100]. Core materials and shell thickness are important factors for stability and ORR performance. Shell thickness helps with long term stability. The thickness of the shell screens the core interactivity, which improves catalytic stability [31, 115]. Gautam et al. reported that a shell material graphene nanosheets appears on behalf of electron collectors and tricks the core ion to form the existing active sites by providing high stability [116]. [116]

#### Irradiation technique

The irradiation process helps improve structural properties and chemical properties. γ-Irradiation helps reduce the oxygen functional group from the GO sheet and increases C=C bands. It also modifies the sp<sup>2</sup> character of C. Some work has been done using gamma irradiation. In the case of few-layered graphene materials, the O/C ratio exhibits a decreasing trend when γ-irradiation dose increases for GO and GONR (nanorod) [117]. A remarkable characteristic has been observed in preparing graphene aerogel (GA) from the GO sheet. GA shows more stability and has a honeycomb structure with a high C/O ratio after irradiation. No significant weight loss can be observed due to γ-irradiation.[118]. However, dose rate, total dose, type of solvent are important parameters for gamma irradiation induced synthesis technique. These parameters can be able to alter the size, chemical, and physical properties of the final product. Sharin and coworkers reported the reduction of GO has occurred when the cumulative dose was 35kGy. They utilized different amounts of irradiation dose,0, 5, 15, 20, and

35kGy on GO powders [119, 126, 127] In an aqueous solution (water/alcohol), Irradiation decompose the water molecules to hydroxyl radical, OH-, hydrogen radical, and hydrated electron, H\* and e- species. Alcohol removes the oxidative OH and converts it into reductive radicals.[121]. In the case of a heterogeneous catalyst, gamma irradiation changes the concentration of the active site of a catalyst surface, whereas electron beam irradiation induces a new active center by switching the chemical bond and creating defects on a catalyst surface [128]. Kakitani et al. reported that Pt-C bond formed during ion-beam irradiation (Ar+). This bond changes the chemical state of Pt nanoparticles and carbon support that suppresses Pt oxidation and improves overall catalytic activity towards ORR [129]. After Ar<sup>+</sup> irradiation, carbon nanofiber-supported PtRu exhibits a lower crystal size (19.5 nm) due to the change in the valence state of support metal, whereas nonirradiated carbon nanofiber-supported PtRu shows a larger crystal size (20.1 nm) [130]. Proton irradiation leads to a break M (metal)-O bond by producing highly active radicals on the metal surface. During irradiation, the 2p orbital of O and the 3d orbital of metal merge, thereby reducing the bang gap, which increases the electronic conductivity and overall performance of the metal catalyst [131]. Ohkubo and co-workers suggested that the electron beam irradiation reduction method can synthesize both alloy and metal oxide on the carbon support simultaneously[132].

#### Conclusion

From the discussions, it is clear that all PGM alloys are comparable catalysts for ORR cathode in both acid and alkaline mediums, though 20% wt of Pt is needed for promising performance. Mixing PGM and transition metal is a good strategy for reducing the use of Pt. PGM-TM alloy catalysts also improve ORR activity and follow the 4e<sup>-</sup> pathway in both types of solutions. However, 50wt% of PGM is required in the PGM-TM cluster for enhancing ORR activity. Most of the TM-based catalysts have been developed with the N supported carbon. N atom produces C-N sites that provide higher active site densities and mass transport. In the absence of the N atom, the TM-based catalysts are not comparable with commercial Pt/C and other PGM catalysts. N supported Fe, and Fe doped Co catalysts

work in acidic solutions, but it is not comparable with commercial Pt/C. All M-N-C (M= transition metal) exhibited better catalytic activity than Pt/C in alkaline solution. Choosing ideal carbon support can improve the catalytic activity of TM alloy in an acidic medium. The amount of nitrogen and carbon defects and metallic particles' existence are common factors for improving performance.

Alloy and pyrolysis are closely related to each other. Homogeneity of alloy catalysts depends on pyrolysis temperature. Core-shell is a popular technique for alloy catalysts. In this process, catalyst behaviour is associated with the mutual interaction between the core metal and the shell metal. Shell thickness also plays a hidden role to facilitates ORR. Nowadays, different types of irradiations have been taken a superior position in research.

#### Acknowledgment

This paper was completed with the financial assistance of Universiti Kebangsaan Malaysia (GUP-2018-041) and the International Atomic Energy Agency (R23130) and support of Fuel Cell Institute, UKM.

#### References

- Rajapakse, R. M. G., Senarathna, K. G. C., Kondo, A., Jayawardena, P. S. and Shimomura, M. (2015). Extremely low-cost alternative for the oxygen reduction catalyst of fuel cell. *Advances in Automobile Engineering*, 4(1): 1.
- Zhang, Y., Huang, N., Zhou, F., He, Q. and Zhan, S. (2018). Research on the oxygen reduction reaction (ORR) mechanism of g-C<sub>3</sub>N<sub>4</sub> doped by Ag based on first-principles calculations. *Journal of the Chinese Chemical Society*, 65(12): 1431-1436.
- She, Y., Chen, J., Zhang, C., Lu, Z., Ni, M., Sit, P. H. L. and Leung, M. K. H. (2017). Oxygen Reduction reaction mechanism of nitrogen-doped graphene derived from ionic liquid. *Energy Procedia*, 142: 1319-1326.
- Hazarika, K. K., Goswami, C., Saikia, H., Borah, B.
   J. and Bharali, P. (2018). Cubic Mn<sub>2</sub>O<sub>3</sub>
   nanoparticles on carbon as bifunctional
   electrocatalyst for oxygen reduction and oxygen
   evolution reactions. *Molecular Catalysis*, 451: 153 160.

- Laurent-Brocq, M., Job, N., Eskenazi, D. and Pireaux, J. J. (2014). Pt/C catalyst for PEM fuel cells: Control of Pt nanoparticles characteristics through a novel plasma deposition method. *Applied Catalysis B: Environmental*, 147: 453-463.
- Shao-Horn, Y., Sheng, W. C., Chen, S., Ferreira, P. J., Holby, E. F. and Morgan, D. (2007). Instability of supported platinum nanoparticles in low-temperature fuel cells. *Topics in Catalysis*, 46(3–4): 285–305.
- 7. Dombrovskis, J. K. and Palmqvist, A. E. C. (2016). Recent progress in synthesis, characterization and evaluation of non-precious metal catalysts for the oxygen reduction reaction. *Fuel Cells*, 16(1): 4-22.
- 8. Holton, O. and Stevenson, J. (2013). The role of platinum in proton exchange membrane fuel cells Johnson Matthey technology review. *Platinum Metals Reviews*, 57(4): 259-271.
- Mustain, W. E., Shrestha, S., Ashegi, S., Timbro, J., Lang, C. M. and Mustain, W. E. (2011). ORR and fuel cell performance of Pt supported on Nfunctionalized mesoporous carbon, ECS Transactions, 41(1): 1183.
- 10. Ghosh, S., Mondal, S. and Retna Raj, C. (2014). Carbon nanotube-supported dendritic Pt-on-Pd nanostructures: Growth mechanism and electrocatalytic activity towards oxygen reduction reaction. *Journal of Materials Chemistry A*, 2(7): 2233-2239.
- Guha, A., Lu, W., Zawodzinski, T. A. and Schiraldi, D. A. (2007). Surface-modified carbons as platinum catalyst support for PEM fuel cells, *Carbon*, 45: 1506-1517.
- 12. Mun, Y., Lee, S., Kim, K., Kim, S., Lee, S., Han, J. W. and Lee, J. (2019). Versatile strategy for tuning ORR activity of a single Fe-N4 site by controlling electron-withdrawing/donating properties of a carbon plane. *Journal of the American Chemical Society*, 141(15): 6254-6262.
- 13. Kodali, M., Santoro, C., Serov, A., Kabir, S., Artyushkova, K., Matanovic, I. and Atanassov, P. (2017). Air breathing cathodes for microbial fuel cell using Mn-, Fe-, Co- and Ni-containing platinum group metal-free catalysts. *Electrochimica Acta*, 231: 115-124.

- Song, M., Song, Y., Sha, W., Xu, B., Guo, J. and Wu, Y. (2020). Recent advances in non-precious transition metal/nitrogen-doped carbon for oxygen reduction electrocatalyst. *Catalysts*, 10(1): 141.
- Mao, J., Liu, P., Du, C., Liang, D., Yan, J. and Song, W. (2019). Tailoring 2D MoS<sub>2</sub> heterointerfaces for promising oxygen reduction reaction electrocatalysis. *Journal of Materials Chemistry A*, 7(15): 8785-8789.
- Ma, R., Lin, G., Zhou, Y., Liu, Q., Zhang, T., Shan, G. and Wang, J. (2019). A review of oxygen reduction mechanisms for metal-free carbon-based electrocatalysts. NPJ Computational Materials, 5(1): 1-15.
- 17. Tang, Z., Wu, W. and Wang, K. (2018). Oxygen reduction reaction catalyzed by noble metal clusters. *Catalysts*, 8(2): 65.
- Kim, J. Y., Oh, T. K., Shin, Y., Bonnett, J. and Weil, K. S. (2011). A novel non-platinum group electrocatalyst for PEM fuel cell application. *International Journal of Hydrogen Energy*, 36(7): 4557-4564.
- 19. Wang, B. (2005). Recent development of non-platinum catalysts for oxygen reduction reaction. *Journal of Power Sources*, 152(1–2): 1-15.
- Sui, S., Wang, X., Zhou, X., Su, Y., Riffat, S. and Liu, C. J. (2017). A comprehensive review of Pt electrocatalysts for the oxygen reduction reaction: Nanostructure, activity, mechanism and carbon support in PEM fuel cells. *Journal of Materials Chemistry A*, 5(5): 1808-1825.
- 21. Raciti, D., Kubal, J., Ma, C., Barclay, M., Gonzalez, M., Chi, M. and Wang, C. (2016). Pt<sub>3</sub>Re alloy nanoparticles as electrocatalysts for the oxygen reduction reaction. *Nano Energy*, 20: 202-211.
- 22. Hyun, K., Lee, J. H., Yoon, C. W. and Kwon, Y. (2013). The effect of platinum based bimetallic electrocatalysts on oxygen reduction reaction of proton exchange membrane fuel cells. *International Journal of Electrochemical Science*, 8(10): 11752-11767
- 23. Tian, J., Wu, W., Tang, Z., Wu, Y., Burns, R., Tichnell, B. and Chen, S. (2018). Oxygen reduction reaction and hydrogen evolution reaction catalyzed by Pd–Ru nanoparticles encapsulated in porous carbon nanosheets. *Catalysts*, 8(8): 1-15.

- Zhou, Z. M., Shao, Z. G., Qin, X. P., Chen, X. G., Wei, Z. D. and Yi, B. L. (2010). Durability study of Pt-Pd/C as PEMFC cathode catalyst. *International Journal of Hydrogen Energy*, 35(4): 1719-1726.
- 25. Wang, W., Wang, Z., Wang, J., Zhong, C. J. and Liu, C. J. (2017). Highly active and stable Pt–Pd Alloy catalysts synthesized by room-temperature electron reduction for oxygen reduction reaction. *Advanced Science*, 4(4): 1-9.
- Yusof, M. S. M., Jalil, A. A., Ahmad, A., Triwahyono, S., Othman, M. H. D., Abdullah, T. A. T. and Nabgan, W. (2019). Effect of Pt–Pd/C coupled catalyst loading and polybenzimidazole ionomer binder on oxygen reduction reaction in high-temperature PEMFC. *International Journal of Hydrogen Energy*, 2019: 20760-20769.
- Thanasilp, S. and Hunsom, M. (2011). Effect of Pt: Pd atomic ratio in Pt-Pd/C electrocatalyst-coated membrane on the electrocatalytic activity of ORR in PEM fuel cells. *Renewable Energy*, 36(6): 1795-1801.
- 28. Jackson, C., Conrad, O. and Levecque, P. (2017). Systematic study of Pt-Ru/C catalysts prepared by chemical deposition for direct methanol fuel cells. *Electrocatalysis*, 8(3): 224-234.
- Huang, H., Zhu, J., Li, D., Shen, C., Li, M., Zhang, X. and Wu, Y. (2017). Pt nanoparticles grown on 3D RuO<sub>2</sub>-modified graphene architectures for highly efficient methanol oxidation. *Journal of Materials Chemistry A*, 5(9): 4560-4567.
- 30. Yang, G., Sun, Y., Lv, P., Zhen, F., Cao, X., Chen, X. and Kong, X. (2016). Preparation of Pt–Ru/C as an oxygen-reduction electrocatalyst in microbial fuel cells for wastewater treatment. *Catalysts*, 6(10): 150.
- 31. Jackson, A., Strickler, A., Higgins, D. and Jaramillo, T. F. (2018). Engineering Ru@Pt coreshell catalysts for enhanced electrochemical oxygen reduction mass activity and stability. *Nanomaterials*, 8(1): 38.
- 32. Tolmachev, Y. V. and Petrii, O. A. (2017). Pt–Ru electrocatalysts for fuel cells: developments in the last decade. *Journal of Solid State Electrochemistry*, 21(3): 613-639.

- Durst, J., Simon, C., Hasché, F. and Gasteiger, H. A. (2015). Hydrogen oxidation and evolution reaction kinetics on carbon supported Pt, Ir, Rh, and Pd electrocatalysts in acidic media. *Journal of The Electrochemical Society*, 162(1): F190-F203.
- 34. Zeng, M., Wang, X. X., Tan, Z. H., Huang, X. X. and Wang, J. N. (2014). Remarkable durability of Pt-Ir alloy catalysts supported on graphitic carbon nanocages. *Journal of Power Sources*, 264: 272-281.
- 35. Zheng, H. B., An, L., Zheng, Y., Qu, C., Fang, Y., Liu, Q. and Dang, D. (2018). Tuning the catalytic activity of Ir@Pt nanoparticles through controlling ir core size on cathode performance for PEM fuel cell application. *Frontiers in Chemistry*, 6(7): 1-7.
- 36. Fang, D., Tang, X., Yang, L., Xu, D., Zhang, H., Sun, S. and Yi, B. (2019). Facile synthesis of Ptdecorated Ir black as a bifunctional oxygen catalyst for oxygen reduction and evolution reactions. *Nanoscale*, 11(18): 9091-9102.
- Zhu, J., Elnabawy, A. O., Lyu, Z., Xie, M., Murray,
   E. A., Chen, Z., Xia, Y. (2019). Facet-controlled
   Pt–Ir nanocrystals with substantially enhanced activity and durability towards oxygen reduction.
   Materials Today, 2019: 1-9.
- 38. Lin, C., Wu, G., Li, H., Geng, Y., Xie, G., Yang, J. and Jin, J. (2017). Rh nanoparticles supported on ultrathin carbon nanosheets for high-performance oxygen reduction reaction and catalytic hydrogenation. *Nanoscale*, 9(5): 1834-1839.
- Paál, Z., Gyorffy, N., Wootsch, A., Tóth, L., Bakos, I., Szabó, S. and Schlögl, R. (2007). Preparation, physical characterization and catalytic properties of unsupported Pt-Rh catalyst. *Journal of Catalysis*, 250(2): 254-263.
- Narayanamoorthy, B., Datta, K. K. R., Eswaramoorthy, M. and Balaji, S. (2014). Selfstabilized Pt–Rh bimetallic nanoclusters as durable electrocatalysts for dioxygen reduction in PEM fuel cells. RSC Advances, 4(98): 55571-55579.
- 41. Goswami, C., Hazarika, K. K. and Bharali, P. (2018). Transition metal oxide nanocatalysts for oxygen reduction reaction. *Materials Science for Energy Technologies*, 1(2): 117–128.
- 42. Xin, L., Zhang, Z., Wang, Z., Qi, J. and Li, W. (2013). Carbon supported Ag nanoparticles as high

- performance cathode catalyst for  $H_2/O_2$  anion exchange membrane fuel cell. *Frontiers in Chemistry*, 1: 16.
- 43. Esfandiari, A., Kazemeini, M. and Bastani, D. (2016). Synthesis, characterization and performance determination of an Ag@Pt/C electrocatalyst for the ORR in a PEM fuel cell. *International Journal of Hydrogen Energy*, 41(45): 20720-20730.
- 44. Chiwata, M., Yano, H., Ogawa, S., Watanabe, M., Iiyama, A. and Uchida, H. (2016). Oxygen reduction reaction activity of carbon-supported Pt-Fe, Pt-Co, and Pt-Ni alloys with stabilized Pt-skin layers. *Electrochemistry*, 84(3), 133–137.
- 45. Li, W., Pan, Z., Huang, Z., Zhou, Q., Xu, Y., Wu, S., Hu, G. (2018). Pt nanoparticles supported on titanium iron nitride nanotubes prepared as a superior electrocatalysts for methanol electrooxidation. *International Journal of Hydrogen Energy*, 43(20): 9777-9786.
- 46. Termpornvithit, C., Chewasatn, N. and Hunsom, M. (2012). Stability of Pt-Co/C and Pt-Pd/C based oxygen reduction reaction electrocatalysts prepared at a low temperature by a combined impregnation and seeding process in PEM fuel cells. *Journal of Applied Electrochemistry*, 42(3): 169-178.
- Cui, Y., Wu, Y., Wang, Z., Yao, X., Wei, Y., Kang, Y., Gan, L. (2020). Mitigating metal dissolution and redeposition of Pt-Co catalysts in PEM fuel cells: Impacts of structural ordering and particle size. *Journal of The Electrochemical Society*, 167(6): 064520.
- 48. Rohendi, D., Rachmat, A. and Syarif, N. (2018). Fabrication and characterization of Pt-Co/C catalyst for fuel cell electrode. *Journal of Physics: Conference Series*, 1095(1): 012007.
- 49. Singh, R. N. (2012). Preparation of bimetallic Pd-Co nanoparticles on graphene support for use as methanol tolerant oxygen reduction electrocatalysts. *Engineering*, *Technology & Applied Science Research*, 2(6): 295-301.
- 50. Ramli, Z. A. C. and Kamarudin, S. K. (2018). Platinum-based catalysts on various carbon supports and conducting polymers for direct methanol fuel cell applications: a review. *Nanoscale Research Letters*, 13: 1-25.

- Mechler, A. K., Sahraie, N. R., Armel, V., Zitolo, A., Sougrati, M. T., Schwämmlein, J. N. and Jaouen, F. (2018). Stabilization of iron-based fuel cell catalysts by non-catalytic platinum. *Journal of The Electrochemical Society*, 165(13): F1084–F1091.
- 52. Mohanraju, K. and Cindrella, L. (2014). Impact of alloying and lattice strain on ORR activity of Pt and Pd based ternary alloys with Fe and Co for proton exchange membrane fuel cell applications. *RSC Advances*, 4(23): 11939-11947.
- 53. Li, X. P., Xiang, X. D., Yang, H. Y., Wang, X. J., Tan, C. L. and Li, W. S. (2013). Hydrogen tungsten bronze-supported platinum as electrocatalyst for methanol oxidation. *Fuel Cells*, 13(2): 314-318.
- 54. Seselj, N., Engelbrekt, C. and Zhang, J. (2015). Graphene-supported platinum catalysts for fuel cells. *Science Bulletin*, 60(9): 864-876.
- 55. Lv, H., Li, D., Strmcnik, D., Paulikas, A. P., Markovic, N. M. and Stamenkovic, V. R. (2016). Recent advances in the design of tailored nanomaterials for efficient oxygen reduction reaction. *Nano Energy*, 29: 149-165.
- Thippani, T., Mandal, S., Wang, G., Ramani, V. K. and Kothandaraman, R. (2016). Probing oxygen reduction and oxygen evolution reactions on bifunctional non-precious metal catalysts for metal-air batteries. *RSC Advances*, 6(75): 71122-71133.
- 57. Osgood, H., Devaguptapu, S. V., Xu, H., Cho, J. and Wu, G. (2016). Transition metal (Fe, Co, Ni, and Mn) oxides for oxygen reduction and evolution bifunctional catalysts in alkaline media. *Nano Today*, 11(5): 601-625.
- Akbari, A., Amini, M., Tarassoli, A., Eftekhari-Sis, B., Ghasemian, N. and Jabbari, E. (2018). Transition metal oxide nanoparticles as efficient catalysts in oxidation reactions. *Nano-Structures* and *Nano-Objects*, 14: 19-48.
- Ren, G., Gao, L., Teng, C., Li, Y., Yang, H., Shui,
   J. and Dai, L. (2018). Ancient Chemistry
   "pharaoh's Snakes" for Efficient Fe-/N-Doped
   Carbon Electrocatalysts. ACS Applied Materials
   and Interfaces, 10(13): 10778–10785.
- 60. Gu, L., Jiang, L., Li, X., Jin, J., Wang, J. and Sun, G. (2016). A Fe-N-C catalyst with highly dispersed iron in carbon for oxygen reduction reaction and its

- application in direct methanol fuel cells. *Cuihua Xuebao/Chinese Journal of Catalysis*, 37(4): 539-548.
- 61. Park, M., Lee, J., Hembram, K., Lee, K.-R., Han, S., Yoon, C. and Kim, J. (2016). Oxygen reduction electrocatalysts based on coupled iron nitride nanoparticles with nitrogen-doped carbon. *Catalysts*, 6(6): 86.
- 62. Rahman, K. R., Kok, K. Y., Wong, W. Y., Yang, H. and Lim, K. L. (2021). Effect of iron loading on the catalytic activity of Fe/N-doped reduced graphene oxide catalysts via irradiation. *Applied Sciences* (*Switzerland*), 11(1): 1-10.
- 63. Xi, J., Wang, F., Mei, R., Gong, Z., Fan, X., Yang, H. and Luo, Z. (2016). Catalytic performance of a pyrolyzed graphene supported Fe-N-C composite and its application for acid direct methanol fuel cells. *RSC Advances*, 6(93): 90797-90805.
- 64. Meng, H., Chen, X., Gong, T., Liu, H., Liu, Y., Li, H. and Zhang, Y. (2019). N, P, S/Fe-codoped carbon derived from feculae bombycis as an efficient electrocatalyst for oxygen reduction reaction. *ChemCatChem*, 11(24): 6015-6021.
- 65. Basri, S. and Kamarudin, S. K. (2018). Nanocatalyst FeN<sub>4</sub>/C molecular orbital behaviour for oxygen reduction reaction (ORR) in cathode direct methano fuel cell (DMFC). *Jurnal Kejuruteraan*, 1(2): 59-64.
- 66. Jiang, W. J., Gu, L., Li, L., Zhang, Y., Zhang, X., Zhang, L. J. and Wan, L. J. (2016). Understanding the high activity of Fe-N-C electrocatalysts in oxygen reduction: Fe/Fe<sub>3</sub>C nanoparticles boost the activity of Fe-Nx. *Journal of the American Chemical Society*, 138(10): 3570-3578.
- 67. Hossen, M. M., Artyushkova, K., Atanassov, P. and Serov, A. (2018). Synthesis and characterization of high performing Fe-N-C catalyst for oxygen reduction reaction (ORR) in alkaline exchange membrane fuel cells. *Journal of Power Sources*, 375: 214-221.
- 68. Zhan, Y., Xie, F., Zhang, H., Lin, Z., Huang, J., Zhang, W. and Meng, H. (2018). Non noble metal catalyst for oxygen reduction reaction and its characterization by simulated fuel cell test. *Journal* of The Electrochemical Society, 165(15): J3008-J3015.

- Kim, S., Park, H. and Li, O. L. (2020). Cobalt nanoparticles on plasma-controlled nitrogen-doped carbon as high-performance ORR electrocatalyst for primary Zn-Air battery. *Nanomaterials*, 10(2): 223.
- Zang, J., Wang, F., Cheng, Q., Wang, G., Ma, L., Chen, C. and Yang, H. (2020). Cobalt/zinc dualsites coordinated with nitrogen in nanofibers enabling efficient and durable oxygen reduction reaction in acidic fuel cells. *Journal of Materials Chemistry A*, 8(7): 3686-3691.
- Grinberg, V. A., Mayorova, N. A., Pasynskii, A. A., Modestov, A. D., Shiryaev, A. A., Vysotskii, V. V. and Nogai, A. S. (2018). Nanostructured platinumfree catalysts of oxygen reduction based on metal chalcogenide cobalt clusters. *Russian Journal of Coordination Chemistry*, 44(10): 589-595.
- Winey, K. I., Li, J., Doan-Nguyen, V. V. T., Murray, C. B., Su, D., Trigg, E. B. and Agarwal, R. (2015). Synthesis and X-ray characterization of cobalt phosphide (Co<sub>2</sub>P) nanorods for the oxygen reduction reaction. ACS Nano, 9(8): 8108-8115.
- 73. Zhao, H., Xing, T., Li, L., Geng, X., Guo, K., Sun, C. and An, B. (2019). Synthesis of cobalt and nitrogen co-doped carbon nanotubes and its ORR activity as the catalyst used in hydrogen fuel cells. *International Journal of Hydrogen Energy*, 44(46): 25180-25187.
- 74. Liang, G., Huang, J., Li, J., Wu, Y., Huang, G., Jin, Y. Q., ... and Meng, H. (2020). Improving the catalytic performance of Co/N/C catalyst for oxygen reduction reaction by alloying with Fe. Journal of The Electrochemical Society, 167(10), 104502.
- 75. An, L., Jiang, N., Li, B., Hua, S., Fu, Y., Liu, J. and Sun, Z. (2018). A highly active and durable iron/cobalt alloy catalyst encapsulated in N-doped graphitic carbon nanotubes for oxygen reduction reaction by a nanofibrous dicyandiamide template. *Journal of Materials Chemistry A*, 6(14): 5962-5970
- Liu, P., Ran, J., Xia, B., Xi, S., Gao, D. and Wang, J. (2020). Bifunctional oxygen electrocatalyst of mesoporous Ni/NiO nanosheets for flexible rechargeable Zn–Air batteries. *Nano-Micro Letters*, 12(1), 1–12.

- 77. Hao, Y., Xu, Y., Liu, J. and Sun, X. (2017). Nickel-cobalt oxides supported on Co/N decorated graphene as an excellent bifunctional oxygen catalyst. *Journal of Materials Chemistry A*, 5(11): 5594-5600.
- 78. Trześniewski, B. J., Diaz-Morales, O., Vermaas, D. A., Longo, A., Bras, W., Koper, M. T. M. and Smith, W. A. (2015). In situ observation of active oxygen species in Fe-containing Ni-based oxygen evolution catalysts: The effect of pH on electrochemical activity. *Journal of the American Chemical Society*, 137(48): 15112-15121.
- Zhuang, Z., Giles, S. A., Zheng, J., Jenness, G. R., Caratzoulas, S., Vlachos, D. G. and Yan, Y. (2016). Nickel supported on nitrogen-doped carbon nanotubes as hydrogen oxidation reaction catalyst in alkaline electrolyte. *Nature Communications*, 7: 1–8.
- 80. Faubert, P., Kondov, I., Qazzazie, D., Yurchenko, O. and Müller, C. (2018). A non-noble Cr-Ni-based catalyst for the oxygen reduction reaction in alkaline polymer electrolyte fuel cells. *MRS Communications*, 8(1): 160-167.
- 81. Kabir, S., Lemire, K., Artyushkova, K., Roy, A., Odgaard, M., Schlueter, D. and Serov, A. (2017). Platinum group metal-free NiMo hydrogen oxidation catalysts: High performance and durability in alkaline exchange membrane fuel cells. *Journal of Materials Chemistry A*, 5(46): 24433-24443.
- 82. Xie, X., Liu, J., Li, T., Song, Y. and Wang, F. (2018). Post-formation copper-nitrogen species on carbon black: their chemical structures and active sites for oxygen reduction reaction. *Chemistry A European Journal*, 24(39): 9968-9975.
- 83. Hamedi, M., Wigenius, J., Tai, F. I., Björk, P. and Aili, D. (2010). Polypeptide-guided assembly of conducting polymer nanocomposites. *Nanoscale*, 2(10): 2058-2061.
- 84. Kang, Y. S., Heo, Y., Kim, P. and Yoo, S. J. (2017). Preparation and characterization of Cu–N–C electrocatalysts for oxygen reduction reaction in alkaline anion exchange membrane fuel cells. *Journal of Industrial and Engineering Chemistry*, 52(3): 35-41.

- 85. He, Q., Yang, X., Ren, X., Koel, B. E., Ramaswamy, N., Mukerjee, S. and Kostecki, R. (2011). A novel CuFe-based catalyst for the oxygen reduction reaction in alkaline media. *Journal of Power Sources*, 196(18): 7404-7410.
- 86. Qiao, Y., Ni, Y., Kong, F., Li, R., Zhang, C., Kong, A. and Shan, Y. (2019).
   Pyrolytic carbon-coated Cu-Fe alloy nanoparticles with high catalytic performance for oxygen electroreduction. *Chemistry An Asian Journal*, 14(15): 2676-2684.
- 87. Cui, L., Cui, L., Li, Z., Zhang, J., Wang, H., Lu, S. and Xiang, Y. (2019). A copper single-atom catalyst towards efficient and durable oxygen reduction for fuel cells. *Journal of Materials Chemistry A*, 7(28): 16690-16695.
- 88. Mosa, I. M., Biswas, S., El-Sawy, A. M., Botu, V., Guild, C., Song, W. and Suib, S. L. (2015). Tunable mesoporous manganese oxide for high performance oxygen reduction and evolution reactions. *Journal of Materials Chemistry A*, 4(2): 620-631.
- 89. Liu, J., Yu, M., Wang, X., Wu, J., Wang, C., Zheng, L. and Wang, W. (2017). Investigation of high oxygen reduction reaction catalytic performance on Mn-based mullite SmMn<sub>2</sub>O<sub>5</sub>. *Journal of Materials Chemistry A*, 5(39): 20922-20931.
- 90. Zhang, R., Zhang, J., Ma, F., Wang, W. Y. and Li, R. F. (2014). Preparation of Mn-N-C catalyst and its electrocatalytic activity for the oxygen reduction reaction in alkaline medium. *Ranliao Huaxue Xuebao/Journal of Fuel Chemistry and Technology*, 42(4): 467-475.
- 91. Stoerzinger, K. A., Risch, M., Han, B. and Shao-Horn, Y. (2015). Recent insights into manganese oxides in catalyzing oxygen reduction kinetics. *ACS Catalysis*, 5(10): 6021-6031.
- 92. Shao, Y., Liu, J., Wang, Y. and Lin, Y. (2009). Novel catalyst support materials for PEM fuel cells: Current status and future prospects. *Journal of Materials Chemistry*, 19(1): 46-59.
- Qin, C., Wang, J., Yang, D., Li, B. and Zhang, C.
   (2016). Proton exchange membrane fuel cell reversal: A review. *Catalysts*, 6(12), 197.
- 94. Chong, S. T., Lee, T. K., Samad, S., Loh, K. S.,

- Wong, W. Y., Wan Daud, W. R. and Sunarso, J. (2018). Carbon and non-carbon support materials for platinum-based catalysts in fuel cells. *International Journal of Hydrogen Energy*, 43(16): 7823-7854.
- 95. Devrim, Y., Arıca, E. D. and Albostan, A. (2018). Graphene based catalyst supports for high temperature PEM fuel cell application. *International Journal of Hydrogen Energy*, 43(26): 11820-11829.
- 96. Khan, A. S. A., Ahmed, R. and Mirza, M. L. (2010). Performance evaluation of platinum-based catalysts for the development of proton exchange membrane fuel cells. *Turkish Journal of Chemistry*, 34(2): 193-206.
- 97. Choi, S. M., Seo, M. H., Kim, H. J. and Kim, W. B. (2011). Synthesis of surface-functionalized graphene nanosheets with high Pt-loadings and their applications to methanol electrooxidation. *Carbon*, 49(3): 904-909.
- 98. Suda, Y., Ozaki, M., Tanoue, H. and Takikawa, H. (2013). Supporting PtRu catalysts on various types of carbon nanomaterials for fuel cell applications. *Journal of Physics: Conference Series*, 433(1): 012008.
- Molina-García, M. A. and Rees, N. V. (2016). Effect of catalyst carbon supports on the oxygen reduction reaction in alkaline media: A comparative study. RSC Advances, 6(97): 94669-94681.
- 100. Esfandiari, A. and Kazemeini, M. (2018). Investigating electrochemical behaviors of Ag@Pt core—shell nanoparticles supported upon different carbon materials acting as PEMFC's cathodes. *Chemical Engineering Transactions*, 70: 2161-2166.
- Minitha, C. R. and Rajendrakumar, R. T. (2013).
   Synthesis and characterization of reduced graphene oxide. *Advanced Materials Research*, 678: 56-60.
- 102. Kang, S. Y., Kim, H. J. and Chung, Y. H. (2018). Recent developments of nano-structured materials as the catalysts for oxygen reduction reaction. *Nano Convergence*, 5(1): 1-15.

- 103. Grigoriev, S. A., Fateev, V. N., Pushkarev, A. S., Pushkareva, I. V., Ivanova, N. A. and Kalinichenko, V. N., Wei, X. (2018). Reduced graphene oxide and its modifications as catalyst supports and catalyst layer modifiers for PEMFC. *Materials*, 11(8): 1405.
- 104. Alam, S. N., Sharma, N. and Kumar, L. (2017). Synthesis of graphene oxide (GO) by modified hummers method and its thermal reduction to obtain reduced graphene oxide (rGO). *Graphene*, 6(1): 118
- 105. Liu, J., Choi, H. J. and Meng, L. Y. (2018). A review of approaches for the design of highperformance metal/graphene electrocatalysts for fuel cell applications. *Journal of Industrial and Engineering Chemistry*, 64: 1-15.
- 106. Santoro, C., Serov, A., Stariha, L., Kodali, M., Gordon, J., Babanova, S. and Atanassov, P. (2016). Iron based catalysts from novel low-cost organic precursors for enhanced oxygen reduction reaction in neutral media microbial fuel cells. *Energy and Environmental Science*, 9(7): 2346-2353.
- 107. Soo, L. T., Loh, K. S., Mohamad, A. B., Daud, W. R. W. and Wong, W. Y. (2015). An overview of the electrochemical performance of modified graphene used as an electrocatalyst and as a catalyst support in fuel cells. *Applied Catalysis A: General*, 497: 198-210.
- 108. Xiao, M., Zhu, J., Feng, L., Liu, C. and Xing, W. (2015). Meso/macroporous nitrogen-doped carbon architectures with iron carbide encapsulated in graphitic layers as an efficient and robust catalyst for the oxygen reduction reaction in both acidic and alkaline solutions. Advanced Materials, 27(15): 2521-2527.
- 109. Liang, Y., Wang, H., Zhou, J., Li, Y., Wang, J., Regier, T. and Dai, H. (2012). Covalent hybrid of spinel manganese-cobalt oxide and graphene as advanced oxygen reduction electrocatalysts. *Journal of the American Chemical Society*, 134(7): 3517-3523.
- 110. Choi, H. J., Jung, S. M., Seo, J. M., Chang, D. W., Dai, L. and Baek, J. B. (2012). Graphene for energy conversion and storage in fuel cells and supercapacitors. *Nano Energy*, 1(4): 534-551.

- 111. Anastasopoulos, A., Blake, J. and Hayden, B. E. (2011). Non-noble intertransition binary metal alloy electrocatalyst for hydrogen oxidation and hydrogen evolution. *Journal of Physical Chemistry C*, 115(39): 19226-19230.
- 112. Osmieri, L. (2019). Transition metal–nitrogen–carbon (M–N–C) catalysts for oxygen reduction reaction. insights on synthesis and performance in polymer electrolyte fuel cells. *ChemEngineering*, 3(1): 16.
- 113. Li, L., Shen, S., Wei, G., Li, X., Yang, K., Feng, Q. and Zhang, J. (2019). A comprehensive investigation on pyrolyzed fe-n-c composites as highly efficient electrocatalyst toward the oxygen reduction reaction of PEMFCs. ACS Applied Materials and Interfaces, 11: 14126-14135.
- 114. Chen, Z., Higgins, D., Yu, A., Zhang, L. and Zhang, J. (2011). A review on non-precious metal electrocatalysts for PEM fuel cells. *Energy and Environmental Science*, 4(9): 3167-3192.
- 115. Ren, X., Lv, Q., Liu, L., Liu, B., Wang, Y., Liu, A. and Wu, G. (2019). Current progress of Pt and Pt-based electrocatalysts used for fuel cells. Sustainable Energy and Fuels, 4(1): 15-30.
- 116. Gautam, J., Huu Tuan, L., Kim, N. H., Van Hien, H., Thanh Tran, D., Lee, J. H. and Dinh Chuong, N. (2018). Emerging core-shell nanostructured catalysts of transition metal encapsulated by two-dimensional carbon materials for electrochemical applications. *Nano Today*, 22: 100-131.
- 117. Ansón-Casaos, A., Puértolas, J. A., Pascual, F. J., Hernández-Ferrer, J., Castell, P. and Benito, A. M., Martínez, M. T. (2014). The effect of gammairradiation on few-layered graphene materials. *Applied Surface Science*, 301: 264-272.
- 118. He, Y., Li, J., Li, L. and Li, J. (2016). Gamma-ray irradiation-induced reduction and self-assembly of graphene oxide into three-dimensional graphene aerogel. *Materials Letters*, 177(1): 76-79.
- 119. Abidin, Z., Muhamad, E., Ahmad Daud, N., Ibrahim, N., Chieng, B. and Talib, Z. (2017). Functionalizing graphene oxide with alkylamine by gamma-ray irradiation method. *Nanomaterials*, 7(6): 135.

- 120. Wang, W., Zhao, X., Shi, H., Liu, L., Deng, H., Xu, Z. and Miao, X. (2020). Shape inducer-free polygonal angle platinum nanoparticles in graphene oxide as oxygen reduction catalyst derived from gamma irradiation. *Journal of Colloid and Interface Science*, 575: 1-15.
- 121. Xu, Z., Chen, L., Zhou, B., Li, Y., Li, B., Niu, J. and Qian, X. (2013). Nano-structure and property transformations of carbon systems under γ-ray irradiation: A review. *RSC Advances*, 3(27): 10579-10597.
- 122. Park, H. Y., Yang, D. S., Bhattacharjya, D., Song, M. Y. and Yu, J. S. (2014). A highly efficient carbon-supported Pt electrocatalyst prepared by γ-irradiation for cathodic oxygen reduction. *International Journal of Hydrogen Energy*, 39(4): 1688-1697.
- 123. Meku, E., Du, C., Wang, Y. and Du, L. (2016). Impact of different synthesis methods on the electrocatalytic activity and stability of Pd-Fe/C nanoparticles for oxygen reduction reaction in fuel cells. 2016 International Conference on Engineering and Technology Innovations: pp. 127-131.
- 124. Hung, T. F., Tu, M. H., Tsai, C. W., Chen, C. J., Liu, R. S., Liu, W. R. and Lo, M. Y. (2013). Influence of pyrolysis temperature on oxygen reduction reaction activity of carbonincorporating iron nitride/nitrogen-doped graphene nanosheets catalyst. *International Journal of Hydrogen Energy*, 38(10): 3956-3962.
- 125. Jeon, M. K. and McGinn, P. J. (2012). Coalloying effect of Co and Cr with Pt for oxygen electro-reduction reaction. *Electrochimica Acta*, 64(3): 147-153.
- 126. Sharin, S., Rahman, I. A., Ahmad, A. F., Mohd, H. M. K., Mohamed, F., Radiman, S., ... and Bastamam, I. S. A. (2015). Penurunan grafin oksida kepada grafin menggunakan sinar gama. *Malaysian Journal of Analytical Sciences*, 19(6): 1223-1228.

- 127. Li, Z., Yang, Y., Relefors, A., Kong, X., Siso, G. M., Wickman, B. and Soroka, I. L. (2021). Tuning morphology, composition and oxygen reduction reaction (ORR) catalytic performance of manganese oxide particles fabricated by γ-radiation induced synthesis. *Journal of Colloid and Interface Science*, 583: 71-79.
- 128. Mashentseva, A. A., Shlimas, D. I., Kozlovskiy, A. L., Zdorovets, M. V., Russakova, A. V., Kassymzhanov, M. and Borisenko, A. N. (2019). Electron beam induced enhancement of the catalytic properties of ion-track membranes supported copper nanotubes in the reaction of the P-nitrophenol reduction. *Catalysts*, 9(9): 737.
- 129. Kakitani, K., Kimata, T., Yamaki, T., Yamamoto, S., Shimoyama, I., Matsumura, D. and Terai, T. (2017). Activity enhancement of platinum nanoparticle catalysts on ion-beam-irradiated carbon support. *National Institutes for Quantum and Radiological Science and Technology*, 34: 2016-2018.
- 130. Nakagawa, N., Ishitobi, H., Abe, S., Kakinuma, M., Koshikawa, H., Yamamoto, S. and Yamaki, T. (2019). A novel method to enhance the catalytic activity of PtRu on the support using CeO<sub>2</sub> by high-energy ion-beam irradiation. *Catalysis Today*, 364: 118-124.
- 131. Choi, Y., Lim, D., Oh, E., Lim, C. and Baeck, S. H. (2019). Effect of proton irradiation on electrocatalytic properties of MnO<sub>2</sub> for oxygen reduction reaction. *Journal of Materials Chemistry A*, 7(19): 11659-11664.
- 132. Ohkubo, Y., Hamaguchi, Y., Seino, S., Nakagawa, T., Kageyama, S., Kugai, J. and Yamamoto, T. A. (2013). Preparation of carbon-supported PtCo nanoparticle catalysts for the oxygen reduction reaction in polymer electrolyte fuel cells by an electron-beam irradiation reduction method. *Journal of Materials Science*, 48(14): 5047-5054.